

Neuroscience Bulletin

The Official Journal of The Chinese Neuroscience Society

神经科学通报

Volume 30
Number 5
October 2014



**Special Issue on
Neuro-Molecular Imaging**

 SIBS  Springer

www.neurosci.cn

NEUROSCIENCE BULLETIN (Bimonthly)

October 1, 2014 Vol. 30 No. 5

Contents

Special Issue on Neuro-Molecular Imaging

Editorial

711 Neuro-molecular imaging. *Hong Zhang*

Reviews

- 713 PET imaging in ischemic cerebrovascular disease: current status and future directions. *Wolf-Dieter Heiss*
- 733 Recent advances in parametric neuroreceptor mapping with dynamic PET: basic concepts and graphical analyses. *Seongho Seo, Su Jin Kim, Dong Soo Lee, Jae Sung Lee*
- 755 Neurostatistical imaging for diagnosing dementia: translational approach from laboratory neuroscience to clinical routine. *Etsuko Imabayashi, Tomio Inoue*
- 765 Brain dopaminergic system changes in drug addiction: a review of positron emission tomography findings. *Haifeng Hou, Chunyan Wang, Shaowei Jia, Shu Hu, Mei Tian*
- 777 Development of ^{18}F -labeled radiotracers for neuroreceptor imaging with positron emission tomography. *Peter Brust, Jörg van den Hoff, Jörg Steinbach*
- 812 Role of cortical spreading depression in the pathophysiology of migraine. *Yilong Cui, Yosky Kataoka, Yasuyoshi Watanabe*
- 823 Brain network markers of abnormal cerebral glucose metabolism and blood flow in Parkinson's disease. *Shichun Peng, David Eidelberg, Yilong Ma*

Original Articles

- 838 Small-animal PET demonstrates brain metabolic change after using bevacizumab in a rat model of cerebral ischemic injury. *Ying Dong, Fahuan Song, Jianjuan Ma, Xuexin He, Said Amer, Weizhong Gu, Mei Tian*
- 845 Paradoxical reduction of cerebral blood flow after acetazolamide loading: a hemodynamic and metabolic study with ^{15}O PET. *Tadashi Watabe, Eku Shimosegawa, Hiroki Kato, Kayako Isohashi, Mana Ishibashi, Mitsuki Tatsumi, Kazuo Kitagawa, Toshiyuki Fujinaka, Toshiki Yoshimine, Jun Hatazawa*
- 857 CBF/CBV maps in normal volunteers studied with ^{15}O PET: a possible index of cerebral perfusion pressure. *Tadashi Watabe, Eku Shimosegawa, Hiroki Kato, Kayako Isohashi, Mana Ishibashi, Jun Hatazawa*

* * * * *

Research Highlight

863 The medial preoptic area and the regulation of parental behavior. *Kumi O. Kuroda, Michael Numan*

Original Articles

866 Activation of extrasynaptic GABA_A receptors inhibits cyclothiazide-induced epileptiform activity in hippocampal CA1 neurons. *Li Wan, Xu Liu, Zheng Wu, Wanting Ren, Shuzhen Kong, Raya Abou Dargham, Longzhen Cheng, Yun Wang*

877 Orexin A attenuates the sleep-promoting effect of adenosine in the lateral hypothalamus of rats. *Yanping Cun, Lin Tang, Jie Yan, Chao He, Yang Li, Zhian Hu, Jianxia Xia*

About the Cover:

As a discipline at the intersection of molecular biology and *in vivo* imaging, molecular imaging enables real-time, noninvasive visualization of cellular function. This is becoming more and more important for scientific and medical research, especially in the field of neuroscience. In this special issue, we present a collection of articles that discuss advances in the applications of molecular imaging to study neuronal functions and diseases. Adapted from the work of Imabayashi *et al.* and Watabe *et al.* in this issue, the cover image showcases colorful and informative molecular images of human brains. (Cover art by Yefei Li)

Neuro-molecular imaging

Hong Zhang*

Department of Nuclear Medicine, The Second Affiliated Hospital of Zhejiang University School of Medicine; Zhejiang University Medical PET Center; Institute of Nuclear Medicine and Molecular Imaging of Zhejiang University; Key Laboratory of Medical Molecular Imaging of Zhejiang Province, Hangzhou 310009, China

*Guest Editor of the Special Issue. E-mail: hzhang21@gmail.com

© Shanghai Institutes for Biological Sciences, CAS and Springer-Verlag Berlin Heidelberg 2014

Neuroscience is the scientific study of how the nervous system develops, its structure, and what it does. With the development of different sciences and technologies, neuroscience has become an interdisciplinary science that collaborates with other fields, and the research approach of neuroscience has also changed greatly. Molecular imaging is a powerful tool for neuroscience that can be used for understanding disease, identifying biomarkers, and developing novel therapeutics. Molecular imaging plays an important role in neuroimaging, especially for investigations of the living brain. While CT and MRI provide important structural and anatomical information on the brain, neuro-molecular imaging allows the *in vivo* visualization and measurement of cellular/molecular processes in the living brain.

The topics covered in this special issue include advances in PET/CT and CT imaging in neurological disease, tracer development for neuroreceptors, brain function evaluation, stroke therapy, and the translational imaging approach in dementia. For instance, changes in cerebral blood flow (CBF) and cerebral glucose metabolism have often been associated with regional neuronal activity in brain function. Advances in biomarkers in PET imaging for parkinsonism and middle cerebral arterial disease such as the ratio of CBF to cerebral blood volume as a marker of regional cerebral perfusion pressure^[1,2], and brain network makers of cerebral glucose metabolism and blood flow^[3] are reported and discussed. These biomarkers can serve as clinically useful markers of disease severity and therapeutic response, as well as aid in the differential diagnosis of parkinsonism. Along this line, Heiss^[4] reviews PET applications to pathophysiological changes caused

by cerebrovascular diseases, which have broadened our understanding of flow and metabolic thresholds critical for the maintenance of brain function and morphology.

Imaging tracers provide possibilities for molecular imaging in neuroscience. PET uses biomolecules as tracers that are labeled with radionuclides with short half-lives, synthesized prior to imaging studies. The administration of such radiotracers to the brain provides images of transport, metabolic, and neurotransmission processes on the molecular level. The contribution by Peter *et al.*^[5] reviews the strategy of radiotracer development bridging from basic science to biomedical application; this allows molecular neuroreceptor imaging studies in various small-animal models of disease including genetically-engineered animals, and can be used for *in vivo* pharmacology during the process of pre-clinical drug development to identify new drug targets, to investigate pathophysiology, to discover potential drug candidates, and to evaluate the pharmacokinetics and pharmacodynamics of drugs *in vivo*.

Tracer kinetic modeling in dynamic PET has been widely used to investigate the characteristic distribution patterns or dysfunction of neuroreceptors in brain diseases. Seo and co-workers^[6] review graphical analysis (GA) which is a major parametric mapping technique that is independent of any compartmental model configuration, robust to noise, and computationally efficient. They describe recent advances in the parametric mapping of neuroreceptor binding based on GA methods. Hou and co-workers^[7] discuss the value of PET in drug addiction and review the major findings of PET imaging studies on the involvement of dopamine (DA) in drug addiction, including presynaptic DA synthesis, vesicular monoamine transporter

2, the DA transporter, and postsynaptic DA receptors. Imabayashi *et al.*^[9] review the superiority of neurostatistical imaging for diagnosing dementia using PET, MRI, and CT. Dong and co-workers^[9] report a study on the effect and safety margin of bevacizumab on the infarction area of cerebral ischemia using PET. They demonstrate an inhibitory effect on metabolic recovery after bevacizumab therapy in a rat model of cerebral ischemia. Cui *et al.*^[10] review the role of cortical spreading depression in the pathophysiology of migraine.

In summary, neuro-molecular imaging can integrate metabolomics and neurobiology and provides novel insights into pathophysiology in the brain. This special issue provides a platform on neuroscience research from molecular imaging technology which may have a high impact on brain science from basic to translational medicine.

REFERENCES

- [1] Watabe T, Shimosegawa E, Kato H, Isohashi K, Ishibashi M, Hatazawa J. CBF/CBV maps in normal volunteers studied with ¹⁵O PET: a possible index of cerebral perfusion pressure. *Neurosci Bull* 2014, 30: 857–862.
- [2] Watabe T, Shimosegawa E, Kato H, Isohashi K, Ishibashi M, Tatsumi M, *et al.* Paradoxical reduction of cerebral blood flow after acetazolamide loading: a hemodynamic and metabolic study with ¹⁵O PET. *Neurosci Bull* 2014, 30: 845–856.
- [3] Peng S, Eidelberg D, Ma Y. Brain network markers of abnormal cerebral glucose metabolism and blood flow in Parkinson's disease. *Neurosci Bull* 2014, 30: 823–837.
- [4] Heiss WD. PET Imaging in ischemic cerebrovascular disease: current status and future directions. *Neurosci Bull* 2014, 30: 713–732.
- [5] Brust P, van den Hoff J, Steinbach J. Development of ¹⁸F-labeled radiotracers for neuroreceptor imaging with positron emission tomography. *Neurosci Bull* 2014, 30: 777–811.
- [6] Seo S, Kim SJ, Lee DS, Lee JS. Recent advances in parametric neuroreceptor mapping with dynamic PET: basic concepts and graphical analyses. *Neurosci Bull* 2014, 30: 733–754.
- [7] Hou H, Wang C, Jia S, Hu S, Tian M. Brain dopaminergic system changes in drug addiction: a review of positron emission tomography findings. *Neurosci Bull* 2014, 30: 765–776.
- [8] Imabayashi E, Inoue T. Neurostatistical imaging for diagnosing dementia: translational approach from laboratory neuroscience to clinical routine. *Neurosci Bull* 2014, 30: 755–764.
- [9] Dong Y, Song F, Ma J, He X, Amer S, Gu W, *et al.* Small-animal PET demonstrates functional change after using bevacizumab in a rat model of cerebral ischemic injury. *Neurosci Bull* 2014, 30: 838–844.
- [10] Cui Y, Kataoka Y, Watanabe Y. Role of cortical spreading depression in the pathophysiology of migraine. *Neurosci Bull* 2014, 30: 812–822.

PET imaging in ischemic cerebrovascular disease: current status and future directions

Wolf-Dieter Heiss

Max Planck Institute for Neurological Research, Cologne, Germany

Corresponding author: Wolf-Dieter Heiss. E-mail: wdh@nf.mpg.de

© Shanghai Institutes for Biological Sciences, CAS and Springer-Verlag Berlin Heidelberg 2014

Cerebrovascular diseases are caused by interruption or significant impairment of the blood supply to the brain, which leads to a cascade of metabolic and molecular alterations resulting in functional disturbance and morphological damage. These pathophysiological changes can be assessed by positron emission tomography (PET), which permits the regional measurement of physiological parameters and imaging of the distribution of molecular markers. PET has broadened our understanding of the flow and metabolic thresholds critical for the maintenance of brain function and morphology: in this application, PET has been essential in the transfer of the concept of the penumbra (tissue with perfusion below the functional threshold but above the threshold for the preservation of morphology) to clinical stroke and thereby has had great impact on developing treatment strategies. Radioligands for receptors can be used as early markers of irreversible neuronal damage and thereby can predict the size of the final infarcts; this is also important for decisions concerning invasive therapy in large (“malignant”) infarctions. With PET investigations, the reserve capacity of blood supply to the brain can be tested in obstructive arteriosclerosis of the supplying arteries, and this again is essential for planning interventions. The effect of a stroke on the surrounding and contralateral primarily unaffected tissue can be investigated, and these results help to understand the symptoms caused by disturbances in functional networks. Chronic cerebrovascular disease causes vascular cognitive disorders, including vascular dementia. PET permits the detection of the metabolic disturbances responsible for cognitive impairment and dementia, and can differentiate vascular dementia from degenerative diseases. It may also help to understand the importance of neuroinflammation after stroke and its interaction with amyloid deposition in the development of dementia. Although the clinical application of PET investigations is limited, this technology had and still has a great impact on research into cerebrovascular diseases.

Keywords: stroke; dementia; PET; brain metabolism; brain ischemia

Introduction

The burden of cerebrovascular disease (CVD) is extremely high: in 2000 there were 15.3 million strokes world-wide, 5.5 million of which resulted in death^[1]. But CVD accounts not only for 10% of all deaths; it is also the leading cause of disability in patients surviving the insult^[2]. However, there exists a high variation in stroke burden and mortality, with >85% of strokes occurring in low- and middle-income countries^[3]. In addition, CVD not only causes strokes, but is also associated with a high incidence of silent infarcts and

microhemorrhages that lead to cognitive and behavioral changes, finally presenting as vascular dementia or cognitive impairment. Eight percent of the US population aged over 65 years experience a stroke, 8% suffer from dementia, and 17% from mild cognitive impairment of predominantly vascular origin^[4].

Requirements for Brain Function

The energy demands of nervous tissue are very high and therefore sufficient blood supply to the brain must

be maintained consistently. A normal adult male's brain containing ~130 billion neurons (21.5 billion in the neocortex)^[5] comprises only 2% of total body mass, yet consumes at rest ~20% of the body's total basal oxygen supplied by 16% of the cardiac output. The brain's oxygen uptake is almost entirely for the oxidative metabolism of glucose, which in normal physiological conditions is the almost exclusive substrate for its energy requirements^[6]. The glucose metabolized in neurons is mainly to support cellular vegetative functions and the glucose consumption of neuronal cell bodies is essentially unaffected by functional activation, which is confined to synapse-rich regions, i.e. neuropil. The magnitudes of related increases in metabolism and blood-flow are linearly related to the frequency of action potentials in the afferent pathways regardless of whether they are excitatory or inhibitory. Increased metabolism by functional activation is mainly used to restore the ionic gradients across the cell membrane degraded by the spike activity and is rather high compared to the demand of the cell body^[7]. Overall, 87% of the energy consumed is required by action potential propagation and postsynaptic ion fluxes, and only 13% is used for maintaining membrane resting potential^[8].

The consequence of CVD in tissue is ischemic cell death. This results from circulatory disturbances and an insufficient blood supply leading to a complex cascade of deleterious biochemical and molecular events, which in principle are amenable to therapeutic intervention^[9, 10]. Better understanding of these complex processes in ischemic stroke has improved treatment in the last decade. Pathophysiological changes that lead to irreversible tissue damage must be targets for the development of effective therapies. For therapeutic interventions in acute ischemic stroke, the concepts of the penumbra (reduced tissue perfusion and disturbed function but preserved morphological integrity) and of the time-dependent progression of irreversible tissue damage play a central role. These concepts are based on results from animal experiments, and their translation into the management of stroke patients is difficult and requires specific methods.

The Concept of the Ischemic Penumbra and Identification by Imaging

Experimental studies on the ischemic flow thresholds of

brain tissue have demonstrated the existence of two critical levels of decreased perfusion: first, a level representing the flow threshold for reversible functional failure (functional threshold); and second, a lower threshold below which irreversible membrane failure and morphological damage occur. The range of perfusion values between these limits is called the "ischemic penumbra"^[11], characterized by the potential for functional recovery without morphological damage, provided that local blood flow can be reestablished at a sufficient level. Whereas neuronal function is impaired immediately when blood flow drops below the threshold, the development of irreversible morphological damage is time-dependent. The interaction between severity and duration of ischemia in the development of irreversible cell damage has been established in simultaneous recordings of cortical neuronal activity and local blood flow^[12]. These results complement the concept of the ischemic penumbra: the potential for post-ischemic recovery of functionally impaired cells is determined not only by the level of residual flow in the ischemic phase but also by the duration of the flow disturbance.

Autoradiographic procedures cannot demonstrate the gradual disappearance of the penumbra with increasing duration of ischemia, the progression of irreversible damage, or the recovery of functionally impaired tissue after reperfusion. To follow these pathophysiological changes, non-invasive imaging modalities, which permit repeated measurements of regional cerebral blood flow (rCBF) and regional cerebral blood volume (rCBV), as well as regional cerebral metabolic rate of oxygen (rCMRO₂) and of glucose (rCMRGlc), must be applied. To date, only positron emission tomography (PET) is able to quantify these variables repeatedly.

Early PET studies of stroke identified various tissue compartments within a cerebral region compromised by ischemia^[13-16]. Tissue with rCBF <12 mL/100 g/min or rCMRO₂ <65 μmol/100 g/min at the time of measurement (usually several hours after stroke) was found to be infarcted on late CTs. Relatively preserved CMRO₂ is an indicator of maintained neuronal integrity in regions with CBF reduced to 12–22 mL/100 g/min. This pattern, coined misery perfusion^[14], serves as a surrogate for the penumbra: it is the area with an increased oxygen extraction fraction (OEF) (to >80% from the normal value of ~40%). PET studies allow the classification of three regions

within the disturbed vascular territory: the ischemic core with a flow <12 mL/100 g/min usually showing a transition into necrosis; a penumbra region with a flow between 12 and 22 mL/100 g/min of still viable tissue but with uncertain chances for infarction or recovery; and a hypoperfused area (>22 mL/100 g/min) not primarily damaged by the reduced blood supply. The conversion of the penumbra into infarction is a dynamic process, and irreversible damage spreads from the core to its border. This process can be imaged with advanced PET equipment, by which changes in regional blood-flow and oxygen consumption have been studied after occlusion of the middle cerebral artery (MCA) in baboons and cats (reviewed in ^[17-19]).

In the cat, changes after MCA occlusion are immediate

and severe. Sequential studies of rCBF, rCMRO₂, and rCMR_{Gl}c from control to the endpoint 24 h after occlusion recorded an immediate decrease in CBF within the MCA territory to $<30\%$ (Fig. 1) of control upon arterial occlusion. rCMRO₂ was preserved at an intermediate level and OEF was increased, indicating misery perfusion. Over time OEF decreased, reflecting progressive necrosis spreading from the core to the periphery of the ischemic territory. Reversible ischemia was studied by reopening the MCA after 60 min. If OEF remained elevated throughout the ischemic episode, reperfusion prevented large infarcts. In contrast, if the initial OEF increase disappeared during ischemia, large infarcts developed and intracranial pressure increased fatally. These experimental findings

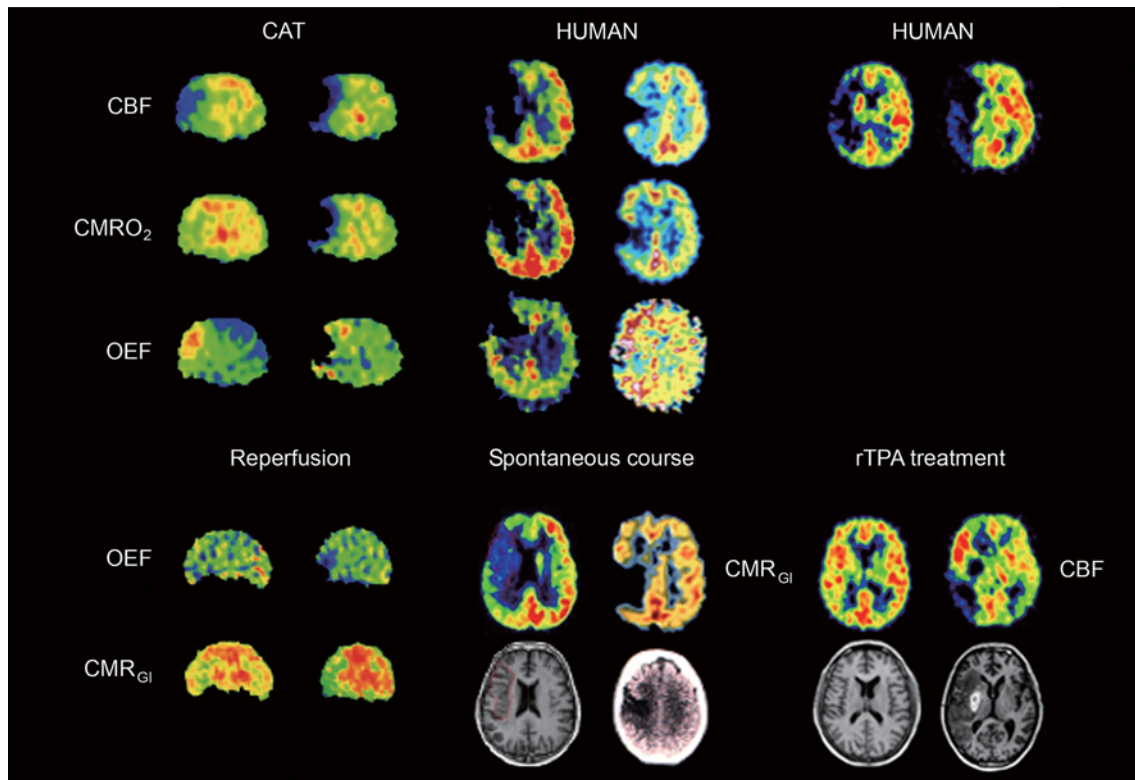


Fig.1. Sequential PET images of CBF, CMRO₂, and OEF after MCA occlusion in cats compared to images from patients after stroke (modified from Heiss WD. Stroke 2012^[19]). Left columns: In the right cat panel, the progressive decrease of CMRO₂ and the reduction of OEF predict infarction and cannot benefit from reperfusion. Only if OEF is increased until the start of reperfusion can it be salvaged (left cat panel). Middle panels: in the patient, the areas with preserved OEF are not infarcted and can survive in the spontaneous course (posterior part of ischemic cortex in the left, and anterior part in the right patient as indicated on late MRI and CT). Right panels: in patients receiving recombinant tissue plasminogen activator treatment, measurements of CMRO₂ and OEF are not feasible, but flow determinations show the effect. If reperfusion occurs early enough and before tissue damage, tissue can be salvaged (left patient). If reperfusion is achieved too late, tissue cannot be salvaged despite hyperperfusion in some parts (right patient).

from sequential studies and clinical investigations at different time-points after the attack (Fig. 1)^[20, 21] imply that the extent of the penumbra, i.e. of morphologically intact but functionally impaired tissue, depends on the time of measurement relative to the onset of ischemia. Flow measurements in the first hours after a stroke allow the identification of various tissue compartments and their contribution to the final infarct on CT/MRI. When the threshold for probable infarction was set to the conventional value of 12 mL/100 g/min and that for the upper limit of the penumbra to 18 mL/100 g/min, a large compartment of the final infarct (70%) was perfused at <12 mL/100 g/min, a level that predicts necrosis, while a smaller portion (18%) had flow values in the penumbra range (12–18 mL/100 g/min), and a fairly small compartment (12%) had perfusion at a higher level^[20]. Only the tissue with CBF >12 mL/100 g/min could benefit from thrombolysis.

Non-invasive Imaging of the Penumbra

Measurement of rCBF, rCMRO₂, and OEF by ¹⁵O-PET necessitates arterial blood sampling. A marker of neuronal integrity is needed that can identify irreversible tissue damage irrespective of the time after the vascular attack without the necessity of arterial blood sampling. The central benzodiazepine receptor ligand flumazenil (FMZ) binds to the GABA receptors abundant in the cerebral cortex. These receptors are damaged early by ischemia and indicate early neuronal loss. In cats with transient MCA occlusion, reduction in FMZ-binding predicts the size of the final infarcts, whereas preserved FMZ-binding indicates an intact cortex^[17, 22]. With this tracer (Fig. 2), the pathophysiological changes early after ischemic stroke can be accurately specified: 55% of the volume of the final infarct had decreased FMZ uptake, indicating infarction in the first hours after stroke; and 21% of the final infarct had flow <14 mL/100 g/min, but FMZ uptake above the critical value, indicating penumbra tissue^[17]. However, selective neuronal loss can occur in tissue outside the documented penumbra or in re-perfused penumbra areas, and this can be documented by decreased cortical FMZ-binding^[23]. These results indicate the potential and the limits of therapy in acute stroke: early reperfusion cannot reverse the already-developed neuronal damage, but is crucial for salvaging the penumbra.

MR studies using diffusion and perfusion imaging might provide a differentiation between the core and the penumbra: the early diffusion-weighted imaging (DWI) lesion might define the ischemic core and adjacent critically hypoperfused tissue might be identified with perfusion-weighted imaging (PWI)^[24]. Therefore, brain regions with hypoperfusion assessed by PWI but without restricted diffusion (PWI/DWI mismatch) have been assumed to represent the penumbra, but this surrogate definition has several uncertainties^[25]. Several studies have been performed to validate this mismatch as a surrogate of the penumbra in the PET-derived discrimination of irreversibly damaged, critically perfused “at risk”, and oligemic “not at risk” tissue. These studies demonstrated that DWI is a rather reliable predictor of the finally infarcted tissue^[26], but contains up to 25% false-positive, i.e. surviving tissue. The inaccuracy in defining the penumbra with the PWI/DWI mismatch is mainly related to the PWI, which uses variable parameters to estimate perfusion. As a consequence, the perfusion lesion size differs markedly depending on the parameters calculated^[27] and is usually overestimated. Time-to-peak delays of 4 and 6 s reliably identify hypoperfused and exclude normoperfused tissue but overestimate the volume of critically perfused but salvageable tissue, i.e. the penumbra^[28]. The mismatch volume in PWI/DWI as conventionally calculated therefore does not reliably reflect misery perfusion, i.e. the penumbra as defined by PET (Fig. 3). Several validation studies of various perfusion parameters calculated from PW-MRI on the flow values obtained from H₂¹⁵O-PET^[29, 30] resulted in corrections permitting reliable classification of critical, but potentially reversible ischemia (T_{max}, CBF, and time-to-peak). These thresholds have been implemented in recent clinical trials to improve the efficiency of therapeutic interventions for stroke^[31]. With the advances of arterial spin-labelling MR techniques^[32] and CT perfusion studies for the determination of cerebral perfusion^[33], it will be necessary to validate the results of flow values from quantitative methods.

Detection of Hypoxic Tissue

Markers of hypoxia have been investigated with respect to their sensitivity in identifying penumbral tissue. Increased uptake of labeled nitroimidazole-derivatives is found in

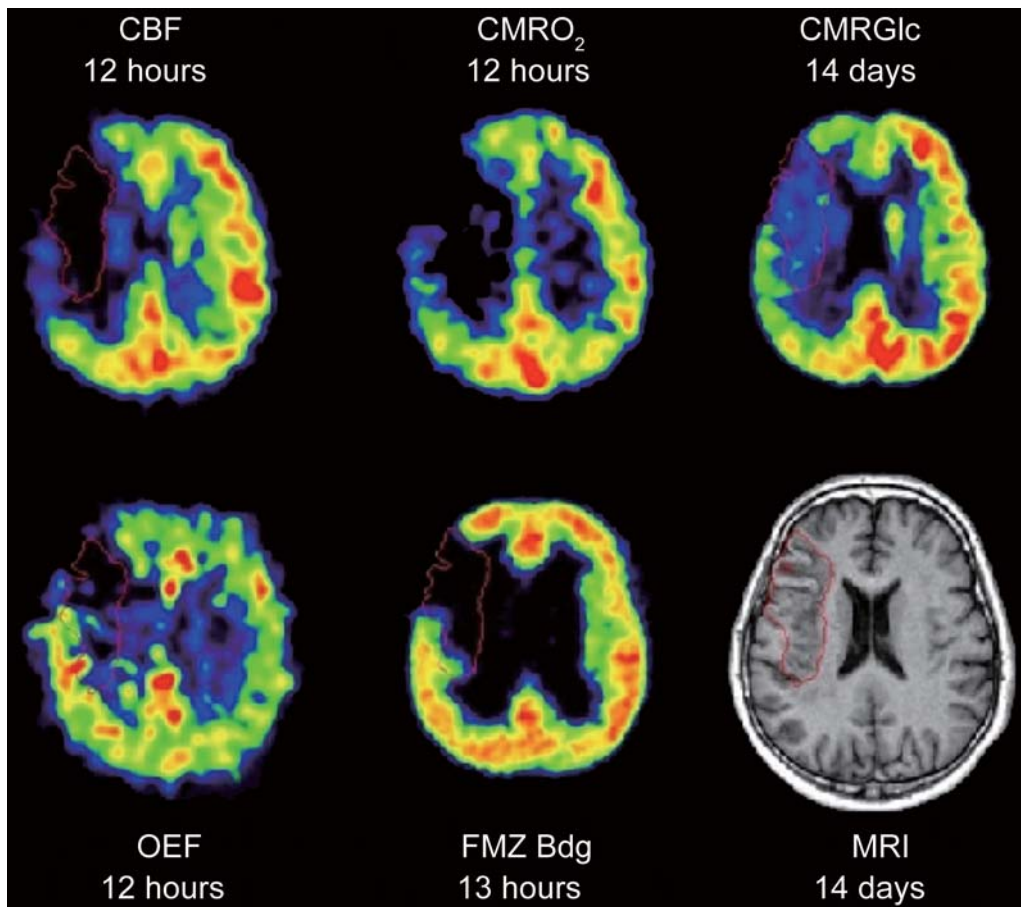


Fig. 2. Co-registered transaxial PET images at the caudate/ventricular level of CBF, steady-state FMZ binding (Bdg), and OEF at 12 h, as well as CMRGlc (glucose consumption) and MRI at 2 weeks after moderate left hemiparesis and hemihyesthesia of acute onset in a 52-year-old male patient (adapted from Heiss WD *et al.* *Stroke* 1998^[12]). The large territorial defect is visible in all PET modalities with different extensions. The contour delineates the cortical infarct as determined on late MRI. FMZ-binding precisely predicts the extension of the final infarct, whereas CBF and FMZ distribution (as markers of perfusion) delineate a considerably larger volume of disturbed perfusion. In the cortical region outside the infarct with initially disturbed perfusion, OEF is increased, indicating preserved CMRO₂ at 12 h post-ictus. The permanently decreased CMRGlc in this region could be caused by neuronal loss and/or diaschisis.

the histologically-damaged ischemic core and in adjacent areas that are intact at follow up^[34, 35]. The nitroimidazole-derivative misonidazole labeled with ¹⁸F-fluoromisonidazole (FMISO), was first used by Yeh *et al.* in 1994^[36] to investigate ischemic stroke in patients and revealed increased uptake surrounding a zone without FMISO uptake. The high uptake disappeared during the chronic phase, indicating that the FMISO-positive tissue had either infarcted or recovered. These results were confirmed in a larger study by Read *et al.* in 1998^[37]: in 9 cases, FMISO-trapping was detected 6.25–42.5 h after stroke onset, but was absent in later examinations. Tissue with increased FMISO uptake was

usually present in the periphery of the infarct identified on the co-registered late CT, but extended into normal tissue adjacent to the infarct in a few cases. The volume of tissue with increased FMISO uptake declined after stroke onset. The proportions of hypoxic tissue that infarcted or survived varied between patients. Within 6 h of stroke onset, ~90% of the FMISO-positive region was included in the final infarct but this percentage was reduced later on^[38]. In addition, the volume of initially affected tissue is correlated with the initial severity of neurologic deficits, and the proportion of initially affected tissue progressing to infarction is correlated with neurological deterioration during the first week after stroke^[39].

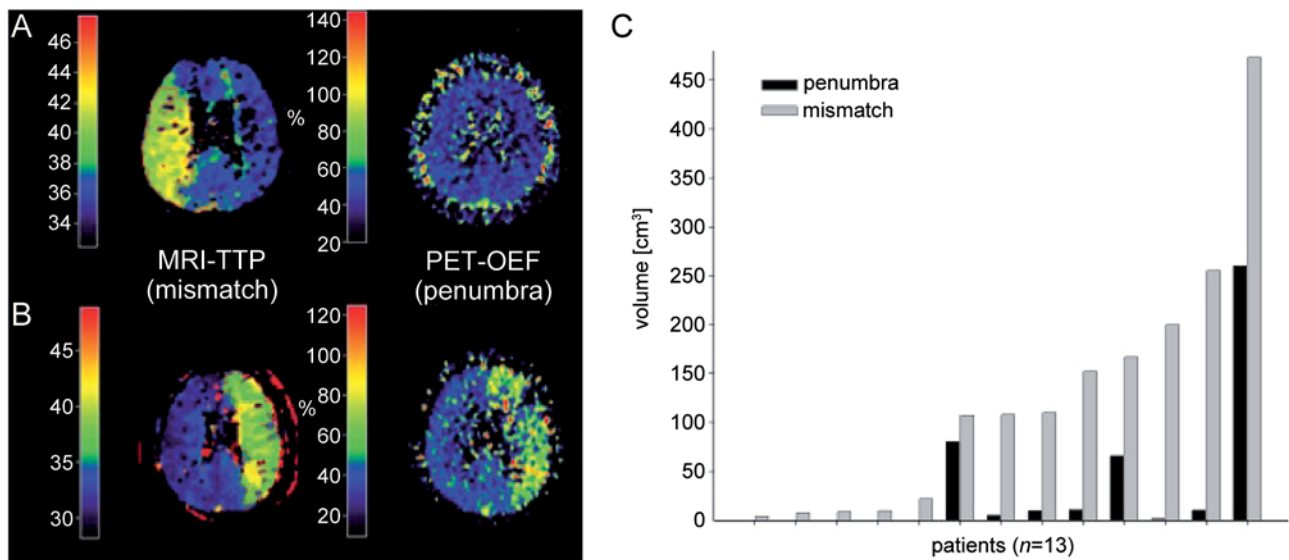


Fig. 3. A, B: Volumetric comparison of time-to-peak (TTP) (MRI) and OEF (PET) images in 2 patients in the chronic phase of stroke. In both patients, a TTP delay of 4 s indicates a considerable mismatch volume (red contour on TTP images). The mismatch volumes were 473 cm³ for patient A and 199.7 cm³ for patient B. However, only patient B had a corresponding volume of penumbra (260 cm³). **C:** Volumes of penumbra and mismatch defined by TTP >4 s in 13 patients. All 13 showed mismatch, but only 8 showed a penumbra, which comprised 1–75% of the mismatch volume (modified from Sobesky J *et al.*, *Stroke* 2005^[28]).

As high FMISO uptake in these areas fulfills the definition of the penumbra, the topography of FMISO-trapping can be used to generate a “penumbragram”^[40].

After 2-h transient occlusion of the MCA in the rat, the area of FMISO uptake is much larger than the area of subsequent infarctions, since a variable portion of the tissue detected by FMISO uptake does not go on to infarct if untreated^[41]. However, in order to provide adequate time for the washout of unbound tracer, scanning of FMISO uptake cannot be performed until 2 h after injection. In addition, due to tracer dynamics, the timing of imaging is crucial with an optimal time of 2 h for the identification of tissue at risk^[42]. In permanent experimental MCA occlusion^[43] and in human stroke^[44], a portion of the FMISO-trapping area may lie outside the final infarct and a portion of the final infarct may not exhibit early tracer mapping, indicating that FMISO-trapping does not accurately identify preventable infarction and therefore may not be specific to the penumbra. This may indicate that the hypoxia necessary for FMISO-binding is less severe than the oxygen depletion responsible for neuronal necrosis^[18]. The required delay between tracer injection and imaging (>2 h) further limits the value of FMISO for the selection of effective treatment in acute ischemic stroke.

PET as a Surrogate Marker for Treatment Efficiency

The efficacy of treatment in ischemic stroke can only be established by controlled, randomized, double-blind clinical trials, as successfully performed for thrombolysis with intravenous recombinant tissue plasminogen activator (rtPA)^[45]. Such controlled trials require large groups of patients from many stroke centers, usually take a long time, and are expensive. Therefore surrogate markers may help to predict therapeutic effects in small groups of patients. Effects demonstrated with surrogate markers must be confirmed in controlled trials with sufficient patient populations. In recent years, identification of salvageable tissue by neuroimaging has attracted much interest as a surrogate marker for treatment efficiency in stroke.

The effect of thrombolysis, the only approved treatment for acute ischemic stroke, has been shown in imaging studies, in which reperfusion to penumbral tissue is associated with improvement in neurological deficits (Fig. 4): reperfusion significantly improves in rtPA-treated patients compared to controls^[46]. The volume of tissue salvaged by reperfusion was determined by H₂¹⁵O-PET within 3 h of stroke onset and compared with the volume of

infarction assessed on MRI 3 weeks after the stroke^[47]. The percentage of voxels with an initial flow below the threshold of 12 mL/100 g/min that became re-perfused predicted the degree of clinical improvement within 3 weeks. Overall, only 22.7% of the grey matter initially perfused below the conventional threshold of critical ischemia became necrotic after thrombolytic therapy in this small sample, indicating that a considerable portion of the critically hypoperfused tissue is salvaged by this therapy. However, hypoperfused tissue can benefit from reperfusion only if cortical flumazenil-binding is not reduced below a critical value^[48]. This marker identifies irreversibly damaged tissue that is not amenable to treatment.

In 34 patients with ischemic changes in >50% of the MCA territory in early cerebral CT scans, PET was performed with ¹¹C-FMZ to assess CBF and irreversible neuronal damage. Thereafter, probes for microdialysis and for measurement of intracranial pressure and tissue oxygen pressure were placed in the ipsilateral frontal lobe^[53]. PET studies within 24 h after stroke identified larger volumes of ischemic core and larger volumes of irreversible neuronal damage in patients with a subsequent malignant course (i.e., edema formation with midline shift) than in patients with a benign course (Fig. 5). CBF within the ischemic core was significantly lower and the penumbra was smaller in the malignant than in the benign group. Therefore, PET may allow the prediction of malignant MCA infarction within the time window suggested for hemicraniectomy. Neuromonitoring helps to classify the clinical courses by characterizing the pathophysiological sequelae of malignant edema formation. In contrast to PET, however, it does not predict a fatal outcome early enough for the successful implementation of invasive therapies.

Microglial Activation as an Indicator of Inflammation

Microglia constitute up to 10% of the total cell population of the brain. As resident macrophages of the central nervous system (CNS), microglia phagocytose cellular debris, present foreign antigens, and are sensors of pathological events, including ischemia^[54]. Microglia change from a resting to an activated state in response to CNS insults and function as phagocytes. In this activation process, they undergo a shift in their effector program by transforming their morphology, proliferating,

releasing pro-inflammatory compounds, and increasing the expression of immunomodulatory surface antigens^[55]. As one consequence, the translocator protein 18 kDa (TSPO), formerly known as the peripheral benzodiazepine receptor (PBR), is upregulated in the mitochondria of activated microglia and may thus serve as a biomarker of inflammation. Several radioligands have been developed to image the activation of microglia in experimental models and in various diseases of the CNS^[56]. Early studies in ischemia models using ³H-PK 11195 autoradiography demonstrated increased binding sites in the area of infarction and in the boundary zones between major arteries in hypertensive animals. These were associated with reactive glial cells and macrophages and reached a maximum 4–8 days after the induction of local ischemia. When high-resolution microPET was applied to the expression of TSPO/PBR in transient experimental ischemia, a high signal was detected in the ischemic core starting on day 4 and increasing to day 7, and this strong signal was associated with microglia/macrophages. A less prominent signal indicating elevated TSPO expression was observed in the region surrounding the infarct at day 7, and this could be attributed to reactive astrocytes. These results demonstrated that the cellular heterogeneity of TSPO/PBR expression depends on the intrinsic features of inflammatory cells^[57, 58]. In permanent ischemia induced by microspheres injection into the MCA of rats, no increase in ³H-PK 11195-binding was found in the infarct core 7 days after the attack, but the permanent MCA ischemia caused increased tracer-binding in the normoperfused peri-infarct zone, which was co-localized with increased glucose metabolism and accumulated microglia and macrophages. This peri-infarct neuroinflammation might contribute to the extension of tissue damage^[59]. After temporary (45 min) MCA occlusion in hypertensive rats, significant increases in ¹¹C-PK 11195-binding in both the infarct and the surrounding areas were observed after 14 days, and less but still increased uptake was already present after 2 days^[60]. With multimodal imaging including a tracer for mitochondrial complex I activity, neuronal damage is identifiable in the areas with neuroinflammation^[61].

Many histological studies have identified activated microglia in the ischemic brain after stroke in humans, especially in the ischemic core within 1 to 2 days after stroke. Over time, they extend from the ischemic core into

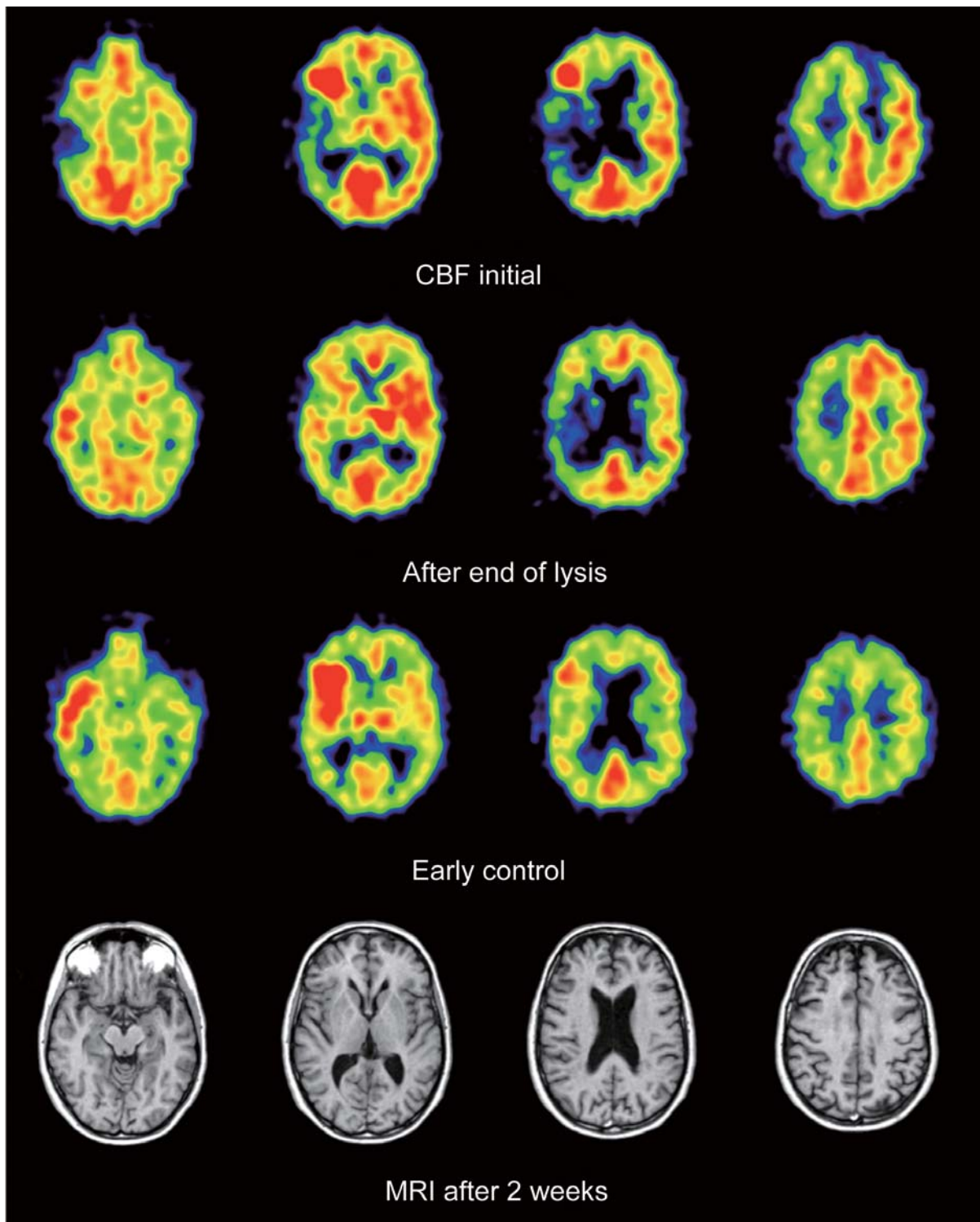


Fig. 4. Effect of thrombolysis (intravenous rTPA) in a 45-year-old woman with stroke due to multiple cerebral emboli *via* an open foramen ovale originating from deep vein thrombosis. The patient showed defects in the right MCA and left ACA territories at initial CBF PET, then lysis reperfusion was applied to both territories. Early control after 1 day showed hyperperfusion in the right MCA. MRI after 2 weeks did not indicate permanent tissue damage, indicating the patient had completely recovered.

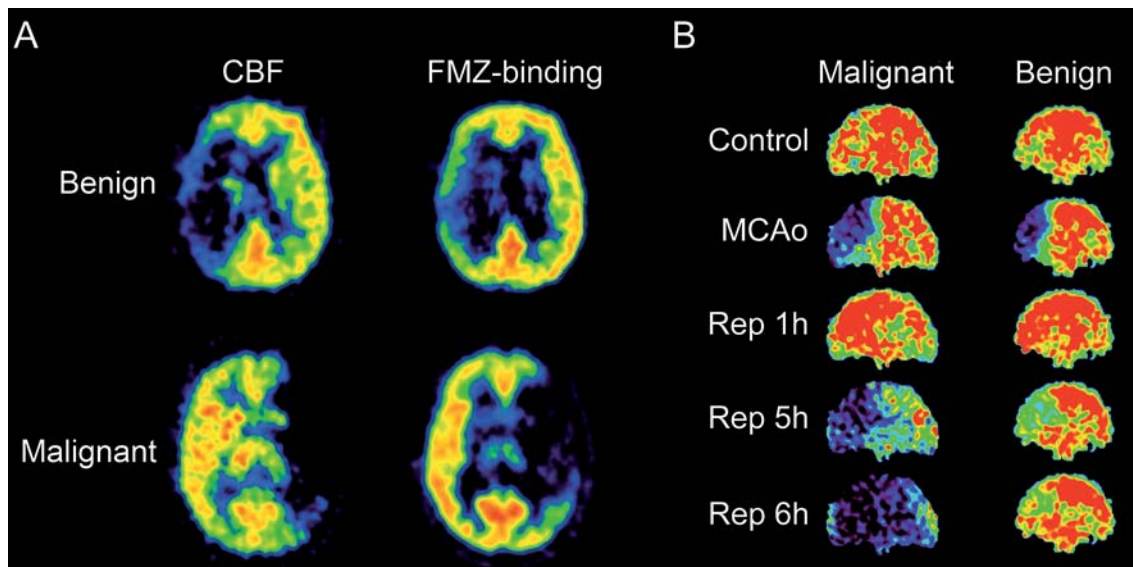


Fig. 5. Benign and malignant infarction in patients and cats (adapted from Heiss WD. Stroke 2012^[19]). A: FMZ-distribution and FMZ-binding in patients with large MCA infarcts. In benign infarcts, the volumes of severe hypoperfusion and neuronal damage, i.e. reduced FMZ binding, were smaller than those in patients with a malignant course. B: Sequential PET CBF images in 2 cats with malignant (left) and benign (right) courses after transient MCA occlusion. Note the hyperperfusion immediately following recirculation and subsequent deterioration extending even to the contralateral hemisphere in the cat with malignant infarct.

the peri-infarct zones^[55, 62]. In several studies, increased ¹¹C-PK11195 uptake has been observed around the ischemic lesions after several days, but also in regions distant from the lesion^[56]. Increased PK-binding has also been documented in the ipsilateral thalamus and in the subcortical white matter. This relationship between neuroinflammation and the integrity of fiber tracts has been investigated more systematically by combining microglia PET with diffusion tensor imaging (DTI), which yields information about the anisotropic diffusion of water molecules along white-matter fiber tracts. Using DTI in a prospective controlled study, Radlinska *et al.*^[63] demonstrated that microglial activation occurs along the pyramidal tract anterograde to the lesion only in those patients with acute subcortical stroke where the cortico-spinal tract is affected. These anterograde regions of the tract undergo Wallerian degeneration in the weeks and months after the stroke. This relationship was further investigated in a similarly-designed but longitudinal study^[64], in which the extent of anterograde microglial activity in the brainstem was found to be linearly related to the extent of pyramidal tract damage (Fig. 6). This remote

microglial activity is positively associated with the outcome, suggesting a neuroprotective role or repair function of microglial cells along the tract regions undergoing Wallerian degeneration. In contrast, local microglial activity in the area of the infarct is only related to persisting tract damage in the chronic phase and is correlated negatively with clinical outcome.

Hemodynamic and Metabolic Reserve

Patients with arterial occlusive disease are protected against ischemic damage to a certain extent by compensatory mechanisms, which help to prevent critical ischemia when perfusion pressure drops. In patients with uni- or bilateral carotid artery disease, PET using ¹⁵O-labelled tracers^[66] indicates regional vasodilatation as a focal increase in cerebral blood volume (CBV) in the respective territory, and the ratio of CBF to CBV is used as an indicator of local perfusion pressure. By calculating CBF/CBV ratio (normal value 10), the territories of patent carotids, unilateral occlusion, occlusion with contralateral stenoses, and bilateral occlusions can be discriminated. The reciprocal of the local mean vascular transit time is a

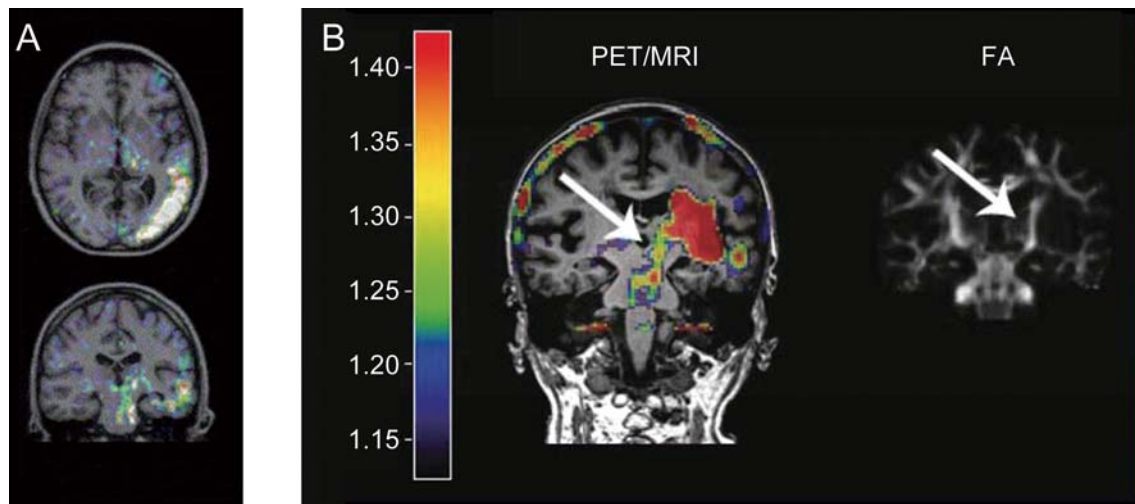


Fig. 6. Microglial activation in infarct and peri-infarct areas (A) (adapted from Gerhard A *et al.* Neuroimage 2005^[62]) and in remote fiber tracts imaged by ¹¹C-PK11195-PET (B) (adapted from Thiel A *et al.* Stroke 2011^[65]): ¹¹C-PK11195-PET is overlaid on T1-weighted MRI (left) and the fractional anisotropy (FA) image shows fiber tracts (right). Tracer binding is high in the infarct but also follows the pyramidal tract (arrows) in an anterograde direction to the level of the pons. Scale indicates uptake ratios.

measure of the perfusion reserve: the lower its value, the lower the flow velocity and the longer the residence time. The lowest ratios are found in patients with symptoms indicating a hemodynamic rather than a thrombotic cause of the ischemia. At maximal vasodilatation, the perfusion reserve is exhausted and a further decrease in arterial pressure produces a proportional decrease in CBF and the CBF/CBV ratio. With this hemodynamic decompensation, the brain must draw upon the oxygen-carriage reserve to prevent energy failure and the OER is increased from the normal value of 40% to up to 85%^[66-68]. Patients with submaximal elevations of OER represent 10% to 15% of the patients with cervical occlusive disease^[66]; their clinical symptoms are suggestive of hemodynamic ischemia.

On the basis of such PET measurements, it is therefore possible to discriminate patients with impaired hemodynamics only, as well as to quantify the impairment of perfusion reserve, using the CBF/CBV ratio. In addition, patients who are in a more precarious physiological state can be identified because (a) their hemodynamic reserve is exhausted and (b) their focal OER is increased. These two homeostatic mechanisms seem to act in series, thereby preventing a fall in CMRO₂ and, hence, preventing functional disorder. Therefore, elevated OEF is an independent predictor for subsequent stroke in patients

with symptomatic internal carotid artery disease, increasing the relative risk for ipsilateral stroke to ~ 7 ^[69-71]. The exhausted metabolic reserve can lead to selective neuronal loss in the cortex; this cannot be detected by morphological imaging (CT or MRI) but can be documented by FMZ-PET^[72]. Removal of the arterial lesion by endarterectomy or stenting is successful in preventing further ischemic attacks; repeated multiparametric PET can reveal accompanying improvements in CBF, perfusion pressure, and oxygen metabolism^[73].

Deactivation of Remote Tissue (Diaschisis)

Even the earliest PET studies of ischemic brain lesions^[74] revealed reduction of metabolism and blood flow exceeding the extent of morphologically damaged tissue (Fig. 7) – a regular finding since then with other functional imaging modalities as well, such as single-photon emission CT. The most conspicuous effect is a reduction of CBF and metabolism in the contralateral cerebellum, called “crossed cerebellar diaschisis” (CCD)^[75], occurring immediately after a stroke and persisting permanently in patients suffering from lesions involving the cortico-ponto-cerebellar pathways, but it is reversed by successful reperfusion therapy^[76] (Fig. 7). This CCD is clearly due to a neuronally-

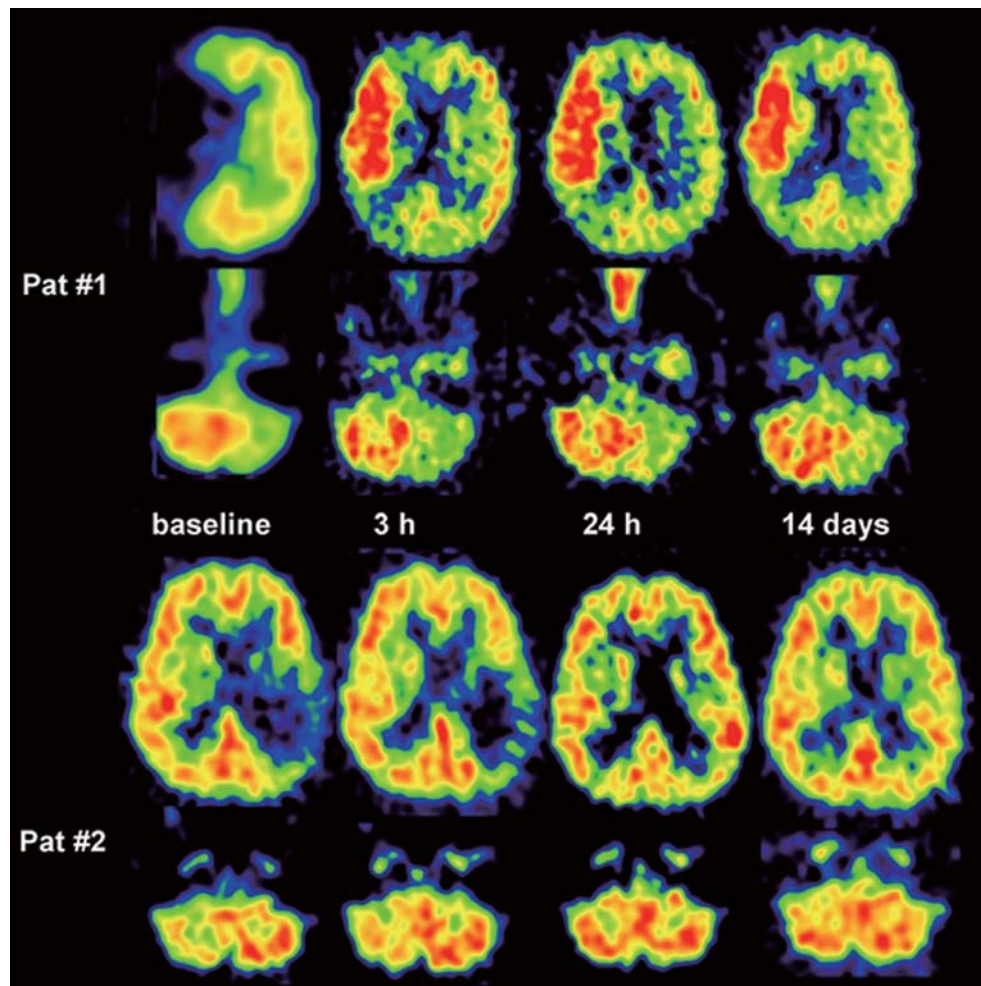


Fig. 7. Crossed cerebellar diaschisis (CCD) in acute stroke and response to supratentorial reperfusion. In patient #1, CCD persisted despite marked supratentorial reperfusion/hyperperfusion. Infarct volume was 60 cm³, clinical outcome was poor (National Institutes of Health stroke scale (NIHSS) 9). In patient #2, supratentorial reperfusion was accompanied by a CCD decrease. Follow-up CT showed no infarct and the NIHSS outcome score was 0 (from Sobesky J *et al.* *J Cereb Blood Flow Metab* 2005^[76]).

mediated functional effect, since a primary vascular cause can be excluded on account of the remote vascular territory. Further remote effects include reductions of CBF and metabolism in the ipsilateral cortex and basal ganglia. Their cause is less clear, since selective ischemic neuronal loss or inadequate blood supply could also contribute in these areas. However, similar effects have also been observed in non-ischemic lesions such as brain tumors and intracerebral hematomas, so they seem therefore to be more closely related to the site than to the nature of the primary lesion^[77]. Among cortical and subcortical lesions, infarcts of the parietal and frontal lobes most often

cause significant reductions of CBF and metabolism in the ipsilateral basal ganglia and the contralateral cerebellum. Infarcts of the basal ganglia may induce ipsilateral cerebral as well as contralateral cerebellar deactivation. Thalamic infarcts have mainly diffuse ipsilateral cortical effects; lesions of the medial thalamic nuclei apparently cause more widespread cortical metabolic reductions than those restricted to the anterior, ventrolateral, and posterior nuclei^[78]. Infarcts of the brainstem and the cerebellum usually do not cause significant asymmetric inactivations of forebrain structures. It is important to note that diaschisis cannot be reliably detected by the usual PWI parameters^[79].

Clinical symptoms not explained by the infarct proper can often be related to remote effects, and the severity of the metabolic changes appears to have an impact on functional recovery^[80]. Especially in complex syndromes affecting parts of widespread functional networks, disturbance of a distinct function (e.g. language comprehension) is closely associated with the metabolic deactivation of a defined region (left temporo-parietal area) irrespective of infarct location^[81]. Therefore, regional deactivation in specialized parts of a functional network plays a major role in the presentation of clinical syndromes and their resolution; re-organization of the affected network is of great importance for the recovery and rehabilitation of stroke victims. This complex topic is discussed in several reviews^[82–85].

Vascular Dementia and Vascular Cognitive Impairment

Vascular cognitive disorders (VCDs)^[86] include vascular cognitive impairment, vascular dementia (VaD, characterized by predominant deficits in executive functions and less prominent memory defects), and mixed Alzheimer VaD, and are responsible for cognitive deficits in 5% of people over the age of 65 years^[87]. VCDs are heterogeneous diseases and may be caused by multiple neuropathological substrates^[88, 89]. For the diagnosis of VaD and its differentiation from Alzheimer disease (AD), the presence of vascular risk factors and clinical features such as acute onset, stepwise progression, and emotional lability are used^[90, 91]. In addition, neuroimaging can detect the location and extent of pathological changes related to disturbed brain function^[92].

Overall, PET studies in patients with VaD demonstrate reduced CBF and CMRO₂, but normal OEF due to chronic ischemia^[93]. In patients with large infarcts, leukoaraiosis and deep white-matter abnormalities, decreased CBF and CMRO₂ in the overlying grey matter are associated with the severity of cognitive impairment^[94].

In VaD, fludeoxyglucose (FDG) PET shows focal cortical and subcortical hypometabolism, a pattern different from the changes in metabolism in AD (Fig. 8) affecting the association areas^[95]. However, various patterns of disturbance of CBF and metabolism are observed in different conditions of vascular pathology (details in review^[92]).

Post-stroke dementia (PSD) is a special case with cognitive impairment developing after the stroke, irrespective of signs of pre-existing cognitive decline. The prevalence of PSD is ~30%, i.e. 3.5 to 5.8 times greater than age-matched controls^[96]. The high rate of cognitive impairment after a stroke could be caused by vascular risk factors and AD-typical metabolic changes. Clinical and experimental studies (summarized in^[97]) indicate a link between vascular risk factors and degenerative dementia which is mediated by inflammation. In animal models, microglial activation after ischemia is exacerbated in the presence of amyloid and infarcts over time^[98]. The processes responsible for the development of PSD can be investigated by multi-tracer PET and may serve as a basis for the development of preventive therapy.

Complex Activation Studies

Regional cerebral metabolism and blood flow are dependent on the functional state of the brain tissue. This has been well established in animal experiments using autoradiography^[99]. A direct coupling of neuronal activity and focal blood flow has been demonstrated directly by simultaneous recordings with microelectrodes^[100]. The transfer to human studies was achieved by the ¹³³Xenon clearance method for the measurement of regional cerebral blood flow^[101], by which two-dimensional cortical activation patterns for various tasks including speech and memory were obtained. With the advance of PET, three-dimensional regional activation studies became feasible in healthy controls and in patients with various CNS disorders^[102]. Due to the radiation exposure and the complex logistics required by PET, these activation studies were taken over by fMRI with the availability of high-resolution MR equipment^[103]. However, PET activation studies are still required and justified for the detection of changes in the complex patterns elicited by stimulation procedures not feasible in MRI.

Our group has long experience with activation studies in aphasia^[84]. In the brain of right-handers and many left-handers, language is a function of the left, dominant hemisphere. This asymmetry is established during maturation and maintained by fiber bundles connecting both hemispheres across the corpus callosum. These fibers are glutaminergic and are connected to inhibitory interneurons

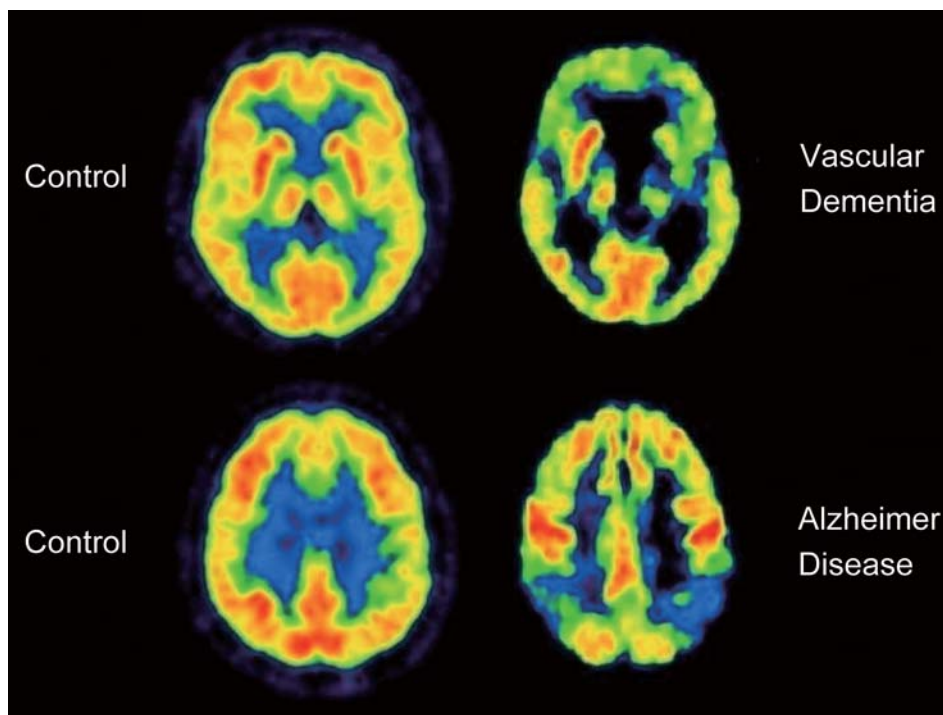


Fig. 8. Glucose metabolism in a normal control, in a patient with vascular dementia (VaD), and a patient with Alzheimer disease (AD) (Adapted from Heiss WD *et al.* J Neurol Sci 2012^[92]). The severity of dementia was comparable, and the pattern of pathologic changes differentiated these two cases: patchy metabolic defects in VaD in the frontal lobe, basal ganglia, and thalamus; bilateral hypometabolism in the parieto-temporal cortex and to a lesser degree in the frontal association areas in AD.

in the non-dominant hemisphere. This means that language areas active in Broca's area suppress homologous areas in the non-dominant hemisphere (transcallosal inhibition). The existence of these inhibitory mechanisms has been deduced from imaging studies in patients with brain lesions and has been demonstrated directly in normal subjects using imaging-guided repetitive transcranial magnetic stimulation (rTMS) (Fig. 9)^[104]. A lesion in the language areas of the dominant hemisphere not only reduces activity in the affected hemisphere, but also activates areas in the unaffected hemisphere by interrupting transcallosal inhibitory fibers^[105]. This activity of regions in areas of the non-dominant hemisphere after a stroke has been repeatedly detected in imaging studies^[106]. In the following weeks and months, activation shifts back to the dominant hemisphere. This backward shift varies considerably and might be responsible for the successful recovery of language function^[107]. For successful rehabilitation, the reactivation of networks in the dominant hemisphere seems to be a more efficient strategy than recruiting homologous

brain regions in the unaffected non-dominant hemisphere. Right-hemispheric regions can be compensatory in chronic aphasics^[108], but this seems to be a less effective long-term strategy if left-hemisphere areas can no longer be recruited. Based on these data, a strategy for the rehabilitation of language function should suppress the right hemisphere and enhance left-hemisphere activity after stroke. Results from a study in post-stroke aphasia show that activity of the non-lesioned hemisphere can be decreased by inhibitory rTMS. The induced shift of activation to the dominant hemisphere is associated with an improvement in language function. Speech therapy combined with inhibitory rTMS of the area in the non-dominant hemisphere homologous to Broca's area might be a successful treatment for post-stroke aphasia^[109].

Future Perspectives: Multimodal Imaging

With technical developments for the integration of different modalities, e.g. MRI and PET, the investigation of various

Models of focal brain lesions

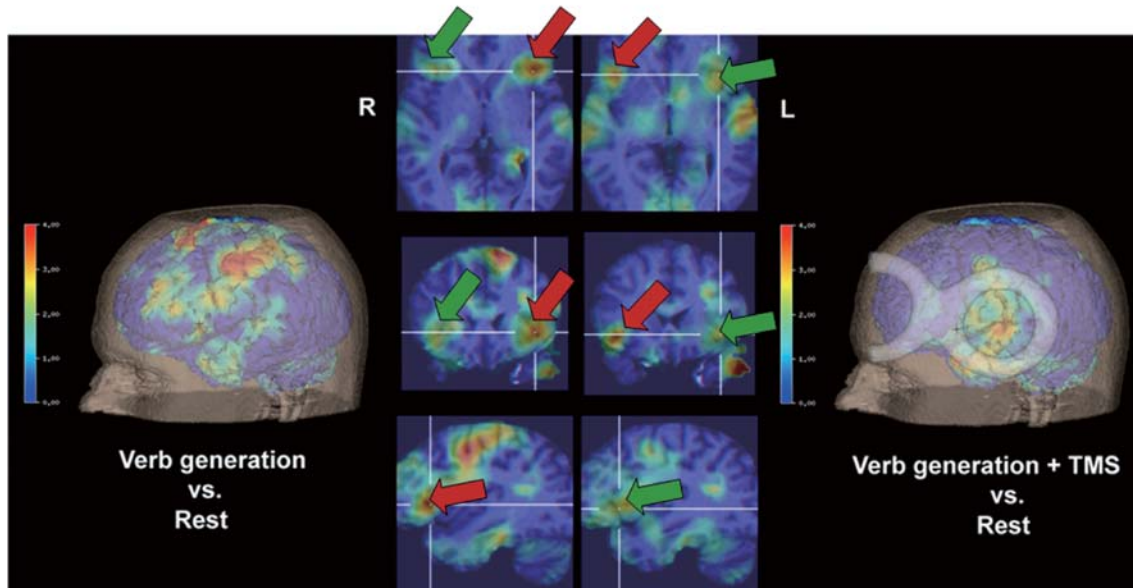


Fig. 9. Effect of repetitive transcranial magnetic stimulation on the activation pattern during verb generation. The activation pattern (left panel) and coil position (right panel) are shown in 3D rendering. Middle panels: left side, images in 3D show activation of the left inferior frontal gyrus during verb generation (red arrows); right side, decreased activation on the left (green arrows), and increased activity on the right (red arrows) during rTMS interference (modified from Thiel A *et al.* *J Cereb Blood Flow Metab* 2006^[110]).

parameters (morphology, metabolism, blood flow and perfusion, and molecular activities) can be performed simultaneously. Combining the functional metabolic values in the picomolar range provided by PET with the fast high-resolution information in the micromolar range from MRI already has widespread applications in experimental research^[111] and promising potential in humans^[112-114]. The co-registration of various parameters also improves the quality of results: MR data are used for the correction of partial volume effects in small structures and dynamic information from MRI can be used for the quantification of parametric values by PET (Fig. 10).

Simultaneous multifunctional and multiparametric imaging might have a significant impact in stroke research: it guarantees exactly the same physiological state for comparative measurements of perfusion by PET and MRI; it permits differentiation of core and penumbra, demonstrates time-dependent growth of infarction, and may be used to determine the optimal therapy for a certain time after the stroke; the vascular origin of the stroke can be detected by magnetic resonance angiography, and

perfusion or oxy/deoxyhemoglobin changes (the BOLD effect) can be related to the extent of oxygen deprivation (¹⁵O) and hypoxia (FMISO) and to changes in metabolic markers (FDG-PET, MR spectroscopy (MRS) for lactate, choline, N-acetylaspartate) – complimentary information important for therapeutic decisions. This high-resolution anatomical information is complemented by diffusion-based tractography, and can be related to the activation or inhibition of neurotransmitter and receptor activity as well as to inflammatory reactions.

Another field of new applications may open up by combining MRS and PET. Monitoring glucose metabolism by FDG yields precise information about glycolysis. Other molecules important in glucose metabolism, such as lactate and pyruvate, can be detected by ¹³C-MRS, which could be used together with FDG-PET to monitor different aspects of glucose metabolism in various diseases^[116].

Some innovative strategies might result from the transfer of experimental findings into clinical applications of PET/MR: imaging of angiogenesis by ¹⁸F-galacto RGD (a cyclic growth factor receptor peptide) combined with

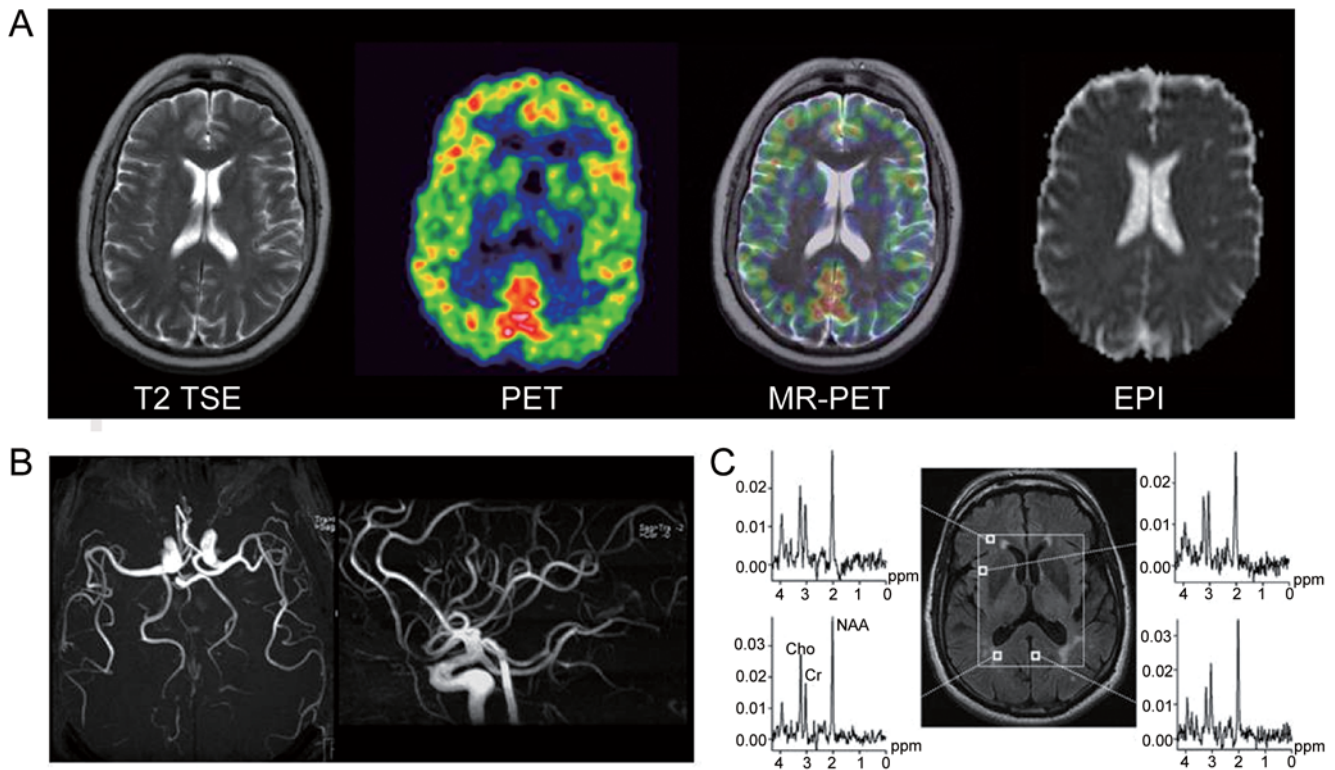


Fig. 10. The first simultaneous PET/MR acquired on the BrainPET prototype, Siemens, Knoxville, TN: Complete set of acquired MR and PET data from a 66-year-old man after injection of 370 MBq of FDG. A: T2-TSE, tracer distribution in PET recorded for 20 min at steady-state, superimposed combined PET/MR and EPI; B: time-of-flight MR-angiography; C: proton MR-spectroscopy showing increased choline relative to creatine in white matter areas (left spectra) compared to normal gray matter (right spectra) (modified from Schlemmer HP *et al.* Radiology 2008^[115]).

dynamic contrast-enhanced MR might become feasible and yield information on revascularization processes in the course after stroke^[117]. Monitoring the location and following the migration of grafted stem or progenitor cells will be essential in the development of cell replacement strategies for the treatment of various neurological disorders. The cells can be labelled with iron oxide particles and their survival and migration to the ischemic lesion can be followed by MRI^[118]. Combining MRI for tracking cells with PET for detecting their biological activity could demonstrate the viability of the cells as well as their integration into functional networks^[119, 120].

Conclusion

Over the years, PET has been the most efficient technique for providing accurate quantitative *in vivo* regional measurements of cerebral blood flow, cerebral metabolism,

and cerebral molecular markers in human subjects. It therefore has played a prominent role in the translation of research concepts from experimental models to clinical application, which is fundamental for understanding the pathophysiology and for developing treatment strategies in various brain diseases including stroke. With the advent of high-resolution integrated PET/MRI facilities, simultaneous investigations of several molecular, metabolic, perfusional, and morphological parameters are feasible, and these might enhance our insights into brain function and disorders.

Received date: 2014-03-13; Accepted date: 2014-04-10

REFERENCES

- [1] World Health Organisation 2008. Burden of Disease Statistics. Geneva: WHO Press.

- [2] Lopez AD, Mathers CD, Ezzati M, Jamison DT, Murray CJ. Global and regional burden of disease and risk factors, 2001: systematic analysis of population health data. *Lancet* 2006, 367: 1747–1757.
- [3] Johnston SC, Mendis S, Mathers CD. Global variation in stroke burden and mortality: estimates from monitoring, surveillance, and modelling. *Lancet Neurol* 2009, 8: 345–354.
- [4] Leary MC, Saver JL. Annual incidence of first silent stroke in the United States: a preliminary estimate. *Cerebrovasc Dis* 2003, 16: 280–285.
- [5] Pakkenberg B, Gundersen HJ. Neocortical neuron number in humans: effect of sex and age. *J Comp Neurol* 1997, 384: 312–320.
- [6] Clarke DD, Sokoloff L. Circulation and energy metabolism of the brain. In: Siegel GJ, Agranoff BW, Albers RW, *et al.* (Eds.). *Basic Neurochemistry: Molecular, Cellular, and Medical Aspects*, 6th ed. Philadelphia: Lippincott-Raven, 1999: 637–669.
- [7] Sokoloff L. Energetics of functional activation in neural tissues. *Neurochem Res* 1999, 24: 321–329.
- [8] Laughlin SB, Attwell D. The metabolic cost of neural information: from fly eye to mammalian cortex. In: Frackowiak RSI, Magistretti PI, Shulman RG, *et al.* (Eds.). *Neuroenergetics: Relevance for Functional Brain Imaging*. Strasbourg: HFSP Workshop XI, 2001: 54–64.
- [9] Dirnagl U, Iadecola C, Moskowitz MA. Pathobiology of ischaemic stroke: an integrated view. *Trends Neurosci*. 1999, 22: 391–397.
- [10] Hossmann KA. Pathophysiological basis of translational stroke research. *Folia Neuropathol* 2009, 47: 213–227.
- [11] Astrup J, Siesjö BK, Symon L. Thresholds in cerebral ischemia - the ischemic penumbra. *Stroke* 1981, 12: 723–725.
- [12] Heiss WD, Rosner G. Functional recovery of cortical neurons as related to degree and duration of ischemia. *Ann Neurol* 1983, 14: 294–301.
- [13] Ackerman RH, Correia JA, Alpert NM, Baron JC, Gouliamos A, Grotta JC, *et al.* Positron imaging in ischemic stroke disease using compounds labeled with oxygen 15. Initial results of clinicophysiological correlations. *Arch Neurol* 1981, 38: 537–543.
- [14] Baron JC, Bousser MG, Comar D, Soussaline F, Castaigne P. Noninvasive tomographic study of cerebral blood flow and oxygen metabolism in vivo. Potentials, limitations, and clinical applications in cerebral ischemic disorders. *Eur Neurol* 1981, 20: 273–284.
- [15] Lenzi GL, Frackowiak RSJ, Jones T. Cerebral oxygen metabolism and blood flow in human cerebral ischemic infarction. *J Cereb Blood Flow Metab* 1982, 2: 321–335.
- [16] Powers WJ, Grubb RL, Jr., Darriet D, Raichle ME. Cerebral blood flow and cerebral metabolic rate of oxygen requirements for cerebral function and viability in humans. *J Cereb Blood Flow Metab* 1985, 5: 600–608.
- [17] Heiss WD. Ischemic penumbra: evidence from functional imaging in man. *J Cereb Blood Flow Metab* 2000, 20: 1276–1293.
- [18] Powers WJ, Zazulia AR. PET in cerebrovascular disease. *PET Clin* 2010, 5: 83106.
- [19] Heiss WD. David sherman lecture 2012: the role of positron emission tomography for translational research in stroke. *Stroke* 2012, 43: 2520–2525.
- [20] Heiss WD, Huber M, Fink GR, Herholz K, Pietrzyk U, Wagner R, *et al.* Progressive derangement of periinfarct viable tissue in ischemic stroke. *J Cereb Blood Flow Metab* 1992, 12: 193–203.
- [21] Baron JC. Mapping the ischaemic penumbra with PET: implications for acute stroke treatment. *Cerebrovasc Dis* 1999, 9: 193–201.
- [22] Graf R, Löttgen J, Ohta K, Wagner R, Rosner G, Pietrzyk U, *et al.* Dynamics of postischemic perfusion following transient MCA occlusion in cats determined by sequential PET. *J Cereb Blood Flow Metab* 1997, 17, Suppl. 1: S323.
- [23] Guadagno JV, Jones PS, Aigbirhio FI, Wang D, Fryer TD, Day DJ, *et al.* Selective neuronal loss in rescued penumbra relates to initial hypoperfusion. *Brain* 2008, 131: 2666–2678.
- [24] Barber PA, Darby DG, Desmond PM, Yang Q, Gerraty RP, Jolley D, *et al.* Prediction of stroke outcome with echoplanar perfusion-weighted and diffusion-weighted MRI. *Neurology* 1998, 51: 418–426.
- [25] Kidwell CS, Alger JR, Saver JL. Beyond mismatch: evolving paradigms in imaging the ischemic penumbra with multimodal magnetic resonance imaging. *Stroke* 2003, 34: 2729–2735.
- [26] Heiss WD, Sobesky J, Smekal U, Kracht LW, Lehnhardt FG, Thiel A, *et al.* Probability of cortical infarction predicted by flumazenil binding and diffusion-weighted imaging signal intensity: a comparative positron emission tomography/magnetic resonance imaging study in early ischemic stroke. *Stroke* 2004, 35: 1892–1898.
- [27] Kane I, Carpenter T, Chappell F, Rivers C, Armitage P, Sandercock P, *et al.* Comparison of 10 different magnetic resonance perfusion imaging processing methods in acute ischemic stroke: effect on lesion size, proportion of patients with diffusion/perfusion mismatch, clinical scores, and radiologic outcomes. *Stroke* 2007, 38: 3158–3164.
- [28] Sobesky J, Weber OZ, Lehnhardt FG, Hesselmann V, Neveling M, Jacobs A, *et al.* Does the mismatch match the penumbra? Magnetic resonance imaging and positron emission tomography in early ischemic stroke. *Stroke* 2005, 36: 980–985.
- [29] Takasawa M, Jones PS, Guadagno JV, Christensen S,

- Fryer TD, Harding S, *et al.* How reliable is perfusion MR in acute stroke? Validation and determination of the penumbra threshold against quantitative PET. *Stroke* 2008, 39: 870–877.
- [30] Zaro-Weber O, Moeller-Hartmann W, Heiss WD, Sobesky J. The performance of MRI-based cerebral blood flow measurements in acute and subacute stroke compared with ¹⁵O-water positron emission tomography: identification of penumbral flow. *Stroke* 2009, 40: 2413–2421.
- [31] Olivot JM, Albers GW. Diffusion-perfusion MRI for triaging transient ischemic attack and acute cerebrovascular syndromes. *Curr Opin Neurol* 2011, 24: 44–49.
- [32] Hernandez DA, Bokkers RP, Mirasol RV, Luby M, Henning EC, Merino JG, *et al.* Pseudocontinuous arterial spin labeling quantifies relative cerebral blood flow in acute stroke. *Stroke* 2012, 43: 753–758.
- [33] Campbell BC, Christensen S, Levi CR, Desmond PM, Donnan GA, Davis SM, *et al.* Cerebral blood flow is the optimal CT perfusion parameter for assessing infarct core. *Stroke* 2011, 42: 3435–3440.
- [34] Mathias CJ, Welch MJ, Kilbourn MR, Jerabek PA, Patrick TB, Raichle ME, *et al.* Radiolabeled hypoxic cell sensitizers: Tracers for assessment of ischemia. *Life Sci* 1987, 41: 199–206.
- [35] Hoffman JM, Rasey JS, Spence AM, Shaw DW, Krohn KA. Binding of the hypoxia tracer [³H]misonidazole in cerebral ischemia. *Stroke* 1987, 18: 168–176.
- [36] Yeh SH, Liu RS, Hu HH, *et al.* Ischemic penumbra in acute stroke: demonstration by PET with fluorine-18 fluoromisonidazole. *J Nucl Med* 1994, 35: 205P.
- [37] Read SJ, Hirano T, Abbott DF, Sachinidis JI, Tochon-Danguy HJ, Chan JG, *et al.* Identifying hypoxic tissue after acute ischemic stroke using PET and ¹⁸F-fluoromisonidazole. *Neurology* 1998, 51: 1617–1621.
- [38] Markus R, Reutens DC, Kazui S, Read S, Wright P, Chambers BR, *et al.* Topography and temporal evolution of hypoxic viable tissue identified by ¹⁸F-fluoromisonidazole positron emission tomography in humans after ischemic stroke. *Stroke* 2003, 34: 2646–2652.
- [39] Read SJ, Hirano T, Abbott DF, Markus R, Sachinidis JI, Tochon-Danguy HJ, *et al.* The fate of hypoxic tissue on ¹⁸F-fluoromisonidazole PET after ischemic stroke. *Ann Neurol* 2000, 48: 228–235.
- [40] Markus R, Donnan G, Kazui S, Read S, Reutens D. Penumbral topography in human stroke: methodology and validation of the ‘Penumbrogram’. *Neuroimage* 2004, 21: 1252–1259.
- [41] Saita K, Chen M, Spratt NJ, Porritt MJ, Liberatore GT, Read SJ, *et al.* Imaging the ischemic penumbra with ¹⁸F-fluoromisonidazole in a rat model of ischemic stroke. *Stroke* 2004, 35: 975–980.
- [42] Spratt NJ, Donnan GA, Howells DW. Characterisation of the timing of binding of the hypoxia tracer FMISO after stroke. *Brain Res* 2009, 1288: 135–142.
- [43] Takasawa M, Beech JS, Fryer TD, Jones PS, Ahmed T, Smith R, *et al.* Single-subject statistical mapping of acute brain hypoxia in the rat following middle cerebral artery occlusion: a microPET study. *Exp Neurol* 2011, 229: 251–258.
- [44] Alawneh JA, Moustafa RR, Marrapu ST, Jensen-Kondering U, Morris RS, Jones PS, *et al.* Diffusion and perfusion correlates of the F-MISO PET lesion in acute stroke: pilot study. *Eur J Nucl Med Mol Imaging* 2014, 41: 736–744.
- [45] Lees KR, Bluhmki E, von Kummer R, Brodt TG, Toni D, Grotta JC, *et al.* Time to treatment with intravenous alteplase and outcome in stroke: an updated pooled analysis of ECASS, ATLANTIS, NINDS, and EPITHET trials. *Lancet* 2010, 375: 1695–1703.
- [46] Grotta JC, Alexandrov AV. tPA-associated reperfusion after acute stroke demonstrated by SPECT. *Stroke* 1998, 29: 429–432.
- [47] Heiss WD, Grond M, Thiel A, von Stockhausen HM, Rudolf J, Ghaemi M, *et al.* Tissue at risk of infarction rescued by early reperfusion: a positron emission tomography study in systemic recombinant tissue plasminogen activator thrombolysis of acute stroke. *J Cereb Blood Flow Metab* 1998, 18: 1298–1307.
- [48] Heiss WD, Kracht L, Grond M, Rudolf J, Bauer B, Wienhard K, *et al.* Early [¹¹C]Flumazenil/H₂O positron emission tomography predicts irreversible ischemic cortical damage in stroke patients receiving acute thrombolytic therapy. *Stroke* 2000, 31: 366–369.
- [49] Hossmann KA. Pathophysiology and therapy of experimental stroke. *Cell Mol Neurobiol* 2006, 26: 1057–1083.
- [50] Nakamura H, Strong AJ, Dohmen C, Sakowitz OW, Vollmar S, Sue M, *et al.* Spreading depolarizations cycle around and enlarge focal ischaemic brain lesions. *Brain* 2010, 133: 1994–2006.
- [51] Dohmen C, Sakowitz OW, Fabricius M, Bosche B, Reithmeier T, Ernestus RI, *et al.* Spreading depolarizations occur in human ischemic stroke with high incidence. *Ann Neurol* 2008, 63: 720–728.
- [52] Juttler E, Bosel J, Amiri H, Schiller P, Limprecht R, Hacke W, *et al.* DESTINY II: DEcompressive Surgery for the Treatment of malignant INfarction of the middle cerebral artery II. *Int J Stroke* 2011, 6: 79–86.
- [53] Dohmen C, Bosche B, Graf R, Staub F, Kracht L, Sobesky J, *et al.* Prediction of malignant course in MCA infarction by PET and microdialysis. *Stroke* 2003, 34: 2152–2158.
- [54] Hanisch UK, Kettenmann H. Microglia: active sensor and versatile effector cells in the normal and pathologic brain. *Nat*

- Neurosci 2007, 10: 1387–1394.
- [55] Weinstein JR, Koerner IP, Moller T. Microglia in ischemic brain injury. *Future Neurol* 2010, 5: 227–246.
- [56] Thiel A, Heiss WD. Imaging of microglia activation in stroke. *Stroke* 2011, 42: 507–512.
- [57] Rojas S, Martin A, Arranz MJ, Pareto D, Purroy J, Verdaguer E, *et al.* Imaging brain inflammation with [(11)C]PK11195 by PET and induction of the peripheral-type benzodiazepine receptor after transient focal ischemia in rats. *J Cereb Blood Flow Metab* 2007, 27: 1975–1986.
- [58] Demerle-Pallardy C, Duverger D, Spinnewyn B, Pirotzky E, Braquet P. Peripheral type benzodiazepine binding sites following transient forebrain ischemia in the rat: effect of neuroprotective drugs. *Brain Res* 1991, 565: 312–320.
- [59] Schroeter M, Dennin MA, Walberer M, Backes H, Neumaier B, Fink GR, *et al.* Neuroinflammation extends brain tissue at risk to vital peri-infarct tissue: a double tracer [11C]PK11195- and [18F]FDG-PET study. *J Cereb Blood Flow Metab* 2009, 29: 1216–1225.
- [60] Hughes JL, Jones PS, Beech JS, Wang D, Menon DK, Aigbirhio FI, *et al.* A microPET study of the regional distribution of [11C]-PK11195 binding following temporary focal cerebral ischemia in the rat. Correlation with post mortem mapping of microglia activation. *Neuroimage* 2012, 59: 2007–2016.
- [61] Tsukada H, Ohba H, Nishiyama S, Kanazawa M, Kakiuchi T, Harada N. PET imaging of ischemia-induced impairment of mitochondrial complex I function in monkey brain. *J Cereb Blood Flow Metab* 2014, 34: 708–714
- [62] Gerhard A, Schwarz J, Myers R, Wise R, Banati RB. Evolution of microglial activation in patients after ischemic stroke: a [11C](R)-PK11195 PET study. *Neuroimage* 2005, 24: 591–595.
- [63] Radlinska BA, Ghinani SA, Lyon P, Jolly D, Soucy JP, Minuk J, *et al.* Multimodal microglia imaging of fiber tracts in acute subcortical stroke. *Ann Neurol* 2009, 66: 825–832.
- [64] Thiel A, Radlinska BA, Paquette C, Sidel M, Soucy JP, Schirmacher R, *et al.* The temporal dynamics of poststroke neuroinflammation: a longitudinal diffusion tensor imaging-guided PET study with ¹¹C-PK11195 in acute subcortical stroke. *J Nucl Med* 2010, 51: 1404–1412.
- [65] Thiel A, Heiss W-D. Imaging of microglia activation in stroke. *Stroke* 2011, 42: 507–512.
- [66] Gibbs JM, Wise RJ, Leenders KL, Jones T. Evaluation of cerebral perfusion reserve in patients with carotid-artery occlusion. *Lancet* 1984, 1: 310–314.
- [67] Powers WJ, Press GA, Grubb RL, Jr., Gado M, Raichle ME. The effect of hemodynamically significant carotid artery disease on the hemodynamic status of the cerebral circulation. *Ann Intern Med* 1987, 106: 27–35.
- [68] Sette G, Baron JC, Mazoyer B, Levasseur M, Pappata S, Crouzel C. Local brain haemodynamics and oxygen metabolism in cerebrovascular disease. Positron emission tomography. *Brain* 1989, 112: 931–951.
- [69] Grubb RL, Jr., Derdeyn CP, Fritsch SM, Carpenter DA, Yundt KD, Videen TO, *et al.* Importance of hemodynamic factors in the prognosis of symptomatic carotid occlusion. *JAMA* 1998, 280: 1055–1060.
- [70] Yamauchi H, Fukuyama H, Nagahama Y, Nabatame H, Ueno M, Nishizawa S, *et al.* Significance of increased oxygen extraction fraction in five-year prognosis of major cerebral arterial occlusive diseases. *J Nucl Med* 1999, 40: 1992–1998.
- [71] Hokari M, Kuroda S, Shiga T, Nakayama N, Tamaki N, Iwasaki Y. Impact of oxygen extraction fraction on long-term prognosis in patients with reduced blood flow and vasoreactivity because of occlusive carotid artery disease. *Surg Neurol* 2009, 71: 532–538; discussion 538, 538–539.
- [72] Baron JC, Yamauchi H, Fujioka M, Endres M. Selective neuronal loss in ischemic stroke and cerebrovascular disease. *J Cereb Blood Flow Metab* 2014, 34: 2–18.
- [73] Matsubara S, Moroi J, Suzuki A, Sasaki M, Nagata K, Kanno I, *et al.* Analysis of cerebral perfusion and metabolism assessed with positron emission tomography before and after carotid artery stenting. Clinical article. *J Neurosurg* 2009, 111: 28–36.
- [74] Kuhl DE, Phelps ME, Kowell AP, Metter EJ, Selin C, Winter J. Effects of stroke on local cerebral metabolism and perfusion: Mapping by emission computed tomography of ¹⁸F-FDG and ¹³NH₃. *Ann Neurol* 1980, 8: 47–60.
- [75] Baron JC, Boussier MG, Comar D, Castaigne P. “Crossed cerebellar diaschisis” in human supratentorial brain infarction. *Trans Am Neurol Assoc* 1980, 105: 459–461.
- [76] Sobesky J, Thiel A, Ghaemi M, Hilker RH, Rudolf J, Jacobs AH, *et al.* Crossed cerebellar diaschisis in acute human stroke: a PET study of serial changes and response to supratentorial reperfusion. *J Cereb Blood Flow Metab* 2005, 25: 1685–1691.
- [77] Feeney DM, Baron JC. Diaschisis. *Stroke* 1986, 17: 817–830.
- [78] Szelies B, Herholz K, Pawlik G, Karbe H, Hebold I, Heiss WD. Widespread functional effects of discrete thalamic infarction. *Arch Neurol* 1991, 48: 178–182.
- [79] Madai VI, Altaner A, Stengl KL, Zaro-Weber O, Heiss WD, von Samson-Himmelstjerna FC, *et al.* Crossed cerebellar diaschisis after stroke: can perfusion-weighted MRI show functional inactivation? *J Cereb Blood Flow Metab* 2011, 31: 1493–1500.
- [80] Kushner M, Reivich M, Fieschi C, Silver F, Chawluk J, Rosen M, *et al.* Metabolic and clinical correlates of acute ischemic infarction. *Neurology* 1987, 37: 1103–1110.

- [81] Karbe H, Herholz K, Szekely B, Pawlik G, Wienhard K, Heiss WD. Regional metabolic correlates of Token test results in cortical and subcortical left hemispheric infarction. *Neurology* 1989, 39: 1083–1088.
- [82] Nudo RJ. Mechanisms for recovery of motor function following cortical damage. *Curr Opin Neurobiol* 2006, 16: 638–644.
- [83] Mountz JM. Nuclear medicine in the rehabilitative treatment evaluation in stroke recovery. Role of diaschisis resolution and cerebral reorganization. *Eura Medicophys* 2007, 43: 221–239.
- [84] Heiss WD. WSO Leadership in Stroke Medicine Award Lecture Vienna, September 26, 2008: Functional imaging correlates to disturbance and recovery of language function. *Int J Stroke* 2009, 4: 129–136.
- [85] Cramer SC, Nudo RJ (Eds.). *Brain Repair after Stroke*. Cambridge: Cambridge University Press, 2010.
- [86] Roman GC, Sachdev P, Royall DR, Bullock RA, Orgogozo JM, Lopez-Pousa S, *et al*. Vascular cognitive disorder: a new diagnostic category updating vascular cognitive impairment and vascular dementia. *J Neurol Sci* 2004, 226: 81–87.
- [87] Rockwood K, Wentzel C, Hachinski V, Hogan DB, MacKnight C, McDowell I. Prevalence and outcomes of vascular cognitive impairment. *Vascular Cognitive Impairment Investigators of the Canadian Study of Health and Aging*. *Neurology* 2000, 54: 447–451.
- [88] Ferrer I. Cognitive impairment of vascular origin: Neuropathology of cognitive impairment of vascular origin. *J Neurol Sci* 2010, 299(1–2): 139–149
- [89] Jellinger KA. The pathology of “vascular dementia”: a critical update. *J Alzheimers Dis* 2008, 14: 107–123.
- [90] Hachinski VC, Lassen NA, Marshall J. Multi-infarct dementia. A cause of mental deterioration in the elderly. *Lancet* 1974, 2: 207–210.
- [91] Moorhouse P, Rockwood K. Vascular cognitive impairment: current concepts and clinical developments. *Lancet Neurol* 2008, 7: 246–255.
- [92] Heiss WD, Zimmermann-Meinzingen S. PET imaging in the differential diagnosis of vascular dementia. *J Neurol Sci* 2012, 322: 268–273.
- [93] Frackowiak RSJ, Pozzilli C, Legg NJ, Du Boulay GH, Marshall J, Lenzi GL, *et al*. Regional cerebral oxygen supply and utilization in dementia. A clinical and physiological study with oxygen-15 and positron tomography. *Brain* 1981, 104: 753–778.
- [94] Meguro K, Hatazawa J, Yamaguchi T, Itoh M, Matsuzawa T, Ono S, *et al*. Cerebral circulation and oxygen metabolism associated with subclinical periventricular hyperintensity as shown by magnetic resonance imaging. *Ann Neurol* 1990, 28: 378–383.
- [95] Benson DF, Kuhl DE, Hawkins RA, Phelps ME, Cummings JL, Tsai SY. The fluorodeoxyglucose ^{18}F scan in Alzheimer's disease and multi-infarct dementia. *Arch Neurol* 1983, 40: 711–714.
- [96] Leys D, Henon H, Mackowiak-Cordoliani MA, Pasquier F. Poststroke dementia. *Lancet Neurol* 2005, 4: 752–759.
- [97] Cechetto DF, Hachinski V, Whitehead SN. Vascular risk factors and Alzheimer's disease. *Expert Rev Neurother* 2008, 8: 743–750.
- [98] Whitehead SN, Cheng G, Hachinski VC, Cechetto DF. Progressive increase in infarct size, neuroinflammation, and cognitive deficits in the presence of high levels of amyloid. *Stroke* 2007, 38: 3245–3250.
- [99] Sokoloff L, Ingvar DH, Lassen NA. Influence of functional activity on local cerebral glucose utilization. *Brain Work* 1975: 385–388.
- [100] Heiss WD, Turnheim M, Vollmer R, Rappelsberger P. Coupling between neuronal activity and focal blood flow in experimental seizures. *Electroenceph Clin Neurophysiol* 1979, 47: 396–403.
- [101] Ingvar DH. Functional landscapes of the dominant hemisphere. *Brain Res* 1976, 107: 181–197.
- [102] Phelps ME, Mazziotta JC. Positron emission tomography: Human brain function and biochemistry. *Science* 1985, 228: 799–809.
- [103] Raichle ME. Behind the scenes of functional brain imaging: a historical and physiological perspective. *Proc Natl Acad Sci U S A* 1998, 95: 765–772.
- [104] Thiel A, Schumacher B, Wienhard K, Gairing S, Kracht LW, Wagner R, *et al*. Direct demonstration of transcallosal disinhibition in language networks. *J Cereb Blood Flow Metab* 2006, 26: 1122–1127.
- [105] Thiel A, Habedank B, Herholz K, Kessler J, Winhuisen L, Haupt WF, *et al*. From the left to the right: How the brain compensates progressive loss of language function. *Brain Lang* 2006, 98: 57–65.
- [106] Saur D, Lange R, Baumgaertner A, Schraknepper V, Willmes K, Rijntjes M, *et al*. Dynamics of language reorganization after stroke. *Brain* 2006, 129: 1371–1384.
- [107] Heiss WD, Kessler J, Thiel A, Ghaemi M, Karbe H. Differential capacity of left and right hemispheric areas for compensation of poststroke aphasia. *Ann Neurol* 1999, 45: 430–438.
- [108] Richter M, Miltner WH, Straube T. Association between therapy outcome and right-hemispheric activation in chronic aphasia. *Brain* 2008, 131: 1391–1401.
- [109] Thiel A, Hartmann A, Rubi-Fessen I, Anglade C, Kracht L, Weiduschat N, *et al*. Effects of noninvasive brain stimulation on language networks and recovery in early poststroke aphasia. *Stroke* 2013, 44: 2240–2246.

- [110] Thiel A, Schumacher B, Wienhard K, Gairing S, Kracht LW, Wagner R, *et al.* Direct demonstration of transcallosal disinhibition in language networks. *J Cereb Blood Flow Metab* 2006, 26: 1122–1127.
- [111] Wehrl HF, Judenhofer MS, Wiehr S, Pichler BJ. Pre-clinical PET/MR: technological advances and new perspectives in biomedical research. *Eur J Nucl Med Mol Imaging* 2009, 36: S56–68.
- [112] Heiss W-D. The potential of PET/MR for brain imaging. *Eur J Nucl Med Mol Imaging* 2009, 36. Suppl 1: 105–112.
- [113] Sauter AW, Wehrl HF, Kolb A, Judenhofer MS, Pichler BJ. Combined PET/MRI: one step further in multimodality imaging. *Trends Mol Med* 2010, 16: 508–515.
- [114] Catana C, Drzezga A, Heiss WD, Rosen BR. PET/MRI for neurologic applications. *J Nucl Med* 2012, 53: 1916–1925.
- [115] Schlemmer HP, Pichler BJ, Schmand M, Burbar Z, Michel C, Ladebeck R, *et al.* Simultaneous MR/PET imaging of the human brain: Feasibility study. *Radiology* 2008, 248: 1028–1035.
- [116] Lanfermann H, Kugel H, Heindel W, Herholz K, Heiss WD, Lackner K. Metabolic changes in acute and subacute cerebral infarctions: findings at proton MR spectroscopic imaging. *Radiology* 1995, 196: 203–210.
- [117] Hsu AR, Chen X. Advances in anatomic, functional, and molecular imaging of angiogenesis. *J Nucl Med* 2008, 49: 511–514.
- [118] Hoehn M, Himmelreich U, Kruttwig K, Wiedermann D. Molecular and cellular MR imaging: potentials and challenges for neurological applications. *J Magn Reson Imaging* 2008, 27: 941–954.
- [119] Bliss T, Guzman R, Daadi M, Steinberg GK. Cell transplantation therapy for stroke. *Stroke* 2007, 38: 817–826.
- [120] Wang J, Chao F, Han F, Zhang G, Xi Q, Li J, *et al.* PET demonstrates functional recovery after transplantation of induced pluripotent stem cells in a rat model of cerebral ischemic injury. *J Nucl Med* 2013, 54: 785–792.
- [121] Heiss WD, Grond M, Thiel A, Ghaemi M, Sobesky J, Rudolf J, Bauer B, Wienhard K. Permanent cortical damage detected by flumazenil positron emission tomography in acute stroke. *Stroke* 1998, 29: 454–461.

Recent advances in parametric neuroreceptor mapping with dynamic PET: basic concepts and graphical analyses

Seongho Seo^{1,2,3}, Su Jin Kim³, Dong Soo Lee^{1,3,4}, Jae Sung Lee^{1,2,3,5}

¹Department of Nuclear Medicine, College of Medicine; ²Department of Brain and Cognitive Sciences, College of Natural Sciences; ³Institute of Radiation Medicine, Medical Research Center; ⁴Department of Molecular Medicine and Biopharmaceutical Sciences, Graduate School of Convergence Science and Technology; ⁵Department of Biomedical Sciences, College of Medicine, Seoul National University, Seoul, Korea

Corresponding author: Jae Sung Lee. E-mail: jaes@snu.ac.kr

© Shanghai Institutes for Biological Sciences, CAS and Springer-Verlag Berlin Heidelberg 2014

Tracer kinetic modeling in dynamic positron emission tomography (PET) has been widely used to investigate the characteristic distribution patterns or dysfunctions of neuroreceptors in brain diseases. Its practical goal has progressed from regional data quantification to parametric mapping that produces images of kinetic-model parameters by fully exploiting the spatiotemporal information in dynamic PET data. Graphical analysis (GA) is a major parametric mapping technique that is independent on any compartmental model configuration, robust to noise, and computationally efficient. In this paper, we provide an overview of recent advances in the parametric mapping of neuroreceptor binding based on GA methods. The associated basic concepts in tracer kinetic modeling are presented, including commonly-used compartment models and major parameters of interest. Technical details of GA approaches for reversible and irreversible radioligands are described, considering both plasma input and reference tissue input models. Their statistical properties are discussed in view of parametric imaging.

Keywords: dynamic positron emission tomography; graphical analysis; neuroreceptor imaging; parametric image; tracer kinetic modeling

Introduction

Tracer kinetic modeling in dynamic positron emission tomography (PET) has played a leading role in quantitative *in vivo* studies on the functional and molecular bases of brain diseases, mainly because of its high sensitivity and quantitative accuracy^[1–5]. Using a tiny amount of radioactive tracer or radioligand injected into the living body, dynamic neuroreceptor PET can accurately capture the temporally changing spatial distribution of the radioligand in the brain, which reflects the targeted receptor's density and dynamic interaction with the radioligand^[6–8]. Nevertheless, the spatiotemporal distribution also contains other distracting information such as the inherent statistical noise associated with radioactive decay, and physiological factors of

secondary interest^[3, 7, 9]. The techniques of tracer kinetic modeling, through a mathematical framework, can refine this noisy information from PET data into several quantitative parameters that characterize the receptor distribution and/or the binding process in the brain^[1, 6, 10]. Therefore, in both clinical and basic research, this method has been widely used to investigate the characteristic distribution patterns of neuroreceptors or their dysfunction, which is related to brain diseases, and the effects of new drugs^[11–16].

Over the last few decades, the practical goal of tracer kinetic modeling in PET has progressed from an analysis of regional data to the production of images of kinetic-model parameters^[17–19]. The typical procedure of tracer kinetic modeling involves fitting a suitable kinetic model to the tissue time-activity curves (TACs)

at the regional or voxel level that are collected from the reconstructed dynamic PET images^[3, 17, 20]. The regional analysis can be easily performed at a lower computational cost and with better statistical properties owing to the smaller number and lower noise-level of the regional TACs that are usually obtained by averaging the voxel TACs within a predefined region-of-interest (ROI). However, the delineation of ROIs requires prior knowledge of the receptor distribution and is operator-dependent and time- and labor-consuming when done manually^[5, 8]. More importantly, the results from regional analysis can provide only the average information within a given ROI, and their accuracy is dependent on the size of the ROI. On the contrary, the analysis of voxel TACs can fully exploit the spatiotemporal information captured in dynamic PET frames, and produce images of kinetic-model parameters that quantitatively characterize the targeted neuroreceptor system^[8, 21]. Furthermore, such parametric images allow the analysis of the entire brain volume regardless of specific anatomy, such as in voxel-based statistical analysis using the SPM package (Statistical Parametric Mapping, University College London, UK)^[16, 19, 22]. Therefore, the estimation of parametric images is becoming preferable, though regional analysis is still important for the exploration of the overall characteristics of tracer kinetics.

Because of the huge numbers of voxels in dynamic images and the high-level noise therein, parametric imaging is more challenging in terms of computational complexity and statistical reliability than ROI-based analysis^[4, 8, 18, 19, 22]. This issue will become more crucial as the resolution of PET images improves or the injection dose of a radioligand diminishes, based on the advancement of PET scanners (e.g., high-resolution research tomography^[23]). Thus, parametric imaging techniques need to be very robust to noise, computationally efficient, and moreover user-independent and automatic^[17, 19].

Conceptually, most kinetic analysis techniques are applicable for the estimation of both regional parameters and parametric images. In practice, however, methods based on nonlinear parameter estimation are undesirable for parametric imaging because of a higher computational burden and less reliability than those relying on linear techniques^[8, 21, 22]. Therefore, the use of compartmental analysis has long been limited mostly to regional data,

although it is now being extended to voxel data thanks to the recently increased computational power and regularization techniques^[24–27] developed to address the high noise-susceptibility issue. In parametric image generation, instead, preferable approaches have relied on the linearization of the standard compartment models in various ways so that computationally efficient and reliable linear estimation techniques are applicable.

One major linearization technique is to integrate the compartment model equations to produce a simple linear regression model that is linear in the parameters^[17]. This method based on the simple model is called graphical analysis (GA), and its parameter estimation depends on a linear estimation technique that has a closed form solution and is thus computationally simple. In contrast to compartment modeling, in which the best model configuration needs to be determined in advance, this method achieves a level of model independence by fitting only the later portion of the measured data to a simple linear model with only two parameters^[17]; this strategy enables the use of common properties among the compartmental models (steady state of specific binding). Furthermore, the results are relatively stable because they are estimated using only late time frames, which have a relatively higher signal-to-noise ratio (SNR) than earlier time frames^[8]. In sum, both the simplicity of the model and the closed-form linear least squares (LLS) solution enable simple, reliable, and computationally efficient parameter estimation.

In this article, we introduce recent advances in these GA approaches, focusing on parametric image generation for neuroreceptor ligand PET studies. Although extensive applications of these approaches are based mostly on relatively fast, simple, and reliable parameter estimation rather than various other techniques, they may suffer from complicated noise structures or a limited amount of data. Hence, their statistical properties are discussed.

Basic Theory in Tracer Kinetic Modeling

Before introducing the GA methods, we briefly describe the basic concepts in tracer kinetic modeling for neuroreceptor PET studies. Throughout this paper, we follow the consensus nomenclature suggested by Innis *et al.*^[28] as

much as possible. More detailed concepts and principles of tracer kinetic modeling have been presented in numerous studies^[3-5, 7-9, 29-31].

Dynamic PET Acquisition

In dynamic neuroreceptor PET studies, a very small amount of radioligand with high specific activity, which is designed to follow a substrate physiological and biochemical process of interest without disturbing the associated system, is introduced into the bloodstream of an individual participant (mostly by a single intravenous bolus). The radioligand administered is delivered to capillaries in the brain by arterial blood flow, is subsequently extracted from arterial blood into tissue space across the blood-brain barrier in the capillaries, and finally binds to high-affinity receptors in the tissue through the targeted biochemical process^[9]. Accordingly, the radioligand is differentially accumulated into and cleared from diverse brain tissues over time, along with the physiological and biochemical properties of the radioligand as well as the target process^[8].

The characteristic spatiotemporal distribution of the radioligand in the brain can be imaged by a dynamic PET scan in which the radioactivity from the delivered radioligand is counted and then recorded in a series of image frames over irregular time intervals. Although an individual i th dynamic frame represents the average spatial distribution of radioactivity during the frame duration, it is usually assumed to be instantaneous at the midpoint of the frame (t_i). After a number of corrections (including a radioactivity-decay correction), reconstruction, and calibration, each dynamic PET image then represents the instantaneous measurement ($C_T^*(t_i)$) at the frame time of the time-varying radioligand concentration in each tissue region, $C_T(t)$, (Bq/mL); t is the post-injection time and the superscript * denotes noisy measurement. Therefore, by collecting the time course of the measurements from each voxel of dynamic PET images (or averaging them over the voxels within a specific ROI), we obtain voxel-wise TACs (or ROI TACs).

Compartmental Models

The measured PET data can be described with a mathematical model or a comprehensive description of the underlying processes that is developed based on a prior understanding of the kinetic behavior of radioligands in brain tissue^[7-9]. Most widely used is a compartmental model that forms the basis for tracer kinetic modeling in PET^[3, 29].

With prior knowledge of their expected *in vivo* kinetics, the injected radioligands can be assumed to form a limited number of separate pools, called compartments, according to their physical and chemical states. In general, the concentration of unmetabolized parent radioligand in plasma (C_P) (Bq/mL) is considered as one compartment because it serves as the input for the radioligands delivered into the tissue. As for the radioligands in the tissue, the following pools are considered plausible in studies of receptor-ligand binding: those in free form (C_F), those specifically bound to the receptor of interest (C_S), and those nonspecifically bound to other proteins (C_{NS}). Then, we have the following relationship:

$$C_T(t) = C_F(t) + C_{NS}(t) + C_S(t). \quad (1)$$

Together with several assumptions, such as homogeneous concentration and instantaneous mixing of radioligands within a compartment, the small injection dose and high specific activity enable the use of first-order rate constants to describe exchanges of radioligand between compartments^[1, 2, 6, 9, 32], so, the transport and binding rates of the radioligand are assumed to be linearly related to the concentration differences between compartments. These considerations lead to linear compartment models.

Figure 1 (top) depicts the standard two-tissue compartment model (2TCM) that involves only two compartments to represent the radioligand concentration within the tissue and that is commonly used to study neuroreceptor ligand binding. By assuming a rapid equilibrium between free and nonspecifically-bound tissue compartments, the two compartments can be considered as one unified compartment, called the non-displaceable compartment (C_{ND})^[1, 2, 10]. This assumption applies well to most neuroreceptor ligand studies because of the limited temporal resolution and statistical quality of the PET data; usually, the aforementioned model containing three tissue compartments is in practice too complex to provide reliable results^[3, 10]. In this model, the exchanges of radioligand are described by four rate constants: K_1 (mL/cm³ per min) is for the delivery of the radioligand from arterial plasma to tissue while k_2 (min⁻¹) is for its efflux from tissue; and k_3 and k_4 (min⁻¹) are for the binding and release from the neuroreceptor, that is, the exchange between $C_{ND}(t)$ and $C_S(t)$.

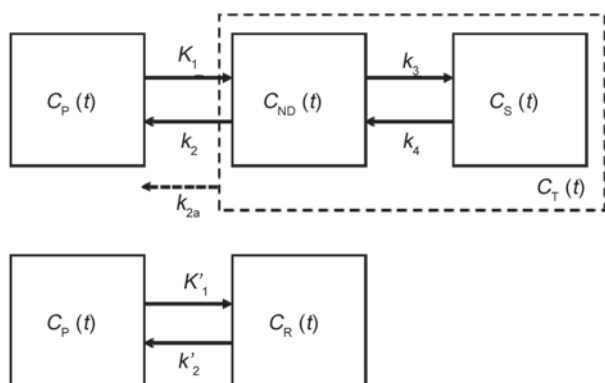


Fig. 1. Standard two-tissue compartment model for a target region or tissue (top) and one-tissue compartment model for a reference region (bottom) to describe the *in vivo* kinetic behavior of neuroreceptor radioligands. Top: concentrations (Bq/mL) of radioligands in the same states are represented as compartments: plasma concentration of unmetabolized parent radioligand (C_P), that of non-displaceable (free and nonspecifically bound) radioligand (C_{ND}), that of specifically bound radioligand (C_S); their exchanges between compartments are explained with the rate constants: K_1 (mL/cm³ per min) and k_2 – k_4 (min⁻¹); and C_T represents the total tissue concentration, that is, the sum of C_{ND} and C_S . In addition, k_{2a} denotes the apparent efflux rate constant from tissue when the tissue region can be approximately described with one compartment (dashed box) because of the equilibrium between C_{ND} and C_S . Bottom: C_R represents the total concentration in the reference region and K'_1 (mL/cm³ per min) and K'_2 (min⁻¹) are the rate constants for their influx and efflux from C_P .

For radioligands showing fast kinetics, i.e., where the binding and release of the radioligand from the receptor are rapid enough and thereby $C_{ND}(t)$ and $C_S(t)$ are indistinguishable, the model can be further simplified into a one-tissue compartment model (1TCM)^[10, 33]. In this case, the efflux rate constant k_2 is replaced by the apparent one $k_{2a} = k_2 / \left(1 + \frac{k_3}{k_4}\right)$. Furthermore, the 2TCM is also commonly used for irreversibly-binding radioligands whose binding process is intrinsically irreversible or seems so during the time period of PET studies. The irreversible accumulation of these radioligands can be analyzed by assuming that $k_4 = 0$.

In compartmental modeling, the final goal is to estimate the rate constants, which characterize the kinetics of the radioligand, from the measured data. Besides the measured PET data $C_T^*(t_i)$, the input function $C_P(t)$ also needs to be measured to obtain the rate constants. The

process of measuring $C_P(t)$ generally relies on frequent invasive arterial blood sampling^[34, 35] under the assumption that the arterial plasma concentration is the same as the capillary plasma concentration^[8]; arterial blood samples are measured separately during the dynamic PET acquisition and subsequently are corrected for metabolites since the standard model assumes that no plasma metabolites cross the blood-brain barrier. As the sampling times of blood data are incompatible with dynamic frame times, some simple signal processing may be required to match them. Contrary to the measured tissue data $C_T^*(t_i)$, where t_i is the matched sampling time for the i th measurement, we also maintain $C_P(t)$ without the superscript for the measured input data, because the data are usually refined through plasma input modeling^[36].

Although the arterial blood sampling method is considered to be the gold standard of measuring $C_P(t)$ based on its accuracy^[8], it has several disadvantages such as invasiveness and technical demands^[8, 31, 37]. Therefore, to minimize or eliminate the need for invasive and technically-demanding blood sampling and metabolite correction, the following approaches have been proposed and applied^[37, 38]: image-derived methods^[39–41], model-based methods^[42–44], reference region methods^[33, 45–48] and other sophisticated approaches^[49–55].

In reference region methods, the kinetics of the radioligand in the tissue is described as a function of a reference region by assuming that there exists a reference area of brain tissue effectively devoid of specific binding sites^[29]. Therefore, they require an additional compartment $C_R(t)$ and related rate constants K'_1 (mL/cm³ per min) and K'_2 (min⁻¹) as shown in Figure 1 (bottom) (hereafter, the superscript ' is used for the parameters in reference tissue). As these additions increase the complexity of the model and thus uncertainty in the resulting estimates, a series of assumptions is usually made to reduce the complexity^[21]: (1) nonspecific binding is the same in both areas though delivery is not, and (2) an equilibrium is rapidly achieved between C_{ND} and C_S so that tissue kinetics effectively follows the 1TCM.

Parameters of Interest in Neuroreceptor Ligand Study

In studies of reversible neuroreceptor-ligand binding, the primary outcome is the equilibrium concentration of

the radioligand specifically bound to the target receptor (C_S) that reflects the density and affinity of the receptors available to react with the radioligand *in vivo*^[28]. Since the density and affinity are inseparable under the single tracer injection protocol, the concentration of specific radioligand binding is usually quantified as its equilibrium ratio to another pool of radioligand concentration, termed binding potential (BP)^[6]. In the literature, there are three different practical definitions of *in vivo* BP depending on the use of distinct normalization factors (or the input measurements): non-displaceable concentration in tissue (C_{ND}), total concentration in plasma (C_P), or its free fraction ($f_P C_P$)^[28]. These *in vivo* BPs represent the potential of available receptors to bind with the radioligand, and reflect the density of available receptors under the assumption that there are no substantial regional changes in receptor affinity.

For consistency throughout this article, however, we limit ourselves to $BP_{ND} = C_S(t)/C_{ND}(t)$ (unitless) because only BP_{ND} can be obtained from both the reference region model (usually directly) and from the plasma input model (indirectly) that we describe. Although the other parameters, $BP_P = C_S(t)/C_P(t)$ and $BP_F = C_S(t)/(f_P C_P(t))$, are considered to be more suitable to describe specific binding than BP_{ND} , the measurement of plasma concentration or its free fraction is necessary to estimate them. Therefore, BP_{ND} is also frequently used (in a variety of applications) mainly because of practicality. However, the interpretation of BP_{ND} requires careful attention because its use is based on the assumption that V_{ND} (more precisely, its free fraction) has no regional or group difference; the comparison of BP_{ND} may not clearly reveal the group difference associated with specific binding when V_{ND} has a group difference or treatment effect^[28, 56].

Another common endpoint is the volume of distribution of total radioligand concentration in tissue (V_T). In the field of *in vivo* imaging, volume of distribution refers to the volume (mL) of plasma (with a certain concentration) required to account for the amount at equilibrium of radioligand in the unit volume (1 cm³) of the target region, and is therefore usually represented as the ratio of the radioligand concentration in the target (tissue or compartment) to that in the plasma (mL/cm³). Thus, V_T has the following relationship with the volume of distribution of

each compartment:

$$V_T = \frac{C_T(t)}{C_P(t)} = \frac{C_{ND}(t)}{C_P(t)} + \frac{C_S(t)}{C_P(t)} = V_{ND} + V_S \quad (2)$$

where V_{ND} and V_S are the volumes of distribution for nondisplaceable and specific binding compartments, respectively.

Though V_T does not directly reflect specific binding, but rather total radioligand uptake in tissue, it is also widely used in studies of neuroreceptor binding^[57]. Indeed, most GA using the plasma input function provides V_T as a major outcome. Because these methods yield a V_{ND} estimate for a receptor-free region, BP_{ND} can be indirectly computed as $BP_{ND} = V_T/V_{ND} - 1$. Similarly, even most reference region methods produce estimates of the tissue-to-reference ratio of V_T (V_T/V_{ND}), called the distribution volume ratio (DVR), to derive BP_{ND} . Furthermore, it is noteworthy that the V_S is BP_P in itself; thus, for a tracer with a high level of specific binding and/or a low level of nonspecific binding (e.g. [¹¹C] flumazenil), V_T ($\approx V_T - V_{ND} = V_S$) can yield a good estimate of the receptor density^[10].

Meanwhile, the concept of BP or volume of distribution is not useful for irreversibly binding radioligands. The major outcome of interest for these radioligands is the influx rate constant (K_{in} , mL/cm³ per min) which is the net influx rate of the radioligand from plasma into the irreversible compartment. K_{in} can be directly obtained from GA using the plasma input function, while only relative values normalized by reference region information such as K_{in}/V_T or K_{in}/K'_{in} can be acquired from reference region methods^[29].

The aforementioned parameters can be related to the rate constants of the 2TCM for reversibly binding radioligands as follows^[10]:

$$V_T = \frac{K_1}{k_2} \left(1 + \frac{k_3}{k_4} \right), \quad (3)$$

$$V_{ND} = \frac{K_1}{k_2}, \quad (4)$$

$$BP_{ND} = \frac{k_3}{k_4} = \frac{V_T}{V_{ND}} - 1. \quad (5)$$

Similarly, when the 2TCM can be simplified, we can consider the following relationship:

$$V_T = \frac{K_1}{k_{2a}} = \frac{K_1}{k_2} \left(1 + \frac{k_3}{k_4} \right). \quad (6)$$

For a reference region commonly described by the 1TCM^[57, 58],

we have

$$V_T' = V_{ND}' = \frac{K_1'}{k_2'} \quad (7)$$

Therefore, under the assumption $V_{ND} = \frac{K_1}{k_2} = \frac{K_1'}{k_2'} = V_{ND}' = V_T'$,

reference region methods can provide direct estimation of BP by using reference region data to acquire information about the non-displaceable component in tissue. Hence, the identification of a reliable reference region effectively devoid of specific binding is crucial^[56]. On the other hand, when modeling the kinetics of irreversible binding radioligands using the 2TCM with $k_4 = 0$, we have

$$K_{in} = \frac{K_1 k_3}{k_2 + k_3} \quad (8)$$

Limitations in Parametric Image Generation

Although the standard compartment model describes a linear system, it is not linear in parameters. Therefore, the estimation of parameters in compartment models requires nonlinear estimation techniques. Because of its optimal statistical accuracy and reliability^[59], the NLS method is considered to be the method of choice for tracer kinetic modeling and is often used as the gold standard to assess the performance of other methods in terms of ROI parameters^[8, 17]. However, nonlinear fitting approaches have no closed-form solution and are usually solved in an iterative way. This iterative approach imposes a tremendous computational burden when applied to voxel-by-voxel analysis. Furthermore, the performance of nonlinear fitting is dependent on the initial guessing of parameters; poor initial values result in finding incorrect optima at local minima of the cost function and slow convergence. In addition, an appropriate convergence threshold and constraints on the parameters should be determined by experience^[5].

Graphical Analysis

The GA method is the simplest approach that relies on a linear parameter estimation technique. In some literature, the term 'graphical analysis' has been used to indicate specific early methods such as the Gjedde-Patlak (GP) plot for an irreversible system^[60-62] or the Logan plot for a reversible one^[57, 63]. However, it is now considered as a category rather than a specific method, since several different GA models have also been developed to measure

different parameters or to improve other models^[64-67]. Table 1 lists the characteristics of all GA methods.

In each GA approach, the kinetic behavior of the radioligand is described by only two variables (for a simple linear regression) that are transformed from the measured data, including input functions, and that establish a linear relationship partially and asymptotically. The slope and intercept of that asymptotic linear portion can be interpreted as physiologically meaningful parameters, such as V_T or K_{in} ^[68]. Hence, first the linearity of the relationship is examined graphically by plotting one variable *versus* the other (which is why it is called graphical analysis; see Fig. 2) and then the slope and intercept are estimated by fitting a straight line to the specified linear portion *via* the LLS method.

To model the linear portion, GA methods rely on a simple linear regression model, or a linear model with a single independent variable, of the following matrix form:

$$\mathbf{y} = \beta_1 \mathbf{x}_1 + \beta_0 \mathbf{1} + \boldsymbol{\epsilon} = \mathbf{X}\boldsymbol{\beta} + \boldsymbol{\epsilon}, \quad (9)$$

where \mathbf{y} and \mathbf{x}_1 are $n \times 1$ vectors of dependent and independent variables, respectively; $\mathbf{X} = [\mathbf{x}_1, \mathbf{1}]$ is an $n \times 2$ matrix of the \mathbf{x}_1 and all-ones vector ($\mathbf{1}$) for the intercept term; $\boldsymbol{\beta} = [\beta_1, \beta_0]^T$ is a vector of the 2 parameters, slope (β_1) and intercept (β_0); and $\boldsymbol{\epsilon} = [\epsilon_1, \dots, \epsilon_n]^T$ is an $n \times 1$ vector of the error term. Then, the slope (β_1) and the intercept (β_0) characterizing the linear portion are usually obtained by solving the LLS problem:

$$\min_{\boldsymbol{\beta}} \|\mathbf{X}\boldsymbol{\beta} - \mathbf{y}\|_2^2, \quad (10)$$

which has the following closed form solution or the LLS estimator:

$$\hat{\boldsymbol{\beta}}_{LLS} = (\mathbf{X}^T \mathbf{X})^{-1} \mathbf{X}^T \mathbf{y}. \quad (11)$$

The GA methods have several advantages that are mainly attained by linearizing compartment model equations into the simple linear model so that the LLS approach can be used^[67, 68]. Both the simplicity of the model and the closed-form solution of the LLS method enable simple, reliable, and computationally efficient parameter estimation. Furthermore, in contrast to standard compartmental modeling, the GA methods are consistently applicable across different tissue data with no *a priori* knowledge on the best model structure for each tissue, because their equations are derived from a general multi-compartment model in which an arbitrary number of

Table 1. Overview of graphical analysis methods

	Logan plot	RE plot	GP plot	RE-GP plot	Ito plot	Noninvasive Logan	Noninvasive RE	Noninvasive GP
Binding type	Reversible	Reversible	Irreversible	Reversible	Reversible	Reversible	Reversible	Irreversible
Input function	C_p	C_p	C_p	C_p	C_p	C_R	C_R	C_R
Model equations	Eq. (12)	Eq. (18)	Eq. (24)	Eqs. (18), (24), (27)–(29)	Eq. (30)	Eq. (17)	Eq. (19)	Eq. (25) ¹ (or (26)) ²
Major parameters of interest	V_T	V_T	K_{in}	V_T	V_{ND} and V_T	V_T/V_T'	V_T/V_T'	K_{in}/V_T' (or K_{in}/K_{fin})
Necessity of reference region or C_R	Need only to obtain BP_{ND}	Need only to obtain BP_{ND}	No	Need only to obtain BP_{ND}	No (optional for BP_{ND})	Yes	Yes	Yes (or Yes)
Model variable containing noisy data C_T'	Both dependent & independent	None	Dependent	Dependent	Dependent	Both	Dependent	Dependent (or both)
Major effect of noise on LLS estimates	Negative bias	Variance	High variance	Variance	High variance	Negative bias	Variance	High variance (or negative bias)
Linearity condition	$\frac{C_S(t)}{C_T(t)} \rightarrow const$ (1TCM after t^*)	$\frac{C_T(t)}{C_p(t)} \rightarrow const$	$\frac{C_{ND}(t)}{C_p(t)} \rightarrow const$	$\frac{C_S(t)}{C_T(t)} \rightarrow const$ (1TCM after t^*)	$\frac{C_S(t)}{C_T(t)} \rightarrow const$ (1TCM after t^*)	Logan condition for tissue and reference	RE condition for tissue and reference	Logan for reversible and GP for irreversible
Reference	Logan et al. (1990) ^[63]	Zhou et al. (2009) ^[66]	Gjedde (1981) ^[60] and Patlak et al. (1983) ^[61]	Zhou et al. (2010) ^[67]	Yokoi et al. (1993) ^[64] and Ito et al. (2010) ^[65]	Logan et al. (1996) ^[57]	Zhou et al. (2009) ^[66]	Patlak and Blasberg (1985) ^[62] , Wu (2008) ^[37] , and Zheng et al. (2012) ^[38]

¹Model for reference region with reversible kinetics. ²Model for reference region with irreversible kinetics (note that this is not a typical graphical analysis). BP_{ND} , *in vivo* binding potential given as the ratio at equilibrium of specifically bound radioligand to that of non-displaceable radioligand in tissue; C_{ND} (or C_S), concentration of non-displaceable (or nonspecifically bound) radioligand in tissue; C_p , plasma concentration of unmetabolized parent radioligand; C_R , total concentration in reference region; C_T' , measure PET data (total concentration in tissue); GP, Gjedde-Patlak; K_{in} , net influx rate of the radioligand from plasma into the irreversible compartment; LLS, linear least squares; RE, relative equilibrium; V_T (or V_{ND}), volume of distribution of total tissue (or non-displaceable) radioligand concentration (superscript prime means that the parameter is associated with reference region).

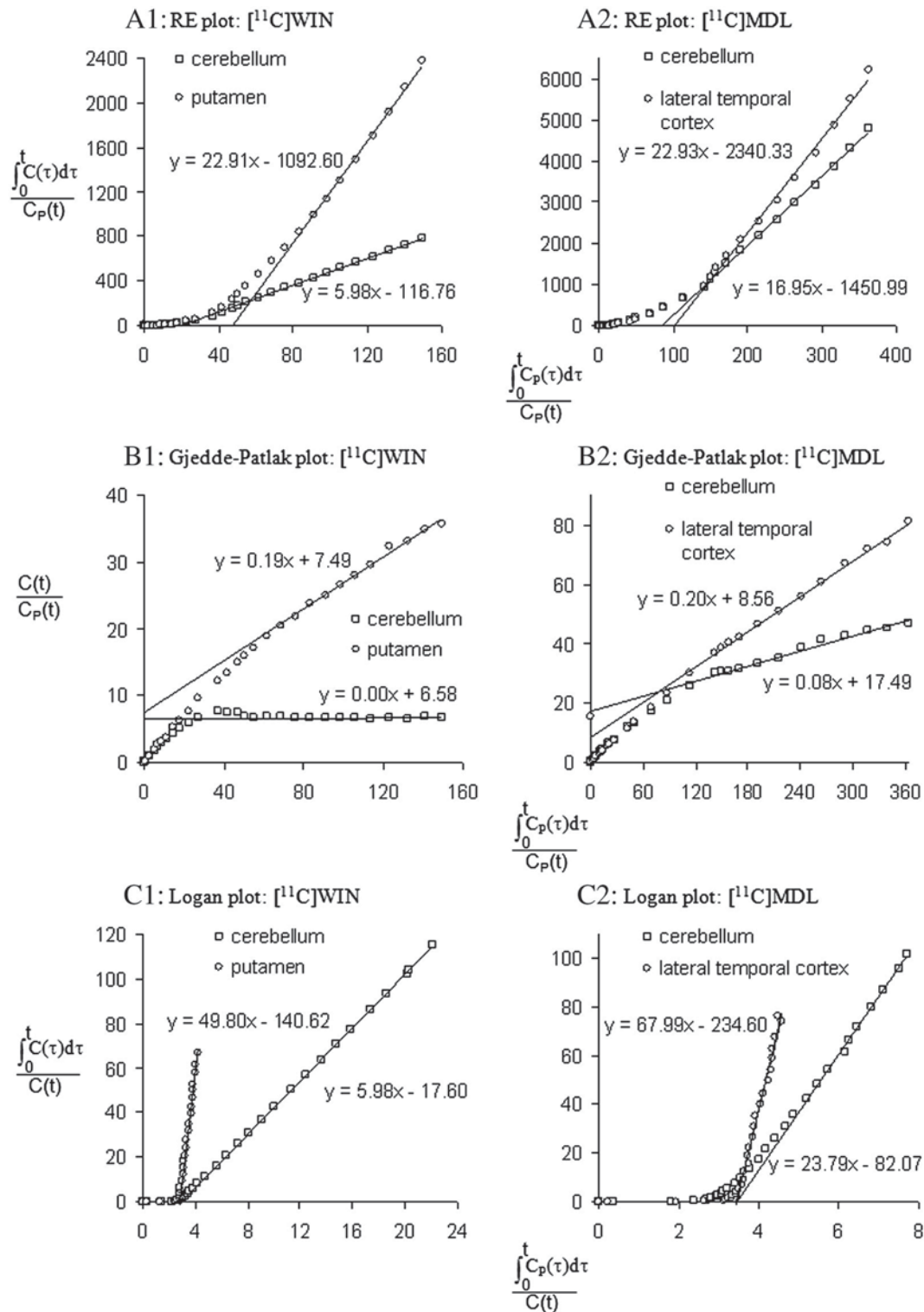


Fig. 2. Various graphical plots for the slow kinetic radiotracers, $[^{11}\text{C}]\text{WIN}$ (left) and $[^{11}\text{C}]\text{MDL}$ (right). (A) Relative equilibrium (RE), (B) Gjedde-Patlak, and (C) Logan plots (reprinted from Zhou *et al.* Neuroimage 2010^[67] with permission).

compartments is assumed^[61, 63]. These strengths of GA methods can greatly facilitate the generation of parametric images in which numerous voxels covering various brain regions can be analyzed.

However, a series of assumptions underlie the linearization and simplification of kinetic models for GA that allows the use of simple linear regression and thus provides various advantages. First, GA methods require the determination of t^* , the time when the plot becomes linear, because the model is valid only for the later part of the dynamic frames. A poor determination can yield erroneous estimates by violating the linearity requirement. In addition, slow kinetic tracers have a late starting point of the linear portion that reduces the amount of data available for estimation. Thus, the results can suffer from high uncertainty because of limited data. Moreover, unbiased parameter estimation in the simple linear regression depends on basic assumptions of LLS: that there are no or negligible errors in the independent variable of the linear model, and that the independent variables are uncorrelated with the error term. Any violation of these conditions can lead to inaccurate results.

Because most PET radioligands bind reversibly, reversible radioligand models have been used extensively^[1, 69]. Therefore, though most of them were extended from the GP plot for an irreversibly binding radioligand (the first GA method), we introduce the reversible radioligand models first.

Reversible Radioligand Models

Logan plot The Logan plot (Fig. 2) is a representative graphical method used to analyze a reversible radioligand-receptor binding^[57, 63]. The model equation using the plasma input function is given by

$$\frac{\int_0^t C_T(s) ds}{C_T(t)} = V_{T, \text{Logan}} \frac{\int_0^t C_P(s) ds}{C_T(t)} + \beta_{\text{Logan}} \text{ for } t > t^*, \quad (12)$$

where $V_{T, \text{Logan}}$ is the total distribution volume, and t^* is the time when the intercept β_{Logan} becomes effectively constant. Given the measured noisy TAC, $C_T^*(t_i)$ ($1 \leq i \leq n$) obtained from n sequential dynamic frames, we have

$$y_i = \int_0^{t_i} C_T^*(s) ds / C_T^*(t_i), \quad x_{1i} = \int_0^{t_i} C_P(s) ds / C_T^*(t_i),$$

and $\beta = [V_{T, \text{Logan}}, \beta_{\text{Logan}}]^T$ for $1 \leq i \leq n$. y_i and x_{1i} are the i th elements of \mathbf{y} and \mathbf{x}_1 , respectively. Here, $\int_0^{t_i} C_T^*(s) ds$

represents the numerical integration of $C_T^*(t_i)$ that are discrete sample data, not the integral of a continuous function.

As in other GA methods, the Logan plot is consistently applicable to data from different voxels or ROIs regardless of their underlying model configurations. However, if a particular model configuration is assumed for the given data, $V_{T, \text{Logan}}$ and β_{Logan} can be related to the specific rate constants included in that configuration; usually the 1TCM or the 2TCM is considered for receptor-ligand studies. The slopes are differently interpreted as Equations (3) or (7), according to the model configurations. For the 1TCM (without k_3 and k_4), the linearity is simply met for all the frame times since $\beta_{\text{Logan}} = -1/k_2$. On the contrary, for the 2TCM, we have to determine t^* because the intercept is not actually a constant:

$$\beta_{\text{Logan}} = -\frac{1}{k_2} \left(1 + \frac{k_3}{k_4} \right) - \frac{1}{k_4} \frac{C_S(t)}{C_T(t)}. \quad (13)$$

The limit value $-1/k_2$ is defined at the steady-state condition of tissue tracer kinetics ($\frac{dC_{\text{ND}}(t)}{dt} = 0$ & $\frac{dC_S(t)}{dt} = 0$):

$$\beta_{\text{Logan}} \rightarrow -\frac{1}{k_2} \left(1 + \frac{k_3}{k_4} \right) - \frac{1}{k_4} \frac{k_3}{k_3 + k_4} = -\frac{1}{k_{2a}^*}. \quad (14)$$

However, the constancy of β_{Logan} can be approximately achieved before the steady state, yielding a good estimate of $V_{T, \text{Logan}}$ ^[63, 68, 70].

Meanwhile, the Logan equation can be re-written for a reference region:

$$\frac{\int_0^t C_R(s) ds}{C_R(t)} = V'_{T, \text{Logan}} \frac{\int_0^t C_P(s) ds}{C_R(t)} + \beta'_{\text{Logan}} \text{ for } t > t^*. \quad (15)$$

Rearranging Equation (15) gives

$$\int_0^t C_P(s) ds = \frac{1}{V'_{T, \text{Logan}}} \left(\int_0^t C_R(s) ds - \beta'_{\text{Logan}} C_R(t) \right). \quad (16)$$

Then, by approximating the plasma integral in Equation (12) using Equation (16), the noninvasive Logan plot based on a reference TAC can be obtained as follows:

$$\frac{\int_0^t C_T(s) ds}{C_T(t)} = \frac{V_{T, \text{Logan}}}{V'_{T, \text{Logan}}} \left(\frac{\int_0^t C_R(s) ds}{C_T(t)} - \frac{\beta'_{\text{Logan}} C_R(t)}{C_T(t)} \right) + \beta_{\text{Logan}}. \quad (17)$$

If the reference region is approximately devoid of receptor sites, BP_{ND} can be determined as $V_{T, \text{Logan}}/V'_{T, \text{Logan}} - 1$ under the assumption that $\frac{K_1}{k_2} = \frac{K'_1}{k'_2}$.

There are several tips for technical efficiency in the implementation of the noninvasive Logan plot. The slope in Equation (17), the DVR, may be stably

estimated by using a population average of β'_{Logan} , $\bar{\beta}'_{\text{Logan}}$, (or the more physiologically meaningful \bar{k}'_2) in place of the individual β'_{Logan} (or k'_2). In this case, the inter-subject variability in β'_{Logan} is blended into an error term of the model and then removed by the fitting process. In addition, the term $\frac{\beta'_{\text{Logan}} C_R(t)}{C_T(t)}$ can be ignored when it is relatively small or becomes constant^[57]; in fact, the term is merged into the error or the intercept term. It is noteworthy that, although the term in parenthesis in Equation (17) is treated as one independent variable in the noninvasive Logan plot method, it can be used as two separate variables for the parameter estimation^[71] that requires multiple linear regression analysis.

Because of its diverse merits, such as model independence, computational efficiency, simple implementation, and statistical reliability under low-noise data, the Logan plot has been extensively used in neuroreceptor binding studies. However, the Logan plot suffers from a crucial limitation, especially in parametric imaging (Figs. 3 and 4), in that it produces a severe negative bias in $V_{T,\text{Logan}}$ or $\frac{V_{T,\text{Logan}}}{V'_{T,\text{Logan}}}$ when $C_T(t)$ is highly contaminated^[72-74]. As shown in Equations (12) and (17), the noise in $C_T(t)$ is entered into both the independent and dependent variables of its model equation while establishing a correlation between them, which therefore makes the model violate the LLS assumptions mentioned. Furthermore, the magnitude of the bias depends on the noise level that is also dependent (but not linearly) on the radioactivity concentration^[72-75]. The effect of noise is also not consistent throughout the parametric image space; high-binding regions usually undergo more severe underestimation. One minor disadvantage of the Logan plot is the requirement of full dynamic scanning to compute $\int_0^t C_T(s) ds$, though only the later parts of the measurements (after t^*) are used for parameter estimation.

Relative equilibrium plot To address the noise-dependent bias issue in the Logan plot, the relative equilibrium-based graphical method (RE plot) was developed for both plasma and reference tissue input functions^[66]. When the tissue to plasma concentration ratio, $\frac{C_T(t)}{C_P(t)}$, becomes a constant, i.e., the RE established after a certain time t^* (Fig. 5, left), tracer

concentrations satisfy the following relationship:

$$\frac{\int_0^t C_T(s) ds}{C_P(t)} = V_{T,\text{RE}} \frac{\int_0^t C_P(s) ds}{C_P(t)} + \beta_{\text{RE}} \text{ for } t > t^*. \quad (18)$$

This model can be derived from compartment model equations or by multiplying the Logan plot model (Equation (12)) by $\frac{C_T(t)}{C_P(t)}$. Note that the constant ratio of tissue-to-plasma concentrations can be achieved at the steady state, but it is also possible to achieve it earlier than the steady state. However, this generally requires somewhat longer times than the Logan linearity condition ($\frac{C_S(t)}{C_T(t)} \rightarrow \text{const}$)^[68].

In addition, when a reference region is also in the RE state for $t > t^*$ ($\frac{C_R(t)}{C_P(t)} = r$), we have the noninvasive RE plot model as follows:

$$\frac{\int_0^t C_T(s) ds}{C_R(t)} = \frac{V_{T,\text{RE}} \int_0^t C_R(s) ds}{V'_{T,\text{RE}} C_R(t)} + \frac{1}{r} \left(\beta_{\text{RE}} - \frac{V_{T,\text{RE}}}{V'_{T,\text{RE}}} \beta'_{\text{RE}} \right), \quad (19)$$

where $V'_{T,\text{RE}}$ and β'_{RE} are the slope and intercept of the RE plot in the reference region. Thus, the invasive RE plot can provide BP_{ND} if the non-receptor region is used for the reference region.

One merit of the RE plot is its high computational efficiency. As shown in Equations (18) and (19), the independent variable is not dependent on the tissue data and is common over all voxel TACs. Therefore, once \mathbf{X} ($x_{1i} = \int_0^{t_i} C_P(s) ds / C_P(t_i)$ or $\int_0^{t_i} C_R^*(s) ds / C_R^*(t_i)$) is computed from the input function, it can be used for all tissue data, that is, only one matrix conversion is required for parametric image generation. However, in the case of the Logan plot, \mathbf{X} needs to be computed and inverted for every voxel. In addition, it is noteworthy that both independent and dependent variables in Equations (18) and (19) have a much lower noise level compared with $C_T(t)$ because the integration reduces fluctuations in the later part of TAC, and $C_R(t)$ is obtained by averaging voxel TACs over a reference ROI. Therefore, the RE plot can achieve effectively unbiased estimation with low variance provided that linearity is established. However, for linearity, tissue tracer kinetics must be at a relative equilibrium state during PET scans, and thus only late data points can be used for the estimation. Thus, good precision properties obtained from a less noisy dependent variable could be

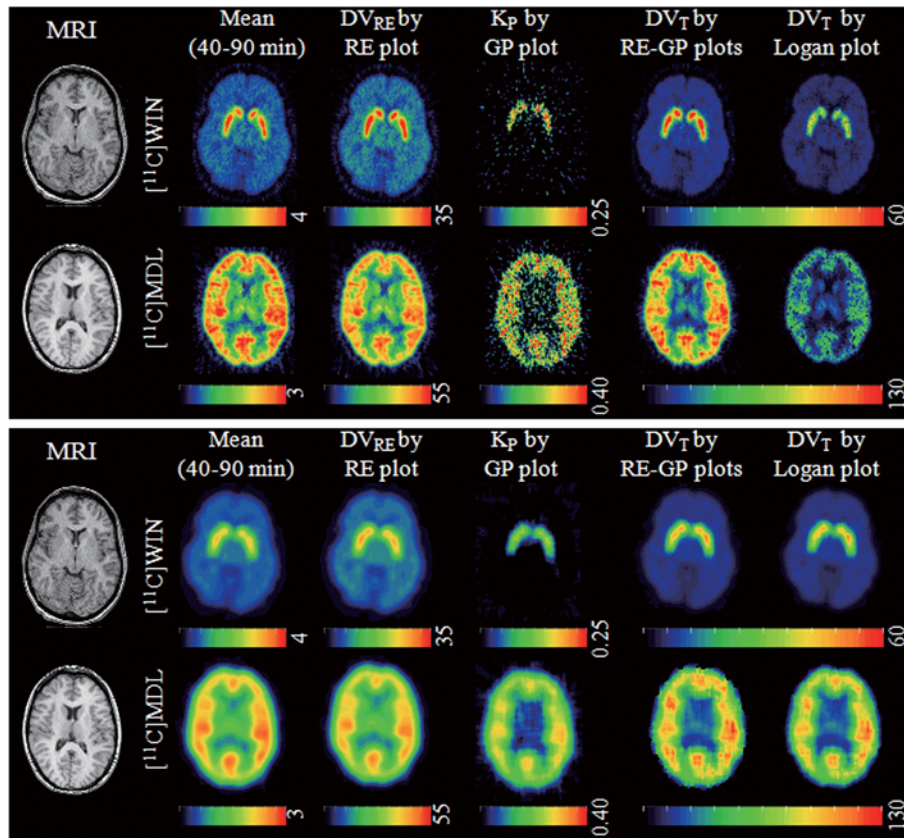


Fig. 3. Top: parametric images of V_T (represented as DV_{RE} or DV_T) and K_{in} (represented as K_p) from various methods: RE plot, RE-GP plot, and Logan plot (reprinted from Zhou et al. Neuroimage 2010^[67] with permission). Bottom: results from de-noised dynamic images (reprinted from Zhou et al. Neuroimage 2010^[67] with permission).

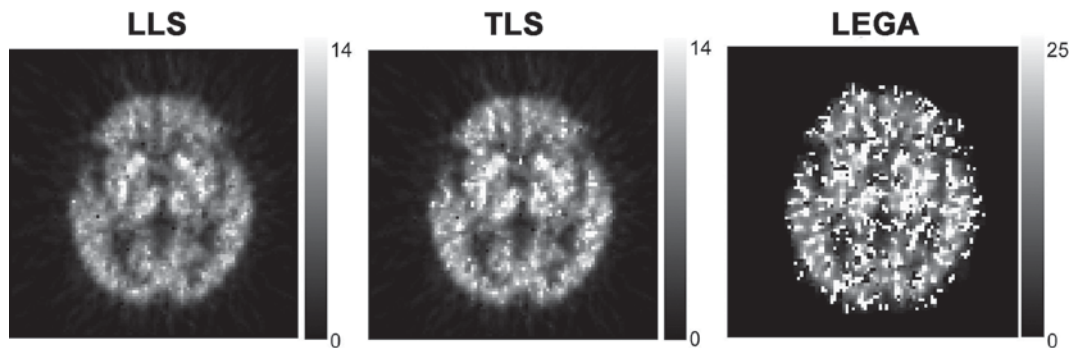


Fig. 4. V_T images from the Logan plot with linear least squares (LLS), total least squares (TLS), and likelihood estimation in graphical analysis (LEGA). The images were made from the same original PET data using $[^{11}C]SA4503$, a radioligand for the σ_1 receptor (reprinted from Kimura et al. Ann Nucl Med 2007^[75] with permission).

compromised with the data reduction because of the relatively late t^* .

Bias reduction for Logan plot In addition to the RE plot, there have been a variety of attempts to reduce the bias in

the LLS estimates from the Logan plot^[19, 36, 56, 69, 76-80]. Those approaches can be categorized by (1) methods to increase the SNR in dynamic images, and (2) those that adopt more sophisticated estimation techniques. In this subsection, we

introduce these two categories.

Data de-noising The most simple and straightforward solution to the bias issue in the Logan plot may be to apply smoothing techniques directly to the dynamic data. Although smoothing approaches are effective, they are not a direct improvement over the Logan plot^[81] and thus can be applied not only to GA but also to all other methods that are affected by noise in the dynamic data. Logan *et al.*^[76] used generalized linear least squares (GLLS)^[42, 82] as a temporal smoothing technique to reduce noise in TAC data, and subsequently applied the Logan plot to the noise-reduced TACs, the result of GLLS. This combination of the Logan plot and GLLS yielded unbiased estimates of V_T up to intermediate noise levels, but suffered from overestimation and significant variability at high noise levels. Joshi *et al.*^[79] suggested the use of principal component analysis (PCA) for the temporal smoothing of TACs. This PCA-based approach demonstrated good performance with both increased accuracy and precision. However, it requires pre-processing for the selection of optimal principal components, and too many components may reintroduce a bias. For spatial domain de-noising, grouping TACs with similar properties such as proximity or functional relations may also be useful^[68, 77, 83]. The main drawback of spatial smoothing techniques is a loss of spatial resolution and additional partial volume effects (Fig. 3 bottom)^[67]. Cselényi *et al.*^[19, 80] proposed two wavelet-based de-noising techniques that can overcome the noise susceptibility with generally good accuracy and not much loss of spatial resolution. However, these techniques are computationally demanding compared with other approaches. In addition to these methods, many other approaches aimed at increasing the SNR of the reconstructed images are also applicable^[27].

Total least squares (TLS) Varga and Szabo^[78] proposed the use of TLS estimation^[84], also referred to as the ‘perpendicular linear regression model’, instead of LLS for the Logan plot model because the TLS considers the noise in the independent as well as in the dependent variables. The TLS method seeks to minimize the following sum of squared orthogonal distances from the measured points to the fitted line (or hyperplane), by perturbing all the noisy variables \mathbf{X} and \mathbf{y} , as follows:

$$\min_{\beta=[\beta_1, \beta_0]^T} \frac{\|\mathbf{X}\beta - \mathbf{y}\|_2^2}{1 + \beta_1^2}, \quad (20)$$

Although this approach may seem to be complicated, it has a closed form solution and thus maintains computational simplicity like LLS.

In the original work^[78], using this TLS method showed that the bias was dramatically reduced and thus the resulting V_T was consistent in accuracy regardless of the noise levels of the TAC but at the expense of increasing variance (Fig. 4). However, such good performance was not reproduced well in other studies where the TLS only partially removed bias^[19, 68, 75, 85]. Although the reason for such discrepancy in the performance between studies is unclear, there are some speculated sources for the remaining bias: a heterogeneity of variances or a correlation between the noise in all the variables^[84, 85]. We speculate that the poor performance of TLS in the Logan plot is mainly due to high noise correlation because the same noise is shared in all the variables of the Logan model through the denominator ($C_T^+(t)$).

Likelihood estimation in graphical analysis (LEGA) Ogden^[36] proposed the LEGA method to suppress the noise-induced bias in the result of the Logan plot. However, the LEGA method implicitly uses the Logan model, unlike other bias-reduction approaches that transform the measured TAC and then directly use the Logan model equation^[19, 69, 76-80]; the Logan model is converted into the following recurrence relation to generate the noise-free TAC predicted by the model,

$$C_T(t_i) = \frac{\sum_{j=1}^{i-1} \Delta t_j C_T(t_j) + \frac{1}{8} \Delta t_i C_T(t_{i-1}) - V_{T, \text{Logan}} \int_0^{t_i} C_P(s) ds}{\beta_{\text{Logan}} - \frac{3}{8} \Delta t_i}, \quad (21)$$

for $k \leq i \leq n$, where Δt_i denotes the duration of the i th frame, $C_T(t_i)$ is the predicted tissue concentration at the mid-frame time t_i (for $k \leq i \leq n$), and k is the index of the first frame satisfying $t_i > t^*$. Then, the solution of the following least squares problem,

$$\min_{V_{T, \text{Logan}} \& \beta_{\text{Logan}}} \left\{ \sum_{i=k}^n C_T^*(t_i) - C_T(t_i) \right\}^2, \quad (22)$$

provides maximum likelihood estimators for $V_{T, \text{Logan}}$ and β_{Logan} under the assumption that errors in the values of the measured TAC, $C_T^+(t)$, are independently and identically distributed normal random variables with zero mean. Because Equation (21) is valid only for $k \leq i \leq n$, the measured values of $C_T^+(t_i)$ for $1 \leq i \leq k-1$ are used for the calculation of $C_T(t_k)$. The LEGA that was originally

developed for the plasma input function was also extended to a reference region method with more complicated update equations for both target tissue and reference tissue TACs^[56].

Since the LEGA method applies the likelihood estimation not to the transformed data but to the original TAC ($C_T(t_i)$), it can circumvent the bias issue associated with the Logan model. However, it does not provide any graphical inspection of the binding characteristic, in contrast to the Logan plot. Hence, to choose a proper value of t^* or k , it needs to rely on the Logan plot or other t^* -selection approaches^[85]. Furthermore, because of the recurrence of predicted values and the nonlinear involvement of $V_{T, \text{Logan}}$ and β_{Logan} , the solution must be computed using an iterative nonlinear optimization algorithm (at least over one-dimensional parameter space for β_{Logan}); the results of the Logan plot may be used for the initial values for the iteration, and for surrogate values when numerical instability occurs.

The major drawback of LEGA in parametric imaging is that the improved accuracy is accomplished at the expense of precision loss that contributes to noisy parametric images as shown in Figure 4^[81, 86]. To improve the variance properties of LEGA, Shidahara *et al.*^[81] suggested a new method based on a maximum *a posteriori* estimation, where a physiological range of parameters is incorporated as prior knowledge and the measured TAC is compared with the predicted TAC, not in the original TAC space, but in the lower-dimensional space that is reduced from the original space using PCA.

Instrumental variable (IV) Logan *et al.*^[69] introduced the IV method^[87, 88] to address the bias problem encountered

in the Logan plot because of the noise in the independent variable. In several disciplines including statistics, the IV method is basically used to remove a correlation between the independent variables (\mathbf{X}) and the error term (ϵ) that can lead to biased estimates in standard linear regression. Although the correlation between \mathbf{X} and ϵ can stem from the noise in the independent variable (even if it is uncorrelated with the noise in the dependent variable) as well as several other sources, the IV method can eliminate the bias regardless of its source^[89]. In addition, TLS can also be considered as a variation on the IV method with a specific instrument that is nonetheless not used explicitly; however, the IV method makes no assumptions about the noise models, unlike the TLS^[90].

The key concept in the IV method is the use of one or more extra variables (not in the model), called instrumental variables or instruments, to separate the (exogenous) part of \mathbf{X} that is uncorrelated with ϵ from the remaining (endogenous) part that is correlated with ϵ . Only the segregated exogenous part of \mathbf{X} is then used for the parameter estimation because the endogenous part is the source of bias in the LLS estimates; given the instruments \mathbf{Z} , the IV estimator is defined as

$$\hat{\beta}_{\text{IV}} = (\mathbf{Z}^T \mathbf{X})^{-1} \mathbf{Z}^T \mathbf{y} \quad (23)$$

This estimator yields unbiased estimates if \mathbf{Z} is uncorrelated with ϵ , and if it is correlated with the endogenous independent variables after removing the effect on them of the other uncorrelated exogenous variables (i.e., conditional on the other independent variables).

The critical point of the IV method is to construct legitimate instruments satisfying these requirements. Logan *et al.*^[69] suggested two methods for the construction: an

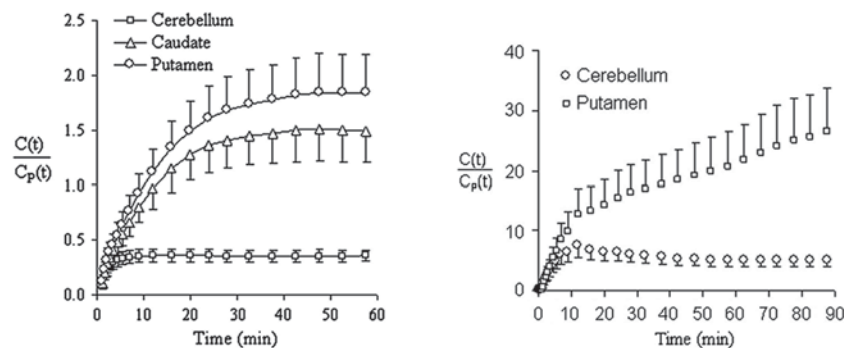


Fig. 5. Left: relative equilibrium (RE) state after $t^* = 42.5$ min in $[^{11}\text{C}]\text{raclopride}$ PET (reprinted from Zhou *et al.* Neuroimage 2009^[66] with permission). Right: violation of RE condition in $[^{11}\text{C}]\text{WIN}$ PET (reprinted from Zhou *et al.* Neuroimage 2010^[67] with permission).

iterative approach proposed by Minchin^[91] and another based on less noisy regional TACs. The main idea common to the two methods is to use $Z = [\int_0^{t_i} C_P(s)ds/C_T(t_i), 1]$, the denoised version of \mathbf{X} that can be considered as the exogenous part of \mathbf{X} by itself when the correlation between \mathbf{X} and ϵ is primarily due to the noise in \mathbf{X} . The first method involves the prediction of $C_T(t_i)$ using Equation (21) and the parameter estimates from the original Logan plot, and the subsequent computation of $\hat{\beta}_{IV}$; this process is repeated until $\hat{\beta}_{IV}$ converges. In the second method, a regional TAC of a large ROI is used for $C_T(t)$, and $\hat{\beta}_{IV}$ is estimated without any iteration. Because the iterative approach has convergence issues, the second method is preferable. Furthermore, according to Logan *et al.*^[69], the second method showed good results when the smoothed reference TAC was used in \mathbf{Z} . On the other hand, the IV approach was extended to the noninvasive Logan plot but \mathbf{Z} was constructed using only the second method based on ROI TACs.

The IV methods successfully reduce the bias but at the expense of variance, much as in other bias-reduction approaches. Instead of improving the IV method itself, to reduce both the bias and variability, Logan *et al.*^[69] suggested the use of the median of the values determined by various modifications of the Logan plot as well as the IV method, methods that have different noise characteristics for the same data.

Irreversible Tracer Models

Invasive Gjedde-Patlak (GP) plot methods For a tracer with an irreversible binding, the GP plot^[60-62] (Fig. 2) has been widely used. Although the term ‘Patlak plot’ or simply ‘graphical analysis’ is often used for this method, we keep the ‘GP plot’ for consistency with the RE-GP plot throughout the paper.

The model equation including the plasma input function (Equation (24)) can be obtained from the 2TCM by assuming $k_4 = 0$ as well as from a general multi-compartment model^[61, 63]. When an equilibrium has been established between the plasma and reversible components (or $\frac{C_{ND}(t)}{C_P(t)}$ becomes effectively constant) for $t > t^*$, the following linear model achieves an asymptotic linearity for an irreversibly-binding tracer:

$$\frac{C_T(t)}{C_P(t)} = K_{in,GP} \frac{\int_0^t C_P(s)ds}{C_P(t)} + \beta_{GP} \text{ for } t > t^*, \quad (24)$$

where the influx rate constant $K_{in,GP} = \frac{K_1 k_3}{k_2 + k_3}$ and the intercept term $\beta_{GP} = \frac{k_2}{k_2 + k_3} \frac{C_{ND}(t)}{C_P(t)}$. Thus, β_{GP} has a positive value in contrast to its equivalents in the Logan or RE plots.

In addition to the common advantages of GA methods, the GP plot has a discriminative one in that it does not require a full dynamic scan because the integration of $C_T(t)$ is not involved, in contrast to other methods such as the Logan plot or the RE plot. Furthermore, it is noteworthy that the GP plot has a model equation very similar to the RE plot (Equation (18)), except for how $C_T(t)$ is involved in a dependent variable. Therefore, the two methods share similar bias properties and computational efficiency owing to using the same independent variable. On the other hand, the variance of the parameter estimate from the GP plot is more sensitive to noise (Fig. 6) than that from the RE plot because $C_T(t)$ (i.e., more noisy data) is directly involved in the dependent variable of the GP plot, while its integration (i.e., less noisy data) is used in the RE plot. This noise sensitivity of the GP plot can be improved through multiple linear analysis for irreversible radiotracers (MLAIR) methods^[22]. Moreover, for a tracer assumed to have effectively irreversible binding ($k_4 \approx 0$) over the scan duration, $K_{in,GP}$ may be underestimated if the dissociation of binding is appreciable^[6]; in such a case, a more general model equation is required to obtain unbiased results^[62].

Noninvasive GP plot methods Concerning the reference region model, the GP plot has two different model equations according to the tracer’s binding type in the reference region. When the reference region has only reversible binding sites, the relationship between $C_P(t)$ and $C_R(t)$ can be represented by the Logan plot equation with a slope $V'_{T,Logan}$ and an intercept β'_{Logan} (for $t > t^*$). Then, by multiplying both sides of Equation (24) by $\frac{C_P(t)}{C_R(t)}$ and substituting Equation (16) into Equation (24), a noninvasive GP plot model can be obtained as follows:

$$\frac{C_T(t)}{C_R(t)} = \frac{K_{in,GP}}{V'_{T,Logan}} \frac{\int_0^t C_R(s)ds}{C_R(t)} + \left\{ \frac{C_P(t)}{C_R(t)} \beta_{GP} - \frac{K_{in,GP}}{V'_{T,Logan}} \beta'_{Logan} \right\}. \quad (25)$$

Thus, the slope and the intercept terms can be estimated using simple linear regression when $\frac{C_P(t)}{C_R(t)} \beta_{GP}$ ($\propto \frac{C_{ND}(t)}{C_R(t)}$) and β'_{Logan} become effectively constant for $t > t^*$ ^[62, 68]. Meanwhile, for a reference region with irreversible uptake, the invasive GP equation is used to describe $C_P(t)$ using

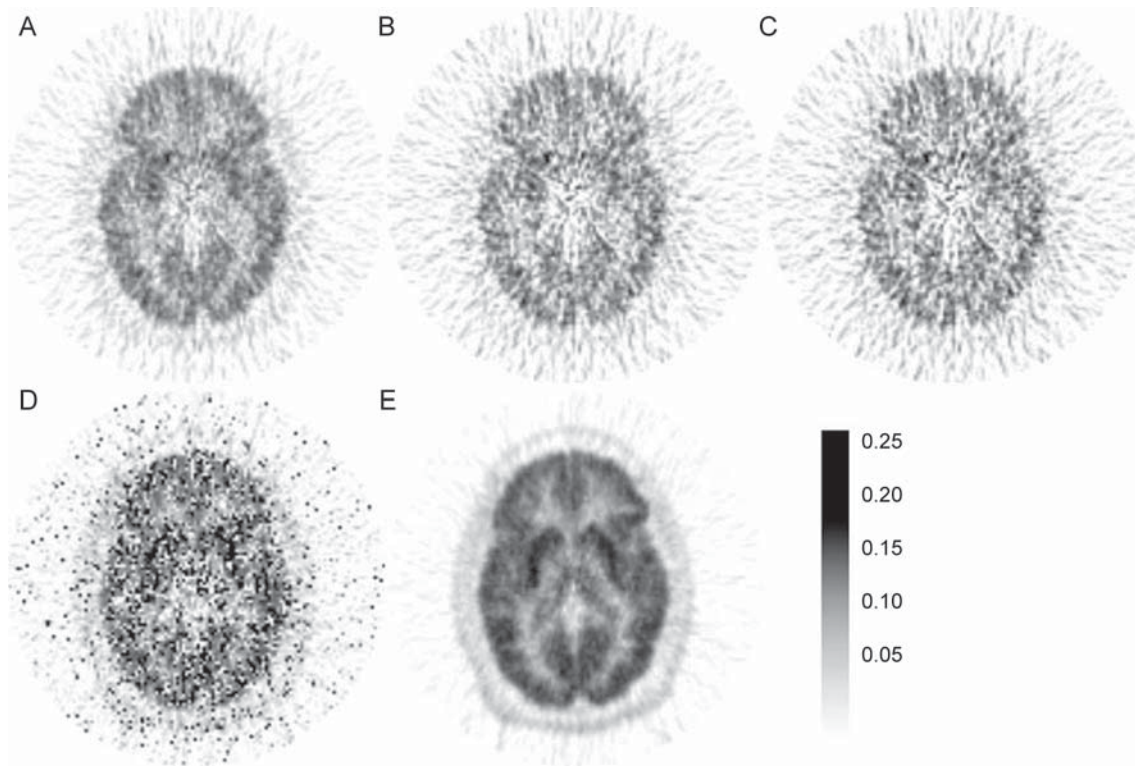


Fig. 6. K_{in} parametric images from 90-min $[^{11}\text{C}]\text{MeNTI}$ PET of a healthy volunteer obtained using various methods: (A) GP plot using $t' = 10$ min, (B) GP plot using $t' = 20$ min, (C) GP plot using $t' = 30$ min, (D) MLAIR1, and (E) MLAIR2 (reprinted from Kim *et al.* *J Cereb Blood Flow Metab* 2008^[22] with permission; GP: Gjedde-Paltak, MLAIR: multiple linear analysis for irreversible radiotracers).

$C_R(t)$. Then, another linear model of a noninvasive GP plot can be obtained as follows^[37, 38],

$$\int_{t^*}^t C_T(s) ds = \frac{K_{in,GP}}{K'_{in,GP}} \int_{t^*}^t C_R(s) ds + \frac{\beta_{GP}}{K'_{in,GP}} [C_R(t) - C_R(t^*)] - \frac{\beta'_{GP}}{K'_{in,GP}} [C_T(t) - C_T(t^*)] \text{ for } t > t^*, \quad (26)$$

where $K'_{in,GP}$ and β'_{GP} are the slope and intercept of the invasive GP plot applied to the reference region. This method requires that the kinetics of the radioligand in both the tissue and reference regions can be modeled using the invasive GP plot (Equation (24)).

The former noninvasive model would inherit all the properties of the original invasive GP plot model, provided that a sufficiently large ROI size is used so as to obtain $C_R(t)$ with as low a noise-level as that of $C_p(t)$; otherwise, the accuracy of the resulting estimates can be damaged by the noisy independent variable, like in the Logan plot. On the contrary, the latter noninvasive model has several distinct features compared with the original invasive and the

former noninvasive models. First, this model is not a simple linear regression model but a multiple linear regression model. Therefore, a graphical plot with a straight-line fit is not provided; although the visualization of 3-dimensional hyper-plane fit is possible instead, its interpretation is not as straightforward as that of GA. In addition, this model includes the integration of $C_T(t)$ in contrast to the others. Nevertheless, it also avoids the requirement of a full dynamic scan like the others; this property of the original GP plot model is just transformed into the integration from t^* to t .

One drawback of these noninvasive methods is that the net accumulation of radioligand is acquired only in a relative or normalized form. Nevertheless, the former noninvasive model has found applications because of its history going back to 1985; the method has been frequently used in 6- $[^{18}\text{F}]\text{fluoro-L-dopa}$ studies because of a good correlation between its own results and those from the invasive counterpart^[92-95]. However, the latter method was

introduced in relatively recent years and thus has not been sufficiently investigated or used, and has been applied only to ROI data. Although the ROI results have shown good accuracy and precision, future parametric imaging may suffer from severe underestimation because $C_T(t)$ is used for independent variables.

Bi-graphical Analysis

Although GA generally provides robust parameter estimation by focusing on only two parameters, it may end up missing some information or exploiting only fragmentary information from given data. However, a combination of two methods or a dual application to different parts of the data may take full advantage of the data. In this sense, graphical methods to estimate V_T , which we went through in the previous subsections, can also be viewed as a bi-graphical technique when they are applied to target and reference regions separately to provide BP_{ND} computation.

RE-GP plots Recently, a bi-graphical analysis, named the RE-GP plot, has been proposed for the quantification of reversible tracer binding that may not be at the RE state during a PET scan because of slow binding kinetics as shown in Fig. 5 (right). Its model equation is given as follows,

$$\frac{\int_0^t C_T(s) ds}{C_T(t)} = V_{T,REGP} \frac{\int_0^t C_P(s) ds}{C_T(t)} + \beta_{REGP} \text{ for } t > t^*, \quad (27)$$

$$V_{T,REGP} = V_{T,RE} - \frac{\beta_{RE}}{\beta_{GP}} K_{in,GP}, \quad (28)$$

$$\beta_{REGP} = \frac{\beta_{RE}}{\beta_{GP}}, \quad (29)$$

where $V_{T,RE}$ and β_{RE} , (or $K_{in,GP}$ and β_{GP}) are the slope and intercept of the RE plot (or the GP plot) based on a plasma input function, respectively. Note that this RE-GP equation is the same as Equation (12) of the Logan plot except for the parameters. However, the parameters $V_{T,REGP}$ and β_{REGP} are estimated not by regression as in the Logan plot, but by arithmetic operations on the parameter estimates obtained by applying the RE plot and the GP plot separately. Thus, the RE-GP method requires the measurement of the plasma input function to estimate the parameters of the RE and GP plots.

The linearity period $t > t^*$ for the RE-GP method mainly follows that of the Logan plot^[67]. It is better to use the t^* suitable for the Logan plot in each application of the RE

plot and the GP plot rather than to determine and use the individual t^* for each plot; the t^* for each may be uncertain because of the slightly curved shape of the RE plot or high fluctuation in the GP plot as shown in Fig. 2.

The RE-GP plot maintains the properties of both plots, such as computational efficiency and statistical characteristics. As the RE plot and the GP plot have the same effectively noise-free independent variable in their model equation, accuracies of their target parameter estimates and thus those of the RE-GP method are not affected by noisy $C_T(t)$ in contrast to the Logan plot. However, the GP parameters are usually of high variance because of noisy $C_T(t)$ in the dependent variable (Figs. 3 and 6). Therefore, it is advantageous to apply a spatial smoothing filter to the GP parametric images before computing the parametric images of $V_{T,REGP}$ and β_{REGP} ^[67].

The original RE-GP can circumvent not only the bias issue in the Logan plot but also that of the RE plot (Fig. 3). As we introduced previously, the RE plot yields an underestimated V_T when sufficient time is not allowed for the tracer kinetics to reach the RE state (Fig. 3). The missing information, which the RE plot failed to capture because of the violation of the RE requirement, can be compensated for by the results from the GP plot (Fig. 3). In other words, the results of the RE plot describe the components achieving the RE state during the PET scan while those of the GP plot compensate for non-relative equilibrium components.

Ito plot Ito *et al.*^[65] developed a form of bi-graphical analysis where the Yokoi plot^[64] is applied to the early part of the data frames and the later part separately, and then the resulting parameters from the separate applications are combined to generate BP_{ND} , the parameter of interest; the Yokoi plot was originally proposed to estimate the cerebral blood flow (K_1) and the total distribution volume (V_T) only for tracers well described by the 1TCM, and was recently generalized into the Ito plot^[65] for the neuroreceptor-radioligand binding studies where the 2TCM is involved. The Yokoi plot and thus the Ito plot rely upon the following linear relationship:

$$\frac{C_T(t)}{\int_0^t C_P(s) ds} = \beta_1 \frac{\int_0^t C_T(s) ds}{\int_0^t C_P(s) ds} + \beta_2 \text{ for } t > t^* \text{ or } t \rightarrow 0. \quad (30)$$

Equation (30) yields a straight line through all data

frames (Fig. 7) when there is no specific binding in a target region (e.g., the Yokoi plot for 1TCM configuration tracers), and the slope (β_1), y -intercept (β_2), and x -intercept (β_2/β_1) of the regression line represent $-k_2$, K_1 , and $V_T (= V_{ND})$, respectively. On the contrary, when applied to regions with specific binding (e.g., the Ito plot for 2TCM configuration tracers), Equation (30) generates a curve (Fig. 7) that reflects the dynamic effect of specific binding concentration on the measured tissue data. The fitted regression line can be characterized by $-k_2$ (slope), K_1 (y -intercept), and V_{ND} (x -intercept) for the early part of the data for $t \rightarrow 0$ in which $C_{ND}(t)$ dominates the measured tissue concentration $C_T(t)$. The line can be specified by $-k_{2a}^*$, $k_{2a}^* V_T$ and $V_T (= V_{ND} + V_S)$, respectively, for late-part data ($t > t^*$) that can be approximately described with the 1TCM and its apparent rate constants $k_{2a}^* V_T$ (for influx) and k_{2a}^* (for efflux) after t^* (Ito et al. 2010^[65, 67]); k_{2a}^* becomes k_{2a} (Fig. 1 and Equation (6)) when rapid equilibrium is established at $t^* \approx 0$ owing to relatively large k_3 and k_4 . Care should be taken in V_{ND} estimation because the use of more data points increases not only the reliability of estimation but also the bias due to the violation of $C_T(t) \approx C_{ND}(t)$ for $t \rightarrow 0$ ^[96].

Based upon the plot characteristics that vary according

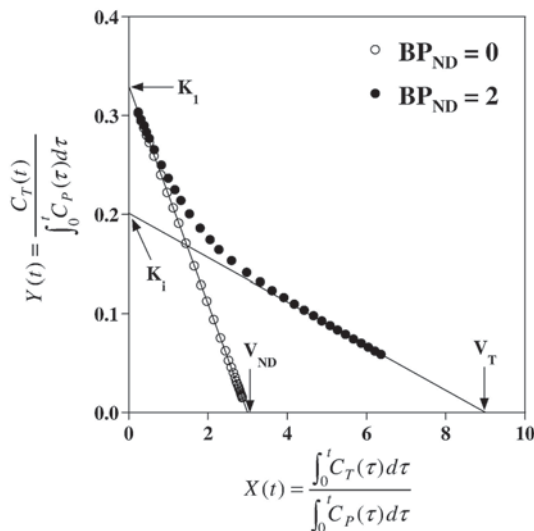


Fig. 7. An example of Ito plot analysis. The y - and x -intercepts of the regression line represent K_1 and V_{ND} , respectively, for early data frames, whereas $K_1 = k_{2a}^* V_T$ and V_T for the late part of the data (after the equilibrium time) (reprinted from Ito et al. Neuroimage 2010^[65] with permission). Open (or filled) circles display examples of applications for one- (or two-) tissue compartment model data.

to the model configuration, the Ito plot model (Equation (30)) can be useful for graphically distinguishing whether a target region is devoid of specific binding or not^[65]. Furthermore, the Ito plot can be used to compute BP_{ND} using the resulting V_{ND} and V_T estimates. The major distinction between this and other reference region methods is that *a priori* knowledge of the reference region is not required. These features may be obtained with the Logan plot because the Ito plot and the Logan plot are based on the same linear relationship except for the different arrangement of parameters and variables (thereby, different noise characteristics). Note that the Yokoi and Ito plots are both GA techniques for V_T estimation, even though we introduce them here as bi-graphical analysis methods for BP_{ND} generation.

On the other hand, the main drawback of the Yokoi and Ito plots is that the precision of estimates is usually low because of noise effects^[65, 69, 96], particularly at the voxel-level, for several reasons: (1) the dependent variable includes $C_T(t)$, the major source of noise in kinetic modeling, as its numerator; (2) the estimation of V_{ND} involves early time frames, usually with a very low SNR^[8]; and (3) the parameters of interest, V_T and V_{ND} , are computed by dividing the y -intercept by the slope. Therefore, as shown in Figure 8, the de-noising of dynamic images is essential to improve the SNR of parametric images^[8, 96].

Summary

PET research has greatly contributed to advance our understanding of the brain in health and disease^[4, 97-102], quantitative neuroreceptor mapping with kinetic modeling has played a key role in such contributions by offering accurate visualization and voxel-wise analysis of the distribution and activity of various neuroreceptors that are the most influential structures in the brain.

In this article, we have presented an overview of GA-based parametric image generation from dynamic neuroreceptor PET data. Although parametric imaging may cover broad concepts, including the voxel-wise measurement of standard uptake values from a single static image, or other standard kinetic parameters such as peak concentration from dynamic data^[5, 8, 31], throughout the paper, it refers to a voxel-wise application of specific mathematical modeling approaches to analyze

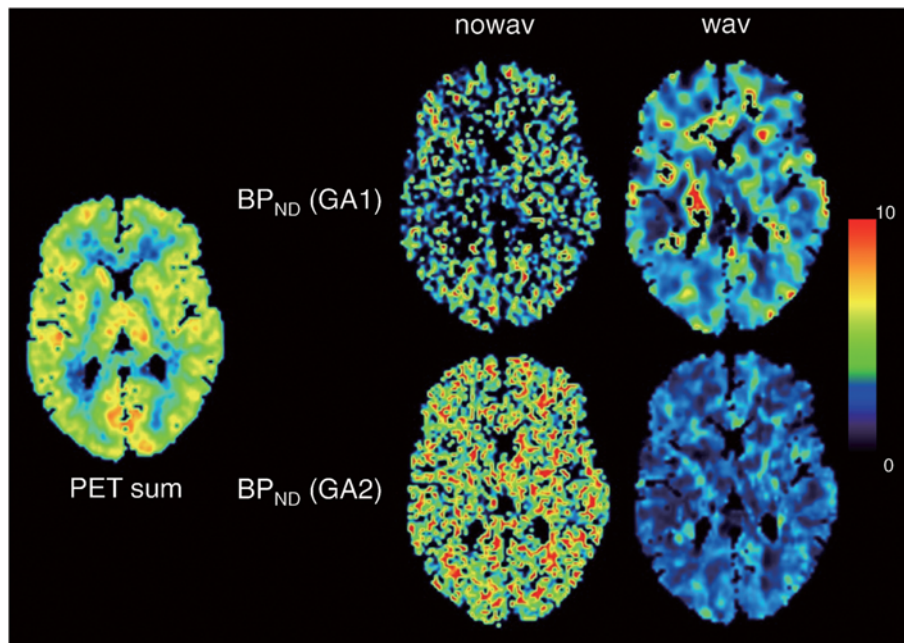


Fig. 8. BP_{ND} images obtained by the Ito plot (upper, GA1) and the Logan plot (lower, GA2) from dynamic PET with [^{18}F]FEDAA1106, a radioligand for translocator protein imaging, before wavelet de-noising (nowav) and after wavelet de-noising (wav) (reprinted from Ikoma *et al.* Neuroimage 2013^[96] with permission).

reconstructed dynamic PET images. In GA methods, a simple linear model with only two parameters is used to fit only the later portion of the measured data. Thanks to the linearization and simplification of the underlying model, GA methods achieve very desirable parametric imaging that is independent of any compartmental model configuration, robust to noise, and computationally efficient. However, both the linearization and simplification depend on several assumptions that are commonly hard to satisfy simultaneously. Therefore, the recent advances in GA approaches have been mainly based on a reduction of specific assumptions or replacement with new ones.

Recently, parametric imaging techniques have shown two major trends: a conventional pipeline of analyzing the reconstructed dynamic data and a direct reconstruction of parametric images from coincidence count data^[17, 20]. Although the direct reconstruction technique is considered as the ultimate path for parametric image generation because of its potential advantages in high-resolution PET^[17], this field was inactive until recently despite its early emergence and has several challenges to address, such as high algorithmic complexity^[20]. Therefore, we believe that

the indirect parametric imaging methods, especially the GA techniques we have considered, are still invaluable and furthermore will play a leading role in achieving the ultimate goal. We refer readers interested in direct parametric imaging to a comprehensive review by Wang and Qi^[20], since it is beyond the scope of this paper.

ACKNOWLEDGMENTS

This review was supported by a grant from the Korea Healthcare Technology R&D Project, Ministry of Health & Welfare, Republic of Korea (HI13C01630200) and by the Industrial Strategic Technology Development Program (10030030) funded by the Ministry of Trade, Industry & Energy, Korea.

Received date: 2014-06-08; Accepted date: 2014-08-15

REFERENCES

- [1] Ichise M, Meyer JH, Yonekura Y. An introduction to PET and SPECT neuroreceptor quantification models. *J Nucl Med* 2001, 42: 755–763.
- [2] Meyer JH, Ichise M. Modeling of receptor ligand data in PET and SPECT imaging: A review of major approaches. *J*

- Neuroimaging 2001, 11: 30–39.
- [3] Watabe H, Ikoma Y, Kimura Y, Naganawa M, Shidahara M. PET kinetic analysis—compartmental model. *Ann Nucl Med* 2006, 20: 583–588.
- [4] Zaidi H, Shidahara M. Neuroreceptor imaging. In: Choi IY and Gruetter R (Eds.). *Neural Metabolism In Vivo*. New York, USA: Springer, 2012: 305–329.
- [5] Lee JS, Lee DS. Tracer kinetic analysis for PET and SPECT. *Medical Imaging: Technology and Applications* 2013.
- [6] Mintun MA, Raichle ME, Kilbourn MR, Wooten GF, Welch MJ. A quantitative model for the *in vivo* assessment of drug binding sites with positron emission tomography. *Ann Neurol* 1984, 15: 217–227.
- [7] Carson RE. Tracer kinetic modeling in PET. In: Bailey DL, Townsend DW, Valk PE, Maisey MN (Eds). *Positron Emission Tomography*. London, Springer, 2005: 127–159.
- [8] Feng DD. *Biomedical Information Technology*. Academic Press, 2008.
- [9] Cherry SR, Sorenson JA, Phelps ME. *Physics in Nuclear Medicine*. Elsevier Health Sciences, 2012.
- [10] Koeppe R, Holthoff V, Frey K, Kilbourn M, Kuhl D. Compartmental analysis of [¹¹C]flumazenil kinetics for the estimation of ligand transport rate and receptor distribution using positron emission tomography. *J Cereb Blood Flow Metab* 1991, 11: 735–744.
- [11] Kazumata K, Dhawan V, Chaly T, Antonini A, Margouleff C, Belakhlef A, *et al.* Dopamine transporter imaging with fluorine-18-FPCIT and PET. *J Nucl Med* 1998, 39: 1521–1530.
- [12] Chen M-K, Lee J-S, McGlothlan JL, Furukawa E, Adams RJ, Alexander M, *et al.* Acute manganese administration alters dopamine transporter levels in the non-human primate striatum. *Neurotoxicology* 2006, 27: 229–236.
- [13] Lim K, Kwon J, Jang I, Jeong J, Lee J, Kim H, *et al.* Modeling of brain D₂ receptor occupancy-plasma concentration relationships with a novel antipsychotic, YKP1358, using serial PET scans in healthy volunteers. *Clin Pharmacol Ther* 2007, 81: 252–258.
- [14] Weerts EM, Kim YK, Wand GS, Dannals RF, Lee JS, Frost JJ, *et al.* Differences in δ - and μ -opioid receptor blockade measured by positron emission tomography in naltrexone-treated recently abstinent alcohol-dependent subjects. *Neuropsychopharmacology* 2008, 33: 653–665.
- [15] Kim JW, Lee JS, Kim SJ, Hoigebazar L, Shin KH, Yu KS, *et al.* Compartmental modeling and simplified quantification of [¹¹C]sertraline distribution in human brain. *Arch Pharm Res* 2012, 35: 1591–1597.
- [16] Lee JY, Seo SH, Kim YK, Yoo HB, Kim YE, Song IC, *et al.* Extrastriatal dopaminergic changes in Parkinson's disease patients with impulse control disorders. *J Neurol Neurosurg Psychiatry* 2014, 85: 23–30.
- [17] Carson RE. Tracer kinetic parametric imaging in PET. In: 2004 2nd IEEE International Symposium on Biomedical Imaging: Nano to Macro. 2004: 611–615.
- [18] Lee JS, Lee DS, Ahn JY, Yeo JS, Cheon GJ, Kim S-K, *et al.* Generation of parametric image of regional myocardial blood flow using H₂¹⁵O dynamic PET and a linear least-squares method. *J Nucl Med* 2005, 46: 1687–1695.
- [19] Cselényi Z, Olsson H, Halldin C, Gulyás B, Farde L. A comparison of recent parametric neuroreceptor mapping approaches based on measurements with the high affinity PET radioligands [¹¹C]FLB 457 and [¹¹C]WAY 100635. *Neuroimage* 2006, 32: 1690–1708.
- [20] Wang G, Qi J. Direct estimation of kinetic parametric images for dynamic PET. *Theranostics* 2013, 3: 802–815.
- [21] Gunn RN, Lammertsma AA, Hume SP, Cunningham VJ. Parametric imaging of ligand-receptor binding in PET using a simplified reference region model. *Neuroimage* 1997, 6: 279–287.
- [22] Kim SJ, Lee JS, Kim YK, Frost J, Wand G, McCaul ME, *et al.* Multiple linear analysis methods for the quantification of irreversibly binding radiotracers. *J Cereb Blood Flow Metab* 2008, 28: 1965–1977.
- [23] Wienhard K, Schmand M, Casey ME, Baker K, Bao J, Eriksson L, *et al.* The ECAT HRRT: performance and first clinical application of the new high resolution research tomograph. *IEEE Transactions on Nuclear Science* 2002, 49: 104–110.
- [24] Zhou Y, Huang SC, Bergsneider M, Wong DF. Improved parametric image generation using spatial-temporal analysis of dynamic PET studies. *Neuroimage* 2002, 15: 697–707.
- [25] Alpert NM, Yuan F. A general method of Bayesian estimation for parametric imaging of the brain. *Neuroimage* 2009, 45: 1183–1189.
- [26] Dean Fang Y-H, El Fakhri G, Becker JA, Alpert NM. Parametric imaging with Bayesian priors: A validation study with ¹¹C-Altropane PET. *Neuroimage* 2012, 61: 131–138.
- [27] Kamasak M. Effects of spatial regularization on kinetic parameter estimation for dynamic PET. *Biomed Signal Process Control* 2014, 9: 6–13.
- [28] Innis RB, Cunningham VJ, Delforge J, Fujita M, Gjedde A, Gunn RN, *et al.* Consensus nomenclature for *in vivo* imaging of reversibly binding radioligands. *J Cereb Blood Flow Metab* 2007, 27: 1533–1539.
- [29] Gunn RN, Gunn SR, Cunningham VJ. Positron emission tomography compartmental models. *J Cereb Blood Flow Metab* 2001, 21: 635–652.
- [30] Morris ED, Endres CJ, Schmidt KC, Christian BT, Muzic RFJ, Fisher RE. Kinetic modeling in positron emission tomography. In: Wernick MN, Aarsvold JN. *Emission Tomography: The*

- Fundamentals of PET and SPECT. Elsevier, 2004: 499–540.
- [31] Bentourkia Mh, Zaidi H. Tracer kinetic modeling in PET. *PET Clinics* 2007, 2: 267–277.
- [32] Huang S-C, Barrio JR, Phelps ME. Neuroreceptor assay with positron emission tomography: equilibrium versus dynamic approaches. *J Cereb Blood Flow Metab* 1986, 6: 515–521.
- [33] Lammertsma AA, Hume SP. Simplified reference tissue model for PET receptor studies. *Neuroimage* 1996, 4: 153–158.
- [34] Phelps M, Huang S, Hoffman E, Selin C, Sokoloff L, Kuhl D. Tomographic measurement of local cerebral glucose metabolic rate in humans with (F–18) 2-fluoro-2-deoxy-D-glucose: validation of method. *Ann Neurol* 1979, 6: 371–388.
- [35] Huang S-C, Phelps ME, Hoffman EJ, Sideris K, Selin CJ, Kuhl DE. Noninvasive determination of local cerebral metabolic rate of glucose in man. *Am J Physiol* 1980, 238: E69–E82.
- [36] Ogden RT. Estimation of kinetic parameters in graphical analysis of PET imaging data. *Stat Med* 2003, 22: 3557–3568.
- [37] Wu YG. Noninvasive quantification of local cerebral metabolic rate of glucose for clinical application using positron emission tomography and ¹⁸F-fluoro-2-deoxy-D-glucose. *J Cereb Blood Flow Metab* 2008, 28: 242–250.
- [38] Zheng X, Wen L, Yu SJ, Huang SC, Feng DD. A study of non-invasive Patlak quantification for whole-body dynamic FDG-PET studies of mice. *Biomed Signal Process Control* 2012, 7: 438–446.
- [39] Chen K, Bandy D, Reiman E, Huang SC, Lawson M, Feng D, *et al.* Noninvasive quantification of the cerebral metabolic rate for glucose using positron emission tomography, ¹⁸F-fluoro-2-deoxyglucose, the Patlak method, and an image-derived input function. *J Cereb Blood Flow Metab* 1998, 18: 716–723.
- [40] Kim SJ, Lee JS, Im KC, Kim SY, Park SA, Lee SJ, *et al.* Kinetic modeling of 3'-deoxy-3'-¹⁸F-fluorothymidine for quantitative cell proliferation imaging in subcutaneous tumor models in mice. *J Nucl Med* 2008, 49: 2057–2066.
- [41] Kim JH, Kim YH, Kim YJ, Yang BY, Jeong JM, Youn H, *et al.* Quantitative positron emission tomography imaging of angiogenesis in rats with forelimb ischemia using ⁶⁸Ga-NOTA-c(RGDyK). *Angiogenesis* 2013, 16: 837–846.
- [42] Feng D, Huang SC, Wang X. Models for computer simulation studies of input functions for tracer kinetic modeling with positron emission tomography. *Int J Biomed Comput* 1993, 32: 95–110.
- [43] Phillips RL, Chen CY, Wong DF, London ED. An improved method to calculate cerebral metabolic rates of glucose using PET. *J Nucl Med* 1995, 36: 1668–1679.
- [44] Takikawa S, Dhawan V, Spetsieris P, Robeson W, Chaly T, Dahl R, *et al.* Noninvasive quantitative fluorodeoxyglucose PET studies with an estimated input function derived from a population-based arterial blood curve. *Radiology* 1993, 188: 131–136.
- [45] Cunningham VJ, Hume SP, Price GR, Ahier RG, Cremer JE, Jones A. Compartmental analysis of diprenorphine binding to opiate receptors in the rat *in vivo* and its comparison with equilibrium data *in vitro*. *J Cereb Blood Flow Metab* 1991, 11: 1–9.
- [46] Hume SP, Myers R, Bloomfield PM, Opacka-Juffry J, Cremer JE, Ahier RG, *et al.* Quantitation of Carbon-11-labeled raclopride in rat striatum using positron emission tomography. *Synapse* 1992, 12: 47–54.
- [47] Lammertsma A, Bench C, Hume S, Osman S, Gunn K, Brooks D, *et al.* Comparison of methods for analysis of clinical [¹¹C]raclopride studies. *J Cereb Blood Flow Metab* 1996, 16: 42–52.
- [48] Watabe H, Carson R, Iida H. The reference tissue model: Three compartments for the reference region. *Neuroimage* 2000, 11: S12.
- [49] Feng D, Wong KP, Wu CM, Siu WC. A technique for extracting physiological parameters and the required input function simultaneously from PET image measurements: Theory and simulation study. *IEEE Trans Inf Technol Biomed* 1997, 1: 243–254.
- [50] Watabe H, Channing MA, Riddell C, Jousse F, Libutti SK, Carrasquillo JA, *et al.* Noninvasive estimation of the aorta input function for measurement of tumor blood flow with [¹⁵O] water. *IEEE Trans Med Imaging* 2001, 20: 164–174.
- [51] Wu HM, Hoh CK, Choi Y, Schelbert HR, Hawkins RA, Phelps ME, *et al.* Factor analysis for extraction of blood time-activity curves in dynamic FDG-PET studies. *J Nucl Med* 1995, 36: 1714–1722.
- [52] Lee JS, Lee DS, Ahn JY, Cheon GJ, Kim SK, Yeo JS, *et al.* Blind separation of cardiac components and extraction of input function from H₂¹⁵O dynamic myocardial PET using independent component analysis. *J Nucl Med* 2001, 42: 938–943.
- [53] Ahn JY, Lee DS, Lee JS, Kim SK, Cheon GJ, Yeo JS, *et al.* Quantification of regional myocardial blood flow using dynamic H₂¹⁵O PET and factor analysis. *J Nucl Med* 2001, 42: 782–787.
- [54] Naganawa M, Kimura Y, Ishii K, Oda K, Ishiwata K, Matani A. Extraction of a plasma time-activity curve from dynamic brain PET images based on independent component analysis. *IEEE Trans Biomed Eng* 2005, 52: 201–210.
- [55] Parker BJ, Feng DD. Graph-based Mumford-Shah segmentation of dynamic PET with application to input function estimation. *IEEE Trans Nucl Sci* 2005, 52: 79–89.
- [56] Zanderigo F, Ogden RT, Parsey RV. Reference region

- approaches in PET: a comparative study on multiple radioligands. *J Cereb Blood Flow Metab* 2013, 33: 888–897.
- [57] Logan J, Fowler JS, Volkow ND, Wang GJ, Ding YS, Alexoff DL. Distribution volume ratios without blood sampling from graphical analysis of PET data. *J Cereb Blood Flow Metab* 1996, 16: 834–840.
- [58] Wong DF, Wagner HN, Dannals RF, Links JM, Frost JJ, Ravert HT, *et al.* Effects of age on dopamine and serotonin receptors measured by positron tomography in the living human brain. *Science* 1984, 226: 1393–1396.
- [59] Beck JV, Arnold KJ. *Parameter Estimation in Engineering and Science*. New York: John Wiley & Sons, 1977.
- [60] Gjedde A. High- and low-affinity transport of D-glucose from blood to brain. *J Neurochem* 1981, 36: 1463–1471.
- [61] Patlak CS, Blasberg RG, Fenstermacher JD. Graphical evaluation of blood-to-brain transfer constants from multiple-time uptake data. *J Cereb Blood Flow Metab* 1983, 3: 1–7.
- [62] Patlak CS, Blasberg RG. Graphical evaluation of blood-to-brain transfer constants from multiple-time uptake data. Generalizations. *J Cereb Blood Flow Metab* 1985, 5: 584–590.
- [63] Logan J, Fowler JS, Volkow ND, Wolf AP, Dewey SL, Schlyer DJ, *et al.* Graphical analysis of reversible radioligand binding from time-activity measurements applied to [N - ^{11}C -methyl]-(-)-cocaine PET studies in human subjects. *J Cereb Blood Flow Metab* 1990, 10: 740–747.
- [64] Yokoi T, Iida H, Itoh H, Kanno I. A new graphic plot analysis for cerebral blood flow and partition coefficient with iodine-123-iodoamphetamine and dynamic SPECT validation studies using oxygen-15-water and PET. *J Nucl Med* 1993, 34: 498–505.
- [65] Ito H, Yokoi T, Ikoma Y, Shidahara M, Seki C, Naganawa M, *et al.* A new graphic plot analysis for determination of neuroreceptor binding in positron emission tomography studies. *Neuroimage* 2010, 49: 578–586.
- [66] Zhou Y, Ye W, Brašić JR, Crabb AH, Hilton J, Wong DF. A consistent and efficient graphical analysis method to improve the quantification of reversible tracer binding in radioligand receptor dynamic PET studies. *Neuroimage* 2009, 44: 661–670.
- [67] Zhou Y, Ye W, Brašić JR, Wong DF. Multi-graphical analysis of dynamic PET. *Neuroimage* 2010, 49: 2947–2957.
- [68] Logan J. A review of graphical methods for tracer studies and strategies to reduce bias. *Nucl Med Biol* 2003, 30: 833–844.
- [69] Logan J, Alexoff D, Fowler JS. The use of alternative forms of graphical analysis to balance bias and precision in PET images. *J Cereb Blood Flow Metab* 2011, 31: 535–546.
- [70] Schmidt KC, Turkheimer FE. Kinetic modeling in positron emission tomography. *quarterly J Nucl Med* 2002, 46: 70–85.
- [71] Ichise M, Ballinger JR, Golan H, Vines D, Luong A, Tsai S, *et al.* Noninvasive quantification of dopamine D_2 receptors with iodine-123-IBF SPECT. *J Nucl Med* 1996, 37: 513–520.
- [72] Carson RE. PET parameter estimation using linear integration methods: Bias and variability considerations. In: Uemura K, Lassen NA, Jones Y, Kanno I (Eds). *Quantification of Brain Function: Tracer Kinetics and Image Analysis in Brain PET*. Amsterdam: Elsevier Science Publishers, 1993.
- [73] Abi-Dargham A, Martinez D, Mawlawi O, Simpson N, Hwang DR, Slifstein M, *et al.* Measurement of striatal and extrastriatal dopamine D_1 receptor binding potential With [^{11}C] NNC 112 in humans: validation and reproducibility. *J Cereb Blood Flow Metab* 2000, 20: 225–243.
- [74] Slifstein M, Laruelle M. Effects of statistical noise on graphic analysis of PET neuroreceptor studies. *J Nucl Med* 2000, 41: 2083–2088.
- [75] Kimura Y, Naganawa M, Shidahara M, Ikoma Y, Watabe H. PET kinetic analysis—Pitfalls and a solution for the Logan plot. *Ann Nucl Med* 2007, 21: 1–8.
- [76] Logan J, Fowler JS, Volkow ND, Ding YS, Wang GJ, Alexoff DL. A strategy for removing the bias in the graphical analysis method. *J Cereb Blood Flow Metab* 2001, 21: 307–320.
- [77] Logan J, Fowler JS, Ding YS, Franceschi D, Wang GJ, Volkow ND, *et al.* Strategy for the formation of parametric images under conditions of low injected radioactivity applied to PET studies with the irreversible monoamine oxidase A tracers [^{11}C]Clorgyline and Deuterium-substituted [^{11}C] Clorgyline. *J Cereb Blood Flow Metab* 2002, 22: 1367–1376.
- [78] Varga J, Szabo Z. Modified regression model for the Logan plot. *J Cereb Blood Flow Metab* 2002, 22: 240–244.
- [79] Joshi A, Fessler JA, Koeppe RA. Improving PET receptor binding estimates from Logan plots using principal component analysis. *J Cereb Blood Flow Metab* 2008, 28: 852–865.
- [80] Cselényi Z, Olsson H, Farde L, Gulyás B. Wavelet-aided parametric mapping of cerebral dopamine D_2 receptors using the high affinity PET radioligand [^{11}C]FLB 457. *Neuroimage* 2002, 17: 47–60.
- [81] Shidahara M, Seki C, Naganawa M, Sakata M, Ishikawa M, Ito H, *et al.* Improvement of likelihood estimation in Logan graphical analysis using maximum a posteriori for neuroreceptor PET imaging. *Ann Nucl Med* 2009, 23: 163–171.
- [82] Feng D, Huang SC, Wang Z, Ho D. An unbiased parametric imaging algorithm for nonuniformly sampled biomedical system parameter estimation. *IEEE Trans Med Imaging* 1996, 15: 512–518.
- [83] Kimura Y, Hsu H, Toyama H, Senda M, Alpert NM. Improved signal-to-noise ratio in parametric images by cluster analysis. *Neuroimage* 1999, 9: 554–561.
- [84] Van Huffel S, Vandewalle J. The total least squares problem:

- computational aspects and analysis. *Frontiers Appl Math SIAM*, Philadelphia, 1991.
- [85] Ichise M, Toyama H, Innis RB, Carson RE. Strategies to improve neuroreceptor parameter estimation by linear regression analysis. *J Cereb Blood Flow Metab* 2002, 22: 1271–1281.
- [86] Parsey RV, Ogden RT, Mann JJ. Determination of volume of distribution using likelihood estimation in graphical analysis: elimination of estimation bias. *J Cereb Blood Flow Metab* 2003, 23: 1471–1478.
- [87] Young PC. An instrumental variable method for real-time identification of a noisy process. *Automatica* 1970, 6: 271–287.
- [88] Stoica P, Soderstrom T. Optimal instrumental variable estimation and approximate implementations. *IEEE Trans Automat Contr* 1983, 28: 757–772.
- [89] Stock JH, Watson MW. *Introduction to Econometrics*. Addison Wesley, 2003.
- [90] Van Huffel S, Vandewalle J. Comparison of total least squares and instrumental variable methods for parameter estimation of transfer function models. *Int J Contr* 1989, 50: 1039–1056.
- [91] Minchin P. Analysis of tracer profiles with applications to phloem transport. *J Exp Bot* 1978, 29: 1441–1450.
- [92] Brooks D, Salmon E, Mathias C, Quinn N, Leenders K, Bannister R, *et al*. The relationship between locomotor disability, autonomic dysfunction, and the integrity of the striatal dopaminergic system in patients with multiple system atrophy, pure autonomic failure, and Parkinson's disease, studied with PET. *Brain* 1990, 113: 1539–1552.
- [93] Howes OD, Montgomery AJ, Asselin M, Murray RM, Grasby PM, McGUIRE PK. Molecular imaging studies of the striatal dopaminergic system in psychosis and predictions for the prodromal phase of psychosis. *Br J Psychiatry* 2007, 191: s13–s18.
- [94] Howes OD, Montgomery AJ, Asselin MC, Murray RM, Valli I, Tabraham P, *et al*. Elevated striatal dopamine function linked to prodromal signs of schizophrenia. *Arch Gen Psychiatry* 2009, 66: 13–20.
- [95] Kumakura Y, Cumming P. PET studies of cerebral levodopa metabolism: a review of clinical findings and modeling approaches. *Neuroscientist* 2009, 15: 635–650.
- [96] Ikoma Y, Takano A, Varrone A, Halldin C. Graphic plot analysis for estimating binding potential of translocator protein (TSPO) in positron emission tomography studies with [¹⁸F]FEDAA1106. *Neuroimage* 2013, 69: 78–86.
- [97] Heiss WD, Herholz K. Brain receptor imaging. *J Nucl Med* 2006, 47: 302–312.
- [98] Woo S, Kim S, Zhou J, Kim E, Seo JM, Park J, *et al*. Imaging of activated cortical areas after light and electrical stimulation of the rabbit retina: F-18 FDG PET-guided brain mapping. *Biomed Eng Lett* 2012, 2: 111–117.
- [99] Jin S, Oh M, Oh S, Oh J, Lee S, Chung S, *et al*. Differential diagnosis of Parkinsonism using dual-phase F-18 FP-CIT PET imaging. *Nucl Med Mol Imaging* 2013, 47: 44–51.
- [100] Park E, Hwang Y, Lee CN, Kim S, Oh S, Kim Y, *et al*. Differential diagnosis of patients with inconclusive Parkinsonian features using [18F]FP-CIT PET/CT. *Nucl Med Mol Imaging* 2014, 48: 106–113.
- [101] Lee SH, Park H. Parametric response mapping of longitudinal PET scans and their use in detecting changes in Alzheimer's diseases. *Biomed Eng Lett* 2014, 4: 73–79.
- [102] Brust P, Hoff J, Steinbach J. Development of ¹⁸F-labeled radiotracers for neuroreceptor imaging with positron emission tomography. *Neurosci Bull* 2014. Doi: 10.1007/s12264-014-1460-6.

Neurostatistical imaging for diagnosing dementia: translational approach from laboratory neuroscience to clinical routine

Etsuko Imabayashi¹, Tomio Inoue²

¹*Integrative Brain Imaging Center, National Center of Neurology and Psychiatry, Tokyo 187-8551, Japan*

²*Department of Radiology, Yokohama City University Graduate School of Medicine and School of Medicine, Yokohama 236-0004, Japan*

Corresponding author: Etsuko Imabayashi. E-mail: embysh@ncnp.go.jp

© Shanghai Institutes for Biological Sciences, CAS and Springer-Verlag Berlin Heidelberg 2014

Statistical analysis in neuroimaging (referred to as “neurostatistical imaging”) is important in clinical neurology. Here, neurostatistical imaging and its superiority for diagnosing dementia are reviewed. In neurodegenerative dementia, the proportional distribution of brain perfusion, metabolism, or atrophy is important for understanding the symptoms and status of patients and for identifying regions of pathological damage. Although absolute quantitative changes are important in vascular disease, they are less important than relative values in neurodegenerative dementia. Even under resting conditions in healthy individuals, the distribution of brain perfusion and metabolism is asymmetrical and differs among areas. To detect small changes, statistical analysis such as the Z-score – the number of standard deviations by which a patient’s voxel value differs from the normal mean value – comparing normal controls is useful and also facilitates clinical assessment. Our recent finding of a longitudinal one-year reduction of glucose metabolism around the olfactory tract in Alzheimer’s disease using the recently-developed DARTEL normalization procedure is also presented. Furthermore, a newly-developed procedure to assess brain atrophy with CT-based voxel-based morphometry is illustrated. The promising possibilities of CT in neurostatistical imaging are also presented.

Keywords: neurostatistical imaging; Neurostat; 3DSSP; eZIS; VSRAD; neurodegenerative disease; CT segmentation

Introduction

Statistical analysis in neuroimaging (described here as “neurostatistical imaging”) is crucial in clinical neurology as, for example, 3DSSP (three-dimensional stereotactic surface projections) in Neurostat^[1]. Neurostatistical imaging can be applied not only to the functional imaging like brain perfusion single photon emission computed tomography (SPECT) or glucose metabolism positron emission tomography (PET), but also to morphological images like magnetic resonance imaging (MRI) with voxel-based morphometry (VBM). Useful information can be extracted by the superimposition of statistical results onto high-resolution images like MRI. Accordingly, even though

the original image resolution is low, additional anatomical information can be obtained.

Neuroimaging in Diagnosing Dementia

An essential part of neuroimaging for the clinical investigation of dementia is to differentiate the underlying disease after systemic diseases have been excluded by blood chemistry or other clinical examinations. In vascular disorders of the brain, absolute quantitative regional changes are clinically important. In the same way, in brain tumors, focal information about the tissue surrounding tumors is important. In both diseases, direct inspection of the original images is useful and important. When the symptoms indicate the possibility of idiopathic normal-pressure hydrocephalus (iNPH),

not only the disproportionately enlarged subarachnoid space hydrocephalus pattern in the original morphological images, but also the distribution pattern of neurostatistical imaging are helpful for diagnosis^[2]. In iNPH, neurostatistical imaging demonstrates inhomogeneity of the distribution of cerebrospinal fluid (CSF) space, which modifies the statistical results in both volumetric and functional images, according to the partial volume effect. Adjacent gray matter volume, perfusion, or metabolism is proportionally reduced if neighboring gyri are far, due to focal CSF abundance. On the contrary, these parameters are proportionally increased if neighboring gyri are closer, resulting from apparent focal CSF reduction. That is, fake significant reductions of gray matter volume, perfusion, and metabolism are observed surrounding the Sylvian fissure and ventricles and fake significant increases are observed in the area of the convexity.

Contribution of Neurostatistical Imaging to Neurodegenerative Dementia

When neurodegenerative dementia is suspected, the proportional distribution of whole-brain perfusion, metabolism, or atrophy should be examined using neurostatistical imaging, because slight changes resulting from early degeneration or remote effects of that degeneration can be extracted. Even in resting conditions, the distribution of brain perfusion or metabolism in normal controls is asymmetrical and inhomogeneous. This inhomogeneity makes it difficult to assess the slight changes by visual inspection of the original tomographic images. Statistical analysis comparing normal controls makes the slight changes clear because the asymmetry and inhomogeneity in normal controls can be canceled out. In many cases of neurodegenerative disease, the changes are too obscure to detect without using neurostatistical imaging.

To diagnose the disease underlying dementia, the symptoms or status of patients are assessed, the region of pathological damage is predicted, and the dysfunction or volume loss of the lesion or remote areas is estimated. Combining the original tomographic images, neurostatistical imaging, and clinical information, the pattern of damage distribution is judged based on whether or not they match the suspected disease. Recently, more accurate analysis has been achieved due to the development of computer technology.

Historical Background of Neurostatistical Imaging

In 1994, Minoshima *et al.*^[3] showed that glucose metabolism decreases in the posterior cingulate in Alzheimer's disease (AD) using Neurostat (Department of Radiology, University of Washington, Seattle, WA^[3], <http://www.rad.washington.edu/research/Research/groups/nbl/neurostat-3d-ssp>). At that time, statistical parametric mapping (SPM, <http://www.fil.ion.ucl.ac.uk/spm/>) had already been developed and used for functional analysis in neuroscientific studies. Compared with SPM that had been used for statistical analysis of many subjects, the Z-score analysis in Neurostat was developed to analyze a single individual's data against a normal database obtained from many control subjects. The Z-score is calculated as: (mean voxel value of normal controls – patient voxel value) / standard deviation of normal controls. In 1997, after the launch of Donepezil (donepezil hydrochloride, E-2020, Aricept; Eisai Co., Ltd, Tokyo, Japan) as the first drug for the symptomatic treatment of AD in the UK, many imaging studies were performed to diagnose AD as early as possible. In 2001, Ohnishi *et al.*^[4] applied VBM to AD patients. Subsequently, in 2004, brain amyloid deposition was visualized using PET^[5], and in 2013, even brain tau protein was observed using a PET scanner^[6].

Neurostatistical Imaging and Alzheimer's Disease

Findings in the Alzheimer Brain

In neurostatistical imaging, usually images from all participants in the patient and normal control groups are anatomically standardized into the same space using templates, and voxel-based comparisons are performed to detect the specific lesions associated with the target disease. This is one of the objective methods available to avoid subjectivity and dependence on an *a priori* hypothesis, and to adopt the principle of data-driven analysis^[7].

For example, group comparison between AD patients and normal controls shows a significant decrease in glucose metabolism in the posterior cingulate and precuneus in AD^[8]. Also, Kogre *et al.* reported reduced perfusion in the posterior cingulate and precuneus in very early stages of AD using ^{99m}Tc-ethylcysteinate dimer SPECT^[9].

Morphologically, because gray-matter thickness reflects the number of residual neurons, MRI has been used to derive anatomical and tissue volume information for the gray and white matter. The VBM technique maps gray-matter or white-matter loss on a voxel-by-voxel basis after anatomical standardization. In patients with AD, a significant reduction of gray-matter volume in the hippocampal formation and the entorhinal cortex has been described^[4, 10].

Estimation of Evidence for Diagnosis of AD Using Z-score Analysis

As described in the former section, the Z-score is calculated as: (mean voxel value of normal controls – patient voxel value) / standard deviation of normal controls (Fig. 1). After anatomical standardization, the Z-score of each voxel in an image is calculated and superimposed on an image such as the MRI template. Before Z-score calculation, all values in voxels are globally normalized to the mean whole-brain value or the mean cerebellar value. Finally, the Z-score map of one patient compared with many normal controls is obtained, and inspection of the Z-score image is considered along with the symptoms and status.

To estimate the diagnostic accuracy of a Z-score map, a volume of interest (VOI) is placed on the Z-score map where a significant reduction was determined by

group comparison^[11]. By averaging the Z-scores within the VOIs and using these values as thresholds, the receiver operating characteristic (ROC) curves discriminating patients from controls are drawn and then the accuracy is calculated. From the results, the areas that contribute most are chosen as diagnostic tools.

Evidence for the discrimination of AD from other forms of dementia has accumulated. By evaluating atrophy using three-dimensional (3D) T1 images with MRI, using the VBM method and VOIs in the hippocampus and parahippocampus, Hirata *et al.*^[10] reported a discrimination accuracy of 87.8% between AD in the very early stage (amnesic type of mild cognitive impairment) and age-matched healthy controls. By evaluating the distribution of the decrease in brain glucose metabolism, Kawachi *et al.* reported an accuracy of 88.5% using VOIs in the bilateral posterior cingulate gyri and the right parietotemporal cortex^[12]. Using SPECT, we reported an accuracy of 86.2% using VOIs in the posterior cingulate and precuneus^[11].

Evidence-based Practice for Clinical Discrimination of AD from Other Forms of Dementia

For MRI, more than 2 000 institutes in Japan use VSRAD® (Eizai Co., Ltd.) for Z-score analysis of brain volumetry. In this software, tissue segmentation is first applied to the 3D-volume T1-weighted image, and gray-matter and white-

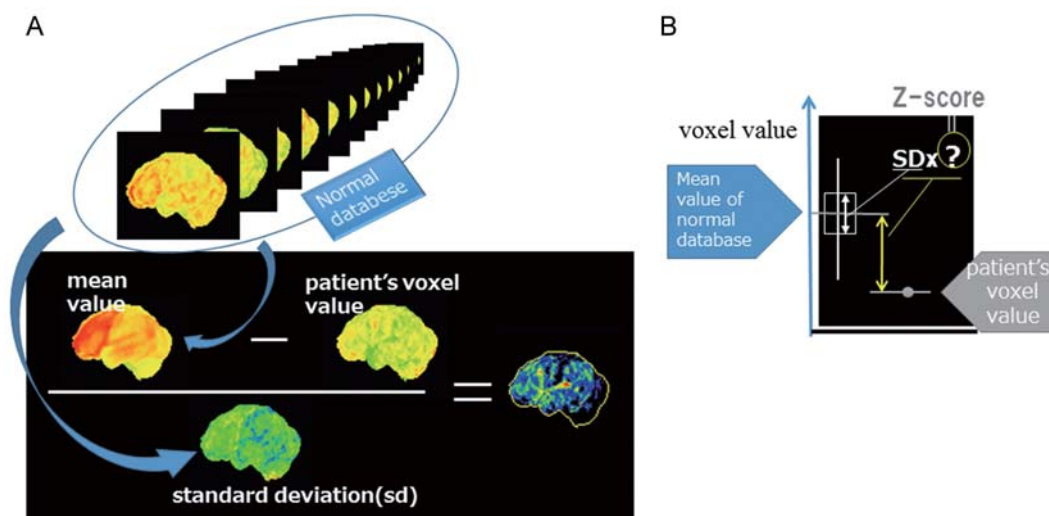


Fig. 1. Z-score analysis for diagnosis. Even with only one patient, the value can be calculated. A: Schema of Z-score calculation. $Z\text{-score} = (\text{mean voxel value of normal controls} - \text{patient voxel value}) / \text{standard deviation of normal controls}$. The Z-score is an absolute value that can be used both for an increase and a decrease. B: Schematic of evaluation of Z-score.

matter images are obtained from each individual. Then, diffeomorphic anatomical registration using the exponential Lie algebra (DARTE) algorithm in SPM8 is used for spatial normalization. Both gray- and white-matter atrophy can be estimated using this software.

For nuclear medicine images, in Japan, two types of software for Z-score analysis of SPECT images are mainly used, eZIS^[13] (easy Z-score imaging analysis; Fujifilm RI Pharma Co., Ltd, Tokyo, Japan) and iSSP (Nihon Medi-Physics Co., Ltd, Tokyo, Japan)^[14].

eZIS includes spatial normalization parameters in SPM2. Normal databases are included in this software and inter-institutional differences can be corrected. That is, correction can be made for data obtained in the institute where the database was built, using previously-scanned phantom data. Otherwise, an original database can be built.

iSSP includes spatial normalization parameters in Neurostat. Normal databases are included and can be used as they are or an original database can be built.

The results of Z-score analysis of a suspected AD patient are shown in Fig. 2. MRI was analyzed with VSRAD®, and SPECT from the same patient was analyzed with eZIS. Voxels with significant gray-matter reduction or reduced perfusion, that is, voxels with Z-scores >2, were superimposed on the MRI template. VOIs within the areas of significant atrophy or reduced perfusion were assessed by group comparison.

Preparation of Normal Database

Neuroimaging is affected by many factors, such as (1) age, race, sex, and education, (2) institution, machine, and reconstruction method, and (3) head position and functional activity during the build-up time when the functional image is obtained.

Concerning age, race, sex, and education, selection of the normal database affects the results of analysis. The more similar the conditions, the higher the sensitivity obtained. However, as the precision of subject selection increases, the size of the database decreases. As for age, if each group in the normal database consists of only a single decade, then the number is less than a database with two or three decades. In many cases, the size of the normal database is limited, and conditions are usually merged.

As for institution, machine, and reconstruction method, data acquisition should be performed in the

same way, using the same machine, with the same procedure, especially in functional imaging like SPECT and PET. When anatomical data like MRI are used for VBM, the limitation is expanded to machines with the same specifications. Concerning SPECT data, with eZIS software, inter-institutional differences can be corrected using the 3D Hoffman phantom as an intermediary. In most other cases, including other modalities like PET, an original normal database or disease control should be built. When examining the subjects, head position and brain functional activity during the build-up time should be carefully considered. In SPECT, if the tracer is injected in a bright room with the individual's eyes open, activity in the occipital region is much higher than when injected in a dark room.

Moreover, it is very important that only clinical non-image data and anatomical data are used for subject selection. The anatomical data are used for screening the space occupying lesion like infarction, tumor or hemorrhage. The functional data itself should never be used. Clinical information is of importance when choosing normal data. Normal database should not be selected only from functional image appearance, as we can hardly differentiate normal distribution from abnormal distribution with visual inspection.

Neurostatistical Imaging of Other Neurodegenerative Dementias

Dementia with Lewy Bodies versus AD

Reduced occipital metabolism and perfusion or loss of dopamine transporters is used to supplement the clinical diagnosis of dementia with Lewy bodies (DLB). Recently, it has been reported that glucose metabolism in the posterior cingulate cortex in DLB^[15] appears to be relatively spared compared with that in AD. Lim *et al.*^[15] found that reduced glucose metabolism in the medial occipital area and the cingulate island is a highly specific sign of DLB, with specificities of 97% and 100%, respectively, while the sensitivity of visual inspection ranged from 43% to 50% for the medial occipital and from 62% to 86% for the cingulate island.

Using VBM with VSRAD®, Nakatsuka *et al.*^[16] examined its ability to discriminate between DLB and AD. Atrophy in the midbrain, pons, and cerebellum was

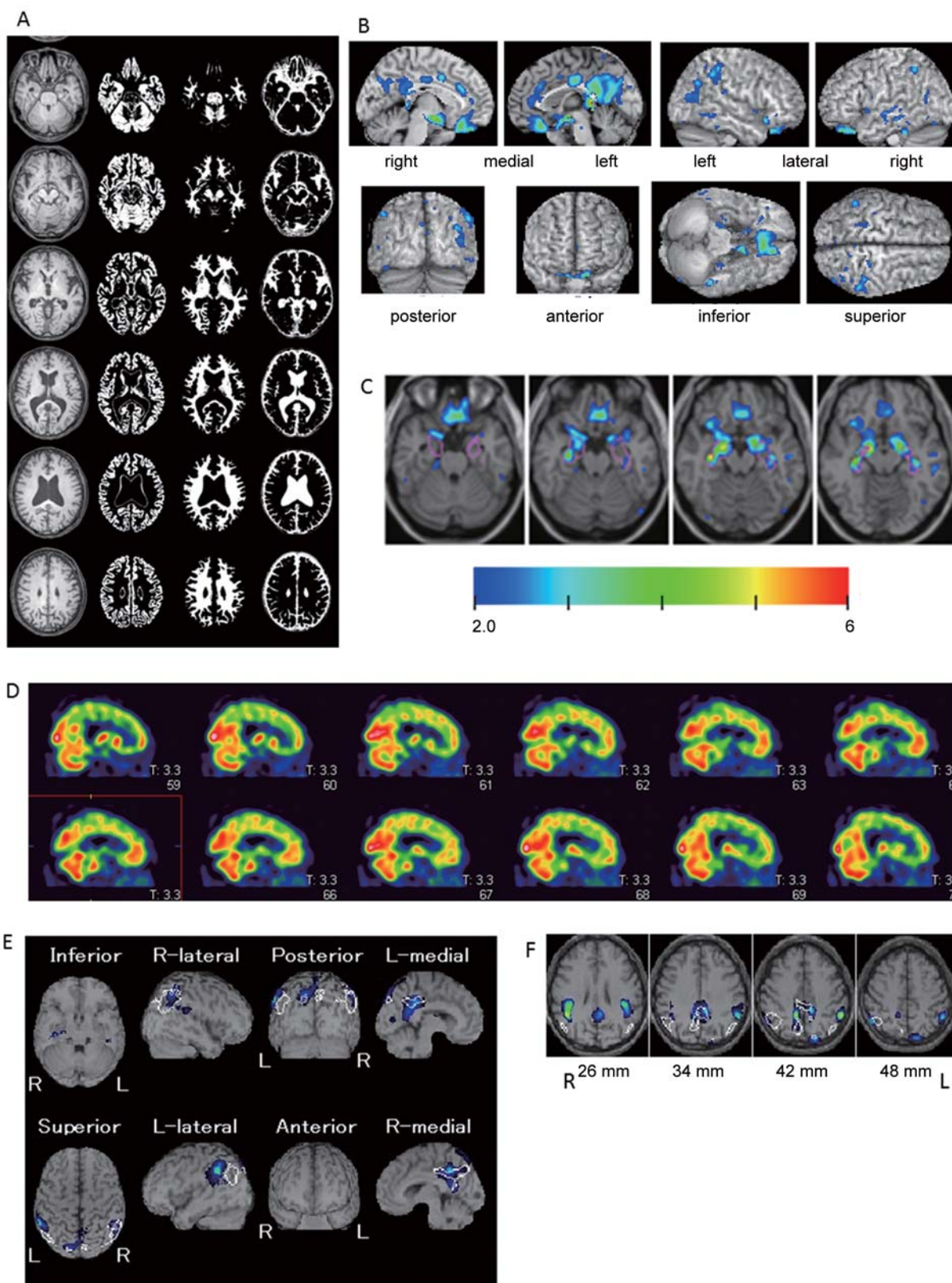


Fig. 2. A clinical case of suspected Alzheimer's disease (AD). A–C: VBM analyzed with VSRAD®. A: Segmented results for quality check of the procedure. Left column: original transaxial MR images; next 3 columns: extracted gray matter, white matter, and cerebrospinal fluid images, respectively. B: Z-scores superimposed on the cortical surface T1-weighted 3D volume MR image. C: Z-scores superimposed on the transaxial T1-weighted MR image. Purple VOIs indicate voxels with significant volume reduction in early AD by group comparison. D–F: Z-score analysis with eZIS. D: ^{99m}Tc-ethylcysteinate dimer SPECT sagittal images from the same patient. E: Z-scores calculated from SPECT superimposed on the cortical surface T1-weighted 3D volume MR image. F: Z-scores calculated from SPECT superimposed on the transaxial T1-weighted MR image. White VOIs indicate voxels with significant volume reduction in early AD by group comparison.

observed as white matter atrophy in DLB compared with AD. Using averaged Z-scores in VOIs in the midbrain, ROC analysis showed a sensitivity of 80%, a specificity of 64%, and an accuracy of 72%^[16] for discrimination of DLB from AD.

Differential Diagnosis of Frontotemporal Lobe Degeneration: Progressive Supranuclear Palsy versus Corticobasal Syndrome

Corticobasal disease (CBD) and progressive supranuclear palsy (PSP) are difficult to diagnose because of the wide variety of symptoms and overlaps in symptoms and neurological findings. Sakurai *et al.*^[17] evaluated the utility of white-matter atrophy to differentiate patients with clinically diagnosed CBD (corticobasal syndrome, CBS) and PSP (Richardson's syndrome, RS). They found that with the target VOIs for CBS in the bilateral frontal white matter, the two diseases are discriminated with sensitivity of 89%, specificity of 100%, and accuracy of 96% with a cutoff Z-score of 1.30, and with the target VOI for RS in the midbrain, they were discriminated with sensitivity of 81%, specificity of 81%, and accuracy of 81% with a cutoff Z-score of 0.97.

New Findings Owing to Technology Development

Recently, the resolution of medical equipment and the precise procedures for image analysis have progressed tremendously. With these methods, particularly DARTEL for normalization, we compared the longitudinal reduction of glucose metabolism in AD patients and cognitively normal volunteers. With DARTEL, precise anatomical normalization generates relatively homogeneously-shaped images. Nine ¹¹C-PiB-positive AD patients and 10 ¹¹C-PiB-negative normal volunteers were studied. Two ¹⁸F-FDG PET scans were performed at an interval of 12 months, and all images were spatially normalized using the DARTEL

algorithm and analyzed with SPM8. The one-year reduction of glucose metabolism in AD patients was significantly greater in the area surrounding the orbital sulcus, including from the subgenual area to the anterior olfactory nucleus (AON) in addition to the posterior cingulate and medial temporal lesions, where decreases in glucose metabolism have been described (Fig. 3). Fouquet *et al.*^[18] reported that although the largest annual decrease in metabolism occurs in the posterior cingulate-precuneus area, patients who convert to AD have a significantly greater decrease than non-converters in two ventro-medial prefrontal areas, the subgenual (BA25) and anterior cingulate (BA24/32). Moreover, Villain *et al.*^[19] suggested that hippocampal atrophy in AD patients progressively leads to disruption of the cingulum bundle and uncinate fasciculus, which in turn leads to glucose hypometabolism in the cingulate and subgenual cortices. We speculate that the AON may be included in this subgenual area where decreased metabolism occurs^[20]. Pathologically, amyloid deposition and neurofibrillary changes have been reported in the AON of AD patients. The AON has connections to the piriform cortex, anterior amygdala, periamygdaloid cortex, rostral entorhinal cortex, hypothalamus, and habenula. Due to these pathways, the AON is rich in dendrites and astrocytes, resulting in abundant glucose consumption in this small region. We also speculate that reduction of glucose metabolism in the AON is responsible for the olfactory disturbances in AD patients.

Prospective Application of Neurostatistical Imaging

Brain CT has more homogeneity and less distortion than MRI, even when using different machines or scan protocols. It is also relatively economical and widely available. Moreover, nowadays, CT data are easily available from

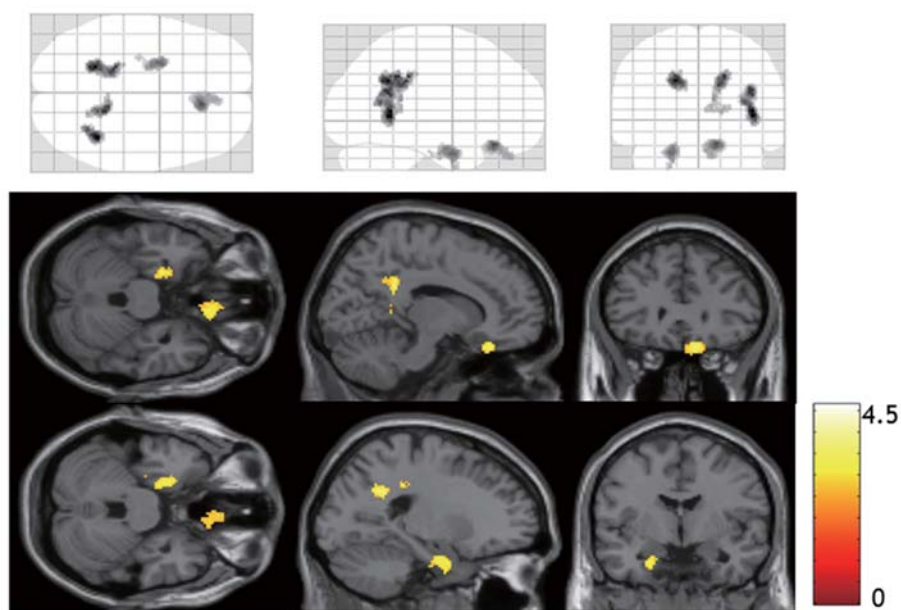


Fig. 3. One-year reduction of glucose metabolism is proportionally greater in Alzheimer’s disease (AD) patients than in cognitively normal volunteers. The one-year proportional reduction of glucose metabolism was significantly greater in AD patients than in controls in the bilateral posterior cingulate gyri, right precuneus, bilateral parahippocampal gyri, left amygdala, right rectal gyrus, and medial orbital gyrus, including caudal to the right rectal gyrus and the olfactory sulcus corresponding to the right olfactory tract (threshold at uncorrected $P < 0.01$; $k > 150$ voxels). The SPM of the t -statistics is displayed in a standard format as a maximum intensity projection viewed from the top, right-hand side and the back (top three images from left to right respectively), and as orthogonal sections (middle and bottom ranks).

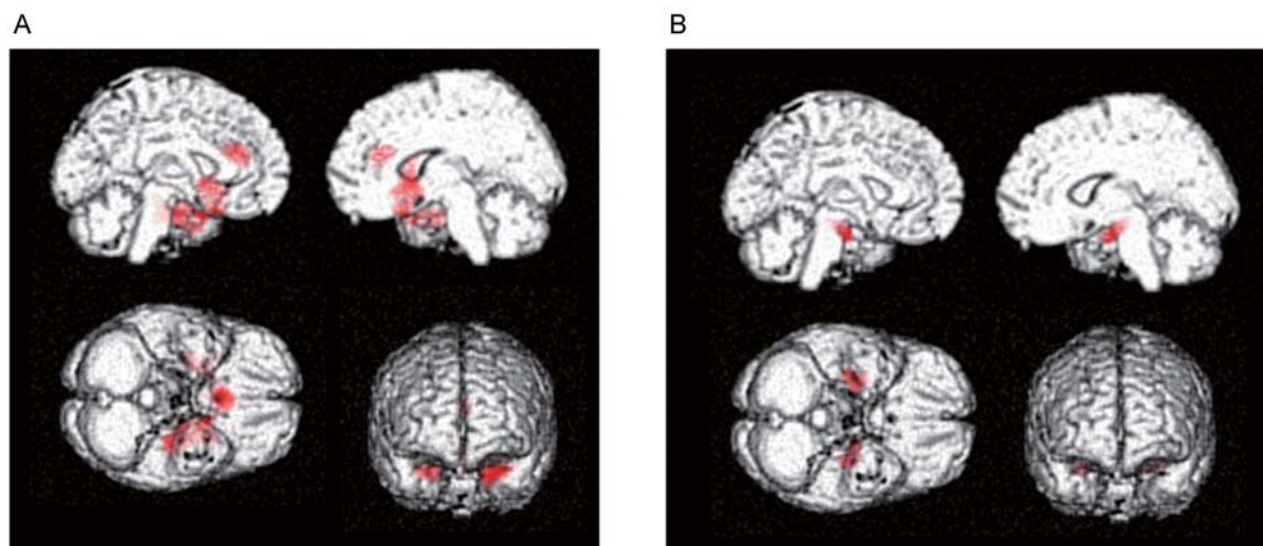


Fig. 4. A: Significant reduction of regional gray matter volume in the bilateral medial temporal cortex, temporopolar areas, right caudate, and anterior cingulate in Alzheimer’s disease (AD) patients with CT-VBM. Significance maps of decreased gray matter volume in AD patients superimposed on a T1-weighted surface MRI template image in MNI space. B: Significant reduction of regional gray matter volume in the bilateral medial temporal cortex in AD patients with MR-VBM. Significance maps of decreased gray matter volume in AD patients superimposed on a surface T1-weighted MRI template image in MNI space.

routine PET/CT studies. We compared the results from CT-VBM with those from MRI-based VBM (MR-VBM) in the same individuals^[21]. All of the AD patients showed positive ¹¹C-PiB accumulation and none of the cognitively normal controls showed an accumulation. In CT-VBM, the AD group showed a significant decrease of gray matter volume in the bilateral entorhinal cortex, left hippocampus, left anterior cingulate gyrus, right temporopolar area, and right head of the caudate, compared to a cognitively normal group (Fig. 4). In MR-VBM, the AD group showed a significant decrease of gray matter volume in the bilateral hippocampus and left entorhinal cortex at BA28 compared to the cognitively normal group (Fig. 4). The most significant atrophy was observed in the left hippocampus.

The results of Z-score analysis comparing one ¹¹C-PiB positive AD patient with a normal database are shown in Figure 5. The normal database was constructed with gray matter extracted from CT images. Blue color in bilateral medial temporal regions shows significant volume reduction in this AD patient's CT image.

Although for clinical use, a simpler and proper program for CT-VBM or an advanced scanning technique for more precise tissue contrast without heavier radiation exposure is desirable, our results suggest that CT-VBM has the potential to replace MR-VBM for diagnosing AD. Moreover, the cortical gray matter volume from CT can also be used for partial volume correction (PVC); especially in amyloid imaging, PVC may be necessary for accurate assessment

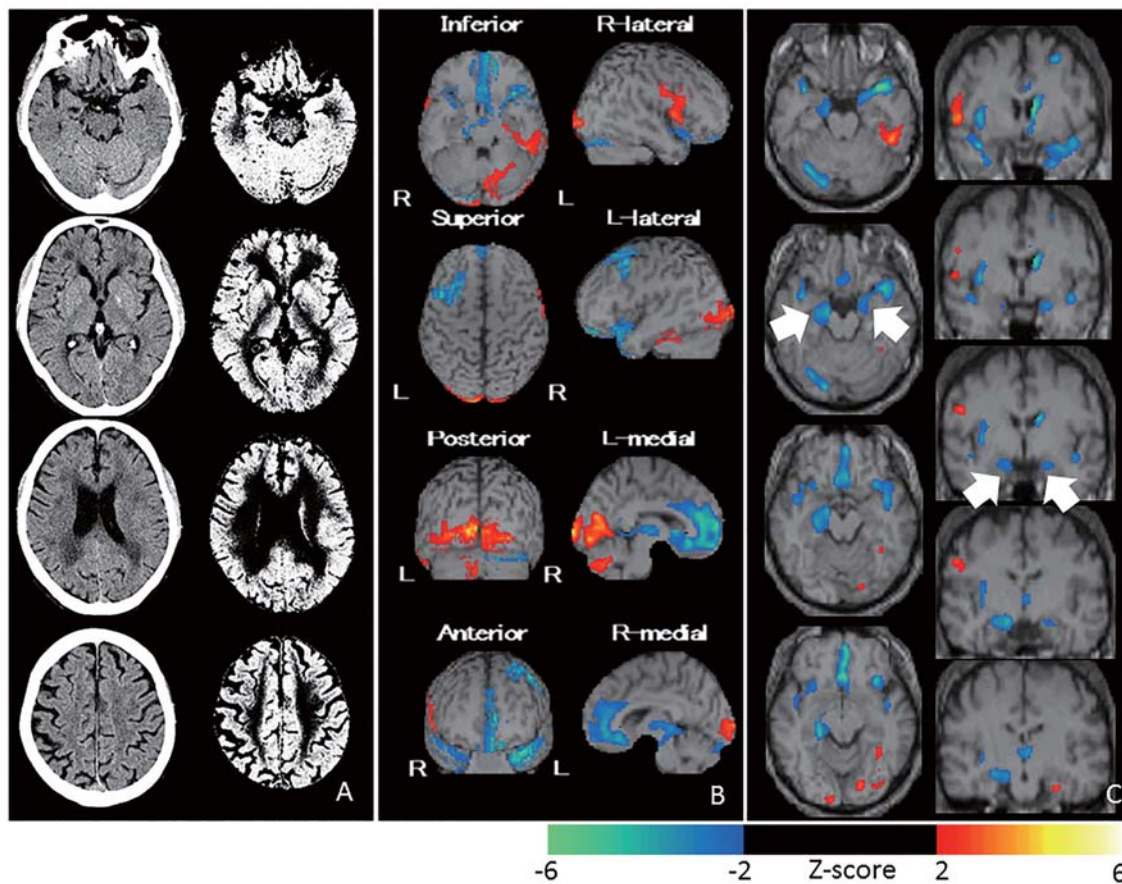


Fig. 5. CT-based VBM. **A:** CT images from an ¹¹C-PiB-positive 60-year-old female AD patient. Left column, original CT images; right column, segmented gray matter from CT images. **B and C:** Z-scores obtained from gray matter image in **A** superimposed on the cortical surface (**B**) and transaxial and coronal (**C**) images of a T1-weighted 3D volume MR image in MNI space. Warm color indicates increase and cool color indicates decrease. That is, blue color in bilateral medial temporal regions (white arrow) shows significant volume reduction in this AD patient's CT image.

of the increased accumulation in the atrophied brain in AD. Without PVC, more atrophied brain in AD patients than in healthy volunteer shows underestimation of PiB accumulation. The availability of PET/CT scanners allows the application of PET data with CT-based PVC and VBM for patients with a single visit. Furthermore, when PET/MRI is used more frequently, these PVC and VBM procedures can be more precisely and easily approached.

Conclusion

In diagnosing neurodegenerative dementia, recently many procedures using new technology like machine learning have been developed. In the near future, better procedures for automatic diagnosis may be developed. At present, as shown in this article, Z-score analysis of each patient's image is useful for routine clinical use, especially after the diagnostic accuracy is estimated. This can be used for both anatomical and metabolic images.

Many artifacts can occur in these traditional procedures due to mis-segmentation, mis-registration, normalization errors, and calculation errors. Accordingly, when neurostatistical imaging is used, it should always be compared to the original tomographic images to confirm a tendency in the neurostatistical analysis. Inconsistencies should be further investigated. When neurostatistical imaging is used adequately, much useful and beneficial information is revealed.

Received date: 2014-04-30; Accepted date: 2014-06-14

REFERENCES

- [1] Minoshima S, Frey KA, Koeppe RA, Foster NL, Kuhl DE. A diagnostic approach in Alzheimer's disease using three-dimensional stereotactic surface projections of fluorine-18-FDG PET. *J Nucl Med* 1995, 36: 1238–1248.
- [2] Kobayashi S, Tateno M, Utsumi K, Takahashi A, Morii H, Saito T. Two-layer appearance on brain perfusion SPECT in idiopathic normal pressure hydrocephalus: a qualitative analysis by using easy Z-score imaging system, eZIS. *Dement Geriatr Cogn Disord* 2009, 28: 330–337.
- [3] Minoshima S, Foster NL, Kuhl DE. Posterior cingulate cortex in Alzheimer's disease. *Lancet* 1994, 344: 895.
- [4] Ohnishi T, Matsuda H, Tabira T, Asada T, Uno M. Changes in brain morphology in Alzheimer disease and normal aging: is Alzheimer disease an exaggerated aging process? *AJNR Am J Neuroradiol* 2001, 22: 1680–1685.
- [5] Klunk WE, Engler H, Nordberg A, Wang YM, Blomqvist G, Holt DP, *et al.* Imaging brain amyloid in Alzheimer's disease with Pittsburgh Compound-B. *Ann Neurol* 2004, 55: 306–319.
- [6] Maruyama M, Shimada H, Suhara T, Shinotoh H, Ji B, Maeda J, *et al.* Imaging of tau pathology in a tauopathy mouse model and in Alzheimer patients compared to normal controls. *Neuron* 2013, 79: 1094–1108.
- [7] Ashburner J, Friston KJ. Voxel-based morphometry - The methods. *Neuroimage* 2000, 11: 805–821.
- [8] Minoshima S, Giordani B, Berent S, Frey KA, Foster NL, Kuhl DE. Metabolic reduction in the posterior cingulate cortex in very early Alzheimer's disease. *Ann Neurol* 1997, 42: 85–94.
- [9] Kogure D, Matsuda H, Ohnishi T, Asada T, Uno M, Kunihiro T, *et al.* Longitudinal evaluation of early Alzheimer's disease using brain perfusion SPECT. *J Nucl Med* 2000, 41: 1155–1162.
- [10] Hirata Y, Matsuda H, Nemoto K, Ohnishi T, Hirao K, Yamashita F, *et al.* Voxel-based morphometry to discriminate early Alzheimer's disease from controls. *Neurosci Lett* 2005, 382: 269–274.
- [11] Imabayashi E, Matsuda H, Asada T, Ohnishi T, Sakamoto S, Nakano S, *et al.* Superiority of 3-dimensional stereotactic surface projection analysis over visual inspection in discrimination of patients with very early Alzheimer's disease from controls using brain perfusion SPECT. *J Nucl Med* 2004, 45: 1450–1457.
- [12] Kawachi T, Ishii K, Sakamoto S, Sasaki M, Mori T, Yamashita F, *et al.* Comparison of the diagnostic performance of FDG-PET and VBM-MRI in very mild Alzheimer's disease. *Eur J Nucl Med Mol Imaging* 2006, 33: 801–809.
- [13] Matsuda H, Mizumura S, Nagao T, Ota T, Iizuka T, Nemoto K, *et al.* Automated discrimination between very early Alzheimer disease and controls using an easy Z-score imaging system for multicenter brain perfusion single-photon emission tomography. *Am J Neuroradiol* 2007, 28: 731–736.
- [14] Mito Y, Yoshida K, Yabe I, Makino K, Hirotani M, Tashiro K, *et al.* Brain 3D-SSP SPECT analysis in dementia with Lewy bodies, Parkinson's disease with and without dementia, and Alzheimer's disease. *Clin Neurol Neurosurg* 2005, 107: 396–403.
- [15] Lim SM, Katsifis A, Villemagne VL, Best R, Jones G, Saling M, *et al.* The ¹⁸F-FDG PET cingulate island sign and comparison to ¹²³I-β-CIT SPECT for diagnosis of dementia with Lewy bodies. *J Nucl Med* 2009, 50: 1638–1645.
- [16] Nakatsuka T, Imabayashi E, Matsuda H, Sakakibara R, Inaoka T, Terada H. Discrimination of dementia with Lewy bodies from Alzheimer's disease using voxel-based morphometry of white matter by statistical parametric mapping 8 plus diffeomorphic anatomic registration through

- exponentiated Lie algebra. *Neuroradiology* 2013, 55: 559–566.
- [17] Sakurai K, Imabayashi E, Tokumaru AM, Hasebe S, Murayama S, Morimoto S, *et al.* The feasibility of white matter volume reduction analysis using SPM8 plus DARTEL for the diagnosis of patients with clinically diagnosed corticobasal syndrome and Richardson's syndrome. *Neuroimage Clin* 2014. DOI: 10.1016/j.nicl.2014.02.009
- [18] Villain N, Fouquet M, Baron JC, Mezenge F, Landeau B, de La Sayette V, *et al.* Sequential relationships between grey matter and white matter atrophy and brain metabolic abnormalities in early Alzheimer's disease. *Brain* 2010, 133: 3301–3314.
- [19] Fouquet M, Desgranges B, Landeau B, Duchesnay E, Mezenge F, de la Sayette V, *et al.* Longitudinal brain metabolic changes from amnesic mild cognitive impairment to Alzheimer's disease. *Brain* 2009, 132: 2058–2067.
- [20] Imabayashi E, Matsuda H, Yoshimaru K, Kuji I, Seto A, Shimano Y, *et al.* Pilot data on telmisartan short-term effects on glucose metabolism in the olfactory tract in Alzheimer's disease. *Brain Behav* 2011, 1: 63–69.
- [21] Imabayashi E, Matsuda H, Tabira T, Arima K, Araki N, Ishii K, *et al.* Comparison between brain CT and MRI for voxel-based morphometry of Alzheimer's disease. *Brain Behav* 2013, 3: 487–493.

Brain dopaminergic system changes in drug addiction: a review of positron emission tomography findings

Haifeng Hou^{1,2,3,4,*}, Chunyan Wang^{5,*}, Shaowei Jia⁶, Shu Hu⁶, Mei Tian^{1,2,3,4}

¹Department of Nuclear Medicine, the Second Affiliated Hospital of Zhejiang University School of Medicine, ²Zhejiang University Medical PET Center, ³Institute of Nuclear Medicine and Molecular Imaging, Zhejiang University, ⁴Key Laboratory of Medical Molecular Imaging of Zhejiang Province, Hangzhou 310009, China

⁵Beijing 307 Hospital, Beijing 100071, China

⁶Department of Nuclear Medicine, Peking University Shenzhen Hospital, Shenzhen 518036, China

*These authors contributed equally to this work.

Corresponding author: Mei Tian. E-mail: meitian@gmail.com

© Shanghai Institutes for Biological Sciences, CAS and Springer-Verlag Berlin Heidelberg 2014

Dopamine (DA) is considered crucial for the rewarding effects of drugs of abuse, but its role in addiction remains unclear. Positron emission tomography (PET) is the first technology used for *in vivo* measurement of components of the dopaminergic system in the human brain. In this article, we review the major findings from PET imaging studies on the involvement of DA in drug addiction, including presynaptic DA synthesis, vesicular monoamine transporter 2, the DA transporter, and postsynaptic DA receptors. These results have corroborated the role of DA in addiction and increased the understanding of its underlying mechanisms.

Keywords: dopamine; dopaminergic system; drug addiction; positron emission tomography

Brain Dopaminergic System

Dopamine (DA) is a catecholamine neurotransmitter in the nervous system. It has many functions in the brain, including punishment, reward, voluntary movement, mood, attention, motivation, sleep, working memory, and learning^[1]. DA is synthesized by the hydroxylation and decarboxylation of L-tyrosine in DA neurons and, before being released into the synapse in response to an action potential, it is stored within presynaptic vesicles (Fig. 1). The action of DA occurs by binding to postsynaptic DA receptors, resulting in the formation of second messengers. There are five subtypes of DA receptors, which can be grouped into two classes or families: D1-like and D-2 like^[1,2]. The D1-like receptor family comprises the D1 and D5 receptors, encoded by genes with no introns, acting by way of Gs-proteins and activating adenylyl cyclase, thus increasing cAMP production^[3,4]. The D2-like receptor family comprises the D2, D3, and D4 receptors, encoded by genes containing introns. D2-

like receptors act *via* Gi-proteins, inhibit adenylyl cyclase activity, and thus decrease cAMP activity^[3,5].

The action of DA in the synapse is terminated primarily by reuptake to the presynaptic membrane through the dopamine transporter (DAT)^[6]. Otherwise, DA is partially removed by oxidation by monoamine oxidase or catechol-O-methyltransferase in the synaptic cleft (Fig. 1).

The dopaminergic neurons, whose primary neurotransmitter is DA, interconnect many areas of the brain to form a system which originates in the substantia nigra (SN) pars compacta, ventral tegmental area (VTA), and hypothalamus. The dopaminergic system is typically divided into four major pathways: mesocortical (from the VTA to the frontal cortex), mesolimbic (from the VTA to the nucleus accumbens), nigrostriatal (from the SN to the striatum), and tuberoinfundibular (from the hypothalamus to the pituitary gland). The mesostriatal and mesocortical pathways are currently recognized to contribute most to drug addiction^[7].

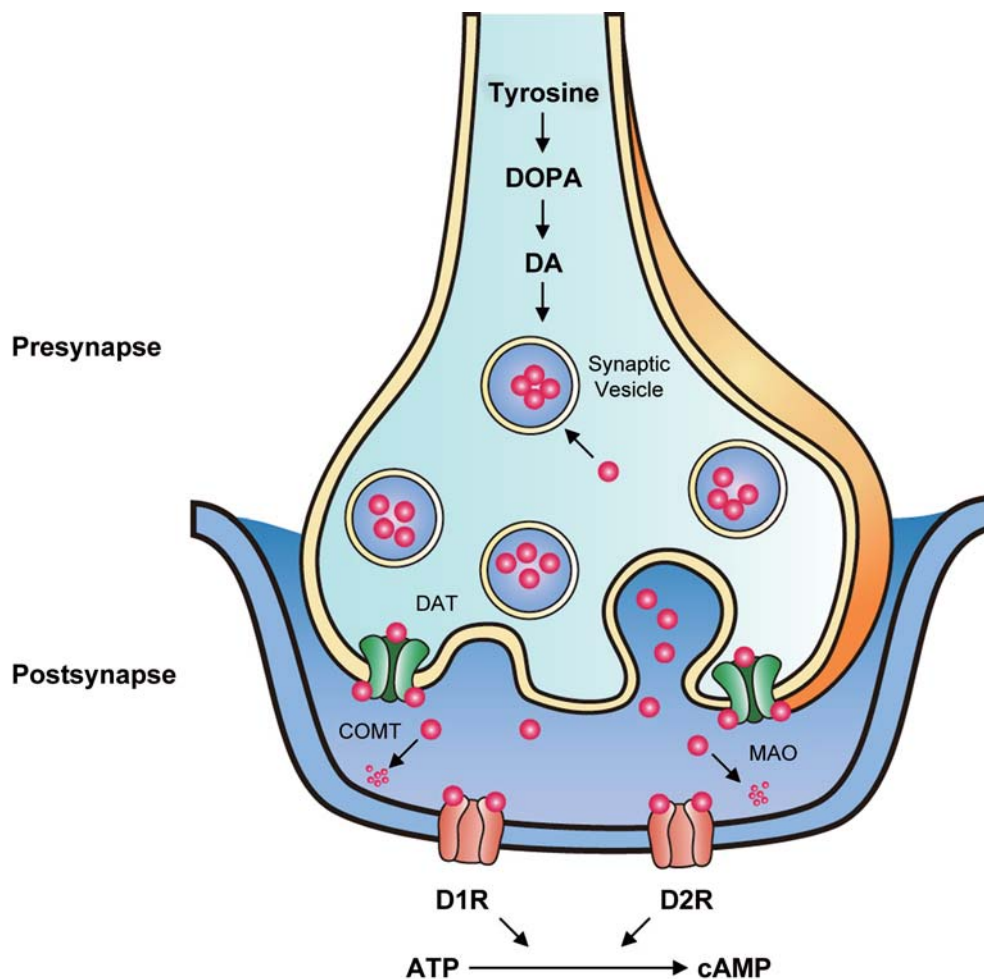


Fig. 1. Schematic representation of a dopaminergic synapse. ATP, adenosine triphosphate; cAMP, cyclic adenosine monophosphate; COMT, catechol-O-methyltransferase; D1R, dopamine receptor 1; D2R, dopamine receptor 2; DA, dopamine; DAT, dopamine transporter; DOPA, dihydroxyphenylalanine; MAO, monoamine oxidase.

Drug Addiction

The term addiction is derived from the Latin verb *addicere*, which referred to the Roman court action of binding a person to another. From the 17th century, addiction has been used to refer to psychoactive substances (e.g. alcohol, tobacco, heroin) which cross the blood-brain barrier, temporarily altering the chemical milieu of the brain^[8]. Currently, addiction is identified as continued involvement with a drug, despite the negative consequences associated with it — such as compulsive drug seeking and taking, loss of control over drug-taking, or emergence of a negative emotional state (e.g., dysphoria, anxiety, irritability) — when access to the drug is prevented or terminated^[9].

Recently, “behavioral addiction” has also been proposed, but is beyond this review and has been described in detail elsewhere^[10–18].

The neuronal basis of addiction has been guided by the premise that the motivation of an addict to take drugs results from the desire to experience the hedonic (i.e., rewarding) effects or from the desire to avoid the anhedonia and aversive consequences of withdrawal^[19]. There are mounting studies suggesting that the rewarding properties of addictive drugs depend on their ability to provoke DA release in the brain^[20–22].

Over the past few decades, the progressive development of functional neuroimaging technology, especially positron emission tomography (PET), has made possible

the elucidation of brain functions associated with addiction^[23-25].

PET Imaging of Alterations of the Brain Dopaminergic System in Drug Addiction

PET is a technique that measures the radioactivity released by specific radioligands, and can therefore be used to generate cross-sectional brain images with anatomical or detailed functional information about changes in neurotransmitter responsiveness or receptor expression^[26]. The commonly-used isotopes ¹¹C, ¹³N, ¹⁵O, and ¹⁸F have short half-lives, making possible repeated studies within a short time-span. Moreover, the quantity of PET tracers injected is too low (in the nanomolar range) to cause harm.

The dopaminergic system has been identified as a key substrate for the rewarding effects of abused drugs and PET was the first technology that enabled the direct measurement of components of the DA system in the living human brain^[27]. PET imaging studies have also shown that in drug-addicted individuals, DA function is markedly disrupted^[25, 28]. In this article, we review PET radiotracers that are currently available for imaging the dopaminergic system in drug addiction and the main findings of *in vivo* imaging studies.

PET Studies of Presynaptic DA Synthesis

Addictive drugs exhibit a wide range of structures and actions, but the unifying principle appears to be that they each acutely enhance DA neurotransmission by means that dissociate it from normal drive by environmental cues^[29, 30]. The function of DA synthesis in the presynaptic neuron can be currently measured in preclinical animal studies and in human subjects. Thus, if DA synthesis by the presynaptic DA neurons in drug-addicted individuals were impaired, this would be expected to translate into a blunted DA response.

L-dopa (*L*-dihydroxyphenylalanine) is the immediate precursor of DA. Although DA in the circulation does not cross the blood-brain barrier, *L*-dopa is carried into the brain by the large neutral amino-acid transport system, is then converted into DA by *L*-aromatic amino-acid decarboxylase, and is stored in intraneuronal vesicles from which DA is released when the neuron fires^[31]. ¹⁸F- or ¹¹C-labeled *L*-dopa is an analog of *L*-dopa, and this positron-emitting compound is used clinically to trace the dopaminergic pathway and to evaluate presynaptic function. Uptake

of *L*-dopa labeled with a positron-emitting radionuclide reflects the synthesis rate of DA in the terminals, under the conditions of PET^[32, 33]. Studies with PET and radionuclide-labeled *L*-dopa and their main findings are summarized in Table 1.

In cocaine addiction, PET imaging with [¹⁸F] dopa (6-[¹⁸F] fluoro-*L*-dopa) shows a delayed decrease in DA terminal activity in the striatum of detoxified cocaine abusers compared with controls^[34, 35]. Also, a decrease in presynaptic DA activity during cocaine abstinence or withdrawal is associated with relapse^[36, 37].

Methamphetamine (MA), another prevalent psychostimulant drug of abuse, induces more deleterious changes in the brain than cocaine when a toxic dose is used^[35]. This is evident from the significant reductions in striatal [¹⁸F] dopa uptake in MA-treated mice, suggesting the neurodegeneration of dopaminergic cells and DA synthesis in MA abuse^[35].

In alcohol addiction, although there is no difference in the net influx of striatal [¹⁸F] dopa (an index of DA synthesis) between detoxified alcoholic patients and control subjects^[33], findings from several studies have shown that low DA synthesis correlates with alcohol craving, negative mood states, and a high risk of relapse^[33, 38]. Further, among late-onset (type 1) alcoholics, [¹⁸F] dopa uptake is elevated in the putamen and caudate, which is correlated with poor performance on the Wisconsin Card Sorting Test. This study suggests that the magnitude of the change in presynaptic DA function correlates with the patients' degree of inability to modify their behavior^[39].

In smokers, significantly higher [¹⁸F] dopa uptake occurs in the putamen and caudate than in non-smokers, which suggests that smoking is related to greater DA activity in the human basal ganglia, and nicotine-induced DA activity may be a mechanism relevant to dependence on cigarette smoking^[40].

Ecstasy (+/-3,4-methylenedioxymethamphetamine, MDMA) is a popular recreational drug with known neurotoxicity. Its potential long-term effects on dopaminergic function have been verified recently by an *in vivo* PET study in human subjects. In the study by Tai *et al.*^[41] [¹⁸F] dopa uptake in the putamen was 9% higher in ex-users of ecstasy than in controls, even after >3 years of abstinence.

Table 1. PET imaging of presynaptic DA synthesis in drug addiction

Ref.	Radioligand	Drug	Subjects	Controls	Main findings
[34]	[¹⁸ F] dopa	Cocaine	11 cocaine addicts	8 normal participants	(↓) [¹⁸ F] dopa uptake negatively correlated with days off cocaine
[35]	[¹⁸ F] dopa	Cocaine	10 male mice treated with cocaine (30 mg/kg) for 7 days	10 male mice treated with saline for 7 days	(↓)
[35]	[¹⁸ F] dopa	MA	10 male mice treated with MA (30 mg/kg) for 7 days	10 male mice treated with saline for 7 days	(↓)
[33]	[¹⁸ F] dopa	Alcohol	12 detoxified male alcoholics	13 age-matched healthy men	(-) [¹⁸ F] dopa uptake positively correlated with alcohol craving
[38]	[¹⁸ F] dopa	Alcohol	11 detoxified male alcoholics	13 normal controls	(-)
[39]	[¹⁸ F] dopa	Alcohol	10 type 1 alcoholics	8 normal controls	(↑) [¹⁸ F] dopa uptake in putamen and caudate negatively correlated with Wisconsin Card Sorting Test performance among alcoholics
[40]	[¹⁸ F] dopa	Nicotine	9 smoking men	10 normal controls	(↑)
[41]	[¹⁸ F] dopa	MDMA	14 ex-MDMA users (abstinent >3 years)	12 normal controls	(↑)

(↓) striatal radioligand uptake decreased, (↑) increased, or (-) did not significantly differ from healthy controls; MA, methamphetamine; MDMA, ecstasy (+/-3,4-methylenedioxymethamphetamine).

PET Studies of Vesicular Monoamine Transporter 2

Vesicular monoamine transporter 2 (VMAT2) is a protein responsible for transporting monoamine neurotransmitters from the cytoplasm into synaptic vesicles^[42], so it plays an important role in regulating the presynaptic DA concentration. The most-used ligand in VMAT2-binding studies *in vivo* is ¹¹C-labeled dihydrotetrabenazine (DTBZ). Binding of [¹¹C] DTBZ to VMAT2 is commonly considered to be a stable marker of DA neuronal integrity and an *in vivo* marker of DA nerve terminals^[43]. PET imaging studies of VMAT2 in drug addiction and the main findings are summarized in Table 2.

Postmortem studies comparing the VMAT2 density in cocaine abusers with healthy subjects using radiolabeled DTBZ found significantly reduced [³H] DTBZ binding in the striatum of cocaine abusers^[44]. A recent *in vivo* PET study with [¹¹C] DTBZ confirmed the previous *in vitro* findings, suggesting compensatory down-regulation of the DA storage vesicles in response to chronic cocaine abuse and/or a loss of dopaminergic terminals^[45].

Animal studies and preclinical investigations have established that drugs of abuse produce long-term changes in DA neuronal integrity. In a PET imaging investigation of “heavy” MA users, the striatal [¹¹C] DTBZ binding was decreased by 10%, even after at least 3 months of abstinence, reflecting the long-lasting effect of MA on VMAT2^[46]. And in the study of Boileau *et al.*^[43], who used human subjects to measure striatal [¹¹C] DTBZ binding after an acute oral dose of amphetamine (AMPH), a slight decrease of [¹¹C] DTBZ binding was also found.

However, in a subsequent study, the striatal [¹¹C] DTBZ binding in early-abstinence MA abusers (mean, 19 days; range, 1–90 days) was increased^[47]. One potential explanation for this increase is that [¹¹C] DTBZ binding not only reflects DA synaptic integrity, but also indicates changes in the endogenous vesicular DA storage levels with unchanged VMAT2 protein expression^[47]. This hypothesis was verified by Kilbourn *et al.*^[48], who conducted a systematic study in rats, in which *in vivo* PET analysis of [¹¹C] DTBZ binding was examined as a function of DA

Table 2. PET imaging of vesicular monoamine transporter 2 in drug addiction

Ref.	Radioligand	Drug	Subjects	Controls	Main findings
[43]	[¹¹ C] DTBZ	AMPH	9 non-drug-using subjects with low-dose AMPH (0.4 mg/kg)	Same subjects before drug use	(↓)
[46]	[¹¹ C] DTBZ	MA	16 MA users	18 normal controls	(↓)
[47]	[¹¹ C] DTBZ	MA	16 recently withdrawn MA users (mean 19 days)	14 normal controls	(↑)

(↓) striatal radioligand uptake decreased or (↑) increased compared with healthy controls; MA, methamphetamine; AMPH, amphetamine.

depletion with alpha-methyl-para-tyrosine (AMPT) and repletion with *L*-dopa. Repeated treatment with AMPT at doses that markedly depleted (-75%) brain DA levels resulted in increased (+36%) *in vivo* [¹¹C] DTBZ binding to VMAT2 in the striatum. This increase in binding was completely reversed by treatment with *L*-dopa to restore the DA levels. But there were no changes in the total number of VMAT2 binding sites, as measured by *in vitro* autoradiography. Further, Boileau *et al.* attributed their findings of a slight decrease in [¹¹C] DTBZ binding caused by AMPH not to changes in presynaptic VMAT2 but an insufficient drug dose to significantly deplete striatal DA^[43]. Therefore, more systematic preclinical studies are required to optimally guide the extraction of clinically useful information from [¹¹C] DTBZ PET imaging of the human brain^[49].

PET Studies of the Dopamine Transporter

The DAT is a membrane-spanning protein that pumps DA from the extracellular space into the presynaptic neuronal cytosol, from which other transporters sequester DA into vesicles for storage and later release (Fig. 1). DA reuptake *via* the DAT is the primary mechanism by which DA is cleared from synapses and DATs have been used as markers of presynaptic DA terminals^[50]. The DAT is also a target for addictive drugs such as cocaine and AMPH. Currently, there are several positron-emitting radionuclide-labeled tracers for PET imaging of the DAT *in vivo*, such as [¹¹C] cocaine, [¹¹C] β-CIT, [¹⁸F] FCT, WIN 35,428, and [¹¹C] d-threo-MP. And the neuroimaging studies have demonstrated that chronic use of addictive drugs has long-term impact on DAT levels and activity, resulting in dopaminergic dysfunction by mechanisms not well understood^[51] (Table 3).

Cocaine was initially labeled with ¹¹C to track the

distribution and pharmacokinetics of this powerful stimulant and drug of abuse in the human brain and body. It was soon discovered that [¹¹C] cocaine is also a sensitive radiotracer for DAT availability^[52]. Because the major molecular target of cocaine is the DAT, the question of whether chronic cocaine use alters the DAT has been investigated^[53]. Although postmortem studies have shown decreased DAT in cocaine addicts^[54], one PET study using [¹¹C] cocaine reported no significant differences in DAT binding between cocaine-dependent individuals who had withdrawn for >5 days and controls^[53].

Besides cocaine *per se*, some of its congeners have also been labeled with positron-releasing radionuclides to study the function of the DAT in drug addiction *in vivo*. 2β-carboxymethoxy-3β-(4-iodophenyl) tropane (β-CIT), one of these congeners, has been labeled with ¹¹C for PET studies. In an autoradiographic study on human brain sections and a PET study of monkeys and humans, [¹¹C] β-CIT was found to accumulate markedly in the striatum where DATs are mostly located^[55]. In an *in vivo* PET study with [¹¹C] β-CIT, decreased DAT has been found in the putamen in early Parkinson's disease^[56], but so far it has not been used in the study of drug abuse.

In 2000, [¹⁸F]-(1)-N-(4-fluorobenzyl)-2b-propanoyl-3b-(4-chlorophenyl) tropane ([¹⁸F] FCT), a structural congener of cocaine, was found to have a high affinity for the DAT and a relatively low affinity for the serotonin transporter, indicating that it is a suitable tracer for studying the DAT *in vivo* with PET^[57]. In the PET study with [¹⁸F] FCT in the cocaine self-administration model with monkeys, the laterality of DAT function was changed even before enough cocaine was consumed to produce significant overall changes in receptor and transporter availability^[58].

Table 3. PET imaging of the dopamine transporter in drug addiction

Ref.	Radioligand	Drug	Subjects	Controls	Main findings
[53]	[¹¹ C] cocaine	Cocaine	12 detoxified cocaine abusers (>5 days)	20 normal controls	(-)
[58]	[¹⁸ F] FCT	Cocaine	12 adult male cocaine-naive rhesus macaques with drug self-administration (9 weeks)	same monkeys before drug use	(-)
[62]	[¹¹ C] WIN 35,428	Heroin	11 heroin users abstinent for 6 months, and 10 on methadone maintenance for 6 months	10 normal controls	(↓); (↓) (comparison to the abstinent subjects); [¹¹ C] WIN 35,428 uptake correlated with subjective anxiety in methadone maintenance subjects
[63]	[¹¹ C] WIN 35,428	MA	6 abstinent MA users	10 normal controls	(↓)
[64]	[¹¹ C] WIN 35,428	MA	baboons treated with one of three doses of MA [0.5 mg/kg (<i>n</i> = 2), 1 mg/kg (<i>n</i> = 2) and 2 mg/kg (<i>n</i> = 3)]	3 baboons treated with saline	(↓) [¹¹ C] WIN 35,428 uptake correlated with MA dose
[65]	[¹¹ C] WIN 35,428	MA	11 male MA users	9 normal controls	(↓) [¹¹ C] WIN 35,428 uptake associated with duration of MA use and closely related to severity of persistent psychiatric symptoms
[69]	[¹¹ C] d-threo-MP	Alcohol	5 alcoholics	16 normal controls	(-)

(↓) striatal radioligand uptake decreased or (-) did not differ significantly from healthy controls; MA, methamphetamine.

Other cocaine analogs, WIN 35,428 and CFT [2β-carbomethoxy-3 beta-(4-fluorophenyl) tropane], have been extensively characterized as selective inhibitors of DA uptake with high affinity for the DAT^[59]. Human studies have shown that the extent of [¹¹C] WIN 35,428 binding can be used to differentiate normal people from those with DA system disorders^[60, 61]. A PET imaging study with [¹¹C] WIN 35,428 demonstrated that heroin users have a significantly lower DAT uptake than healthy controls^[62]. [¹¹C] WIN 35,428 has also revealed a reduction of the DAT in MA abusers and in baboons after MA injection^[63-66].

Methylphenidate (MP, Ritalin), a psychostimulant, is commonly used to treat attention deficit hyperactivity disorder and narcolepsy. The psychostimulant properties of

MP are linked to its binding to a site on the DAT, resulting in inhibition of DA reuptake and enhanced levels of synaptic DA. The more active d-enantiomer (d-threo-MP) has been labeled with [¹¹C] and animal studies have demonstrated the saturable, reversible, and specific binding of [¹¹C] d-threo-MP to the DAT, suggesting that it is a useful PET tracer for imaging presynaptic dopaminergic neurons^[67]. A PET imaging study using pretreatment with MP showed a marked decrease of [¹¹C] d-threo-MP binding in the human brain^[68]. However, PET imaging did not find a significant difference of [¹¹C] d-threo-MP distribution between alcoholics and non-alcoholics, which means that prolonged alcohol abuse might have no significant impact on DAT availability^[69].

PET Studies of Postsynaptic DA Receptors

The radiolabeled ligands for PET imaging of DA receptors in drug addiction and the main findings are listed in Table 4.

Spiroperidol (spiperone) is a potent D2 receptor antagonist^[70]. In 1984, *in vivo* studies in rats and primates showed that ¹⁸F-labeled spiroperidol has high specific activity for D2 receptors^[71]. Latterly, N-methylspiroperidol (NMSP), the amide N-methyl analog, has also been radiolabeled with ¹⁸F. *In vivo* PET imaging in the baboon brain showed that striatal uptake and retention is five-fold higher for [¹⁸F] NMSP than for [¹⁸F] spiroperidol, which suggested that [¹⁸F] NMSP is an ideal choice for studies of the D2 receptor in humans^[72]. In PET studies with [¹⁸F] NMSP, cocaine abusers show significantly lower D2 receptor availability than normal controls, especially during early detoxification^[53, 73], and this may be present even 3–4 months after detoxification^[74]. D2 receptor availability was also found to be associated with decreased metabolism in several regions of the frontal lobe, most markedly the orbito-frontal cortex and cingulate gyri^[73]. *In vivo* PET imaging in baboons showed that AMPH pretreatment induces decreases in [¹⁸F] NMSP in the corpus striatum, suggesting that PET imaging with [¹⁸F] NMSP can also be used to monitor drug-induced elevations in endogenous DA levels^[75].

Raclopride is a synthetic compound that acts as an antagonist on D2 receptors and ¹¹C-labeled raclopride is the most commonly-used tracer in the PET imaging of addiction to cocaine^[76], alcohol^[69, 77, 78], MA^[79], and heroin^[80]. In cocaine abusers with intravenous administration of 48 mg cocaine (a typical “street” dose), [¹¹C] raclopride occupancy at D2 receptors was decreased significantly, suggesting that higher DA concentrations compete at the receptor site^[76]. Alcoholics showed lower D2 receptor levels in the caudate and putamen during early detoxification and in the caudate during late detoxification, which is in line with the idea that D2 mechanisms are involved in alcohol dependence^[69, 77, 78]. Heroin-dependent individuals^[80] and MA abusers^[79] both showed significantly lower D2 receptor availability than comparison subjects.

[¹⁸F]FCP ([¹⁸F] 4-fluorocleobopride) is a fluorine-18 labeled benzamide derivative that binds reversibly to D2 receptors^[81]. In PET imaging with [¹⁸F] FCP, Nader and colleagues^[82] found that the baseline D2 receptor

availability is negatively correlated with the rate of cocaine self-administration.

[¹⁸F] fallypride, an analog of epidepride, is a selective and high-affinity antagonist of D2/D3 receptors. In an [¹⁸F] fallypride PET imaging study, nicotine-dependent smokers displayed significantly less availability of D2/D3 receptors within the bilateral putamen, functionally covering parts of the dorsal striatum, compared to never-smoking subjects^[83]. [¹⁸F] desmethoxyfallypride ([¹⁸F] DMFP), another selective D2/D3 receptor antagonist, has also been developed and used to find that a low availability of D2/3 receptors in the ventral striatum and adjacent putamen is associated with a high level of craving for alcohol^[33].

For the D1 receptor, [¹¹C] NNC 112, a new benzazepine [(+)-8-chloro-5-(7-benzofuranyl)-7-hydroxy-3-methyl-2,3,4,5-tetra-hydro-1H-3-benzazepine], has been reported to be a useful PET radioligand for the quantitation of D1 receptors in humans^[84], and its D1 receptor selectivity has recently been re-evaluated^[85]. With PET and the radiotracer [¹¹C] NNC 112, Martinez *et al.*^[86] found no difference between cocaine abusers and normal controls. However, within the cocaine abusers, low D1 receptor availability in the ventral striatum was associated with the choice to self-administer cocaine, suggesting that low D1 receptor availability may be associated with an increased risk of relapse. Another radioligand, [¹¹C] SCH23390 [(R)-(+)-7-chloro-8-hydroxy-3-methyl-1-phenyl -2,3,4,5-tetrahydro-1H-3-benzazepine], the first selective D1-like receptor antagonist, is recognized as the standard ligand for PET studies of striatal D1 receptors^[87]. A significant reduction in [¹¹C] SCH23390 binding potential has been found in the striatum of smokers compared to nonsmokers, most prominently in the ventral striatum, suggesting a reduction in D1 receptor density in the ventral striatum of cigarette smokers^[88, 89].

Conclusions

PET imaging studies have corroborated the role of DA in drug addiction. The increases in DA caused by addictive drugs and the subsequent fast and marked activation of postsynaptic DA receptors are relevant for drug reinforcement. The adaptive changes in the dopaminergic system after long-term drug abuse may lead to the

Table 4. PET imaging of postsynaptic DA receptors in drug addiction

Ref.	target	Radioligand	Drug	Subjects	Controls	Main findings
[73]	D2	[¹⁸ F] NMSP	Cocaine	10 cocaine abusers	10 normal controls	(↓) (detoxified for 1 week); (-) (detoxified for 1 month)
[74]	D2	[¹⁸ F] NMSP	Cocaine	20 male cocaine abusers	20 normal male controls	(↓)
[75]	D2	[¹⁸ F] NMSP	AMPH	3 adult female baboons treated with AMPH (1.0 mg/kg)	before drug use	(↓)
[76]	D2	[¹¹ C] raclopride	Cocaine	11 male cocaine abusers with intravenous administration of 48 mg cocaine	before drug use	(↓)
[53]	D2	[¹⁸ F] NMSP	Cocaine	10 cocaine abusers	9 normal controls	(↓)
[69]	D2	[¹¹ C] raclopride	Alcohol	10 alcoholics	10 normal controls	(↓)
[77]	D2	[¹¹ C] raclopride	Alcohol	9 male alcoholics abstinent for 1-68 weeks	8 normal male controls	(↓)
[78]	D2	[¹¹ C] raclopride	Alcohol	14 type 2 alcoholics tested within 6 weeks of detoxification and re-tested 1-4 months later while alcohol-free	11 normal controls	(↓); (-) (between early and late detoxification)
[79]	D2	[¹¹ C] raclopride	MA	15 MA abusers	20 normal controls	(↓) [¹¹ C] raclopride uptake positively correlated with rate in orbitofrontal cortex in abusers
[80]	D2	[¹¹ C] raclopride	Heroin	11 opiate-dependent individuals	11 normal controls	(↓)
[81]	D2	[¹⁸ F] FCP	Cocaine	12 rhesus macaques with cocaine self-administration	Self control	(↓) (by 15-20% within 1 week initiating self-administration); of (↓) (by 20% during 1 year of drug exposure)
[83]	D2/D3	[¹⁸ F] fallypride	Nicotine	17 heavy smokers	21 age-matched normal controls	(-); [¹⁸ F] fallypride uptake positively correlated with nicotine craving in the ventral striatum but negatively correlated in the anterior cingulate and inferior temporal cortex
[33]	D2/D3	[¹⁸ F] DMFP	Alcohol	12 alcoholics	12 normal controls	(↓) (negatively correlated with alcohol craving)
[86]	D1	[¹¹ C] NNC 112	Cocaine	25 cocaine abusers	23 normal controls	(-) [¹¹ C] NNC 112 uptake in ventral striatum negatively correlated with cocaine relapse
[88]	D1	[¹¹ C] SCH23390	Nicotine	11 smokers	18 normal controls	(↓)
[89]	D1	[¹¹ C] SCH23390	Nicotine	12 smokers	12 normal controls	(↓) trend of increase of [¹¹ C] SCH23390 uptake after smoking abstinence

(↓) striatal radioligand uptake decreased and (-) not significantly different from healthy controls; MA, methamphetamine; AMPH, amphetamine.

persistent use of drugs and cause relapse. Neuroimaging studies have provided evidence of how the human brain changes as the individual becomes addicted. With the appropriate radiotracers, PET enables visualization of the presynaptic and postsynaptic sites in the dopaminergic system. Imaging these markers provides key insights into the pathophysiology of drug addiction, and understanding of the involvement of DA in drug abuse may also offer directions for the development of new strategies for pharmacological interventions for addiction. The therapeutic interventions that are driven by the imaging findings on DA can be divided into those that interfere with the acute effects of a drug and those that compensate for the chronic effects of long-term use linked to its dopaminergic effects^[90].

In the future, the role of PET may become more important in drug-addiction diagnosis and guiding therapy. Enhancements in image resolution and specific molecular tags will permit accurate diagnoses, based on both structural and molecular changes in the brain. For widespread application, advances in molecular imaging should include the characterization of new radiotracers, application of modeling techniques, standardization and automation of image-processing techniques, and appropriate clinical settings in large multicenter trials. The growing field of neuroimaging is helping nuclear medicine physicians to incorporate pathways into personalized patient care.

However, the use of PET to study the role of the dopaminergic system in drug addiction is still in its infancy. Although available PET studies have mainly focused on DA, its interactions with other neurotransmitters such as GABA, glutamate, and serotonin also play important roles in modulating the magnitude of DA responses to drugs. Currently, several imaging modalities complement each other, and image fusion has become common in diagnostics and treatment^[91]. In recent years, the multimodality imaging technologies such as PET/CT and PET/MRI have shown promising results, indicating great potential for clinical and preclinical uses^[92]. There is no doubt that future PET research on drug addiction will benefit greatly from multimodal imaging approaches. Furthermore, the development of new PET tracers that are sensitive to the targets of DA and other neurotransmitter systems, along with the findings of multimodal imaging studies that are integrated into genetic and neurobiological research, will

increase our understanding of the mechanisms underlying drug addiction.

ACKNOWLEDGEMENTS

This review was partly sponsored by the National Basic Research Development Program of China (2013CB329506), the National Natural Science Foundation of China (81301243 and 81271601), the Research Fund for the Doctoral Program of Higher Education of China (20120101120031 and 20130101110015), grants from the Health Bureau of Zhejiang Province (2014KYA095, and WKJ2013-2-016), the Scientific Research Foundation for Doctors of Second Affiliated Hospital of Zhejiang University School of Medicine (Y560252013), and the Natural Science Foundation of Zhejiang Province, China (LR13H180001).

Received date: 2014-04-24; Accepted date: 2014-06-02

REFERENCES

- [1] Smythies J. Section II. The dopamine system. *Int Rev Neurobiol* 2005, 64: 123–172.
- [2] Callier S, Snapyan M, Le Crom S, Prou D, Vincent JD, Vernier P. Evolution and cell biology of dopamine receptors in vertebrates. *Biol Cell* 2003, 95: 489–502.
- [3] Lee D, Huang W, Lim AT. Dopamine induces a biphasic modulation of hypothalamic ANF neurons: a ligand concentration-dependent effect involving D5 and D2 receptor interaction. *Mol Psychiatry* 2000, 5: 39–48.
- [4] Vallone D, Picetti R, Borrelli E. Structure and function of dopamine receptors. *Neurosci Biobehav Rev* 2000, 24: 125–132.
- [5] Missale C, Nash SR, Robinson SW, Jaber M, Caron MG. Dopamine receptors: from structure to function. *Physiol Rev* 1998, 78: 189–225.
- [6] Garris PA, Ciolkowski EL, Pastore P, Wightman RM. Efflux of dopamine from the synaptic cleft in the nucleus accumbens of the rat brain. *J Neurosci* 1994, 14: 6084–6093.
- [7] Wise RA. Roles for nigrostriatal—not just mesocorticolimbic—dopamine in reward and addiction. *Trends Neurosci* 2009, 32: 517–524.
- [8] Maddux JF, Desmond DP. Addiction or dependence? *Addiction* 2000, 95: 661–665.
- [9] Koob GF, Le Moal M. Drug abuse: hedonic homeostatic dysregulation. *Science* 1997, 278: 52–58.
- [10] Holden C. 'Behavioral' addictions: do they exist? *Science* 2001, 294: 980–982.
- [11] Bancroft J, Vukadinovic Z. Sexual addiction, sexual compulsivity, sexual impulsivity, or what? Toward a theoretical model. *J Sex Res* 2004, 41: 225–234.

- [12] Block JJ. Issues for DSM-V: internet addiction. *Am J Psychiatry* 2008, 165: 306–307.
- [13] Pelchat ML. Food addiction in humans. *J Nutr* 2009, 139: 620–622.
- [14] Grant JE, Potenza MN, Weinstein A, Gorelick D A. Introduction to behavioral addictions. *Am J Drug Alcohol Abuse* 2010, 36: 233–241.
- [15] Holden C. Psychiatry. Behavioral addictions debut in proposed DSM-V. *Science* 2010, 327: 935.
- [16] O'Brien C. Addiction and dependence in DSM-V. *Addiction* 2011, 106: 866–867.
- [17] Tian M, Chen Q, Zhang Y, Du F, Hou H, Chao F, *et al.* PET imaging reveals brain functional changes in internet gaming disorder. *Eur J Nucl Med Mol Imaging*, 2014, 41: 1388–1397
- [18] Mansi L, Cuccurullo V, Ciarmiello A. From Homo sapiens to Homo in nexu (connected man): could functional imaging redefine the brain of a "new human species"? *Eur J Nucl Med Mol Imaging* 2014, 41: 1385–1387.
- [19] Koob GF, Stinus L, Le Moal M, Bloom FE. Opponent process theory of motivation: neurobiological evidence from studies of opiate dependence. *Neurosci Biobehav Rev* 1989, 13: 135–140.
- [20] Cami J, Farre M. Drug addiction. *N Engl J Med* 2003, 349: 975–986.
- [21] Franken I H, Booij J, van den Brink W. The role of dopamine in human addiction: from reward to motivated attention. *Eur J Pharmacol* 2005, 526: 199–206.
- [22] Goodman A. Neurobiology of addiction. An integrative review. *Biochem Pharmacol* 2008, 75: 266–322.
- [23] Volkow ND, Wang GJ, Fowler JS, Tomasi D, Telang F. Quantification of Behavior Sackler Colloquium: Addiction: Beyond dopamine reward circuitry. *Proc Natl Acad Sci U S A* 2011, 108: 15037–15042.
- [24] Volkow ND, Fowler JS, Wang GJ, Baler R, Telang F. Imaging dopamine's role in drug abuse and addiction. *Neuropharmacology* 2009, 56 Suppl 1: 3–8.
- [25] Hou H, Tian M, Zhang H. Positron emission tomography molecular imaging of dopaminergic system in drug addiction. *Anat Rec (Hoboken)* 2012, 295: 722–733.
- [26] Schiffer WK, Lee DE, Brodie JD, Dewey SL. Imaging addiction with PET: is insight in sight? *Drug Discov Today* 2005, 10: 547–562.
- [27] Christman DR, Hoyte RM, Wolf AP. Organic radiopharmaceuticals labeled with isotopes of short half-life. I. 11C-1-dopamine hydrochloride. *J Nucl Med* 1970, 11: 474–478.
- [28] Volkow ND, Fowler JS, Wang GJ. Positron emission tomography and single-photon emission computed tomography in substance abuse research. *Semin Nucl Med* 2003, 33: 114–128.
- [29] Fischman MW, Foltin RW. Utility of subjective-effects measurements in assessing abuse liability of drugs in humans. *Br J Addict* 1991, 86: 1563–1570.
- [30] Volkow ND, Ding YS, Fowler JS, Wang GJ, Logan J, Gatley JS, *et al.* Is methylphenidate like cocaine? Studies on their pharmacokinetics and distribution in the human brain. *Arch Gen Psychiatry* 1995, 52: 456–463.
- [31] Nanni C, Fanti S, Rubello D. ¹⁸F-DOPA PET and PET/CT. *J Nucl Med* 2007, 48: 1577–1579.
- [32] Turjanski N, Lees AJ, Brooks DJ. Striatal dopaminergic function in restless legs syndrome: 18F-dopa and 11C-raclopride PET studies. *Neurology* 1999, 52: 932–937.
- [33] Heinz A, Siessmeier T, Wrase J, Buchholz HG, Grunder G, Kumakura Y, *et al.* Correlation of alcohol craving with striatal dopamine synthesis capacity and D2/3 receptor availability: a combined [18F]DOPA and [18F]DMFP PET study in detoxified alcoholic patients. *Am J Psychiatry* 2005, 162: 1515–1520.
- [34] Wu JC, Bell K, Najafi A, Widmark C, Keator D, Tang C, *et al.* Decreasing striatal 6-FDOPA uptake with increasing duration of cocaine withdrawal. *Neuropsychopharmacology* 1997, 17: 402–409.
- [35] Klongpanichapak S, Govitrapong P, Sharma SK, Ebadi M. Attenuation of cocaine and methamphetamine neurotoxicity by coenzyme Q10. *Neurochem Res* 2006, 31: 303–311.
- [36] Dackis CA, Gold MS. New concepts in cocaine addiction: the dopamine depletion hypothesis. *Neurosci Biobehav Rev* 1985, 9: 469–477.
- [37] Markou A, Koob GF. Postcocaine anhedonia. An animal model of cocaine withdrawal. *Neuropsychopharmacology* 1991, 4: 17–26.
- [38] Kienast T, Schlagenhauf F, Rapp MA, Wrase J, Daig I, Buchholz HG, *et al.* Dopamine-modulated aversive emotion processing fails in alcohol-dependent patients. *Pharmacopsychiatry* 2013, 46: 130–136.
- [39] Tiihonen J, Vilkkumäki H, Rasanen P, Ryyanen OP, Hakko H, Bergman J, *et al.* Striatal presynaptic dopamine function in type 1 alcoholics measured with positron emission tomography. *Mol Psychiatry* 1998, 3: 156–161.
- [40] Salokangas RK, Vilkkumäki H, Ilonen T, Taiminen T, Bergman J, Haaparanta M, *et al.* High levels of dopamine activity in the basal ganglia of cigarette smokers. *Am J Psychiatry* 2000, 157: 632–634.
- [41] Tai YF, Hoshi R, Brignell CM, Cohen L, Brooks DJ, Curran HV, *et al.* Persistent nigrostriatal dopaminergic abnormalities in ex-users of MDMA ('Ecstasy'): an 18F-dopa PET study. *Neuropsychopharmacology* 2011, 36: 735–743.
- [42] Martin WR, Wieler M, Stoessl AJ, Schulzer M. Dihydrotrabenazine positron emission tomography imaging in early, untreated Parkinson's disease. *Ann Neurol* 2008, 63: 388–394.
- [43] Boileau I, Houle S, Rusjan PM, Furukawa Y, Wilkins D, Tong

- J, *et al.* Influence of a low dose of amphetamine on vesicular monoamine transporter binding: a PET (+)[11C]DTBZ study in humans. *Synapse* 2010, 64: 417–420.
- [44] Little KY, Zhang L, Desmond T, Frey KA, Dalack GW, Cassin BJ. Striatal dopaminergic abnormalities in human cocaine users. *Am J Psychiatry* 1999, 156: 238–245.
- [45] Narendran R, Lopresti BJ, Martinez D, Mason NS, Himes M, May MA, *et al.* In vivo evidence for low striatal vesicular monoamine transporter 2 (VMAT2) availability in cocaine abusers. *Am J Psychiatry* 2012, 169: 55–63.
- [46] Johanson CE, Frey KA, Lundahl LH, Keenan P, Lockhart N, Roll J, *et al.* Cognitive function and nigrostriatal markers in abstinent methamphetamine abusers. *Psychopharmacology (Berl)* 2006, 185: 327–338.
- [47] Boileau I, Rusjan P, Houle S, Wilkins D, Tong J, Selby P, *et al.* Increased vesicular monoamine transporter binding during early abstinence in human methamphetamine users: Is VMAT2 a stable dopamine neuron biomarker? *J Neurosci* 2008, 28: 9850–9856.
- [48] Kilbourn MR, Butch ER, Desmond T, Sherman P, Harris PE, Frey KA. In vivo [11C]dihydrotrabenazine binding in rat striatum: sensitivity to dopamine concentrations. *Nucl Med Biol* 2010, 37: 3–8.
- [49] Eiden LE, Weihe E. VMAT2: a dynamic regulator of brain monoaminergic neuronal function interacting with drugs of abuse. *Ann N Y Acad Sci* 2011, 1216: 86–98.
- [50] Volkow ND, Chang L, Wang GJ, Fowler JS, Franceschi D, Sedler M, *et al.* Loss of dopamine transporters in methamphetamine abusers recovers with protracted abstinence. *J Neurosci* 2001, 21: 9414–9418.
- [51] Urban NB, Martinez D. Neurobiology of addiction: insight from neurochemical imaging. *Psychiatr Clin North Am* 2012, 35: 521–541.
- [52] Fowler JS, Volkow ND, Wang GJ, Gatley SJ, Logan J. [(11)C]Cocaine: PET studies of cocaine pharmacokinetics, dopamine transporter availability and dopamine transporter occupancy. *Nucl Med Biol* 2001, 28: 561–572.
- [53] Volkow ND, Wang GJ, Fowler JS, Logan J, Hitzemann R, Gatley SJ, *et al.* Cocaine uptake is decreased in the brain of detoxified cocaine abusers. *Neuropsychopharmacology* 1996, 14: 159–168.
- [54] Hurd YL, Herkenham M. Molecular alterations in the neostriatum of human cocaine addicts. *Synapse* 1993, 13: 357–369.
- [55] Farde L, Halldin C, Muller L, Suhara T, Karlsson P, Hall H. PET study of [11C]beta-CIT binding to monoamine transporters in the monkey and human brain. *Synapse* 1994, 16: 93–103.
- [56] Rinne JO, Laihininen A, Nagren K, Ruottinen H, Ruotsalainen U, Rinne UK. PET examination of the monoamine transporter with [11C]beta-CIT and [11C]beta-CFT in early Parkinson's disease. *Synapse* 1995, 21: 97–103.
- [57] Mach RH, Nader MA, Ehrenkauf RL, Gage HD, Childers SR, Hodges LM, *et al.* Fluorine-18-labeled tropine analogs for PET imaging studies of the dopamine transporter. *Synapse* 2000, 37: 109–117.
- [58] Czoty PW, Gage HD, Nader SH, Reboussin BA, Bounds M, Nader MA. PET imaging of dopamine D2 receptor and transporter availability during acquisition of cocaine self-administration in rhesus monkeys. *J Addict Med* 2007, 1: 33–39.
- [59] Canfield DR, Spealman RD, Kaufman MJ, Madras BK. Autoradiographic localization of cocaine binding sites by [3H]CFT ([3H]WIN 35,428) in the monkey brain. *Synapse* 1990, 6: 189–195.
- [60] Frost JJ, Rosier AJ, Reich SG, Smith JS, Ehlers MD, Snyder SH, *et al.* Positron emission tomographic imaging of the dopamine transporter with 11C-WIN 35,428 reveals marked declines in mild Parkinson's disease. *Ann Neurol* 1993, 34: 423–431.
- [61] Rinne JO, Laihininen A, Nagren K, Ruottinen H, Ruotsalainen U, Rinne UK. PET examination of the monoamine transporter with [11C]beta-CIT and [11C]beta-CFT in early Parkinson's disease. *Synapse* 1995, 21: 97–103.
- [62] Shi J, Zhao LY, Copersino ML, Fang YX, Chen Y, Tian J, *et al.* PET imaging of dopamine transporter and drug craving during methadone maintenance treatment and after prolonged abstinence in heroin users. *Eur J Pharmacol* 2008, 579: 160–166.
- [63] Mccann UD, Wong DF, Yokoi F, Villemagne V, Dannals RF, Ricaurte GA. Reduced striatal dopamine transporter density in abstinent methamphetamine and methcathinone users: evidence from positron emission tomography studies with [11C]WIN-35,428. *J Neurosci* 1998, 18: 8417–8422.
- [64] Villemagne V, Yuan J, Wong DF, Dannals RF, Hatzidimitriou G, Mathews WB, *et al.* Brain dopamine neurotoxicity in baboons treated with doses of methamphetamine comparable to those recreationally abused by humans: evidence from [11C]WIN-35,428 positron emission tomography studies and direct in vitro determinations. *J Neurosci* 1998, 18: 419–427.
- [65] Sekine Y, Iyo M, Ouchi Y, Matsunaga T, Tsukada H, Okada H, *et al.* Methamphetamine-related psychiatric symptoms and reduced brain dopamine transporters studied with PET. *Am J Psychiatry* 2001, 158: 1206–1214.
- [66] Sekine Y, Minabe Y, Ouchi Y, Takei N, Iyo M, Nakamura K, *et al.* Association of dopamine transporter loss in the orbitofrontal and dorsolateral prefrontal cortices with methamphetamine-related psychiatric symptoms. *Am J Psychiatry* 2003, 160: 1699–1701.
- [67] Ding YS, Fowler JS, Volkow ND, Logan J, Gatley SJ, Sugano Y. Carbon-11-d-threo-methylphenidate binding to dopamine transporter in baboon brain. *J Nucl Med* 1995, 36: 2298–

- 2305.
- [68] Ding YS, Fowler JS, Volkow ND, Dewey SL, Wang GJ, Logan J, *et al.* Chiral drugs: comparison of the pharmacokinetics of [¹¹C] d-threo and L-threo-methylphenidate in the human and baboon brain. *Psychopharmacology (Berl)* 1997, 131: 71–78.
- [69] Volkow ND, Wang GJ, Fowler JS, Logan J, Hitzemann R, Ding YS, *et al.* Decreases in dopamine receptors but not in dopamine transporters in alcoholics. *Alcohol Clin Exp Res* 1996, 20: 1594–1598.
- [70] De Jesus OT, Friedman AM. Radiobrominated spiroperidol for the study of dopamine D2 receptors. *Int J Rad Appl Instrum A* 1986, 37: 719–726.
- [71] Welch MJ, Raichle ME, Kilbourn MR, Mintun MA. [¹⁸F] spiroperidol: a radiopharmaceutical for the in vivo study of the dopamine receptor. *Ann Neurol* 1984, 15 Suppl: S77–S78.
- [72] Arnett CD, Fowler JS, Wolf AP, Shiue CY, McPherson DW. [¹⁸F]-N-Methylspiroperidol: the radioligand of choice for PET studies of the dopamine receptor in human brain. *Life Sci* 1985, 36: 1359–1366.
- [73] Volkow ND, Fowler JS, Wolf AP, Schlyer D, Shiue CY, Alpert R, *et al.* Effects of chronic cocaine abuse on postsynaptic dopamine receptors. *Am J Psychiatry* 1990, 147: 719–724.
- [74] Volkow ND, Fowler JS, Wang GJ, Hitzemann R, Logan J, Schlyer DJ, *et al.* Decreased dopamine D2 receptor availability is associated with reduced frontal metabolism in cocaine abusers. *Synapse* 1993, 14: 169–177.
- [75] Dewey SL, Logan J, Wolf AP, Brodie JD, Angrist B, Fowler JS, *et al.* Amphetamine induced decreases in (18F)-N-methylspiroperidol binding in the baboon brain using positron emission tomography (PET). *Synapse* 1991, 7: 324–327.
- [76] Schlaepfer TE, Pearlson GD, Wong DF, Marengo S, Dannals RF. PET study of competition between intravenous cocaine and [¹¹C]raclopride at dopamine receptors in human subjects. *Am J Psychiatry* 1997, 154: 1209–1213.
- [77] Hietala J, West C, Syvalahti E, Nagren K, Lehtikoinen P, Sonninen P, *et al.* Striatal D2 dopamine receptor binding characteristics in vivo in patients with alcohol dependence. *Psychopharmacology (Berl)* 1994, 116: 285–290.
- [78] Volkow ND, Wang GJ, Maynard L, Fowler JS, Jayne B, Telang F, *et al.* Effects of alcohol detoxification on dopamine D2 receptors in alcoholics: a preliminary study. *Psychiatry Res* 2002, 116: 163–172.
- [79] Volkow ND, Chang L, Wang GJ, Fowler JS, Ding YS, Sedler M, *et al.* Low level of brain dopamine D2 receptors in methamphetamine abusers: association with metabolism in the orbitofrontal cortex. *Am J Psychiatry* 2001, 158: 2015–2021.
- [80] Wang GJ, Volkow ND, Fowler JS, Logan J, Abumrad NN, Hitzemann RJ, *et al.* Dopamine D2 receptor availability in opiate-dependent subjects before and after naloxone-precipitated withdrawal. *Neuropsychopharmacology* 1997, 16: 174–182.
- [81] Mach RH, Nader MA, Ehrenkauser RL, Line SW, Smith CR, Gage HD, *et al.* Use of positron emission tomography to study the dynamics of psychostimulant-induced dopamine release. *Pharmacol Biochem Behav* 1997, 57: 477–486.
- [82] Nader MA, Morgan D, Gage HD, Nader SH, Calhoun TL, Buchheimer N, *et al.* PET imaging of dopamine D2 receptors during chronic cocaine self-administration in monkeys. *Nat Neurosci* 2006, 9: 1050–1056.
- [83] Fehr C, Yakushev I, Hohmann N, Buchholz HG, Landvogt C, Deckers H, *et al.* Association of low striatal dopamine d2 receptor availability with nicotine dependence similar to that seen with other drugs of abuse. *Am J Psychiatry* 2008, 165: 507–514.
- [84] Halldin C, Foged C, Chou YH, Karlsson P, Swahn CG, Sandell J, *et al.* Carbon-11-NNC 112: a radioligand for PET examination of striatal and neocortical D1-dopamine receptors. *J Nucl Med* 1998, 39: 2061–2068.
- [85] Slifstein M, Kegeles L S, Gonzales R, Frankle WG, Xu X, Laruelle M, *et al.* [¹¹C]NNC 112 selectivity for dopamine D1 and serotonin 5-HT(2A) receptors: a PET study in healthy human subjects. *J Cereb Blood Flow Metab* 2007, 27: 1733–1741.
- [86] Martinez D, Slifstein M, Narendran R, Foltin RW, Broft A, Hwang DR, *et al.* Dopamine D1 receptors in cocaine dependence measured with PET and the choice to self-administer cocaine. *Neuropsychopharmacology* 2009, 34: 1774–1782.
- [87] Hirvonen J, Nagren K, Kajander J, Hietala J. Measurement of cortical dopamine d1 receptor binding with [¹¹C]SCH23390: a test-retest analysis. *J Cereb Blood Flow Metab* 2001, 21: 1146–1150.
- [88] Dagher A, Bleicher C, Aston JA, Gunn RN, Clarke PB, Cumming P. Reduced dopamine D1 receptor binding in the ventral striatum of cigarette smokers. *Synapse* 2001, 42: 48–53.
- [89] Yasuno F, Ota M, Ando K, Ando T, Maeda J, Ichimiya T, *et al.* Role of ventral striatal dopamine D1 receptor in cigarette craving. *Biol Psychiatry* 2007, 61: 1252–1259.
- [90] Volkow ND, Fowler JS, Wang GJ, Swanson JM. Dopamine in drug abuse and addiction: results from imaging studies and treatment implications. *Mol Psychiatry* 2004, 9: 557–569.
- [91] Pichler BJ, Kolb A, Nagele T, Schlemmer HP. PET/MRI: paving the way for the next generation of clinical multimodality imaging applications. *J Nucl Med* 2010, 51: 333–336.
- [92] Pichler BJ, Judenhofer MS, Pfannenberger C. Multimodal imaging approaches: PET/CT and PET/MRI. *Handb Exp Pharmacol* 2008: 109–132.

Development of ^{18}F -labeled radiotracers for neuroreceptor imaging with positron emission tomography

Peter Brust, Jörg van den Hoff, Jörg Steinbach

Helmholtz-Zentrum Dresden-Rossendorf, Institute of Radiopharmaceutical Cancer Research, Permoserstrasse 15, Leipzig 04318, Germany

Corresponding author: Peter Brust. E-mail: p.brust@hzdr.de

© Shanghai Institutes for Biological Sciences, CAS and Springer-Verlag Berlin Heidelberg 2014

Positron emission tomography (PET) is an *in vivo* molecular imaging tool which is widely used in nuclear medicine for early diagnosis and treatment follow-up of many brain diseases. PET uses biomolecules as probes which are labeled with radionuclides of short half-lives, synthesized prior to the imaging studies. These probes are called radiotracers. Fluorine-18 is a radionuclide routinely used in the radiolabeling of neuroreceptor ligands for PET because of its favorable half-life of 109.8 min. The delivery of such radiotracers into the brain provides images of transport, metabolic, and neurotransmission processes on the molecular level. After a short introduction into the principles of PET, this review mainly focuses on the strategy of radiotracer development bridging from basic science to biomedical application. Successful radiotracer design as described here provides molecular probes which not only are useful for imaging of human brain diseases, but also allow molecular neuroreceptor imaging studies in various small-animal models of disease, including genetically-engineered animals. Furthermore, they provide a powerful tool for *in vivo* pharmacology during the process of pre-clinical drug development to identify new drug targets, to investigate pathophysiology, to discover potential drug candidates, and to evaluate the pharmacokinetics and pharmacodynamics of drugs *in vivo*.

Keywords: Alzheimer's disease; autoradiography; blood-brain barrier; brain tumor; cholinergic system; kinetic modeling; metabolism; molecular imaging; neurodegeneration; positron emission tomography; precursor; psychiatric disorder; radiotracer; sigma receptor

Introduction

Positron emission tomography (PET) is an *in vivo* molecular imaging tool widely used in nuclear medicine for early diagnosis and treatment follow-up of many brain diseases. Positron-emitting radionuclide-labeled substances allow the visualization, characterization, and measurement of biological processes at the molecular and cellular levels in humans and other living systems by highly sensitive coincidence-detection^[1]. This is based on 511 keV photons (gamma radiation) originating from positron-electron annihilation. PET differs in that aspect from other modalities such as single-photon emission computed tomography (SPECT), magnetic resonance imaging

(MRI), optical imaging, and ultrasound. Because of their high sensitivity ($\sim 10^{-9}$ to 10^{-12} M) PET and SPECT offer advantages over the other methods. Therefore, in the past, they were the only modalities that allowed noninvasive imaging of biochemical receptor sites. Nowadays, the other imaging modalities compete in that aspect although precise absolute quantitation in terms of biochemical parameters has not been achieved yet.

Recently, multimodal imaging approaches, specifically PET/CT and PET/MRI, have been suggested to bring a new perspective into the fields of clinical and preclinical imaging. Clinical cases have shown that the combination of anatomical structures, revealed by CT and MRI, and the functional information from PET into one image, with high

fusion accuracy, provides an advanced diagnostic tool and research platform^[2, 3].

PET and SPECT use biomolecules as probes, labeled with radionuclides of short half-lives, synthesized prior to the imaging studies. These probes are called radiotracers. According to the concept developed by George von Hevesy^[4] a radiotracer is a chemical compound in which one or more atoms have been replaced by its radioisotope. By virtue of its radioactive decay, it can be used to follow the original compound as it acts in the same manner. Due to the extremely small concentrations required, the radiotracer does not disturb the systemic processes to be studied. This allows the tracing of chemical, biochemical, and physiological processes and investigation of their functions and capacities.

Although SPECT is the most common imaging tool in clinical nuclear medicine, this review is focused on PET. SPECT primarily uses radioiodine, e.g. ¹²³I, or radiometals, e.g. ^{99m}Tc as the label. Iodine is rarely present and metals are usually absent from the protein-binding drugs that serve as lead structures. Therefore, the applicability of SPECT for neuroimaging is rather limited, because labeling with ¹²³I or ^{99m}Tc causes strong and unpredictable alterations of target affinities and blood-brain-barrier (BBB) permeability. The positron-emitting radionuclides ¹¹C and ¹⁸F, introduced as an isotopic modification (¹¹C for ¹²C; “isotopic labeling”) or an atomic substitute (¹⁸F for ¹H, OH; “isosteric, isoelectronic, or biososteric labeling”), generate rather small affinity changes, if any. ¹⁸F is considered the most suitable radionuclide for PET because of its five-fold longer half-life (109.8 min) than ¹¹C, its high β^+ yield (97%) and its lower positron energy maximum of 640 keV (IAEA, Nuclear Data Services, <https://www-nds.iaea.org/relnsd/vcharthtml/VChartHTML.html>).

Despite the limitations, the principles and strategies for radiotracer development described below also apply to SPECT. Also, aspects of radiation safety, toxicology issues, quality control, licensing, and regulatory control, which need to be considered for the production of radiopharmaceuticals suitable for administration to humans, have been reviewed extensively elsewhere^[5]. Meanwhile, a highly regulated system for radiopharmaceutical production has been established in most of the developed countries (http://ec.europa.eu/health/documents/eudralex/vol-4/index_en.htm). This topic is therefore excluded from further consideration.

Successful radiotracer design as described below

does not necessarily lead to human application. Nowadays, special PET and SPECT devices are available for small-animal imaging, allowing molecular neuroreceptor imaging studies in various models of disease including genetically-engineered animals^[6, 7]. They provide a powerful tool for *in vivo* pharmacology during the process of pre-clinical drug development to identify new drug targets, to investigate pathophysiology, to discover potential drug candidates, and to evaluate the pharmacokinetics and pharmacodynamics of drugs *in vivo*^[8].

The general sequence of radiotracer development is shown in Fig. 1 and can be followed up in a short video available at <http://www.beilstein.tv/tvpost/toxic-epibatidine-was-structurally-modified-to-image-alzheimer%C2%B4s-disease/>. This demonstrates how chemical/pharmaceutical and biochemical/pharmacological steps interact to finally decide whether to break-off or continue the development process. PET radiotracers that have been developed for neuroreceptor imaging and have already been used in humans are listed in Table 1.

Target Selection and Identification of Lead Structures

Careful selection of the target to be imaged in combination

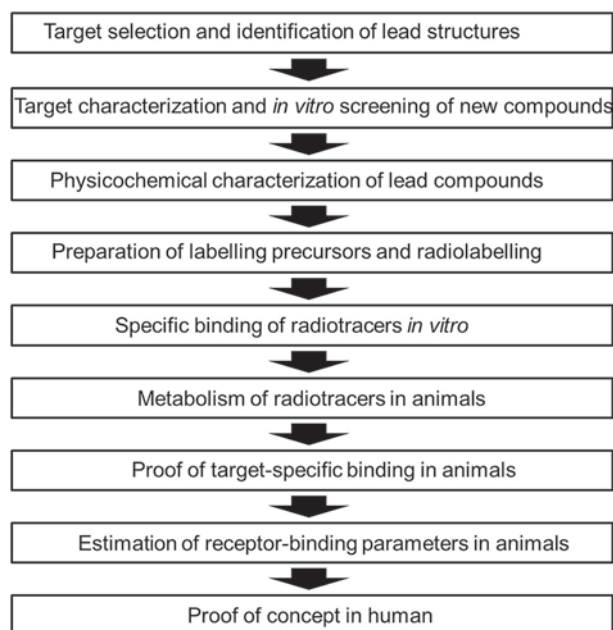


Fig. 1. Strategy for development of new PET radiotracers for neuroimaging.

Table 1. Neuroreceptor targets^a that have been used for successful PET radiotracer development

Neuroreceptor	PET radiotracer	Selected reference for human use
Acetylcholine receptor: muscarinic	[^{11}C]scopolamine	Frey <i>et al.</i> 1992 ^[9]
Acetylcholine receptor: muscarinic	[N- ^{11}C -methyl]-benztropine	Xie <i>et al.</i> 2004 ^[10]
Acetylcholine receptor: muscarinic	[^{11}C](+)-3-MPB	Yamamoto <i>et al.</i> 2012 ^[11]
Acetylcholine receptor: muscarinic M2	[^{18}F]FP-TZTP	Ichise <i>et al.</i> 2008 ^[12]
Acetylcholine receptor: nicotinic $\alpha 4\beta 2$	2-[^{18}F]fluoro-A-85380	Sabri <i>et al.</i> 2008 ^[13]
Acetylcholine receptor: nicotinic $\alpha 4\beta 2$	6-[^{18}F]fluoro-A-85380	Ding <i>et al.</i> 2004 ^[14]
Acetylcholine receptor: nicotinic $\alpha 4\beta 2$	[^{18}F]AZAN	Wong <i>et al.</i> 2013 ^[15]
Acetylcholine receptor: nicotinic $\alpha 4\beta 2$	(-)-[^{18}F]flubatine	Sabri <i>et al.</i> 2011 ^[16]
Acetylcholine receptor: nicotinic $\alpha 7$	[^{11}C]CHIBA-1001	Toyohara <i>et al.</i> 2009 ^[17]
Adenosine receptor: A ₁	[^{18}F]CPFPX	Bauer <i>et al.</i> 2003 ^[18]
Adenosine receptor: A ₁	[^{11}C]MPDX	Fukumitsu <i>et al.</i> 2008 ^[19]
Adenosine receptor: A _{2A}	[^{11}C]TMSX	Mishina <i>et al.</i> 2011 ^[20]
Adenosine receptor: A _{2A}	[^{11}C]SCH442416	Ramlackhansingh <i>et al.</i> 2011 ^[21]
Cannabinoid receptor: CB ₁	[^{18}F]MK-9470	Burns <i>et al.</i> 2007 ^[22]
Cannabinoid receptor: CB ₁	[^{11}C]MePPEP	Terry <i>et al.</i> 2010 ^[23]
Cannabinoid receptor: CB ₁	[^{18}F]FMPEP-d	Terry <i>et al.</i> 2010 ^[23]
Cannabinoid receptor: CB ₁	[^{11}C]OMAR	Wong <i>et al.</i> 2010 ^[24]
Cannabinoid receptor: CB ₂	[^{11}C]NE40	Ahmad <i>et al.</i> 2013 ^[25]
Dopamine receptor: D ₁	[^{11}C]SCH 23390	Farde <i>et al.</i> 1987 ^[26]
Dopamine receptor: D ₁	[^{11}C]NNC687	Karlsson <i>et al.</i> 1993 ^[27]
Dopamine receptor: D ₁	[^{11}C]NNC756	Karlsson <i>et al.</i> 1993 ^[27]
Dopamine receptor: D ₁	[^{11}C]NNC112	Slifstein <i>et al.</i> 2008 ^[28]
Dopamine receptor: D ₂ -D ₃	[^{11}C]raclopride	Farde <i>et al.</i> 1986 ^[29]
Dopamine receptor: D ₂ -D ₃	[^{11}C]NMSP	Wong <i>et al.</i> 1986 ^[30]
Dopamine receptor: D ₂ -D ₃	[^{11}C]NPA	Narendran <i>et al.</i> 2009 ^[31]
Dopamine receptor: D ₂ -D ₃	[^{11}C]MNPA	Otsuka <i>et al.</i> 2009 ^[32]
Dopamine receptor (extrastriatal): D ₂ /D ₃	[^{11}C]FLB457	Farde <i>et al.</i> 1997 ^[33]
Dopamine receptor (extrastriatal): D ₂ /D ₃	[^{18}F]fallypride	Mukherjee <i>et al.</i> 2002 ^[34]
Dopamine receptor: D ₃ >D ₂	[^{11}C]-(+)-PHNO	Ginovart <i>et al.</i> 2007 ^[35]
Estrogen receptor	[^{18}F]FES	Moresco <i>et al.</i> 1997 ^[36]
Glutamate receptor: mGluR1	[^{11}C]ITMM	Toyohara <i>et al.</i> 2013 ^[37]
Glutamate receptor: mGluR5	[^{11}C]ABP688	Ametamey <i>et al.</i> 2007 ^[38]
Glutamate receptor: mGluR5	[^{18}F]SP203	Brown <i>et al.</i> 2008 ^[39]
Glutamate receptor: mGluR5	[^{11}C]JAZD9272	Kagedal <i>et al.</i> 2012 ^[40]
Glutamate receptor: mGluR5	[^{18}F]FPEB	Wong <i>et al.</i> 2013 ^[41]
Glutamate NMDA receptor: PCP site	[^{11}C]ketamine	Kumlien <i>et al.</i> 1999 ^[42]
Glutamate NMDA receptor: PCP site	[^{11}C]CNS-5161	Hammers <i>et al.</i> 2004 ^[43]
Glutamate NMDA receptor: PCP site	[^{18}F]fluoromemantine	Ametamey <i>et al.</i> 2002 ^[44]
Glutamate NMDA receptor: PCP site	[^{18}F]GE-179	McGinnity <i>et al.</i> 2014 ^[45]
Glutamate NMDA receptor: glycine-site	[^{11}C]AcL703	Matsumoto <i>et al.</i> 2007 ^[46]
Histamine receptor: H1	[^{11}C]doxepin	Yanai <i>et al.</i> 1991 ^[47]

(To be continued)

(Continued)

Histamine receptor: H3	[¹¹ C]GSK189254	Ashworth <i>et al.</i> 2010 ^[46]
GABA-benzodiazepine receptor: α 1	[¹¹ C]flumazenil	Persson <i>et al.</i> 1985 ^[49]
GABA-benzodiazepine receptor: α 1	[¹⁸ F]fluoroethyl-flumazenil	Leveque <i>et al.</i> 2003 ^[50]
GABA-benzodiazepine receptor: α 1	[¹⁸ F]fluoroflumazenil	Lee <i>et al.</i> 2007 ^[51]
GABA-benzodiazepine receptor: α 1	[¹⁸ F]flumazenil	Massaweh <i>et al.</i> 2009 ^[52]
GABA-benzodiazepine receptor: α 5	[¹¹ C]Ro15-4513	Lingford-Hughes <i>et al.</i> 2002 ^[53]
Opioid receptor: μ	[¹¹ C]carfentanil	Frost <i>et al.</i> 1990 ^[54]
Opioid receptor: δ	[¹¹ C]methylnaltrindol	Madar <i>et al.</i> 1997 ^[55]
Opioid receptor: κ	[¹¹ C]GR103545	Tomasi <i>et al.</i> 2010 ^[56]
Opioid receptor: unselective	[¹¹ C]diprenorphine	Frost <i>et al.</i> 1990 ^[54]
Opioid receptor: unselective	[¹⁸ F]FcyF	Cohen <i>et al.</i> 2000 ^[57]
Opioid receptor: unselective	[¹⁸ F]fluorethyldiprenorphine	Baumgärtner <i>et al.</i> 2006 ^[58]
Neuropeptide Y receptor: Subtype 1	[¹⁸ F]Y1-973	Hostetler <i>et al.</i> 2011 ^{[59]b}
Serotonin receptor: 5-HT _{1A}	[¹¹ C]WAY-100635	Pike <i>et al.</i> 1995 ^[60]
Serotonin receptor: 5-HT _{1A}	[carbonyl- ¹¹ C]WAY-100635	Parsey <i>et al.</i> 2000 ^[61]
Serotonin receptor: 5-HT _{1A}	[carbonyl- ¹¹ C]DWAY	Andree <i>et al.</i> 2002 ^[62]
Serotonin receptor: 5-HT _{1A}	[¹¹ C]CPC-222	Houle <i>et al.</i> 1997 ^[63]
Serotonin receptor: 5-HT _{1A}	[¹¹ C]CUMI-101	Milak <i>et al.</i> 2010 ^[64]
Serotonin receptor: 5-HT _{1A}	[¹⁸ F]MPPF	Costes <i>et al.</i> 2002 ^[65]
Serotonin receptor: 5-HT _{1A}	[¹⁸ F]FCWAY	Theodore <i>et al.</i> 2006 ^[66]
Serotonin receptor: 5-HT _{1B}	[¹¹ C]P943	Gallezot <i>et al.</i> 2010 ^[67]
Serotonin receptor: 5-HT _{1B}	[¹¹ C]AZ10419369	Varnäs <i>et al.</i> 2011 ^[68]
Serotonin receptor: 5-HT _{1B}	[¹¹ C]P943	Murrrough <i>et al.</i> 2011 ^[69]
Serotonin receptor: 5-HT _{2A}	[¹¹ C]MDL100907	Hinz <i>et al.</i> 2007 ^[70]
Serotonin receptor: 5-HT _{2A}	[¹⁸ F]altanserin	Rosier <i>et al.</i> 1996 ^[71]
Serotonin receptor: 5-HT _{2A}	[¹⁸ F]deuteroaltanserin	Van Dyck <i>et al.</i> 2000 ^[72]
Serotonin receptor: 5-HT _{2A}	[¹⁸ F]setoperone	Trichard <i>et al.</i> 1998 ^[73]
Serotonin receptor: 5-HT _{2A}	[¹⁸ F]Cimbi-36	Ettrup <i>et al.</i> 2014 ^[74]
Serotonin receptor: 5-HT ₄	[¹¹ C]SB207145	Marnier <i>et al.</i> 2009 ^[75]
Serotonin receptor: 5-HT ₆	[¹¹ C]GSK215083	Parker <i>et al.</i> 2012 ^[76]
Sigma receptor: σ_1	[¹¹ C]SA4503	Mishina <i>et al.</i> 2005 ^[77]
Sigma receptor: σ_1	[¹⁸ F]FPS	Waterhouse <i>et al.</i> 2004 ^[78]
Translocator protein (TSPO) ^b	[¹¹ C]PK11195	Junck <i>et al.</i> 1989 ^[79]
Translocator protein (TSPO)	(<i>R</i>)-[¹¹ C]PK11195	Banati <i>et al.</i> 1999 ^[80]
Translocator protein (TSPO)	[¹¹ C]PBR28	Brown <i>et al.</i> 2007 ^[81]
Translocator protein (TSPO)	[¹¹ C]DPA-713	Endres <i>et al.</i> 2009 ^[82]
Translocator protein (TSPO)	[¹¹ C]DAA1106	Yasuno <i>et al.</i> 2012 ^[83]
Translocator protein (TSPO)	[¹¹ C]vinpocetine	Gulyas <i>et al.</i> 2012 ^[84]
Translocator protein (TSPO)	[¹⁸ F]F-PBR06	Fujimura <i>et al.</i> 2009 ^[85]
Translocator protein (TSPO)	[¹⁸ F]DPA-714	Arlicot <i>et al.</i> 2012 ^[86]
Translocator protein (TSPO)	[¹⁸ F]FEPPA	Mizrahi <i>et al.</i> 2012 ^[87]
Translocator protein (TSPO)	[¹⁸ F]PBR-111	Guo <i>et al.</i> 2013 ^[88]

^aNeurotransmitter transporters are not considered; ^bformerly known as peripheral benzodiazepine receptor.

with proper identification of a lead structure and subsequently an appropriate lead compound is one of the most important steps in the process of radiotracer development. Considering the resources needed to obtain a radiopharmaceutical ready for human application, strong biomedical or even pathological relevance of the chosen target is needed. Major groups of brain diseases such as neurodegenerative diseases, affective disorders, and brain tumors are expected to be of multifactorial origin, i.e., interactions between multiple genes influenced by internal and external factors occur, and this may have pathological or protective consequences.

Imaging with a single radiotracer offers the chance of picking out only one dedicated piece of the whole scenario of physiological interactions. Thus, it is important to select those key proteins as rational targets which are predominantly altered in pathophysiological states. Ideally, they are causally involved in the etiology of the disease, providing the possibility that their imaging may have impact on both diagnosis and therapeutic drug development.

A schematic view of this complex situation, identifying important molecules involved in the three classes of diseases noted above, is shown in Fig. 2. Notably, many of them are identical though occurring in different contexts. Therefore, it is highly likely that radiotracers designed, for instance, for imaging a certain key protein in the etiology of Alzheimer's disease (AD) may also be of major importance for other diseases, which further justifies the efforts expended on radiotracer development.

For example, sigma₁ (σ_1) receptors are chaperones involved in the suppression of oxidative stress, a feature that links them to numerous brain diseases^[89]. Post-mortem studies have shown loss of σ_1 binding sites in the hippocampus of patients with AD^[90] and in the cortex of patients with schizophrenia^[91]. Overexpression of σ receptors has been found in many brain tumor cell lines and in human brain tumors^[92]. The neuroprotective potential of σ_1 receptor agonists has been shown in different models of neurodegeneration^[89, 93] and is expected to be important for cancerous diseases as well^[92, 94].

As another example, impaired cholinergic neurotransmission is a key feature of AD and the related cognitive impairment is at least partially associated with loss of cortical nicotinic acetylcholine receptors (nAChRs)^[6, 95]. There is evidence that both subtypes with the highest

expression in the brain are involved: $\alpha 4\beta 2$ and $\alpha 7$ nAChRs. Accordingly, these subtypes have been chosen for radiotracer development^[6, 96, 97]. However, these nAChRs are not only key proteins in neurodegenerative diseases (Fig. 2A) but also in many other brain diseases such as drug addiction, schizophrenia (Fig. 2B), and possibly cancer (Fig. 2C). This offers the advantage that corresponding radiotracers may also be used to answer questions related to these diseases.

The radiotracer (S)-[^{11}C]nicotine, one of the very first positron-emitting receptor ligands, was initially developed to investigate the distribution of nicotine *in vivo* and later tested for PET imaging of nAChRs in the human brain^[6, 98]. However, co-administration of unlabeled nicotine failed to displace much of the radioligand, indicating that the PET signal did not sensitively reveal specific binding to nAChRs. Cerebral (S)-[^{11}C]nicotine uptake proved mainly to be determined by blood flow, rather than the local abundance of nAChRs *in vivo*^[6]. This indicates the importance not only of target but also of lead structure identification. Clearly, nicotine failed for the purpose of nAChR imaging. The discovery of various nAChR subtypes during the last two decades and their investigation have revealed different distributions and functions in various brain regions^[6, 99]. Accordingly, different lead structures are needed to image them separately.

The selection process for development of ^{18}F -labeled radiotracers resembles the strategy used by the pharmaceutical industry in drug discovery. Although some features of radiotracers and drugs are different, the principal need remains: specific target binding. As discussed below, some selection criteria, such as affinity, selectivity, kinetic behavior, and metabolism may be even stronger for radiotracers than for common drugs. On the other side, characteristics like bioavailability, side-effects, and pharmacological efficacy are negligible. Regardless of the differences, the lead structures of pharmaceutical interest are usually the basis for radiopharmaceutical development.

Target Characterization and *in vitro* Screening of New Compounds

High-affinity binding is one of the most important prerequisites for radiotracers targeting neuroreceptors^[100, 101]. As

a rule of thumb, a binding potential ($BP = B_{max}/K_D$) of >2 is required for a good PET radioligand^[102]. This implies the need to search for higher target affinity ($1/K_D$) if the receptor density (B_{max}) is low. For example, the receptor densities for $\alpha7$ nAChRs in the human brain are between 2 and 16 fmol/mg tissue^[96]. Accordingly, a K_D between 1 and 8 nmol/L is required to fulfil the minimal criteria. The best $\alpha7$ nAChR PET radiotracers available so far have affinities between 0.3 and 10 nmol/L^[6].

Other important prerequisites for PET radiotracers

are target selectivity and low non-specific binding^[100, 101]. The displacement of radiotracer binding by ligands specific for non-target sites indicates lack of selectivity. This is a general disadvantage, because the specific signal obtained in neuroimaging studies is reduced (i.e. constitutes only a fraction of the total signal) in the presence of binding to non-target sites^[100]. nAChRs, for example, comprise many subtypes expressed by at least 16 different genes^[6, 103]. Many of them share a high degree of sequence identity and similarity with other nAChRs and also with other ligand-

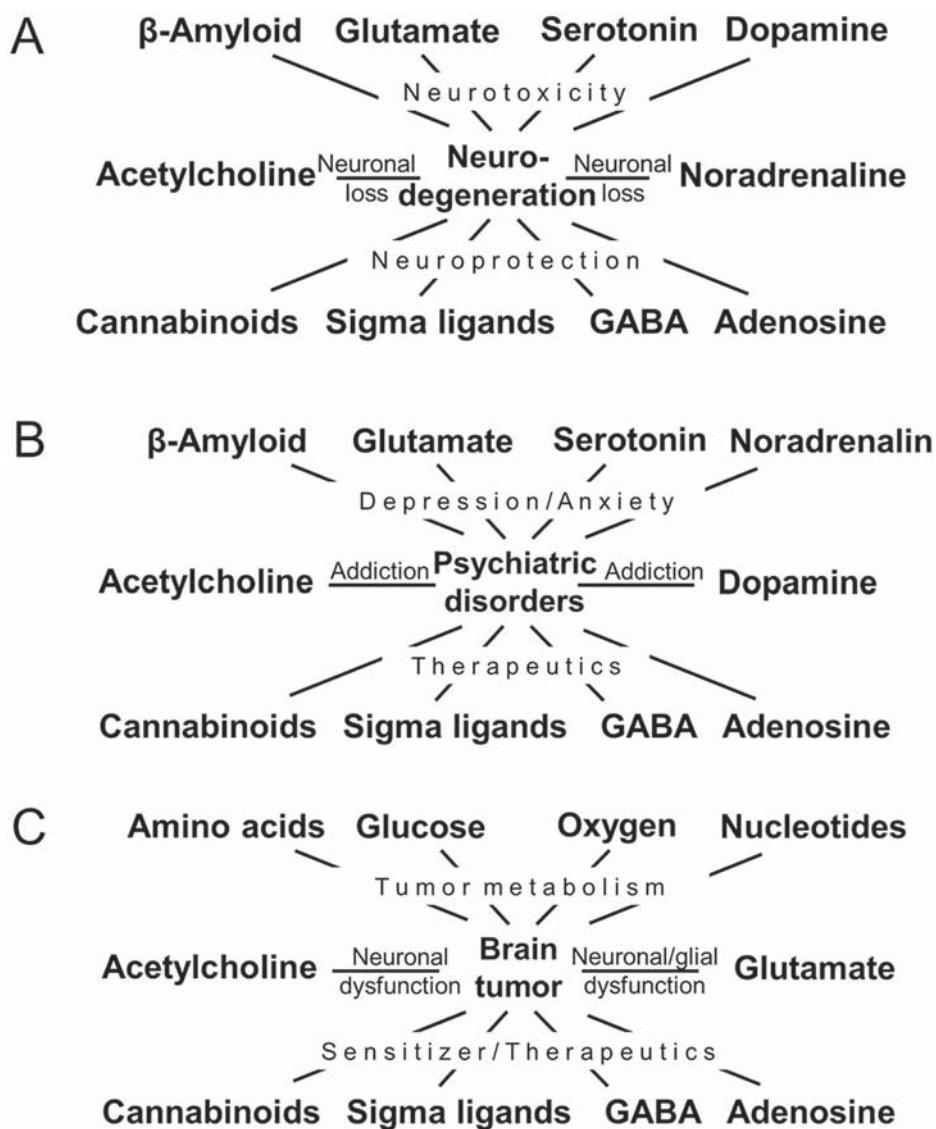


Fig. 2. Key molecules for development of new PET radiotracers for neuroimaging neurodegeneration (A), psychiatric disorders (B), and brain tumors (C).

gated ion channels^[104]. Therefore, detailed investigation of non-target sites is important for the development of PET radiotracers for neuroimaging of nAChRs. In some cases, it is not the sequence-similarity of target proteins that is responsible for cross-reactivity but the chosen lead structure. A well-known example is vesamicol, which is the only known lead structure for targeting the vesicular acetylcholine transporter (VAChT). It has only a ten-fold higher affinity for VAChT than for σ receptors in the brain^[105]. Improving this selectivity is still a challenge in the development of PET radiotracers for the VAChT^[106].

The receptor densities and affinities of the respective ligands in target tissues are parameters that can be quantified *in vivo* by molecular imaging with PET. They are important during radiotracer development. To obtain such information, *in vitro* radioligand-binding assays can be used^[100, 101]. The total binding measured in these assays is always a sum of target-specific binding, which has limited capacity and is saturable, and non-specific binding, which has a high capacity and is non-saturable at pharmacologically meaningful concentrations^[100].

Given that the receptor density is determined by the target, higher BP values can only be achieved by higher ligand affinity. The binding affinity *in vitro* and *in vivo* may differ considerably because of the presence of different affinity states and other confounding factors^[107]. Therefore, *in vitro* binding assays are the methods of choice to experimentally determine the affinity of new ligands. In particular, homogenate-binding or cell-binding assays allow high-throughput screening if needed. Alternatively, autoradiography on brain slices may be used; this is much

more time-consuming but allows additional investigation of the regional distribution of receptors in the brain^[100, 108].

With regard to nAChRs, the $\alpha 4\beta 2$ subunit distribution has been investigated by *in vitro* autoradiography using [^3H]cytisine^[109, 110] while the $\alpha 7$ nAChR has been characterized using [^{125}I] α -bungarotoxin^[111, 112] or [^3H]methyllycaconitine^[113]. For various reasons, these three ligands are not suitable as lead compounds for PET radiotracer development^[6]. However, these highly selective compounds can be used to obtain information on the specific receptor binding of new drugs. For example, the highly-selective $\alpha 7$ nAChR ligand NS10743^[114] (for structure see Fig. 7) is able to displace the binding of [^{125}I] α -bungarotoxin in the mouse brain (Fig. 3).

Concerning the $\alpha 4\beta 2$ nAChR subtype, epibatidine has been used successfully as a lead compound since it has long been known for its high affinity for heteromeric nAChRs^[115]. However, it has rather high toxicity arising from its potency and capacity to activate many different neuronal nAChR subtypes^[116].

In order to improve the subtype selectivity, the fluoro-chloro-substituted homoepibatidine analogue, flubatine (previously called NCFHEB), has been synthesized^[117] (Fig. 4). Results from [^3H]epibatidine binding assays performed with HEK293 cells expressing the human $\alpha 4\beta 2$ nAChR (Fig. 5) show that both enantiomers of flubatine have affinities comparable to that of epibatidine and that the (+)-enantiomer has two-fold higher affinity than the other stereoisomer^[117].

As expected from previous studies with fluoro- and norchloro-analogues of epibatidine^[116], the newly-designed homoepibatidine analogues have 20- to 60-fold lower

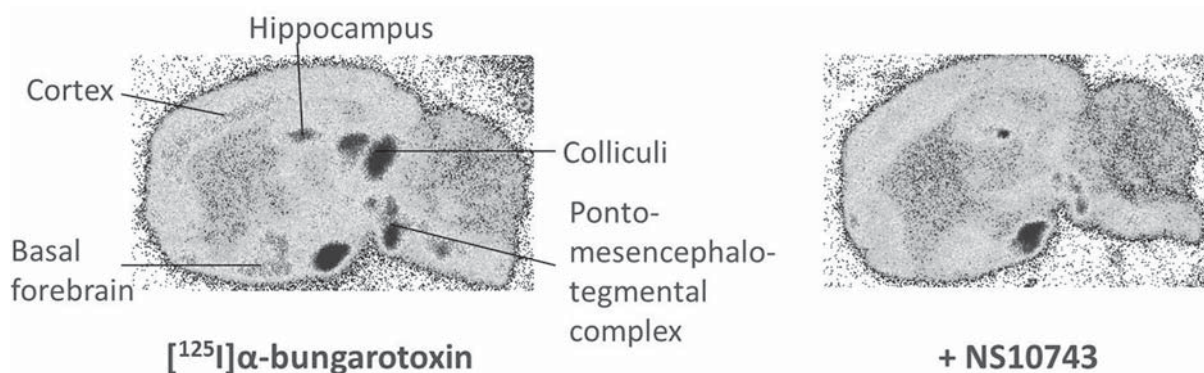


Fig. 3. NS10743, a lead compound for $\alpha 7$ nAChRs, displaces *in vitro* binding of the highly-selective [^{125}I] α -bungarotoxin in mouse brain.

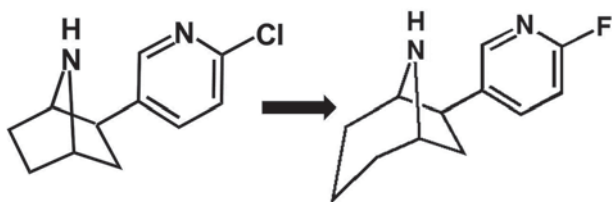


Fig. 4. Toxic epibatidine (left) and its less toxic derivative norchloro-fluoro-homoepibatidine (flubatine, right).

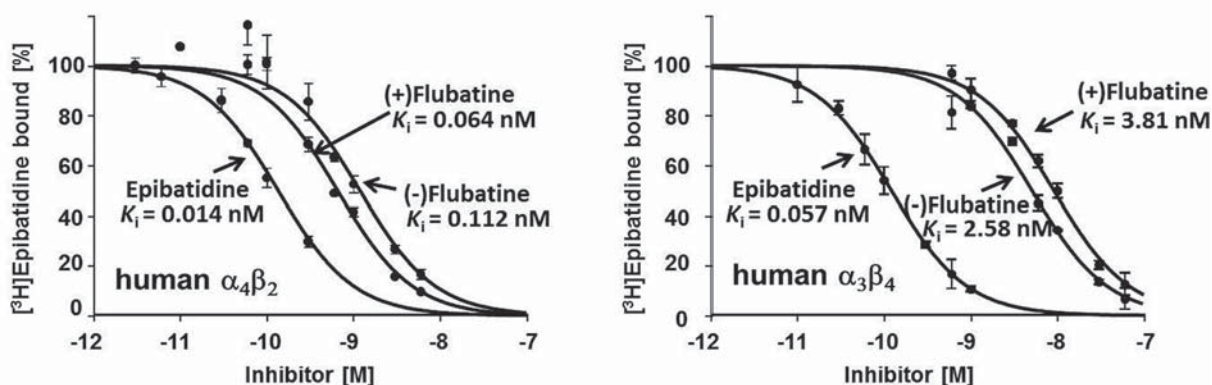


Fig. 5. Competition binding assays of [3 H]epibatidine on membranes prepared from cultured HEK293 cells stably transfected with $\alpha_4\beta_2$ and HEK293 $\alpha_3\beta_4$ cells. Increasing concentrations of epibatidine or flubatine were used for competition. Non-specific binding was determined in the presence of 300 $\mu\text{mol/L}$ (-)-nicotine tartrate and subtracted from the total binding (adapted from Deuther-Conrad *et al.* *Farmaco* 2004^[117]).

and 1.55 $\mu\text{g/kg}$ for (+)-flubatine after i.v. injection^[119]. These values are about ten-fold higher than those reported for *N*-methylepibatidine^[120] and fluoro-norchloroepibatidine^[121].

Regarding α_7 nAChRs, many drug companies are developing receptor agonists and/or positive allosteric modulators for the treatment of schizophrenia and dementia^[97]. Recently, NS10743, developed by NeuroSearch A/S (Ballerup, Denmark), has been characterized as a lead structure for PET radiotracer development. [3 H]Epibatidine-binding studies performed with HEK293 cells expressing the human α_7 , $\alpha_3\beta_4$, or $\alpha_4\beta_2$ nAChR have revealed K_i -values of NS10743 of 12 nmol/L, 84 nmol/L, and >10 $\mu\text{mol/L}$, respectively^[114]. Together with autoradiographic evidence of specific receptor binding as shown in Fig. 3, these data encouraged the radiolabeling of NS10743 to obtain an α_7 nAChR-selective PET radiotracer^[114].

Occasionally, there is a lack of specific drugs that interact with certain brain proteins. For example, only a single lead compound AH5183, later called vesamicol^[122, 123],

affinities to ganglionic $\alpha_3\beta_4$ nAChRs than to the $\alpha_4\beta_2$ subtype^[117]. For flubatine, the increase in subtype selectivity seemingly results in decreased pharmacological side-effects compared to epibatidine. Intraperitoneal injection of 25 $\mu\text{g/kg}$ (+)-flubatine or (-)-flubatine into awake mice is without important pharmacological effects^[118]. Extended single-dose toxicity studies in rodents have shown a NOEL (No Observed Effect Level) of 6.2 $\mu\text{g/kg}$ for (-)-flubatine

has been identified for the VACHT so far. Accordingly, all the PET radioligands that have been developed for neuroimaging the VACHT are derivatives of this lead structure^[106]. Major drawbacks of vesamicol are the relatively low affinity ($K_i >10$ nmol/L) and lack of selectivity. It binds to σ receptors with only ten-fold lower affinity^[105] as well as to a "vesamicol-binding-protein"^[124]. Similar affinity and selectivity have been found for (-)-FEOBV^[125], a radioligand first described in 1993^[126] and recently chosen for human VACHT studies^[127]. Autoradiographic investigations of the human brain have revealed that [18 F]FEOBV binding is decreased by 33% in the prefrontal cortex, 25% in hippocampal CA3, and 20% in the CA1 region of patients with AD^[128]. Although this was interpreted as cholinergic depletion, reduced σ_1 receptor binding cannot be excluded, because a 26% loss of this receptor has also been described in the CA1 region of patients with AD^[90]. So far, no ideal PET radiotracer for the VACHT has been developed^[106] and optimization of the binding affinity

of vesamicol-type ligands has been hampered by the lack of respective quantitative structure-activity relationships. Therefore, molecular modeling approaches have been used to predict the binding affinity of vesamicol-type/like ligands for VACHT from their molecular structures^[125, 129].

A completely different situation is found with regard to radiotracer development for σ_1 receptor imaging. These receptors have an unusual multi-drug binding spectrum and the respective ligands cover diverse structural classes^[89]. Therefore, selectivity not only for the other subtype (σ_2 receptor) but also for a great variety of further potential binding sites needs to be considered. Choosing spiropiperidines as lead structures, which fulfill these criteria and display a lack of significant binding to a great variety of different targets^[130-132], has enabled successful PET radiotracer development^[89]. However, structural modification was needed to introduce fluorine in a suitable labeling position. Accordingly, various series of derivatives have been synthesized to select those with the highest affinity, selectivity, and *in vitro* metabolic stability^[133-138]. Very high selectivity towards the VACHT has been found, excluding cross-reactions with this target^[139].

Physicochemical Characterization of Lead Compounds

Besides affinity and selectivity, some basic physicochemical properties of the parent compound have to be considered before radiolabeling. Lipophilicity, measured for example as $\log P$ and/or $\log D$ in octanol/water partition experiments, and molecular weight are important determinants for the compound's ability to cross the BBB^[140, 141]. Small-molecule drugs may sufficiently cross the BBB *via* lipid-mediated free diffusion if they have a molecular weight <400 g/mol and form <8 hydrogen bonds^[141]. However, the majority of small-molecule drugs and all large-molecule drugs lack these chemical properties^[141]. Considering these limitations, increasing lipophilicity may enhance the BBB permeability, but it also tends to increase plasma protein binding, causing a decrease of drug availability. Consequently, a parabolic relationship exists between lipophilicity and BBB permeability^[107]. For a series of benzamides targeting the dopamine D_2 receptor, an optimal $\log P$ between 2 and 3 has been determined^[142]. Accordingly, there is a rather small window of appropriate combinations of lipophilicity, molecular weight, and affinity. Nevertheless, a nearly infinite

number of substances can theoretically be synthesized from basic organic elements within the restraints described above.

Significant deviations from the above parabolic relationship have been found, which can be ascribed to the existence of multiple mechanisms of drug transport through the BBB^[143]. There is clear evidence that the expression of active efflux pumps like the multidrug transporter P-glycoprotein (P-gP) at the BBB accounts for the poor permeability of certain drugs (see below). Undoubtedly, P-gP is an important barrier to the entry of hydrophobic drugs into the brain^[144]. Thus, proper prediction needs to consider active transport phenomena.

Furthermore, a variety of nutrient transporters expressed at the BBB are able to transport certain xenobiotics and drugs^[141, 143]. Recently, it has been shown that the $\alpha 4\beta 2$ nAChR PET radiotracer [^{18}F]flubatine (formerly called [^{18}F]NCFHEB) interacts with carrier-mediated choline transport at the BBB^[118].

Preparation of Labeling Precursors and Radio-labeling

Considering the short half-lives of the radionuclides used for radiolabeling (e.g., 20.4 min for ^{11}C and 109.8 min for ^{18}F) they need to be incorporated into appropriate precursor molecules quickly. Ideally, the precursor molecules should allow rapid labeling in a maximum of two synthetic steps. As a rule of thumb, the whole labeling procedure including purification and formulation of the final product, should not last longer than two to three half-lives (for ^{11}C). Accordingly, labeling precursors are not necessarily chemically similar to the respective radiolabeled compound/non-radiolabeled reference compound.

Furthermore the precursor should allow (1) high reproducibility of the reaction, (2) automation of the production process (labeling, purification, formulation), and (3) accomplishment of an absolute radiochemical yield (RCY) of the formulated product high enough to permit human application. Ideally, the latter should enable routine as well as commercial production of the radiopharmaceutical.

Fluorine forms very strong covalent C-F bonds that provide valuable chemical, physical, and biological properties to organic molecules that contain one or more

fluorine atoms attached to aromatic carbon. However, because of the reactivity and hazards of elemental fluorine and hydrogen fluoride, the task of introducing fluorine into organic molecules has been a particular challenge to synthetic chemists and has led to the development of specialized fluorination techniques and reagents^[145, 146].

Generally, fluorine can be introduced into organic molecules by electrophilic fluorination reactions using elemental fluorine or by nucleophilic fluorination using inorganic and other ionic fluorides. Although various fluorinating agents have been reported in organic fluorination reactions, only two agents are suitable for direct radiofluorination reactions with ^{18}F : $[^{18}\text{F}]\text{F}_2$ and its derivatives (such as $[^{18}\text{F}]\text{acetylhypofluorite}$ for electrophilic fluorination and $[^{18}\text{F}]\text{fluoride}$ for nucleophilic substitutions^[147-149]). For regioselective introduction of ^{18}F , activated precursor molecules like trialkylstannyl-substituted arenes are needed.

Electrophilic fluorination is quite fast and efficient, making it a highly desirable synthetic method to obtain metabolic radiopharmaceuticals such as the glucose derivative $[^{18}\text{F}]\text{FDG}$ (via the old-fashioned synthetic pathway using glycals) or the amino acid $[^{18}\text{F}]\text{FDOPA}$. Unfortunately, the products suffer from low specific activity owing to the carrier-added non-radioactive fluorine^[147, 148] and thus are excluded from use for neuroreceptor imaging.

The only exception is the post-target-produced highly specific $[^{18}\text{F}]\text{F}_2$ of up to 55 GBq/ μmol ^[150] and its use for $[^{18}\text{F}]\text{CFT}$ synthesis, a dopamine transporter ligand^[151]. Therefore, no further attention is given to electrophilic radiofluorination in this review. Furthermore, special methods for ^{18}F -labeling of peptides and proteins are not considered, because these molecules are not suitable for brain imaging due to their very low BBB transport rates^[152].

Nucleophilic substitution primarily depends on the activation of the $[^{18}\text{F}]\text{fluoride}$ ion ($[^{18}\text{F}]\text{F}^-$) – so-called “naked fluoride” – starting from irradiated ^{18}O -enriched target water. This is reached by the generation of ion pairs consisting of bulky counter-ions for the $[^{18}\text{F}]\text{F}^-$ such as K^+ -chelating agents or tetraalkylammonium ions^[153, 154].

In the presence of aprotic or very weakly-acidic protic solvents, the counter-ion/ $[^{18}\text{F}]\text{F}^-$ ion pair is available as a highly reactive nucleophile. In combination with suitable precursors provided with properly reactive leaving groups, nucleophilic substitution reactions may occur.

Nucleophilic substitution depends on properly active leaving groups for the ^{18}F -fluoride exchange reaction. Its selection depends on various chemical properties of the compounds to be labeled. For radiosynthesis of a desired ^{18}F -labeled compound via nucleophilic substitution, a distinction generally has to be made between aliphatic and aromatic procedures.

For aliphatic nucleophilic substitutions^[155], in most cases, the anions of sulfonic acids such as triflate, tosylate, mesylate, or nosylate groups are the preferred leaving groups. An option to introduce ^{18}F to aliphatic (or even deactivated aromatic) moieties of a molecule is the use of its halide derivatives. The approximate order of increasing suitability for aliphatic reactions is: $\text{I} > \text{Br} > \text{Cl} > \text{F}$, which is the reverse of that found in aromatic nucleophilic substitution reactions^[156]. In the radiolabeling of various fluoro-alkyl indiplon derivatives, the use of bromine as the leaving group has an RCY (38-43%) similar to the use of a tosylate leaving group^[157-159]. Notably, depending on the length of the alkyl chain, O-tosyl-containing precursor molecules gradually decompose over months^[159]. Using a halide leaving group, even isotopic ^{19}F (stable fluorine) for ^{18}F exchange with minor precursor amounts is an option^[160]. Ring opening of cyclic reactive entities offers another method for the introduction of radiofluorine^[161].

Fluoro-aromatic compounds are known to be extraordinarily stable. This is true for the C-F bond too. Accordingly, radiofluorinated derivatives are very suitable radiotracers. For their no-carrier-added radiosynthesis, aromatic nucleophilic substitutions on deactivated (electron-deficient) aromatic ring systems (i.e. activated in terms of nucleophilic reactions) with suitable leaving groups are needed. This activation is caused by electron withdrawing groups, whereas trialkylammonium ($-\text{N}(\text{Me}_3)^+$) or nitro groups or special combinations of both act as leaving groups^[162]. For aromatic nucleophilic substitution reactions, the $-\text{N}(\text{Me}_3)^+$ group is preferred because it usually allows more reproducible radiosynthesis with higher RCYs. Beside deactivated carbocyclic aromates, pyridine rings are a valuable tool to be radiofluorinated as they are already deactivated moieties. Recently, seven different strategies for radiolabeling the $\alpha 4\beta 2$ nAChR ligands (-)/(+)- $[^{18}\text{F}]\text{flubatine}$ were compared^[163]. The original radiosynthesis using a bromo-pyridine precursor and an ethoxycarbonyl protecting group at the tropane

nitrogen requires a microwave reaction followed by chiral HPLC separation of the enantiomers and provides overall RCYs of only 2%, which is insufficient for routine clinical PET investigation^[164]. Several variations of leaving groups coupled in the ortho-position to pyridine nitrogen (-Cl, -NO₂, -N(Me₃)⁺/iodide, -N(Me₃)⁺/triflate) and protecting groups (-Boc, -Trityl, -Fmoc) have been investigated. The use of chlorine was unsuccessful, while the use of -NO₂ revealed ~75% lower labeling efficiency than that of -N(Me₃)⁺/iodide or -N(Me₃)⁺/triflate. A combination of the N(Me₃)⁺/iodide precursor and a Boc-protecting group provided the best results with an RCY of 60 ± 5%^[163]. The radiosynthesis was independent of the use of a microwave and was easily transferable to automated synthesis modules to prepare for human application. Recently, automated synthesis has been reported by two institutions with RCYs of 30%^[165] and 25%^[166].

The above-mentioned electron withdrawing groups (-I effect, -M effect) bound to aromatic moieties are a definite need to enable a nucleophilic attack. In a recent study on radiolabeling of cannabinoid receptor type 2-selective compounds (Fig. 6), the summarized effect of bromine in the *meta*-position to the leaving group -NO₂ was regarded to be not strong enough to achieve an RCY >3%^[167]. An introduction of nitrogen into the aromatic ring facilitated the nucleophilic substitution (RCY >28%) but reduced the affinity by a factor of 30^[167]. To retain the affinity ($K_i = 4.3$ nmol/L), a -N(Me₃)⁺ precursor was synthesized and used for radiolabeling and provided RCYs between 30% and 35%^[168].

Besides low labeling yields, the use of bromine precursors may have further disadvantages such as an unsatisfactory quantitative separation of the radiolabeled product and its precursor (Fig. 7). Initial attempts to use a bromine precursor for radiolabeling of NS10743, a highly

selective $\alpha 7$ nAChR ligand, failed.

For some molecules, the structure does not allow nucleophilic substitution or the radiotracers decompose under the accompanying harsh conditions. In these cases, labeling can be achieved by a multistep procedure using small generic groups that allow both derivatisation with fluorine as well as convenient introduction of radiofluorine. These groups are referred to as secondary labeling precursors or prosthetic groups^[148, 169, 170]. A large number of these ^{18}F -labeled intermediates have been prepared and investigated, such as amines, alcohols, aldehydes, ketones, carboxylic acids, esters, and halides^[148]. In particular, [^{18}F]fluoroalkynes and [^{18}F]fluoroalkylazides are interesting prosthetic groups as they can be coupled to a variety of molecules using the Huisgen "click" reaction which proceeds in high RCYs in aqueous solution under mild conditions. Thus, it can be used for the radiolabeling of water-soluble biomolecules^[148, 171-175]. Generally, careful selection of prosthetic groups is critical for radiotracer development as they often exert great influence on target binding and/or *in vivo* stability^[169].

A further path to ^{18}F -labeled radiotracers is starting the labeling of a pre-prepared substance (reactive precursor) in a first step and its chemical transformation in a subsequent reaction into the final product. This is demonstrated by means of a ring closure reaction (McMurry coupling, Fig. 8).

We have recently used ^{18}F -labeled alkyltosylates for the radiolabeling of phenolic precursors *via* etherification to obtain high-affinity and selective radiotracers for the serotonin transporter^[177] and the enzyme phosphodiesterase 10A^[178], respectively, with RCYs between 11% and 25%. High metabolic stability of the ether bond is expected because negligible defluorination was observed^[178].

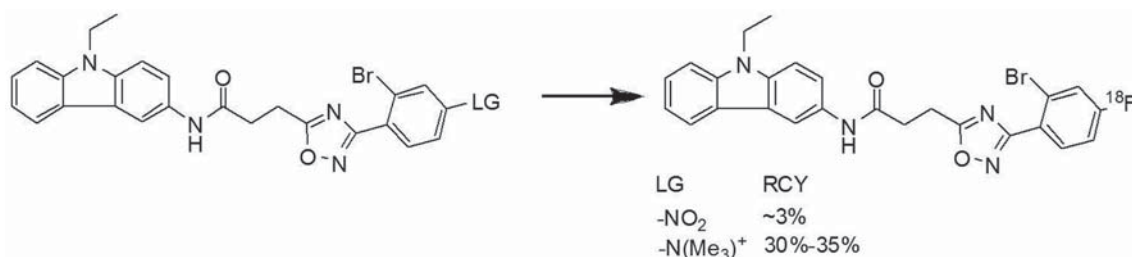


Fig. 6. Effect of leaving group (LG) on radiolabeling yield of a new cannabinoid receptor type 2-selective drug. RCY, radiochemical yield.

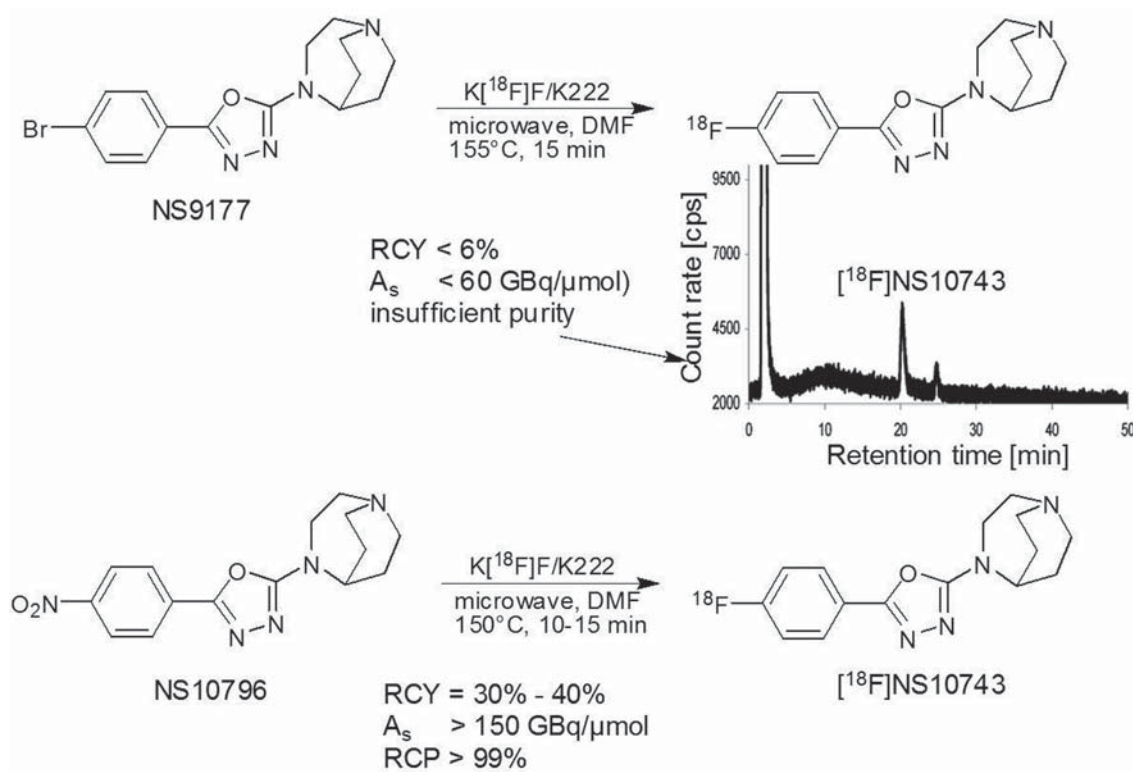


Fig. 7. Radiosynthesis of the $\alpha 7$ nAChR ligand [^{18}F]NS10743 using two different precursors. The bromo precursor NS9177 proved unsuitable for radiolabeling. The radio-HPLC sample is from the reaction mixture with the bromo precursor. RCY, radiochemical yield.

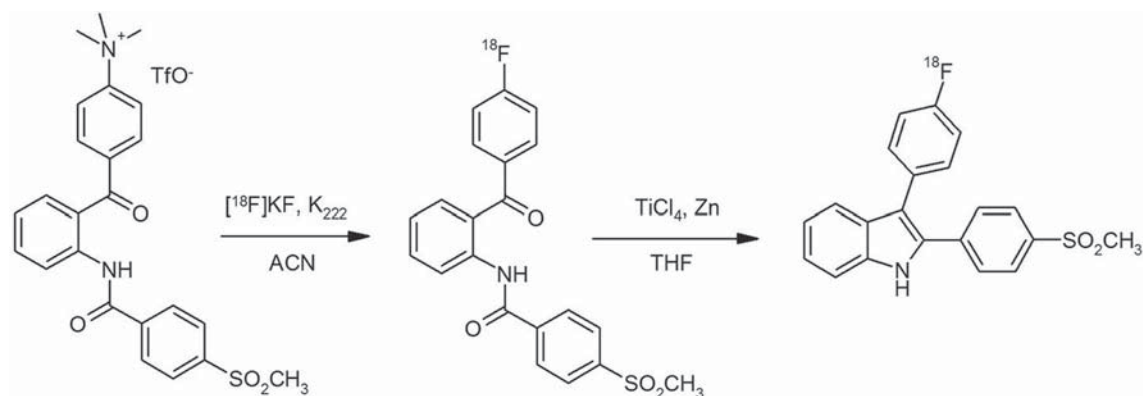


Fig. 8. Introduction of [^{18}F]fluoride into a complex molecule in a first step and subsequent McMurry coupling to the final product, a PET-tracer for imaging cyclooxygenase-2^[176].

By contrast, [^{18}F]fluoroacetamides have proven to be metabolically unstable due to hydrolytic cleavage^[169]. Thus, high-affinity and selective radiotracers for the VACHT^[179] and the GABA_A receptor^[180], respectively, are not suitable

for *in vivo* imaging because metabolites that cross the BBB are generated. The metabolic instability is caused by the action of hydrolytic enzymes, e.g. carboxylesterase^[169]. In such cases, the use of [^{18}F]fluoropropane sulfonamides

can be recommended because of their stability against carboxylesterase-mediated hydrolysis^[169].

Specific Binding of Radiotracers *in vitro*

To determine the specific target binding of newly developed radiotracers, various *in vitro* binding assays can be used^[100]. These provide specific features useful for target characterization and *in vitro* screening; an example of affinity determination of [^{18}F]NS10743^[114] is shown in

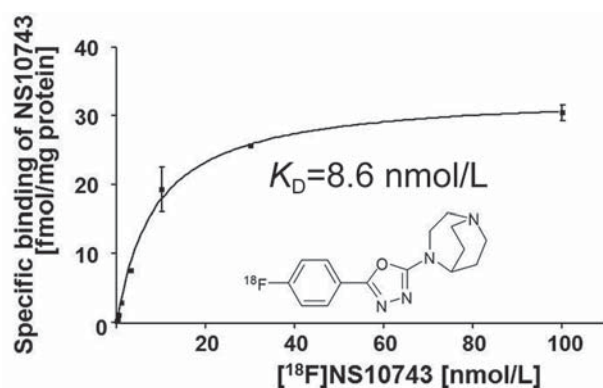


Fig. 9. Saturation analysis of [^{18}F]NS10743 binding on membranes prepared from cultured SHSY5Y cells expressing the human $\alpha 7$ nAChR. Non-specific binding was determined in the presence of 300 $\mu\text{mol/L}$ (-)-nicotine tartrate and subtracted from total binding.

Fig. 9. In a homologous competitive binding assay using SHSY5Y cells expressing the human $\alpha 7$ nAChR and increasing concentrations of [^{18}F]NS10743 as radiotracer, an equilibrium dissociation constant K_D of ~ 9 nmol/L was estimated. Non-specific binding was determined in the presence of 300 $\mu\text{mol/L}$ (-)-nicotine tartrate and subtracted from the total binding.

Alternatively, *in vitro* binding affinity can also be determined by autoradiography, where brain slices are incubated with increasing radiotracer concentrations. Although more time-consuming, this technology has the advantage that additional information on the regional distribution of the target within the brain is available. As an example, Fig. 10 shows the distribution of $\alpha 4\beta 2$ nAChRs in rat brain as determined with the two enantiomers of [^{18}F]flubatine. Brain slices were incubated with increasing radiotracer concentrations to obtain data on target density and radiotracer affinity. As expected, these clearly show the highest receptor densities in the thalamus, superior colliculus, and nucleus interpeduncularis^[181]. Unexpectedly, different affinities were estimated for the various regions. In principle, this may be caused (1) by a remaining part of the endogenous ligand (ACh) competing with the radiotracers, (2) different allosteric receptor regulation in the various regions, or (3) by additional binding to (an)other target(s).

In another experiment (Fig. 11), additional information was obtained on the selectivity of (-)-[^{18}F]flubatine for $\alpha 4\beta 2$

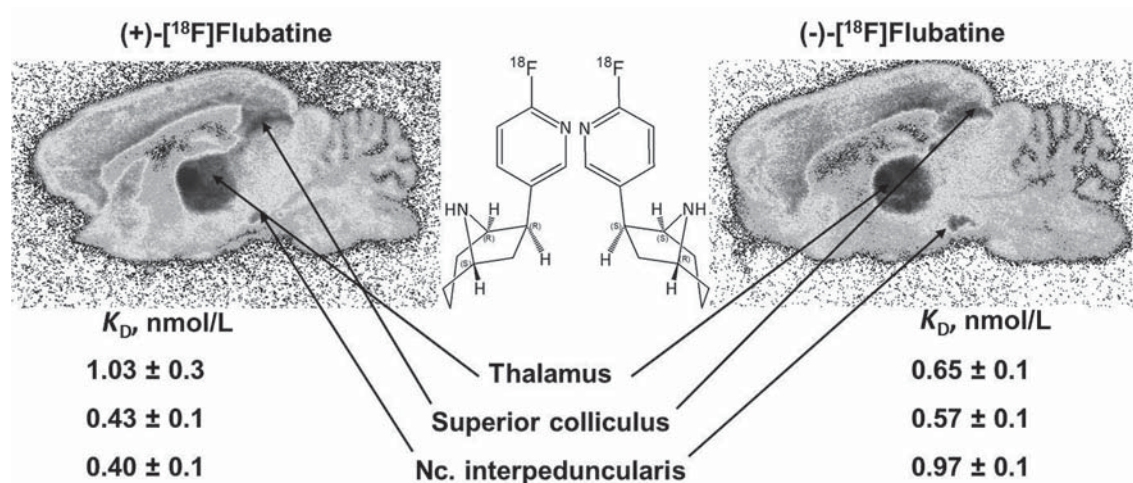


Fig. 10. *In vitro* autoradiographs of $\alpha 4\beta 2$ nAChR distribution in rat brain using (+)-[^{18}F]flubatine and (-)-[^{18}F]flubatine as radioligands. Increasing concentrations of flubatine were used for homologous competition. Non-linear regression analysis was used to estimate the affinities ($1/K_D$) in various brain regions. Nc, nucleus.

nAChRs. The radiotracer binding in pig brain was inhibited by co-incubation with various drugs of different selectivities for nAChRs. The nonselective inhibitor epibatidine^[182] and the $\beta 2$ -subtype-selective inhibitors A-85380^[183] and cytisine^[182] clearly reduced the (-)-[¹⁸F]flubatine binding, whereas the $\alpha 7$ -subtype-selective inhibitor MLA^[184] did not.

Furthermore, autoradiographic experiments are well-suited to compare various radiotracers and target binding in different species. For example, the distribution of GABA_A receptors in pig brain as measured with the gold-standard [³H]flunitrazepam and a new ¹⁸F-labeled indiplon^[185] derivative^[186] is similar to that in rat brain (Fig. 12). Another example shows the use of [³H]citalopram, the most selective serotonin transporter radioligand^[187], to obtain *in vitro* autoradiographs of serotonin transporter (SERT) distribution in the pig brain (Fig. 13). Cresyl violet staining of parallel slices allowed the precise delineation of numerous brain regions and correlation analysis between autoradiographs of the gold-standard ([³H]citalopram) and a new PET radiotracer ([¹⁸F]FMe-McN5652). A highly

significant correlation between the radioligands ($r = 0.9$, $P < 0.001$) was found^[188].

Usually, *in vitro* autoradiography is a good predictor of the imaging properties of a new radiotracer. However, radiotracers with unacceptable *in vitro* data are still able to provide good images *in vivo*. An example is the dopamine transporter-selective SPECT radiotracer [^{99m}Tc]TRODAT-1. *In vitro* autoradiography with this radiotracer shows a high non-specific background with less conspicuous binding in the rat striatum, a dopamine-transporter-rich brain region^[189]. Meanwhile, [^{99m}Tc]TRODAT-1 has been introduced into the clinic as a tool for the diagnosis of Parkinson's disease^[190].

Metabolism of Radiotracers in Animals

Investigation of radiotracer metabolism *in vivo* needs special consideration, especially for neuroimaging. Because of the exceptionally great functional diversity of the brain compared to other organs, there is a need to precisely differentiate between various brain regions with

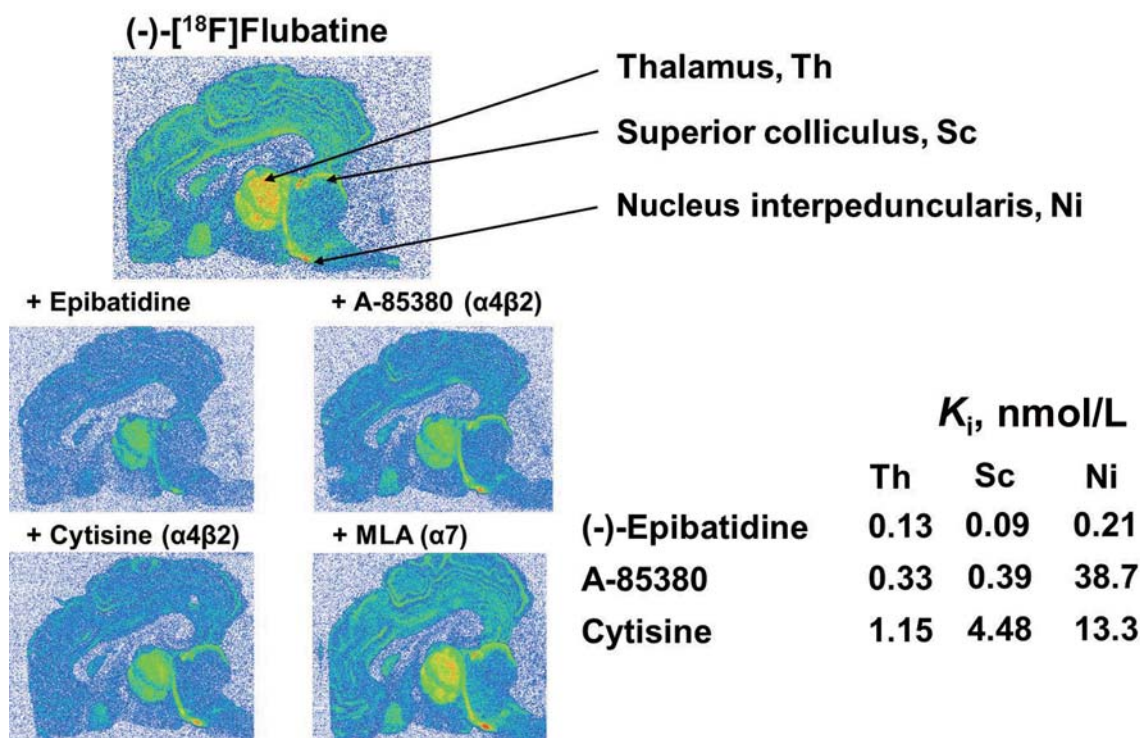


Fig. 11. *In vitro* autoradiographs of $\alpha 4 \beta 2$ nAChR distribution in pig brain using (-)-[¹⁸F]flubatine as radioligand. Epibatidine, A-85380, cytisine and MLA were used as competitors to assess the specificity and selectivity of radiotracer binding to $\alpha 4 \beta 2$ nAChRs.

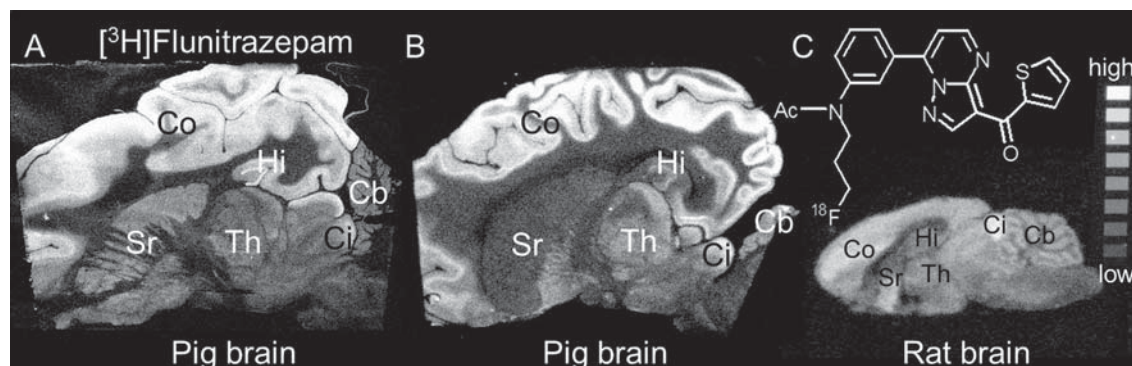


Fig. 12. *In vitro* autoradiographs of GABA_A receptor distribution in pig and rat brain using $[^3\text{H}]$ flunitrazepam and a new ^{18}F -labeled indiplon derivative^[186] as radioligands (adapted from Deuther-Conrad et al. *Curr Radiopharm* 2009^[158]).

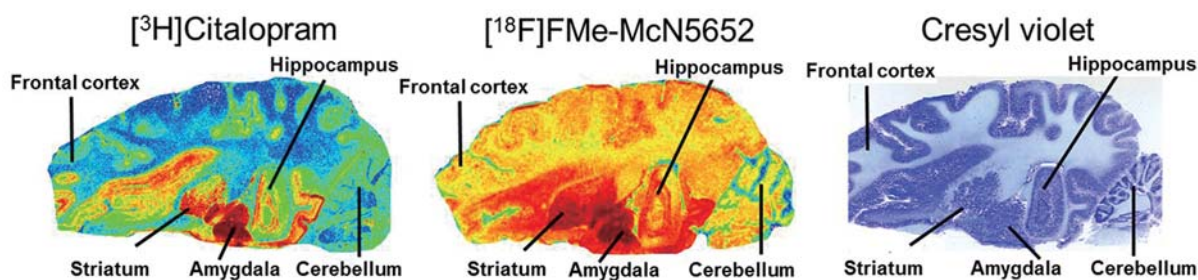


Fig. 13. *In vitro* autoradiographs of serotonin transporter distribution in pig brain using $[^3\text{H}]$ citalopram and $[^{18}\text{F}]$ FMe-McN5652 as radioligands, compared to an adjacent cresyl violet-stained brain slice (adapted from Kretzschmar et al. *Eur Neuropsychopharmacol* 2003^[188]).

regard to specific radiotracer binding and target density. Therefore, it has to be ensured that the PET image is derived from the radiotracer only and not blurred by the presence of radiolabeled metabolites. Consequently, the potential presence of radiometabolites in the brain needs to be investigated and ideally excluded. Furthermore, the use of compartmental models for the quantitation of receptor binding parameters depends on an exact measurement of the radiotracer availability for brain uptake. Accordingly, the radioactivity measured in blood samples needs to be corrected by subtraction of the amount of radiometabolites.

Standard chromatographic methods such as high-performance liquid chromatography (HPLC), thin-layer chromatography (TLC) and solid-phase extraction (SPE) are used to separate the radiotracer and its metabolites. In principle, all methods are based on the different interactions of various analytes with the stationary and mobile phases. After separation has been achieved, the

activity of the analytes is determined by special online activity detectors integrated into the HPLC system, by autoradiography of TLC plates, or by measurement of eluted substances in well-counters. While HPLC and TLC are standard procedures during radiotracer development, SPE offers advantages in the clinical setting because of its high throughput and low cost. However, SPE has to be validated by comparison with HPLC or TLC before use.

A common concern in the development of PET radiotracers for neuroimaging is the presence of lipophilic metabolites in blood, because they are likely to cross the BBB just because of their lipophilicity^[107]. Such metabolites may either be active, i.e. having a target-affinity high enough for significant binding, or inactive. In the former case, quantification is highly confounded because the measured signal represents undetermined proportions of parent tracer and metabolite, each of which may have a different affinity for the target^[107]. In the latter case, non-

specific binding is increased, leading to a decreased signal-to-noise ratio.

For example, the 5-HT_{2A} receptor PET radiotracer [¹⁸F]altanserin is metabolized by reduction of ketone to yield [¹⁸F]altanserinol, which is transported across the BBB^[191]. In the brain, it contributes to non-specific binding. However, the signal obtained from specific receptor binding is regarded to be unchanged because the affinity of altanserinol for serotonin receptors is negligible^[191]. This offers the possibility of using [¹⁸F]altanserin together with a constant infusion paradigm for quantification of 5-HT_{2A} receptor availability in the brain^[191, 192]. Alternatively, the use of the simplified reference tissue model (see below) allows consideration of the presence of radiometabolites in brain, as long as their contribution to non-specific binding is homogenous throughout and there is a reference region without specific binding^[193].

Confounding effects of brain metabolites on dopamine transporter (DAT) imaging have been observed for a variety of radiotracers such as [¹²³I]β-CIT^[194], [¹¹C]β-CIT^[195], [¹⁸F]FECNT^[196], [¹¹C]PE2I^[197], and [¹¹C]/[¹⁸F]LBT-999^[198].

In the case of β-CIT, lipophilic metabolites have been detected^[194, 195]. Accordingly, labeling of β-CIT with ¹¹C by either *N*-methylation or *O*-methylation has resulted in radioligands with different kinetics in the monkey brain. Preparation of two of the putative labeled metabolites [*N*-methyl-¹¹C]β-CIT-acid and [*O*-methyl-¹¹C]nor-β-CIT, and investigation of their brain uptake, revealed that <0.4% of the injected [*N*-methyl-¹¹C]β-CIT-acid entered the brain whereas 5%–6% of the more lipophilic [*O*-methyl-¹¹C]nor-β-CIT entered and accumulated in the striatum and thalamus. Notably, nor-β-CIT has been found to specifically bind to the serotonin transporter^[199], providing an additional confounding effect.

Regarding [¹¹C]PE2I, a benzyl alcohol metabolite derived from biotransformation by cytochrome P450 enzymes residing predominantly in the liver^[200], has been shown to cross the BBB^[197]. In the brain, it is supposed to be further metabolized by alcohol and aldehyde dehydrogenases. Also, for [¹¹C]LBT-999 and [¹⁸F]LBT-999, hydroxylated derivatives have been found. Their accumulation in the striatum indicates specific binding to the DAT^[198].

For [¹⁸F]FECNT, *N*-dealkylation has been shown to provide a brain-penetrant radiometabolite of even

higher *in vitro* DAT affinity than the parent compound itself, preventing the use of a reference tissue model for quantitation^[196, 201].

Lipophilicity is not necessarily a prerequisite for brain uptake of radiometabolites. [¹⁸F]fluoroacetamides have been shown to be metabolically unstable due to hydrolytic cleavage of the amide bond. The resulting highly hydrophilic [¹⁸F]fluoroacetate is transported into the brain^[202–204], at least partly mediated by carboxylic acid transporters at the BBB^[205]. [¹⁸F]fluoroacetate was proposed as a major metabolite of radiotracers for imaging the VAcHT, e.g. [¹⁸F]FAMV^[179] and [¹⁸F]FAA^[206], or GABA_A receptors^[180], preventing the use of these radiotracers for neuroimaging. Interestingly, it was found that fluoroacetate is defluorinated by glutathione *S*-transferases^[207] which are highly expressed in brain tissue^[208]. To explain the high amounts of radioactivity in rat ventricles after injection of [¹⁸F]FAMV, it was proposed that the elimination of brain metabolites may occur by clearance *via* the cerebrospinal fluid^[179].

Besides knowledge regarding the potential of radiometabolites to cross the BBB, information on the precise amounts of radiometabolites in plasma is often needed for quantitation of receptor binding of PET radiotracers *in vivo* (see below). The faster the metabolism, the stronger the alterations of the input functions and the influence of potential bias. Determination of metabolites in rodents or larger animals such as pig or monkey provides suitable estimates for clinical PET studies. Because of the higher surface-to-volume ratio, the influence of metabolism on the PET quantitation of human data is usually overestimated when investigated in experimental animals. Thus, for the serotonin transporter PET radiotracers (+)-[¹¹C]McN5652 and [¹⁸F]FMe-McN5652, the metabolism in pigs^[209] is about twice as fast as measured in humans^[210, 211]. Another very good example is the α4β2 nAChR PET radiotracer (–)-[¹⁸F]flubatine. Rather strong differences between pigs and humans have been reported. While ~60% of metabolites were found in pig plasma at 2 h after injection^[212], this value was only ~10%–15% in humans^[213]. Because of this very low amount of radiolabeled metabolites, full kinetic modeling was possible even without metabolite correction of the input function^[214], which is of great advantage for routine clinical use.

The high metabolic stability of flubatine has recently

been confirmed in an *in vitro* study comparing mouse and human microsomal preparations (containing enriched cytochrome P450 enzymes^[215, 216]), where a 5–6-times faster metabolism was found in mice. Interestingly, the (–)-enantiomer is significantly less stable than the (+)-enantiomer (unpublished data). Stereoselective metabolism of drugs by P450 enzymes is a common phenomenon and may also explain differences in the metabolism of other enantiomeric PET radiotracers, such as (+)-/(-)-[¹¹C]McN5652^[211] or the σ_1 receptor-selective (R)-/(S)-[¹⁸F]fluspidine^[136].

Proof of Target-specific Binding in Animals

Usually one of the first steps to demonstrate target-specific binding *in vivo* is the investigation of radiotracer biodistribution in mice or rats. Although *in vitro* studies allow the estimation of target affinities, the bioavailability of radiotracers is a confounding factor for target binding *in vivo*. The bioavailability of radiotracers is influenced by blood flow, plasma protein binding, membrane permeability, and metabolism. Furthermore, the optimized settings used for radioligand binding assays usually differ from the physiological conditions found *in vivo* where different pH and temperature as well as the presence of endogenous competitors may be confounding factors. The complex interaction of all these parameters can only be investigated *in vivo* and justifies the approval of animal experiments by legislative authorities.

Information on the time-dependent biodistribution of radiotracers can be obtained by *ex vivo* tissue sampling or small-animal imaging^[7, 100]. The two methods are rather complementary than competitive, both offering advantages and disadvantages (see Table 2). More detailed information is available elsewhere^[100].

In addition to the use of rodents for *ex vivo* tissue sampling or small-animal imaging, larger animals such as monkeys or pigs are used for PET imaging with human scanners.

Independent of the type of *in vivo* study chosen, the strategy to obtain certain information about the radiotracer is similar. Studies have to show that the brain uptake is sufficiently high, specific, and selective to justify human application for neuroimaging. Furthermore, data obtained on whole-body radiotracer kinetics can also be used to estimate the absorbed radiation dose as a prerequisite for human application^[217].

The magnitude of brain uptake is mainly determined by the size, lipophilicity, and H-bonding capacity of the radiotracer^[141, 218], i.e. parameters accessible by *in vitro* investigations. The brain uptake may occasionally be confounded by affinity for efflux transporters at the BBB. A variety of *in vitro* systems representing the BBB have been described, but the optimal use of these data, in terms of extrapolation to human unbound brain concentration profiles, remains to be fully exploited^[219]. Therefore, animal experiments are still indispensable to investigate this aspect. Notably, the expression of the various efflux

Table 2. Advantages and limitations of *ex vivo* tissue sampling and small-animal imaging

Parameter	<i>Ex vivo</i> tissue sampling	Small-animal imaging
Anesthesia	Just before death	Throughout the study
Applied activity (per mass)	~ Human dosage	>> Human dosage
Radiation damage	Unlikely	Possible
Estimation of absorbed radiation dose	Possible	Possible (preferred)
Multiple time point measurements	Multiple subjects needed	Single subjects
Longitudinal studies	Not possible	Possible
Animal models of disease	Relatively high expenses	Possible
Tracer kinetic modeling	Relatively high expenses	Possible
Physiology	Unaffected	Potentially affected
Blocking effects of drugs	Unaffected by applied dosage	Potentially affected by applied dosage

transporters at the BBB differs significantly between species^[220, 221]. Among drug transporters, breast cancer resistance protein appears to be most abundant with an expression level ~2-fold greater in humans than in mice. By contrast, the expression level of P-gP in humans is ~2.5-fold lower than the corresponding *mdr1a* gene in mice^[221]. Consequently, low brain uptake in rodents does not necessarily forecast the uptake in other species like humans. For example, the brain uptake of the high-affinity and selective $\alpha 7$ nAChR ligand [¹⁸F]NS14492 is ~10-times higher in pigs than in mice, suggesting suitability for human brain imaging^[222]. Similar species differences between rats, guinea pigs, and monkeys have been reported for the 5-HT_{2A} receptor ligand [¹⁸F]altanserin, the NK1 receptor antagonist [¹¹C]GR205171, and the classical P-gP substrate [¹¹C]verapamil^[223].

The specificity and selectivity of brain uptake is another important issue to consider in animal experiments^[7]. For targets with a heterogeneous distribution, the ratio of brain uptake between a region with high target expression and a region with negligible or low target expression represents a reasonable measure of specific binding. A typical example is the dopamine D₂ receptor. The caudate/cerebellum ratio was used to verify specific binding of the first (D₂-receptor specific) PET radiotracers, 3-*N*-[¹¹C]methylspiperone and [¹¹C]raclopride, in human and monkey^[224, 225]. Since these early studies, the cerebellum has often been used as suitable reference region for the development of PET radiotracers for other dopamine receptors^[226], serotonin 5-HT_{1A} and 5-HT₂ receptors^[227, 228], muscarinic and nicotinic ACh receptors^[229-231], histamine receptors^[232], and the serotonin transporter^[188, 233]. An example of *ex vivo* autoradiography of SERT distribution in rat brain where the radiotracer

[¹⁸F]FMe-McN5652 (30 MBq) was injected intravenously is shown in Fig. 14B. The animal was sacrificed 90 min later and the brain subjected to autoradiography. Regions with the highest SERT expression such as frontal cortex, striatum, and substantia nigra^[187, 234] clearly showed the highest radiotracer accumulation, providing evidence for radiotracer selectivity^[188]. Furthermore, comparison with an *in vitro* autoradiograph of rat brain (Fig. 14A) using the same radiotracer clearly showed a high correlation of SERT binding between the approaches.

An example of how an *ex vivo* binding ratio has been used to identify the radiotracer with the highest σ_1 receptor binding in mouse brain among a series with various lengths of the alkyl side chain is shown in Fig. 15. Notably, for the σ_1 receptor, as for metabotropic glutamate receptor 1 (mGluR1)^[59] and the GABA_A receptor^[180], the cerebellum is among the regions with the highest expression and cannot be used as a reference region in this case. The ratio between the region with lowest radiotracer accumulation (olfactory bulb) and that with highest accumulation (facial nucleus) was chosen for the estimation of specific receptor binding. Consistent with the highest brain-to-plasma ratio at 60 min post-injection and the highest target affinity, this ratio was highest for the ethyl derivative [¹⁸F]fluspidine^[89].

Besides the use of reference regions for the evaluation of specific receptor binding in brain, blocking studies are recommended. A high concentration of a drug that binds specifically to the receptor site is injected before or together with the radiotracer and thereby prevents its specific binding to the target^[100]. From the difference between a control study and the blocking study, information on the specific binding can be obtained. Using a similar setup, the target selectivity of the radiotracer can be investigated. As shown

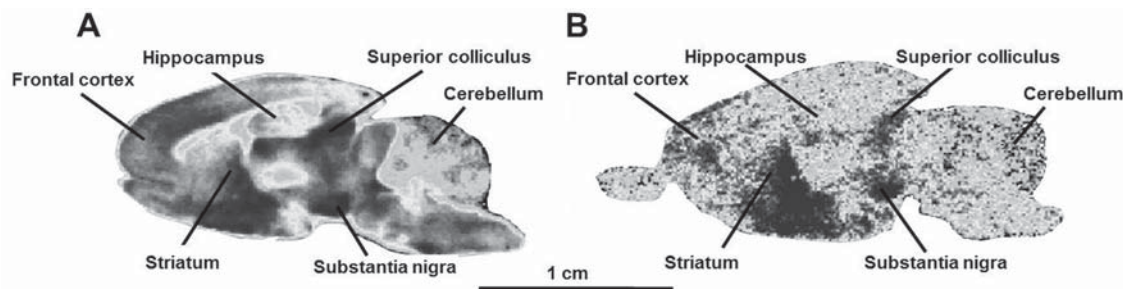


Fig. 14. Comparison of *in vitro* (A) and *ex vivo* (B) autoradiographs of serotonin transporter distribution in rat brain using [¹⁸F]FMe-McN5652 as radioligand (adapted from Kretschmar *et al.* Eur Neuropsychopharmacol 2003^[188]).

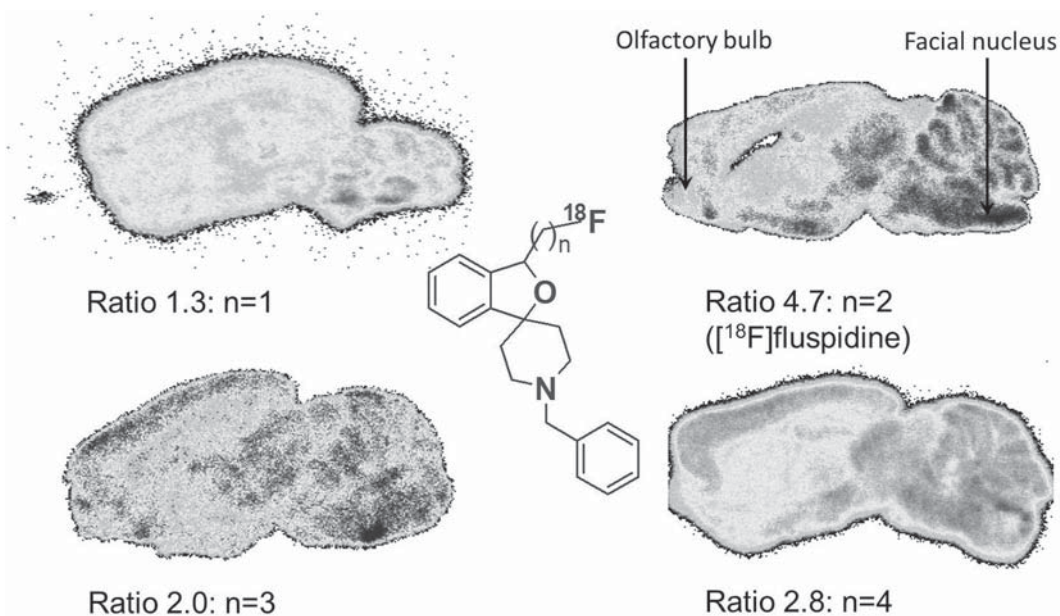


Fig. 15. Comparison of *ex vivo* autoradiographs of σ_1 receptor distribution in rat brain using (\pm)- ^{18}F fluspidine and derivatives with various lengths of the alkyl side-chain as radioligands (adapted from Brust *et al.* *Curr Med Chem* 2014^[69]).

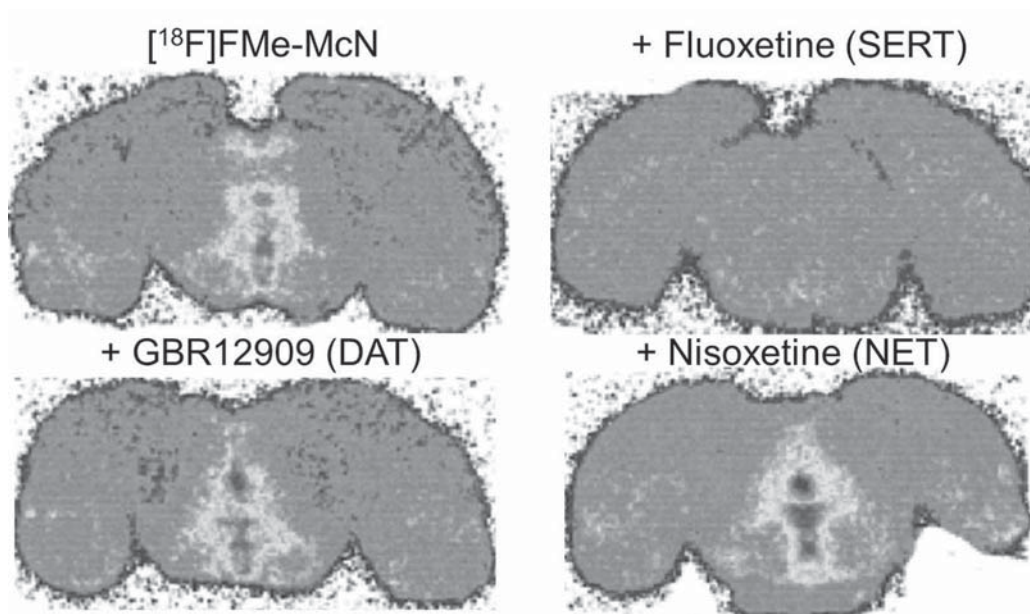


Fig. 16. Comparison of *ex vivo* autoradiographs of serotonin transporter distribution in rat brain using ^{18}F FMe-McN5652 as radioligand. Specific transporter inhibitors were used to assess the selectivity of transporter binding (adapted from Marjamäki *et al.* *Synapse* 2003^[235]).

in Fig. 16, the selectivity of the new SERT radiotracer ^{18}F FMe-McN5652 was assessed by *ex vivo* autoradiography performed on rat brain at 120 min after radiotracer injection and 180 min after administration of nisoxetine, a specific norepinephrine uptake inhibitor, or GBR12909, a specific

dopamine uptake inhibitor^[235]. In contrast to the selective SERT inhibitor fluoxetine, neither drug inhibited binding of ^{18}F FMe-McN5652 to the rat midbrain, a region with high SERT expression.

In comparison to autoradiography, PET images of

animal brains suffer from low resolution. This can clearly be seen in Fig. 17 where an *ex vivo* autoradiograph of a mouse brain (volume 0.4 mL) is compared to a PET image of a pig brain (volume 110 mL). Despite this limitation, the specificity

of radiotracer binding may be determined in animal PET studies. The coronal PET images in Fig. 17 show that administration of the σ_1 receptor ligand SA4503 prevents the specific target binding of (S)-[18 F]fluspidine in pig brain^[236].

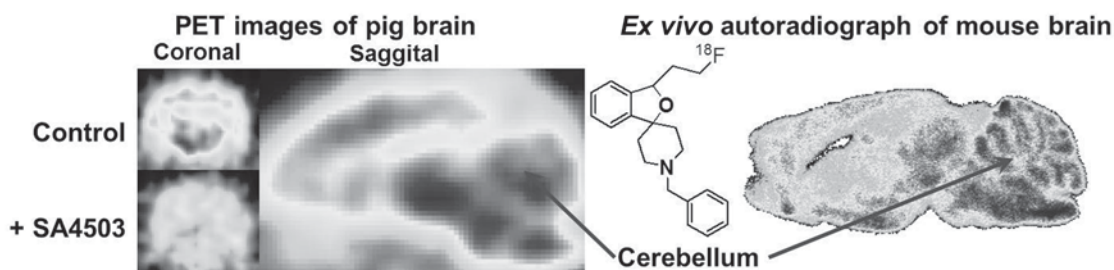


Fig. 17. PET images of a pig brain (left; volume 110 mL) and an *ex vivo* autoradiograph of a mouse brain (right; volume 0.4 mL) are compared to demonstrate the difference in resolution between the two imaging modalities (adapted from Brust *et al.* J Nucl Med 2014^[237]).

Estimation of Receptor-binding Parameters in Animals

One of the great advantages of PET is the possibility of precise quantitation of local tracer concentrations in tissue; this ultimately enables the estimation of receptor binding parameters *in vivo*. Preclinical PET studies in animals are suitable for this purpose^[7, 8] and hence permit appropriate radiotracer evaluation. Initially, the PET scanner's resolution was rather low (~ 10 mm)^[238] allowing successful quantitation only in the brains of larger animals such as primates^[239, 240], dogs^[241-243], cats^[244, 245], and pigs^[246-248]. During the last decade, various dedicated PET cameras for imaging in small animals have been developed, providing a resolution of 1–2 mm^[6, 249].

Moreover, the first PET/MRI systems have become available for both human and small-animal imaging, allowing more accurate identification of brain regions^[250]. Thus, accurate quantitation is possible and similar to that achievable with autoradiography^[7]. In addition, pharmacokinetic, multiple-tracer, and longitudinal studies can be performed in single subjects constituting a great potential for basic neuroscience research^[251], neuropharmacology^[8, 252], and the investigation of animal models of neurological and neuropsychiatric disorders^[7].

While *in vitro* autoradiography was the method of choice for receptor mapping for more than three decades,

the suitability of animal PET/MRI for that purpose has recently been proven. For example, Syvänen^[253] determined the GABA_A receptor density, B_{\max} , in rat brain using four doses (between 4 μ g and 400 μ g) of [11 C]flumazenil. Five regions with high GABA_A receptor expression were investigated and the highest B_{\max} was found in the hippocampus (44 ng/mL) and the lowest in the cerebellum (33 ng/mL). No significant regional differences in the receptor affinity, K_D (5.9 ng/mL), were detected. Using the same setup, an experimental model of epilepsy was investigated and a significant decrease of B_{\max} by 12% was reported, while K_D remained unchanged^[253].

Although convincing in animals, a similar protocol applied to humans has major drawbacks. Multiple radiotracer injections significantly increase the radiation burden. Furthermore, use of pharmacological doses requires much stronger safety regulations. Therefore, a common and generally-accepted approach to quantify radiotracer receptor binding in humans is estimation of the binding potential, $BP = B_{\max}/K_D$ ^[107]. Assuming that K_D remains unchanged, changes of BP are directly proportional to changes in B_{\max} , a postulate which holds in the majority of such studies.

The BP can be estimated by compartmental modeling^[254-259]. A compartment model is a linear mathematical model that describes the transfer of a radiotracer among various compartments which are regarded to be

homogenous at all times with respect to the radiotracer concentration. Compartmental models describe the tracer kinetics as a first-order process which is in general, but not always, justified in view of the very low concentrations in which the tracer is present in the investigated organism.

Also, one should keep in mind that the different compartments do not necessarily correspond to unique spaces (e.g. extracellular *versus* intracellular) but usually rather represent different chemical modifications in which the radioactive label resides (see above, the radiotracer and its metabolites). For this reason, all compartmental concentrations in PET are usually referred to the same common volume (total tissue space). This has to be considered when interpreting the numerical results in order to avoid misconceptions. In other words, compartmental models superficially relate tracer concentrations in the different compartments, but in fact represent (local) mass-balance equations. Radiotracer exchange between the different compartments is described by rate constants (usual unit: 1/min) specifying the fractional change of concentration per unit time in the respective compartment due to the process modeled by that specific rate constant.

As long as the tracer kinetics can be considered linear (which is usually a valid assumption) a sufficiently comprehensive compartmental model (with a sufficient number of compartments) will be able to describe any given system. Increasing the number of compartments sufficiently, one can even model diffusive processes (which

inherently imply the presence of concentration gradients). For the evaluation of PET data, however, this is not a feasible strategy. It rather turns out that very simple one- or two-tissue compartmental models suffice to adequately describe the data at the given limits of spatial and temporal resolution. For a more in-depth description of the basics of compartmental modeling we refer the reader to the literature^[258, 259].

Typical examples of compartmental models are shown in Fig. 18, where C_a refers to the arterial plasma concentration of the unmetabolized radiotracer, M_t to the total amount of radiotracer, M_f to the free fraction, and M_b to the bound fraction. Linear systems of ordinary differential equations describe the changes of radiotracer contents in these models. Based on these equations, the rate constants for the blood-brain and brain-blood transfer (K_1 and k_2' or k_2''), and the rate constants for the specific binding/release (k_3' and k_4), can be estimated by nonlinear least-squares fits. Distribution volumes calculated from the rate constants provide parameters related to receptor density. For the one-tissue compartmental model, the respective parameter is the total distribution volume V_T (equal to K_1/k_2'). For the two-tissue compartmental model the total distribution volume $V_T = V_{ND} + V_S = (K_1/k_2')(1 + k_3'/k_4)$, the specific distribution volume $V_S = (K_1/k_2')(k_3'/k_4)$, and the binding potential $BP = k_3'/k_4$ provide measures of the specific binding.

Fig. 19 shows an example, where a two-tissue compartment model was used to estimate BP of the SERT

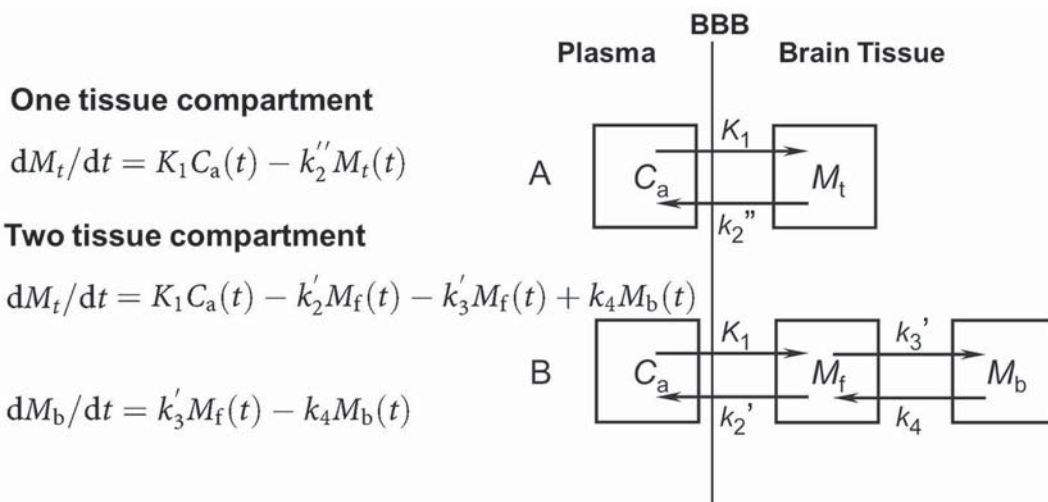


Fig. 18. Compartmental models used to describe receptor binding of radiotracers in brain.

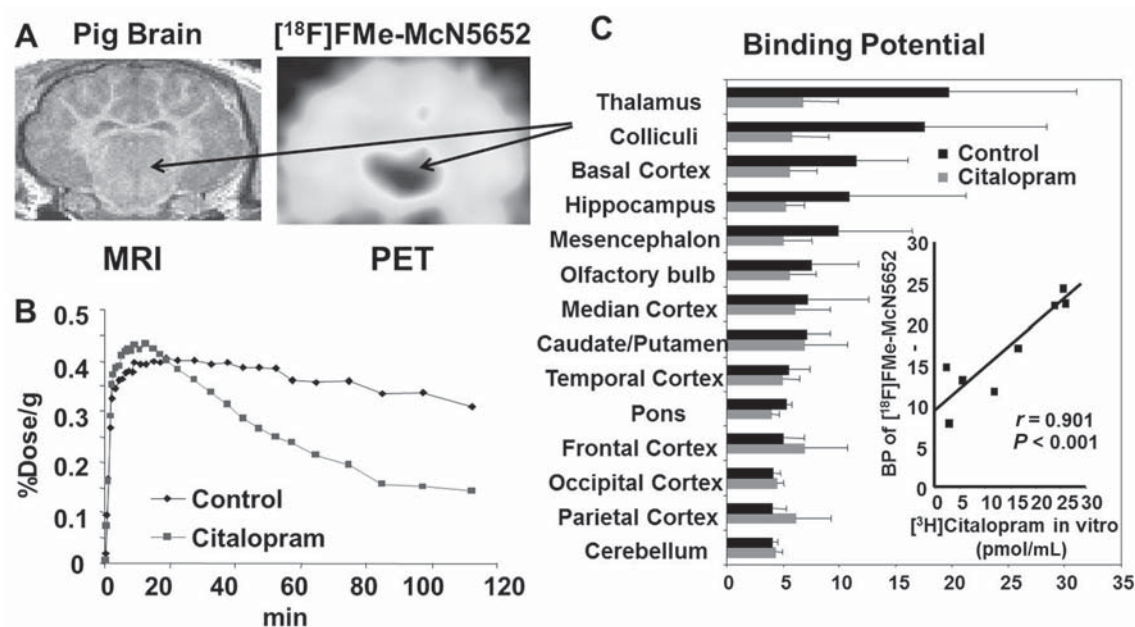


Fig. 19. Comparative PET and autoradiographic study of serotonin distribution in pig brain using [^{18}F]FMe-McN5652 and [^3H]citalopram as radioligands. Binding potential values estimated from time-activity curves (B) of a PET study in various brain regions (A) are compared to results from an *in vitro* autoradiographic study using [^3H]citalopram (C) (adapted from Brust *et al.* *Neuropsychopharmacology* 2003^[209] and Brust *et al.* *Synapse* 2003^[212]).

radiotracer [^{18}F]FMe-McN5652 in anesthetized pigs under control conditions and after i.v. injection of the highly-selective SERT inhibitor citalopram (5 mg/kg). Under control conditions, BP values clearly reflected the SERT distribution as demonstrated by correlation analysis with [^3H]citalopram autoradiography with the highest values in the thalamus and the lowest in the cerebellum. Pre-injection of citalopram significantly inhibited [^{18}F]FMe-McN5652 accumulation, as demonstrated by the time-activity curves, and BP estimated from these curves^[209, 260]. This clearly demonstrated the specificity of the radiotracer uptake. The selectivity for the norepinephrine transporter (NET) was demonstrated by pre-injection of maprotilin, a selective NET inhibitor^[209].

Accurate measurement of the arterial plasma time-activity curve as well as consideration and correct determination of metabolites in plasma is important for receptor quantitation based on compartmental models using an arterial input function. This poses substantial problems in imaging of small animals and humans. Therefore, alternative quantification strategies, called “reference tissue models” have been developed^[261, 262].

These models rest on the observation that (apart from minor effects of different arrival times) the arterial input function is identical in different brain regions. Then, it is possible to use the tissue response to this input function in one region as an indirect measure of the input function if that region is devoid of the targeted receptor. This obviates the need for actual measurement of the arterial plasma time-activity curve and also makes metabolite analysis unnecessary. Furthermore, this strategy can be used even in the presence of brain metabolites. Although these techniques have several advantages compared to arterial blood sampling (especially non-invasiveness), they quite sensitively rely on several assumptions and should be used with great care. For example, the existence of any specific binding in the reference region results in an underestimation of specific binding in the target region^[257].

PET also allows the visualization of specific receptor binding by estimation of the binding parameters in each voxel, i.e. each image point in the three-dimensional rectangular grid^[263]. The higher the number of voxels, the higher the number of calculations to be executed. To be able to perform about a million estimations in a

reasonable time, graphical methods are available allowing linear rather than non-linear regression. For radiotracers with irreversible binding the Gjedde-Patlak graphical analysis^[264-266] and for those with reversible binding the Logan graphical analysis^[267] have become the methods of choice. For the two-tissue compartmental model, the slope of the regression line in the Logan plot represents the total distribution volume V_T , defined by $K_1/k_2(1+k_3/k_4) + \text{fbv}$ (fbv = fractional blood volume in the target region, $k_3/k_4 = \text{BP}^{[267]}$).

Fig. 20A shows a parametric map of V_T of the $\alpha 7$ nAChR radiotracer [^{18}F]NS10743 resampled into the MR-based common stereotactic space for the brain of a juvenile pig^[230]. Fig. 20B shows V_T of [^{18}F]NS10743 after administration of the selective $\alpha 7$ nAChR antagonist NS6740. This clearly demonstrates specific radiotracer binding in pig brain.

Newer developments include proposals to obtain parametric images even in cases without either an arterial input function or a reference region^[268], direct reconstruction algorithms of linear and nonlinear parametric images, and joint estimation of parametric images and input function^[263]. Further validation of these concepts is still needed.

Proof-of-Concept in Humans

The final step in PET radiotracer development is proof-

of-concept in humans. A prerequisite to get permission for such studies is the transition of the biomarker from research-grade radiochemical to a radiopharmaceutical, for which higher standards of product quality must be met^[269]. Many aspects of radiation safety, toxicology issues, quality control, licensing, and regulatory control need to be considered for the production of radiopharmaceuticals and these have been extensively reviewed elsewhere^[5, 100, 270, 271]. The regulatory framework has become increasingly restrictive during the last two decades. Therefore, the time between first successful radiosynthesis of a new PET radiotracer and its first human use is at least between 5 and 10 years. For example, in the case of the $\alpha 2\beta 2$ nAChR radiotracer ($-$)-[^{18}F]flubatine, the time between the first report on radiosynthesis^[164] and the first report on human use^[16] was 8 years. For [^{18}F]FMe-McN5652 it was 10 years^[210, 272], and for [^{18}F]FEOBV^[126], a radiotracer for the VAcHT, it has been almost 20 years^[273]. At the beginning of neuroreceptor imaging with PET this transition time was much shorter, in the range of 1–2 years as exemplified by [^{11}C]raclopride^[225, 274], 3-*N*-[^{11}C]methylspiperone^[224], and [^{11}C]flumazenil^[49, 275].

However, even if a radiotracer is not further developed into a radiopharmaceutical for imaging in human subjects it may find widespread use in preclinical studies with special animal PET devices^[276] to investigate animal models of diseases^[7] or new drugs^[8, 252].

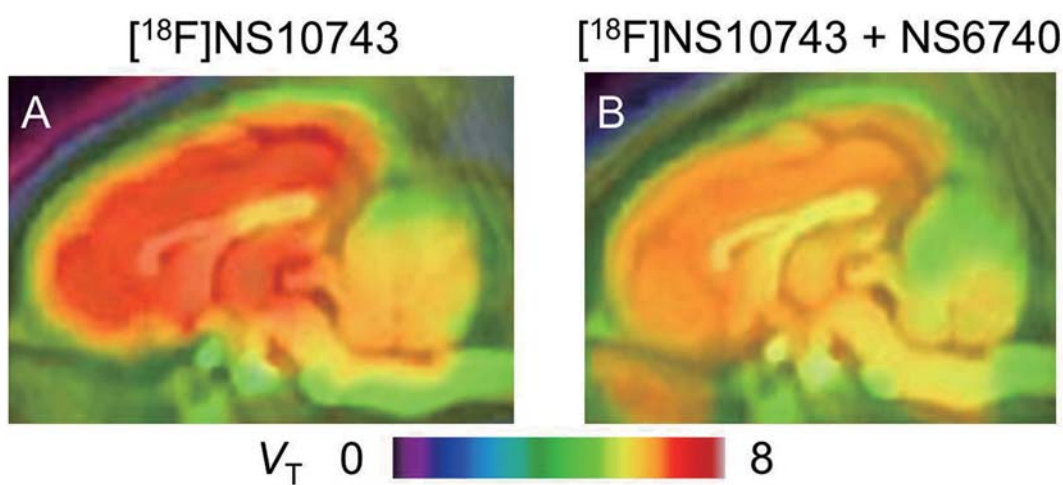


Fig. 20. Parametric maps of the distribution volumes (V_T , mL/g) of [^{18}F]NS10743 under baseline (A) and blocking (B) conditions in sagittal plane of pig brain. The V_T values were calculated by the classic Logan method using the arterial input function for [^{18}F]NS10743 (adapted from Deuther-Conrad *et al.* Eur J Nucl Med Mol Imaging 2011^[230]).

Conclusion

The main focus of this review is the development and evaluation of radiolabeled ligands (radiotracers) in order to investigate brain functions in living organisms. Application of radiotracers provides images of transport, metabolic, and neurotransmission processes on the molecular level. PET is a method used in humans to acquire such information. It is the most sensitive and specific molecular *in vivo* imaging method available at present. Through the integration of chemical/radiochemical, pharmaceutical/radiopharmaceutical, biochemical and radiopharmacological basic research, computational chemistry, and with the aid of nuclear medicine diagnostics, a new approach in neuroscience has been made available. The foremost importance of this approach is the diagnosis and therapeutic monitoring of brain diseases.

ACKNOWLEDGEMENTS

Many valuable contributions of our colleagues at HZDR are gratefully acknowledged.

Received date: 2014-04-19; Accepted date: 2014-06-02

REFERENCES

- [1] Mankoff DA. A definition of molecular imaging. *J Nucl Med* 2007, 48: 18N, 21N.
- [2] Pichler BJ, Judenhofer MS, Pfannenbergl C. Multimodal imaging approaches: PET/CT and PET/MRI. *Handb Exp Pharmacol* 2008: 109–132.
- [3] Drzezga A, Barthel H, Minoshima S, Sabri O. Potential clinical applications of PET/MR imaging in neurodegenerative diseases. *J Nucl Med* 2014, 55: 1–9.
- [4] Levi H. George von Hevesy memorial lecture. George Hevesy and his concept of radioactive indicators--in retrospect. *Eur J Nucl Med* 1976, 1: 3–10.
- [5] Sampson CD (Ed.). *Textbook of Radiopharmacy: Theory and Practice*. 3rd. ed. Amsterdam: Gordon and Breach Science Publishers, 1999.
- [6] Brust P, Deuther-Conrad W, Donat CK, Barthel H, Riss P, Paterson L, *et al*. Preclinical aspects of nicotinic acetylcholine receptor imaging. In: Dierckx RAJ, Otte A, de Vries EFJ, *et al*. (Eds.). *PET and SPECT of Neurobiological Systems*. Springer, 2014: 465–512.
- [7] Virdee K, Cumming P, Caprioli D, Jupp B, Rominger A, Aigbirhio FI, *et al*. Applications of positron emission tomography in animal models of neurological and neuropsychiatric disorders. *Neurosci Biobehav Rev* 2012, 36: 1188–1216.
- [8] Melhem M. Translation of central nervous system occupancy from animal models: application of pharmacokinetic/pharmacodynamic modeling. *J Pharmacol Exp Ther* 2013, 347: 2–6.
- [9] Frey KA, Koeppe RA, Mulholland GK, Jewett D, Hichwa R, Ehrenkaufel RL, *et al*. *In vivo* muscarinic cholinergic receptor imaging in human brain with [¹¹C]scopolamine and positron emission tomography. *J Cereb Blood Flow Metab* 1992, 12: 147–154.
- [10] Xie G, Gunn RN, Dagher A, Daloz T, Plourde G, Backman SB, *et al*. PET quantification of muscarinic cholinergic receptors with [N-11C-methyl]-benztropine and application to studies of propofol-induced unconsciousness in healthy human volunteers. *Synapse* 2004, 51: 91–101.
- [11] Yamamoto S, Ouchi Y, Nakatsuka D, Tahara T, Mizuno K, Tajima S, *et al*. Reduction of [¹¹C](+)-3-MPB binding in brain of chronic fatigue syndrome with serum autoantibody against muscarinic cholinergic receptor. *PLoS One* 2012, 7: e51515.
- [12] Ichise M, Cohen RM, Carson RE. Noninvasive estimation of normalized distribution volume: application to the muscarinic-2 ligand [¹⁸F]FP-TZTP. *J Cereb Blood Flow Metab* 2008, 28: 420–430.
- [13] Sabri O, Kendziorra K, Wolf H, Gertz HJ, Brust P. Acetylcholine receptors in dementia and mild cognitive impairment. *Eur J Nucl Med Mol Imaging* 2008, 35 Suppl 1: S30–45.
- [14] Ding YS, Fowler JS, Logan J, Wang GJ, Telang F, Garza V, *et al*. 6-[¹⁸F]Fluoro-A-85380, a new PET tracer for the nicotinic acetylcholine receptor: studies in the human brain and *in vivo* demonstration of specific binding in white matter. *Synapse* 2004, 53: 184–189.
- [15] Wong DF, Kuwabara H, Kim J, Brasic JR, Chamroonrat W, Gao Y, *et al*. PET imaging of high-affinity $\alpha_4\beta_2$ nicotinic acetylcholine receptors in humans with ¹⁸F-AZAN, a radioligand with optimal brain kinetics. *J Nucl Med* 2013, 54: 1308–1314.
- [16] Sabri O, Wilke S, Gräf S, Schönknecht P, Becker G, Patt M, *et al*. Cerebral $\alpha_4\beta_2$ nicotinic acetylcholine receptors (nAChRs) in early Alzheimer disease (AD) assessed with the new PET tracer (-)-[¹⁸F]-norchloro-fluoro-homoepibatidine (NCFHEB). *J Nucl Med* 2011, 52 (Suppl. 1): 1267.
- [17] Toyohara J, Sakata M, Wu J, Ishikawa M, Oda K, Ishii K, *et al*. Preclinical and the first clinical studies on [¹¹C]CHIBA-1001 for mapping α_7 nicotinic receptors by positron emission tomography. *Ann Nucl Med* 2009, 23: 301–309.
- [18] Bauer A, Holschbach MH, Meyer PT, Boy C, Herzog H, Olsson RA, *et al*. *In vivo* imaging of adenosine A₁ receptors in the human brain with [¹⁸F]CPPFX and positron emission

- tomography. *Neuroimage* 2003, 19: 1760–1769.
- [19] Fukumitsu N, Ishii K, Kimura Y, Oda K, Hashimoto M, Suzuki M, *et al.* Adenosine A_1 receptors using 8-dicyclopropylmethyl-1- ^{11}C methyl-3-propylxanthine PET in Alzheimer's disease. *Ann Nucl Med* 2008, 22: 841–847.
- [20] Mishina M, Ishiwata K, Naganawa M, Kimura Y, Kitamura S, Suzuki M, *et al.* Adenosine A_{2A} receptors measured with ^{11}C TMSX PET in the striata of Parkinson's disease patients. *PLoS One* 2011, 6: e17338.
- [21] Ramlackhansingh AF, Bose SK, Ahmed I, Turkheimer FE, Pavese N, Brooks DJ. Adenosine 2_A receptor availability in dyskinetic and nondyskinetic patients with Parkinson disease. *Neurology* 2011, 76: 1811–1816.
- [22] Burns HD, Van Laere K, Sanabria-Bohorquez S, Hamill TG, Bormans G, Eng WS, *et al.* ^{18}F MK-9470, a positron emission tomography (PET) tracer for *in vivo* human PET brain imaging of the cannabinoid-1 receptor. *Proc Natl Acad Sci U S A* 2007, 104: 9800–9805.
- [23] Terry GE, Hirvonen J, Liow JS, Seneca N, Tauscher JT, Schaus JM, *et al.* Biodistribution and dosimetry in humans of two inverse agonists to image cannabinoid CB1 receptors using positron emission tomography. *Eur J Nucl Med Mol Imaging* 2010, 37: 1499–1506.
- [24] Wong DF, Kuwabara H, Horti AG, Raymont V, Brasic J, Guevara M, *et al.* Quantification of cerebral cannabinoid receptors subtype 1 (CB1) in healthy subjects and schizophrenia by the novel PET radioligand ^{11}C OMAR. *Neuroimage* 2010, 52: 1505–1513.
- [25] Ahmad R, Koole M, Evens N, Serdons K, Verbruggen A, Bormans G, *et al.* Whole-body biodistribution and radiation dosimetry of the cannabinoid type 2 receptor ligand ^{11}C -NE40 in healthy subjects. *Mol Imaging Biol* 2013.
- [26] Farde L, Halldin C, Stone-Elander S, Sedvall G. PET analysis of human dopamine receptor subtypes using ^{11}C -SCH 23390 and ^{11}C -raclopride. *Psychopharmacology* 1987, 92: 278–284.
- [27] Karlsson P, Farde L, Halldin C, Swahn CG, Sedvall G, Foged C, *et al.* PET examination of ^{11}C NNC 687 and ^{11}C NNC 756 as new radioligands for the D_1 -dopamine receptor. *Psychopharmacology* 1993, 113: 149–156.
- [28] Slifstein M, Kolachana B, Simpson EH, Tabares P, Cheng B, Duvall M, *et al.* COMT genotype predicts cortical-limbic D_1 receptor availability measured with ^{11}C NNC112 and PET. *Mol Psychiatry* 2008, 13: 821–827.
- [29] Farde L, Hall H, Ehrin E, Sedvall G. Quantitative analysis of D_2 dopamine receptor binding in the living human brain by PET. *Science* 1986, 231: 258–261.
- [30] Wong DF, Wagner HN, Jr., Tune LE, Dannals RF, Pearson GD, Links JM, *et al.* Positron emission tomography reveals elevated D_2 dopamine receptors in drug-naive schizophrenics. *Science* 1986, 234: 1558–1563.
- [31] Narendran R, Frankle WG, Mason NS, Laymon CM, Lopresti BJ, Price JC, *et al.* Positron emission tomography imaging of $D_{2/3}$ agonist binding in healthy human subjects with the radiotracer ^{11}C -N-propyl-norapomorphine: preliminary evaluation and reproducibility studies. *Synapse* 2009, 63: 574–584.
- [32] Otsuka T, Ito H, Halldin C, Takahashi H, Takano H, Arakawa R, *et al.* Quantitative PET analysis of the dopamine D_2 receptor agonist radioligand ^{11}C -(R)-2-CH₃O-N-n-propylnorapomorphine in the human brain. *J Nucl Med* 2009, 50: 703–710.
- [33] Farde L, Suhara T, Nyberg S, Karlsson P, Nakashima Y, Hietala J, *et al.* A PET-study of ^{11}C FLB 457 binding to extrastriatal D_2 -dopamine receptors in healthy subjects and antipsychotic drug-treated patients. *Psychopharmacology* 1997, 133: 396–404.
- [34] Mukherjee J, Christian BT, Dunigan KA, Shi B, Narayanan TK, Satter M, *et al.* Brain imaging of ^{18}F -fallypride in normal volunteers: blood analysis, distribution, test-retest studies, and preliminary assessment of sensitivity to aging effects on dopamine D-2/D-3 receptors. *Synapse* 2002, 46: 170–188.
- [35] Ginovart N, Willeit M, Rusjan P, Graff A, Bloomfield PM, Houle S, *et al.* Positron emission tomography quantification of ^{11}C -(+)-PHNO binding in the human brain. *J Cereb Blood Flow Metab* 2007, 27: 857–871.
- [36] Moresco RM, Scheithauer BW, Lucignani G, Lombardi D, Rocca A, Losa M, *et al.* Oestrogen receptors in meningiomas: a correlative PET and immunohistochemical study. *Nucl Med Comm* 1997, 18: 606–615.
- [37] Toyohara J, Sakata M, Fujinaga M, Yamasaki T, Oda K, Ishii K, *et al.* Preclinical and the first clinical studies on ^{11}C ITMM for mapping metabotropic glutamate receptor subtype 1 by positron emission tomography. *Nucl Med Biol* 2013, 40: 214–220.
- [38] Ametamey SM, Treyer V, Streffer J, Wyss MT, Schmidt M, Blagojev M, *et al.* Human PET studies of metabotropic glutamate receptor subtype 5 with ^{11}C -ABP688. *J Nucl Med* 2007, 48: 247–252.
- [39] Brown AK, Kimura Y, Zoghbi SS, Simeon FG, Liow JS, Kreisl WC, *et al.* Metabotropic glutamate subtype 5 receptors are quantified in the human brain with a novel radioligand for PET. *J Nucl Med* 2008, 49: 2042–2048.
- [40] Kagedal M, Cselenyi Z, Nyberg S, Jonsson S, Raboisson P, Stenkrona P, *et al.* Non-linear mixed effects modelling of positron emission tomography data for simultaneous estimation of radioligand kinetics and occupancy in healthy volunteers. *Neuroimage* 2012, 61: 849–856.
- [41] Wong DF, Waterhouse R, Kuwabara H, Kim J, Brasic JR, Chamroonrat W, *et al.* ^{18}F -FPEB, a PET radiopharmaceutical for quantifying metabotropic glutamate 5 receptors: a first-

- in-human study of radiochemical safety, biokinetics, and radiation dosimetry. *J Nucl Med* 2013, 54: 388–396.
- [42] Kumlien E, Hartvig P, Valind S, Oye I, Tedroff J, Langström B. NMDA-receptor activity visualized with (S)-[N-methyl-¹¹C] ketamine and positron emission tomography in patients with medial temporal lobe epilepsy. *Epilepsia* 1999, 40: 30–37.
- [43] Hammers A, Asselin M, Brooks DJ, Luthra SK, Hume SP, Thompson PJ, *et al.* Correlation of memory function with binding of [C-11]CNS 5161, a novel putative NMDA ion channel PET ligand. *Neuroimage* 2004, 22(Suppl 2): T54–55.
- [44] Ametamey SM, Bruehlmeier M, Kneifel S, Kokic M, Honer M, Arigoni M, *et al.* PET studies of ¹⁸F-memantine in healthy volunteers. *Nucl Med Biol* 2002, 29: 227–231.
- [45] McGinnity CJ, Hammers A, Riano Barros DA, Luthra SK, Jones PA, Trigg W, *et al.* Initial evaluation of ¹⁸F-GE-179, a putative PET Tracer for activated N-methyl D-aspartate receptors. *J Nucl Med* 2014, 55: 423–430.
- [46] Matsumoto R, Haradahira T, Ito H, Fujimura Y, Seki C, Ikoma Y, *et al.* Measurement of glycine binding site of N-methyl-D-aspartate receptors in living human brain using 4-acetoxy derivative of L-703,717, 4-acetoxy-7-chloro-3-[3-(4-[¹¹C] methoxybenzyl) phenyl]-2(1H)-quinolone (AcL703) with positron emission tomography. *Synapse* 2007, 61: 795–800.
- [47] Yanai K, Watanabe T, Itoh M, Hatazawa J, Iwata R, Ido T. Labeling of histamine H1-receptors *in vivo*: a compartment model analysis and positron emission tomographic imaging. *Agents Actions Suppl* 1991, 33: 381–386.
- [48] Ashworth S, Rabiner EA, Gunn RN, Plisson C, Wilson AA, Comley RA, *et al.* Evaluation of ¹¹C-GSK189254 as a novel radioligand for the H3 receptor in humans using PET. *J Nucl Med* 2010, 51: 1021–1029.
- [49] Persson A, Ehrin E, Eriksson L, Farde L, Hedström CG, Litton JE, *et al.* Imaging of [¹¹C]-labelled Ro 15-1788 binding to benzodiazepine receptors in the human brain by positron emission tomography. *J Psychiatric Res* 1985, 19: 609–622.
- [50] Leveque P, Sanabria-Bohorquez S, Bol A, De Volder A, Labar D, Van Rijckevorsel K, *et al.* Quantification of human brain benzodiazepine receptors using [¹⁸F]fluoroethylflumazenil: a first report in volunteers and epileptic patients. *Eur J Nucl Med Mol Imaging* 2003, 30: 1630–1636.
- [51] Lee JD, Park HJ, Park ES, Kim DG, Rha DW, Kim EY, *et al.* Assessment of regional GABA_A receptor binding using ¹⁸F-fluoroflumazenil positron emission tomography in spastic type cerebral palsy. *Neuroimage* 2007, 34: 19–25.
- [52] Massaweh G, Schirrmacher E, la Fougere C, Kovacevic M, Wängler C, Jolly D, *et al.* Improved work-up procedure for the production of [¹⁸F]flumazenil and first results of its use with a high-resolution research tomograph in human stroke. *Nucl Med Biol* 2009, 36: 721–727.
- [53] Lingford-Hughes A, Hume SP, Feeney A, Hirani E, Osman S, Cunningham VJ, *et al.* Imaging the GABA-benzodiazepine receptor subtype containing the alpha5-subunit *in vivo* with [¹¹C]Ro15 4513 positron emission tomography. *J Cereb Blood Flow Metab* 2002, 22: 878–889.
- [54] Frost JJ, Mayberg HS, Sadzot B, Dannals RF, Lever JR, Ravert HT, *et al.* Comparison of [¹¹C]diprenorphine and [¹¹C] carfentanil binding to opiate receptors in humans by positron emission tomography. *J Cereb Blood Flow Metab* 1990, 10: 484–492.
- [55] Madar I, Lesser RP, Krauss G, Zubieta JK, Lever JR, Kinter CM, *et al.* Imaging of σ - and μ -opioid receptors in temporal lobe epilepsy by positron emission tomography. *Ann Neurol* 1997, 41: 358–367.
- [56] Tomasi G, Zheng M-Q, Weinzimmer D, Lin S-F, Nabulsi N, Williams W, *et al.* Kinetic modeling of the kappa agonist tracer [¹¹C]GR103545 in humans. *J Nucl Med* 2010, 51 (Supplement 2): 1293.
- [57] Cohen RM, Carson RE, Sunderland T. Opiate receptor avidity in the thalamus is sexually dimorphic in the elderly. *Synapse* 2000, 38: 226–229.
- [58] Baumgärtner U, Buchholz HG, Bellosevich A, Magerl W, Siessmeier T, Rolke R, *et al.* High opiate receptor binding potential in the human lateral pain system. *Neuroimage* 2006, 30: 692–699.
- [59] Hostetler ED, Sanabria-Bohorquez S, Fan H, Zeng Z, Gantert L, Williams M, *et al.* Synthesis, characterization, and monkey positron emission tomography (PET) studies of [¹⁸F]Y1-973, a PET tracer for the neuropeptide Y Y₁ receptor. *Neuroimage* 2011, 54: 2635–2642.
- [60] Pike VW, McCarron JA, Lammerstma AA, Hume SP, Poole K, Grasby PM, *et al.* First delineation of 5-HT_{1A} receptors in human brain with PET and ¹¹C WAY-100635. *Eur J Pharmacol* 1995, 283: R1–3.
- [61] Parsey RV, Slifstein M, Hwang DR, Abi-Dargham A, Simpson N, Mawlawi O, *et al.* Validation and reproducibility of measurement of 5-HT_{1A} receptor parameters with [carbonyl-¹¹C]WAY-100635 in humans: comparison of arterial and reference tissue input functions. *J Cereb Blood Flow Metab* 2000, 20: 1111–1133.
- [62] Andree B, Halldin C, Pike VW, Gunn RN, Olsson H, Farde L. The PET radioligand [carbonyl-¹¹C]desmethyl-WAY-100635 binds to 5-HT_{1A} receptors and provides a higher radioactive signal than [carbonyl-¹¹C]WAY-100635 in the human brain. *J Nucl Med* 2002, 43: 292–303.
- [63] Houle S, Wilson AA, Inaba T, Fisher N, DaSilva JN. Imaging 5-HT_{1A} receptors with positron emission tomography: initial human studies with [¹¹C]CPC-222. *Nucl Med Comm* 1997, 18: 1130–1134.
- [64] Milak MS, DeLorenzo C, Zanderigo F, Prabhakaran J, Kumar JS, Majo VJ, *et al.* *In vivo* quantification of human serotonin

- 1A receptor using ^{11}C -CUMI-101, an agonist PET radiotracer. *J Nucl Med* 2010, 51: 1892–1900.
- [65] Costes N, Merlet I, Zimmer L, Lavenne F, Cinotti L, Delforge J, *et al.* Modeling [^{18}F]MPPF positron emission tomography kinetics for the determination of 5-hydroxytryptamine $_{1A}$ receptor concentration with multiinjection. *J Cereb Blood Flow Metab* 2002, 22: 753–765.
- [66] Theodore WH, Giovacchini G, Bonwetsch R, Bagic A, Reeves-Tyer P, Herscovitch P, *et al.* The effect of antiepileptic drugs on 5-HT-receptor binding measured by positron emission tomography. *Epilepsia* 2006, 47: 499–503.
- [67] Gallezot JD, Nabulsi N, Neumeister A, Planeta-Wilson B, Williams WA, Singhal T, *et al.* Kinetic modeling of the serotonin 5-HT $_{1B}$ receptor radioligand [^{11}C]P943 in humans. *J Cereb Blood Flow Metab* 2010, 30: 196–210.
- [68] Varnäs K, Nyberg S, Halldin C, Varrone A, Takano A, Karlsson P, *et al.* Quantitative analysis of [^{11}C]AZ10419369 binding to 5-HT $_{1B}$ receptors in human brain. *J Cereb Blood Flow Metab* 2011, 31: 113–123.
- [69] Murrough JW, Henry S, Hu J, Gallezot JD, Planeta-Wilson B, Neumaier JF, *et al.* Reduced ventral striatal/ventral pallidal serotonin $_{1B}$ receptor binding potential in major depressive disorder. *Psychopharmacology* 2011, 213: 547–553.
- [70] Hinz R, Bhagwagar Z, Cowen PJ, Cunningham VJ, Grasby PM. Validation of a tracer kinetic model for the quantification of 5-HT $_{2A}$ receptors in human brain with [^{11}C]MDL 100,907. *J Cereb Blood Flow Metab* 2007, 27: 161–172.
- [71] Rosier A, Dupont P, Peuskens J, Bormans G, Vandenberghe R, Maes M, *et al.* Visualisation of loss of 5-HT $_{2A}$ receptors with age in healthy volunteers using [^{18}F]altanserin and positron emission tomographic imaging. *Psychiatry Res* 1996, 68: 11–22.
- [72] van Dyck CH, Soares JC, Tan PZ, Staley JK, Baldwin RM, Amici LA, *et al.* Equilibrium modeling of 5-HT $_{2A}$ receptors with [^{18}F]deuteroaltanserin and PET: feasibility of a constant infusion paradigm. *Nucl Med Biol* 2000, 27: 715–722.
- [73] Trichard C, Paillere-Martinot ML, Attar-Levy D, Recassens C, Monnet F, Martinot JL. Binding of antipsychotic drugs to cortical 5-HT $_{2A}$ receptors: a PET study of chlorpromazine, clozapine, and amisulpride in schizophrenic patients. *Am J Psychiatry* 1998, 155: 505–508.
- [74] Ettrup A, da Cunha-Bang S, McMahon B, Lehel S, Dyssegaard A, Skibsted AW, *et al.* Serotonin 2 $_A$ receptor agonist binding in the human brain with [^{11}C]Cimbi-36. *J Cereb Blood Flow Metab* 2014.
- [75] Marnier L, Gillings N, Comley RA, Baare WF, Rabiner EA, Wilson AA, *et al.* Kinetic modeling of ^{11}C -SB207145 binding to 5-HT $_4$ receptors in the human brain *in vivo*. *J Nucl Med* 2009, 50: 900–908.
- [76] Parker CA, Gunn RN, Rabiner EA, Slifstein M, Comley R, Salinas C, *et al.* Radiosynthesis and characterization of ^{11}C -GSK215083 as a PET radioligand for the 5-HT $_6$ receptor. *J Nucl Med* 2012, 53: 295–303.
- [77] Mishina M, Ishiwata K, Ishii K, Kitamura S, Kimura Y, Kawamura K, *et al.* Function of sigma1 receptors in Parkinson's disease. *Acta Neurol Scand* 2005 112: 103–107.
- [78] Waterhouse RN, Nobler MS, Zhou Y, Chang RC, Morales O, Kuwabara H, *et al.* First evaluation of the sigma1 receptor radioligand [^{18}F]1-3-fluoropropyl-4-((4-cyanophenoxy)-methyl)piperidine ([^{18}F]FPS) in healthy humans. *Neuroimage* 2004, 22: T29.
- [79] Junck L, Olson JM, Ciliax BJ, Koeppe RA, Watkins GL, Jewett DM, *et al.* PET imaging of human gliomas with ligands for the peripheral benzodiazepine binding site. *Ann Neurol* 1989, 26: 752–758.
- [80] Banati RB, Goerres GW, Myers R, Gunn RN, Turkheimer FE, Kreutzberg GW, *et al.* [^{11}C](R)-PK11195 positron emission tomography imaging of activated microglia *in vivo* in Rasmussen's encephalitis. *Neurology* 1999, 53: 2199–2203.
- [81] Brown AK, Fujita M, Fujimura Y, Liow JS, Stabin M, Ryu YH, *et al.* Radiation dosimetry and biodistribution in monkey and man of ^{11}C -PBR28: a PET radioligand to image inflammation. *J Nucl Med* 2007, 48: 2072–2079.
- [82] Endres CJ, Pomper MG, James M, Uzuner O, Hammoud DA, Watkins CC, *et al.* Initial evaluation of ^{11}C -DPA-713, a novel TSPO PET ligand, in humans. *J Nucl Med* 2009, 50: 1276–1282.
- [83] Yasuno F, Kosaka J, Ota M, Higuchi M, Ito H, Fujimura Y, *et al.* Increased binding of peripheral benzodiazepine receptor in mild cognitive impairment-dementia converters measured by positron emission tomography with [^{11}C]DAA1106. *Psychiatry Res* 2012, 203: 67–74.
- [84] Gulyas B, Toth M, Schain M, Airaksinen A, Vas A, Kostulas K, *et al.* Evolution of microglial activation in ischaemic core and peri-infarct regions after stroke: a PET study with the TSPO molecular imaging biomarker [^{11}C]vinpocetine. *J Neurol Sci* 2012, 320: 110–117.
- [85] Fujimura Y, Zoghbi SS, Simeon FG, Taku A, Pike VW, Innis RB, *et al.* Quantification of translocator protein (18 kDa) in the human brain with PET and a novel radioligand, F-18-PBR06. *J Nucl Med* 2009, 50: 1047–1053.
- [86] Arlicot N, Vercouillie J, Ribeiro MJ, Tauber C, Venel Y, Baulieu JL, *et al.* Initial evaluation in healthy humans of [^{18}F]DPA-714, a potential PET biomarker for neuroinflammation. *Nucl Med Biol* 2012, 39: 570–578.
- [87] Mizrahi R, Rusjan PM, Kennedy J, Pollock B, Mulsant B, Suridjan I, *et al.* Translocator protein (18 kDa) polymorphism (rs6971) explains *in-vivo* brain binding affinity of the PET radioligand [^{18}F]FEPPA. *J Cereb Blood Flow Metab* 2012, 32: 968–972.

- [88] Guo Q, Colasanti A, Owen DR, Onega M, Kamalakaran A, Bennacef I, *et al.* Quantification of the specific translocator protein signal of ^{18}F -PBR111 in healthy humans: a genetic polymorphism effect on *in vivo* binding. *J Nucl Med* 2013, 54: 1915–1923.
- [89] Brust P, Deuther-Conrad W, Lehmkuhl K, Jia H, Wünsch B. Molecular imaging of σ_1 receptors *in vivo*: current status and perspectives. *Curr Med Chem* 2014, 21: 35–69.
- [90] Jansen KL, Faull RL, Storey P, Leslie RA. Loss of sigma binding sites in the CA1 area of the anterior hippocampus in Alzheimer's disease correlates with CA1 pyramidal cell loss. *Brain Res* 1993, 623: 299–302.
- [91] Weissman AD, Casanova MF, Kleinman JE, London ED, De Souza EB. Selective loss of cerebral cortical sigma, but not PCP binding sites in schizophrenia. *Biol Psychiatry* 1991, 29: 41–54.
- [92] van Waarde A, Rybczynska AA, Ramakrishnan N, Ishiwata K, Elsinga PH, Dierckx RA. Sigma receptors in oncology: therapeutic and diagnostic applications of sigma ligands. *Curr Pharm Des* 2010, 16: 3519–3537.
- [93] Banister SD, Kassiou M. The therapeutic potential of sigma (σ) receptors for the treatment of central nervous system diseases: evaluation of the evidence. *Curr Pharm Des* 2012, 18: 884–901.
- [94] Megalizzi V, Le Mercier M, Decaestecker C. Sigma receptors and their ligands in cancer biology: overview and new perspectives for cancer therapy. *Med Res Rev* 2012, 32: 410–427.
- [95] Schliebs R, Arendt T. The cholinergic system in aging and neuronal degeneration. *Behav Brain Res* 2011, 221: 555–563.
- [96] Brust P, Deuther-Conrad W. Molecular imaging of $\alpha 7$ nicotinic acetylcholine receptors *in vivo*: current status and perspectives. In: Bright P (Ed). *Neuroimaging - Clinical Applications*. InTech, 2012: 533–558.
- [97] Brust P, Peters D, Deuther-Conrad W. Development of radioligands for the imaging of $\alpha 7$ nicotinic acetylcholine receptors with positron emission tomography. *Curr Drug Targets* 2012, 13: 594–601.
- [98] Kadir A, Almkvist O, Wall A, Langström B, Nordberg A. PET imaging of cortical ^{11}C -nicotine binding correlates with the cognitive function of attention in Alzheimer's disease. *Psychopharmacology* 2006, 188: 509–520.
- [99] Papke RL. Merging old and new perspectives on nicotinic acetylcholine receptors. *Biochem Pharmacol* 2014. doi: 10.1016/j.bcp.2014.1001.1029.
- [100] Moerlein SM. Molecular imaging and the development of new radiopharmaceuticals. In: Kowalsky RJ, Falen SW (Eds.). *Radiopharmaceuticals in Nuclear Pharmacy and Nuclear Medicine*. American Pharmacists Association (APhA), 2011: 741.
- [101] Davenport AP, Russel FD. Radioligand Binding Assays: Theory and Practice. In: Mather SJ (Ed.). *Current Directions in Radiopharmaceutical Research and Development*. Kluwer Academic Publisher, 1996: 169–179.
- [102] Koeppe RA. A panel discussion on the future of pharmacology and experimental tomography. In: Gjedde A, Hansen SB, Knudsen GM, Paulson OB (Eds.). *Physiological Imaging of the Brain with PET*. Academic Press, 2001: 402.
- [103] Hurst R, Rollema H, Bertrand D. Nicotinic acetylcholine receptors: from basic science to therapeutics. *Pharmacol Ther* 2013, 137: 22–54.
- [104] Lendvai B, Kassai F, Szajli A, Nemethy Z. $\alpha 7$ Nicotinic acetylcholine receptors and their role in cognition. *Brain Res Bull* 2013, 93: 86–96.
- [105] Sorger D, Scheunemann M, Vercouillie J, Grossmann U, Fischer S, Hiller A, *et al.* Neuroimaging of the vesicular acetylcholine transporter by a novel 4- ^{18}F fluoro-benzoyl derivative of 7-hydroxy-6-(4-phenyl-piperidin-1-yl)-octahydrobenzo[1,4]oxazines. *Nucl Med Biol* 2009, 36: 17–27.
- [106] Giboureau N, Som IM, Boucher-Arnold A, Guilloteau D, Kassiou M. PET radioligands for the vesicular acetylcholine transporter (VAcHT). *Curr Top Med Chem* 2010, 10: 1569–1583.
- [107] Fujita M, Innis RB. *In vivo* molecular imaging: ligand development and research applications. In: Borroni E and Kupfer DJ (Eds.). *Neuropsychopharmacology: The Fifth Generation of Progress*. New York: Raven Press Ltd, 2002, Section 3: 411–425.
- [108] Blower PJ. Microautoradiography. In: Mather SJ (Ed.). *Current Directions in Radiopharmaceutical Research and Development*. Kluwer Academic Publisher, 1996: 219–232.
- [109] Lapchak PA, Araujo DM, Hefti F. Effects of chronic nerve growth factor treatment on hippocampal [^3H]cytisine/nicotinic binding sites and presynaptic nicotinic receptor function following fimbrial transections. *Neuroscience* 1994, 60: 293–298.
- [110] Rubboli F, Court JA, Sala C, Morris C, Perry E, Clementi F. Distribution of neuronal nicotinic receptor subunits in human brain. *Neurochem Int* 1994, 25: 69–71.
- [111] Baddick CG, Marks MJ. An autoradiographic survey of mouse brain nicotinic acetylcholine receptors defined by null mutants. *Biochem Pharmacol* 2011, 82: 828–841.
- [112] Morley BJ, Kemp GE, Salvaterra P. α -Bungarotoxin binding sites in the CNS. *Life Sci* 1979, 24: 859–872.
- [113] Whiteaker P, Davies AR, Marks MJ, Blagbrough IS, Potter BV, Wolstenholme AJ, *et al.* An autoradiographic study of the distribution of binding sites for the novel $\alpha 7$ -selective nicotinic radioligand [^3H]-methyllycaconitine in the mouse brain. *Eur J Neurosci* 1999, 11: 2689–2696.

- [114] Deuther-Conrad W, Fischer S, Hiller A, Nielsen EO, Timmermann DB, Steinbach J, *et al.* Molecular imaging of $\alpha 7$ nicotinic acetylcholine receptors: design and evaluation of the potent radioligand [^{18}F]NS10743. *Eur J Nucl Med Mol Imaging* 2009, 36: 791–800.
- [115] Daly JW. Thirty years of discovering arthropod alkaloids in amphibian skin. *J Nat Prod* 1998, 61: 162–172.
- [116] Avalos M, Parker MJ, Maddox FN, Carroll FI, Luetje CW. Effects of pyridine ring substitutions on affinity, efficacy, and subtype selectivity of neuronal nicotinic receptor agonist epibatidine. *J Pharmacol Exp Ther* 2002, 302: 1246–1252.
- [117] Deuther-Conrad W, Patt JT, Feuerbach D, Wegner F, Brust P, Steinbach J. Norchloro-fluoro-homoepibatidine: specificity to neuronal nicotinic acetylcholine receptor subtypes *in vitro*. *Farmaco* 2004, 59: 785–792.
- [118] Deuther-Conrad W, Patt JT, Lockman PR, Allen DD, Patt M, Schildan A, *et al.* Norchloro-fluoro-homoepibatidine (NCFHEB) - A promising radioligand for neuroimaging nicotinic acetylcholine receptors with PET. *Eur Neuro-psychopharmacol* 2008, 18: 222–229.
- [119] Smits R, Fischer S, Hiller A, Deuther-Conrad W, Wenzel B, Patt M, *et al.* Synthesis and biological evaluation of both enantiomers of [^{18}F]flubatine, promising radiotracers with fast kinetics for the imaging of $\alpha_4\beta_2$ -nicotinic acetylcholine receptors. *Bioorg Med Chem* 2014, 22: 804–812.
- [120] Patt JT, Spang JE, Westera G, Buck A, Schubiger PA. Synthesis and *in Vivo* studies of [C-11]N-methylepibatidine: comparison of the stereoisomers. *Nucl Med Biol* 1999, 26: 165–173.
- [121] Molina PE, Ding YS, Carroll FI, Liang F, Volkow ND, Pappas N, *et al.* Fluoro-norchloroepibatidine: preclinical assessment of acute toxicity. *Nucl Med Biol* 1997, 24: 743–747.
- [122] Gandiha A, Marshall IG. The effects of 2-(4-phenylpiperidino)-cyclohexanol (AH5183) on the acetylcholine content of, and output from, the chick biventer cervicis muscle preparation. *Int J Neurosci* 1973, 5: 191–196.
- [123] Prior C, Marshall IG, Parsons SM. The pharmacology of vesamicol: an inhibitor of the vesicular acetylcholine transporter. *Gen Pharmacol* 1992, 23: 1017–1022.
- [124] Hicks BW, Rogers GA, Parsons SM. Purification and characterization of a nonvesicular vesamicol-binding protein from electric organ and demonstration of a related protein in mammalian brain. *J Neurochem* 1991, 57: 509–519.
- [125] Kovac M, Mavel S, Deuther-Conrad W, Meheux N, Glockner J, Wenzel B, *et al.* 3D QSAR study, synthesis, and *in vitro* evaluation of (+)-5-FBVM as potential PET radioligand for the vesicular acetylcholine transporter (VACHT). *Bioorg Med Chem* 2010, 18: 7659–7667.
- [126] Mulholland GK, Jung YW, Wieland DM, Kilbourn MR, Kuhl DE. Synthesis of [^{18}F] fluoroethoxy-benzovesamicol, a radiotracer for cholinergic neurons. *J Labelled Comp Radiopharm* 1993, 33: 583–591.
- [127] Petrou M, Frey KA, Kilbourn MR, Scott PJ, Raffel DM, Bohnen NI, *et al.* *In vivo* imaging of human cholinergic nerve terminals with (-)-5- ^{18}F -fluoroethoxybenzovesamicol: biodistribution, dosimetry, and tracer kinetic analyses. *J Nucl Med* 2014. doi:10.2967/jnumed.113.124792.
- [128] Parent MJ, Bedard MA, Aliaga A, Minuzzi L, Mechawar N, Soucy JP, *et al.* Cholinergic depletion in Alzheimer's disease shown by [^{18}F]FEOBV autoradiography. *Int J Mol Imaging* 2013, 2013: 205045.
- [129] Szymoszek A, Wenzel B, Scheunemann M, Steinbach J, Schüürmann G. First CoMFA characterization of vesamicol analogs as ligands for the vesicular acetylcholine transporter. *J Med Chem* 2008, 51: 2128–2136.
- [130] Maier CA, Wünsch B. Novel spiro piperidines as highly potent and subtype selective σ -receptor ligands. Part 1. *J Med Chem* 2002, 45: 438–448.
- [131] Maier CA, Wünsch B. Novel σ receptor ligands. Part 2. SAR of spiro[[2]benzopyran-1,4'-piperidines] and spiro[[2] benzofuran-1,4'-piperidines] with carbon substituents in position 3. *J Med Chem* 2002, 45: 4923–4930.
- [132] Maier CA, Wünsch B. Novel σ receptor ligands, Part 3: Synthesis and SAR studies of 3-substituted 1'-benzylspiro[[2] benzoxepine-1,4'-piperidines]. *Eur J Org Chem* 2003: 714–720.
- [133] Große Maestrup E, Fischer S, Wiese C, Schepmann D, Hiller A, Deuther-Conrad W, *et al.* Evaluation of spirocyclic 3-(3-fluoropropyl)-2-benzofurans as σ_1 receptor ligands for neuroimaging with positron emission tomography. *J Med Chem* 2009, 52: 6062–6072.
- [134] Große Maestrup E, Wiese C, Schepmann D, Brust P, Wünsch B. Synthesis, pharmacological activity and structure affinity relationships of spirocyclic σ_1 receptor ligands with a (2-fluoroethyl) residue in 3-position. *Bioorg Med Chem* 2011, 19: 393–405.
- [135] Große Maestrup E, Wiese C, Schepmann D, Hiller A, Fischer S, Scheunemann M, *et al.* Synthesis of spirocyclic sigma(1) receptor ligands as potential PET radiotracers, structure-affinity relationships and *in vitro* metabolic stability. *Bioorg Med Chem* 2009, 17: 3630–3641.
- [136] Holl K, Falck E, Köhler J, Schepmann D, Humpf HU, Brust P, *et al.* Synthesis, characterization, and metabolism studies of fluspidine enantiomers. *Chem Med Chem* 2013, 8: 2047–2056.
- [137] Maisonia A, Grosse Maestrup E, Fischer S, Hiller A, Scheunemann M, Wiese C, *et al.* A ^{18}F -labeled fluorobutyl-substituted spirocyclic piperidine derivative as a selective radioligand for PET Imaging of σ_1 receptors. *Chem Med Chem* 2011, 6: 1401–1410.

- [138] Maisonia A, Grosse Maestrup E, Wiese C, Hiller A, Schepmann D, Fischer S, *et al.* Synthesis, radiofluorination and pharmacological evaluation of a fluoromethyl spirocyclic PET tracer for central σ_1 receptors and comparison with fluoroalkyl homologs. *Bioorg Med Chem* 2012, 20: 257–269.
- [139] Fischer S, Wiese C, Grosse Maestrup E, Hiller A, Deuther-Conrad W, Scheunemann M, *et al.* Molecular imaging of sigma receptors: synthesis and evaluation of the potent σ_1 selective radioligand [^{18}F]fluspidine. *Eur J Nucl Med Mol Imaging* 2011, 38: 540–551.
- [140] Bickel U. How to measure drug transport across the blood-brain barrier. *NeuroRx* 2005, 2: 15–26.
- [141] Pardridge WM. Drug transport across the blood-brain barrier. *J Cereb Blood Flow Metab* 2012, 32: 1959–1972.
- [142] Kessler RM, Ansari MS, de Paulis T, Schmidt DE, Clanton JA, Smith HE, *et al.* High affinity dopamine D_2 receptor radioligands. 1. Regional rat brain distribution of iodinated benzamides. *J Nucl Med* 1991, 32: 1593–1600.
- [143] Tsuji A. Small molecular drug transfer across the blood-brain barrier via carrier-mediated transport systems. *NeuroRx* 2005, 2: 54–62.
- [144] Ecker GF, Noe CR. In silico prediction models for blood-brain barrier permeation. *Curr Med Chem* 2004, 11: 1617–1628.
- [145] Gouverneur V, Müller K. Fluorine in Pharmaceutical and Medicinal Chemistry: From Biophysical Aspects to Clinical Applications. Singapore: World Scientific Publishing 2012.
- [146] Tressaud A, Haufe G (Eds.). Fluorine and Health, Molecular Imaging, Biomedical Materials and Pharmaceuticals. Elsevier Science, 2008.
- [147] Alauddin MM. Positron emission tomography (PET) imaging with ^{18}F -based radiotracers. *Am J Nucl Med Mol Imaging* 2012, 2: 55–76.
- [148] Ross TL, Wester HJ. ^{18}F : Labeling chemistry and labeled compounds. In: Vértés A, Nagy S, Klencsár Z, Lovas R, Rösch F (Eds.). *Handbook of Nuclear Chemistry: Radiochemistry and Radiopharmaceutical Chemistry in Life Sciences*, 2nd Ed. Springer, 2011, 4: 2021–2071.
- [149] Schubiger PA, Lehmann L, Friebe M. PET Chemistry: The Driving Force in Molecular Imaging. Springer, 2007.
- [150] Bergman J, Solin O. Fluorine-18-labeled fluorine gas for synthesis of tracer molecules. *Nucl Med Biol* 1997, 24: 677–683.
- [151] Forsback S, Marjamäki P, Eskola O, Bergman J, Rokka J, Grönroos T, *et al.* [^{18}F]CFT synthesis and binding to monoamine transporters in rats. *EJNMMI Res* 2012, 2: 3.
- [152] Ermisch A, Brust P, Kretschmar R, Rühle HJ. Peptides and Blood-Brain Barrier Transport. *Physiol Rev* 1993, 73: 489–527.
- [153] Coenen HH, Hamacher K, Schüller M, Stöcklin G, Klatte B, Knöchel A. Process for the preparation of fluorine-18 labelled compounds by nucleophilic exchange. EP0167103 A2, 1985.
- [154] Coenen HH, Colosimo M, Schüller M, Stöcklin G. Preparation of n.c.a. [^{18}F]CH₂BrF via aminopolyether supported nucleophilic substitution. *J Labelled Compd Radiopharm* 1986, 23: 587–595.
- [155] Roeda D, Dolle F. Aliphatic nucleophilic radiofluorination. *Curr Radiopharm* 2010, 3: 81–108
- [156] Cai LS, Lu SY, Pike VW. Chemistry with [^{18}F]fluoride ion. *European J Org Chem* 2008: 2853–2873.
- [157] Hoepping A, Scheunemann M, Fischer S, Deuther-Conrad W, Hiller A, Wegner F, *et al.* Radiosynthesis and biological evaluation of an ^{18}F -labeled derivative of the novel pyrazolopyrimidine sedative-hypnotic agent indiplon. *Nucl Med Biol* 2007, 34: 559–570.
- [158] Deuther-Conrad W, Fischer S, Scheunemann M, Hiller A, Diekers M, Friemel A, *et al.* GABA_A receptor specific pyrazolopyrimidines as potential imaging agents: *In vivo* characteristics of a new ^{18}F -labelled Indiplon derivative. *Curr Radiopharm* 2009, 2: 24–31.
- [159] Fischer S, Hiller A, Scheunemann M, Deuther-Conrad W, Hoepping A, Diekers M, *et al.* Radiosynthesis of novel ^{18}F -labelled derivatives of indiplon as potential GABA_A receptor imaging tracers for PET. *J Labelled Comp Radiopharm* 2008, 51: 123–131.
- [160] Schirmacher R, Bradtmöller G, Schirmacher E, Thews O, Tillmanns J, Siessmeier T, *et al.* ^{18}F -labeling of peptides by means of an organosilicon-based fluoride acceptor. *Angew Chem Int Ed Engl* 2006, 45: 6047–6050.
- [161] Römer J, Füchtner F, Steinbach J, Kasch H. Automated synthesis of 16 α -[^{18}F]fluoroestradiol-3,17 β -disulphamate. *Appl Radiat Isot* 2001, 55: 631–639.
- [162] Ermert J, Coenen HH. Nucleophilic ^{18}F -fluorination of complex molecules in activated carbocyclic aromatic position. *Curr Radiopharm* 2010, 3: 109–126
- [163] Fischer S, Hiller A, Smits R, Hoepping A, Funke U, Wenzel B, *et al.* Radiosynthesis of racemic and enantiomerically pure (-)-[^{18}F]flubatine-A promising PET radiotracer for neuroimaging of $\alpha_4\beta_2$ nicotinic acetylcholine receptors. *Appl Radiat Isot* 2013, 74C: 128–136.
- [164] Patt JT, Deuther-Conrad W, Wohlfarth K, Feuerbach D, Brust P, Steinbach J. Norchloro-fluoro-homoepibatidine: ^{18}F -labelling and evaluation of affinity and selectivity at neuronal nicotinic acetylcholine receptors. *J Labelled Compd Radiopharm* 2003, 46 (S1): S 168.
- [165] Patt M, Schildan A, Habermann B, Fischer S, Hiller A, Deuther-Conrad W, *et al.* Fully automated radiosynthesis of both enantiomers of [^{18}F]Flubatine under GMP conditions for human application. *Appl Radiat Isot* 2013, 80: 7–11.
- [166] Hockley BG, Stewart MN, Sherman P, Quesada C, Kilbourn MR, Albin RL, *et al.* (-)-[^{18}F]Flubatine: evaluation

- in rhesus monkeys and a report of the first fully automated radiosynthesis validated for clinical use. *J Labelled Comp Radiopharm* 2013, 56: 595–599.
- [167] Rühl T, Deuther-Conrad W, Fischer S, Günther R, Hennig L, Krautscheid H, *et al.* Cannabinoid receptor type 2 (CB₂)-selective N-aryl-oxadiazolyl-propionamides: synthesis, radiolabelling, molecular modelling and biological evaluation. *Org Med Chem Lett* 2012, 2: 32.
- [168] Teodoro R, Moldovan RP, Lueg C, Günther R, Donat CK, Ludwig FA, *et al.* Radiofluorination and biological evaluation of N-aryl-oxadiazolyl-propionamides as potential radioligands for PET imaging of cannabinoid CB₂ receptors. *Org Med Chem Lett* 2013, 3: 11.
- [169] Löser R, Fischer S, Hiller A, Köckerling M, Funke U, Maisonia A, *et al.* Use of 3- ^{18}F fluoropropanesulfonyl chloride as a prosthetic agent for the radiolabelling of amines: Investigation of precursor molecules, labelling conditions and enzymatic stability of the corresponding sulfonamides. *Beilstein J Org Chem* 2013, 9: 1002–1011.
- [170] Wüst F, Köhler L, Berndt M, Pietzsch J. Systematic comparison of two novel, thiol-reactive prosthetic groups for ^{18}F labeling of peptides and proteins with the acylation agent succinimidyl-4- ^{18}F fluorobenzoate (^{18}F SFB). *Amino Acids* 2009, 36: 283–295.
- [171] Serdons K, Verbruggen A, Bormans GM. Developing new molecular imaging probes for PET. *Methods* 2009, 48: 104–111.
- [172] Pretze M, Kuchar M, Bergmann R, Steinbach J, Pietzsch J, Mamat C. An efficient bioorthogonal strategy using CuAAC click chemistry for radiofluorinations of SNEW peptides and the role of copper depletion. *Chem Med Chem* 2013, 8: 935–945.
- [173] Pretze M, Pietzsch D, Mamat C. Recent trends in bioorthogonal click-radiolabeling reactions using fluorine-18. *Molecules* 2013, 18: 8618–8665.
- [174] Ramenda T, Kniess T, Bergmann R, Steinbach J, Wüst F. Radiolabelling of proteins with fluorine-18 via click chemistry. *Chem Commun (Camb)* 2009: 7521–7523.
- [175] Ramenda T, Steinbach J, Wüst F. 4- ^{18}F Fluoro-N-methyl-N-(propyl-2-yn-1-yl)benzenesulfonamide (^{18}F F-SA): a versatile building block for labeling of peptides, proteins and oligonucleotides with fluorine-18 via Cu(I)-mediated click chemistry. *Amino Acids* 2013, 44: 1167–1180.
- [176] Kniess T, Laube M, Bergmann R, Sehn F, Graf F, Steinbach J, *et al.* Radiosynthesis of a ^{18}F -labeled 2,3-diarylsubstituted indole via McMurry coupling for functional characterization of cyclooxygenase-2 (COX-2) *in vitro* and *in vivo*. *Bioorg Med Chem* 2012, 20: 3410–3421.
- [177] Funke U, Fischer S, Hiller A, Scheunemann M, Deuther-Conrad W, Brust P, *et al.* 3-(4-(6-Fluoroalkoxy-3,4-dihydroisoquinoline-2(1H)-yl)cyclohexyl)-1H-indol e-5-carbonitriles for SERT imaging: chemical synthesis, evaluation *in vitro* and radiofluorination. *Bioorg Med Chem Lett* 2008, 18: 4727–4730.
- [178] Funke U, Schwan G, Maisonia A, Scheunemann M, Deuther-Conrad W, Fischer S, *et al.* Radiosynthesis and radiotracer properties of a 7-(2- ^{18}F fluoroethoxy)-6-methoxy-pyrrolidinylquinazoline for imaging of phosphodiesterase 10A with PET. *Pharmaceuticals (Basel)* 2012, 5: 169–188.
- [179] Sorger D, Scheunemann M, Grossmann U, Fischer S, Vercouille J, Hiller A, *et al.* A new ^{18}F -labeled fluoroacetylmorpholino derivative of vesamicol for neuroimaging of the vesicular acetylcholine transporter. *Nucl Med Biol* 2008, 35: 185–195.
- [180] Hoepping A, Scheunemann M, Fischer S, Deuther-Conrad W, Hiller A, Wegner F, *et al.* Radiosynthesis and biological evaluation of an ^{18}F -labeled derivative of the novel pyrazolopyrimidine sedative-hypnotic agent indiplon. *Nucl Med Biol* 2007, 34: 559–570.
- [181] Donat CK, Schuhmann MU, Voigt C, Nieber K, Deuther-Conrad W, Brust P. Time-dependent alterations of cholinergic markers after experimental traumatic brain injury. *Brain Res* 2008, 1246: 167–177.
- [182] Perry DC, Kellar KJ. [^3H]epibatidine labels nicotinic receptors in rat brain: an autoradiographic study. *J Pharmacol Exp Ther* 1995, 275: 1030–1034.
- [183] Vaupel DB, Mukhin AG, Kimes AS, Horti AG, Koren AO, London ED. *In vivo* studies with [125I]5-I-A-85380, a nicotinic acetylcholine receptor radioligand. *Neuroreport* 1998, 9: 2311–2317.
- [184] Davies AR, Hardick DJ, Blagbrough IS, Potter BV, Wolstenholme AJ, Wonnacott S. Characterisation of the binding of [^3H]methyllycaconitine: a new radioligand for labelling $\alpha 7$ -type neuronal nicotinic acetylcholine receptors. *Neuropharmacology* 1999, 38: 679–690.
- [185] No-authors-listed. Indiplon. Indiplon modified-release, indiplon MR, NBI 34060, NBI 34060 modified-release, NBI 34060 MR. *Drugs R D* 2002, 3: 197–199.
- [186] Hoepping A, Diekers M, Deuther-Conrad W, Scheunemann M, Fischer S, Hiller A, *et al.* Synthesis of fluorine substituted pyrazolopyrimidines as potential leads for the development of PET-imaging agents for the GABAA receptors. *Bioorg Med Chem* 2008, 16: 1184–1194.
- [187] Brust P, Scheffel U, Szabo Z. Radioligands for the study of the 5-HT transporter *in vivo*. *IDrugs* 1999, 2: 129–145.
- [188] Kretzschmar M, Brust P, Zessin J, Cumming P, Bergmann R, Johannsen B. Autoradiographic imaging of the serotonin transporter in the brain of rats and pigs using S-([^{18}F] Fluoromethyl)-(+)-McN5652. *Eur Neuropsychopharmacol* 2003, 13: 387–397.

- [189] Kung MP, Stevenson DA, Plössl K, Meegalla SK, Beckwith A, Essman WD, *et al.* [^{99m}Tc]TRODAT-1: a novel technetium-99m complex as a dopamine transporter imaging agent. *European J Nucl Med* 1997, 24: 372–380.
- [190] Kung HF, Kung MP, Wey SP, Lin KJ, Yen TC. Clinical acceptance of a molecular imaging agent: a long march with [Tc-99m]TRODAT. *Nucl Med Biol* 2007, 34: 787–789.
- [191] Tan PZ, Baldwin RM, Van Dyck CH, Al-Tikriti M, Roth B, Khan N, *et al.* Characterization of radioactive metabolites of 5-HT_{2A} receptor PET ligand [¹⁸F]altanserin in human and rodent. *Nucl Med Biol* 1999, 26: 601–608.
- [192] van Dyck CH, Tan PZ, Baldwin RM, Amici LA, Garg PK, Ng CK, *et al.* PET quantification of 5-HT_{2A} receptors in the human brain: a constant infusion paradigm with [¹⁸F]altanserin. *J Nucl Med* 2000, 41: 234–241.
- [193] Liptrot M, Adams KH, Martiny L, Pinborg LH, Lonsdale MN, Olsen NV, *et al.* Cluster analysis in kinetic modelling of the brain: a noninvasive alternative to arterial sampling. *Neuroimage* 2004, 21: 483–493.
- [194] Bergström KA, Halldin C, Kuikka JT, Swahn CG, Tiihonen J, Hiltunen J, *et al.* Lipophilic metabolite of [¹²³I]β-CIT in human plasma may obstruct quantitation of the dopamine transporter. *Synapse* 1995, 19: 297–300.
- [195] Lundkvist C, Halldin C, Swahn CG, Ginovart N, Farde L. Different brain radioactivity curves in a PET study with [¹¹C]β-CIT labelled in two different positions. *Nucl Med Biol* 1999, 26: 343–350.
- [196] Zoghbi SS, Shetty HU, Ichise M, Fujita M, Imaizumi M, Liow JS, *et al.* PET imaging of the dopamine transporter with ¹⁸F-FECNT: a polar radiometabolite confounds brain radioligand measurements. *J Nucl Med* 2006, 47: 520–527.
- [197] Shetty HU, Zoghbi SS, Liow JS, Ichise M, Hong J, Musachio JL, *et al.* Identification and regional distribution in rat brain of radiometabolites of the dopamine transporter PET radioligand [¹¹C]PE2I. *Eur J Nucl Med Mol Imaging* 2007, 34: 667–678.
- [198] Peyronneau MA, Saba W, Dolle F, Goutal S, Coulon C, Bottlaender M, *et al.* Difficulties in dopamine transporter radioligand PET analysis: the example of LBT-999 using [¹⁸F] and [¹¹C] labelling: part II: Metabolism studies. *Nucl Med Biol* 2012, 39: 347–359.
- [199] Bergström KA, Halldin C, Hall H, Lundkvist C, Ginovart N, Swahn CG, *et al.* *In vitro* and *in vivo* characterisation of nor-β-CIT: a potential radioligand for visualisation of the serotonin transporter in the brain. *European J Nucl Med* 1997, 24: 596–601.
- [200] Guengerich FP. Common and uncommon cytochrome P450 reactions related to metabolism and chemical toxicity. *Chem Res Toxicol* 2001, 14: 611–650.
- [201] Carroll FI, Blough BE, Nie Z, Kuhar MJ, Howell LL, Navarro HA. Synthesis and monoamine transporter binding properties of 3beta-(3',4'-disubstituted phenyl)tropane-2beta-carboxylic acid methyl esters. *J Med Chem* 2005, 48: 2767–2771.
- [202] Mori T, Sun LQ, Kobayashi M, Kiyono Y, Okazawa H, Furukawa T, *et al.* Preparation and evaluation of ethyl [¹⁸F]fluoroacetate as a praradiotracer of [¹⁸F]fluoroacetate for the measurement of glial metabolism by PET. *Nucl Med Biol* 2009, 36: 155–162.
- [203] Diemel GA, Popp D, Drew PD, Ball K, Krisht A, Cruz NF. Preferential labeling of glial and meningial brain tumors with [2-¹⁴C]acetate. *J Nucl Med* 2001, 42: 1243–1250.
- [204] Lear JL, Ackermann RF. Evaluation of radiolabeled acetate and fluoroacetate as potential tracers of cerebral oxidative metabolism. *Metab Brain Dis* 1990, 5: 45–56.
- [205] Davson H, Segal MB. *Physiology of the CSF and Blood-Brain Barriers*. Boca Raton, USA: CRC Press, 1996.
- [206] Rogers GA, Stone-Elander S, Ingvar M, Eriksson L, Parsons SM, Widen L. ¹⁸F-labelled vesamicol derivatives: syntheses and preliminary *in vivo* small animal positron emission tomography evaluation. *Nucl Med Biol* 1994, 21: 219–230.
- [207] Tu LQ, Wright PF, Rix CJ, Ahokas JT. Is fluoroacetate-specific defluorinase a glutathione S-transferase? *Comp Biochem Physiol C Toxicol Pharmacol* 2006, 143: 59–66.
- [208] Johnson JA, el Barbary A, Kornguth SE, Brugge JF, Siegel FL. Glutathione S-transferase isoenzymes in rat brain neurons and glia. *J Neurosci* 1993, 13: 2013–2023.
- [209] Brust P, Hinz R, Kuwabara H, Hesse S, Zessin J, Pawelke B, *et al.* *In vivo* measurement of the serotonin transporter with (S)-([¹⁸F]fluoromethyl)-(+)-McN5652. *Neuropsychopharmacology* 2003, 28: 2010–2019.
- [210] Hesse S, Brust P, Mäding P, Becker GA, Patt M, Seese A, *et al.* Imaging of the brain serotonin transporters (SERT) with ¹⁸F-labelled fluoromethyl-McN5652 and PET in humans. *Eur J Nucl Med Mol Imaging* 2012, 39: 1001–1011.
- [211] Szabo Z, Scheffel U, Mathews WB, Ravert HT, Szabo K, Kraut M, *et al.* Kinetic analysis of [¹¹C]McN5652: a serotonin transporter radioligand. *J Cereb Blood Flow Metab* 1999, 19: 967–981.
- [212] Brust P, Patt JT, Deuther-Conrad W, Becker G, Patt M, Schildan A, *et al.* *In vivo* measurement of nicotinic acetylcholine receptors with [¹⁸F]norchloro-fluoro-homoepibatidine. *Synapse* 2008, 62: 205–218.
- [213] Patt M, Becker GA, Grossmann U, Habermann B, Schildan A, Wilke S, *et al.* Evaluation of metabolism, plasma protein binding and other biological parameters after administration of (-)-[¹⁸F]flubatine in humans. *Nucl Med Biol* 2014. doi: org/10.1016/j.nucmedbio.2014.1003.1018.
- [214] Becker GA, Wilke S, Schönknecht P, Patt M, Luthardt J, Hesse S, *et al.* Comparison of (-)-[¹⁸F]-flubatine and 2-[¹⁸F]FA-85380 binding to nicotinic alpha4beta2 acetylcholine receptors in human brains. *Eur J Nucl Med Mol Imaging*

- 2013, 40 (Suppl. 2): S271.
- [215] Fasinu P, Bouic PJ, Rosenkranz B. Liver-based *in vitro* technologies for drug biotransformation studies - a review. *Curr Drug Metab* 2012, 13: 215–224.
- [216] Davydov DR. Microsomal monooxygenase as a multienzyme system: the role of P450-P450 interactions. *Expert Opin Drug Metab Toxicol* 2011, 7: 543–558.
- [217] Stabin MG. *Fundamentals of Nuclear Medicine Dosimetry*. Springer, 2008.
- [218] van de Waterbeemd H, Camenisch G, Folkers G, Chretien JR, Raevsky OA. Estimation of blood-brain barrier crossing of drugs using molecular size and shape, and H-bonding descriptors. *J Drug Target* 1998, 6: 151–165.
- [219] Ball K, Bouzom F, Scherrmann JM, Walther B, Declèves X. Physiologically based pharmacokinetic modelling of drug penetration across the blood-brain barrier-towards a mechanistic IVIVE-based approach. *AAPS J* 2013, 15: 913–932.
- [220] Shawahna R, Declèves X, Scherrmann JM. Hurdles with using *in vitro* models to predict human blood-brain barrier drug permeability: a special focus on transporters and metabolizing enzymes. *Curr Drug Metab* 2013, 14: 120–136.
- [221] Uchida Y, Ohtsuki S, Katsukura Y, Ikeda C, Suzuki T, Kamiie J, *et al.* Quantitative targeted absolute proteomics of human blood-brain barrier transporters and receptors. *J Neurochem* 2011, 117: 333–345.
- [222] Rötering S, Scheunemann M, Fischer S, Hiller A, Peters D, Deuther-Conrad W, *et al.* Radiosynthesis and first evaluation in mice of [¹⁸F]NS14490 for molecular imaging of $\alpha 7$ nicotinic acetylcholine receptors. *Bioorg Med Chem* 2013, 21: 2635–2642.
- [223] Syvänen S, Lindhe O, Palner M, Kornum BR, Rahman O, Langström B, *et al.* Species differences in blood-brain barrier transport of three positron emission tomography radioligands with emphasis on P-glycoprotein transport. *Drug Metab Dispos* 2009, 37: 635–643.
- [224] Wagner HN, Jr., Burns HD, Dannals RF, Wong DF, Langström B, Delfer T, *et al.* Imaging dopamine receptors in the human brain by positron tomography. *Science* 1983, 221: 1264–1266.
- [225] Ehrn E, Farde L, de Paulis T, Eriksson L, Greitz T, Johnström P, *et al.* Preparation of ¹¹C-labelled Raclopride, a new potent dopamine receptor antagonist: preliminary PET studies of cerebral dopamine receptors in the monkey. *Int J Appl Radiat Isot* 1985, 36: 269–273.
- [226] Chan GL, Holden JE, Stoessl AJ, Doudet DJ, Wang Y, Dobko T, *et al.* Reproducibility of the distribution of carbon-11-SCH 23390, a dopamine D₁ receptor tracer, in normal subjects. *J Nucl Med* 1998, 39: 792–797.
- [227] Parsey RV, Arango V, Olvet DM, Oquendo MA, Van Heertum RL, John Mann J. Regional heterogeneity of 5-HT_{1A} receptors in human cerebellum as assessed by positron emission tomography. *J Cereb Blood Flow Metab* 2005, 25: 785–793.
- [228] Biver F, Goldman S, Luxen A, Monclus M, Forestini M, Mendlewicz J, *et al.* Multicompartmental study of F-18 altanserin binding to brain 5HT₂ receptors in humans using positron emission tomography. *Eur J Nucl Med* 1994, 21: 937–946.
- [229] Itoh T, Tanaka M, Kobayashi K, Suzuki K, Inoue O. Binding kinetics of ¹¹C-N-methyl piperidyl benzilate (¹¹C-NMPB) in a rhesus monkey brain using the cerebellum as a reference region. *Ann Nucl Med* 2005, 19: 499–505.
- [230] Deuther-Conrad W, Fischer S, Hiller A, Becker G, Cumming P, Xiong G, *et al.* Assessment of $\alpha 7$ nicotinic acetylcholine receptor availability in porcine brain with [¹⁸F]NS10743. *Eur J Nucl Med Mol Imaging* 2011, 38: 1541–1549.
- [231] Flesher JE, Scheffel U, London ED, Frost JJ. *In vivo* labeling of nicotinic cholinergic receptors in brain with [³H]cytisine. *Life Sci* 1994, 54: 1883–1890.
- [232] Ishiwata K, Kawamura K, Wang WF, Tsukada H, Harada N, Mochizuki H, *et al.* Evaluation of *in vivo* selective binding of [¹¹C]doxepin to histamine H₁ receptors in five animal species. *Nucl Med Biol* 2004, 31: 493–502.
- [233] Kish SJ, Furukawa Y, Chang LJ, Tong J, Ginovart N, Wilson A, *et al.* Regional distribution of serotonin transporter protein in postmortem human brain: Is the cerebellum a SERT-free brain region? *Nucl Med Biol* 2005, 32: 123–128.
- [234] Brust P, Hesse S, Müller U, Szabo Z. Neuroimaging of the serotonin transporter - possibilities and pitfalls. *Curr Psychiat Rev* 2006, 2: 111–149.
- [235] Marjamäki P, Zessin J, Eskola O, Grönroos T, Haaparanta M, Bergman J, *et al.* S-[¹⁸F]fluoromethyl-(+)-McN5652, a PET tracer for the serotonin transporter: Evaluation in rats. *Synapse* 2003, 47: 45–53.
- [236] Deuther-Conrad W, Maisoniai A, Patt M, Stittsworth S, Becker G, Habermann B, *et al.* Discovery of enantioselective suitability of (R)-(+)- and (S)-(-)-[¹⁸F]fluspidine for σ_1 receptor imaging. *J Label Comp Radiopharm* 2013, 56: S55.
- [237] Brust P, Deuther-Conrad W, Becker G, Patt M, Donat CK, Stittsworth S, *et al.* Distinctive *in vivo* kinetics of the new sigma1 receptor ligands (R)-(+)- and (S)-(-)-¹⁸F-fluspidine in porcine brain. *J Nucl Med* 2014, pii: jnumed.114.137562.
- [238] Leenders KL, Gibbs JM, Frackowiak RS, Lammertsma AA, Jones T. Positron emission tomography of the brain: new possibilities for the investigation of human cerebral pathophysiology. *Prog Neurobiol* 1984, 23: 1–38.
- [239] Mintun MA, Raichle ME, Kilbourn MR, Wooten GF, Welch MJ. A quantitative model for the *in vivo* assessment of drug binding sites with positron emission tomography. *Ann Neurol* 1984, 15: 217–227.

- [240] Miyoshi S, Mitsuoka K, Nishimura S, Veltkamp SA. Radioisotopes in Drug Research and Development: Focus on Positron Emission Tomography. In: Singh N (Ed). Radioisotopes - Applications in Bio-Medical Science. InTech, 2011: 93–113.
- [241] Yanai K, Ido T, Ishiwata K, Hatazawa J, Watanuki S, Takahashi T, *et al.* Characteristics of specific *in vivo* labeling of neuroleptic binding sites with 3-N-[¹¹C]methylspiperone. *European J Nucl Med* 1986, 11: 438–443.
- [242] Brust P, Shaya EK, Jeffries KJ, Dannals RF, Ravert HT, Wilson AA, *et al.* Effects of vasopressin on blood-brain transfer of methionine in dogs. *J Neurochem* 1992, 59: 1421–1429.
- [243] Kong FL, Ford RJ, Yang DJ. Managing lymphoma with non-FDG radiotracers: current clinical and preclinical applications. *Biomed Res Int* 2013, 2013: 626910.
- [244] Prenen GH, Go KG, Paans AM, Zuiderveen F, Vaalburg W, Kamman RL, *et al.* Positron emission tomographical studies of 1-¹¹C-acetoacetate, 2-¹⁸F-fluoro-deoxy-D-glucose, and L-1-¹¹C-tyrosine uptake by cat brain with an experimental lesion. *Acta Neurochirurgica* 1989, 99: 166–172.
- [245] Ginovart N, Wilson AA, Meyer JH, Hussey D, Houle S. [¹¹C]-DASB, a tool for *in vivo* measurement of SSRI-induced occupancy of the serotonin transporter: PET characterization and evaluation in cats. *Synapse* 2003, 47: 123–133.
- [246] Bauer R, Bergmann R, Beyer GJ, Manfrass P, Steinbach J, Kretschmar M, *et al.* Investigations of cerebral glucose utilization into the newborn brain: a [¹⁸F]-FDG positron emission tomography study using a high resolution multiwire proportional chamber detector device. *Exp Pathol* 1991, 42: 229–233.
- [247] Sauleau P, Lapouble E, Val-Laillet D, Malbert CH. The pig model in brain imaging and neurosurgery. *Animal* 2009, 3: 1138–1151.
- [248] Alstrup AKO, Smith DF. PET neuroimaging in pigs. *Scand J Lab Anim Sci* 2012, 39: 25–45.
- [249] Herzog H. PET/MRI: challenges, solutions and perspectives. *Z Med Phys* 2012, 22: 281–298.
- [250] Herzog H, van den Hoff J. Combined PET/MR systems: an overview and comparison of currently available options. *Q J Nucl Med Mol Imaging* 2012, 56: 247–267.
- [251] Xi W, Tian M, Zhang H. Molecular imaging in neuroscience research with small-animal PET in rodents. *Neurosci Res* 2011, doi:10.1016/j.neures.2010.12.017.
- [252] Lancelot S, Zimmer L. Small-animal positron emission tomography as a tool for neuropharmacology. *Trends Pharmacol Sci* 2010, 31: 411–417.
- [253] Syvänen S, Labots M, Tagawa Y, Eriksson J, Windhorst AD, Lammertsma AA, *et al.* Altered GABA_A receptor density and unaltered blood-brain barrier transport in a kainate model of epilepsy: an *in vivo* study using ¹¹C-flumazenil and PET. *J Nucl Med* 2012, 53: 1974–1983.
- [254] Gunn RN, Gunn SR, Turkheimer FE, Aston JA, Cunningham VJ. Positron emission tomography compartmental models: a basis pursuit strategy for kinetic modeling. *J Cereb Blood Flow Metab* 2002, 22: 1425–1439.
- [255] Schmidt KC, Turkheimer FE. Kinetic modeling in positron emission tomography. *Quarterly J Nucl Med* 2002, 46: 70–85.
- [256] Laruelle M, Slifstein M, Huang Y. Positron emission tomography: imaging and quantification of neurotransmitter availability. *Methods* 2002, 27: 287–299.
- [257] Watabe H, Ikoma Y, Kimura Y, Naganawa M, Shidahara M. PET kinetic analysis--compartmental model. *Ann Nucl Med* 2006, 20: 583–588.
- [258] van den Hoff J. Principles of quantitative positron emission tomography. *Amino Acids* 2005, 29: 341–353.
- [259] van den Hoff J. Kinetic Modelling. In: Kiessling F, Pichler BJ. *Small Animal Imaging: Basics and Practical Guide*. Springer, 2010: 387–404.
- [260] Brust P, Zessin J, Kuwabara H, Pawelke B, Kretschmar M, Hinz R, *et al.* Positron emission tomography imaging of the serotonin transporter in the pig brain using [¹¹C](+)-McN5652 and S-([¹⁸F]fluoromethyl)-(+)-McN5652. *Synapse* 2003, 47: 143–151.
- [261] Lammertsma AA, Bench CJ, Hume SP, Osman S, Gunn K, Brooks DJ, *et al.* Comparison of methods for analysis of clinical C-11 raclopride studies. *J Cereb Blood Flow Metab* 1996, 16: 42–52.
- [262] Lammertsma AA, Hume SP. Simplified reference tissue model for PET receptor studies. *Neuroimage* 1996, 4: 153–158.
- [263] Wang G, Qi J. Direct estimation of kinetic parametric images for dynamic PET. *Theranostics* 2013, 3: 802–815.
- [264] Patlak CS, Blasberg RG, Fenstermacher JD. Graphical evaluation of blood-to-brain transfer constants from multiple-time uptake data. *J Cereb Blood Flow Metab* 1983, 3: 1–7.
- [265] Patlak CS, Blasberg RG. Graphical evaluation of blood-to-brain transfer constants from multiple-time uptake data. Generalizations. *J Cereb Blood Flow Metab* 1985, 5: 584–590.
- [266] Gjedde A. High-and low-affinity transport of D-glucose from blood to brain. *J Neurochem* 1981, 36: 1463–1471.
- [267] Logan J, Fowler JS, Volkow ND, Wolf AP, Dewey SL, Schlyer DJ, *et al.* Graphical analysis of reversible radioligand binding from time-activity measurements applied to [N-¹¹C-methyl]-(-)-cocaine PET studies in human subjects. *J Cereb Blood Flow Metab* 1990, 10: 740–747.
- [268] Wang JZ, Qiu P, Liu RKJ, Szabo Z. Model-Based receptor quantization analysis for PET parametric imaging. *Conf Proc IEEE Eng Med Biol Soc* 2005, 6: 5908–5911.
- [269] Dennen S, Decristoforo Ce. *The Radiopharmacy. A Technologist's Guide*. European Association of Nuclear Medicine,

- 2008.
- [270] Elsinga P, Todde S, Penuelas I, Meyer G, Farstad B, Faivre-Chauvet A, *et al.* Guidance on current good radiopharmacy practice (cGRPP) for the small-scale preparation of radiopharmaceuticals. *Eur J Nucl Med Mol Imaging* 2010, 37: 1049–1062.
- [271] Verbruggen A, Coenen HH, Deverre JR, Guilloteau D, Langstrom B, Salvadori PA, *et al.* Guideline to regulations for radiopharmaceuticals in early phase clinical trials in the EU. *Eur J Nucl Med Mol Imaging* 2008, 35: 2144–2151.
- [272] Zessin J, Eskola O, Steinbach J, Bergman J, Marjamäki P, Brust P, *et al.* Synthesis and first biological evaluation of the [^{18}F]fluoromethyl-analog of (+)-MCN5652, a tracer for imaging the serotonin transporter. *Nuklearmedizin* 2000, 39: A36. [Article in German language]
- [273] Petrou M, Koeppe R, Scott P, Bohnen N, Kilbourn M, Frey K. PET imaging of the vesicular acetylcholine transporter. *J Nucl Med* 2012, 53 (Supplement 1): 290.
- [274] Farde L, Ehrin E, Eriksson L, Greitz T, Hall H, Hedström CG, *et al.* Substituted benzamides as ligands for visualization of dopamine receptor binding in the human brain by positron emission tomography. *Proc Natl Acad Sci U S A* 1985, 82: 3863–3867.
- [275] Maziere M, Hantraye P, Prenant C, Sastre J, Comar D. Synthesis of ethyl 8-fluoro-5,6-dihydro-5- ^{11}C methyl-6-oxo-4H-imidazo [1,5-a] [1,4]benzodiazepine-3-carboxylate (RO 15.1788-11C): a specific radioligand for the *in vivo* study of central benzodiazepine receptors by positron emission tomography. *Int J Appl Radiat Isot* 1984, 35: 973–976.
- [276] Rowland DJ, Cherry SR. Small-animal preclinical nuclear medicine instrumentation and methodology. *Semin Nucl Med* 2008, 38: 209–222.

Role of cortical spreading depression in the pathophysiology of migraine

Yilong Cui, Yosky Kataoka, Yasuyoshi Watanabe

Division of Bio-function Dynamics Imaging, RIKEN Center for Life Science Technologies, 6-7-3 Minatojima minamimachi, Chuo-ku, Kobe, Hyogo 650-0047, Japan

Corresponding author: Yilong Cui. E-mail: cuiyl@riken.jp

© Shanghai Institutes for Biological Sciences, CAS and Springer-Verlag Berlin Heidelberg 2014

A migraine is a recurring neurological disorder characterized by unilateral, intense, and pulsatile headaches. In one-third of migraine patients, the attacks are preceded by a visual aura, such as a slowly-propagating scintillating scotoma. Migraine aura is thought to be a result of the neurovascular phenomenon of cortical spreading depression (SD), a self-propagating wave of depolarization that spreads across the cerebral cortex. Several animal experiments have demonstrated that cortical SD causes intracranial neurogenic inflammation around the meningeal blood vessels, such as plasma protein extravasation and pro-inflammatory peptide release. Cortical SD has also been reported to activate both peripheral and central trigeminal nociceptive pathways. Although several issues remain to be resolved, recent evidence suggests that cortical SD could be the initial trigger of intracranial neurogenic inflammation, which then contributes to migraine headaches *via* subsequent activation of trigeminal afferents.

Keywords: cortical spreading depression; migraine; neurogenic inflammation; PET; trigeminal nociceptive pathway

Introduction

Cortical spreading depression (SD), described first by Leao^[1], is a self-propagating wave of transient neuronal/glia membrane depolarization that is accompanied by a transient negative shift of the direct current (DC) potential^[2] and temporal elevation of cerebral blood flow (CBF)^[3, 4] throughout the cerebral hemisphere at a rate of 2–5 mm/min^[1, 5, 6]. The rate of spreading correlates with the observed spread of the aura of a classical migraine^[7], which is characterized by a spot of flickering light that appears near the center of the visual field and then gradually expands outward^[8–10]. Recently, cortical SD has been hypothesized to be the initial event involved in migraine headaches. Moskowitz *et al.*^[11, 12] proposed that pro-inflammatory peptides, such as substance P and calcitonin gene-related peptide (CGRP), released from trigeminocervical nerve terminals in response to some unknown stimulation,

probably cortical SD, induces vasodilation and plasma protein extravasation. Such neurogenic inflammation is thought to trigger a headache *via* stimulation of trigeminal afferents. Consistent with this hypothesis, cortical SD induced intracranial neurogenic inflammation around the meningeal blood vessels^[13–15], and subsequent activation of both peripheral^[16] and central^[17] trigeminal nociceptive pathways has been described. Here, we review the experimental evidence mainly from neurophysiological studies that has advanced the understanding of whether and how the neurovascular phenomenon of cortical SD causes intracranial neurogenic inflammation, and subsequently participates in triggering a migraine headache.

Migraine Pathophysiology

A migraine is a recurring neurological disorder characterized

by unilateral, intense, and pulsatile headaches lasting 4–72 h^[18], and is often associated with symptoms including nausea, vomiting, and sensitivity to light, sound, or smell^[19]. In one-third of migraine patients, the attack is preceded by transient neurological symptoms like sensory or motor deficits, collectively referred to as a migraine aura^[9, 20, 21]. Most common is a visual aura, a scintillating scotoma, in which a spot of flickering light appears near the center of the visual field and then gradually expands outward^[8-10].

Several theories have been proposed to explain the pathophysiology of migraine: the vascular, neural, and trigeminovascular theories. In the 1930s, Harold Wolff^[22] and colleagues proposed the vascular theory, wherein the neurological symptoms of migraine aura are caused by cerebral vasoconstriction, and the migraine pain is evoked by vasodilatation of the extracranial terminal branches of the external carotid artery. They found that the intensity of migraine pain is closely related to the amplitude of pulsation in the occipital and superficial temporal branches of the external carotid arteries^[22]. In the 1980s, Olesen and colleagues found the presence of spreading oligemia, a 20%–30% reduction of cerebral blood flow that appears first in the posterior part of the brain and then gradually spreads into the parietal and temporal lobes at a rate of 2–3 mm/min during an episode of migraine with aura^[8, 23, 24]. The spread of oligemia does not match the territories of the major cerebral arteries, but follows the cortical surface, implying a neural, rather than a vascular cause^[23]. A highly variable increase in the cerebral blood flow is often followed by oligemia^[25, 26], but the periods of increased cerebral blood flow do not correlate temporally with the experience of migraine headache^[8, 23, 27], suggesting that the intracranial vasodilatation is likely an epiphenomenon, rather than a cause of the migraine headache.

In 1941, Karl Spencer Lashley^[10], a psychologist at Harvard University, described his own experience of a visual aura, where a scotoma started as a small area, then gradually enlarged, and spread toward the periphery of the visual field, and the propagation rate was estimated to be 3 mm/min or less. Three years later, Aristides Leao^[1] reported the phenomenon of cortical SD, characterized by a self-propagating wave of depolarization that begins in the neuronal/glia cells of local areas of the brain and subsequently spreads in all directions at a rate of ~3 mm/

min. The similarity of Lashley's migraine aura and Leao's cortical SD was first picked up by Milner in 1958^[7], and further investigated by Olesen in the 1980s, as described above. Based on both Lashley's description of a spreading scotoma^[10] and Leao's findings of cortical SD^[1], the pathogenic theories changed from primary vascular to primary neural mechanisms.

In the 1980s, Moskowitz and colleagues reconciled the primary vascular and primary neural views and proposed the trigeminovascular theory^[11, 12]. They hypothesized that some unknown stimulation, probably the cortical SD, depolarizes the trigeminocervical nerve terminals innervating the meninges, and pro-inflammatory peptides such as substance P and CGRP are released from the primary meningeal afferents, which further induce vasodilation and plasma protein extravasation. Such neurogenic inflammatory reactions were thought to trigger headache *via* stimulation of the trigeminal afferents. Supporting this theory, plasma extravasation was observed during electrical stimulation of the trigeminal ganglion in the rat^[11], and pro-inflammatory peptides including CGRP and substance P were released in response to electrical stimulation of the trigeminal ganglion in humans and cats^[28]. Moreover, the theory was supported by clinical studies where the CGRP levels were found to be increased in the jugular vein of patients during migraine attacks^[29], and vasogenic leakage from the leptomeningeal vessels has also been shown in at least one case of migraine with aura^[30], two cases of prolonged migraine aura and during spontaneous or familial hemiplegic migraine attacks^[31, 32].

Leao's Cortical Spreading Depression

The mysterious phenomenon of cortical SD was first identified in the rabbit cerebral cortex by Aristides Leao, a young Brazilian neurophysiologist, during his Ph.D. fellowship in the Department of Physiology at Harvard University^[1]. At that time, Leao was studying the electroencephalogram (EEG) of experimental epilepsy in the cerebral cortex of an anesthetized rabbit, but he was distracted by a contradictory and unexpected result that the EEG activity was silenced for a minute, and such suppression propagated slowly across the cerebral hemisphere. This phenomenon was then extensively studied around the world^[33-36], and has been characterized

as a self-propagating wave of depolarization associated with a transient negative shift of the DC potential^[2] and temporal elevation of the CBF^[3, 4]. These changes in DC potential and CBF spread throughout the cortical gray matter at a rate of ~ 3 mm/min^[1, 5, 6].

Cortical SD can be evoked by tetanic electrical stimuli, mechanical stimuli such as pressure on or puncture of the cortex, alkaline pH, low osmolarity, and chemical stimuli such as potassium ions or glutamate^[36–38]. Recently, we demonstrated that transient tissue oxidation in a restricted local area of the rat cerebral cortex also induces cortical SD^[3]. To restrict oxidation within a sub-millimeter region, we used a unique technique, photo-dynamic tissue oxidation (PDTO) technique, developed by Kataoka *et al.* for assessing the spatially- and temporally-controlled brain tissue oxidation from outside the brain within seconds or minutes^[39]. PDTO was carried out by application of rose Bengal, a photo-sensitizing dye, to a discrete region of the brain, followed by photo-irradiation through the dura mater. We found a high-amplitude DC potential shift (~ 50 mV) in the photo-oxidized area, and such a shift of the DC

potential recovered gradually over the next 3 h (Fig. 1)^[3]. A series of DC potential negative shifts with an amplitude of approximately -25 mV was observed in the surrounding area, indicating that a representative cortical SD was induced by prolonged and synchronized membrane depolarization in the photo-irradiated area^[3].

The propagation of cortical SD is thought to involve the release and diffusion of some excitatory chemical mediators, most likely K^+ and glutamate, into the interstitial fluid^[40]. Mechanisms that modulate cortical excitability have been demonstrated to contribute to cortical SD propagation, such as the local distribution of astrocytes, which is known to stabilize the extracellular milieu^[38, 41]. Astrocytes have been reported to remove K^+ from the extracellular space by several mechanisms, including inwardly-rectifying K^+ channels, the Na^+/K^+ -ATPase and $Na^+-K^+-Cl^-$ co-transporters, and spatial K^+ buffering *via* gap junctions^[42, 43]. Indeed, astrocytes have been reported to prevent the occurrence of SD through spatial buffering of the extracellular K^+ ^[44]. Moreover, several studies have reported that the spread of SD stops where white matter

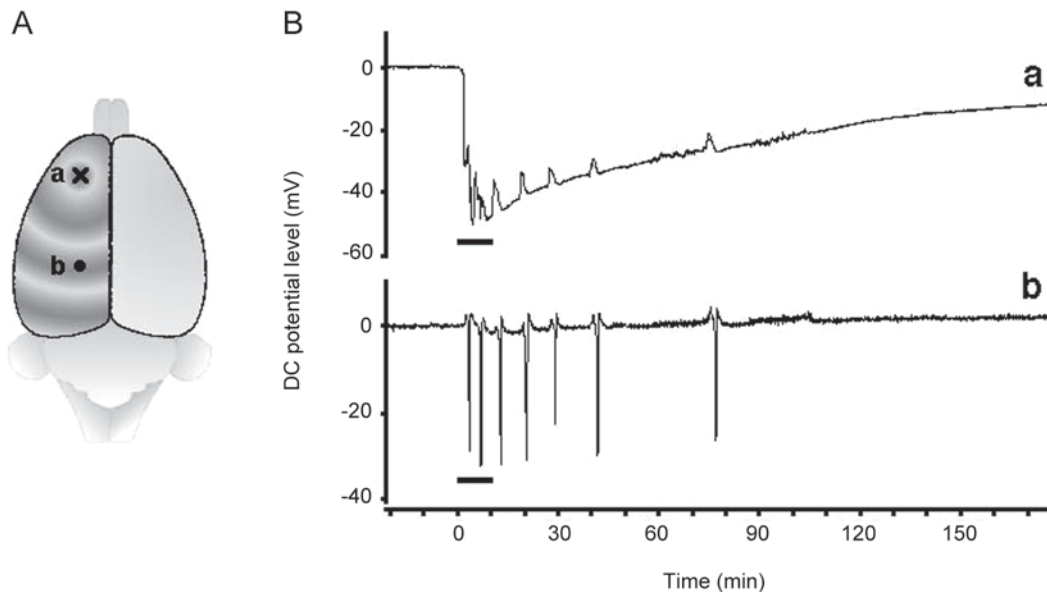


Fig. 1. A: Schematic of the experimental method (brain viewed from above). The rose Bengal was injected into the frontal cortex (point a, represented by a cross), and two microelectrodes were placed in both the dye-injected site (point a) and in the parietal cortex (point b). The dye-injected site (cross) was then photo-irradiated. B: DC potential changes recorded from the dye-injected site (a) and the surrounding area (b). The bars indicate photo-irradiation for 10 min. Note the transient positive deflections in the upper panel, which are thought to be induced by local current passing between the recording site and the neighboring tissue undergoing depolarization (adapted from Cui *et al.* *Biochem Biophys Res Commun* 2003^[3]).

begins and at the edge of glial-fibrous scars left by previous injury or infarction^[45, 46]. Consistent with these observations, we also demonstrated that the velocity of cortical SD gradually decreases from the dorsal to the ventral cortical areas of the insular cortex, in which the volume distribution of astrocyte is known to gradually increase.

Recently, we have also demonstrated that the brain serotonergic system, which is known to modulate the excitability of cortical neurons through activation of several receptor subtypes, in particular, 5-HT_{1A}, 5-HT_{2A}, and 5-HT₃ receptors^[47-49], contributes to the propagation of cortical SD. Pyramidal neurons in the cerebral cortex express 5-HT_{1A} and 5-HT_{2A} receptors, which exert opposing effects on the excitability and firing activity of pyramidal neurons^[47, 49]. Activation of 5-HT_{1A} receptors hyperpolarizes, whereas activation of 5-HT_{2A} receptors depolarizes pyramidal neurons^[47-49]. On the other hand, 5-HT_{2A} receptors are expressed in large and 5-HT₃ receptors in small GABAergic interneurons^[50]. The activation of the excitatory receptors 5-HT_{2A} and 5-HT₃ in GABAergic interneurons directly excites GABAergic interneurons, and indirectly inhibits the firing of pyramidal neurons in the cortex and hippocampus^[51, 52]. Although the activation of 5-HT_{2A} receptors in pyramidal neurons results in the activation of neurons, a preferential inhibitory action of 5-HT has been reported *in vivo*^[48]. Such a preferential inhibitory action of 5-HT on cortical neurons could be explained by the different binding affinities of 5-HT for 5-HT_{1A} and 5-HT₂ receptors. Hoyer *et al.*^[53] reported that 5-HT has a much higher binding affinity for 5-HT_{1A} than 5-HT₂ receptors in the cerebral cortex. We also found that the propagation velocity of cortical SD is increased, possibly by extending the width of the depolarization wave, in neonatal rats treated with 5,7-dihydroxytryptamine^[54], in which the serotonergic innervation in the cerebral cortex is chronically decreased due to pharmacological degeneration of the dorsal raphe serotonergic neurons (Fig. 2). These results indicate that the excitability of the cerebral cortex might be increased by chronic dysfunction of serotonergic innervation in the cerebral cortex, and such a mechanism would explain the facilitation of migraine with a low serotonin disposition. Likewise, increased excitability of the cerebral cortex caused by gene mutation, such as missense mutation of *CACNA1A* (encoding the α_1

subunit of neuronal Cav2.1(P/Q-type) calcium channels), a representative gene mutation in familial hemiplegic migraine (FHM) families, induces migraine susceptibility by lowering the threshold of cortical SD generation^[55].

Cortical SD Induces Neurogenic Inflammation in Rat Cerebral Cortex

Cortical SD is thought to be a trigger of neurogenic inflammation around meningeal blood vessels, and then evokes headache pain *via* the activation of trigeminal afferents^[11, 12, 56]. Bolay *et al.*^[13] demonstrated that cortical SD causes vasodilation of the middle meningeal artery and subsequent plasma protein leakage mediated by the release of pro-inflammatory peptides from trigeminal axon collaterals innervating the meninges. Further evidence^[15] supports the idea that a long-lasting (up to 48 h) disruption of the blood-brain barrier can be induced by cortical SD, due to activation of the matrix metalloproteinase-9 (MMP-9) cascade. The MMP-9 levels increase from 3 to 6 h after the induction of cortical SD in the ipsilateral cerebral hemisphere, reaching a maximum at 24 h and persisting for at least 48 h^[15]. Plasma protein leakage and brain edema are also contemporaneous 3 h after cortical SD induction. These observations suggest that the plasma protein extravasation and pro-inflammatory peptides release from primary meningeal afferents might be a pivotal step in the cortical SD-induced neurogenic inflammatory process and subsequent headache. However, conflicts exist, as several drugs that selectively inhibit plasma protein extravasation in rodents have failed to reduce the pain severity in patients with migraine as evidenced by the failure in clinical trials of substance P and neurokinin-1 antagonists^[57] and specific plasma protein extravasation blockers such as 4991w93^[58] and cp122,288^[59]. Such contradictory evidence indicates that an appropriate method is necessary to investigate whether and how the neuroinflammation is involved in migraine etiology and to verify the extrapolated data from animal studies for the human condition.

Recent advances in non-invasive molecular imaging techniques, such as positron emission tomography (PET), provide powerful tools for quantitative investigation of the tissue distribution and dynamic changes of functional molecules *in vivo*, because of their high sensitivity and

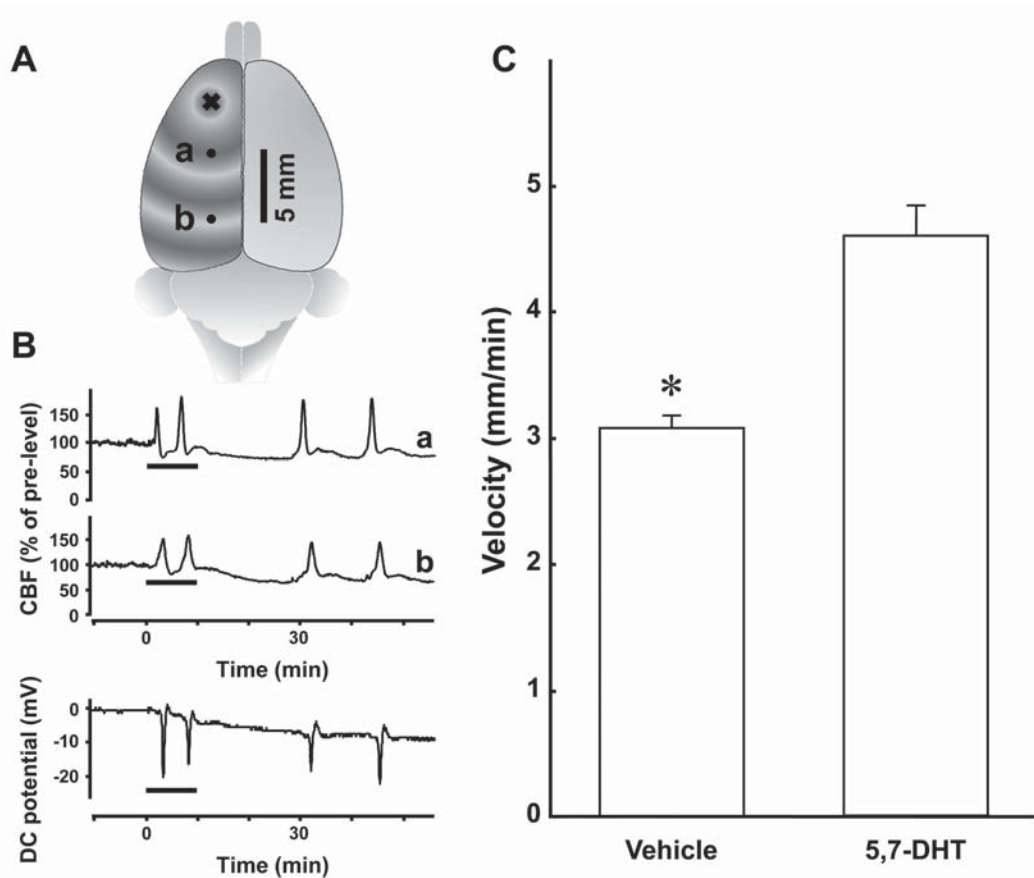


Fig. 2. Increased velocity of cortical SD in 5,7-dihydroxytryptamine (5,7-DHT)-treated rats. **A:** Schematic of the experimental method (brain viewed from above): two laser Doppler flow probes were placed on the same side as the dye-injection (cross) at different distances (point a, 4 mm; point b, 9 mm). A microelectrode was placed near the caudal probe (point b) for recording DC potential changes. **B:** PDTO-induced changes in cerebral blood flow (CBF, upper) and in the DC potential (lower). Bars indicate photo-irradiation for 10 min. **C:** Spreading velocity in 5,7-DHT-treated (65 hyperperfusions in eight animals) and vehicle-treated rats (51 hyperperfusions in six animals). * $P < 0.05$, unpaired t -test (adapted from Cui *et al.* *J Neurosci Res* 2013^[64]).

spatiotemporal resolution. PET imaging with specific probes designed for binding to inflammatory processes, such as [¹¹C]PK11195, [¹¹C]DAA1106, [¹¹C]DPA-713, and [¹¹C]CLINME have been widely used for studying brain inflammation^[60-63]. The principal immune cells in the central nervous system, microglia, are activated in response to inflammatory processes in the brain^[64]. The process of microglial activation is thought to be related to an increase in the number of microglia and the expression of numerous proteins such as the peripheral benzodiazepine receptor (PBR)^[65]. The PBR is a mitochondrial outer membrane protein, and is expressed at a low level on resting microglia and astrocytes in the normal brain. Its

expression is upregulated in activated microglia^[66-68], and the upregulation is well correlated with the state of activation^[69-71]. ¹¹C-labeled PK11195 is a specific PET ligand for PBR to image activated microglia in the brain, and has been extensively used for quantitative evaluation of brain inflammation by PET in a number of neurological disorders, such as stroke^[72], multiple sclerosis^[69], Alzheimer disease^[73], Parkinson disease^[74] and Huntington disease^[75].

Using [¹¹C]PK11195-PET imaging in rats, we demonstrated that unilateral cortical SD induces neurogenic inflammation in the ipsilateral cerebral hemisphere^[14]. The highest [¹¹C]PK11195 radioactivity was seen in the initial area of the cortical SD (KCl-microinjected

site), and moderate radioactivity was observed in the ipsilateral surrounding areas, but not in the corresponding contralateral areas. In sham control rats, however, a slight increase in [^{11}C]PK11195 radioactivity was seen primarily in the NaCl-microinjected site. [^{11}C]PK11195 radioactivity is barely observed within the brain under normal conditions in control rats, except for the lateral, third, and fourth ventricles (Fig. 3). Our immunohistochemical study also confirmed that the number of OX-42-immunopositive microglia is increased in the ipsilateral hemisphere compared with the corresponding area in the contralateral hemisphere in rats with unilateral cortical SD (Fig. 4). Hypertrophied (enlarged, darkened soma with shorter, thicker processes) or amoeboid (densely stained, enlarged soma with a few

short processes) OX-42-immunopositive microglia are often seen in the ipsilateral hemisphere. However, such a difference between the two hemispheres is not observed in sham-operated rats. These results indicate that cortical SD is able to induce microglial activation, a well-known sign of neuroinflammation in the brain.

Cortical SD Activates the Trigeminal Nociceptive Pathway in the Rat Brain

Migraine headaches are thought to be triggered by brain inflammation that activates trigeminal nociceptors in meningeal blood vessels^[76]. However, it is still controversial whether the neurogenic inflammation induced by cortical

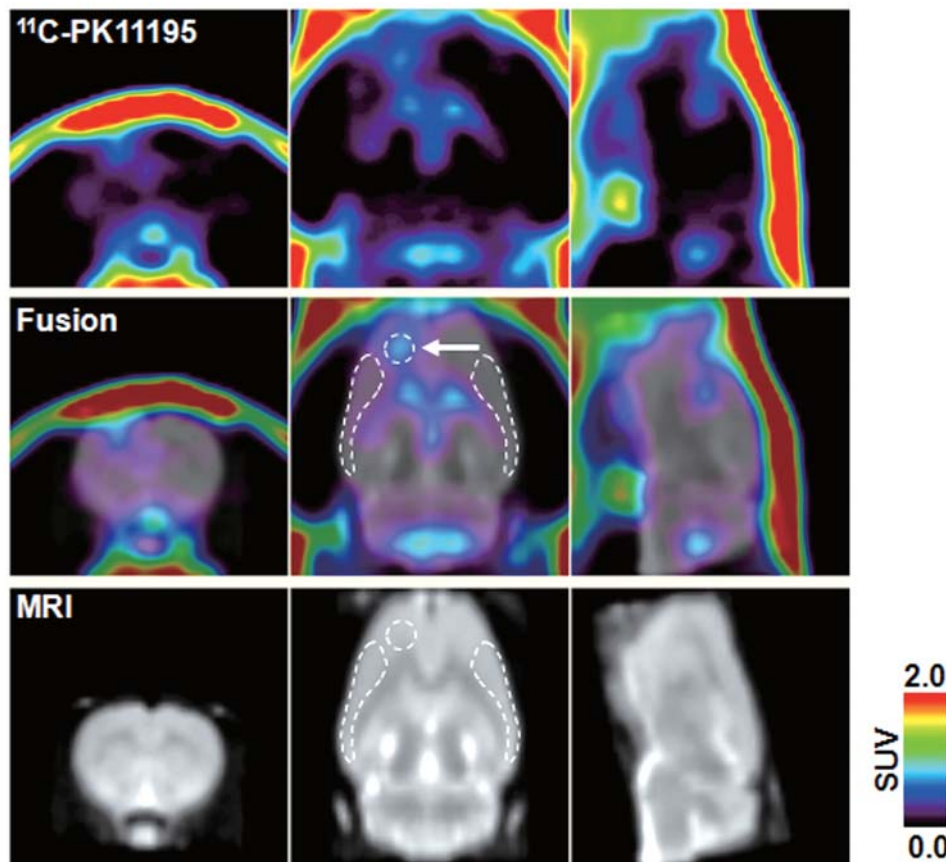


Fig. 3. A representative [^{11}C]PK11195 PET image co-registered with the MRI template eight days after generation of unilateral (left hemisphere) cortical SD. The PET image was reconstructed with the MAP algorithm and summed from 5 to 60 min after radioligand injection. The arrow in the middle panel indicates the KCl-microinjected area. The white broken lines indicate the regions of interest (core, ipsilateral and contralateral). The mean values of binding potential for [^{11}C]PK11195 in the core and ipsilateral side were 0.48 ± 0.18 and 0.26 ± 0.07 , respectively. Binding potential was estimated by Logan-noninvasive graphical analysis using contralateral as the reference region (adapted from Cui *et al.* J Nucl Med 2009^[14]).

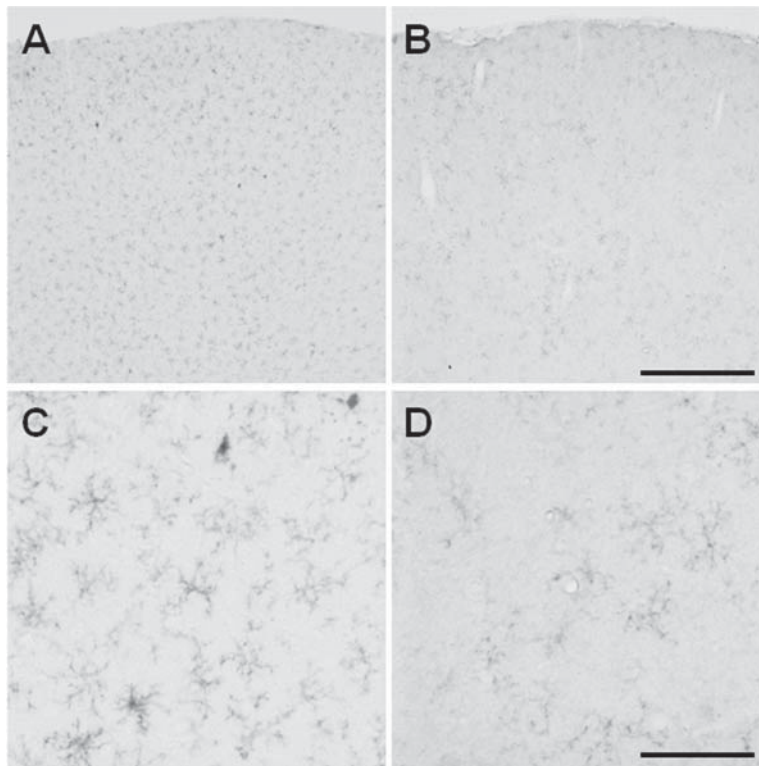


Fig. 4. Photomicrographs of OX-42 immunoreactivity following cortical SD. The images show the OX-42 immunoreactivity 8 days after 2 h of recurrent SD in the left hemisphere (A and C) compared with the contralateral hemisphere (B and D). C and D, magnified views of the OX-42 immunoreactivity. Hypertrophied or amoeboid OX-42-positive microglia were often seen in the left hemisphere. Scale bars, 500 μm in A and B, and 100 μm in C and D (adapted from Cui *et al.* J Nucl Med 2009^[14]).

SD is able to activate the trigeminal nociceptive pathway. Recently, Moskowitz and colleagues demonstrated that c-Fos expression in the trigeminal nucleus caudalis (TNC), the first central site of the trigeminal nociceptive pathway, is significantly increased by cortical SD, and this increase is abolished by trigeminal rhizotomy^[56]. Moreover, cortical SD-evoked single neuron activity in the trigeminal ganglion (peripheral pathway) and the TNC has also been demonstrated directly by electrophysiological studies^[17]. Such activation was observed as a two-fold increase in ~50% of neurons in the trigeminal ganglion and TNC, and persisted for 45 min or longer. However, conflicting reports have shown that the cortical SD does not induce sustained neuronal activity recorded mainly in the deeper laminae of the more rostral trigeminal nucleus up to several hours after either a single or even a series of cortical SD inductions in the rat^[77, 78].

We recently developed a small-animal neuroimaging method combining 2-^[18F]fluoro-2-deoxy-D-glucose (FDG)

PET imaging with statistical parametric mapping analysis to evaluate the regional activity in the entire rat brain. Using the FDG-PET imaging method, we found that cortical SD activates the trigeminal nociceptive pathway, including both second-order and high-order nuclei, such as the thalamus and somatosensory cortex, ~40 h after the induction of unilateral cortical SD (unpublished data). Consistently, several electrophysiological studies have reported that neurons in the high-order nuclei of the trigeminal nociceptive pathway are activated in response to inflammatory stimuli applied to the meninges^[79, 80]. A juxtacellular recording study has further revealed that the neurons located in the trigeminal thalamic areas (ventral posteromedial thalamic nucleus/ posterior thalamic nucleus) are activated by inflammatory stimulation of the meninges, and functionally project to diverse cortical areas, such as the trigeminal primary somatosensory (trigeminal barrel-field region of the primary somatosensory cortex,

S1BF), trunk region of the primary somatosensory cortex, secondary somatosensory cortex, insula, primary visual cortex and primary auditory cortex^[81]. Taken together, these observations suggest that cortical SD is able to activate the trigeminal nociceptive pathway and might contribute to migraine headache.

Summary

A migraine headache is a complex neurobiological disorder that has been hypothesized to be caused by intracranial neurogenic inflammation which activates trigeminal nociceptors in meningeal blood vessels. Since its discovery by Leao, cortical SD has been implicated in the pathophysiology of migraine due to the similar spreading velocity of cortical SD and the scintillating scotoma, a typical visual aura in migraine. Animal studies have demonstrated that cortical SD causes plasma protein extravasation around the meningeal blood vessels due to vasodilation of the middle meningeal artery or long-lasting disruption of the blood-brain barrier. Furthermore, direct and indirect evidence has shown that cortical SD activates both the peripheral (trigeminal ganglion) and the central pathways including the second-order and high-order nuclei of the trigeminal nociceptive pathways. These observations suggest that cortical SD is the initial trigger of prolonged neurogenic inflammation around the meningeal blood vessels, which probably evokes the headache sensation. Although the precise roles of cortical SD in migraine remain unclear, evidence from experimental models in rodents provides a valid platform for understanding the molecular mechanism of migraine and for promoting the development of new migraine therapies.

ACKNOWLEDGMENTS

This review was supported in part by a consignment expense from the Molecular Imaging Program on "Research Base for Exploring New Drugs" and by KAKENHI (24659574) from the Ministry of Education, Culture, Sports, Science, and Technology (MEXT) of the Government of Japan.

Received date: 2014-04-30; Accepted date: 2014-06-21

REFERENCES

[1] Leao AAP. Spreading depression of activity in the cerebral

cortex. *J Neurophysiol* 1944, 7: 359–390.

- [2] Nedergaard M, Hansen AJ. Spreading depression is not associated with neuronal injury in the normal brain. *Brain Res* 1988, 449: 395–398.
- [3] Cui Y, Kataoka Y, Li QH, Yokoyama C, Yamagata A, Mochizuki-Oda N, *et al.* Targeted tissue oxidation in the cerebral cortex induces local prolonged depolarization and cortical spreading depression in the rat brain. *Biochem Biophys Res Commun* 2003, 300: 631–636.
- [4] Fabricius M, Akgoren N, Lauritzen M. Arginine nitric-oxide pathway and cerebrovascular regulation in cortical spreading depression. *Am J Physiol* 1995, 269: H23–H29.
- [5] Hansen AJ, Zeuthen T. Extracellular ion concentrations during spreading depression and ischemia in the rat-brain cortex. *Acta Physiol Scand* 1981, 113: 437–445.
- [6] Lauritzen M, Jorgensen MB, Diemer NH, Gjedde A, Hansen AJ. Persistent oligemia of rat cerebral-cortex in the wake of spreading depression. *Ann Neurol* 1982, 12: 469–474.
- [7] Milner PM. Note on a possible correspondence between the scotomas of migraine and spreading depression of Leao. *Electroencephalogr Clin Neurophysiol* 1958, 10: 705–705.
- [8] Lauritzen M. Pathophysiology of the migraine aura. The spreading depression theory. *Brain* 1994, 117: 199–210.
- [9] Rasmussen BK, Olesen J. Migraine with aura and migraine without aura: an epidemiological study. *Cephalalgia* 1992, 12: 221–228; discussion 186.
- [10] Lashley KS. Patterns of cerebral integration indicated by the scotomas of migraine. *Arch Neuropsych* 1941, 46: 331–339.
- [11] Markowitz S, Saito K, Moskowitz MA. Neurogenically mediated leakage of plasma protein occurs from blood vessels in dura mater but not brain. *J Neurosci* 1987, 7: 4129–4136.
- [12] Moskowitz MA. The neurobiology of vascular head pain. *Ann Neurol* 1984, 16: 157–168.
- [13] Bolay H, Reuter U, Dunn AK, Huang Z, Boas DA, Moskowitz MA. Intrinsic brain activity triggers trigeminal meningeal afferents in a migraine model. *Nat Med* 2002, 8: 136–142.
- [14] Cui Y, Takashima T, Takashima-Hirano M, Wada Y, Shukuri M, Tamura Y, *et al.* ¹¹C-PK11195 PET for the *in vivo* evaluation of neuroinflammation in the rat brain after cortical spreading depression. *J Nucl Med* 2009, 50: 1904–1911.
- [15] Gursoy-Ozdemir Y, Qiu J, Matsuoka N, Bolay H, Berman D, Jin H, *et al.* Cortical spreading depression activates and upregulates MMP-9. *J Clin Invest* 2004, 113: 1447–1455.
- [16] Zhang X, Levy D, Noseda R, Kainz V, Jakubowski M, Burstein R. Activation of meningeal nociceptors by cortical spreading depression: implications for migraine with aura. *J Neurosci* 2010, 30: 8807–8814.
- [17] Zhang X, Levy D, Kainz V, Noseda R, Jakubowski M, Burstein R. Activation of central trigeminovascular neurons

- by cortical spreading depression. *Ann Neurol* 2011, 69: 855–865.
- [18] The International Classification of Headache Disorders: 2nd edition. *Cephalalgia* 2004, 24 Suppl 1: 9–160.
- [19] Blau JN. Migraine: theories of pathogenesis. *Lancet* 1992, 339: 1202–1207.
- [20] Lipton RB, Scher AI, Kolodner K, Liberman J, Steiner TJ, Stewart WF. Migraine in the United States: epidemiology and patterns of health care use. *Neurology* 2002, 58: 885–894.
- [21] Silberstein SD. Migraine. *Lancet* 2004, 363: 381–391.
- [22] Graham JR, Wolff HG. Mechanism of migraine headache and action of ergotamine tartrate. *Arch Neuropsych* 1938, 39: 737–763.
- [23] Olesen J, Larsen B, Lauritzen M. Focal hyperemia followed by spreading oligemia and impaired activation of Rcbf in classic migraine. *Ann Neurol* 1981, 9: 344–352.
- [24] Woods RP, Iacoboni M, Mazziotta JC. Brief report: bilateral spreading cerebral hypoperfusion during spontaneous migraine headache. *N Engl J Med* 1994, 331: 1689–1692.
- [25] Lauritzen M. Cerebral blood flow in migraine and cortical spreading depression. *Acta Neurol Scand Suppl* 1987, 113: 1–40.
- [26] Andersen AR, Friberg L, Olsen TS, Olesen J. Delayed hyperemia following hypoperfusion in classic migraine. Single photon emission computed tomographic demonstration. *Arch Neurol* 1988, 45: 154–159.
- [27] Olesen J, Friberg L, Olsen TS, Iversen HK, Lassen NA, Andersen AR, *et al.* Timing and topography of cerebral blood flow, aura, and headache during migraine attacks. *Ann Neurol* 1990, 28: 791–798.
- [28] Goadsby PJ, Edvinsson L, Ekman R. Release of vasoactive peptides in the extracerebral circulation of humans and the cat during activation of the trigeminovascular system. *Ann Neurol* 1988, 23: 193–196.
- [29] Goadsby PJ, Edvinsson L, Ekman R. Vasoactive peptide release in the extracerebral circulation of humans during migraine headache. *Ann Neurol* 1990, 28: 183–187.
- [30] Arnold G, Reuter U, Kinze S, Wolf T, Einhaupl KM. Migraine with aura shows gadolinium enhancement which is reversed following prophylactic treatment. *Cephalalgia* 1998, 18: 644–646.
- [31] Lindner A, Reiners K, Toyka KV. Meningeal hyperperfusion visualized by MRI in a patient with visual hallucinations and migraine. *Headache* 1996, 36: 53–57.
- [32] Smith M, Cros D, Sheen V. Hyperperfusion with vasogenic leakage by fMRI in migraine with prolonged aura. *Neurology* 2002, 58: 1308–1310.
- [33] Gorji A. Spreading depression: a review of the clinical relevance. *Brain Res Brain Res Rev* 2001, 38: 33–60.
- [34] Cui Y, Kataoka Y, Inui T, Mochizuki T, Onoe H, Matsumura K, *et al.* Up-regulated neuronal COX-2 expression after cortical spreading depression is involved in non-REM sleep induction in rats. *J Neurosci Res* 2008, 86: 929–936.
- [35] Bures J, Buresova O, Krivanek J. The meaning and significance of Leao's spreading depression. *An Acad Bras Cienc* 1984, 56: 385–400.
- [36] Somjen GG. Mechanisms of spreading depression and hypoxic spreading depression-like depolarization. *Physiol Rev* 2001, 81: 1065–1096.
- [37] Guedes RC, do Carmo RJ. Influence of ionic disturbances produced by gastric washing on cortical spreading depression. *Exp Brain Res* 1980, 39: 341–349.
- [38] Marshall WH. Spreading cortical depression of Leao. *Physiol Rev* 1959, 39: 239–279.
- [39] Kataoka Y, Morii H, Imamura K, Cui Y, Kobayashi M, Watanabe Y. Control of neurotransmission, behaviour and development, by photo-dynamic manipulation of tissue redox state of brain targets. *Eur J Neurosci* 2000, 12: 4417–4423.
- [40] Van Harreveld A. Two mechanisms for spreading depression in the chicken retina. *J Neurobiol* 1978, 9: 419–431.
- [41] Leibowitz DH. The glial spike theory. I. On an active role of neuroglia in spreading depression and migraine. *Proc Biol Sci* 1992, 250: 287–295.
- [42] Kofuji P, Newman EA. Potassium buffering in the central nervous system. *Neuroscience* 2004, 129: 1045–1056.
- [43] Olsen ML, Sontheimer H. Functional implications for Kir4.1 channels in glial biology: from K⁺ buffering to cell differentiation. *J Neurochem* 2008, 107: 589–601.
- [44] Gardner-Medwin AR. Possible roles of vertebrate neuroglia in potassium dynamics, spreading depression and migraine. *J Exp Biol* 1981, 95: 111–127.
- [45] Hull CD, Vanharreveld A. Absence of conduction of spreading depression through cortical region damaged by Asphyxiation. *Am J Physiol* 1964, 207: 921–924.
- [46] Van Harreveld A, Terres G, Dernburg EA. Cortical discontinuity and propagation of spreading depression. *Am J Physiol* 1956, 184: 233–238.
- [47] Araneda R, Andrade R. 5-Hydroxytryptamine₂ and 5-hydroxytryptamine_{1A} receptors mediate opposing responses on membrane excitability in rat association cortex. *Neuroscience* 1991, 40: 399–412.
- [48] Puig MV, Artigas F, Celada P. Modulation of the activity of pyramidal neurons in rat prefrontal cortex by raphe stimulation *in vivo*: involvement of serotonin and GABA. *Cereb Cortex* 2005, 15: 1–14.
- [49] Puig MV, Celada P, Diaz-Mataix L, Artigas F. In vivo modulation of the activity of pyramidal neurons in the rat medial prefrontal cortex by 5-HT_{2A} receptors: relationship to thalamocortical afferents. *Cereb Cortex* 2003, 13: 870–882.
- [50] Jakab RL, Goldman-Rakic PS. Segregation of serotonin

- 5-HT_{2A} and 5-HT₃ receptors in inhibitory circuits of the primate cerebral cortex. *J Comp Neurol* 2000, 417: 337–348.
- [51] Kawa K. Distribution and functional properties of 5-HT₃ receptors in the rat hippocampal dentate gyrus: a patch-clamp study. *J Neurophysiol* 1994, 71: 1935–1947.
- [52] Roerig B, Katz LC. Modulation of intrinsic circuits by serotonin 5-HT₃ receptors in developing ferret visual cortex. *J Neurosci* 1997, 17: 8324–8338.
- [53] Hoyer D, Engel G, Kalkman HO. Molecular pharmacology of 5-HT₁ and 5-HT₂ recognition sites in rat and pig brain membranes: radioligand binding studies with [³H]5-HT, [³H]8-OH-DPAT, (-)[¹²⁵I]iodocyanopindolol, [³H]mesulergine and [³H]ketanserin. *Eur J Pharmacol* 1985, 118(1-2): 13–23.
- [54] Cui Y, Li QH, Yamada H, Watanabe Y, Kataoka Y. Chronic degeneration of dorsal raphe serotonergic neurons modulates cortical spreading depression: a possible pathophysiology of migraine. *J Neurosci Res* 2013, 91: 737–744.
- [55] van den Maagdenberg AM, Pietrobon D, Pizzorusso T, Kaja S, Broos LA, Cesetti T, *et al.* A *Cacna1a* knockin migraine mouse model with increased susceptibility to cortical spreading depression. *Neuron* 2004, 41: 701–710.
- [56] Moskowitz MA, Nozaki K, Kraig RP. Neocortical spreading depression provokes the expression of c-fos protein-like immunoreactivity within trigeminal nucleus caudalis via trigeminovascular mechanisms. *J Neurosci* 1993, 13: 1167–1177.
- [57] Goldstein DJ, Wang O, Saper JR, Stoltz R, Silberstein SD, Mathew NT. Ineffectiveness of neurokinin-1 antagonist in acute migraine: a crossover study. *Cephalalgia* 1997, 17: 785–790.
- [58] Earl NL, McDonald SA, Lowy MT. Efficacy and tolerability of the neurogenic inflammation inhibitor, 4991W93, in the acute treatment of migraine. *Cephalalgia* 1999, 19: 357–357.
- [59] Roon KI, Olesen J, Diener HC, Ellis P, Hettiarachchi J, Poole PH, *et al.* No acute antimigraine efficacy of CP-122,288, a highly potent inhibitor of neurogenic inflammation: Results of two randomized, double-blind, placebo controlled clinical trials. *Ann Neurol* 2000, 47: 238–241.
- [60] Venetti S, Lopresti BJ, Wang G, Slagel SL, Mason NS, Mathis CA, *et al.* A comparison of the high-affinity peripheral benzodiazepine receptor ligands DAA1106 and (R)-PK11195 in rat models of neuroinflammation: implications for PET imaging of microglial activation. *J Neurochem* 2007, 102: 2118–2131.
- [61] Boutin H, Chauveau F, Thominaux C, Kuhnast B, Gregoire MC, Jan S, *et al.* *In vivo* imaging of brain lesions with [(11)C]CLINME, a new PET radioligand of peripheral benzodiazepine receptors. *Glia* 2007, 55: 1459–1468.
- [62] Boutin H, Chauveau F, Thominaux C, Gregoire MC, James ML, Trebossen R, *et al.* 11C-DPA-713: a novel peripheral benzodiazepine receptor PET ligand for *in vivo* imaging of neuroinflammation. *J Nucl Med* 2007, 48: 573–581.
- [63] Banati RB. Visualising microglial activation *in vivo*. *Glia* 2002, 40: 206–217.
- [64] Kreutzberg GW. Microglia: a sensor for pathological events in the CNS. *Trends Neurosci* 1996, 19: 312–318.
- [65] Moran LB, Duke DC, Turkheimer FE, Banati RB, Graeber MB. Towards a transcriptome definition of microglial cells. *Neurogenetics* 2004, 5: 95–108.
- [66] Benavides J, Guilloux F, Rufat P, Uzan A, Renault C, Dubroeuq MC, *et al.* *In vivo* labelling in several rat tissues of 'peripheral type' benzodiazepine binding sites. *Eur J Pharmacol* 1984, 99: 1–7.
- [67] Cagnin A, Gerhard A, Banati RB. *In vivo* imaging of neuroinflammation. *Eur Neuropsychopharmacol* 2002, 12: 581–586.
- [68] Casellas P, Gallegue S, Basile AS. Peripheral benzodiazepine receptors and mitochondrial function. *Neurochem Int* 2002, 40: 475–486.
- [69] Banati RB, Newcombe J, Gunn RN, Cagnin A, Turkheimer F, Heppner F, *et al.* The peripheral benzodiazepine binding site in the brain in multiple sclerosis: quantitative *in vivo* imaging of microglia as a measure of disease activity. *Brain* 2000, 123 (Pt 11): 2321–2337.
- [70] Stephenson DT, Schober DA, Smalstig EB, Mincy RE, Gehlert DR, Clemens JA. Peripheral benzodiazepine receptors are colocalized with activated microglia following transient global forebrain ischemia in the rat. *J Neurosci* 1995, 15: 5263–5274.
- [71] Vowinckel E, Reutens D, Becher B, Verge G, Evans A, Owens T, *et al.* PK11195 binding to the peripheral benzodiazepine receptor as a marker of microglia activation in multiple sclerosis and experimental autoimmune encephalomyelitis. *J Neurosci Res* 1997, 50: 345–353.
- [72] Price CJ, Wang D, Menon DK, Guadagno JV, Cleij M, Fryer T, *et al.* Intrinsic activated microglia map to the peri-infarct zone in the subacute phase of ischemic stroke. *Stroke* 2006, 37: 1749–1753.
- [73] Cagnin A, Brooks DJ, Kennedy AM, Gunn RN, Myers R, Turkheimer FE, *et al.* *In-vivo* measurement of activated microglia in dementia. *Lancet* 2001, 358: 461–467.
- [74] Gerhard A, Pavese N, Hotton G, Turkheimer F, Es M, Hammers A, *et al.* *In vivo* imaging of microglial activation with [(11)C](R)-PK11195 PET in idiopathic Parkinson's disease. *Neurobiol Dis* 2006, 21: 404–412.
- [75] Pavese N, Gerhard A, Tai YF, Ho AK, Turkheimer F, Barker RA, *et al.* Microglial activation correlates with severity in Huntington disease: a clinical and PET study. *Neurology* 2006, 66: 1638–1643.
- [76] Ray BS, Wolff HG. Experimental studies on headache - Pain-

- sensitive structures of the head and their significance in headache. *Arch Surg* 1940, 41: 813–856.
- [77] Ebersberger A, Schaible HG, Averbeck B, Richter F. Is there a correlation between spreading depression, neurogenic inflammation, and nociception that might cause migraine headache? *Ann Neurol* 2001, 49: 7–13.
- [78] Lambert GA, Michalicek J, Storer RJ, Zagami AS. Effect of cortical spreading depression on activity of trigeminovascular sensory neurons. *Cephalalgia* 1999, 19: 631–638.
- [79] Davis KD, Dostrovsky JO. Properties of feline thalamic neurons activated by stimulation of the middle meningeal artery and sagittal sinus. *Brain Res* 1988, 454: 89–100.
- [80] Nosedá R, Kainz V, Jakubowski M, Gooley JJ, Saper CB, Digre K, *et al.* A neural mechanism for exacerbation of headache by light. *Nat Neurosci* 2010, 13: 239–245.
- [81] Nosedá R, Jakubowski M, Kainz V, Borsook D, Burstein R. Cortical projections of functionally identified thalamic trigeminovascular neurons: implications for migraine headache and its associated symptoms. *J Neurosci* 2011, 31: 14204–14217.

Brain network markers of abnormal cerebral glucose metabolism and blood flow in Parkinson's disease

Shichun Peng, David Eidelberg, Yilong Ma

Center for Neurosciences, The Feinstein Institute for Medical Research, North Shore-Long Island Jewish Health System, Manhasset, New York, USA

Corresponding author: Yilong Ma. E-mail: yima@nshs.edu

© Shanghai Institutes for Biological Sciences, CAS and Springer-Verlag Berlin Heidelberg 2014

Neuroimaging of cerebral glucose metabolism and blood flow is ideally suited to assay widely-distributed brain circuits as a result of local molecular events and behavioral modulation in the central nervous system. With the progress in novel analytical methodology, this endeavor has succeeded in unraveling the mechanisms underlying a wide spectrum of neurodegenerative diseases. In particular, statistical brain mapping studies have made significant strides in describing the pathophysiology of Parkinson's disease (PD) and related disorders by providing signature biomarkers to determine the systemic abnormalities in brain function and evaluate disease progression, therapeutic responses, and clinical correlates in patients. In this article, we review the relevant clinical applications in patients in relation to healthy volunteers with a focus on the generation of unique spatial covariance patterns associated with the motor and cognitive symptoms underlying PD. These characteristic biomarkers can be potentially used not only to improve patient recruitment but also to predict outcomes in clinical trials.

Keywords: Parkinson's disease; metabolism; blood flow; PET; SPECT; movement disorder; network analysis; imaging biomarkers

Introduction

Functional brain imaging with positron emission tomography (PET) and single-photon emission computed tomography (SPECT) has provided novel insights into the pathophysiology of Parkinson's disease (PD) and related movement disorders. The integrity of the presynaptic nigrostriatal dopaminergic systems can be evaluated by measuring the dopamine storage capacity using [^{18}F] fluorodopa (FDOPA), or dopamine transporter (DAT) binding using radiotracers such as [^{123}I]βCIT and [^{18}F]FPCIT (see reviews^[1,2]). Postsynaptic dopamine receptor systems can be assayed with radioligands that bind specifically to D₁ or D₂ receptors. In addition, PET has been used to study regional neuronal activity by quantifying resting-state regional cerebral glucose metabolism (rCMRglc) with [^{18}F]fluorodeoxyglucose (FDG)^[3] and regional cerebral

blood flow (rCBF) activation responses with [^{15}O]H₂O^[4]. Abnormal rCBF distributions in the resting state can also be measured using PET and SPECT perfusion tracers. In particular, imaging of cerebral metabolism and blood flow has contributed greatly to the understanding of the abnormal brain circuitry underlying the pathophysiology of PD.

PET/SPECT can be particularly useful in assessing the consequences of nigrostriatal dopamine deficiency on the functional networks of the basal ganglia. Although the primary pathological abnormality in PD is located in the substantia nigra, the degeneration of dopaminergic projection neurons to the striatum leads to widespread changes in the functional activity of the basal ganglia^[5]. Specifically, the loss of inhibitory dopaminergic input to the striatum increases the inhibitory output from the putamen to the external globus pallidus (GPe), decreases the inhibitory

output from the GPe to the subthalamic nucleus (STN), and causes functional over-activity of the STN and internal globus pallidus (GPi), resulting in reduced output from the ventrolateral thalamus to the cortex. This classic model has been modified to emphasize the cognitive dysfunction associated with PD^[6] and is linked to concurrent changes in regional glucose metabolism and blood flow.

We review the advances in functional brain imaging studies of PD in the resting state based on analyses of rCMRglc and rCBF in patients and healthy volunteers. As in most neurodegenerative conditions, these two variables are considered to be coupled in PD and related to synaptic activity at the regional level. We also summarize the use of novel analytical techniques in the clinical diagnosis and evaluation of PD. These include both univariate and multivariate statistical approaches such as statistical parametric mapping (SPM) and principal component analysis (PCA) for volume of interest (VOI) or voxel-wise analysis over the whole brain. In addition, we focus on the application of these imaging methods to the selection of suitable candidates for surgical trials and the assessment of their treatment outcome.

Functional Brain Imaging: Univariate Analyses

PET/SPECT imaging of rCMRglc and rCBF has been used extensively to identify changes in regional brain function in patients with PD comparable to those revealed in experimental animal models^[7, 8]. The bulk of this effort is based on the use of SPM to localize regionally specific differences and functional-clinical correlates in PD patients scanned when they are off dopaminergic medications. Functional brain images are spatially transformed into a standard anatomical space to allow mapping analysis on a voxel basis. To reduce inter-individual variability in anatomical and functional substrates, images are usually ratio-normalized to a global mean or other reference value that is assumed to be preserved in the diseased brain. Consequently, only relative measures of functional brain activity are used in most studies.

Cerebral Metabolism Studies

Because the local rate of glucose metabolism is a direct marker of synaptic activity, PET with FDG has been the most common approach to studying abnormal brain function in PD. By using FDG PET images from multiple cohorts

of patients and healthy controls we and other researchers have reported a reproducible pattern of abnormal regional metabolism in PD (Fig. 1) characterized bilaterally by increases in the putamen, thalamus, cerebellum, pons, and sensorimotor cortex (SMC), and decreases in the lateral frontal and parieto-occipital areas^[9-11]. This is in accordance with a dual-tracer PET study with both FDG and [¹⁵O]O₂ showing bilaterally increased energy metabolism in the putamen and pallidum in early unmedicated PD patients^[12]. Regional metabolism in the cerebellum is also elevated in early-stage and advanced PD patients^[13, 14], suggesting that cerebellar hypermetabolic activity in PD is closely linked to akinesia and rigidity but not to tremor. It has been further reported that clinical scores of motor symptoms are correlated positively with rCMRglc in the bilateral putamen and pallidum^[15], and in the midbrain, cerebellum, and motor cortex^[16]. These reports indicate a pathophysiologic association between subcortical hypermetabolism and motor dysfunction in PD.

Unique features of cortical hypometabolism in PD have also been frequently reported. An early study reported pronounced occipital hypometabolism in the more severely affected hemisphere in PD^[17]. The asymmetry in this metabolic reduction correlated inversely with finger-tapping performance in a subset of patients with more unilateral motor impairment. While hypometabolism is limited in the frontal and occipital cortices of PD patients with no cognitive impairment^[18], it becomes more widespread within cortical regions in advanced PD^[14]. Further, the relationships of abnormal rCMRglc with clinical symptoms and impaired striatal DAT binding have been examined in *de novo* untreated PD patients^[19]. Correlation analyses showed that the UPDRS motor ratings were negatively correlated with rCMRglc in the premotor cortex (PMC), while putaminal DAT binding was positively correlated with rCMRglc in the premotor, dorsolateral prefrontal, anterior prefrontal, and orbitofrontal cortices. This method also led to a set of disease-related brain templates for PD and atypical PD to aid single-case differential diagnosis^[10, 11]. These results may represent the cortical functional correlates of nigrostriatal dysfunction in the motor basal ganglia-cortical circuitry in parkinsonism.

FDG PET has also been used to delineate the metabolic functional correlates of PD with cognitive impairment. Regional metabolism is markedly reduced

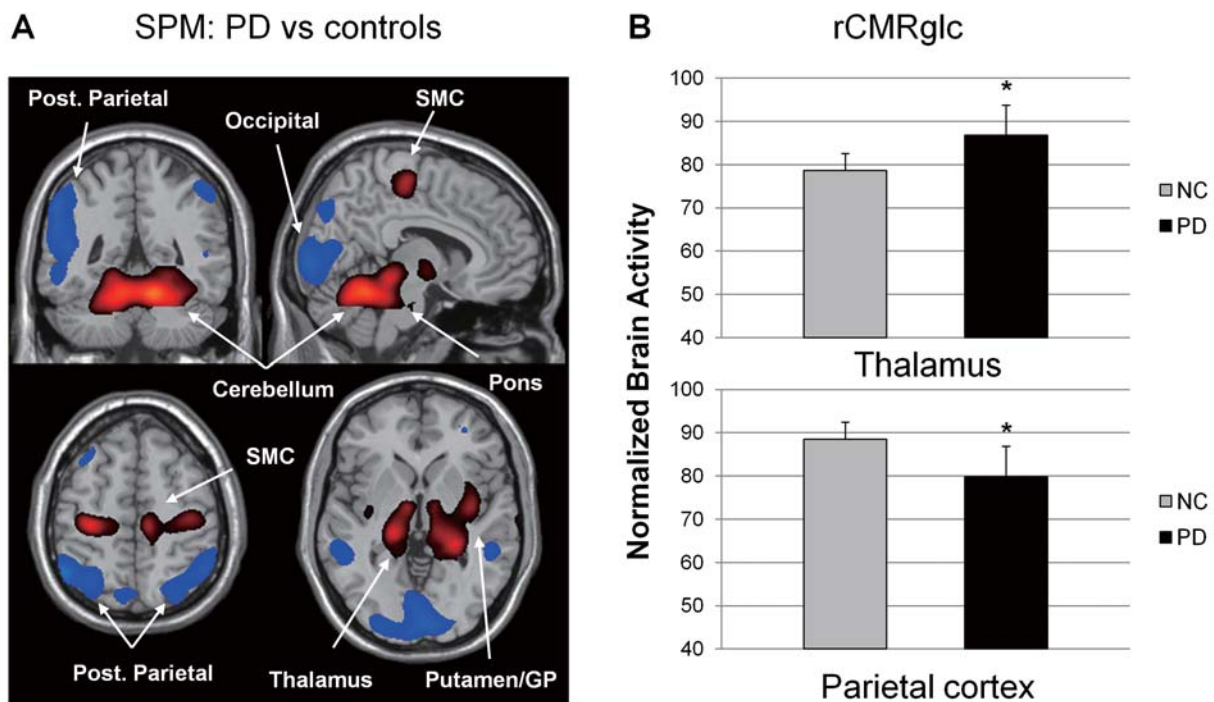


Fig. 1. A: Brain regions with significant metabolic abnormality identified by SPM analysis of resting-state FDG PET scans in patients with Parkinson's disease (PD) and age-matched normal volunteers. PD patients showed relative metabolic increases (red) in the putamen/globus pallidus (GP) and thalamus, in the cerebellum and pons, and in the sensorimotor cortex (SMC), along with metabolic decreases (blue) in the parieto-occipital association areas. B: Bar diagrams (mean \pm standard error) illustrating increased metabolic activity in the subcortical area and decreased activity in the cortex using rCMRglc data ($P < 0.01$) that compared the PD patients to the controls. (Produced by the authors using FDG PET images described by Ma *et al.* *J Cereb Blood Flow Metab* 2007^[39]. The display shows *t*-maps that are significant at $P < 0.001$. The regional brain activity values were obtained *post-hoc* with a spherical VOI 8 mm in diameter centered at the peak of significant SPM clusters.)

in the inferior/superior parietal and occipital cortices in PD patients with autonomic failure^[20], in agreement with the negative correlation reported between intellectual impairment in PD and rCMRglc in posterior association regions such as the bilateral parietal and occipital gyri^[21]. Both studies provided early indications that cortical hypometabolism may be primarily associated with cognitive dysfunction in PD. It was also found that the relative metabolic activity in typically affected cortical regions was significantly correlated with scores for cognition, but not with those for motor performance and behavior in a combined cohort of PD patients without and with dementia^[22]. This measure gave a high sensitivity and specificity of 0.91 and 1.00 for an ultimate clinical diagnosis of dementia. Indeed, we found that worsening executive dysfunction in non-demented PD patients is related bilaterally with lower rCMRglc in parieto-occipital association regions, and with

higher rCMRglc in the cerebellum (Fig. 2). Extensive areas of hypometabolism are also evident in the posterior cortical regions, including the temporo-parieto-occipital, medial parietal, and inferior temporal cortices in PD patients with mild cognitive impairment^[18]. These results support the notion that posterior cortical dysfunction is the primary imaging feature of cognitively-impaired PD patients at risk for developing dementia.

Cerebral Blood Flow Studies

Owing to the short half-life of the radiotracer, H_2O PET has been primarily used in brain activation studies to examine physiological processes underlying motor execution and learning^[23, 24]. Nevertheless, this method has also been used to map rCBF alterations in PD patients at rest. Both rCBF and rCMRglc data measured with PET yield similar patterns of subcortical hyperactivity and cortical hypoactivity in PD patients; these are highly comparable to those from

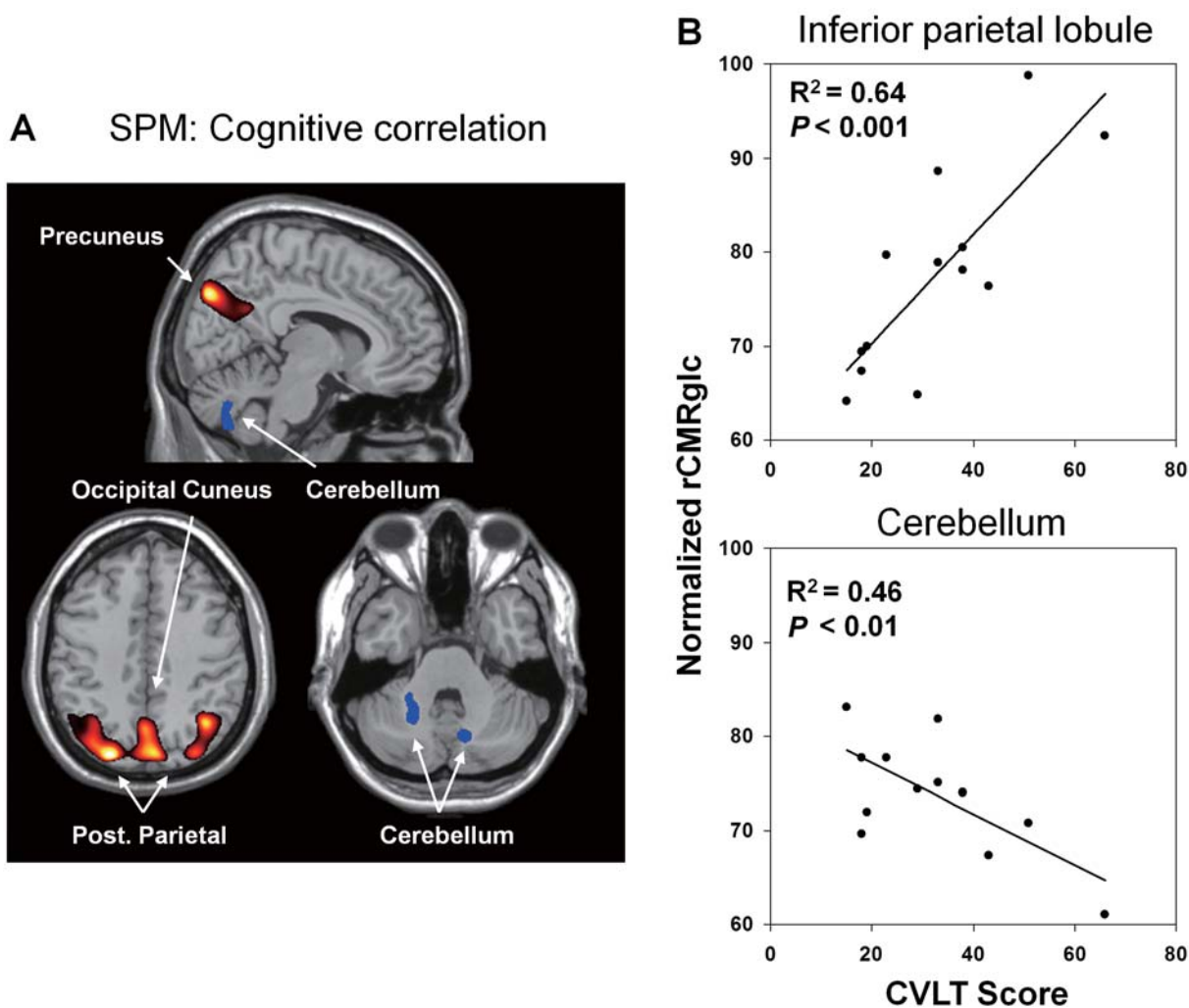


Fig. 2. A: Brain regions with significant behavioral correlations identified by SPM regression analysis of resting-state FDG PET scans in non-demented patients with Parkinson's disease (PD). Scores on the California verbal learning test (CVLT) were positively correlated with metabolic activity in the precuneus and bilateral parieto-occipital association areas (red), and negatively with metabolic activity in the right brainstem and bilateral cerebellum (blue). B: Scatter plots illustrating significant linear relationships between the measure of cognitive dysfunction in PD with decreased brain activity in the parieto-occipital regions and increased brain activity in the cerebellum with rCMRglc data. Note that a lower CVLT score indicated a higher degree of cognitive dysfunction in individual patients. (Produced by the authors using FDG PET and clinical data described by Huang *et al.* *NeuroImage* 2007^[50]. The display represents *t*-maps that are significant at $P < 0.01$. The regional metabolic values were obtained *post-hoc* with a spherical VOI 8 mm in diameter centered at the peak of significant SPM clusters.)

resting-state rCBF studies using SPECT perfusion data. For example, one study compared parametric maps of globally normalized rCBF in PD patients and age-matched normal volunteers using SPECT with ^{99m}Tc-ethyl cysteinate dimer (ECD)^[25]. In patients with early-stage PD, rCBF increased in the bilateral putamen and the right hippocampus relative to controls. In patients with late-stage PD, rCBF increased

in the bilateral putamen, pallidum, hippocampus, and cerebellum, the left ventrolateral thalamus, and the right insula and inferior temporal cortex. Thus, significant rCBF changes in PD are associated with the pathophysiology and progression in the functional architecture of thalamocortico-basal ganglia circuits and related pathways.

By contrast, rCBF declines in the supplementary motor

area (SMA) and the dorsolateral prefrontal cortex (DLPFC) in PD patients using SPECT with 99mTc-hexamethyl propylene amine oxime (HMPAO)^[26]. In a subgroup of patients with Hoehn-Yahr III/IV, rCBF decreased in the SMA, and in the DLPFC and insular cortex. The degree of rCBF decline in the DLPFC or the insular cortex was correlated with UPDRS motor scores. rCBF was also significantly reduced in the bilateral posterior parietal and occipital cortices in non-demented PD patients relative to normal individuals using SPECT with N-isopropyl-p-[¹²³I]iodoamphetamine (IMP)^[27]. There was a strong positive correlation between the scores in a visual-processing task and rCBF in the right visual association area in PD patients. This work demonstrates that posterior parietal and occipital hypoperfusion is a consistent feature in non-demented PD patients and the latter is likely to underlie impaired visual cognition.

SPECT perfusion data have proven useful for characterizing the unique features of cortical hypoperfusion in PD with dementia. Previous studies in patients with Hoehn-Yahr III-IV PD showed significant rCBF decreases in the left frontal/parietal association cortices with IMP^[28] and in the precuneus and inferior parietal regions with HMPAO^[29], consistent with the impaired visuospatial perception in demented PD. Furthermore, temporal and more extensive parietal hypoperfusion are often seen in demented patients^[30]. The cortical hypoperfusion might be clinically useful in discriminating PD patients with dementia from those without cognitive impairment.

In summary, imaging studies of brain metabolism and perfusion have revealed unique and comparable pathological features underlying varying degrees of motor and cognitive dysfunction in patients with PD. The characteristic patterns of abnormal regional cerebral metabolism and perfusion are to a large degree independent of global measures of brain activity in non-demented patients with PD as described previously^[3, 31]. The generally similar findings from these two imaging measures of brain function indicate close coupling between cerebral blood flow and metabolism in PD under resting conditions. These results have established molecular-functional-clinical correlates of the impaired cortico-subcortical circuitry in PD.

Functional Brain Imaging: Multivariate Analyses

The measurements of local metabolic rates or blood flow

changes may not fully account for the complex nature of brain networks involved in neurodegenerative processes and their modulation by therapy. These processes may be better represented by spatial covariance patterns among spatially distributed functional regions that can be altered by the presence of disease or behavioral activation. Many computing methods have been used in the analysis of rCMRglc and rCBF data to compare groups in the same resting state^[32-35] and under brain activation conditions^[36-38]. The resultant topographic patterns describe functional connectivity and are commonly referred to as disease-specific brain networks.

Metabolic Network Analyses

We have developed a statistical modeling approach to detect and quantify regional functional interactions in neurodegenerative disorders^[31, 39]. This method, known originally as the scaled subprofile model (SSM), uses PCA to identify regional covariance patterns using images from a combined group of patients and controls or a single group of individuals (software freely available at our website <http://www.feinsteinneuroscience.org>). These patterns reflect the covariation of increased or decreased activity in regional brain function in patients relative to the normal population or in relation to the correlation with a behavioral variable.

SSMPCA allows for the prospective quantification of covariance pattern expression in individual subjects. Subject scores computed from functional brain images can be correlated with clinical or physiological parameters on a single-case basis^[3]. Of note, these scores have higher signal-to-noise ratios than decreasing levels of dopaminergic markers such as FDOPA or FPCIT with increasing disease severity. Thus, SSMPCA may offer greater sensitivity for detecting spatiotemporal changes in brain network activity during progression or following therapy.

Many imaging studies have been performed to implement and validate network methods for the diagnosis and evaluation of patients with PD and related movement disorders^[39, 40]. Using SSMPCA analysis of FDG PET data we consistently revealed a pattern of regional metabolic covariation characterized by lentiform, thalamic, cerebellar, pontine, and sensorimotor hypermetabolism, along with hypometabolism in the lateral PMC, SMA, and parieto-occipital regions (Fig. 3). The subject scores for this PD-

related covariance pattern (PDRP) are elevated in PD patients, and are correlated positively with clinical disease ratings and negatively with striatal FDOPA uptake or DAT binding^[3, 41, 42]. This pattern has been confirmed in multiple cohorts of PD patients^[43-45] and parkinsonian primates^[46] scanned with different tomographs. In addition, PDRP expression showed an excellent test-retest reproducibility [intra-class correlation coefficient (ICC) >0.94] between FDG PET imaging sessions conducted OFF and ON medications in independent groups of PD patients at early and advanced stages^[39]. Moreover, disease-specific covariance patterns for multiple system atrophy (MSA), progressive supranuclear palsy and parkinsonian tremor have also been developed for more accurate differential diagnosis of PD from atypical parkinsonism on a single-case basis^[45, 47-49].

SSMPCA analysis of FDG PET data can also

reveal the specific networks associated with cognitive dysfunction in PD. By using this method in non-demented PD patients, we identified a covariance pattern that is correlated with memory and executive functioning^[50]. This PD-related cognitive pattern (PDCP) is characterized by hypermetabolism in the cerebellar vermis and dentate nuclei and hypometabolism in frontal and parietal association areas (Fig. 4). Similar results have been reported from VOI-based SSMPCA analysis^[51] and another multivariate method based on partial least squares^[34]. PDCP activity predicted memory or visuospatial function, and perceptual motor speed in a prospective validation sample of PD patients of similar disease duration and severity. In addition, PDCP scores showed excellent test-retest reliability (ICC >0.89) in patients undergoing repeat FDG PET imaging OFF and ON medications. PDCP is orthogonal to PDRP as its expression is independent of

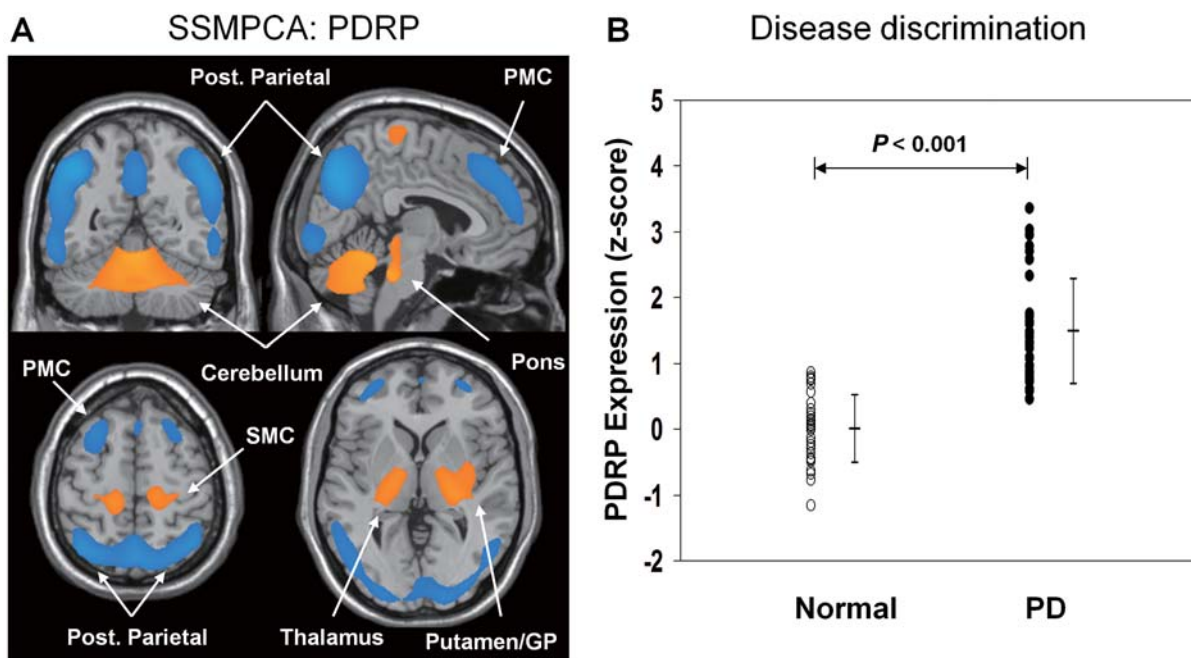


Fig. 3. A: Parkinson's disease-related pattern (PDRP) identified by SSMPCA spatial covariance analysis of resting-state FDG PET scans in patients with Parkinson's disease (PD) and age-matched normal volunteers. This pattern was characterized by relatively increased metabolic activity (yellow) in the putamen/globus pallidus (GP) and thalamus, in the cerebellum and pons, and in the SMC. These changes covaried with relatively decreased metabolic activity (blue) in the lateral premotor cortex (PMC) and in the parieto-occipital association regions. **B:** Scatter plots of individual values and mean (\pm standard deviation) for PDRP expression in healthy controls (open circles) and PD patients (filled circles). PDRP network scores were significantly elevated in patients relative to controls. A higher PDRP score corresponded with more severe motor symptoms in individual patients. [Reproduced by the authors using FDG PET images described by Ma *et al.* *J Cereb Blood Flow Metab* 2007^[39]. The display represents voxels that contributed significantly to the network at $P \leq 0.001$, and were demonstrated to be reliable ($P < 0.001$) on bootstrap estimation.]

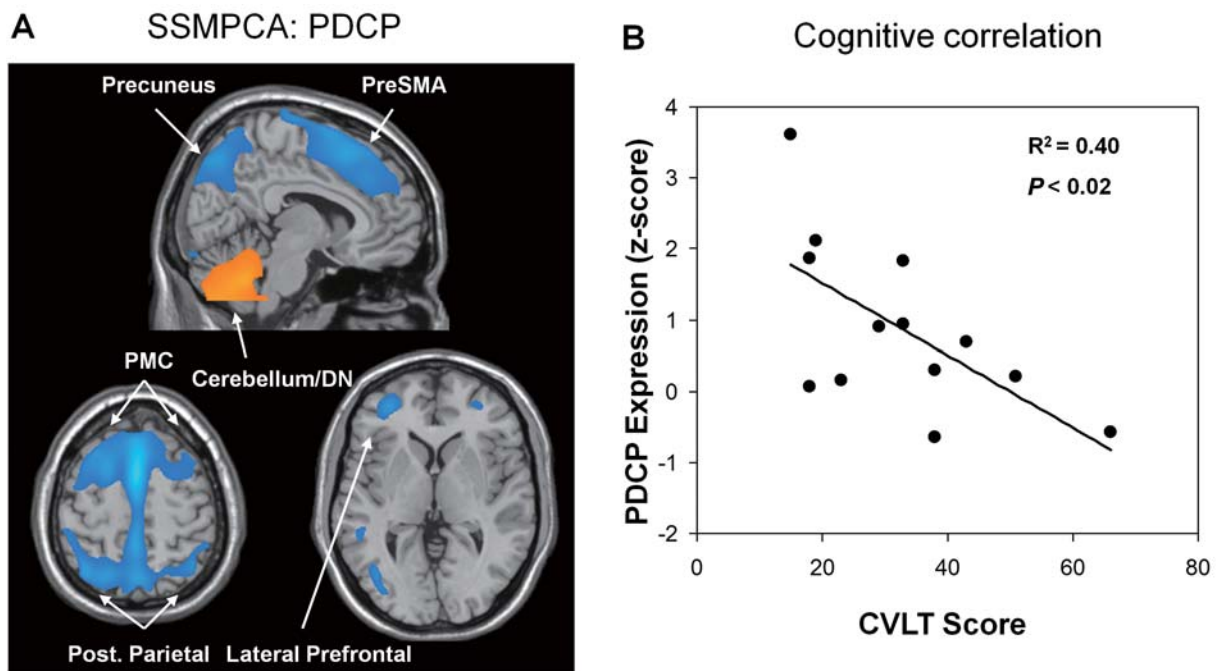


Fig. 4. A: Parkinson's disease-related cognitive pattern (PDCP) identified by SSMPCA spatial covariance analysis of resting-state FDG PET scans in non-demented PD patients. This pattern was characterized by covarying metabolic reductions (blue) in the rostral supplementary motor area (pre-SMA) and precuneus, as well as in the dorsal premotor (PMC) and posterior parietal regions, and in the left prefrontal cortex. Relative metabolic increases (yellow) in the cerebellar vermis and dentate nuclei (DN) were also evident as part of this topography. **B:** Brain-behavioral correlations between PDCP network expression and neuropsychological performance in non-demented PD patients. There was a significant linear relationship between PDCP network activity and scores in the California verbal learning test (CVLT). Note that a lower CVLT score and higher PDCP activity indicated a greater degree of cognitive dysfunction in individual patients. (Reproduced by the authors using FDG PET and clinical data described by Huang *et al.* *NeuroImage* 2007^[50].) The display represents regions that contributed significantly to the network at $P \leq 0.01$ and were demonstrated to be reliable ($P < 0.05$) by bootstrap estimation.

UPDRS motor scores in individual PD patients.

Importantly, the topography of the PD-related metabolic covariance pattern identified in these studies is in line with experimental models of parkinsonism^[3, 46]. Specifically, this supports the notion of enhanced pallidothalamic inhibition as the main functional substrate of parkinsonian bradykinesia. The subject scores for PDRP correlate with objective disease severity ratings and with independent measures of nigrostriatal dopamine function. Furthermore, the PDRP scores and rCMRglc within key hypermetabolic regions obtained from preoperative FDG PET scans are related to neuronal firing rates in the GPi and STN measured during stereotaxic neurosurgery^[52, 53]. On the contrary, the PDCP scores did not show such relationships despite their correlation with cognitive impairment in patients. This is further evidence that the

PDRP is an indirect measure of an abnormal physiological signal resulting from hyperactivity in the basal ganglia-thalamic-motor cortical loop.

Blood Flow Network Analyses

PD-related brain network patterns based on SSMPCA can be directly identified and prospectively accessed by using rCBF images from PET or SPECT. VOI-based network analysis of ECD SPECT data from PD patients and age-matched healthy controls revealed a pattern characterized by relative increases in putaminal, thalamic, and cerebellar perfusion along with decreases in the frontal operculum and in the medial temporal cortex^[54]. The subject scores for this PDRP pattern were significantly increased in PD patients relative to healthy control and MSA groups. These features agree very well with those reported in the PDRP derived from FDG PET images.

Notably, the PET-derived PDRP scores computed from ECD SPECT scans more accurately separate PD patients from normal controls and MSA patients^[54, 55]. Receiver operating characteristic analysis indicated that the PDRP measures yielded an overall diagnostic accuracy of 0.91, with a sensitivity of 0.97 and specificity of 0.71 and 0.80 for distinguishing PD from the other two groups. Hence, the disease-related patterns identified with FDG PET can be reliably assessed in SPECT perfusion scans to discriminate between healthy controls and patients with PD and atypical parkinsonism.

The disease-related patterns seen in PDRP derived from FDG PET and ECD SPECT images are also similar to those revealed by another multivariate brain mapping method based on independent component analysis (ICA). A SPECT study compared differences in rCBF between PD patients and age-matched controls with SPM after decomposing the images into disease-related and unrelated components^[33]. In the disease-related components, PD patients revealed significantly higher normalized rCBF in the putamen, pallidum, thalamus, brainstem, and cerebellum, and significant hypoperfusion in the parieto-temporo-occipital cortex, DLPFC, insula, and cingulate gyrus. Importantly, motor UPDRS scores in patients correlated negatively with rCBF in the insula and cingulate gyrus. The abnormal regions revealed by both ICA and PCA are consistent with the current model of parkinsonism.

We have validated the PDRP or PDCP network as a reliable measure of parkinsonism or cognitive dysfunction by computing its activity prospectively in H₂O and FDG PET scans from PD patients and healthy volunteers^[56]. PDRP expression was significantly elevated in PD patients, using either H₂O or FDG PET scans. A significant correlation was present between PDRP/PDCP scores computed from H₂O and FDG images in the same cohort of PD patients. This relationship has established the clinical utility of network quantification with rCBF data in the early differential diagnosis of PD. For example, PDRP/PDCP scores were computed in a prospective cohort of normal controls and patients with early- and late-stage PD who underwent H₂O PET imaging. We found that PDRP scores performed better than those for PDCP in separating early PD from controls. This difference in PDRP and PDCP scores from

cross-sectional data is in line with the observation from a longitudinal study of disease progression with FDG PET^[42], indicating that the manifestation of motor symptoms precedes cognitive dysfunction in early PD.

The reliability of PDRP/PDCP expression computed in rCBF scans has also been evaluated within subjects using a test–retest design in mild and advanced PD patients^[56]. These patients were scanned twice within one H₂O PET imaging session at baseline and during treatment with levodopa (LD) infusion or deep brain stimulation (DBS). PDRP/PDCP scores measured with rCBF data have very high reproducibility (ICC >0.92), comparable to that from rCMRglc data acquired between FDG PET sessions separated by up to 2 months. This high reproducibility is evident in both early-stage and advanced PD patients scanned at baseline and during treatment.

PDRP/PDCP expression can also be assessed prospectively with rCBF data acquired from arterial spin labeling (ASL) perfusion MRI. We have shown that ASL MRI is comparable to FDG PET in quantifying PDRP network activity in individual patients and healthy controls^[57]. Indeed, the PDRP scores in PD patients measured concurrently with both rCBF and rCMRglc images were equally elevated from the controls and significantly correlated with each other. With further technical refinement this imaging modality has been successful in deriving analogous spatial covariance patterns associated with motor and cognitive dysfunction in PD^[58].

In summary, the motor and cognitive symptoms of PD have been linked to abnormal spatial covariance patterns involving different aspects of the basal ganglia-thalamocortical pathways. These patterns closely resemble specific physiological and anatomical brain networks known to be operating in disease states, and are highly reproducible across independent patient populations and tomographs at separate institutions. Individual subject scores for the motor-related topography are significantly elevated in PD patients and correlate with bradykinesia and rigidity ratings. In addition, subject scores for the cognition-related topography predict behavioral performance. Besides the use of FDG PET data, pattern derivation and prospective assessment can also be achieved with rCBF data obtained from PET and more routine SPECT methods as well as newly-developed MRI perfusion techniques.

Functional Neuroimaging in the Evaluation of Therapeutic Interventions

Reliable *in vivo* markers of neuronal activity are necessary to assess the medical or surgical outcome in PD. Currently available clinical rating scales are inherently variable and relatively insensitive, and may not accurately reflect the extent of therapy-mediated changes in regional brain function. Conversely, quantitative functional imaging markers of cerebral metabolism and blood flow in the resting state may serve as suitable outcome measures for the treatment of PD. These measures may help select patients for clinical trials by providing more accurate diagnosis on an individual case basis and may afford a useful tool in predicting clinical outcomes for certain neurosurgical interventions.

Effects of Dopaminergic Therapy on Brain Function

PET/SPECT has been used to quantify regional functional changes associated with successful drug therapy. We reported that LD infusion significantly decreased rCMRglc in the putamen, thalamus, cerebellum, and primary motor cortex, along with a significant decline in PDRP expression^[59] (Fig. 5). Changes in pallidal metabolism and PDRP activity were negatively correlated with clinical improvement in UPDRS motor ratings. These confirmed that lentiform hypermetabolism or hyperfusion in PD may be in part reversible by LD^[60]. The response to dopaminergic therapy in PD patients may be mediated by the modulation of cortico-striato-pallido-thalamocortical pathways.

PET has played a key role in unraveling the metabolic and neurovascular effects of LD therapy for PD. Both H₂O and FDG PET images have been used to quantify LD-mediated changes in the expression of motor- and cognition-related PD covariance patterns as well as in rCBF and rCMRglc in PD patients before and after intravenous LD infusion^[61]. There was a significant dissociation between rCBF and rCMRglc in the modulation of the PDRP by LD treatment, characterized by decreases in network activity in the rCMRglc images but concurrent increases in the rCBF images. This treatment also induced decreases in rCMRglc and increases in rCBF in the putamen/pallidum, dorsal midbrain/pons, STN, and ventral thalamus. These

are the same regions that exhibit increased brain activity in PD with either rCMRglc or rCBF data obtained off medication as described above. These results indicate that flow–metabolism dissociation is a unique feature of LD treatment. The elevations in rCBF and in the corresponding PDRP network activity may be attributed to a direct action of dopaminergic drugs on the microvasculature in the close proximity of monoaminergic terminals. This LD-mediated disassociation between blood flow and metabolism calls for great caution when interpreting rCBF findings in patients who have taken dopaminergic medications or undergone insufficient washout before imaging.

Stereotaxic Surgical Therapies

Neurosurgery can provide effective symptomatic relief in patients with advanced PD by performing localized interventions on several deep nuclei that serve as key relay stations within the basal-ganglia-cortical motor circuitry and related pathways. DBS at high frequency offers a reversible treatment for PD without the permanent side-effects caused by an ablative lesion. In addition, DBS parameters can be adjusted postoperatively for optimal clinical benefits on an individual basis. A number of subcortical targets have been stimulated to achieve long-term improvement in the motor and non-motor symptoms of PD^[62-64], including mainly pallidal and subthalamic DBS to improve general motor features and ventral intermediate (Vim) thalamic DBS to suppress tremor.

Neuroimaging studies with rCMRglc and rCBF have shed important light on the therapeutic mechanisms underlying these procedures. Ipsilateral and contralateral changes in regional brain function can be detected in the PMC, SMC, SMA, and cerebellum using both FDG and H₂O PET following unilateral DBS at the internal and external parts of the globus pallidus^[9, 65]. Interestingly, unilateral Vim DBS leads to rCBF decreases in the ipsilateral SMC and the contralateral cerebellum, as well as concurrent increases in the ipsilateral ventral thalamus^[66]. Changes in tremor acceleration and rCBF are correlated in the ipsilateral cortical regions; changes in tremor frequency and rCBF are correlated in the contralateral cerebellum and pons. These results suggest that DBS delivers symptomatic relief by modulating the activity of cerebello-thalamo-cortical pathways.

Stimulation at the STN is considered to be more

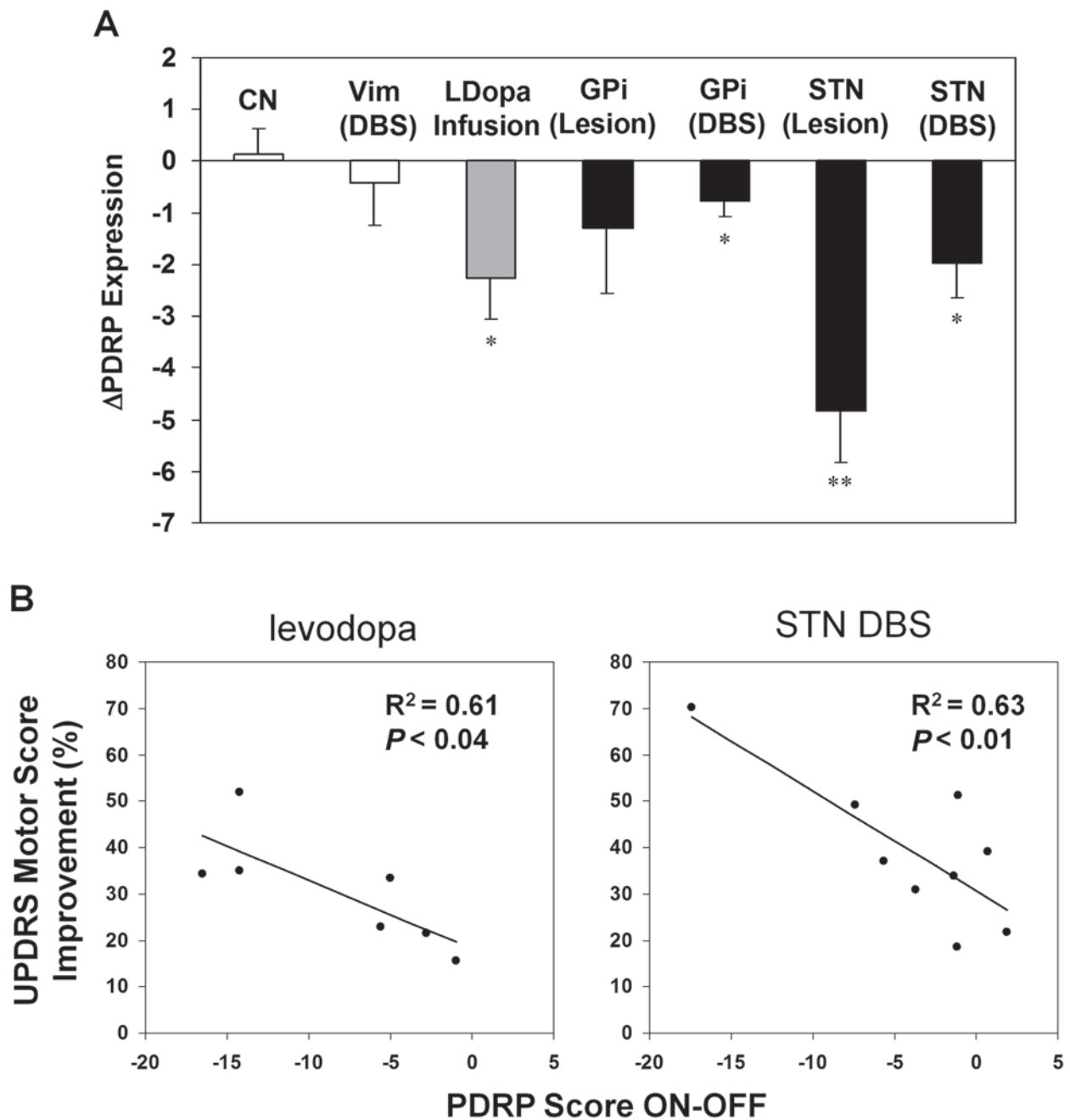


Fig. 5. Network modulation and clinical correlation with antiparkinsonian interventions in patients assessed with FDG PET. A: Bar graph (mean \pm SE) illustrating relative changes in the expression of the PD-related metabolic covariance pattern (PDRP) during antiparkinsonian therapy with LD infusion (shaded bar) and ventral pallidotomy, pallidal and STN DBS, and subthalamotomy (filled bars). Reduction in PDRP activity was greater in lesion versus DBS at the same target or in STN versus GPi by either lesion or DBS. For unilateral surgical intervention, PDRP reflected changes in network activity in the operated hemisphere. With LD infusion, the PDRP changes were averaged across hemispheres. CN, Control. B: Correlations between clinical improvement in UPDRS motor rating and treatment-mediated changes in PDRP activity. The clinical outcome in individual patients was significantly correlated with the degree of PDRP suppression following levodopa administration in mild PD patients and STN DBS in advanced PD patients. (Reproduced by the authors using FDG PET and clinical data described by Feigin *et al.* Neurology 2001^[59] and Asanuma *et al.* Brain 2006^[67]. * $P < 0.01$; ** $P < 0.005$ vs untreated condition)

effective than at the GPi in improving PD symptoms by affecting more than one inhibitory output area of the basal ganglia, i.e. both the GPi and the substantia nigra pars reticulata. An FDG PET study showed that rCMRglc decreased in the left rostral cerebellum with STN-DBS, but increased in both lower thalami extending to the midbrain area and remotely in the right frontal, temporal, and parietal cortices^[14]. These data demonstrate an activating effect of DBS on its target structures and suggest a central role of the STN in motor, association, limbic, and cerebellar-basal ganglia circuits.

FDG PET has proven to be useful for directly comparing the specific metabolic effects of different interventions. It has been reported that metabolism is reduced in the GPi and caudal midbrain but elevated in the posterior parietal region following STN stimulation and subthalamotomy^[16]. While the metabolic decline in the GPi is greater with a lesion, the metabolic increase is greater with stimulation. PDRP expression is similarly reduced with both treatments. Moreover, we reported that both STN stimulation and LD therapy result in significant metabolic reductions in the putamen/pallidum, SMC, and cerebellar vermis, as well as elevations in the precuneus^[67]. Reduction in the lentiform metabolism may reflect deactivation of the inhibitory basal ganglia output nuclei following suppression of the synaptic activity of STN projections. Comparable declines in PDRP activity have also been observed with both interventions (Fig. 5), and they are correlated with clinical improvement. This is in excellent agreement with the findings reported with FDG PET in subthalamotomy^[68] and DBS at the GPi^[9] and STN^[69]. These results suggest that effective treatments for PD are facilitated by a common mechanism involving the modulation of pathological brain networks.

It is of interest to note that PDCP expression assessed by rCMRglc and rCBF scans in the same patients was not changed by symptomatic therapy with either intravenous LD infusion or STN-DBS^[61]. Hence, PDCP assessment did not reveal any flow-metabolism disassociation evident with LD administration in PDRP noted above. These findings support the hypothesis that PDCP network activity is a reproducible imaging biomarker of cognitive function in PD and this measure may prove useful in clinical trials targeting the non-motor symptoms of PD.

H₂O PET has been used to measure resting rCBF responses to STN-DBS. Cerebral blood flow increases in the thalamus and midbrain, but declines bilaterally in premotor cortex^[70]. Of note, significant correlations are present between improved rigidity and decreased rCBF in the SMA, between improved bradykinesia and increased rCBF in the thalamus, and between improved postural reflexes and decreased rCBF in the pedunculo-pontine nucleus (PPN). Increased rCBF in the thalamus and midbrain agrees with the rCMRglc results from FDG PET^[14, 67]. These data indicate that STN stimulation appears to increase the firing of STN output neurons, which enhances inhibition of the thalamocortical projections, ultimately decreasing blood flow in cortical targets. Furthermore, blood flow increases bilaterally in the STN and in the left lentiform during bilateral STN DBS^[71], but declines in the left SMA (BA 6), left ventrolateral thalamus, and right cerebellum. Changes in rCBF in the basal ganglia or the SMA and thalamus are both correlated with the improvement in motor function. STN DBS in resting patients may also result in deactivation of the thalamic anteroventral and ventrolateral nuclei and the SMA.

STN-DBS in PD has also been examined by measuring resting-state rCBF with SPECT. In patients with stable clinical improvement during a long-term follow-up study^[72], STN-DBS at 5 months induced a reversible increase of rCBF in the pre-SMA, PMC, and DLPFC regions from the preoperative baseline. Blood flow increased further from 5 to 42 months in these frontal areas, and also in the primary sensorimotor cortices, pallidum, ventral lateral thalamus, cerebellum, pons, and midbrain, involving the substantia nigra. The improvement in motor scores was correlated with the rCBF increase in the pre-SMA and PMC. Long-term STN-DBS leads to progressive improvement in neural activity in the frontal motor/association areas, along with increased activity in subcortical structures in the later phase.

There are bound to be agreements and discrepancies across the many neuroimaging studies on the functional effects of STN-DBS. The major disagreement is likely to come from different neurosurgical protocols, imaging techniques, and analytical methods. The second difference may stem from varied and limited sample sizes, and the inhomogeneous clinical characteristics of PD patients included in the study. The third difference may be the

use of rCBF or rCMRglc as an outcome measure for the therapeutic trial. Although STN stimulation results in similar changes in regional brain activity and PDRP expression whether in rCMRglc or rCBF scans, a small difference may still arise from the potential residual effects of dopaminergic medications on rCBF values across studies.

H₂O PET can also detect the rCBF activation patterns induced by STN-DBS under task conditions. One study disclosed that rCBF increases significantly in the SMA, cingulate cortex, and DLPFC with STN stimulation during a motor activation task^[73]. This suggests that STN DBS plays a role in enhancing non-primary motor cortical areas, especially the DLPFC showing greater activation than in the GPi during effective stimulation. Bilateral STN DBS worsened the performance of a fast-paced cognitive task of random number generation in PD^[74]. Cerebral blood flow was reduced in the left dorsal and inferior frontal gyri, DLPFC, and the posterior and right anterior cingulate, but increased in the right GPi during the task. STN stimulation activates its output neurons to the GPi and significantly changes pallidal coupling with prefrontal, cingulate, and temporal cortices during the performance of a cognitive experiment.

It has been proposed that the axial symptoms in PD can be effectively improved by stimulation at the PPN. Cerebral blood flow was measured by H₂O PET at rest and during a self-paced motor task of the lower limbs in patients with advanced PD who were treated with unilateral PPN-DBS^[75]. Stimulation induced significantly increased rCBF in subcortical regions such as the thalamus, cerebellum, and midbrain as well as in different cortical areas involving the medial SMC extending into the caudal SMA (BA 4/6). Some of these regions are similar to the H₂O PET observations during STN-DBS. An FDG PET study also demonstrated that PPN DBS can improve non-motor function in the cognitive domain as indicated by relative prefrontal and cingulate hypermetabolism and cerebellar hypometabolism^[76]. It remains to be seen in a large sample how PPN-DBS affects the clinical correlates of regional brain function and whether it can modulate PDRP activity as evident in other interventions.

In summary, PET/SPECT imaging of rCMRglc and rCBF is a useful experimental method for assessing the modulation of structure/functional relationships during the successful treatment of PD. Treatment with LD or DBS

surgery in patients with PD alters activity in the putamen, pallidum, thalamus, and cerebellum, and partly restores the physiological substrate in limbic and associative cortical regions of the basal ganglia. In addition, clinical improvement is correlated with the changes in regional brain activity as well as in the expression of a PD-related covariance pattern. These interventions are consistently associated with modulation of regional brain function and suppression of a specific functional network involving elements of the cortico-striato-pallido-thalamocortical and the cerebello-cortical motor loops.

Conclusion

PET/SPECT has been widely used to identify changes in regional cerebral glucose metabolism and blood flow in PD. The measurements of cerebral metabolism and perfusion provide unique information on the topography of widespread functional alterations in the brains of PD patients, which is not available from studies with presynaptic or postsynaptic dopaminergic radioligands. Much effort has been devoted to the development of novel analytical methods for the validation of brain networks in functional imaging data. Such spatial covariance patterns may afford clinically useful markers in the differential diagnosis of parkinsonism and in the evaluation of disease severity and therapeutic response. Many studies have established the specific roles of imaging in preoperative patient selection for clinical trials in parkinsonism. A major contribution in this line of research has been a complementary analytical approach using both voxel-wise brain mapping and network modeling strategies to determine the relationships between localized functional abnormality and the expression of widely distributed brain networks. Applications of these techniques may provide greater insights into the pathophysiology of PD and offer more accurate assessment of the inherent functional changes that occur with disease onset, progression, and successful therapy.

ACKNOWLEDGEMENTS

This review was supported by NIH (R01 NS 35069) and the Morris K. Udall Center of Excellence for Parkinson's Disease Research (NIH P50 NS 071675) at The Feinstein Institute for Medical Research, USA.

Received date: 2014-07-25; Accepted date: 2014-09-14

REFERENCES

- [1] Thobois S, Jahanshahi M, Pinto S, Frackowiak R, Limousin-Dowsey P. PET and SPECT functional imaging studies in Parkinsonian syndromes: from the lesion to its consequences. *Neuroimage* 2004, 23: 1–16.
- [2] Peng S, Doudet DJ, Dhawan V, Ma Y. Dopamine PET imaging and Parkinson's disease. *PET Clin* 2013, 8: 469–485.
- [3] Ma Y, Tang C, Moeller JR, Eidelberg D. Abnormal regional brain function in Parkinson's disease: truth or fiction? *Neuroimage* 2009, 45: 260–266.
- [4] Catalan MJ, Ishii K, Honda M, Samii A, Hallett M. A PET study of sequential finger movements of varying length in patients with Parkinson's disease. *Brain* 1999, 122: 483–495.
- [5] Wichmann T, DeLong MR. Functional neuroanatomy of the basal ganglia in Parkinson's disease. *Adv. Neurol.* 2003, 91: 9–18.
- [6] Braak H, Del Tredici K. Cortico-basal ganglia-cortical circuitry in Parkinson's disease reconsidered. *Exp Neurol* 2008, 212: 226–229.
- [7] Brownell AL, Canales K, Chen YI, Jenkins BG, Owen C, Livni E, *et al.* Mapping of brain function after MPTP-induced neurotoxicity in a primate Parkinson's disease model. *Neuroimage* 2003, 20: 1064–1075.
- [8] Guigoni C, Dovero S, Aubert I, Li Q, Bioulac BH, Bloch B, *et al.* Levodopa-induced dyskinesia in MPTP-treated macaques is not dependent on the extent and pattern of nigrostriatal lesioning. *Eur. J. Neurosci.* 2005, 22: 283–287.
- [9] Fukuda M, Mentis MJ, Ma Y, Dhawan V, Antonini A, Lang AE, *et al.* Networks mediating the clinical effects of pallidal brain stimulation for Parkinson's disease: a PET study of resting-state glucose metabolism. *Brain* 2001, 124: 1601–1609.
- [10] Eckert T, Barnes A, Dhawan V, Frucht S, Gordon MF, Feigin AS, *et al.* FDG PET in the differential diagnosis of parkinsonian disorders. *Neuroimage* 2005, 26: 912–921.
- [11] Teune LK, Bartels AL, de Jong BM, Willemsen AT, Eshuis SA, de Vries JJ, *et al.* Typical cerebral metabolic patterns in neurodegenerative brain diseases. *Mov Disord* 2010, 25: 2395–2404.
- [12] Powers WJ, Videen TO, Markham J, Black KJ, Golchin N, Perlmutter JS. Cerebral mitochondrial metabolism in early Parkinson's disease. *J Cereb Blood Flow Metab* 2008, 28: 1754–1760.
- [13] Ghaemi M, Raethjen J, Hilker R, Rudolf J, Sobesky J, Deuschl G, *et al.* Monosymptomatic resting tremor and Parkinson's disease: a multitracer positron emission tomographic study. *Mov Disord* 2002, 17: 782–788.
- [14] Hilker R, Voges J, Weisenbach S, Kalbe E, Burghaus L, Ghaemi M, *et al.* Subthalamic nucleus stimulation restores glucose metabolism in associative and limbic cortices and in cerebellum: evidence from a FDG-PET study in advanced Parkinson's disease. *J Cereb Blood Flow Metab* 2004, 24: 7–16.
- [15] Lozza C, Marie RM, Baron JC. The metabolic substrates of bradykinesia and tremor in uncomplicated Parkinson's disease. *Neuroimage* 2002, 17: 688–699.
- [16] Trost M, Su S, Su P, Yen RF, Tseng HM, Barnes A, *et al.* Network modulation by the subthalamic nucleus in the treatment of Parkinson's disease. *Neuroimage* 2006, 31: 301–307.
- [17] Bohnen NI, Minoshima S, Giordani B, Frey KA, Kuhl DE. Motor correlates of occipital glucose hypometabolism in Parkinson's disease without dementia. *Neurology* 1999, 52: 541–546.
- [18] Hosokai Y, Nishio Y, Hirayama K, Takeda A, Ishioka T, Sawada Y, *et al.* Distinct patterns of regional cerebral glucose metabolism in Parkinson's disease with and without mild cognitive impairment. *Mov Disord* 2009, 24: 854–862.
- [19] Berti V, Polito C, Ramat S, Vanzi E, De Cristofaro MT, Pellicano G, *et al.* Brain metabolic correlates of dopaminergic degeneration in de novo idiopathic Parkinson's disease. *Eur J Nucl Med Mol Imaging* 2010, 37: 537–544.
- [20] Arahata Y, Hirayama M, Ieda T, Koike Y, Kato T, Tadokoro M, *et al.* Parieto-occipital glucose hypometabolism in Parkinson's disease with autonomic failure. *J Neurol Sci* 1999, 163: 119–126.
- [21] Wu JC, Iacono R, Ayman M, Salmon E, Lin SD, Carlson J, *et al.* Correlation of intellectual impairment in Parkinson's disease with FDG PET scan. *Neuroreport* 2000, 11: 2139–2144.
- [22] Liepelt I, Reimold M, Maetzler W, Godau J, Reischl G, Gaenslen A, *et al.* Cortical hypometabolism assessed by a metabolic ratio in Parkinson's disease primarily reflects cognitive deterioration-[18F]FDG-PET. *Mov Disord* 2009, 24: 1504–1511.
- [23] Boecker H, Ceballos-Baumann A, Bartenstein P, Weindl A, Siebner HR, Fassbender T, *et al.* Sensory processing in Parkinson's and Huntington's disease: investigations with 3D H(2)(15)O-PET. *Brain* 1999, 122: 1651–1665.
- [24] Fukuda M, Mentis M, Ghilardi MF, Dhawan V, Antonini A, Hammerstad J, *et al.* Functional correlates of pallidal stimulation for Parkinson's disease. *Ann Neurol* 2001, 49: 155–164.
- [25] Imon Y, Matsuda H, Ogawa M, Kogure D, Sunohara N. SPECT image analysis using statistical parametric mapping in patients with Parkinson's disease. *J Nucl Med* 1999, 40: 1583–1589.
- [26] Kikuchi A, Takeda A, Kimpara T, Nakagawa M, Kawashima R, Sugiura M, *et al.* Hypoperfusion in the supplementary

- motor area, dorsolateral prefrontal cortex and insular cortex in Parkinson's disease. *J Neurol Sci* 2001, 193: 29–36.
- [27] Abe Y, Kachi T, Kato T, Arahata Y, Yamada T, Washimi Y, *et al.* Occipital hypoperfusion in Parkinson's disease without dementia: correlation to impaired cortical visual processing. *J Neurol Neurosurg Psychiatry* 2003, 74: 419–422.
- [28] Matsui H, Nishinaka K, Oda M, Hara N, Komatsu K, Kubori T, *et al.* Heterogeneous factors in dementia with Parkinson's disease: IMP-SPECT study. *Parkinsonism Relat Disord* 2007, 13: 174–181.
- [29] Firbank MJ, Colloby SJ, Burn DJ, McKeith IG, O'Brien JT. Regional cerebral blood flow in Parkinson's disease with and without dementia. *Neuroimage* 2003, 20: 1309–1319.
- [30] Osaki Y, Morita Y, Fukumoto M, Akagi N, Yoshida S, Doi Y. Three-dimensional stereotactic surface projection SPECT analysis in Parkinson's disease with and without dementia. *Mov Disord* 2005, 20: 999–1005.
- [31] Spetsieris PG, Eidelberg D. Scaled subprofile modeling of resting state imaging data in Parkinson's disease: methodological issues. *Neuroimage* 2011, 54: 2899–2914.
- [32] Moeller JR, Ishikawa T, Dhawan V, Spetsieris P, Mandel F, Alexander GE, *et al.* The metabolic topography of normal aging. *J Cereb Blood Flow Metab* 1996, 16: 385–398.
- [33] Hsu JL, Jung TP, Hsu CY, Hsu WC, Chen YK, Duann JR, *et al.* Regional CBF changes in Parkinson's disease: a correlation with motor dysfunction. *Eur J Nucl Med Mol Imaging* 2007, 34: 1458–1466.
- [34] Mentis MJ, McIntosh AR, Perrine K, Dhawan V, Berlin B, Feigin A, *et al.* Relationships among the metabolic patterns that correlate with mnemonic, visuospatial, and mood symptoms in Parkinson's disease. *Am J Psychiatry* 2002, 159: 746–754.
- [35] Chen K, Reiman EM, Huan Z, Caselli RJ, Bandy D, Ayutyanont N, *et al.* Linking functional and structural brain images with multivariate network analyses: a novel application of the partial least square method. *Neuroimage* 2009, 47: 602–610.
- [36] Friston KJ, Holmes A, Poline JB, Price CJ, Frith CD. Detecting activations in PET and fMRI: levels of inference and power. *Neuroimage* 1996, 4: 223–235.
- [37] McIntosh AR, Bookstein FL, Haxby JV, Grady CL. Spatial pattern analysis of functional brain images using partial least squares. *Neuroimage* 1996, 3: 143–157.
- [38] Carbon M, Eidelberg D. Functional imaging of sequence learning in Parkinson's disease. *J Neurol Sci* 2006, 248: 72–77.
- [39] Ma Y, Tang C, Spetsieris PG, Dhawan V, Eidelberg D. Abnormal metabolic network activity in Parkinson's disease: test-retest reproducibility. *J Cereb Blood Flow Metab* 2007, 27: 597–605.
- [40] Niethammer M, Eidelberg D. Metabolic brain networks in translational neurology: Concepts and Applications. *Ann Neurol* 2012.
- [41] Kaasinen V, Maguire RP, Hundemer HP, Leenders KL. Corticostriatal covariance patterns of 6-[18F]fluoro-L-dopa and [18F]fluorodeoxyglucose PET in Parkinson's disease. *J Neurol* 2006, 253: 340–348.
- [42] Huang C, Tang C, Feigin A, Lesser M, Ma Y, Pourfar M, *et al.* Changes in network activity with the progression of Parkinson's disease. *Brain* 2007, 130: 1834–1846.
- [43] Moeller JR, Nakamura T, Mentis MJ, Dhawan V, Spetsieris P, Antonini A, *et al.* Reproducibility of Regional Metabolic Covariance Patterns: Comparison of Four Populations. *Journal of Nuclear Medicine* 1999, 40: 1264–1269.
- [44] Wu P, Wang J, Peng S, Ma Y, Zhang H, Guan Y, *et al.* Metabolic brain network in the Chinese patients with Parkinson's disease based on 18F-FDG PET imaging. *Parkinsonism Relat Disord* 2013, 19: 622–627.
- [45] Teune LK, Renken RJ, Mudali D, De Jong BM, Dierckx RA, Roerdink JB, *et al.* Validation of parkinsonian disease-related metabolic brain patterns. *Mov Disord* 2013, 28: 547–551.
- [46] Ma Y, Peng S, Spetsieris PG, Sossi V, Eidelberg D, Doudet DJ. Abnormal metabolic brain networks in a nonhuman primate model of parkinsonism. *J Cereb Blood Flow Metab* 2012, 32: 633–642.
- [47] Eckert T, Tang C, Ma Y, Brown N, Lin T, Frucht S, *et al.* Abnormal metabolic networks in atypical parkinsonism. *Mov Disord* 2008, 23: 727–733.
- [48] Poston KL, Tang CC, Eckert T, Dhawan V, Frucht S, Vonsattel JP, *et al.* Network correlates of disease severity in multiple system atrophy. *Neurology* 2012, 78: 1237–1244.
- [49] Mure H, Hirano S, Tang CC, Isaias IU, Antonini A, Ma Y, *et al.* Parkinson's disease tremor-related metabolic network: characterization, progression, and treatment effects. *Neuroimage* 2011, 54: 1244–1253.
- [50] Huang C, Mattis P, Tang C, Perrine K, Carbon M, Eidelberg D. Metabolic brain networks associated with cognitive function in Parkinson's disease. *Neuroimage* 2007, 34: 714–723.
- [51] Lozza C, Baron JC, Eidelberg D, Mentis MJ, Carbon M, Marie RM. Executive processes in Parkinson's disease: FDG-PET and network analysis. *Hum Brain Mapp* 2004, 22: 236–245.
- [52] Eidelberg D, Moeller JR, Kazumata K, Antonini A, Sterio D, Dhawan V, *et al.* Metabolic correlates of pallidal neuronal activity in Parkinson's disease. *Brain* 1997, 120: 1315–1324.
- [53] Lin TP, Carbon M, Tang C, Mogilner AY, Sterio D, Beric A, *et al.* Metabolic correlates of subthalamic nucleus activity in Parkinson's disease. *Brain* 2008, 131: 1373–1380.
- [54] Feigin A, Antonini A, Fukuda M, De Notaris R, Benti R, Pezzoli G, *et al.* Tc-99m ethylene cysteinate dimer SPECT in

- the differential diagnosis of parkinsonism. *Mov Disord* 2002, 17: 1265–1270.
- [55] Eckert T, Van Laere K, Tang C, Lewis DE, Edwards C, Santens P, *et al.* Quantification of Parkinson's disease-related network expression with ECD SPECT. *Eur J Nucl Med Mol Imaging* 2007, 34: 496–501.
- [56] Ma Y, Eidelberg D. Functional imaging of cerebral blood flow and glucose metabolism in Parkinson's disease and Huntington's disease. *Mol Imaging Biol* 2007, 9: 223–233.
- [57] Ma Y, Huang C, Dyke JP, Pan H, Alsop D, Feigin A, *et al.* Parkinson's disease spatial covariance pattern: noninvasive quantification with perfusion MRI. *J Cereb Blood Flow Metab* 2010, 30: 505–509.
- [58] Melzer TR, Watts R, MacAskill MR, Pearson JF, Rueger S, Pitcher TL, *et al.* Arterial spin labelling reveals an abnormal cerebral perfusion pattern in Parkinson's disease. *Brain* 2011, 134: 845–855.
- [59] Feigin A, Fukuda M, Dhawan V, Przedborski S, Jackson-Lewis V, Mentis MJ, *et al.* Metabolic correlates of levodopa response in Parkinson's disease. *Neurology* 2001, 57: 2083–2088.
- [60] Hilker R, Voges J, Thiel A, Ghaemi M, Herholz K, Sturm V, *et al.* Deep brain stimulation of the subthalamic nucleus versus levodopa challenge in Parkinson's disease: measuring the on- and off-conditions with FDG-PET. *J Neural Transm* 2002, 109: 1257–1264.
- [61] Hirano S, Asanuma K, Ma Y, Tang C, Feigin A, Dhawan V, *et al.* Dissociation of metabolic and neurovascular responses to levodopa in the treatment of Parkinson's disease. *J Neurosci* 2008, 28: 4201–4209.
- [62] Krack P, Batir A, Van Blercom N, Chabardes S, Fraix V, Ardouin C, *et al.* Five-year follow-up of bilateral stimulation of the subthalamic nucleus in advanced Parkinson's disease. *The New England journal of medicine* 2003, 349: 1925–1934.
- [63] Follett KA, Weaver FM, Stern M, Hur K, Harris CL, Luo P, *et al.* Pallidal versus subthalamic deep-brain stimulation for Parkinson's disease. *N Engl J Med* 2010, 362: 2077–2091.
- [64] Fasano A, Daniele A, Albanese A. Treatment of motor and non-motor features of Parkinson's disease with deep brain stimulation. *Lancet Neurol* 2012, 11: 429–442.
- [65] Payoux P, Remy P, Miloudi M, Houeto JL, Stadler C, Bejjani BP, *et al.* Contrasting changes in cortical activation induced by acute high-frequency stimulation within the globus pallidus in Parkinson's disease. *J Cereb Blood Flow Metab* 2009, 29: 235–243.
- [66] Fukuda M, Barnes A, Simon ES, Holmes A, Dhawan V, Giladi N, *et al.* Thalamic stimulation for parkinsonian tremor: correlation between regional cerebral blood flow and physiological tremor characteristics. *Neuroimage* 2004, 21: 608–615.
- [67] Asanuma K, Tang C, Ma Y, Dhawan V, Mattis P, Edwards C, *et al.* Network modulation in the treatment of Parkinson's disease. *Brain* 2006, 129: 2667–2678.
- [68] Trost M, Su PC, Barnes A, Su SL, Yen RF, Tseng HM, *et al.* Evolving metabolic changes during the first postoperative year after subthalamotomy. *J Neurosurg* 2003, 99: 872–878.
- [69] Wang J, Ma Y, Huang Z, Sun B, Guan Y, Zuo C. Modulation of metabolic brain function by bilateral subthalamic nucleus stimulation in the treatment of Parkinson's disease. *J Neurol* 2010, 257: 72–78.
- [70] Karimi M, Golchin N, Tabbal SD, Hershey T, Videen TO, Wu J, *et al.* Subthalamic nucleus stimulation-induced regional blood flow responses correlate with improvement of motor signs in Parkinson disease. *Brain* 2008, 131: 2710–2719.
- [71] Geday J, Ostergaard K, Johnsen E, Gjedde A. STN-stimulation in Parkinson's disease restores striatal inhibition of thalamocortical projection. *Hum Brain Mapp* 2009, 30: 112–121.
- [72] Sestini S, Ramat S, Formiconi AR, Ammannati F, Sorbi S, Pupi A. Brain networks underlying the clinical effects of long-term subthalamic stimulation for Parkinson's disease: a 4-year follow-up study with rCBF SPECT. *J Nucl Med* 2005, 46: 1444–1454.
- [73] Limousin P, Greene J, Pollak P, Rothwell J, Benabid AL, Frackowiak R. Changes in cerebral activity pattern due to subthalamic nucleus or internal pallidum stimulation in Parkinson's disease. *Ann Neurol* 1997, 42: 283–291.
- [74] Thobois S, Hotton GR, Pinto S, Wilkinson L, Limousin-Dowsey P, Brooks DJ, *et al.* STN stimulation alters pallidal-frontal coupling during response selection under competition. *J Cereb Blood Flow Metab* 2007, 27: 1173–1184.
- [75] Ballanger B, Lozano AM, Moro E, van Eimeren T, Hamani C, Chen R, *et al.* Cerebral blood flow changes induced by pedunculopontine nucleus stimulation in patients with advanced Parkinson's disease: A [(15)O] H(2)O PET study. *Hum Brain Mapp* 2009, 30: 3901–3909.
- [76] Alessandro S, Ceravolo R, Brusa L, Pierantozzi M, Costa A, Galati S, *et al.* Non-motor functions in parkinsonian patients implanted in the pedunculopontine nucleus: focus on sleep and cognitive domains. *J Neurol Sci* 2010, 289: 44–48.

Small-animal PET demonstrates brain metabolic change after using bevacizumab in a rat model of cerebral ischemic injury

Ying Dong^{1,#}, Fahuan Song^{2,3,4,5,#}, Jianjuan Ma¹, Xuexin He¹, Said Amer⁶, Weizhong Gu⁷, Mei Tian^{2,3,4,5}

¹Department of Oncology, ²Department of Nuclear Medicine, The Second Affiliated Hospital of Zhejiang University School of Medicine, Hangzhou 310009, China

³Zhejiang University Medical PET Center, ⁴Institute of Nuclear Medicine and Molecular Imaging of Zhejiang University, Hangzhou 310009, China

⁵Key Laboratory of Medical Molecular Imaging of Zhejiang Province, Hangzhou 310009, China

⁶Department of Zoology, Faculty of Science, Kafr El Sheikh University, Kafr el-Sheikh, Egypt

⁷Department of Pathology, The Children's Hospital of Zhejiang University School of Medicine, Hangzhou 310003, China

#These authors contributed equally to this work.

Corresponding author: Mei Tian. E-mail: meitian@zju.edu.cn

© Shanghai Institutes for Biological Sciences, CAS and Springer-Verlag Berlin Heidelberg 2014

ABSTRACT

To evaluate the effect of bevacizumab on cerebral ischemia, we used 2-deoxy-2-¹⁸F-fluoro-*D*-glucose (¹⁸F-FDG) small-animal positron emission tomography (PET) in the middle cerebral artery occlusion (MCAO) rat model. After baseline neurologic function tests and PET studies, MCAO Sprague-Dawley rats received bevacizumab or normal saline (controls). Weekly PET imaging and neurologic function tests showed that the ¹⁸F-FDG accumulation in the bevacizumab group was similar to that in the controls during the first 2 weeks, but lower than in controls at weeks 3 and 4. However, no difference was found in neurological scores between the groups. The number of von Willebrand factor-positive cells in the bevacizumab group was lower than that in controls. The expression of vascular endothelial growth factor was higher than in controls at week 4. These results suggested that bevacizumab does not influence functional recovery in this model of cerebral ischemia during a 4-week period, but inhibits vascular formation and metabolic recovery, which may be considered in cancer patients with a recent ischemic stroke.

Keywords: cerebral ischemia; bevacizumab; positron emission tomography; cancer

INTRODUCTION

Cerebrovascular disease (CVD) and cancer are the top two causes of morbidity and mortality in aging populations^[1-3]. Studies have shown that CVD is typically associated with ischemic stroke^[4]. Ischemic stroke featuring functional disturbance and morphological damage of brain is caused by CVD, which affects the brain blood supply and leads to a cascade of metabolic alterations. Clinical presentation of CVD in cancer patients is common: 14.6% of such patients have pathologic evidence of CVD, and 7.4% show clinical symptoms^[5]. Although current therapeutic strategies improve the survival rate and extend the lifetime of cancer patients, increased risk of ischemic stroke is frequently observed in the same individuals^[6]. Therefore, exploring the therapeutic strategies for recent ischemic stroke in cancer patients is a serious challenge.

Currently, anti-angiogenic therapy is widely used in the treatment of various solid cancers. Increasingly, angiogenesis-targeting therapies have been developed by manipulating the vascular endothelial growth factor (VEGF) signaling pathway. Bevacizumab (Avastin, Genentech/Roche, Basel, Switzerland), a recombinant humanized monoclonal antibody against VEGF-A, is the first anti-angiogenic drug approved by the Food and Drug Administration (USA)^[7] for metastatic colorectal cancer^[8],

non-squamous non-small-cell lung cancer^[8], glioblastoma^[9], and metastatic renal cell carcinoma^[10]. Many studies have demonstrated that bevacizumab therapy is associated with an increased risk of gastrointestinal perforation, wound healing complications, hemorrhage, arterial thromboembolism, and reversible posterior leukoencephalopathy syndrome^[11-14]. Therefore, patients with a history of bleeding, cerebrovascular accident, thrombotic disorders, and gastrointestinal perforation were excluded from participation in clinical trials^[11].

Interestingly, our recent clinical observations have shown that significantly increased numbers of elderly cancer patients treated with bevacizumab have a recent ischemic stroke. One study reported that prolonged bevacizumab treatment increases the risk of ischemic stroke^[12]. However, its safety in cancer patients with recent ischemic stroke is still unknown. In the current study, we evaluated the effect of bevacizumab on recent ischemic stroke using a molecular imaging approach.

Positron emission tomography (PET) provides *in vivo* metabolic information based on imaging the distribution of positron-emitting radiopharmaceuticals^[15-16]. PET can not only locate the area of infarction like MRI scanning, but also provide metabolic information, which has led to significant insights into various neurologic disorders, including dementias^[17], movement disorders^[18], epilepsy^[19-20], brain tumors^[21], neurologic infectious, and inflammatory diseases^[22-23]. Furthermore, PET imaging in neurologic disease can detect pathologic changes preceding those seen with structural imaging techniques and even clinical symptoms^[24]. 2-deoxy-2-¹⁸F-fluoro-*D*-glucose (¹⁸F-FDG), the most extensively used PET imaging tracer, can detect subtle changes of glucose metabolism after stroke^[26]. In a previous study, we successfully used ¹⁸F-FDG small-animal PET to evaluate the metabolic recovery of the cerebral infarction in an ischemic stroke model^[27]. In this study, we used ¹⁸F-FDG PET to assess the metabolic changes, along with related immunohistochemical and functional changes, in a rat model of cerebral ischemia treated with bevacizumab.

MATERIALS AND METHODS

Animal and Experimental Design

Eight adult male Sprague-Dawley rats weighing 240–270 g

were randomly assigned into two equal groups: bevacizumab treatment and control groups. All animals underwent reperfusion at 90 min after middle cerebral artery occlusion (MCAO). Rats in the treatment group were administered bevacizumab (Avastin, Genentech/Roche Inc., South San Francisco, CA) *via* tail vein at 5 mg/kg on the day after MCAO. Similarly, all rats in the control group were administered normal saline (NS) in the same way. All rats underwent neurologic function testing followed by ¹⁸F-FDG PET scanning on day 1 (before injection) and weeks 1, 2, 3, and 4 (after injection). Immunohistochemical staining was performed immediately after the last ¹⁸F-FDG PET scan. All experiments were performed with the approval of the Institutional Animal Care and Use Committee of Zhejiang University School of Medicine.

Middle Cerebral Artery Occlusion Procedure

MCAO was induced as previously described^[27]. Briefly, animals were anesthetized intraperitoneally with 1.5% pentobarbital sodium (50 mg/kg). Body temperature was maintained at 37 ± 0.5 °C with a warm pad during the procedure. The right common, internal, and external carotid arteries were exposed. A 3-0 monofilament nylon suture with a rounded tip was inserted from the right common carotid into the internal carotid and then advanced 18–20 mm intracranially from the common carotid bifurcation in order to block the origin of the middle cerebral artery. Approximately 90 min after MCAO, reperfusion was allowed by withdrawal of the suture. Then the muscle and skin were sutured with 4-0 nylon. Animals were given buprenorphine (0.05 mg/kg, subcutaneously) every 8 h^[28] for pain palliation during the first 24 h after operation.

Evaluation of Neurological Deficits

Animals were subjected to a weekly behavioral test for 4 weeks, using the Garcia neurological grading method^[29]. This evaluation is a composite of spontaneous activity (abnormal movement), climbing, forepaw stretching, symmetry in the movement of four limbs, proprioception, and response to vibrissae touch. The score is the sum of the six individual test scores and ranges from 3 to 18. A score of 3 represents the most severe behavioral deficits and 18 means normal behavior. Rats with scores ranging from 7 to 12 were used. Investigators were blinded to the animal group to avoid the bias effect.

PET Scanning and Image Analysis

Rats were anesthetized with isoflurane (2%) and administered ~18.5 MBq (500 mCi) of ^{18}F -FDG *via* tail vein just before bevacizumab or NS injection and at weeks 1, 2, 3, and 4 later. PET images were acquired with a microPET R4 scanner (Siemens Medical Solutions, Munich, Germany) for 10 min static acquisition at 40 min after ^{18}F -FDG injection. Anesthesia was maintained during data acquisition. The images were reconstructed with a modified back-projection algorithm. ^{18}F -FDG uptake was calculated as the percentage of injected dose per gram of tissue, using the AMIDE software package (version 9.2; Stanford University, Santa Clara County, CA). To assess the metabolic changes induced by MCAO, regions of interest (ROIs) 2 mm in diameter were identified in coronal images. The lesion-to-homologous contralateral normal region (L/N) ratios were calculated according to the following formula: L/N ratio = mean counts per pixel of right lesion ROI/mean counts per pixel of contralateral normal area. To assess the therapeutic responses, we calculated the percentage change of L/N ratios according to the following formula: % change of L/N ratio = (L/N ratio – baseline L/N ratio) / baseline L/N ratio. The L/N ratio on day 1 was set as the baseline. The average radioactivity level within the infarct was obtained from the mean pixel values, normalized to that of non-ischemic cortex, and expressed as a percentage.

Immunohistochemical Staining

Immunohistochemical investigation was done to determine the potential effect of bevacizumab on angiogenesis. At the end of week 4, the rats were deeply anesthetized after the last PET scan and perfused transcardially with 0.9% saline followed by 4% ice-chilled paraformaldehyde in PBS (pH 7.4). The brain was immediately removed, sliced, and immersed in the same fixative for 24 h. After that, the 5–10 mm slices were washed in dH_2O for 30 min, dehydrated in ascending ethanols, cleared in xylene, and embedded in paraffin wax. Serial sections were cut at 4 μm throughout the ischemic area, and stained using the EnVisionTM two-step protocol with high-temperature antigen retrieval. The slides were incubated with 3% H_2O_2 for 10 min and rinsed 3 times in PBS for 5 min. Sections were permeabilized with 0.04% Triton X-100, blocked with 10% normal goat serum in PBS for 1 h, and incubated overnight in a

humidified chamber at 4°C with the primary antibodies rabbit polyclonal antibody against VEGF (1:400 dilution; EMD Millipore, Billerica, MA) and rabbit polyclonal antibody against von Willebrand factor (vWF) (1:200 dilution; DAKO, Glostrup, Denmark). The sections were rinsed 3 times with PBS for 10 min each and treated with HRP-conjugated secondary antiserum (DAKO EnVisionTM kit) for 30 min at 37°C. Then the stained sections were washed thoroughly and developed by 0.05% diaminobenzidine with 0.03% H_2O_2 for 3–5 min until a brown reaction product was observed. The number of cells positively-stained for vWF in 5 microscope fields (469 μm × 351 μm) was counted. Hotspots on the section were selected at ×100 magnification in order to evaluate the average integrated optical density (IOD) of VEGF. Individual measurements were then made at ×200 (BX60, Olympus, Japan). Images (5 fields/section, 1 section/animal) were digitized with a camera. The IOD values for VEGF were obtained using Image-ProPlus 5.0 software (Media Cybernetics, Silver Spring, MD).

Statistical Analysis

Data are expressed as mean ± SEM. The independent sample-*t* test was used to evaluate functional recovery, the PET index, and immunohistochemically-positive cells. Statistical analyses were performed with SPSS software (version 15.0, SPSS Inc, Armonk, NY). Values of *P* < 0.05 were considered statistically significant.

RESULTS

Influence of Bevacizumab on Functional Recovery

No significant difference in neurological score was detected between the groups at each time point of the 4-week experimental observation (Fig. 1), suggesting that bevacizumab does not affect functional recovery.

Changes in Glucose Metabolism

The rats were studied using ^{18}F -FDG PET in order to document whether bevacizumab influences glucose metabolism. The scans allowed the visualization (Fig. 2) and quantification (Fig. 3) of glucose metabolism throughout the brain at each time point. Semi-quantitative measurement of ^{18}F -FDG radioactivity in the ischemic area demonstrated no significant differences in the percentage

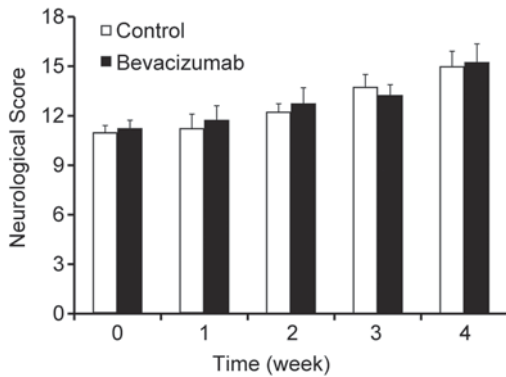


Fig. 1. Neurological scores before and after bevacizumab treatment.

change of the L/N ratio between the two groups on day 1 (before bevacizumab or NS injection) and at weeks 1 and 2 after MCAO. However, the percentage change in the bevacizumab-treated group was significantly lower than that in the NS group at week 3 (0.46 ± 1.15 vs 14.80 ± 2.33 ; $P < 0.05$) and week 4 (6.48 ± 1.91 vs 14.64 ± 0.89 ; $P < 0.05$) (Fig. 3), indicating that bevacizumab reduces glucose metabolism in the ischemic area.

Immunohistochemistry

The results showed that the number of vWF-positive cells in the bevacizumab group was lower than that in the NS

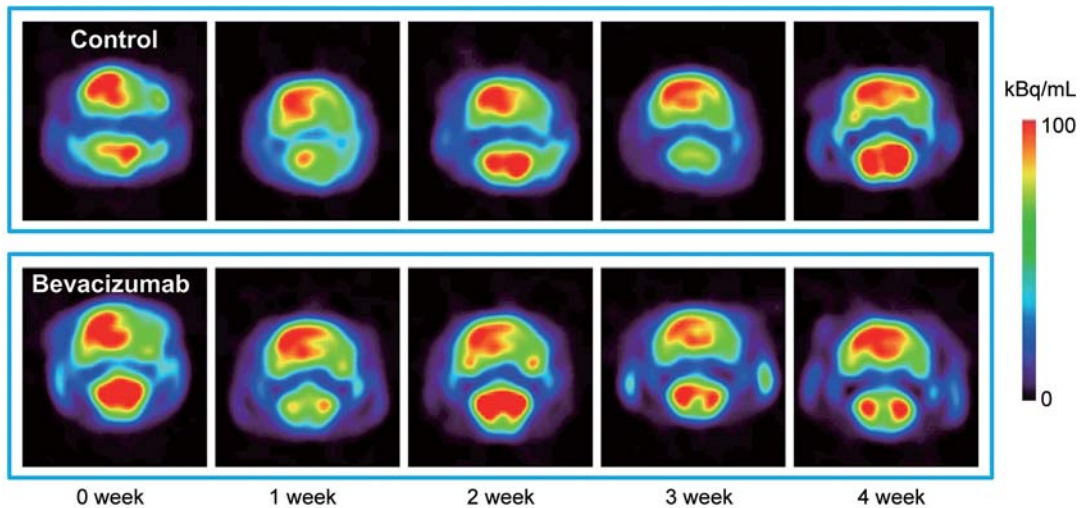


Fig. 2. Serial PET images demonstrating metabolic recovery after MCAO in rats after bevacizumab compared to the control group. Images show the brain in coronal view. Scale indicates signal intensity.

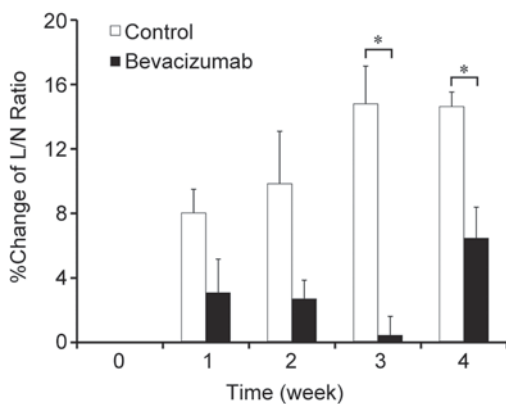


Fig. 3. Semiquantitative analysis of variance of glucose metabolism in each group (shown as % change of L/N ratio at each time point). * $P < 0.05$.

group (7.05 ± 0.43 vs 8.67 ± 0.32 ; $P < 0.01$) (Fig. 4). The IOD of VEGF in the bevacizumab group was higher than that in the NS group (15.22 ± 0.80 vs 12.83 ± 0.76 ; $P < 0.05$) (Fig. 4).

DISCUSSION

Both ischemic stroke and cancer are leading causes of morbidity and mortality among the aged worldwide. Stroke severely impacts cancer patients, while cancer increases the risk of stroke^[30]. CVD occurs commonly in cancer patients, ~15% of whom experience a thromboembolic event during the clinical course^[5].

In the present study, we evaluated the effect of bevacizumab on neurogenic recovery after a recent stroke

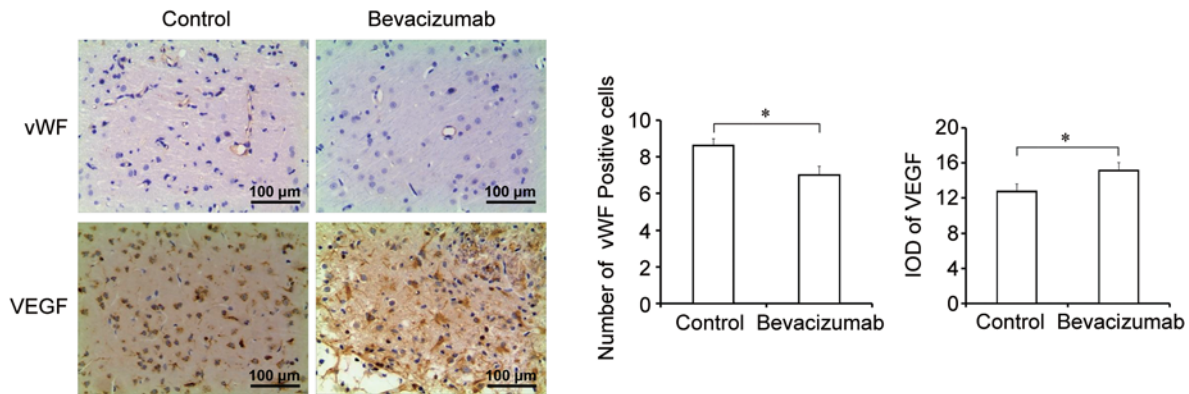


Fig. 4. vWF and VEGF immunohistochemistry. Left, photomicrographs ($\times 200$) of immunohistochemical staining for vWF and VEGF (brown cells) in the ischemic region in bevacizumab-treated and normal saline-injected animals (control). Middle, number of vWF-positive cells after 4 weeks of bevacizumab treatment ($*P < 0.01$). Right, integrated optical density (IOD) of VEGF after 4 weeks of bevacizumab treatment ($*P < 0.05$).

using serial ^{18}F -FDG PET scans combined with neurologic function testing and immunohistochemical investigation. Our results demonstrated that bevacizumab had no effect on functional recovery after a recent ischemic stroke; however, it did suppress the recovery of cerebral glucose metabolism. Immunohistology confirmed a decrease in angiogenesis in the bevacizumab-treated group.

Our study showed no significant difference between the two groups in terms of glucose metabolic changes in the area of infarction during the first 2 weeks after MCAO. However, in the later stage (weeks 3 and 4), significantly lower ^{18}F -FDG accumulation was observed in the infarct in the bevacizumab-treated group than in the control group. These results indicated that bevacizumab does not significantly inhibit metabolism immediately after MCAO and in the early stage (weeks 1 and 2), but does significantly inhibit it in the later stage (weeks 3 and 4), especially at week 3. Interestingly, at week 4, the bevacizumab-treated group showed increased ^{18}F -FDG accumulation compared to that in week 3, indicating that the inhibitory effect of bevacizumab declines over time. These results are consistent with the instructions for bevacizumab, namely, it is safer to do surgery 4 weeks after treatment.

In behavioral tests, there was no significant difference in neurological score between the two groups at any time point, suggesting that bevacizumab does not affect functional recovery. These results demonstrated that bevacizumab is relatively safe in the first 4 weeks in a rat model of cerebral ischemia.

vWF, released upon perturbation of endothelial cells, is a predictive biomarker of vascular injury. VEGF has the capacity to induce physiological and pathological angiogenesis, while bevacizumab can decrease this capacity by preventing the interaction of VEGF with its receptors on the surface of endothelial cells^[31]. In the current study, immunohistochemical analysis of the injured brain showed significantly lower expression of vWF but higher expression of VEGF in the treatment group than in the control group. This result indicated that bevacizumab has a strong effect on decreasing the number of vessels, consistent with a previous study^[32]. However, other cancer studies^[33-34] differ from ours, in that bevacizumab was reported to reduce the high expression of VEGF. We consider that this might be due to the much lower level of VEGF expression in the ischemic brain compared to that in a tumor. In a recent study on candesartan, a drug currently used to treat hypertension, VEGF expression was found to significantly increase at 2 weeks after MCAO compared to baseline^[35]. Ischemic neurons increase VEGF expression by activating astrocytes, and the increase usually occurs within the first few hours of ischemic stroke^[36]. Since the endpoint of our study was 28 days after bevacizumab administration, its effect on VEGF was assumed to be decreased after its biological half-life of ~ 5 days^[37,38].

In conclusion, the present results indicate that attention should be paid when using bevacizumab and careful management should be provided for cancer patients

with recent ischemic stroke. Although the present study was done to evaluate the safety of bevacizumab in cancer patients with recent stroke using a cerebral ischemic rat model, there are several limitations in terms of sample size, dose, investigation time points, and duration of follow-up.

ACKNOWLEDGEMENTS

This work was supported by grants from the National Basic Research Development Program of China (2014CB744505), the National Natural Science Foundation of China (81101023, 81173468, and 81101835), Natural Science Foundation of Zhejiang Province, China (Z2110230 and Y2110299), the Health Bureau of Zhejiang Province, China (2010ZA075 and 2011ZDA013), and the Science and Technology Bureau of Zhejiang Province, China (2012R10040).

Received date: 2014-04-30; Accepted date: 2014-06-21

REFERENCES

- [1] Tang Z, Zhou T, Luo Y, Xie C, Huo D, Tao L, *et al.* Risk factors for cerebrovascular disease mortality among the elderly in Beijing: a competing risk analysis. *PLoS One* 2014, 9: e87884.
- [2] He J, Gu D, Wu X, Reynolds K, Duan X, Yao C, *et al.* Major causes of death among men and women in China. *N Engl J Med* 2005, 353: 1124–1134.
- [3] Feigin VL, Lawes CM, Bennett DA, Barker-Collo SL, Parag V. Worldwide stroke incidence and early case fatality reported in 56 population-based studies: a systematic review. *Lancet Neurol* 2009, 8: 355–369.
- [4] Pappachan J, Kirkham FJ. Cerebrovascular disease and stroke. *Arch Dis Child* 2008, 93: 890–898.
- [5] Graus F, Rogers LR, Posner JB. Cerebrovascular complications in patients with cancer. *Medicine (Baltimore)* 1985, 64: 16–35.
- [6] Kim SJ, Park JH, Lee MJ, Park YG, Ahn MJ, Bang OY. Clues to occult cancer in patients with ischemic stroke. *PLoS One* 2012, 7: e44959.
- [7] Ferrara N, Hillan KJ, Gerber HP, Novotny W. Discovery and development of bevacizumab, an anti-VEGF antibody for treating cancer. *Nat Rev Drug Discov* 2004, 3: 391–400.
- [8] The FDA approves drugs for colorectal cancer, lung cancer. *FDA Consum* 2007, 41: 5.
- [9] Cloughesy T. FDA accelerated approval benefits glioblastoma. *Lancet Oncol* 2010, 11: 1120.
- [10] Summers J, Cohen MH, Keegan P, Pazdur R. FDA drug approval summary: bevacizumab plus interferon for advanced renal cell carcinoma. *Oncologist* 2010, 15: 104–111.
- [11] Hershman DL, Wright JD, Lim E, Buono DL, Tsai WY, Neugut AI. Contraindicated use of bevacizumab and toxicity in elderly patients with cancer. *J Clin Oncol* 2013, 31: 3592–3599.
- [12] Scappaticci FA, Skillings JR, Holden SN, Gerber HP, Miller K, Kabbinavar F, *et al.* Arterial thromboembolic events in patients with metastatic carcinoma treated with chemotherapy and bevacizumab. *J Natl Cancer Inst* 2007, 99: 1232–1239.
- [13] Vaughn C, Zhang L, Schiff D. Reversible posterior leukoencephalopathy syndrome in cancer. *Curr Oncol Rep* 2008, 10: 86–91.
- [14] Marinella MA, Markert RJ. Reversible posterior leukoencephalopathy syndrome associated with anticancer drugs. *Intern Med J* 2009, 39: 826–834.
- [15] Phelps ME, Hoffman EJ, Mullani NA, Ter-Pogossian MM. Application of annihilation coincidence detection to transaxial reconstruction tomography. *J Nucl Med* 1975, 16: 210–224.
- [16] Gallagher BM, Fowler JS, Gutterson NI, MacGregor RR, Wan CN, Wolf AP. Metabolic trapping as a principle of radiopharmaceutical design: some factors responsible for the biodistribution of [¹⁸F] 2-deoxy-2-fluoro-D-glucose. *J Nucl Med* 1978, 19: 1154–1161.
- [17] Tatsch K. Positron emission tomography in diagnosis and differential diagnosis of Parkinson's disease. *Neurodegener Dis* 2010, 7: 330–340.
- [18] Bohnen NI, Frey KA. The role of positron emission tomography imaging in movement disorders. *Neuroimaging Clin N Am* 2003, 13: 791–803.
- [19] Kim YK, Lee DS, Lee SK, Kim SK, Chung CK, Chang KH, *et al.* Differential features of metabolic abnormalities between medial and lateral temporal lobe epilepsy: quantitative analysis of (18)F-FDG PET using SPM. *J Nucl Med* 2003, 44: 1006–1012.
- [20] Herholz K, Heiss WD. Positron emission tomography in clinical neurology. *Mol Imaging Biol* 2004, 6: 239–269.
- [21] Kosaka N, Tsuchida T, Uematsu H, Kimura H, Okazawa H, Itoh H. 18F-FDG PET of common enhancing malignant brain tumors. *AJR Am J Roentgenol* 2008, 190: W365–369.
- [22] Hong YT, Veenith T, Dewar D, Outtrim JG, Mani V, Williams C, *et al.* Amyloid imaging with carbon 11-labeled Pittsburgh Compound B for traumatic brain injury. *JAMA Neurol* 2014, 71: 23–31.
- [23] Cash SS, Larvie M, Dalmau J. Case records of the Massachusetts General Hospital. Case 34-2011: A 75-year-old man with memory loss and partial seizures. *N Engl J Med* 2011, 365: 1825–1833.
- [24] Singhal T. Positron emission tomography applications in clinical neurology. *Semin Neurol* 2012, 32: 421–431.
- [25] Phelps ME. Positron emission tomography provides molecular imaging of biological processes. *Proc Natl Acad Sci U S A* 2000, 97: 9226–9233.

- [26] Shalhoub J, Oskrochi Y, Davies AH, Owen DR. Clinical assessment of carotid atherosclerosis inflammation by positron emission tomography. *Curr Mol Med* 2013, 13: 1646–1652.
- [27] Wang J, Chao F, Han F, Zhang G, Xi Q, Li J, *et al.* PET demonstrates functional recovery after transplantation of induced pluripotent stem cells in a rat model of cerebral ischemic injury. *J Nucl Med* 2013, 54: 785–792.
- [28] Curtin LI, Grakowsky JA, Suarez M, Thompson AC, DiPirro JM, Martin LB, *et al.* Evaluation of buprenorphine in a postoperative pain model in rats. *Comp Med* 2009, 59: 60–71.
- [29] Garcia JH, Wagner S, Liu KF, Hu XJ. Neurological deficit and extent of neuronal necrosis attributable to middle cerebral artery occlusion in rats. Statistical validation. *Stroke* 1995, 26: 627–634; discussion 635.
- [30] Bang OY, Seok JM, Kim SG, Hong JM, Kim HY, Lee J, *et al.* Ischemic stroke and cancer: stroke severely impacts cancer patients, while cancer increases the number of strokes. *J Clin Neurol* 2011, 7: 53–59.
- [31] Chowdhary S, Chamberlain M. Bevacizumab for the treatment of glioblastoma. *Expert Rev Neurother* 2013, 13: 937–949.
- [32] Wang CJ, Huang KE, Sun YC, Yang YJ, Ko JY, Weng LH, *et al.* VEGF modulates angiogenesis and osteogenesis in shockwave-promoted fracture healing in rabbits. *J Surg Res* 2011, 171: 114–119.
- [33] Yang H, Jager MJ, Grossniklaus HE. Bevacizumab suppression of establishment of micrometastases in experimental ocular melanoma. *Invest Ophthalmol Vis Sci* 2010, 51: 2835–2842.
- [34] Lu Y, Zhou N, Huang X, Cheng JW, Li FQ, Wei RL, *et al.* Effect of intravitreal injection of bevacizumab-chitosan nanoparticles on retina of diabetic rats. *Int J Ophthalmol* 2014, 7: 1–7.
- [35] Ishrat T, Pillai B, Soliman S, Fouda AY, Kozak A, Johnson MH, *et al.* Low-dose candesartan enhances molecular mediators of neuroplasticity and subsequent functional recovery after ischemic stroke in rats. *Mol Neurobiol* 2014.
- [36] Li YN, Pan R, Qin XJ, Yang WL, Qi Z, Liu W, *et al.* Ischemic neurons activate astrocytes to disrupt endothelial barrier via increasing VEGF expression. *J Neurochem* 2014, 129: 120–129.
- [37] Stewart MW. Predicted biologic activity of intravitreal bevacizumab. *Retina* 2007, 27: 1196–1200.
- [38] Sinapis CI, Routsias JG, Sinapis AI, Sinapis DI, Agrogiannis GD, Pantopoulou A, *et al.* Pharmacokinetics of intravitreal bevacizumab (Avastin(R)) in rabbits. *Clin Ophthalmol* 2011, 5: 697–704.

Paradoxical reduction of cerebral blood flow after acetazolamide loading: a hemodynamic and metabolic study with ^{15}O PET

Tadashi Watabe^{1,5}, Eku Shimosegawa^{2,5,7}, Hiroki Kato^{2,5}, Kayako Isohashi^{2,5}, Mana Ishibashi^{2,5}, Mitsuaki Tatsumi⁶, Kazuo Kitagawa^{3,7}, Toshiyuki Fujinaka^{4,7}, Toshiki Yoshimine^{4,7}, Jun Hatazawa^{2,5,7}

¹Department of Molecular Imaging in Medicine, ²Department of Nuclear Medicine and Tracer Kinetics, ³Department of Neurology, ⁴Department of Neurosurgery, Osaka University Graduate School of Medicine, Suita, Japan

⁵Department of Nuclear Medicine, ⁶Department of Radiology, ⁷Stroke Center, Osaka University Hospital, Suita, Japan

Corresponding author: Tadashi Watabe. E-mail: twatabe@mi.med.osaka-u.ac.jp

© Shanghai Institutes for Biological Sciences, CAS and Springer-Verlag Berlin Heidelberg 2014

ABSTRACT

Paradoxical reduction of cerebral blood flow (CBF) after administration of the vasodilator acetazolamide is the most severe stage of cerebrovascular reactivity failure and is often associated with an increased oxygen extraction fraction (OEF). In this study, we aimed to reveal the mechanism underlying this phenomenon by focusing on the ratio of CBF to cerebral blood volume (CBV) as a marker of regional cerebral perfusion pressure (CPP). In 37 patients with unilateral internal carotid or middle cerebral arterial (MCA) steno-occlusive disease and 8 normal controls, the baseline CBF (CBF_b), CBV, OEF, cerebral oxygen metabolic rate (CMRO_2), and CBF after acetazolamide loading in the anterior and posterior MCA territories were measured by ^{15}O positron emission tomography. Paradoxical CBF reduction was found in 28 of 74 regions (18 of 37 patients) in the ipsilateral hemisphere. High CBF_b (>47.6 mL/100 mL/min, $n = 7$) was associated with normal CBF_b/CBV , increased CBV, decreased OEF, and normal CMRO_2 . Low CBF_b (<31.8 mL/100 mL/min, $n = 9$) was associated with decreased CBF_b/CBV , increased CBV, increased OEF, and decreased CMRO_2 . These findings demonstrated that paradoxical CBF reduction is not always associated with reduction of CPP, but partly includes high- CBF_b regions with normal CPP, which has not been described in previous studies.

Keywords: acetazolamide; cerebral blood flow; paradoxical reduction; positron emission tomography; vasodilatation

INTRODUCTION

Paradoxical reduction of cerebral blood flow (CBF) after administration of vasodilators, termed the “intracerebral steal phenomenon”, was originally described in the core of an acute brain infarct after CO_2 inhalation in a cat experimental model^[1,2]. The vasodilator acetazolamide (ACZ) also reduces CBF in the core of the acute ischemic region after experimental occlusion of the middle cerebral artery (MCA). Expansion of the infarct volume is higher in cats given ACZ than in controls^[3]. These studies indicate that administration of vasodilators for the recovery of CBF in acute brain ischemia is harmful.

A paradoxical CBF reduction has also been documented in patients with steno-occlusive atherosclerotic carotid artery disease^[4-6], and is associated with poor collateral circulation^[7]. Okazawa *et al.* demonstrated that patients with paradoxical CBF reduction show a significantly increased oxygen extraction fraction (OEF), a state of misery perfusion^[8,9]. These studies indicated that the paradoxical CBF reduction is a sign of severe hemodynamic failure due to a reduction of cerebral perfusion pressure (CPP) in patients with chronic ischemic disease.

Regional CPP is not measurable by non-invasive means in patients. However, the regional ratio of CBF to

cerebral blood volume (CBV) has been suggested to be an index of regional CPP^[10,11]. Schumann *et al.* evaluated the CBF/CBV ratio during global CPP manipulation by varying mean arterial blood pressure (MABP) in the anesthetized baboon^[12], and found that the CBF/CBV ratio is significantly correlated with MABP. As the CPP is a function of MABP and intracranial pressure, regional CBF/CBV is considered to be an index of regional CPP in the cerebral parenchyma when intracranial pressure is not pathologically altered^[12].

In the present study, we tested the hypothesis that the paradoxical CBF reduction after ACZ loading is associated with a reduction of regional CPP by evaluating the CBF/CBV ratio in patients with internal carotid artery (ICA)/MCA steno-occlusive disease by means of ¹⁵O positron emission tomography (PET).

PARTICIPANTS AND METHODS

Participants

This retrospective study was conducted in 37 patients (29 men, 8 women; age, 64.9 ± 10.3 years) who were examined for evaluation of hemodynamic status at Osaka University Hospital from August 2007 to January 2011. The clinical information of the patients is summarized in Table 1. All patients had severe stenosis or occlusion of the ICA or MCA on one side. Digital subtraction angiography or magnetic resonance (MR) angiography revealed ICA

occlusion in 11 patients, severe stenosis of the ICA in 10, MCA occlusion in 6, and severe stenosis of the MCA in 10. The severity of the ICA stenosis was >80% by the North American Symptomatic Carotid Endarterectomy Trial criteria^[13]. Ten patients had a minor stroke, 12 had a transient ischemic attack (TIA), and 15 were asymptomatic. All PET studies were performed at least one month after the last ischemic episode.

Eight healthy volunteers (4 men, 4 women; 50.5 ± 4.2 years) were included as normal controls. The criteria for the controls were (1) absence of a history of disease, (2) absence of smoking and alcohol habits, and (3) no significant brain abnormalities by MR imaging and MR angiography.

This study was approved by the Ethics Committee of Osaka University Hospital. Written informed consent was given by all participants.

PET Measurements

PET images were obtained in 3-D mode using the SET-3000 GCT/X scanner (Shimadzu Corp., Kyoto, Japan). The intrinsic spatial resolution was 3.5-mm full-width at half maximum (FWHM) in-plane and 4.2-mm FWHM axially. Transmission scanning with a ¹³⁷Cs point source was performed for attenuation correction. The PET images were reconstructed by a filtered-back projection method after 3D Gaussian smoothing with a 6-mm FWHM. Scattered

Table 1. Characteristics of the 37 patients enrolled in the study

		Number
Characteristics	Age (years)	64.9 ± 10.3
	Sex (male/female)	29 / 8
Angiography	ICA occlusion/stenosis	11 / 10
	MCA occlusion/stenosis	6 / 10
Symptoms	Minor stroke	10
	TIA	12
	Asymptomatic	15
	Interval between the last symptom and PET (months)	23.5 ± 34.2
Underlying disease	Hypertension	25
	Diabetes mellitus	11
	Dyslipidemia	21

ICA, internal carotid artery; MCA, middle cerebral artery; PET, positron emission tomography; TIA, transient ischemic attack.

radiation was corrected by the hybrid dual-energy window method combined with a convolution-subtraction method, and estimation of the true scatter-free component of the standard photopeak window was performed on a sonographic basis^[14,15].

The baseline CBV, the baseline cerebral metabolic rate of oxygen (CMRO_2), the OEF at baseline, the CBF_b , and the CBF after ACZ loading (CBF_{acz}) were measured following C^{15}O and $^{15}\text{O}_2$ gas inhalation, and H_2^{15}O injection^[15]. A cannula was inserted into the radial artery for arterial input. CBV measurement was performed with 4-min static scanning after 1 min of continuous inhalation of C^{15}O gas (3.0 GBq/min) and a 3-min interval^[16]. Arterial blood was collected 3 times during the scanning to measure the whole-blood radioactivity. OEF was measured by 3-min scanning starting simultaneously with 1.5-min $^{15}\text{O}_2$ gas bolus inhalation (1.0 GBq/min). Continuous arterial blood sampling was performed using a β -detector system to determine the whole-arterial blood radioactivity. CMRO_2 and OEF were calculated by an autoradiographic method^[16-19]. The CBV data were used to correct for intravascular hemoglobin-bound $^{15}\text{O}_2$ ^[20]. CBF_b was measured by 3 min of scanning started simultaneously with intravenous bolus injection of H_2^{15}O (370 MBq)^[17,21]. Continuous arterial blood sampling was also performed with a β -detector system. Delay and dispersion occurring in the β -detector system were corrected by the methods described previously^[22]. Quantitation of reconstructed PET images by the 3-D mode PET scanner has been validated in a previous report^[15].

At the end of the study protocol, we examined the CBF_{acz} to determine the cerebrovascular reactivity (CVR)^[5]. ACZ (1 g; Diamox®, Sanwa kagaku kenkyusho Co., Ltd, Nagoya, Japan) was slowly injected intravenously for 2 min, and measurement of CBF_{acz} was started 15 min after the injection using the same protocol as for CBF_b .

Arterial O_2 and CO_2 partial pressures (PaO_2 and PaCO_2), pH, hematocrit (Ht), and hemoglobin concentration (Hb) were measured in arterial blood samples. Systemic blood pressure and heart rate were monitored during the PET study. MABP was calculated as $[\text{diastolic BP} + (\text{systolic BP} - \text{diastolic BP}) / 3]$.

Data Analysis

The CBF_b images were transformed to the standard brain

size and shape of a built-in PET template using SPM2 software (Wellcome Trust Centre for Neuroimaging). Parametric maps of CBV, CMRO_2 , OEF, and CBF_{acz} were created with the same parameters as those for CBF_b normalization. The resultant images had the same anatomical format with an isotropic voxel size of 2 mm. Oval regions of interest (ROI: major axis, 45 mm) were placed on the MCA-anterior branch territory (MCA-an) and MCA-posterior branch territory (MCA-po) on 3 sequential cross-sections on both the ipsilateral and the contralateral sides of all parametric images (Fig. 1). Each ROI was confirmed to include no minor infarct region on the co-registered MRI slices. Mean values of the 3 cross-sections in each region were used to evaluate the hemodynamic status. CVR was calculated as the percentage change in the CBF after ACZ administration using the equation: $\text{CVR} = [(\text{CBF}_{\text{acz}} - \text{CBF}_b) / \text{CBF}_b] \times 100\%$. Paradoxical CBF reduction was defined as a negative value of the CVR. The CBF_b/CBV ratio was calculated as an index of the CPP^[10,12]. All regions on the affected side ($n = 74$) were divided into a paradoxical CBF reduction group (group A: $\text{CVR} < 0\%$) and non-paradoxical CBF reduction groups (group B: $\text{CVR} = 0-15\%$ and group C: $\text{CVR} > 15\%$). The CVR threshold of 15% between groups B and C was determined based on previous studies, which set thresholds from 10% to 20%^[23-25]. The CBF_b , CBV, OEF, CMRO_2 , and CBF_b/CBV ratio were compared between the three groups and evaluated in comparison to the controls. The contralateral sides of each group were also compared.

Furthermore, ipsilateral regions showing the paradoxical CBF reduction were tentatively classified into three subgroups according to the CBF_b value (high- CBF_b : $>20\%$ of the mean value in the controls; moderate- CBF_b ;

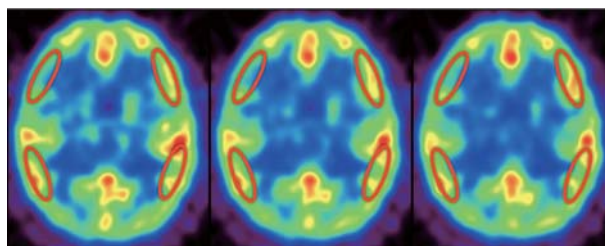


Fig. 1. Locations of regions of interest on three sequential cross-sectional images of baseline cerebral blood flow (22, 24, and 26 mm above the transaxial section with the anterior commissure to the posterior commissure line).

within $\pm 20\%$ of the controls; and low-CBF_b: $< -20\%$ of the controls). The CBV, OEF, CMRO₂, CBF_b/CBV ratio, and CVR values were compared among the ipsilateral and contralateral sides of the three subgroups, and evaluated in comparison to the controls.

Statistical Analysis

Comparisons of the arterial blood gas and MABP data among the three groups (groups A, B, and C) and controls and among the three subgroups of group A were performed using analysis of variance (ANOVA) followed by Tukey's HSD test. Comparisons of PET data among the three groups and among the three subgroups were conducted using the Steel-Dwass test. For each of the three groups or subgroups, comparisons of PET data to the controls were evaluated by the Mann-Whitney test. $P < 0.05$ was considered to denote statistical significance.

RESULTS

The relationships between the CVR and CBF_b in the ipsilateral MCA-an and MCA-po are shown in Fig. 2. Among a total of 74 regions, 28 were classified into group A, 21 into group B, and 25 into group C. In group A, 7, 12, and 9 regions were classified into the high-, moderate-, and low-CBF_b subgroups, respectively.

Comparisons among Groups A, B, and C

The mean values of PaCO₂, MABP, Hb, and Ht are summarized in Table 2. No significant differences were found between each of the three groups and the controls. The MABP after ACZ in group C was increased compared to groups A and B ($P = 0.018$ and $P = 0.012$, respectively). Hb and Ht in group C were higher than those in group A ($P = 0.022$ and $P = 0.031$, respectively).

The mean values of CBF_b, CBV, OEF, CMRO₂, and CBF_b/CBV ratio are shown in Table 3. The bilateral CBF_b in groups B and C were lower than in controls (ipsilateral: $P < 0.001$ and $P < 0.001$, contralateral: $P = 0.044$ and $P = 0.024$, respectively). The ipsilateral CBV in groups A and B were higher than in the controls ($P = 0.011$ and $P = 0.009$, respectively). The bilateral CMRO₂ in groups A, B, and C were lower than in the controls (ipsilateral: $P < 0.001$, $P = 0.002$, and $P < 0.001$; contralateral: $P = 0.006$, $P = 0.003$, and $P = 0.002$, respectively). The ipsilateral CBF_b/CBV ratio in group A and the bilateral CBF_b/CBV ratio in group B were significantly lower than in controls ($P < 0.001$, $P < 0.001$, and $P = 0.001$, respectively).

Comparisons among High-, Moderate-, and Low-CBF_b Subgroups

No significant differences in the physiological parameters were found among the three subgroups (Table 4). The

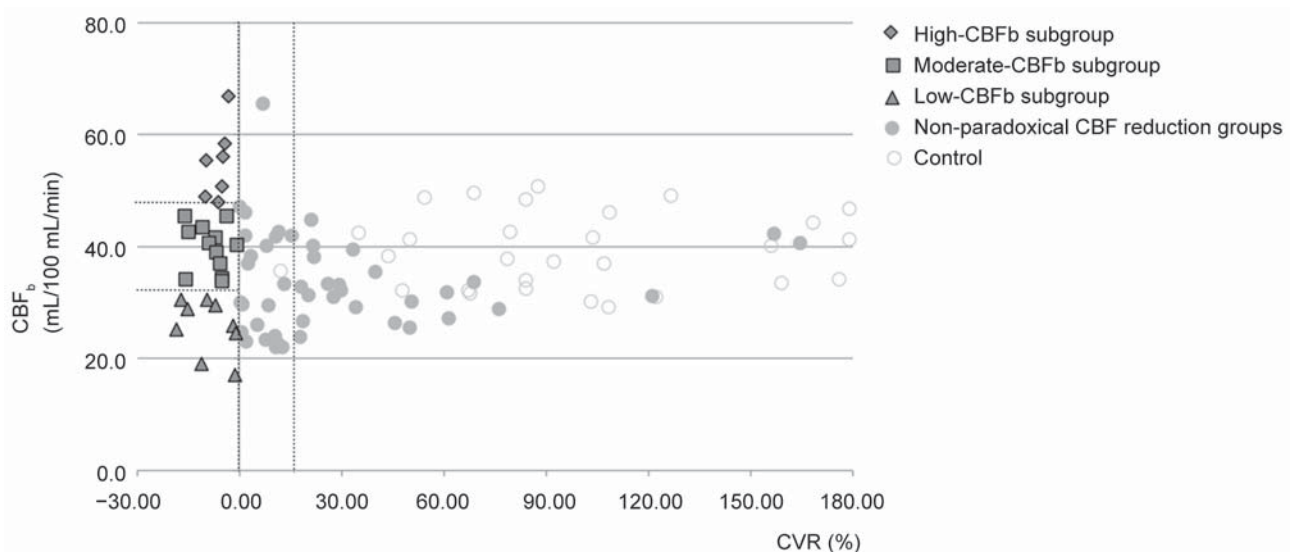


Fig. 2. Relationship between cerebrovascular reactivity (CVR) and baseline cerebral blood flow (CBF_b). The distribution of the paradoxical CBF reduction group was significantly different from the non-paradoxical CBF reduction groups ($P = 0.031$, Mann-Whitney U test).

Table 2. Mean ± SD values of arterial blood gas parameters and blood pressure

	Group A (CVR <0%)	Group B (CVR 0–15%)	Group C (CVR >15%)	Control	<i>P</i> value ^c
PaCO ₂ at baseline (mmHg)	38.8±4.1	38.9±4.1	39.2±2.3	40.1±4.3	0.877
PaCO ₂ after ACZ (mmHg)	36.7±4.7	37.6±4.9	37.7±3.0	39.2±4.2	0.584
MABP at baseline (mmHg)	87.6±9.6	85.9±12.4	95.0±10.2	93.6±10.6	0.072
MABP after ACZ (mmHg)	88.6±11.0 ^a	87.5±12.4 ^A	101.8±12.5 ^{a,A}	97.0±15.2	0.006
Hb (g/dl)	11.9±1.5 ^a	12.8±1.5	13.4±1.4 ^a	12.9±1.3	0.035
Ht (%)	36.7±4.6 ^a	39.4±4.5	41.0±4.0 ^a	39.4±3.8	0.047

ACZ, acetazolamide; CVR, cerebrovascular reactivity; Hb, hemoglobin; Hct, hematocrit; MABP, mean arterial blood pressure; PaCO₂, arterial partial pressure of CO₂. ^aANOVA (analysis of variance), ^a*P* < 0.05 between groups A and C, ^A*P* < 0.05 between groups B and C, Tukey's HSD test.

Table 3. Hemodynamic parameters in the MCA-an and MCA-po regions (mean ± SD)

		Group A (CVR <0%) (<i>n</i> = 28)		Group B (CVR 0–15%) (<i>n</i> = 21)		Group C (CVR >15%) (<i>n</i> = 25)		Control (<i>n</i> = 32)
		Ipsilateral	Contralateral	Ipsilateral	Contralateral	Ipsilateral	Contralateral	
Baseline	CBF _b (mL/100 mL/min)	39.0±12.2	42.3±11.6	33.9±11.2 [†]	36.1±9.6 [‡]	33.3±5.8 [‡]	35.7±5.6 [‡]	39.7±6.4
	CBV (mL/100 mL)	3.62±0.79 ^{b,‡}	2.95±0.58	3.41±0.72 [‡]	3.06±0.50	2.90±0.88 ^b	2.96±0.62	2.91±0.46
	OEF (%)	45.4±7.4	44.3±6.0	45.3±7.6	43.7±7.9	43.5±6.5	42.7±5.8	45.2±5.2
	CMRO ₂ (mL/100 mL/min)	2.52±0.56 [‡]	2.69±0.43 [‡]	2.52±0.64 [‡]	2.60±0.49 [‡]	2.51±0.27 [‡]	2.65±0.36 [‡]	3.07±0.52
	CBF _b /CBV ratio (/min)	11.0±3.3 [‡]	14.5±3.6 ^b	9.9±1.9 ^{a,‡}	11.7±1.8 ^{b,‡}	12.3±3.5 ^a	12.5±2.7	13.8±2.2
After ACZ	CVR (%)	-8.0±5.2 [‡]	35.0±31.4 ^{a,‡}	6.2±4.6 [‡]	36.7±20.2 [‡]	49.3±41.3 [‡]	57.6±43.5 ^{a,‡}	107.3±52.9

ACZ, acetazolamide; an, anterior branch territory; CBF_b, baseline cerebral blood flow; CBV, cerebral blood volume; CMRO₂, cerebral oxygen metabolic rate; CVR, cerebrovascular reactivity; MCA, middle cerebral artery; OEF, oxygen extraction fraction; po, posterior branch territory. ^a*P* < 0.05, ^b*P* < 0.01 by multiple comparison among groups, Steel-Dwass test; [†]*P* < 0.05, [‡]*P* < 0.01 versus control, Mann-Whitney test.

ipsilateral CBV in the high-CBF_b subgroup was higher than that in the moderate- and low-CBF_b subgroups (*P* = 0.030 and 0.034, respectively; Table 5), and the controls (*P* < 0.001). The ipsilateral OEF in the high-CBF_b subgroup was lower than that in the controls (*P* = 0.007), while the ipsilateral OEF in the low-CBF_b subgroup was higher than that in the high-CBF_b subgroup (*P* = 0.002), the moderate-CBF_b subgroup (*P* = 0.034), and the controls (*P* = 0.001)

(Table 5). The ipsilateral CMRO₂ in the low-CBF_b subgroup was lower than that in the high-CBF_b subgroup (*P* = 0.045), the moderate-CBF_b subgroup (*P* = 0.034), and the controls (*P* < 0.001) (Table 5). The ipsilateral CBF_b/CBV ratio in the high-CBF_b subgroup was comparable to the controls while those in the moderate- and low-CBF_b subgroups were significantly lower than in the controls (*P* = 0.007 and *P* < 0.001) (Table 5). In addition, the contralateral CBF_b in the

Table 4. Arterial blood gas parameters and blood pressure in the three subgroups with paradoxical cerebral blood flow reduction (mean ± SD)

	High-CBF _b	Moderate-CBF _b	Low-CBF _b	P value*
PaCO ₂ at baseline (mmHg)	40.8±3.6	38.6±4.6	36.5±4.3	0.270
PaCO ₂ after ACZ (mmHg)	39.3±4.1	36.1±5.0	34.1±5.6	0.242
MABP at baseline (mmHg)	89.4±8.7	87.9±8.8	87.3±10.9	0.931
MABP after ACZ (mmHg)	91.1±5.1	88.7±11.7	90.4±13.2	0.909
Hb (g/dl)	11.4±1.5	12.1±1.5	12.2±1.5	0.685
Ht (%)	35.8±5.0	37.2±4.6	37.4±4.5	0.827

ACZ, acetazolamide; CBF_b, baseline cerebral blood flow; Hb, hemoglobin; Hct, hematocrit; MABP, mean arterial blood pressure; PaCO₂, arterial partial pressure of CO₂. Data were analyzed by ANOVA

Table 5. Hemodynamic parameters in the MCA-an and MCA-po regions of the three subgroups with paradoxical cerebral blood flow reduction (mean ± SD)

		High-CBF _b (n = 7)		Moderate-CBF _b (n = 12)		Low-CBF _b (n = 9)	
		Ipsilateral	Contralateral	Ipsilateral	Contralateral	Ipsilateral	Contralateral
Baseline	CBF _b (mL/100 mL/min)	54.9±6.6 [‡]	55.2±11.9 ^{b‡}	39.8±4.2	42.3±6.9 ^B	25.7±4.9 [‡]	32.3±4.8 ^{b,B,‡}
	CBV (mL/100 mL)	4.41±0.78 ^{a,A,‡}	3.36±0.46 [‡]	3.46±0.59 ^{a,‡}	2.82±0.47	3.22±0.64 ^A	2.79±0.67
	OEF (%)	39.3±5.1 ^{b,‡}	40.7±5.1 ^{a,‡}	44.4±6.7 ^A	44.1±5.9	51.7±4.8 ^{b,A,‡}	47.4±5.7 ^a
	CMRO ₂ (mL/100 mL/min)	2.77±0.54 ^a	2.83±0.51	2.69±0.50 ^A	2.81±0.36	2.11±0.44 ^{a,A,‡}	2.43±0.38 [‡]
	CBF _b /CBV ratio (/min)	13.0±3.8 ^a	17.0±5.6	11.8±2.2 ^{A,‡}	15.1±1.6 ^B	8.4±2.6 ^{a,A,‡}	11.8±1.3 ^{B,‡}
	After ACZ	CVR (%)	-6.2±2.7 [‡]	69.2±43.8 ^{b,a}	-8.3±5.0 [‡]	24.0±14.2 ^{b,‡}	-9.1±6.8 [‡]

ACZ, acetazolamide; an, anterior branch territory; CBF_b, baseline cerebral blood flow; CBV, cerebral blood volume; CMRO₂, cerebral oxygen metabolic rate; CVR, cerebrovascular reactivity; MCA, middle cerebral artery; OEF, oxygen extraction fraction; po, posterior branch territory. ^aP < 0.05, ^bP < 0.01: comparison between high-CBF_b subgroup and moderate- or low-CBF_b subgroup in the same side; ^AP < 0.05 and ^BP < 0.01: comparison between low-CBF_b subgroup and high- or moderate-CBF_b subgroup in the same side, Tukey's HSD test; [‡]P < 0.05, ^{‡‡}P < 0.01, compared with control, Mann-Whitney test.

high-CBF_b subgroup was higher than that in the controls ($P = 0.002$). The contralateral CBV in the high-CBF_b subgroup was also higher than that in the controls ($P = 0.027$).

The relationships between the ipsilateral CBF_b/CBV

ratio and CBF_b, CBF_b/CBV ratio and CBV were similar among the three subgroups (Fig. 3). The low-CBF_b subgroup was located in the inferior edge of groups B and C. The moderate-CBF_b subgroup was located inside groups B, C, and controls. The high-CBF_b subgroup was

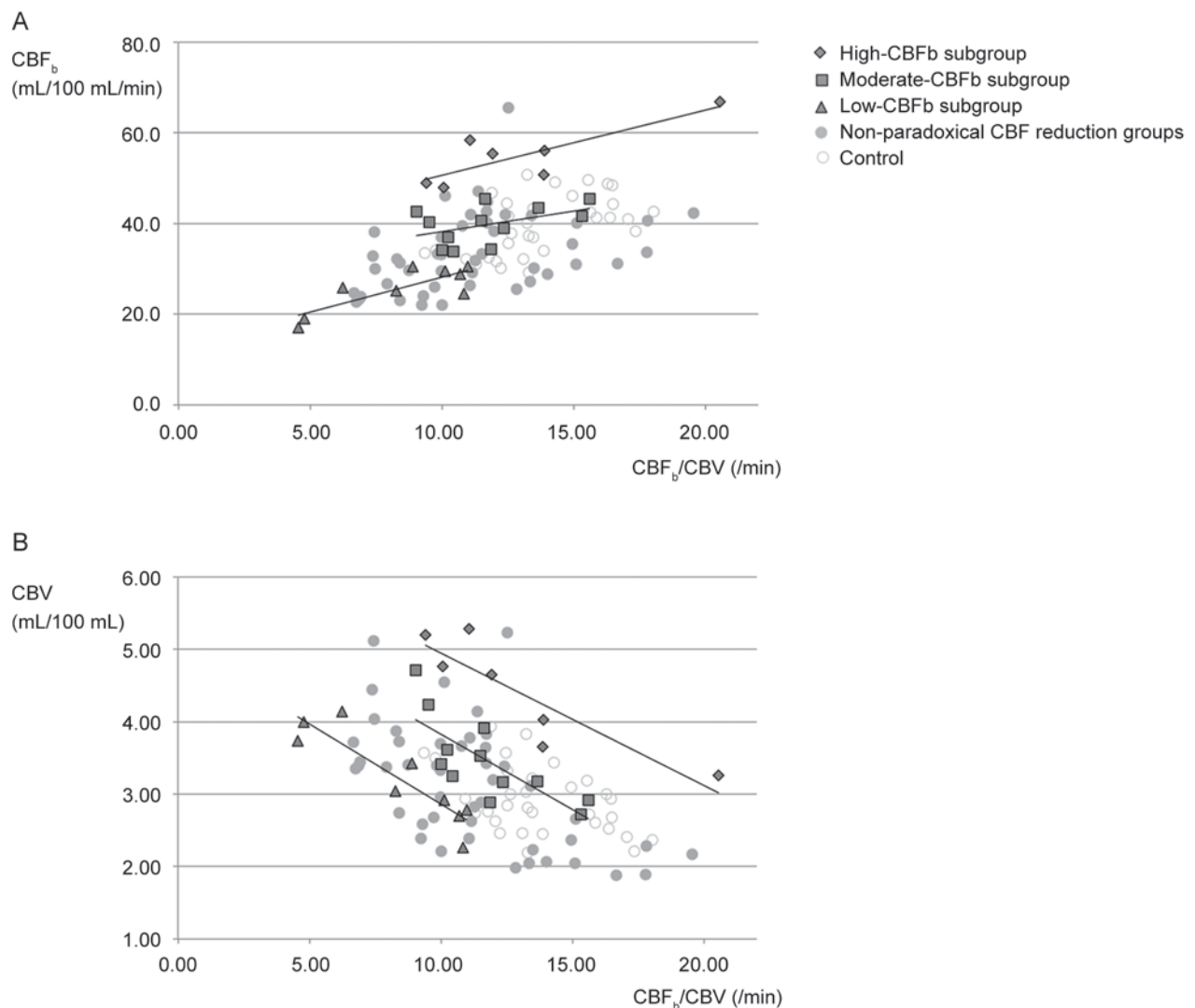


Fig. 3. Relationship between baseline cerebral blood flow to cerebral blood volume (CBF_b/CBV) ratio and CBF_b (A), and between the CBF_b/CBV ratio and CBV (B).

located adjacent to the top of the controls. Figure 4 shows a representative patient with high CBF_b in the regions with paradoxical CBF reduction.

DISCUSSION

The results of the present study demonstrated that the paradoxical CBF reduction after ACZ loading is not always associated with reduction of regional CPP but with various hemodynamic and metabolic states. On the one extreme was “misery perfusion” and stage II ischemia^[26] where CBF_b was decreased, CBF_b/CBV was decreased, OEF

was increased, and CMRO_2 was decreased. On the other was increased CBF_b , normal CBF_b/CBV , increased CBV, decreased OEF, and normal CMRO_2 . The latter condition has not been reported in previous studies.

High Baseline CBF in Paradoxical CBF Reduction

In the high CBF_b regions with paradoxical circulation, the increases in CBF_b and CBV were proportional resulting in normal CBF_b/CBV and thus normal CPP. Low OEF in these regions suggested an excessive CBF_b increase for normal oxygen demand. Originally, increased perfusion without increased CMRO_2 was found after acute ischemia

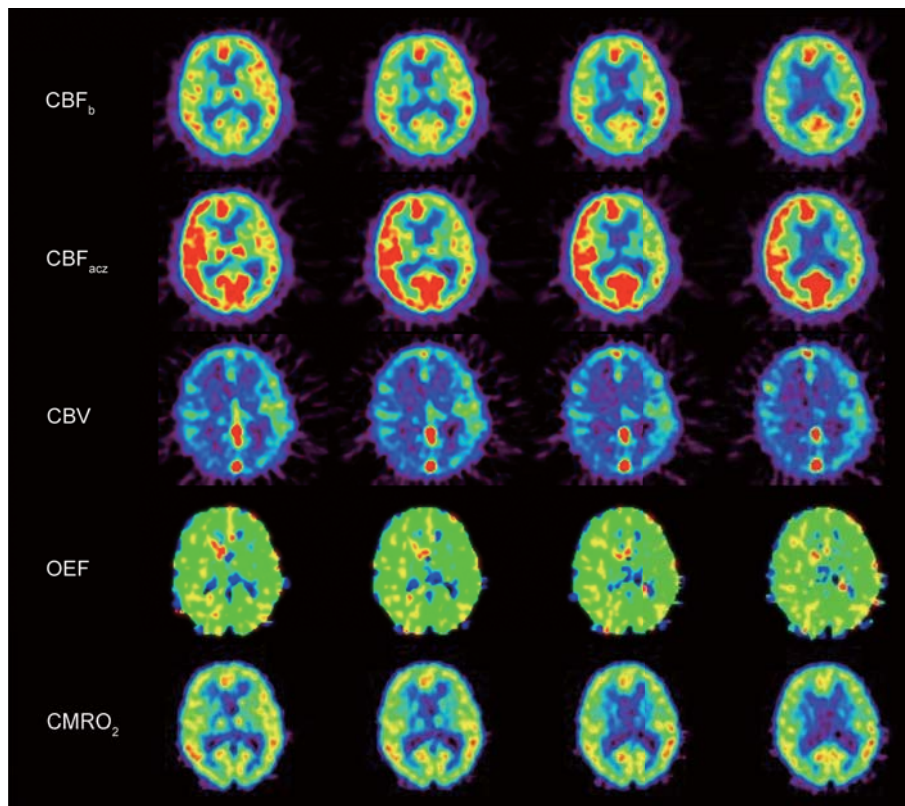


Fig. 4. Representative images from a patient (female, 71 years) with paradoxical cerebral blood flow (CBF) reduction in high-baseline CBF (CBF_b) regions. This patient was diagnosed with chronic severe stenosis of the left ICA. She presented with no ischemic symptoms prior to the positron emission tomography examination. Ipsilateral increase in the CBF_b and cerebral blood volume (CBV), ipsilateral decrease in the CBF after acetazolamide loading (CBF_{acz}), ipsilateral decrease in the oxygen extraction fraction (OEF), and maintained cerebral oxygen metabolic rate ($CMRO_2$) were found in the left ICA territory.

and called the “luxury perfusion” syndrome^[27]. This condition resulted in irreversible brain damage^[28–30]. Our patients showed no clinical signs and MRI evidence of acute cerebral infarction. None of the patients had cerebral infarction after the examination. It is noteworthy that an excessive CBF_b increase was also found in the contralateral hemisphere where the OEF was significantly decreased, the CBV was significantly increased, and the CBF_b/CBV did not significantly change. Therefore, we speculated that the excessive CBF_b and CBV increases in our patients differ from ischemia-related luxury perfusion.

A bilateral hemispheric CBF increase during unilateral ICA occlusion was also found by Torigai *et al.*^[31]. They performed balloon occlusion tests in 4 patients with intracranial aneurysm and in 6 with head and neck tumors. Each hemispheric CBF increase was proportional between

the occluded and non-occluded sides. Although their study induced acute unilateral ICA occlusion, there is a physiological mechanism to increase CBF bilaterally.

Mechanism of High Baseline CBF

One possible mechanism of the bilateral increase of CBF_b in the high- CBF_b subgroup is dilatation of the contralateral carotid artery and/or basilar artery, as well as of the cerebral microvessels. Faraci and Heistad suggested that the large intracranial and extracranial arteries are a major site of resistance to CBF and contribute to total cerebral vascular resistance^[32]. If the contralateral ICA and/or basilar artery in addition to the arterioles were dilated with sufficient collateral circulation through the circle of Willis in a patient with unilateral ICA occlusion, then the CPP may be constant and the CBF_b may be increased. Furst *et al.* also

Table 6. Information on patients with regions showing paradoxical cerebral blood flow reduction

Pt	Age	Sex	Angiography	MCA-an CBFb Subgroup / Ipsi (Contra)	MCA-po CBFb Subgroup / Ipsi (Contra)	Patency of the circle of Willis	Symptom	Interval* (months)	Underlying disease
1	71	F	ICA occlusion	HC 48.0 (41.4)	HC 48.9 (40.6)	A-com, P-com	Asymptomatic		DM
2	71	F	ICA stenosis	HC 56.0 (65.4)	HC 66.9 (70.0)	A-com	TIA	2	HT, DM
3	59	M	ICA occlusion	HC 58.4 (53.1)	(-) 65.5 (60.5)	A-com, P-com	Asymptomatic		HT, DL
4	68	M	ICA stenosis	MC 40.3 (53.2)	HC 55.4 (65.0)	A-com	TIA	2	DM, HT, DL
5	46	M	ICA occlusion	MC 41.6 (45.8)	HC 50.8 (50.7)	P-com	Asymptomatic		
6	63	F	MCA stenosis	MC 43.4 (38.6)	MC 45.4 (47.8)	(-)	MS (Ipsi-BG, Ipsi-CR)	1.5	HT, DL
7	51	F	MCA stenosis	MC 39.0 (40.1)	MC 40.6 (46.0)	(-)	TIA	6	DL
8	62	F	MCA stenosis	(-) 42.7 (49.2)	MC 45.5 (51.4)	(-)	Asymptomatic		DM, DL
9	41	F	ICA stenosis	MC 42.6 (42.4)	(-) 47.2 (43.9)	(-)	MS (Ipsi-parietal, cortex)	19	HT, DL
10	71	M	ICA stenosis	MC 37.0 (42.3)	(-) 41.9 (47.9)	A-com, P-com	Asymptomatic		HT
11	73	M	ICA stenosis	MC 34.3 (33.8)	(-) 42.0 (39.3)	A-com, P-com	Asymptomatic		HT
12	63	M	MCA stenosis	LC 29.6 (31.1)	(-) 33.9 (36.9)	(-)	TIA	4	HT, DL
13	59	M	MCA stenosis	MC 34.1 (30.1)	LC 30.5 (34.3)	(-)	Asymptomatic		HT
14	74	M	ICA occlusion	LC 25.1 (34.5)	LC 30.5 (42.2)	A-com	MS (Ipsi-BG)	1	DM, HT
15	57	M	ICA stenosis	LC 19.1 (32.3)	LC 25.8 (33.2)	(-)	Asymptomatic		HT
16	78	M	ICA occlusion	LC 17.1 (26.0)	(-) 24.8 (28.1)	A-com, P-com	MS (Ipsi-BG)	1	HT, DL
17	63	M	ICA stenosis	LC 28.9 (29.7)	(-) 36.9 (35.8)	A-com	MS (Ipsi-BG, Ipsi-Th)		DM, HT
18	76	M	MCA occlusion	LC 24.5 (26.9)	(-) 23.0 (30.5)	(-)	MS (Contra-parietal, cortex)	17	HT

*Interval between the last symptom and positron emission tomography.

A-com, anterior communicating artery; an, anterior branch territory; BG, basal ganglia; CBF_b, baseline cerebral blood flow; Contra, contralateral; CR, corona radiate; DL, dyslipidemia; DM, diabetes mellitus; DWM, deep white matter; F, female; HC, high-CBF_b subgroup; HT, hypertension; ICA, internal carotid artery; Ipsi, ipsilateral; LC, low-CBF_b subgroup; M, male; MCA, middle cerebral artery; MC, moderate-CBF_b subgroup; MS, minor stroke; P-com, posterior communicating artery; Pt, patient; po, posterior branch territory; Th, thalamus; TIA, transient ischemic attack.

speculated that dilatation of the contralateral large arteries and of the microvessels in the ipsilateral hemisphere may induce bilateral elevation of the CBF_b ^[33]. In the present study, all patients classified into the high- CBF_b subgroup suffered from unilateral ICA occlusion or severe stenosis with a patent circle of Willis (Table 6). We speculated that compensatory dilatation of the contralateral ICA and/or basilar artery induces a bilateral increase of the CBF_b . It is known that sympathetic innervation of the carotid and cerebral vessels and their response to norepinephrine play an important role in maintaining cerebral autoregulation^[34]. The contribution of large arteries to the control of cerebral circulation needs further study in patients with chronic carotid artery steno-occlusive disease.

Prognosis of Patients with High Baseline CBF

Because of the short observation period after PET examination, the prognosis of patients classified into each group and/or subgroup has not yet been precisely analyzed. Derdeyn *et al.* studied the relationship between the OEF and CBV in patients with unilateral carotid artery occlusion and found that an increase in the CBV with an increase of the OEF was associated with a higher risk of stroke^[35]. However, none of the patients with increased CBV and low OEF developed stroke over a mean follow-up period of 3.1 years. We suppose that a high CBF_b in the paradoxical CBF reduction is not indicative of a high risk of ischemic stroke.

Cerebral Oxygen Metabolism in Paradoxical CBF Reduction

Cerebral oxygen metabolism was significantly and exclusively decreased in the low CBF_b regions of the paradoxical CBF reduction, even extending to the contralateral hemisphere. The reduction of $CMRO_2$ in the ipsilateral hemisphere was probably due to selective neuronal loss. In patients with unilateral cerebrovascular disease, selective neuronal necrosis, as represented by a reduction of ^{11}C -flumazenil binding, has been found in the cortical areas in the ipsilateral hemisphere with reduced CBF and reduced CVR^[36,37]. In these studies, no significant reduction of ^{11}C -flumazenil binding was found in the contralateral hemisphere. In the contralateral hemisphere of the low CBF_b subgroup, metabolic reduction

was considered to be attributable to trans-hemispheric functional depression. Recovery of $CMRO_2$ in the contralateral hemisphere after bypass surgery supports this view^[38].

Staging of High Baseline CBF

Powers and Derdeyn *et al.* established a staging for cerebral hemodynamic crisis based on CBF_b , CBV, and OEF^[26,35]. In Stage 0, CBF_b , CBV, and OEF are all normal. In Stage I, CPP is reduced and the cerebral vessels are dilated to maintain CBF_b ; the CBV is increased, while the OEF remains normal. In Stage II, the capacity for compensatory vasodilation is overwhelmed and the CBF_b begins to fall. Nemoto *et al.* added Stage III chronic where OEF returns to normal levels due to impaired $CMRO_2$ and CVR is still compromised. In the present study, we showed that the abnormalities in the low- CBF_b subgroup correspond to Stage II hemodynamic failure, and those in the moderate- CBF_b subgroup correspond to Stage I. However, the abnormalities in the high- CBF_b subgroup could not be clearly categorized into any of the established stages. According to the CBF/CBV in the present study, the reduction of CPP was most severe in the low CBF_b regions of paradoxical CBF reduction (mean $CBF_b/CBV = 8.4$) followed by Group B ($0 < CVR < 15\%$) (mean $CBF_b/CBV = 9.9$), moderate CBF_b (mean $CBF_b/CBV = 11.8$), Group C ($CVR > 15\%$, mean $CBF_b/CBV = 12.3$), and high CBF_b (mean $CBF_b/CBV = 12.5$) in this order. An additional category for high baseline CBF we propose would be located between normal and stage I.

Limitations

There are several limitations of the present study. First, the number of patients was limited and the background characteristics of the patients were heterogeneous. Some were asymptomatic, while others suffered a minor stroke as evidenced by MR, or a TIA. The patients often had hypertension, diabetes mellitus, and dyslipidemia. Second, we determined the presence/absence of the paradoxical CBF reduction by CBF measurements conducted 15 min after ACZ injection. The ACZ effect is reported to reach a maximum at 10 to 20 min after administration^[4]. According to Kuwabara *et al.*, who reported the time-dependency of the effect of ACZ on the cerebral circulation, the paradoxical CBF reduction is most prominent 5 min after injection

compared to 20 min after injection^[7]. The paradoxical CBF reduction might be detectable more frequently in the early phase (at 5 to 10 min). Third, although we speculated about the role of large arteries in controlling the cerebral circulation, we did not evaluate changes in the diameter of the common carotid artery or ICA after ACZ administration. Fourth, we are still following up the patients of the present study, and the prognosis is still uncertain. The contribution of a high CBF_b to the clinical outcome and long-term changes remain unclear. However, regions with increased CBF_b and normal CPP might indicate a protective mechanism against the CBF reduction caused by the changes in circulatory dynamics. We suggest that careful follow-up, rather than revascularization treatment, is desirable in patients with such regions.

In conclusion, we have demonstrated that the paradoxical CBF reduction in patients with chronic unilateral ICA/MCA steno-occlusive disease is not always associated with a reduction of CPP and misery perfusion, but partly includes high CBF regions with normal CPP and an excessive oxygen supply. The high CBF state found in the present study has not been included in the previously-established staging of chronic brain ischemia in patients with steno-occlusive ICA/MCA disease. We consider that the high CBF in these regions might be partly due to vasodilatation of the contralateral carotid and large cerebral arteries.

ACKNOWLEDGEMENTS

This work was partly supported by the Molecular Imaging Program, a grant (21591561) from the Ministry of Education, Culture, Sports, Science, and Technology and the Japan Science and Technology Agency, Japan, by the Research Promotion Program on Health from the National Institute of Biomedical Innovation, Japan, and a Grant-in-Aid (H21-019 and H21-5) from the Ministry of Health, Welfare, and Labour, Japan.

Received date: 2013-12-04; Accepted date: 2014-01-23

REFERENCES

- [1] Symon L. Experimental evidence for "intracerebral steal" following CO₂ inhalation. *Scand J Clin Lab Invest Suppl* 1968, 102: XIII:A.
- [2] Symon L, Pasztor E, Branston NM. The distribution and density of reduced cerebral blood flow following acute middle cerebral artery occlusion: an experimental study by the technique of hydrogen clearance in baboons. *Stroke* 1974, 5: 355–364.
- [3] Regli F, Yamaguchi T, Waltz AG. Effects of acetazolamide on cerebral ischemia and infarction after experimental occlusion of middle cerebral artery. *Stroke* 1971, 2: 456–460.
- [4] Vorstrup S, Henriksen L, Paulson OB. Effect of acetazolamide on cerebral blood flow and cerebral metabolic rate for oxygen. *J Clin Invest* 1984, 74: 1634–1639.
- [5] Vorstrup S, Brun B, Lassen NA. Evaluation of the cerebral vasodilatory capacity by the acetazolamide test before EC-IC bypass surgery in patients with occlusion of the internal carotid artery. *Stroke* 1986, 17: 1291–1298.
- [6] Vorstrup S. Tomographic cerebral blood flow measurements in patients with ischemic cerebrovascular disease and evaluation of the vasodilatory capacity by the acetazolamide test. *Acta Neurol Scand Suppl* 1988, 114: 1–48.
- [7] Kuwabara Y, Ichiya Y, Sasaki M, Yoshida T, Masuda K. Time dependency of the acetazolamide effect on cerebral hemodynamics in patients with chronic occlusive cerebral arteries. Early steal phenomenon demonstrated by [¹⁵O]H₂O positron emission tomography. *Stroke* 1995, 26: 1825–1829.
- [8] Okazawa H, Yamauchi H, Toyoda H, Sugimoto K, Fujibayashi Y, Yonekura Y. Relationship between vasodilatation and cerebral blood flow increase in impaired hemodynamics: a PET study with the acetazolamide test in cerebrovascular disease. *J Nucl Med* 2003, 44: 1875–1883.
- [9] Baron JC, Bousser MG, Rey A, Guillard A, Comar D, Castaigne P. Reversal of focal "misery-perfusion syndrome" by extra-intracranial arterial bypass in hemodynamic cerebral ischemia. A case study with ¹⁵O positron emission tomography. *Stroke* 1981, 12: 454–459.
- [10] Gibbs JM, Wise RJ, Leenders KL, Jones T. Evaluation of cerebral perfusion reserve in patients with carotid-artery occlusion. *Lancet* 1984, 1: 310–314.
- [11] Sette G, Baron JC, Mazoyer B, Levasseur M, Pappata S, Crouzel C. Local brain haemodynamics and oxygen metabolism in cerebrovascular disease. Positron emission tomography. *Brain* 1989, 112 (Pt 4): 931–951.
- [12] Schumann P, Touzani O, Young AR, Morello R, Baron JC, MacKenzie ET. Evaluation of the ratio of cerebral blood flow to cerebral blood volume as an index of local cerebral perfusion pressure. *Brain* 1998, 121 (Pt 7): 1369–1379.
- [13] North American Symptomatic Carotid Endarterectomy Trial Collaborators. Beneficial effect of carotid endarterectomy in symptomatic patients with high-grade carotid stenosis. *N Engl J Med* 1991, 325: 445–453.
- [14] Matsumoto K, Kitamura K, Mizuta T, Tanaka K, Yamamoto S, Sakamoto S, *et al.* Performance characteristics of a new 3-dimensional continuous-emission and spiral-transmission

- high-sensitivity and high-resolution PET camera evaluated with the NEMA NU 2-2001 standard. *J Nucl Med* 2006, 47: 83–90.
- [15] Ibaraki M, Miura S, Shimosegawa E, Sugawara S, Mizuta T, Ishikawa A, *et al.* Quantification of cerebral blood flow and oxygen metabolism with 3-dimensional PET and ^{15}O : validation by comparison with 2-dimensional PET. *J Nucl Med* 2008, 49: 50–59.
- [16] Mintun MA, Raichle ME, Martin WR, Herscovitch P. Brain oxygen utilization measured with O-15 radiotracers and positron emission tomography. *J Nucl Med* 1984, 25: 177–187.
- [17] Herscovitch P, Markham J, Raichle ME. Brain blood flow measured with intravenous H $_2$ (15)O. I. Theory and error analysis. *J Nucl Med* 1983, 24: 782–789.
- [18] Iida H, Jones T, Miura S. Modeling approach to eliminate the need to separate arterial plasma in oxygen-15 inhalation positron emission tomography. *J Nucl Med* 1993, 34: 1333–1340.
- [19] Hatazawa J, Fujita H, Kanno I, Satoh T, Iida H, Miura S, *et al.* Regional cerebral blood flow, blood volume, oxygen extraction fraction, and oxygen utilization rate in normal volunteers measured by the autoradiographic technique and the single breath inhalation method. *Ann Nucl Med* 1995, 9: 15–21.
- [20] Lammertsma AA, Jones T. Correction for the presence of intravascular oxygen-15 in the steady-state technique for measuring regional oxygen extraction ratio in the brain: 1. Description of the method. *J Cereb Blood Flow Metab* 1983, 3: 416–424.
- [21] Kanno I, Iida H, Miura S, Murakami M, Takahashi K, Sasaki H, *et al.* A system for cerebral blood flow measurement using an H $_2$ (15)O autoradiographic method and positron emission tomography. *J Cereb Blood Flow Metab* 1987, 7: 143–153.
- [22] Iida H, Kanno I, Miura S, Murakami M, Takahashi K, Uemura K. Error analysis of a quantitative cerebral blood flow measurement using H $_2$ (15)O autoradiography and positron emission tomography, with respect to the dispersion of the input function. *J Cereb Blood Flow Metab* 1986, 6: 536–545.
- [23] Kuroda S, Shiga T, Ishikawa T, Houkin K, Narita T, Katoh C, *et al.* Reduced blood flow and preserved vasoreactivity characterize oxygen hypometabolism due to incomplete infarction in occlusive carotid artery diseases. *J Nucl Med* 2004, 45: 943–949.
- [24] Imaizumi M, Kitagawa K, Oku N, Hashikawa K, Takasawa M, Yoshikawa T, *et al.* Clinical significance of cerebrovascular reserve in acetazolamide challenge -comparison with acetazolamide challenge H $_2$ O-PET and Gas-PET. *Ann Nucl Med* 2004, 18: 369–374.
- [25] Isozaki M, Arai Y, Kudo T, Kiyono Y, Kobayashi M, Kubota T, *et al.* Clinical implication and prognosis of normal baseline cerebral blood flow with impaired vascular reserve in patients with major cerebral artery occlusive disease. *Ann Nucl Med* 2010, 24: 371–377.
- [26] Powers WJ. Cerebral hemodynamics in ischemic cerebrovascular disease. *Ann Neurol* 1991, 29: 231–240.
- [27] Lassen NA. The luxury-perfusion syndrome and its possible relation to acute metabolic acidosis localised within the brain. *Lancet* 1966, 2: 1113–1115.
- [28] Ackerman RH, Correia JA, Alpert NM, Baron JC, Gouliamos A, Grotta JC, *et al.* Positron imaging in ischemic stroke disease using compounds labeled with oxygen 15. Initial results of clinicophysiological correlations. *Arch Neurol* 1981, 38: 537–543.
- [29] Wise RJ, Bernardi S, Frackowiak RS, Legg NJ, Jones T. Serial observations on the pathophysiology of acute stroke. The transition from ischaemia to infarction as reflected in regional oxygen extraction. *Brain* 1983, 106 (Pt 1): 197–222.
- [30] Hakim AM. The cerebral ischemic penumbra. *Can J Neurol Sci* 1987, 14: 557–559.
- [31] Torigai T, Mase M, Ohno T, Katano H, Nisikawa Y, Sakurai K, *et al.* Usefulness of dual and fully automated measurements of cerebral blood flow during balloon occlusion test of the internal carotid artery. *J Stroke Cerebrovasc Dis* 2011, 22(3): 197–204.
- [32] Faraci FM, Heistad DD. Regulation of large cerebral arteries and cerebral microvascular pressure. *Circ Res* 1990, 66: 8–17.
- [33] Furst H, Hartl WH, Janssen I. Patterns of cerebrovascular reactivity in patients with unilateral asymptomatic carotid artery stenosis. *Stroke* 1994, 25: 1193–1200.
- [34] Omar NM, Marshall JM. Age-related changes in the sympathetic innervation of cerebral vessels and in carotid vascular responses to norepinephrine in the rat: *in vitro* and *in vivo* studies. *J Appl Physiol* 2010, 109: 314–322.
- [35] Derdeyn CP, Videen TO, Yundt KD, Fritsch SM, Carpenter DA, Grubb RL, *et al.* Variability of cerebral blood volume and oxygen extraction: stages of cerebral haemodynamic impairment revisited. *Brain* 2002, 125: 595–607.
- [36] Kuroda S, Shiga T, Houkin K, Ishikawa T, Katoh C, Tamaki N, *et al.* Cerebral oxygen metabolism and neuronal integrity in patients with impaired vasoreactivity attributable to occlusive carotid artery disease. *Stroke* 2006, 37: 393–398.
- [37] Yamauchi H, Nishii R, Higashi T, Kagawa S, Fukuyama H. Silent cortical neuronal damage in atherosclerotic disease of the major cerebral arteries. *J Cereb Blood Flow Metab* 2011, 31: 953–961.
- [38] Samson Y, Baron JC, Bousser MG, Rey A, Derlon JM, David P, *et al.* Effects of extra-intracranial arterial bypass on cerebral blood flow and oxygen metabolism in humans. *Stroke* 1985, 16: 609–616.

CBF/CBV maps in normal volunteers studied with ^{15}O PET: a possible index of cerebral perfusion pressure

Tadashi Watabe^{1,3}, Eku Shimosegawa^{2,3,4}, Hiroki Kato^{2,3}, Kayako Isohashi^{2,3}, Mana Ishibashi^{2,3}, Jun Hatazawa^{2,3,4}

¹Department of Molecular Imaging in Medicine, ²Department of Nuclear Medicine and Tracer Kinetics, Osaka University Graduate School of Medicine, Suita, Japan

³Department of Nuclear Medicine, ⁴Stroke Center, Osaka University Hospital, Suita, Japan

Corresponding author: Tadashi Watabe. E-mail: twatabe@mi.med.osaka-u.ac.jp

© Shanghai Institutes for Biological Sciences, CAS and Springer-Verlag Berlin Heidelberg 2014

ABSTRACT

Local cerebral perfusion pressure (CPP) is a primary factor controlling cerebral circulation and previous studies have indicated that the ratio of cerebral blood flow (CBF) to cerebral blood volume (CBV) can be used as an index of the local CPP. In this study, we investigated whether the CBF/CBV ratio differs among different brain structures under physiological conditions, by means of ^{15}O positron emission tomography. Nine healthy volunteers (5 men and 4 women; mean age, 47.0 ± 1.2 years) were studied by H_2^{15}O bolus injection for CBF measurement and by C^{15}O inhalation for CBV measurement. The CBF/CBV ratio maps were created by dividing the CBF images by the CBV images after anatomical normalization. Regions of interest were placed on the CBF/CBV maps and comparing the regions. The mean CBF/CBV ratio was highest in the cerebellum ($19.3 \pm 5.2/\text{min}$), followed by the putamen (18.2 ± 3.9), pons (16.4 ± 4.6), thalamus (14.5 ± 3.3), cerebral cortices (13.2 ± 2.4), and centrum semiovale (11.5 ± 2.1). The cerebellum and putamen showed significantly higher CBF/CBV ratios than the cerebral cortices and centrum semiovale. We created maps of the CBF/CBV ratio in normal volunteers and demonstrated higher CBF/CBV ratios in the cerebellum and putamen than in the cerebral cortices and deep cerebral white matter. The CBF/CBV may reflect the local CPP and should be studied in hemodynamically

compromised patients and in patients with risk factors for small-artery diseases of the brain.

Keywords: cerebral perfusion pressure; cerebral blood flow; cerebral blood volume; H_2^{15}O ; C^{15}O

INTRODUCTION

Cerebral perfusion pressure (CPP) is one of the essential factors in maintaining the cerebral circulation. Powers and Derdeyn *et al.* proposed a staging method for cerebral hemodynamic crises based on the CPP, cerebral blood flow (CBF), cerebral blood volume (CBV), and oxygen extraction fraction (OEF)^[1,2]. However, the regional CPP in the brain could not be non-invasively measured in humans.

Based on clinical observations, the local CBF/CBV ratio can be used as an index of the local CPP^[3,4]. Schumann *et al.* evaluated the CBF/CBV ratio during global CPP manipulation by varying the mean arterial blood pressure (MABP) in anesthetized baboons^[5] and demonstrated that the CBF/CBV ratio is significantly correlated with the MABP in the range where the cerebral metabolic rate of oxygen is maintained. As the CPP is defined as MABP minus intracranial pressure, the cortical CBF/CBV ratio could be an index of the local CPP in the brain.

In the present study, we created CBF/CBV ratio maps in normal volunteers by means of ^{15}O PET, and examined the possible existence of differences in the CBF/CBV ratio maps among different brain regions under physiological conditions.

PARTICIPANTS AND METHODS

Normal Volunteers

^{15}O PET studies were performed in nine normal volunteers (4 men and 5 women; mean age \pm SD = 50.9 \pm 0.4 years). The criteria for defining “normality” were as follows: (1) no past history of neurological and psychiatric disorders, heart failure, liver and renal dysfunction, respiratory diseases, acute inflammatory disease, autoimmune diseases, or cancer, (2) no smoking or alcohol habit, (3) no significant abnormality on MR imaging or MR angiography of the brain, and (4) no history of medication within the previous 3 months. This study was conducted with the approval of the Ethics Committee of Osaka University Hospital. Written informed consent was given by all participants.

PET Measurements

The PET images were obtained in the 3-D mode using a SET-3000 GCT/X scanner (Shimadzu Corp., Kyoto, Japan), the performance of which has been described^[6]. Briefly, the intrinsic spatial resolution was 3.5-mm full-width at half maximum (FWHM) in-plane and 4.2-mm FWHM axially. Transmission scanning with an external point source (^{137}Cs) was performed for attenuation correction. The PET images were reconstructed by a filtered-back projection method after 3D Gaussian smoothing with a 6-mm FWHM. Scatter events were corrected by the hybrid dual-energy window method combined with a convolution-subtraction method^[6]. Participants were studied under room light and minimal mechanical noise, with their eyes closed and ears unplugged. The head of each participant was immobilized by a belt to minimize any motion during the study and between the CBV and CBF measurements.

A cannula was inserted into the radial artery for measuring the arterial input function. For the CBV study, the participants continuously inhaled C^{15}O gas (3.0 GBq/min) for 1 min. Static 4-min scanning was started 3 min after the completion of C^{15}O inhalation^[7]. Arterial blood was collected 3 times during the scanning period to measure the whole-blood radioactivity. In the equation, the small-to-large vessel hematocrit ratio was fixed at 0.85^[8].

The CBF study was performed more than 10 min after completion of the C^{15}O study to minimize any residual ^{15}O activity. For the CBF study, a bolus of 370 MBq H_2^{15}O was injected intravenously, and simultaneously a 3-D list-mode

data acquisition over a period of 180 s was started^[9,10]. Continuous arterial blood sampling was performed using a β -detector system to determine the whole-arterial blood radioactivity. Delay and dispersion occurring in the β -detector system were corrected by methods described previously^[11]. Quantitative measurement of the CBF and CBV by the 3-D mode PET scanner has been validated^[6].

Partial arterial O_2 pressure (PaO_2), partial arterial CO_2 pressure (PaCO_2), pH, hematocrit (Ht), and hemoglobin concentration (Hb) were monitored continuously during the study. The systemic blood pressure and heart rate were also monitored during the PET study. MABP was calculated as: $[\text{diastolic BP} + (\text{systolic BP} - \text{diastolic BP}) / 3]$.

Data Analysis

The CBF images were transformed to the standard brain size and shape of a built-in PET template, using SPM8 software (Wellcome Department of Imaging Neuroscience: <http://www.fil.ion.ucl.ac.uk/spm/>). Parametric maps of CBV were created using the same parameters as those for CBF normalization. The resultant images had the same anatomic format, with an isotropic voxel size of 2 mm. The CBF/CBV images were created by dividing the normalized CBF images by the normalized CBV images after smoothing (FWHM = 8 mm). PET/MRI fusion images were created with a normalized template of T1-weighted MRI using Osirix software (32-bit, version 3.8.1). Regions of interest (ROIs) were drawn on the normalized CBF, CBV, and CBF/CBV images. Circular ROIs were placed on 3 sequential cross-sections of the pons and thalamus (16 mm in diameter), and elliptical ROIs (16 \times 32 mm) were placed on 3 sequential cross-sections in each of the cerebellum (cerebellar hemisphere), putamen, centrum semiovale, and cerebral cortices (frontal, temporal, occipital, and parietal). All the ROIs were manually set apart from the superior and inferior sagittal sinuses, straight sinus, transverse sinus, sigmoid sinus, cavernous sinus, basilar venous plexus, superior and inferior petrosal sinuses, and large cerebral veins, such as great vein of Galen, internal cerebral vein, and basal vein of Rosenthal. Regional differences in the CBF/CBV ratio were compared by the paired *t* test. Probability values <0.05 determined by Bonferroni's correction for multiple comparisons were considered to denote statistical significance.

RESULTS

There were no significant differences in the physiological parameters between the CBV and CBF measurement periods (Table 1). The mean CBF, CBV and CBF/CBV ratio for each brain region are shown in Table 2. The cerebellum showed the highest CBF/CBV ratio, while the cerebral deep white matter (centrum semiovale) showed the lowest ratio. The mean CBF/CBV ratios in the cerebellum and putamen were higher than those in the cerebral cortices or centrum semiovale ($P < 0.006$). The normalized sum images for

CBF, CBV, and CBF/CBV ratio, along with fusion images of CBF/CBV and MRI T1-weighted images are shown in Figure 1. Among the regions of the cerebral cortex, the frontal cortex showed the highest CBF/CBV ratio, followed by the temporal, parietal, and occipital cortex. The CBF/CBV ratio in the frontal cortex was higher than that in the occipital cortex ($P < 0.006$).

DISCUSSION

In the present study, we created anatomically normalized CBF/CBV ratio maps in normal volunteers based on ¹⁵O PET, and demonstrated that the CBF/CBV ratio was not uniformly distributed in the brain. The cerebellum, putamen, thalamus, and brainstem (pons) showed relatively higher CBF/CBV ratios than the cerebral cortex and deep white matter (centrum semiovale) under physiological conditions.

The CBF/CBV ratios determined here are consistent with the calculated values from previous ¹⁵O PET studies. The regional distribution of the mean transit time (MTT; inverse of the CBF/CBV ratio) in normal young volunteers has been investigated in previous studies. Ibaraki *et al.* studied the distribution of the MTT in seven healthy volunteers (aged 20 to 21 years) based on ¹⁵O-PET ($H_2^{15}O$ and $C^{15}O$)^[12]. Regional differences were observed,

Table 1. Arterial blood gas parameters and blood pressure in $C^{15}O$ and $H_2^{15}O$ studies

	$C^{15}O$ study	$H_2^{15}O$ study	<i>P</i> value
pH	7.403 ± 0.021	7.401 ± 0.015	0.66
PaO ₂ (mmHg)	85.6 ± 8.3	83.2 ± 8.8	0.16
PaCO ₂ (mmHg)	39.8 ± 5.0	40.0 ± 4.1	0.71
MABP (mmHg)	95.0 ± 11.5	93.4 ± 9.9	0.17
Hb (g/dl)	12.5 ± 1.6		
Ht (%)	38.4 ± 4.7		

Mean ± SD; paired *t*-test.

Table 2. CBF, CBV, and CBF/CBV ratio for each brain region

	CBF (mL/100 mL/min)	CBV (mL/100 mL)	CBF/CBV (/min)
Cerebellum	44.3 ± 7.2	2.52 ± 0.40 (2.21 ± 0.35)*	19.3 ± 5.2 (22.0 ± 5.9)*
Putamen	46.3 ± 5.7	2.62 ± 0.41 (2.42 ± 0.38)*	18.2 ± 3.9 (19.7 ± 4.2)*
Pons	42.1 ± 6.0	2.74 ± 0.69	16.4 ± 4.6
Thalamus	45.2 ± 6.9	3.12 ± 0.51	14.5 ± 3.3 ^b
Frontal cortex	38.6 ± 6.6	2.70 ± 0.32	14.4 ± 2.4 ^{a,b}
Temporal cortex	43.1 ± 5.7	3.23 ± 0.22	13.3 ± 2.5 ^{a,b}
Parietal cortex	35.2 ± 4.9	2.65 ± 0.25	13.2 ± 1.9 ^{a,b}
Occipital cortex	39.3 ± 5.6	3.23 ± 0.52	12.1 ± 2.4 ^{a,b,d,e}
Centrum semiovale	21.3 ± 2.7	1.78 ± 0.22	11.5 ± 2.1 ^{a,b,c}

*A small-to-large hematocrit ratio of 0.92 was used for the putamen and 0.97 for the cerebellum in the CBV calculation. $P < 0.05$ versus ^acerebellum,

^bputamen, ^cpons, ^dthalamus, and ^efrontal cortex (adjusted for multiple comparisons); mean ± SD.

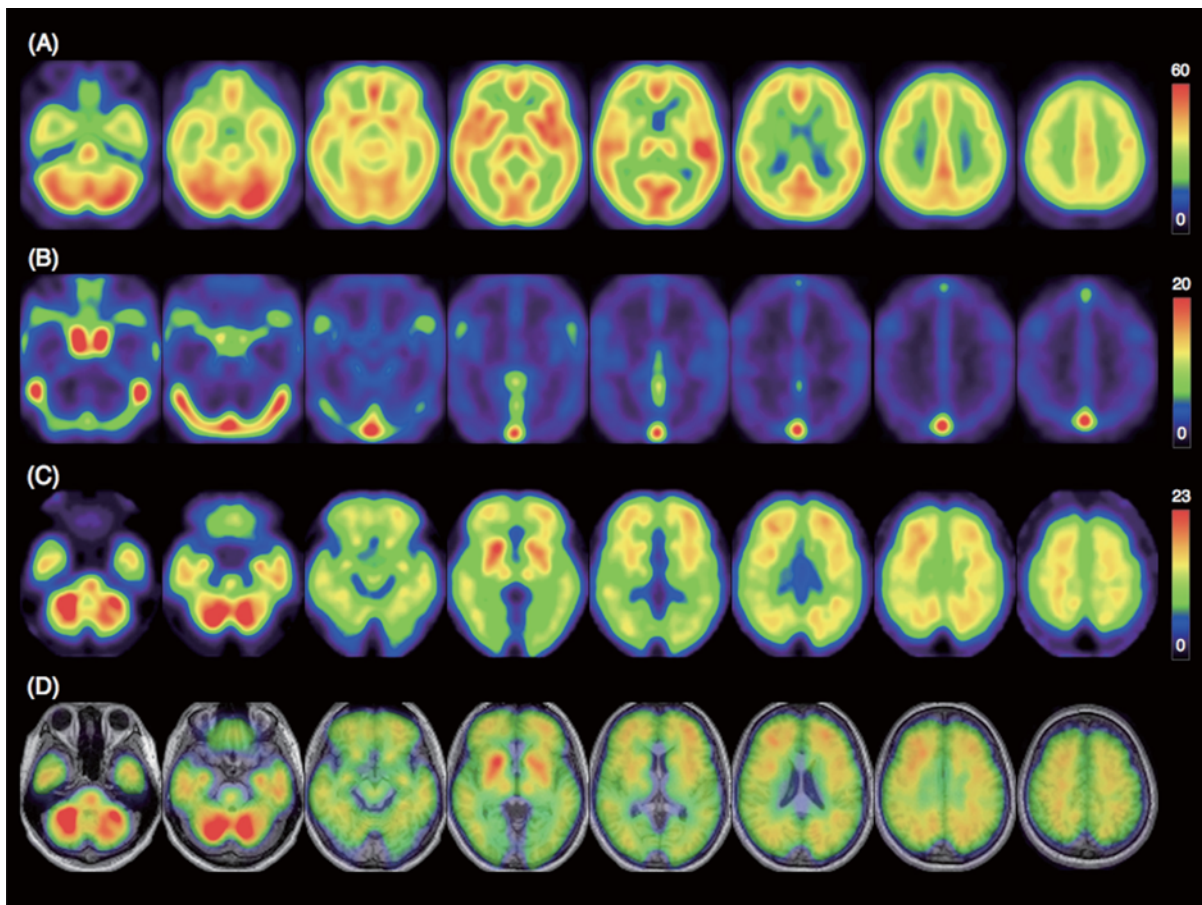


Fig. 1. Average PET images of (A) CBF, (B) CBV, and (C) CBF/CBV ratio with (D) PET/MRI fusion images of CBF/CBV ratio.

the MTTs being shorter in the order thalamus, putamen, cerebellum, cerebral cortex, and centrum semiovale. Ito *et al.* (2003) reported that in young male volunteers (19–27 years of age), the MTT was significantly shorter in the cerebellum, thalamus, and putamen than in all the neocortical regions, and significantly longer in the centrum semiovale than in almost all other regions^[13]. Our results from middle-aged volunteers are consistent with the above findings. The mean CBF/CBV ratio in the temporal cortex was 13.3 in the present study, 15.4 in the study reported by Ibaraki *et al.* and 16.7 in the report by Ito *et al.*^[12,13]. The lower mean CBF/CBV ratio in this study is considered to result from an age-related decline in the CBF and no change in the CBV^[14].

In the CBV measurement by C¹⁵O inhalation, the regional CBV was estimated under the assumption of a constant small-to-large vessel hematocrit ratio (0.85)

among brain structures^[8]. If the hemodilution in the small vessels were to differ among regions, correct estimation of the regional CBV and CBF/CBV ratio may be difficult. Okazawa *et al.* measured the regional red blood cell volume and plasma volume separately by means of C¹⁵O and ⁶²Cu-human serum albumin-dithiosemicarbazone PET^[15]. In their study, the small-to-large vessel hematocrit ratios in the cortical gray matter, white matter, and basal ganglia of normal volunteers were 0.85 ± 0.07 , 0.86 ± 0.07 and 0.92 ± 0.04 , respectively. Yamauchi *et al.*, by means of a similar combined PET study, reported that the cerebellar small-to-large hematocrit ratio was ~ 0.97 ^[16]. When we applied a ratio of 0.92 for the putamen and 0.97 for the cerebellum instead of 0.85 in the CBV calculation, the CBF/CBV ratio increased by 8% for the putamen and by 14% for the cerebellum, further enhancing the regional differences in the CBF/CBV ratio between the cerebellum/basal ganglia

and cerebral cortices/centrum semiovale. Cremer *et al.* reported relatively constant tissue hematocrit values (%) in rats: 31.01 ± 0.61 for the caudate/putamen, 28.66 ± 0.66 for the thalamus, 30.80 ± 0.55 for the cerebellum, and 30.34 ± 0.49 (auditory cortex) to 32.05 ± 0.83 (visual cortex) for the cerebral cortices^[17]. Based on these reports, we considered that the CBF/CBV ratios in the cerebellum and putamen were higher than those in the cerebral cortex and centrum semiovale.

Schumann *et al.* have demonstrated a linear correlation between the cortical CBF/CBV ratio and the MAP, and claimed that the cortical CBF/CBV ratio could be used as an index of the cortical CPP^[5]. However, it was still unknown whether the CBF/CBV ratios in the basal ganglia and cerebellum respond to changes of the MABP as found in the cortical regions. In their study, the CBF/CBV ratio maps of baboons showed proportional changes in the cerebral cortex and putamen/thalamus during hypotension and hypertension. Based on these findings, we speculated that the CBF/CBV ratio maps may reflect the local CPP not only in the cerebral cortices, but in the whole brain. We further speculate that the CPP in the cerebellum, putamen, thalamus, and brainstem may be higher than that in the cerebral cortices and deep white matter.

What are the clinical implications of the findings of the present study? Brain regions showing high CBF/CBV ratios (putamen, thalamus, pons, and cerebellum) are vulnerable to small-artery diseases. Kinoshita *et al.* reported that in hypertensive stroke patients, brain microbleeds were found by MRI in the lentiform nucleus (47%), thalamus (42%), brainstem (34%), and cerebellum (25%)^[18]. Lacunar infarction was associated with a similar finding of microbleeds. Kato *et al.* reported a high incidence of microbleeds in the subcortical white matter, thalamus, basal ganglia, brainstem (predominantly in the pons), and cerebellum^[19]. Further analysis of CBF/CBV ratio maps and the local CPP values may reveal the probability of microangiopathy and the mechanisms of formation of microbleeds/lacunar infarcts in hypertensive patients. In patients with steno-occlusive arterial diseases, the CBF/CBV ratio maps would reveal the extent and magnitude of the CPP decline, as proposed by Gibbs *et al.*, Sette *et al.*, and Schumann *et al.*^[3-5].

In the clinical setting, it is much easier to measure the CBF and CBV by means of SPECT than by ¹⁵O PET.

Several SPECT tracers are available for CBF and for CBV (^{99m}Tc-human serum albumin) imaging. By combining CBF measurements with CBV SPECT, CBF/CBV ratio maps can be prepared for each patient. In ¹⁵O PET studies, we can obtain quantitative images with higher spatial resolution than in SPECT. The CBF/CBV ratio of a small region can be accurately evaluated by ¹⁵O PET.

CONCLUSIONS

In this study we demonstrated, based on the CBF/CBV ratio maps of healthy volunteers, the normal distribution of the local CPP in the brain. The cerebellum and putamen, which are common sites of hypertensive intracerebral hemorrhage, showed higher CBF/CBV ratios than the cerebral cortices and deep white matter under normal physiological conditions. CBF/CBV maps should be studied in further detail in hemodynamically compromised patients and in patients with risk factors for small-artery diseases of the brain.

ACKNOWLEDGMENTS

We thank the staff of the Department of Nuclear Medicine, Osaka University Hospital, for their excellent technical assistance, Sadahiro Naka and Yasukazu Kanai for the supply of the ¹⁵O-gas and water, and Mami Kakuda for collecting the patient data during the PET examination. This work was partly supported by the Molecular Imaging Program, a grant (21591561) from the Ministry of Education, Culture, Sports, Science, and Technology and the Japan Science and Technology Agency, Japan, by the Research Promotion Program on Health from the National Institute of Biomedical Innovation, Japan, and a Grant-in-Aid (H21-019 and H21-5) from the Ministry of Health, Welfare, and Labour, Japan.

Received date: 2013-12-03; Accepted date: 2014-01-18

REFERENCES

- [1] Powers WJ. Cerebral hemodynamics in ischemic cerebrovascular disease. *Ann Neurol* 1991, 29: 231–240.
- [2] Derdeyn CP, Videen TO, Yundt KD, Fritsch SM, Carpenter DA, Grubb RL, *et al.* Variability of cerebral blood volume and oxygen extraction: stages of cerebral haemodynamic impairment revisited. *Brain* 2002, 125: 595–607.
- [3] Gibbs JM, Wise RJ, Leenders KL, Jones T. Evaluation of cerebral perfusion reserve in patients with carotid-artery occlusion. *Lancet* 1984, 1: 310–314.

- [4] Sette G, Baron JC, Mazoyer B, Levasseur M, Pappata S, Crouzel C. Local brain haemodynamics and oxygen metabolism in cerebrovascular disease. Positron emission tomography. *Brain* 1989, 112 (Pt 4): 931–951.
- [5] Schumann P, Touzani O, Young AR, Morello R, Baron JC, MacKenzie ET. Evaluation of the ratio of cerebral blood flow to cerebral blood volume as an index of local cerebral perfusion pressure. *Brain* 1998, 121 (Pt 7): 1369–1379.
- [6] Ibaraki M, Miura S, Shimosegawa E, Sugawara S, Mizuta T, Ishikawa A, *et al.* Quantification of cerebral blood flow and oxygen metabolism with 3-dimensional PET and ^{15}O : validation by comparison with 2-dimensional PET. *J Nucl Med* 2008, 49: 50–59.
- [7] Mintun MA, Raichle ME, Martin WR, Herscovitch P. Brain oxygen utilization measured with O-15 radiotracers and positron emission tomography. *J Nucl Med* 1984, 25: 177–187.
- [8] Phelps ME, Huang SC, Hoffman EJ, Kuhl DE. Validation of tomographic measurement of cerebral blood volume with C-11-labeled carboxyhemoglobin. *J Nucl Med* 1979, 20: 328–334.
- [9] Herscovitch P, Markham J, Raichle ME. Brain blood flow measured with intravenous $\text{H}_2(15)\text{O}$. I. Theory and error analysis. *J Nucl Med* 1983, 24: 782–789.
- [10] Kanno I, Iida H, Miura S, Murakami M, Takahashi K, Sasaki H, *et al.* A system for cerebral blood flow measurement using an H_2^{15}O autoradiographic method and positron emission tomography. *J Cereb Blood Flow Metab* 1987, 7: 143–153.
- [11] Iida H, Kanno I, Miura S, Murakami M, Takahashi K, Uemura K. Error analysis of a quantitative cerebral blood flow measurement using $\text{H}_2(15)\text{O}$ autoradiography and positron emission tomography, with respect to the dispersion of the input function. *J Cereb Blood Flow Metab* 1986, 6: 536–545.
- [12] Ibaraki M, Ito H, Shimosegawa E, Toyoshima H, Ishigame K, Takahashi K, *et al.* Cerebral vascular mean transit time in healthy humans: a comparative study with PET and dynamic susceptibility contrast-enhanced MRI. *J Cereb Blood Flow Metab* 2007, 27: 404–413.
- [13] Ito H, Kanno I, Takahashi K, Ibaraki M, Miura S. Regional distribution of human cerebral vascular mean transit time measured by positron emission tomography. *Neuroimage* 2003, 19: 1163–1169.
- [14] Ibaraki M, Shinohara Y, Nakamura K, Miura S, Kinoshita F, Kinoshita T. Interindividual variations of cerebral blood flow, oxygen delivery, and metabolism in relation to hemoglobin concentration measured by positron emission tomography in humans. *J Cereb Blood Flow Metab* 2010, 30: 1296–1305.
- [15] Okazawa H, Yonekura Y, Fujibayashi Y, Yamauchi H, Ishizu K, Nishizawa S, *et al.* Measurement of regional cerebral plasma pool and hematocrit with copper-62-labeled HSA-DTS. *J Nucl Med* 1996, 37: 1080–1085.
- [16] Yamauchi H, Fukuyama H, Nagahama Y, Okazawa H, Konishi J. A decrease in regional cerebral blood volume and hematocrit in crossed cerebellar diaschisis. *Stroke* 1999, 30: 1429–1431.
- [17] Cremer JE, Seville MP. Regional brain blood flow, blood volume, and haematocrit values in the adult rat. *J Cereb Blood Flow Metab* 1983, 3: 254–256.
- [18] Kinoshita T, Okudera T, Tamura H, Ogawa T, Hatazawa J. Assessment of lacunar hemorrhage associated with hypertensive stroke by echo-planar gradient-echo T_2^* -weighted MRI. *Stroke* 2000, 31: 1646–1650.
- [19] Kato H, Izumiyama M, Izumiyama K, Takahashi A, Itoyama Y. Silent cerebral microbleeds on T_2^* -weighted MRI: correlation with stroke subtype, stroke recurrence, and leukoaraiosis. *Stroke* 2002, 33: 1536–1540.

The medial preoptic area and the regulation of parental behavior

Kumi O. Kuroda¹, Michael Numan²

¹Research Unit for Affiliative Social Behavior, RIKEN Brain Science Institute, Saitama 351-0198, Japan

²Rio Rancho, NM 87144, USA

Corresponding author: Kumi O. Kuroda. E-mail: oyako@brain.riken.jp

© Shanghai Institutes for Biological Sciences, CAS and Springer-Verlag Berlin Heidelberg 2014

The preoptic area (POA) is located in the most anterior part of the hypothalamus and is bordered dorsally by the anterior commissure and anteroventrally by the nucleus of the diagonal band of Broca^[1]. Accumulating evidence from developmental neurobiology suggests, however, that the POA may be a separate entity from hypothalamus, and may actually be part of the basal telencephalon^[2, 3]. Both the hypothalamus and POA are highly complex and heterogeneous areas, containing multiple nuclei, each of which has specific fundamental functions for survival. Among these, the POA contains nuclei involved in the regulation of blood osmolality and temperature (the median preoptic nucleus), sleep (the ventrolateral preoptic and suprachiasmatic nuclei), ovulation (gonadotropin-releasing hormone neurons scattered mainly in the ventral part of the POA), male sexual behavior (the medial preoptic nucleus), and parental behavior (the central part of the medial POA, cMPOA).

Parental behavior in mammals is typically a uniparental maternal care system, while paternal and alloparental behaviors (parental responses toward infants that are not one's biological offspring) are not common. However, paternal and alloparental behaviors do occur in those species where such behaviors have adaptive significance^[4, 5].

A critical role of the medial POA (MPOA) in maternal behavior was initially suggested by Fisher^[6], and has been established in a series of studies by Numan^[7, 8] in laboratory rats. Then it was confirmed in other rodents, such as hamsters^[9], California mice^[10], and laboratory mice^[11], as well as for paternal and alloparental behaviors^[10–13]. The MPOA is also involved in the parental behavior of sheep^[14] and presumably most other mammals. Severing the lateral, in particular the dorsolateral, connections of the MPOA

disrupts maternal behavior most strongly and specifically, compared to cutting the anterior, posterior, or dorsal connections^[15, 16]. These findings are consistent with the fact that the major afferent and efferent connections of the rat medial preoptic nucleus, the largest and central nucleus of the MPOA, enter and leave laterally^[17].

While postpartum maternal behavior is similar in laboratory rats and mice, alloparental behavior in virgin animals differs quite impressively. Virgin female rats initially avoid, and may even attack, young pups, and they require several days of continuous pup exposure (sensitization) before their behavior switches toward displaying parental responses^[18]. Virgin male rats behave similarly^[18]. In contrast, the majority of virgin female mice start retrieving pups and showing other parental responses within 30 to 60 min after their first exposure to pups^[19]. In other words, nulliparous female laboratory mice, unlike most female mammals, do not require pregnancy hormones or extensive pup sensitization to induce immediate maternal care. In contrast to their female counterparts, virgin male laboratory mice behave more like virgin female and male rats, and are more avoidant or even infanticidal on their first exposure to pups^[20]. Significantly, once these male mice become fathers by mating and cohabitation with their pregnant mates, they show extensive paternal care toward their offspring as well as non-offspring pups^[21]. The underlying mechanism for this behavioral switch induced by social experience with the female mate is unknown, although it has been shown that surgical removal of the vomeronasal organ abolishes the infanticidal response and turns virgin male mice toward parental responsiveness^[22]. Interestingly, vomeronasal organ removal also facilitates maternal behavior in virgin female rats^[23], and decreases infanticide in male rats^[24].

It appears that dual neural mechanisms regulating behavioral responses toward infants exist in the brains of most male and female rodents: typical virgin females and males initially avoid pups, while postpartum females, and males of certain species that have mated and cohabitated with females, care for the young. In comparison to most mammals, the spontaneous maternal behavior of virgin female laboratory mice is atypical; indeed, feral female virgin mice are infanticidal^[8] (see ^[4, 5] for a broader analysis of these issues).

Recently, Wu and colleagues reported on the role of galanin neurons in the MPOA for parental behavior in both male and female mice^[25]. They showed that (1) virgin male mice lacking the *Trpc2* gene, which encodes a vomeronasal-organ-specific ion channel, show paternal behavior rather than infanticide; (2) Galanin, a neuropeptide widely expressed in the brain, spinal cord, and gut, is co-expressed with c-Fos induced in MPOA neurons by parental behavior (38.3% of MPOA c-Fos-positive neurons co-express galanin, and 24.8% of MPOA galanin-positive neurons co-express c-Fos in virgin females displaying parental behavior), consistent with a previous publication (47.7% and 29.6%, respectively, in the cMPOA)^[11]; (3) ablation of the galanin neurons within the MPOA causes impairments in parental behavior and male mating behavior; and (4) optogenetic stimulation of MPOA galanin neurons attenuates infanticide and inter-male aggression in virgin males, and facilitates pup grooming (sniffing and licking) as well as general locomotion at the expense of crouching behavior. The strength of this study is the specific manipulation of galanin neurons using a galanin-cre mouse line in combination with sophisticated virus-vector-mediated gene-transfer techniques. Such approaches will become indispensable tools for elucidation of the neuronal circuits of the mammalian parent-infant relationship.

The functional role of galanin is largely unknown, however; it has been implicated in diverse biological processes including lactation *via* prolactin secretion, neural development, feeding, mood regulation, and osmoregulation (see ^[26] for review). Moreover, galanin expression is widely distributed in the MPOA. As such, it is reasonable to assume that the manipulation of MPOA galanin neurons affects not only pup-directed behaviors but also other behaviors and physiological functions. More anatomically-specific targeting of experimental

manipulations within subregions of the MPOA in future studies should provide more information on the neuronal basis of pup-directed behaviors in relation to other social behaviors, in particular the behavioral switch from infanticide to paternal care in male mice that is induced by social interactions with females. Perhaps one population of MPOA neurons is involved in suppressing an avoidance/infanticide circuit, while another population is involved in stimulating a parental circuit^[4, 27]. Significantly, the facts that Wu *et al.*^[25] found that stimulation of MPOA galanin neurons in virgin males reduces infanticide without stimulating parental behaviors, while ablation of these neurons in fathers and postpartum females suppresses parental behavior without inducing infanticide, support the view that there are two functionally distinct MPOA neuronal populations. Obviously, much more research needs to be done to determine, for example, which functional aspects of parental behavior are regulated by MPOA galanin neurons, and whether the critical MPOA-galanin neurons are local-circuit neurons, output projection neurons, or both.

Received date: 2014-06-26; Accepted date: 2014-07-22

REFERENCES

- [1] Simerly RB. Anatomical substrates of hypothalamic integration. In: Paxinos G (Ed). *The Rat Nervous System*. San Diego, CA: Elsevier Academic Press, 2004: 336–368.
- [2] Puelles L, Kuwana E, Puelles E, Bulfone A, Shimamura K, Keleher J, *et al.* Pallial and subpallial derivatives in the embryonic chick and mouse telencephalon, traced by the expression of the genes *Dlx-2*, *Emx-1*, *Nkx-2.1*, *Pax-6*, and *Tbr-1*. *J Comp Neurol* 2000, 424: 409–438.
- [3] Blackshaw S, Scholpp S, Placzek M, Ingraham H, Simerly R, Shimogori T. Molecular pathways controlling development of thalamus and hypothalamus: from neural specification to circuit formation. *J Neurosci* 2010, 30: 14925–14930.
- [4] Numan M. Parental behavior. In: Koob GE, Le Moal M, Thompson RF (Eds). *Encyclopedia of Behavioral Neuroscience* 2010, 3: 14–23.
- [5] Numan M. *Neurobiology of Social Behavior: Toward an understanding of prosocial and antisocial brain*. London: Elsevier, 2015.
- [6] Fisher AE. Maternal and sexual behavior induced by intracranial chemical stimulation. *Science* 1956, 124: 228–229.
- [7] Numan M. Medial preoptic area and maternal behavior in the female rat. *J Comp Physiol Psychol* 1974, 87: 746–759.

- [8] Numan M, Insel TR. The neurobiology of parental behavior. New York: Springer-Verlag, 2003.
- [9] Miceli MO, Malsbury CW. Sagittal knife cuts in the near and far lateral preoptic area-hypothalamus disrupt maternal behaviour in female hamsters. *Physiol Behav* 1982, 28: 856–867.
- [10] Lee AW, Brown RE. Medial preoptic lesions disrupt parental behavior in both male and female California mice (*Peromyscus californicus*). *Behav Neurosci* 2002, 116: 968–975.
- [11] Tsuneoka Y, Maruyama T, Yoshida S, Nishimori K, Kato T, Numan M, *et al.* Functional, anatomical, and neurochemical differentiation of medial preoptic area subregions in relation to maternal behavior in the mouse. *J Comp Neurol* 2013, 521: 1633–1663.
- [12] Sturgis JD, Bridges RS. N-methyl-DL-aspartic acid lesions of the medial preoptic area disrupt ongoing parental behavior in male rats. *Physiol Behav* 1997, 62: 305–310.
- [13] Kalinichev M, Rosenblatt JS, Morrell JI. The medial preoptic area, necessary for adult maternal behavior in rats, is only partially established as a component of the neural circuit that supports maternal behavior in juvenile rats. *Behav Neurosci* 2000, 114: 196–210.
- [14] Perrin G, Meurisse M, Levy F. Inactivation of the medial preoptic area or the bed nucleus of the stria terminalis differentially disrupts maternal behavior in sheep. *Horm Behav* 2007, 52: 461–473.
- [15] Terkel J, Bridges RS, Sawyer CH. Effects of transecting lateral neural connections of the medial preoptic area on maternal behavior in the rat: nest building, pup retrieval and prolactin secretion. *Brain Res* 1979, 169: 369–380.
- [16] Numan M, McSparren J, Numan MJ. Dorsolateral connections of the medial preoptic area and maternal behavior in rats. *Behav Neurosci* 1990, 104: 964–979.
- [17] Simerly RB, Swanson LW. Projections of the medial preoptic nucleus: a Phaseolus vulgaris leucoagglutinin anterograde tract-tracing study in the rat. *J Comp Neurol* 1988, 270: 209–242.
- [18] Rosenblatt JS. Nonhormonal basis of maternal behavior in the rat. *Science* 1967, 156: 1512–1514.
- [19] Leblond CP. Extra-hormonal factors in maternal behavior. *Proc Soc Exp Biol Med* 1940, 38: 66–70.
- [20] Parmigiani S, vom Saal FS. *Infanticide and Parental Care*. Chur, Switzerland: Haywood Academic Publishers GmH, 1994.
- [21] vom Saal FS, Howard LS. The regulation of infanticide and parental behavior: implications for reproductive success in male mice. *Science* 1982, 215: 1270–1272.
- [22] Tachikawa KS, Yoshihara Y, Kuroda KO. Behavioral transition from attack to parenting in male mice: a crucial role of the vomeronasal system. *J Neurosci* 2013, 33: 5120–5126.
- [23] Fleming A, Vaccarino F, Tambosso L, Chee P. Vomeronasal and olfactory system modulation of maternal behavior in the rat. *Science* 1979, 203: 372–374.
- [24] Mennella JA, Moltz H. Infanticide in the male rat: the role of the vomeronasal organ. *Physiol Behav* 1988, 42: 303–306.
- [25] Wu Z, Autry AE, Bergan JF, Watabe-Uchida M, Dulac CG. Galanin neurons in the medial preoptic area govern parental behaviour. *Nature* 2014, 509: 325–330.
- [26] Mechenthaler I. Galanin and the neuroendocrine axes. *Cell Mol Life Sci* 2008, 65: 1826–1835.
- [27] Numan M. Motivational systems and the neural circuitry of maternal behavior in the rat. *Dev Psychobiol* 2007, 49: 12–21.

Activation of extrasynaptic GABA_A receptors inhibits cyclothiazide-induced epileptiform activity in hippocampal CA1 neurons

Li Wan^{1#}, Xu Liu^{2#}, Zheng Wu¹, Wanting Ren¹, Shuzhen Kong¹, Raya Abou Dargham¹, Longzhen Cheng¹, Yun Wang¹
¹Institutes of Brain Science and State Key Laboratory of Medical Neurobiology, ²Neurology Department, Zhongshan Hospital, Fudan University, Shanghai 200032, China

[#]These authors contributed equally to this work.

Corresponding authors: Yun Wang and Longzhen Cheng. E-mail: yunwang@fudan.edu.cn, lzcheng@fudan.edu.cn

© Shanghai Institutes for Biological Sciences, CAS and Springer-Verlag Berlin Heidelberg 2014

ABSTRACT

Extrasynaptic GABA_A receptors (GABA_ARs)-mediated tonic inhibition is reported to involve in the pathogenesis of epilepsy. In this study, we used cyclothiazide (CTZ)-induced *in vitro* brain slice seizure model to explore the effect of selective activation of extrasynaptic GABA_ARs by 4,5,6,7-tetrahydroisoxazolo[5,4-c] pyridine-3-ol (THIP) on the CTZ-induced epileptiform activity in hippocampal neurons. Perfusion with CTZ dose-dependently induced multiple epileptiform peaks of evoked population spikes (PSs) in CA1 pyramidal neurons, and treatment with THIP (5 μmol/L) significantly reduced the multiple PS peaks induced by CTZ stimulation. Western blot showed that the δ-subunit of the GABA_AR, an extrasynaptic specific GABA_AR subunit, was also significantly down-regulated in the cell membrane 2 h after CTZ treatment. Our results suggest that the CTZ-induced epileptiform activity in hippocampal CA1 neurons is suppressed by the activation of extrasynaptic GABA_ARs, and further support the hypothesis that tonic inhibition mediated by extrasynaptic GABA_ARs plays a prominent role in seizure generation.

Keywords: GABA_ARs; tonic inhibition; epilepsy; population spike; cyclothiazide; hippocampal CA1 neurons

INTRODUCTION

Epilepsy is a common neurological disorder, and various

factors such as brain trauma, infection, and genetic factors contribute to its pathogenesis^[1]. This disorder entails abnormal behavior caused by sudden, overriding, and synchronized electrical activity of certain neuronal groups in the central nervous system. Although the exact mechanisms that lead to this abnormal firing are not yet fully understood, a functional imbalance of GABAergic inhibition and glutamatergic excitation is considered to be one of the fundamental etiologies.

Hitherto, many antiepileptic drugs have targeted GABA_A receptors (GABA_ARs)^[2–4]. Current studies show that GABA_ARs are present in, but not confined to the synapse; they are also abundant at extrasynaptic sites, although these receptors contain different subunits^[5, 6]. Synaptic GABA_ARs have relatively a low affinity for GABA, and are principally activated by neurotransmitters released into the perisynaptic space, mainly mediating fast synaptic inhibition. Conversely, extrasynaptic GABA_ARs have a high affinity for GABA and are persistently activated by low concentrations, resulting from the extrasynaptic leakage of the neurotransmitter, and mediate ‘tonic’ inhibition. The δ-subunit-containing GABA_AR is the major extrasynaptic form, particularly localized in the hippocampal area and the cerebellum^[7, 8]. Extrasynaptic GABA_ARs are not sensitive to most of the benzodiazepines; however, they are highly sensitive to 4,5,6,7-tetra-hydroisoxazolo[5,4-c] pyridine-3-ol (THIP)^[5, 9]. The role of synaptic GABA_AR-mediated phasic inhibition in epileptogenesis has been well investigated^[10, 11], yet recent research efforts have also revealed that extrasynaptic GABA_AR-mediated tonic inhibition plays

an equivalent or even more critical role in the regulation of epilepsy^[12, 13]. Moreover, clinical studies have shown that there is a significant down-regulation of δ -subunit-containing GABA_ARs in brain samples from patients with temporal lobe epilepsy^[14], and that mutation of the δ -subunit is one of the pathogenic mechanisms of epilepsy^[15]. Our recent study demonstrated that enhancing tonic inhibition by overexpressing either the α 5- or the δ -subunit-containing extrasynaptic GABA_ARs substantially inhibits the formation of epileptiform activity in hippocampal cultures. Furthermore, the injection of the selective extrasynaptic GABA_AR agonist THIP inhibits both epileptiform burst activity in anesthetized rats and seizure behavior in freely-moving rats^[12, 13].

In this work, we further investigated whether δ -subunit-containing GABA_ARs were deficient during cyclothiazide (CTZ)-induced epileptogenesis in hippocampal brain slices, and whether activation of the extrasynaptic GABA_ARs could reverse the CTZ-induced epileptiform activity.

MATERIALS AND METHODS

Experimental Animals and Hippocampal Slice Preparation

Brain slices were prepared from P21–28 male Sprague-Dawley rats provided by the Shanghai Institutes for Biological Sciences Experimental Animal Center. The rats were housed in a regulated environment ($22 \pm 1^\circ\text{C}$) with a 12 h light–dark cycle, and food and water were available *ad libitum*. All experiments were carried out in accordance with the local animal protection law, and approved by the Experimental Animal Ethics Committee of Fudan University.

Rats were anesthetized by intraperitoneal injection of 1.25% pentobarbital sodium at 0.1 mL per 100 g body weight. After full anesthesia, the rats were decapitated and the brain was removed and cooled in iced artificial cerebrospinal fluid (ACSF; in mmol/L: NaCl 124, KCl 3.3, KH₂PO₄ 1.2, NaHCO₃ 26, CaCl₂ 2.5, MgSO₄ 2.4, glucose 10) for 1 min, then the hippocampus was exposed on ice. After that, the brain was fixed on a vibrating cryotome and bathed in iced ACSF throughout the slicing process. The thickness of the slices used in both field potential recording and western blot was 350 μm . The slices were transferred to ACSF at room temperature, and later to a 33°C water

bath for 30 min, in order to restore neuronal function before they were allowed to recover in room temperature ACSF for 1 h. At the end of this process, the slices were ready for pharmacological treatment and electrophysiological recording.

Evoked Population Spike Recording in Hippocampal Slices

Freshly-prepared hippocampal slices were superfused with normal ACSF using a Peri-star double-channel perfusion system (World Precision Instruments, Sarasota, FL), and the perfusate was continuously bubbled with 95% O₂ and 5% CO₂. The recording pipettes were pulled from borosilicate glass on a P97 microelectrode puller (Sutter Instruments, Novato, CA). The pipette was filled with normal ACSF and the impedance was 4–8 M Ω . Bipolar tungsten electrodes were used for stimulation. The recording electrodes were placed in the CA1 pyramidal layer, while the tungsten electrodes were placed across the Schaffer collaterals. The stimulation strength was set to evoke 60% of the maximal response, and the frequency was set to one per 30 s. The signal was amplified and filtered using the NeuroLog system (Digitimer Ltd, Hartford, UK), and was acquired using the CED1401 data acquisition system and Spike 2 software (CED Electronics, Cambridge, UK). After 30 min of baseline recording, either DMSO (0.1%) or one of the convulsants [(CTZ, kainic acid (KA), bicuculline (BIC), or Mg²⁺-free solution (0-Mg²⁺)] was added to the ACSF, and the recording was continued for another 2 h. In some experiments, after 2 h recording with CTZ (200 $\mu\text{mol/L}$) (Tocris, Northpoint, Bristol, UK), the perfusate was replaced with either DMSO (0.1%) or THIP (5 $\mu\text{mol/L}$) (Sigma Aldrich Chemical Co., Poole, Dorset, UK) for another hour.

Whole-cell Patch-clamp Recording

Whole-cell recordings were performed in voltage-clamp mode using a MultiClamp 700B amplifier (Molecular Devices, Sunnyvale, CA). Patch pipettes were pulled from borosilicate glass and fire-polished (2–6 M Ω). Before the pipettes were immersed in solution, positive pressure was applied to prevent tip blockage. When approaching target cells, the pressure was withdrawn to form a high-impedance seal (>1 G Ω) between the membrane and the pipette. Meanwhile, the membrane potential was held at around -70 mV to facilitate the seal. After the seal

stabilized, appropriate negative pressure was applied to break the cell for whole-cell recording. Data were acquired using pClamp 10 software, sampled at 2–10 kHz, and filtered at 1 kHz. Off-line analysis was done with Clampfit 10 software. Based on previous work, a large depolarization resembling a paroxysmal depolarization shift was defined as ≥ 10 mV depolarization, and ≥ 300 ms duration. And an epileptiform burst in a single neuron was defined by at least five consecutive action potentials superimposed on a large depolarization shift^[16].

Immunoblotting

Slices were dissected to preserve only the hippocampus under a dissecting microscope on ice, and then quickly homogenized in pre-cooled lysis buffer (#K268-50, Biovision, Milpitas, CA). The plasma membrane protein fraction was prepared from the homogenate following the standard procedure using a membrane protein extraction kit (#K268-50, Biovision). The membrane fraction was dissolved in 0.5 % Triton X-100 in PBS, and incubated at 45°C with SDS sample buffer for 45 min for inactivation. Membrane proteins were separated on SDS-PAGE, electrophoretically transferred to polyvinylidene fluoride membranes (Millipore, Billerica, MA), then incubated with primary antibodies raised against the GABA_AR δ -subunit (#AB9752, 1:800; Millipore) or β -actin (#4967, 1:1 000; Cell Signaling Technology, Danvers, MA) in 5% skimmed milk-TBS-T (20 mmol/L Tris, pH 7.6, 137 mmol/L NaCl, 0.05% Tween 20) overnight at 4°C, followed by incubation with peroxidase-conjugated Affinipure goat anti-rabbit (#111-035-003, 1:20 000; Jackson, Noida, India) or rabbit anti-goat (#305-035-003, 1:20 000; Jackson) secondary antibody in TBS-T buffer. Bands were visualized using an ECL detection system (Pierce, Rockford, IL). The immunoreactivity of an individual band was measured by Imagepro plus and normalized to β -actin.

Data Analysis

Group data are expressed as mean \pm SEM. Across different groups of data, statistically significant differences between means were determined using one-way ANOVA with Tukey's HSD *post hoc* analysis. Comparison within a group was carried out using a paired or unpaired *t* test. All analyses were performed using the statistics software Stata 7. The significance level was set at $P < 0.05$.

RESULTS

CTZ-induced Epileptiform Activity in CA1 Pyramidal Neurons of Hippocampal Slices

Previous studies have shown that CTZ induces progressive epileptiform activity including multiple evoked peaks followed by spontaneous epileptiform spike activity, and eventually highly-synchronized burst activity, in rat hippocampal CA1 neurons^[16, 17]. In this study, we first tried to establish a hippocampal slice model of seizures induced by CTZ. Under control condition, a single population spike (PS), without any spontaneous activity, was evoked in CA1 pyramidal neurons after stimulation of the Schaffer collaterals (Fig. 1Aa). However, slices treated with CTZ (50 or 200 $\mu\text{mol/L}$, dissolved in 1% DMSO) dose-dependently induced multiple epileptiform PS peaks in CA1 pyramidal neurons, similar to those reported in anesthetized rats *in vivo*^[16] (Fig. 1Ab, Ac). The latency to the appearance of the second PS peak in the 50 $\mu\text{mol/L}$ CTZ group was 68.1 ± 4.0 min ($n = 9$), which was significantly longer than that of the 200 $\mu\text{mol/L}$ CTZ group (18.3 ± 1.5 min, $n = 6$; $P < 0.001$) (Fig. 1B, Table 1). In addition, CTZ at 200 $\mu\text{mol/L}$ induced multiple PS peaks (3 or more) (Fig. 1Ac), while 50 $\mu\text{mol/L}$ CTZ failed to induce three or more peaks during our 2-h recording paradigm (Fig. 1Ab). These results indicated that CTZ induces concentration-dependent epileptiform activity in hippocampal slices.

Comparison of the Latency to Evoke Epileptiform Multiple PS Peaks among Different *in vitro* Epilepsy Models

Previous studies have reported that KA, BIC, and 0-Mg²⁺ induce epileptiform activity in hippocampal slices, and all are commonly used in the study of epilepsy^[18-20]. We performed a study to compare these models with CTZ. Hippocampal slices continuously superfused with ACSF containing KA (0.5 $\mu\text{mol/L}$), BIC (2 $\mu\text{mol/L}$), or 0-Mg²⁺ all rapidly displayed double or even multiple PS peaks (Fig. 2 C–E), while this process was much slower with CTZ (50/200 $\mu\text{mol/L}$). The CTZ model also induced relatively fewer peaks overall compared with the other three models (Fig. 2A, B). The latencies of the double peaks in these four models were: CTZ (50 $\mu\text{mol/L}$), 68.1 ± 4.0 min, $n = 9$; CTZ (200 $\mu\text{mol/L}$), 18.3 ± 1.5 min, $n = 6$; KA (0.5 $\mu\text{mol/L}$), 3.6 ± 0.4 min, $n = 6$; BIC (2 $\mu\text{mol/L}$), 2.5 ± 0.2 min, $n = 5$; 0-Mg²⁺, 7.4 ± 0.9 min, $n = 5$ (Fig. 2F). These results showed that the

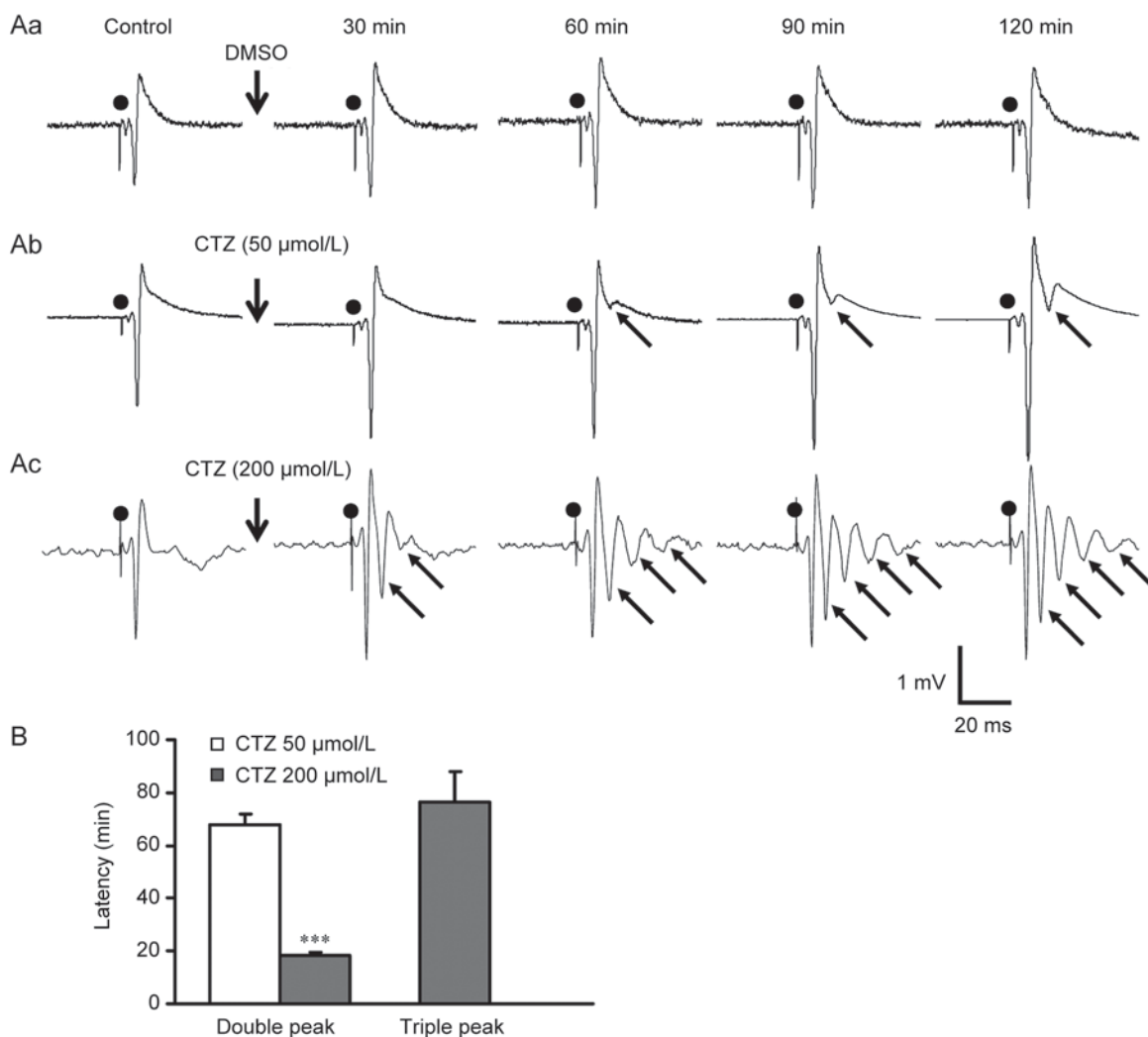


Fig. 1. Progressive change of hippocampal CA1 evoked potentials induced by CTZ in a brain slice. A: CTZ-induced time- and concentration-dependent progressive change of the evoked population spikes (PSs) in a hippocampal CA1 slice. Aa: PS was not significantly changed when superfused with DMSO as control (*n* = 4); Ab–Ac: PS peak number gradually increased after continuous superfusion with either 50 μmol/L (*n* = 9) (b) or 200 μmol/L (*n* = 6) (c) CTZ. B: Bar graph showing the latency to evoke double and triple peaks at different CTZ concentrations. Additional peaks are indicated by the arrows; “•” indicates the stimulus artifact.

Table 1. Summary of double or triple PS peak latency induced by different concentrations of CTZ

Group	Double Peaks (min)	Triple Peaks (min)
DMSO	>120 (<i>n</i> = 4)	>120 (<i>n</i> = 4)
CTZ (50 μmol/L)	68.1 ± 4.0 (<i>n</i> = 9)	>120 (<i>n</i> = 9)
CTZ (200 μmol/L)	18.3 ± 1.5*** (<i>n</i> = 6)	76.7 ± 11.3 (<i>n</i> = 6)

****P* < 0.001 compared with the 50 μmol/L CTZ group.

onset of abnormal epileptiform PSs induced by CTZ was significantly slower (*P* < 0.001, Fig. 2F) than that seen with the classical experimental convulsants. The slow onset of action of CTZ is comparable to that reported in cultured hippocampal neurons^[16].

CTZ-induced Epileptiform Firing in Single Hippocampal CA1 Neurons

A previous study showed that the additional PS peaks

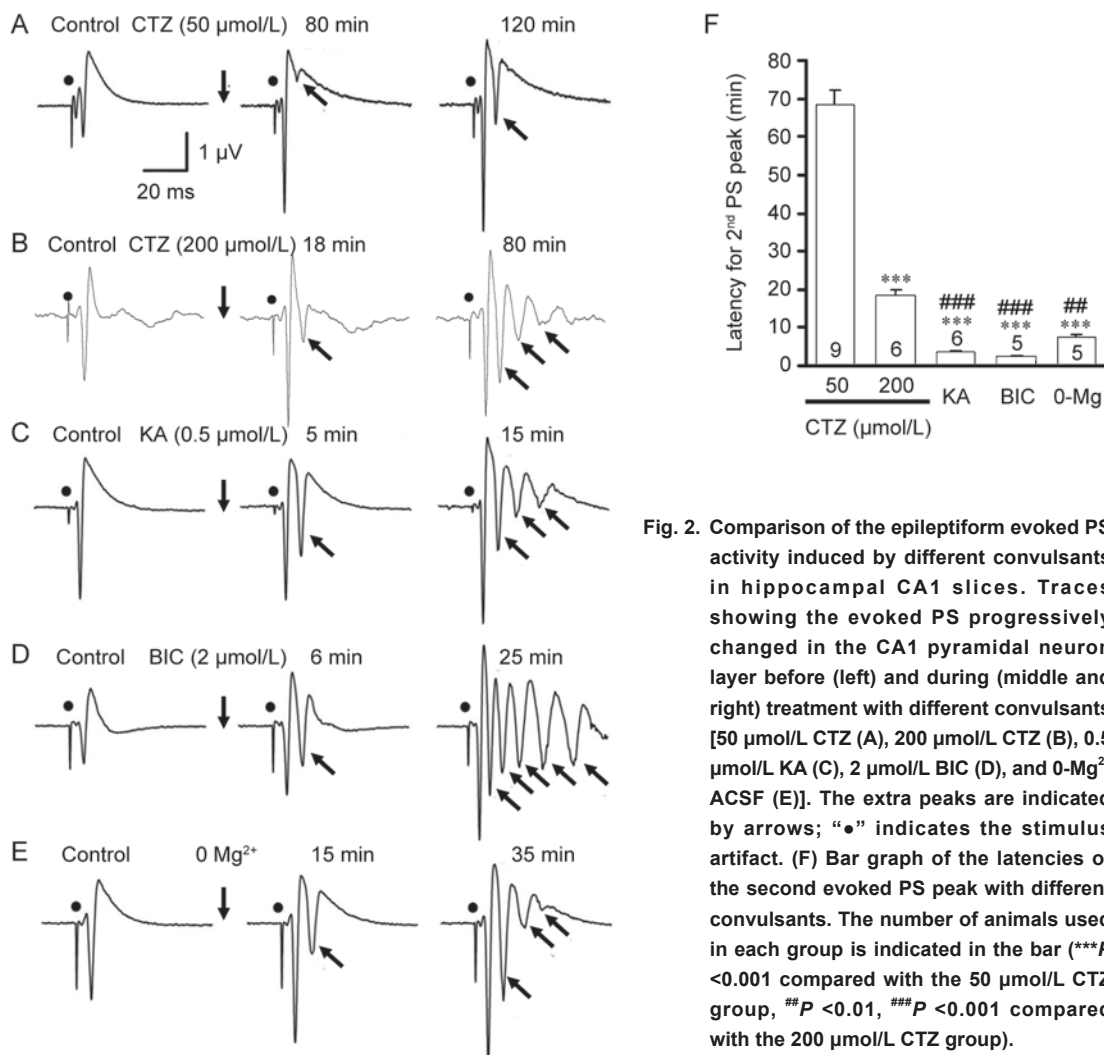


Fig. 2. Comparison of the epileptiform evoked PS activity induced by different convulsants in hippocampal CA1 slices. Traces showing the evoked PS progressively changed in the CA1 pyramidal neuron layer before (left) and during (middle and right) treatment with different convulsants [50 $\mu\text{mol/L}$ CTZ (A), 200 $\mu\text{mol/L}$ CTZ (B), 0.5 $\mu\text{mol/L}$ KA (C), 2 $\mu\text{mol/L}$ BIC (D), and 0- Mg^{2+} ACSF (E)]. The extra peaks are indicated by arrows; “•” indicates the stimulus artifact. (F) Bar graph of the latencies of the second evoked PS peak with different convulsants. The number of animals used in each group is indicated in the bar (*** $P < 0.001$ compared with the 50 $\mu\text{mol/L}$ CTZ group, ** $P < 0.01$, ### $P < 0.001$ compared with the 200 $\mu\text{mol/L}$ CTZ group).

are likely due to the non-synchronized composition of the enhanced electrical activity from different neuronal layers^[21]. Enhanced neuronal activity for epileptiform burst firing^[16], which is at the core of epileptogenesis and network spread^[22-24], has been reported in cultured hippocampal neurons after treatment with CTZ. Therefore, we further explored changes in the firing pattern at the level of single hippocampal CA1 neurons in CTZ-treated hippocampal slices using the patch-clamp technique. Spontaneous action potentials were only occasionally recorded from CA1 pyramidal neurons when the membrane potential was current-clamped at -70 mV (Fig. 3, left). However, neuronal activity was enhanced after the application of CTZ (50 $\mu\text{mol/L}$) (Fig. 3, middle), which eventually induced epileptiform

burst activity (Fig. 3, right), analogous to that reported in cultured hippocampal neurons^[16]. The percentage of neurons that displayed epileptiform burst firing in slices treated with 50 $\mu\text{mol/L}$ CTZ for 2 h was 55.6% ($n = 9$). The above results point towards the possibility of a correlation between epileptiform burst firing in single neurons and synchronization in the neuronal network after CTZ perfusion.

Incubation with CTZ Downregulates Neuronal Cell Membrane Expression of Extrasynaptic GABA_A Receptors in Hippocampal Slices

Extrasynaptic GABA_ARs have been suggested to exert a regulatory function during epileptogenesis and could be

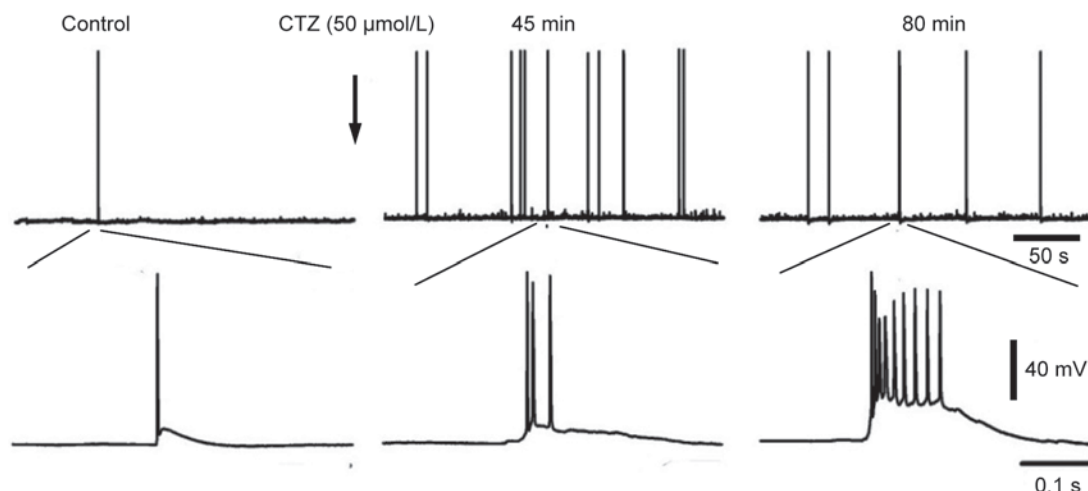


Fig. 3. CTZ-induced robust epileptiform burst activity in a CA1 pyramidal neuron in a rat hippocampal slice. Traces from current-clamp recordings (membrane potential held at -70 mV) in a CA1 pyramidal neuron showing that CTZ (50 $\mu\text{mol/L}$) transformed the firing pattern from single action potentials (left), to grouped (middle), and finally burst-like activity (right).

novel antiepileptic drug targets^[13]. Hence, we went on to examine the variation in expression of the δ subunit, one of the major extrasynaptic GABA_AR subunits, on the neuronal cell membrane after treatment of hippocampal slices with CTZ. Freshly-prepared slices were incubated in ACSF containing 50 $\mu\text{mol/L}$ CTZ or 1% DMSO (solvent control) for 2 h, after which membrane protein was extracted for western blot analysis. Two hours after treatment with CTZ (50 $\mu\text{mol/L}$), the relative level of the GABA_AR δ subunit was markedly decreased to $55.0 \pm 4.3\%$ (Fig. 4) of the DMSO control level. This result demonstrated that the extrasynaptic expression of GABA_ARs is reduced in CTZ-induced epileptogenesis in hippocampal slices.

THIP Suppresses the Epileptiform PSs Induced by CTZ in Hippocampal Slices

Our previous study showed that the sustained tonic inhibition mediated by extrasynaptic GABA_ARs has a significant effect on epileptiform activity^[13]. Therefore, we further tested whether enhancing tonic GABA inhibition by THIP, an agonist specific for the GABA_AR δ -subunit, could suppress the epileptiform activity in hippocampal slices. Perfusion with 200 $\mu\text{mol/L}$ CTZ induced multiple PS peaks in all slices as shown above. After 2 h of continuous superfusion, the induced multiple PS peaks had reached a stable stage with an average of 2.3 ± 0.2 ($n = 9$) extra

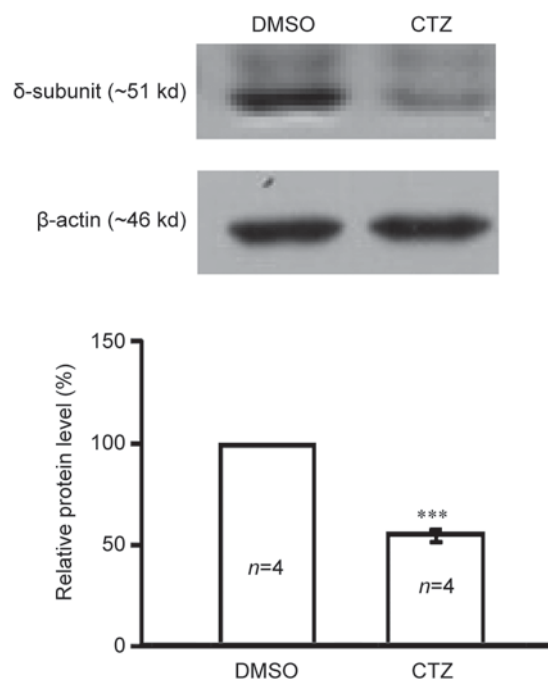


Fig. 4. CTZ treatment suppressed expression of the GABA_AR δ -subunit in the hippocampal cell membrane. **A:** Western blots showing the GABA_AR δ -subunit (upper) and β -actin (lower) in DMSO- and CTZ-treated (2 h) hippocampal slices. **B:** Bar diagrams showing the group data of the change of the GABA_AR δ -subunit after CTZ treatment. The number of animals in each group are indicated in the bar (***) $P < 0.001$ compared with the DMSO group).

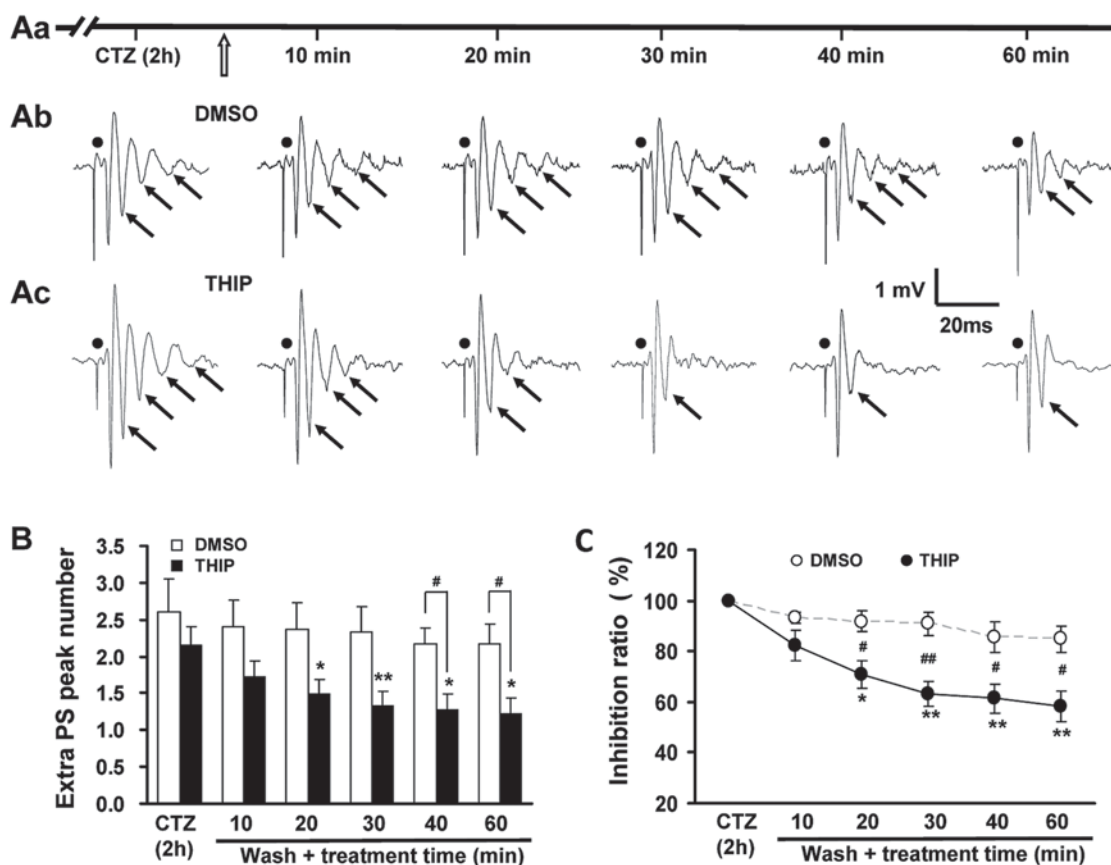


Fig. 5. Stimulation of extrasynaptic GABA_A receptors with THIP suppressed CTZ-induced epileptiform population spike (PS) peaks in hippocampal CA1 region. **Aa:** Line to show the protocol (arrow indicates the superfusate change from CTZ to either DMSO or THIP). **Ab–Ac:** Raw traces showing the change in the extra number of PS peaks (arrows) after the superfusate was changed to either DMSO (**Ab**) or THIP (**Ac**). **B:** Bar diagram showing that THIP (5 μmol/L, *n* = 6) suppressed the CTZ (200 μmol/L, 2 h)-induced multiple PS peaks compared with the DMSO control (*n* = 3) (*P* < 0.001, two-way ANOVA). **C:** Graph showing the reduction ratio of the extra PS peaks in the THIP (filled circles) and DMSO (unfilled circles) groups (**P* < 0.05, ***P* < 0.01 compared with 2-h CTZ control, paired *t*-test; #*P* < 0.05, ##*P* < 0.01 compared with time-matched DMSO control, unpaired *t*-test).

peaks (excluding the first PS) (Fig. 5Ab, Ac). Then slices were randomly washed with ACSF either containing 5 μmol/L THIP (*n* = 6) or 1% DMSO (*n* = 3) as solvent control (Fig. 5Aa). The results showed that superfusion with THIP suppressed the epileptiform extra PS peaks in a time-dependent manner from an average of 2.2 ± 0.3 to 1.3 ± 0.2 at 30 min (*P* < 0.01) and 1.2 ± 0.2 at 60 min (*P* < 0.05), while those superfused with DMSO showed no significant effect on the PS peaks (Fig. 5B). Further analyses showed that, compared with the time-matched DMSO control group, the extra number of peaks was reduced at 40 min (1.3 ± 0.2 versus 2.2 ± 0.2 , *P* < 0.05), and at 60 min (1.2 ± 0.2 versus 2.2 ± 0.3 , *P* < 0.05) after CTZ was washed out with THIP

(Fig. 5B). The reduction ratio of the extra PS peak number in the THIP group was greater than that in the DMSO group (*P* < 0.001, Fig. 5C). These results showed that, although δ-GABA_ARs were down-regulated, the extrasynaptic GABA_AR agonist THIP was still capable of suppressing the CTZ-induced epileptiform activity in hippocampal slices.

DISCUSSION

In this study, we established a novel brain-slice epilepsy model that used the previously-characterized convulsant CTZ^[16]. Using this model, our results demonstrated that extrasynaptic GABA_ARs were downregulated by ~50%

during early CTZ-induced epileptogenesis, and selective stimulation of the remaining extrasynaptic GABA_ARs by THIP was still capable of suppressing the epileptiform activity established by CTZ.

Recently, several studies have shown that CTZ is a potent convulsant capable of inducing epileptiform activity both *in vivo* and in cultured hippocampal neurons^[16, 17, 25], as well as evoking seizure behavior in freely-moving animals^[26]. In the current study, we further extended this epilepsy model to hippocampal slices. CTZ has long been known as a blocker of AMPA receptor desensitization and was also recently found to be a GABA_AR inhibitor^[27]. Although the previous *in vitro* studies on cultured hippocampal neurons have shown that neurons treated with CTZ have a long-lasting alteration in neuronal firing pattern, including the induction of epileptiform burst activity^[16], the change in network activity after CTZ treatment was still not clear. The brain slice is a simple and convenient method that has been widely used in anticonvulsant drug development, and in experimental studies on the neuroprotective roles of these drugs during epilepsy^[28-30]. Thus, the brain-slice model is of special value in the study of epilepsy. Using the hippocampal slice preparation, we showed that not only were individual hippocampal pyramidal neurons induced to generate epileptiform burst firing but also, at the local network level, epileptiform activity was triggered in the form of multiple evoked PS peaks. We also demonstrated that CTZ is a potent convulsant in hippocampal slices, and provided another useful *in vitro* model for studying the mechanisms underlying seizures along with the development of potential anticonvulsant drugs. While the *in vivo* model requires injection of CTZ into the cerebral ventricles due to its inability to cross the blood-brain-barrier, the brain-slice model of epilepsy induced by CTZ is not only easy to establish, but also retains relatively intact neuronal networks. In addition, our previous *in vitro* work has demonstrated that, unlike other convulsants (e.g. kainate), CTZ does not appear to be neurotoxic^[16], and our recent study on a CTZ-induced chronic rat seizure model (data not shown) also indicated that intracerebroventricular application of CTZ, which gives rise to recurrent seizure behavior, has a mild effect on neuronal apoptosis. Thus, the CTZ seizure model has special advantages in the study of epilepsy.

Our previous studies both in anesthetized animals

and in cultured neurons indicated that the process of CTZ-induced epilepsy is relatively moderate with a rather long latency to the induction of the acute phases of seizure^[16]. We further characterized this property by comparing the latency to the onset of epileptiform activity in hippocampal slices with the commonly-used convulsants KA, BIC, and 0-Mg²⁺. We showed that the onset latency to evoke the extra PS peaks in CA1 was significantly longer than any of those convulsants, even after the CTZ concentration had been increased to 200 μmol/L. This discrepancy in latency provides a much longer window period, up to 1 h in the 50 μmol/L CTZ group, as compared to only few minutes with either KA, BIC, or 0-Mg²⁺, to explore the initial seizure induction mechanism. Thus, we have extended the use of the novel convulsant CTZ to this model for epilepsy research. Previous research on anesthetized rats showed that CTZ-induced epilepsy in hippocampal CA1 neurons has a characteristic 3-stage pattern consisting of multiple evoked PS peaks, followed by the appearance of spontaneous high-amplitude spikes that later synchronize to generate high-frequency bursting activity. In the current study on hippocampal slices, we noted that CTZ induced multiple evoked PS peaks, yet no spontaneous epileptiform activity was observed, in contrast with the high-K⁺ model in hippocampal slices reported by Liu and colleagues^[31]. The reason for this disparity may lie in the different experimental conditions; the limited recording time (recording for 2 h after CTZ treatment), and a lower recording temperature (room temperature (25°C) rather than body temperature (~37°C) *in vivo*). Researchers have pointed out that temperature greatly influences the occurrence of spontaneous activity *in vitro* in the brain slice. It has also been noted that the probability of detecting burst-like activity is reduced at a certain range of low temperatures^[32, 33]. Thus, the limited spontaneous epileptiform activity observed in our slice recording is comprehensible. Future studies with longer recording times and higher recording temperatures are required for comparison. However, under our conditions, the pattern of CTZ-induced multiple PS peaks in the slice model was similar to that reported in field potential recordings from anesthetized rats^[16, 17]. The evoked PSs were composed of evoked action potentials from multiple neurons, and are considered to be an important electrophysiological index in the study of excitation/inhibition relationships in the CNS. During the early phase

of treatment with the CTZ convulsant, the PS peaks changed remarkably over time; their amplitude and number gradually increased. The PS peaks, which represent the non-synchronized neuronal activity from different layers, changed from a single peak under control conditions to double or even multiple peaks, which parallel the onset of epilepsy and arrive at a seizure-prone state^[21, 34, 35]. Thus, in this study, we used the PS peak number as a marker for studying the epileptiform activity in hippocampal slices.

Epilepsy itself also has an impact on the inhibition mediated by GABA_ARs; long-term epilepsy may alter the expression of GABA_AR subunits^[36]. It is well known that a functional deficit of synaptic GABAergic inhibition plays an important role in the pathogenesis of epilepsy^[37-40]. Recent studies have also revealed the possible role of 'tonic' GABA inhibition in the modulation of epileptic seizures^[41-43]. Tonic inhibition has been reported in hippocampal dentate gyrus (DG) granule cells^[43], CA1 pyramidal neurons^[44], and hippocampal interneurons^[45]; however, in these three areas, the receptors mediating tonic inhibition are of different composition. Most extrasynaptic GABA_ARs in CA1 pyramidal neurons contain $\alpha 5$ and γ subunits, while in DG cells they mainly contain $\alpha 4$ and δ subunits. In interneurons, δ -GABA_ARs are the main mediator of tonic inhibition^[8, 44, 45]. Our western blot results showed that the δ -subunit-containing GABA_ARs on the cell membrane were significantly down-regulated by up to 50% during CTZ stimulation in hippocampal slices. This downregulation may be due to activation of the BDNF-TrkB signaling pathway, as our previous study showed that CTZ, as well as other classic convulsants, induces epileptiform activity via enhanced TrkB receptor-mediated BDNF function^[17, 46]. In addition, BDNF is a known modulator of the surface expression of δ subunits^[36]. This suggests that the function of the extrasynaptic GABA_ARs was largely impaired and is consistent with previous studies. In animal models of temporal lobe epilepsy, there have been reports of a significant reduction of GABA_AR $\alpha 5$ and δ subunit levels in the hippocampal area^[11, 14, 47]. Moreover, δ -subunit mutations have been mapped in epilepsy patients^[15, 48]. Furthermore, increased δ -subunit levels during the diestrus stage of the ovarian cycle have been associated with less seizure activity in KA-induced epilepsy models^[49]. All these pieces of evidence suggest that tonic inhibition, mediated by extrasynaptic GABA_ARs, play an essential

role in the process of epileptogenesis. Indeed, our recent study demonstrated that enhancing tonic inhibition by increasing the expression of either $\alpha 5$ - or δ -subunit-containing GABA_ARs effectively suppresses epileptiform activity in cultured hippocampal neurons^[13]. *In vivo* studies have further demonstrated that both seizure behavior and epileptiform activity are attenuated by enhancing tonic inhibition in hippocampal neurons^[13]. Based on previous studies and our own research, we therefore hypothesize that enhancing 'tonic' GABA inhibition inhibits epileptiform activity, while reducing tonic inhibition increases the susceptibility to epileptic seizures^[49, 50].

THIP is a GABA_AR agonist that can interact with the receptor at sites different from those usually occupied by benzodiazepines, non-benzodiazepines, and barbiturates. Our recent study showed that THIP at a relatively low concentration selectively activates extrasynaptic GABA_ARs^[13]. In light of this finding, we used THIP to test whether selective activation of the extrasynaptic GABA_ARs could reverse the CTZ-induced epileptiform activity. Indeed, we found that, despite the down-regulation of the membrane δ -subunit of GABA_ARs, THIP effectively suppressed the CTZ-induced multiple PS peaks. One simple explanation could be that THIP, by acting on the remaining extrasynaptic GABA_ARs, enhances tonic inhibition in the whole hippocampal neuronal network and inhibits epileptiform activity. In addition, our previous study disclosed a strong inhibitory effect of THIP on the pronounced neuronal activity induced by both CTZ and KA^[13]. This effect could be due to the increased neuronal activity induced by the convulsants, releasing a substantial amount of GABA^[51], which in turn acts concomitantly with THIP to enhance tonic inhibition and suppress neuronal activity. Furthermore, it is also possible that the tonic current may be an outward rectifying current at depolarized membrane potentials^[52], making the effect of THIP more potent when neurons are hyperexcited. Thus, our findings related to the inhibitory effect of THIP on epileptiform activity in hippocampal slices further support views on the significance of extrasynaptic GABA_ARs in epileptogenesis.

In conclusion, we developed a novel CTZ-induced brain slice seizure model, and using this model, we further demonstrated that the activation of extrasynaptic GABA_ARs with THIP effectively suppressed the progress of epileptogenesis. These results support the notion that

extrasynaptic GABA_ARs may be valuable drug targets for novel antiepileptic drug therapy.

ACKNOWLEDGEMENTS

This work was supported by grants from the National Natural Science Foundation of China (31129003, 81100815, 81171224, 81401082, and 81301108) and the Science and Technology Commission of Shanghai Municipality, China (13DJ1400302, 13ZR1406500, and 11ZR1401700).

Received date: 2013-11-08; Accepted date: 2014-01-17

REFERENCES

- [1] Lytton WW. Computer modelling of epilepsy. *Nat Rev Neurosci* 2008, 9: 626–637.
- [2] Celikyurt IK, Mutlu O, Ulak G, Akar FY, Erden F. Gabapentin, A GABA analogue, enhances cognitive performance in mice. *Neurosci Lett* 2011, 492: 124–128.
- [3] Frye CA. Effects and mechanisms of progestogens and androgens in ictal activity. *Epilepsia* 2010, 51 Suppl 3: 135–140.
- [4] Kusunose N, Koyanagi S, Hamamura K, Matsunaga N, Yoshida M, Uchida T, *et al.* Molecular basis for the dosing time-dependency of anti-allodynic effects of gabapentin in a mouse model of neuropathic pain. *Mol Pain* 2010, 6: 83.
- [5] Belelli D, Harrison NL, Maguire J, Macdonald RL, Walker MC, Cope DW. Extrasynaptic GABAA receptors: form, pharmacology, and function. *J Neurosci* 2009, 29: 12757–12763.
- [6] Zarnowska ED, Keist R, Rudolph U, Pearce RA. GABAA receptor alpha5 subunits contribute to GABAA,slow synaptic inhibition in mouse hippocampus. *J Neurophysiol* 2009, 101: 1179–1191.
- [7] Wei W, Zhang N, Peng Z, Houser CR, Mody I. Perisynaptic localization of delta subunit-containing GABA(A) receptors and their activation by GABA spillover in the mouse dentate gyrus. *J Neurosci* 2003, 23: 10650–10661.
- [8] Stell BM, Brickley SG, Tang CY, Farrant M, Mody I. Neuroactive steroids reduce neuronal excitability by selectively enhancing tonic inhibition mediated by delta subunit-containing GABAA receptors. *Proc Natl Acad Sci U S A* 2003, 100: 14439–14444.
- [9] Wohlfarth KM, Bianchi MT, Macdonald RL. Enhanced neurosteroid potentiation of ternary GABA(A) receptors containing the delta subunit. *J Neurosci* 2002, 22: 1541–1549.
- [10] Palma E, Roseti C, Maiolino F, Fucile S, Martinello K, Mazzuferi M, *et al.* GABA(A)-current rundown of temporal lobe epilepsy is associated with repetitive activation of GABA(A) "phasic" receptors. *Proc Natl Acad Sci USA* 2007, 104: 20944–20948.
- [11] Zhang N, Wei W, Mody I, Houser CR. Altered localization of GABA(A) receptor subunits on dentate granule cell dendrites influences tonic and phasic inhibition in a mouse model of epilepsy. *J Neurosci* 2007, 27: 7520–7531.
- [12] Errington AC, Cope DW, Crunelli V. Augmentation of tonic GABA(A) inhibition in absence epilepsy: therapeutic value of inverse agonists at extrasynaptic GABA(A) receptors. *Adv Pharmacol Sci* 2011, 2011: 790590.
- [13] Sun Y, Wu Z, Kong S, Jiang D, Pitre A, Wang Y, *et al.* Regulation of epileptiform activity by two distinct subtypes of extrasynaptic GABAA receptors. *Mol Brain* 2013, 6: 21.
- [14] Peng Z, Huang CS, Stell BM, Mody I, Houser CR. Altered expression of the delta subunit of the GABAA receptor in a mouse model of temporal lobe epilepsy. *J Neurosci* 2004, 24: 8629–8639.
- [15] Dibbens LM, Feng HJ, Richards MC, Harkin LA, Hodgson BL, Scott D, *et al.* GABRD encoding a protein for extra- or peri-synaptic GABAA receptors is a susceptibility locus for generalized epilepsies. *Hum Mol Genet* 2004, 13: 1315–1319.
- [16] Qi J, Wang Y, Jiang M, Warren P, Chen G. Cyclothiazide induces robust epileptiform activity in rat hippocampal neurons both *in vitro* and *in vivo*. *J Physiol* 2006, 571: 605–618.
- [17] Wang Y, Qi JS, Kong S, Sun Y, Fan J, Jiang M, *et al.* BDNF-TrkB signaling pathway mediates the induction of epileptiform activity induced by a convulsant drug cyclothiazide. *Neuropharmacology* 2009, 57: 49–59.
- [18] Karr L, Rutecki PA. Activity-dependent induction and maintenance of epileptiform activity produced by group I metabotropic glutamate receptors in the rat hippocampal slice. *Epilepsy Res* 2008, 81: 14–23.
- [19] Karnup S, Stelzer A. Seizure-like activity in the disinhibited CA1 minislice of adult guinea-pigs. *J Physiol* 2001, 532: 713–730.
- [20] Stittsworth JD, Jr., Lanthorn TH. Resistance to epileptic, but not anoxic, depolarization in the gerbil hippocampal slice preparation. *Neurosci Lett* 1994, 168: 8–10.
- [21] Durand DM, Warman EN. Desynchronization of epileptiform activity by extracellular current pulses in rat hippocampal slices. *J Physiol* 1994, 480 (Pt 3): 527–537.
- [22] Furshpan EJ. Seizure-like activity in cell culture. *Epilepsy Res* 1991, 10: 24–32.
- [23] Bernardo LS. GABAergic cell grafts control seizure activity. *Epilepsy Curr* 2004, 4: 162–163.
- [24] Maeda T, Hashizume K, Sako K, Tanaka T. The effect of hippocampal dentate granule cell lesions upon the limbic seizure model of rats. *No To Shinkei* 1998, 50: 643–649.
- [25] Qian B, Sun Y, Wu Z, Wan L, Chen L, Kong S, *et al.* Epileptiform response of CA1 neurones to convulsant stimulation by cyclothiazide, kainic acid and pentylenetetrazol in anaesthetized rats. *Seizure* 2011, 20: 312–319.
- [26] Kong S, Qian B, Liu J, Fan M, Chen G, Wang Y. Cyclothiazide induces seizure behavior in freely moving rats. *Brain Res*

- 2010, 1355: 207–213.
- [27] Deng L, Chen G. Cyclothiazide potently inhibits gamma-aminobutyric acid type A receptors in addition to enhancing glutamate responses. *Proc Natl Acad Sci U S A* 2003, 100: 13025–13029.
- [28] Fitzpatrick JS, Shahi K, Baudry M. Effect of seizure activity and calpain inhibitor I on LTP in juvenile hippocampal slices. *Int J Dev Neurosci* 1992, 10: 313–319.
- [29] Wieraszko A, Seyfried TN. Increased amount of extracellular ATP in stimulated hippocampal slices of seizure prone mice. *Neurosci Lett* 1989, 106: 287–293.
- [30] Kovacs R, Rabanus A, Otahal J, Patzak A, Kardos J, Albus K, *et al.* Endogenous nitric oxide is a key promoting factor for initiation of seizure-like events in hippocampal and entorhinal cortex slices. *J Neurosci* 2009, 29: 8565–8577.
- [31] Liu JS, Li JB, Gong XW, Gong HQ, Zhang PM, Liang PJ, *et al.* Spatiotemporal dynamics of high-K⁺-induced epileptiform discharges in hippocampal slice and the effects of valproate. *Neurosci Bull* 2013, 29: 28–36.
- [32] Fujii T, Yoshizaki K. Temperature dependence on the recovery of electrical activities in brain slice during incubation. *Nihon Seirigaku Zasshi* 1976, 38: 43–45.
- [33] Davidson C, Chauhan NK, Knight S, Gibson CL, Young AM. Modelling ischaemia *in vitro*: effects of temperature and glucose concentration on dopamine release evoked by oxygen and glucose depletion in a mouse brain slice. *J Neurosci Methods* 2011, 202: 165–172.
- [34] Margineanu DG, Klitgaard H. Differential effects of cation-chloride co-transport-blocking diuretics in a rat hippocampal slice model of epilepsy. *Epilepsy Res* 2006, 69: 93–99.
- [35] Margineanu DG, Klitgaard H. Can gap-junction blockade preferentially inhibit neuronal hypersynchrony vs. excitability? *Neuropharmacology* 2001, 41: 377–383.
- [36] Brunig I, Penschuck S, Berninger B, Benson J, Fritschy JM. BDNF reduces miniature inhibitory postsynaptic currents by rapid downregulation of GABA(A) receptor surface expression. *Eur J Neurosci* 2001, 13: 1320–1328.
- [37] Treiman DM. GABAergic mechanisms in epilepsy. *Epilepsia* 2001, 42 Suppl 3: 8–12.
- [38] Sperk G, Furtinger S, Schwarzer C, Pirker S. GABA and its receptors in epilepsy. *Adv Exp Med Biol* 2004, 548: 92–103.
- [39] Mann EO, Mody I. The multifaceted role of inhibition in epilepsy: seizure-genesis through excessive GABAergic inhibition in autosomal dominant nocturnal frontal lobe epilepsy. *Curr Opin Neurol* 2008, 21: 155–160.
- [40] Coulter DA, Carlson GC. Functional regulation of the dentate gyrus by GABA-mediated inhibition. *Prog Brain Res* 2007, 163: 235–243.
- [41] Atack JR, Bayley PJ, Seabrook GR, Wafford KA, McKernan RM, Dawson GR. L-655,708 enhances cognition in rats but is not proconvulsant at a dose selective for alpha5-containing GABAA receptors. *Neuropharmacology* 2006, 51: 1023–1029.
- [42] Sierra-Paredes G, Sierra-Marcuno G. Extrasynaptic GABA and glutamate receptors in epilepsy. *CNS Neurol Disord Drug Targets* 2007, 6: 288–300.
- [43] Richerson GB. Looking for GABA in all the wrong places: the relevance of extrasynaptic GABA(A) receptors to epilepsy. *Epilepsy Curr* 2004, 4: 239–242.
- [44] Caraiscos VB, Elliott EM, You-Ten KE, Cheng VY, Beelli D, Newell JG, *et al.* Tonic inhibition in mouse hippocampal CA1 pyramidal neurons is mediated by alpha5 subunit-containing gamma-aminobutyric acid type A receptors. *Proc Natl Acad Sci U S A* 2004, 101: 3662–3667.
- [45] Mann EO, Mody I. Control of hippocampal gamma oscillation frequency by tonic inhibition and excitation of interneurons. *Nat Neurosci* 2010, 13: 205–212.
- [46] Liu X, Liu J, Liu J, Liu XL, Jin LY, Fan W, *et al.* BDNF-TrkB signaling pathway is involved in pentylenetetrazole-evoked progression of epileptiform activity in hippocampal neurons in anesthetized rats. *Neurosci Bull* 2013, 29: 565–575.
- [47] Houser CR, Esclapez M. Downregulation of the alpha5 subunit of the GABA(A) receptor in the pilocarpine model of temporal lobe epilepsy. *Hippocampus* 2003, 13: 633–645.
- [48] Feng HJ, Kang JQ, Song L, Dibbens L, Mulley J, Macdonald RL. Delta subunit susceptibility variants E177A and R220H associated with complex epilepsy alter channel gating and surface expression of alpha4beta2delta GABAA receptors. *J Neurosci* 2006, 26: 1499–1506.
- [49] Maguire JL, Stell BM, Rafizadeh M, Mody I. Ovarian cycle-linked changes in GABA(A) receptors mediating tonic inhibition alter seizure susceptibility and anxiety. *Nat Neurosci* 2005, 8: 797–804.
- [50] Spigelman I, Li Z, Banerjee PK, Mihalek RM, Homanics GE, Olsen RW. Behavior and physiology of mice lacking the GABAA-receptor delta subunit. *Epilepsia* 2002, 43 Suppl 5: 3–8.
- [51] Glykys J, Mody I. Activation of GABAA receptors: views from outside the synaptic cleft. *Neuron* 2007, 56: 763–770.
- [52] Pavlov I, Savtchenko LP, Kullmann DM, Semyanov A, Walker MC. Outwardly rectifying tonically active GABAA receptors in pyramidal cells modulate neuronal offset, not gain. *J Neurosci* 2009, 29: 15341–15350.

Orexin A attenuates the sleep-promoting effect of adenosine in the lateral hypothalamus of rats

Yanping Cun, Lin Tang, Jie Yan, Chao He, Yang Li, Zhian Hu, Jianxia Xia

Department of Physiology, Third Military Medical University, Chongqing 400038, China

Corresponding authors: Jianxia Xia and Zhian Hu. E-mail: xiajxia@163.com, zhianhu@aliyun.com

© Shanghai Institutes for Biological Sciences, CAS and Springer-Verlag Berlin Heidelberg 2014

ABSTRACT

Orexin neurons within the lateral hypothalamus play a crucial role in the promotion and maintenance of arousal. Studies have strongly suggested that orexin neurons are an important target in endogenous adenosine-regulated sleep homeostasis. Orexin A induces a robust increase in the firing activity of orexin neurons, while adenosine has an inhibitory effect. Whether the excitatory action of orexins in the lateral hypothalamus actually promotes wakefulness and reverses the sleep-producing effect of adenosine *in vivo* is less clear. In this study, electroencephalographic and electromyographic recordings were used to investigate the effects of orexin A and adenosine on sleep and wakefulness in rats. We found that microinjection of orexin A into the lateral hypothalamus increased wakefulness with a concomitant reduction of sleep during the first 3 h of post-injection recording, and this was completely blocked by a selective antagonist for orexin receptor 1, SB 334867. The enhancement of wakefulness also occurred after application of the excitatory neurotransmitter glutamate in the first 3 h post-injection. However, in the presence of the NMDA receptor antagonist APV, orexin A did not induce any change of sleep and wakefulness in the first 3 h. Further, exogenous application of adenosine into the lateral hypothalamus induced a marked increase of sleep in the first 3-h post-injection. No significant change in sleep and wakefulness was detected after adenosine application followed by orexin A administration into the same brain area. These

findings suggest that the sleep-promoting action of adenosine can be reversed by orexin A applied to the lateral hypothalamus, perhaps by exciting glutamatergic input to orexin neurons *via* the action of orexin receptor 1.

Keywords: sleep; wakefulness; orexin; adenosine; lateral hypothalamus

INTRODUCTION

The neuropeptides orexin A and orexin B, produced by hypothalamic neurons, play a crucial role in the promotion and maintenance of wakefulness^[1–4]. This arousal-promoting effect of orexins may be realized by excitatory actions on multiple subcortical arousal systems and the cerebral cortex^[5–8]. Two G protein-coupled receptors (orexin receptor 1 and 2) are involved in maintaining a long, consolidated awake period^[5, 9, 10]. Loss of orexin neurons impairs wakefulness^[11], whereas their stimulation facilitates wakefulness^[3]. Thus, modulation of orexin neurons is critical in the regulation of sleep and wakefulness^[12–14]. *In vitro* electrophysiological studies have demonstrated that orexin A directly excites local glutamatergic neurons in the lateral hypothalamus, inducing a substantial depolarization and a robust increase in the firing of orexin neurons^[15, 16]. Whether the excitatory actions of orexins on orexin neurons in the hypothalamus actually promote and maintain wakefulness *in vivo* is still unknown.

In addition, abundant evidence has suggested that orexin neurons are a potential target in the regulation of sleep homeostasis by endogenous adenosine. *In vivo*, local perfusion of an adenosine receptor agonist into the

lateral hypothalamus elicits sleep^[17, 18], while microinjection of adenosine receptor-specific antagonists in the same area increases wakefulness^[17-19]. Our previous study with patch clamp recordings in acute slices showed that under sustained or strong excitatory transmission, endogenous adenosine is released into the lateral hypothalamus and reduces the excitatory glutamatergic input to orexin neurons^[16]. We therefore speculated that adenosine, a product of cellular energy metabolism, accumulates in the lateral hypothalamus during wakefulness and eventually promotes sleep by exerting an inhibitory effect on orexin neurons. Whether orexin A reverses the sleep-promoting effect of adenosine in this brain area has been less investigated.

The aim of the present study was to explore the possible actions of exogenous orexin A applied to the lateral hypothalamus on the sleep-wakefulness cycle and the increase of sleep induced by adenosine using electroencephalographic (EEG) and electromyographic (EMG) recordings *in vivo*.

MATERIALS AND METHODS

Animals

A total of 51 adult male Sprague-Dawley rats weighing 250–300 g were housed in a temperature-controlled room (22°C) and maintained on a 12-h light/12-h dark cycle with food and water available *ad libitum*. The animal use and all experimental protocols were approved by the Third Military Medical University Animal Care Committee.

Reagents

Reagents unless specified otherwise were from Sigma (St. Louis, MO). Orexin A, glutamate, adenosine, and D-2-amino-5-phosphonovaleric acid (APV) were dissolved in artificial cerebral spinal fluid (ACSF) containing (in mmol/L): 126 NaCl, 5 KCl, 1.25 NaH₂PO₄, 2 MgSO₄, 26 NaHCO₃, 2 CaCl₂, and 10 glucose, pH 7.3–7.4. SB 334867 (Tocris Bioscience, Bristol, UK), 8-cyclopentyl-1,3-dipropylxanthine (DPCPX) and 3,7-dimethyl-1-propargylxanthine (DMPX) were dissolved in ACSF containing 10% dimethylsulfoxide (DMSO).

Surgery

Under deep pentobarbital anesthesia (50 mg/kg, *i.p.*),

rats were implanted with cortical EEG and EMG recording electrodes as described previously^[20, 21]. Briefly, two stainless-steel electrodes for EEG recording were screwed through the skull onto the dura over the frontal cortex (anterior: –3 mm; lateral: 3.5 mm) and the parietal cortex (anterior: –4 mm; lateral: –3 mm)^[22]. Two insulated stainless-steel, Teflon-coated wires for monitoring EMG signals were placed bilaterally into the trapezius muscles. In addition, at the stereotaxic coordinates anterior, –3.3 mm; lateral, 1.5 mm; dorsoventral, 8.5 mm, a guide cannula (O.D. 0.67 mm; RWD Life Technology Co., Ltd., Shenzhen, China) for unilateral microinjection was inserted vertically from the skull surface and blocked with stylets. The tip of this guide cannula was 2 mm above the lateral hypothalamus. Each rat was allowed at least 7 days for recovery from surgery, and was habituated individually to the experimental conditions for 3–4 days, where it was connected to the EEG/EMG recording system by a flexible cable.

Microinjection Procedure

All microinjections were unilateral and performed between 09:30 and 10:00 as described previously^[19]. Then the rats were reconnected and recorded from 10:00. Behavioral states were recorded continuously for 4 days, except during microinjections. At the time of infusion, the rats were gently restrained in a towel and an injection cannula was inserted into the guide cannula for microinjection of a volume of 0.2 μ L, at a rate of 0.1 μ L/min. A constant injection rate was maintained using a syringe pump (CMA 402, CMA/Microdialysis, Solna, Sweden). The injection cannula was kept in place for 1–2 min to allow diffusion from the cannula tip.

Procedure 1: Effect of orexin A administration on spontaneous sleep and wakefulness Seven rats were used in this experiment. The experimental protocol is outlined in Table 1. On day 1, EEG and EMG signals without any injection were recorded as baseline. On the second day, either ACSF or orexin A (40 pmol) was microinjected into the lateral hypothalamus^[19]. After recovery on day 3, these animals were given either ACSF or 40 pmol orexin A (whichever had not been injected on the second day) injected into the lateral hypothalamus on day 4. One week after completion of this session, another session using 10 pmol orexin A was initiated. Rats were

Table 1. The protocol for the microinjection procedures

Procedure	Batch	Day 1	Day 2	Day 3	Day 4
Procedure 1	Batch 1 (<i>n</i> = 4)	—	ACSF	—	Orexin A (40 pmol)
	Batch 2 (<i>n</i> = 3)	—	Orexin A (40)	—	ACSF
	Batch 3 (<i>n</i> = 4)	—	ACSF	—	Orexin A (10 pmol)
	Batch 4 (<i>n</i> = 3)	—	Orexin A (10)	—	ACSF
Procedure 2	Batch 1 (<i>n</i> = 3)	—	DMSO+ACSF	—	SB334867+ACSF
	Batch 2 (<i>n</i> = 3)	—	SB334867+ACSF	—	DMSO+ACSF
	Batch 3 (<i>n</i> = 3)	—	DMSO+orexin A (10)	—	SB334867+orexin A (10)
	Batch 4 (<i>n</i> = 3)	—	SB334867+orexin A (10)	—	DMSO+orexin A (10)
Procedure 3	Batch 1 (<i>n</i> = 3)	ACSF	Glutamate (40 ng)	Glutamate (80 ng)	ACSF
	Batch 2 (<i>n</i> = 3)	Glutamate (80)	ACSF	Glutamate (40)	ACSF
Procedure 4	Batch 1 (<i>n</i> = 3)	—	ACSF+ACSF	—	APV (10 nmol)+ACSF
	Batch 2 (<i>n</i> = 3)	—	APV (10)+ACSF	—	ACSF+ACSF
	Batch 3 (<i>n</i> = 3)	—	ACSF+orexin A (10)	—	APV (10)+orexin A (10)
	Batch 4 (<i>n</i> = 3)	—	APV (10)+orexin A (10)	—	ACSF+orexin A (10)
Procedure 5	Batch 1 (<i>n</i> = 3)	ACSF	Adenosine (1 nmol)	Adenosine (10 nmol)	ACSF
	Batch 2 (<i>n</i> = 4)	Adenosine (10)	ACSF	Adenosine (1)	ACSF
	Batch 3 (<i>n</i> = 7)	ACSF	Adenosine (20 nmol)	ACSF	Adenosine (20)
Procedure 6	Batch 1 (<i>n</i> = 3)	—	Adenosine (10)+ACSF	—	Adenosine (10)+orexin A (10)
	Batch 2 (<i>n</i> = 4)	—	Adenosine (10)+orexin A (10)	—	Adenosine (10)+ACSF

—, no injection.

randomly assigned to receive ACSF or orexin A.

Procedure 2: Effect of orexin receptor 1 antagonist application on spontaneous sleep and wakefulness

A total of twelve rats were used. On day 2, the rats (*n* = 6) randomly received unilateral microinjection of ACSF containing 10% dimethylsulfoxide (DMSO) or SB 334867 (0.5 µg) followed by ACSF application at the same site 5–10 min later (Table 1). After one-day recovery, the animals were microinjected with ACSF following DMSO or SB 334857 (0.5 µg) (whichever was not applied on the second day) on day 4. Another group of animals (*n* = 6) received DMSO or SB 334867 (0.5 µg) (whichever was not applied on the second day) followed by orexin A (10 pmol) application on day 2 or 4 randomly.

Procedure 3: Effect of glutamate administration on spontaneous sleep and wakefulness

Two delivery

models and six rats were used in this experiment.

Three rats received ACSF on days 1 and 4, and were microinjected with 40 ng glutamate on day 2 and 80 ng glutamate on day 3. The other three rats were given 80 ng and 40 ng glutamate on days 1 and 3, respectively.

Procedure 4: Effect of the glutamatergic receptor antagonist APV on orexin A-induced alteration of sleep and wakefulness

Two groups of rats were used in this experiment (*n* = 12). On day 2, six rats were randomly microinjected with either ACSF or D-2-amino-5-phosphonovaleric acid (APV) (10 nmol) followed by injection of ACSF 5–10 min later. On day 4, these rats were microinjected with ACSF following APV (10 nmol) or ACSF (whichever was not applied on the second day). The other six rats received 10 pmol orexin A following ACSF or APV (10 nmol) microinjection on days 2 and 4 (Table 1).

Procedure 5: Effect of adenosine on sleep and wakefulness A total of seven rats were used in this experiment. Three rats were randomly selected to be microinjected with 1 nmol and 10 nmol adenosine on days 2 and 3, and the other four were given 10 nmol adenosine on day 1 and 1 nmol adenosine on day 3. One week after completion of the experiments, all seven animals received microinjection of 20 nmol adenosine into the lateral hypothalamus on days 2 and 4, and ACSF administration on days 1 and 3 (Table 1).

Procedure 6: Effect of orexin A on adenosine-induced changes of sleep and wakefulness Seven rats were used in this experiment (Table 1). After basal recording without any treatment on day 1, the rats received unilateral microinjection of adenosine (10 nmol) followed by ACSF or orexin A (10 pmol) 5–10 min later on day 2 or 4.

Acquisition and Analysis of Sleep-wakefulness Data

Amplified and filtered (EEG, 0.5–30 Hz; EMG, 20–200 Hz) on a multichannel data acquisition and processing system (Grass Model 15LT polygraph, model 15A54 amplifiers), the cortical EEG and EMG signals were acquired and digitized at a sampling rate of 128 Hz for on-line viewing (data acquisition program SLEEPSIGN). Continuous data files were saved on a PC for off-line analysis. EEG and EMG recordings were scored by 10-s epochs for sleep-wakefulness state as either wakefulness, non-rapid eye movement (NREM), or rapid eye movement (REM) sleep by SLEEPSIGN software, according to the methods described previously^[23–25].

Histological Localization of Microinjection Site

After completion of the experiments, all rats were killed under deep pentobarbital anesthesia and perfused with cold heparinized 0.9% saline followed by perfusion of 4% paraformaldehyde. The brain was isolated, blocked, and processed for orexin A immunohistochemistry^[20], to illustrate the locations of orexin neurons relative to the track of the drug injector cannula.

Statistical Analysis

All data are presented as mean \pm SEM. Data analyses were conducted with Statistical Product and Service Solutions (SPSS) version 13 software. The time of wakefulness, REM sleep, and NREM sleep after application of drugs was

normalized to the baseline without any treatment. Statistical analysis was carried out using one-way repeated-measures analysis of variance with the Kolmogorov-Smirnov test for normal distribution followed by *post-hoc* multiple comparisons with Newman-Keuls tests where appropriate. $P < 0.05$ was considered statistically significant.

RESULTS

Identification of the Site of Drug Delivery

Three continuous coronal schematics of rat brain through lateral hypothalamus including orexin neurons demonstrated that all microinjection sites were localized in the perifornical lateral hypothalamus and adjoining areas between AP -3.1 and -3.6 mm (Fig. 1A)^[22], consistent with previous reports^[17]. Based on the location of microinjection sites, the areas of perfused drugs were confirmed to include the orexin neurons in the lateral hypothalamus.

Arousal-promoting Effect of Orexin A in the Lateral Hypothalamus

Compared to the ACSF treatment, application of 40 pmol orexin A markedly increased the time of wakefulness during the first 3 h of recording post-injection (Newman-Keuls, $P < 0.01$), accompanied by reduced REM (Newman-Keuls test, $P < 0.05$) and NREM sleep (Newman-Keuls, $P < 0.01$) (Fig. 1B). Similar changes were found for 10 pmol orexin A in the time spent in wakefulness (Newman-Keuls test, $P < 0.01$) and sleep (Newman-Keuls test, REM: $P < 0.05$; NREM: $P < 0.01$) during the first 3 h of post-injection recordings. However, no significant difference was detected in the time spent in wakefulness or sleep between 40 pmol and 10 pmol orexin A (Newman-Keuls test).

Orexin A Promotes Arousal through Activation of Orexin Receptor 1

A preliminary study has demonstrated that a selective antagonist for orexin receptor 1, SB 334867, reverses the arousal-promoting action of orexin A in anesthetized animals^[26]. In this study, we further tested the effect of SB 334867 on spontaneous sleep and wakefulness in conscious rats. Orexin A (10 pmol) increased the time spent in wakefulness and reduced REM and NREM sleep correspondingly (Newman-Keuls test, $P < 0.01$), while pretreatment with SB 334867 (0.5 μ g) blocked

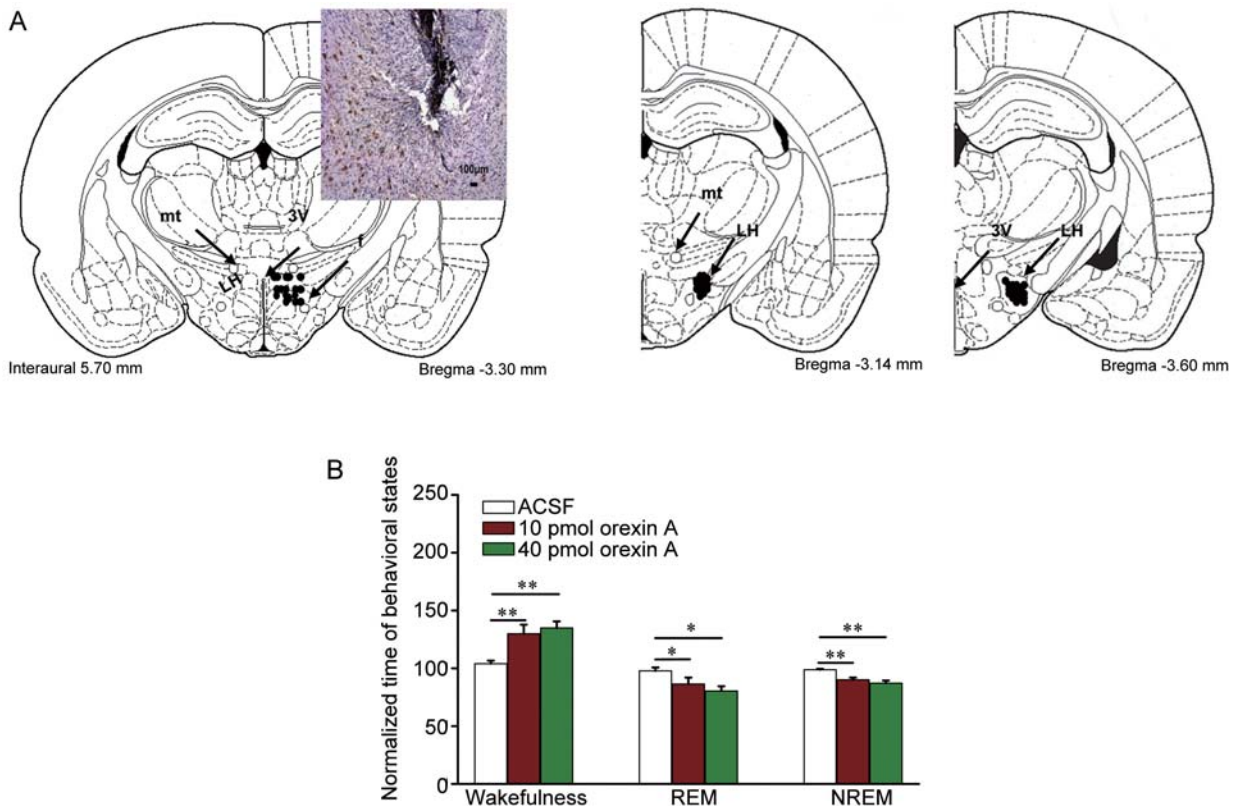


Fig. 1. Microinjection sites and the actions of orexin A on the sleep-wakefulness profile. **A:** Reconstruction of coronal sections through the perifornical and lateral hypothalamus showing the outlines and locations of the microinjection probes used for the unilateral delivery of drugs. Inset is a photomicrograph of a horizontal section showing the track of the microinjection probe localized in the orexin neuronal field (yellow staining). 3V, third ventricle; f: fornix; LH: lateral hypothalamus; mt, mammillothalamic tract. **B:** Normalized time spent in wakefulness, NREM, and REM sleep for the first 3 h after microinjection of ACSF, 40 pmol and 10 pmol orexin A. One-way ANOVA, wakefulness: $F_{(2,18)} = 8.50$, $P < 0.01$; REM sleep: $F_{(2,18)} = 4.16$, $P < 0.05$; NREM sleep: $F_{(2,18)} = 10.12$, $P < 0.01$. * $P < 0.05$, ** $P < 0.01$, Newman-Keuls test.

these effects (Newman-Keuls test, $P > 0.05$). In addition, compared to vehicle (DMSO) followed by ACSF injection, administration of SB 334867 (0.5 μg) with ACSF into the lateral hypothalamus had no effect on the three behavioral states during the first 3-h session (Newman-Keuls test, $P > 0.05$) (Fig. 2).

Involvement of Glutamatergic Synaptic Transmission in Orexin A-induced Promotion of Wakefulness

In vitro electrophysiological experiments have demonstrated that the excitatory action of orexin A on orexin neurons in the lateral hypothalamus is achieved by increasing the excitatory glutamatergic synaptic input to these neurons^[15, 16]. Thus, we further explored the role of the glutamatergic

system in the orexin A-induced arousal-promoting effect *in vivo*. Compared to ACSF treatment, administration of 80 ng but not 40 ng glutamate elevated the time in wakefulness in the first 3 h post-injection (Newman-Keuls test, 80 ng: $P < 0.05$; 40 ng: $P > 0.05$) (Fig. 3A). Concomitantly, compared with the recordings of ACSF treatment in the same rats, application of 80 ng but not 40 ng glutamate decreased the time of NREM sleep (Newman-Keuls test, $P < 0.01$). And a significant difference between 80 ng and 40 ng glutamate was detected in the time spent in wakefulness and NREM sleep (Newman-Keuls test, $P < 0.05$) but not in REM sleep.

Compared to the two administrations (at a 5–10 min interval) of ACSF, administration of the NMDA receptor antagonist APV (10 nmol) followed by ACSF significantly

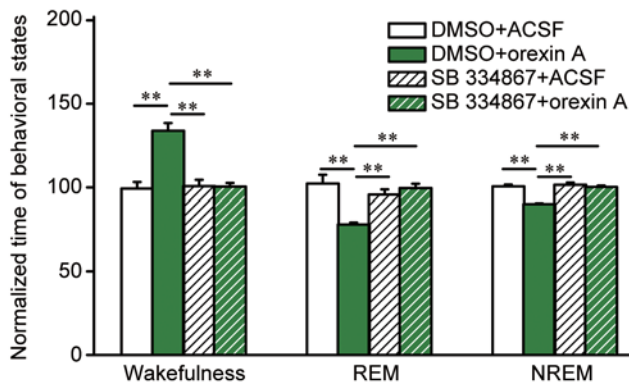


Fig. 2. Effect of orexin receptor 1 antagonist SB 334867 on sleep and wakefulness. Pooled data showing the normalized time in behavioral states during the first 3 h after application of 0.5 μ g SB 334867 and 10 pmol orexin A. One-way ANOVA, wakefulness: $F_{(3,20)} = 19.88$, $P < 0.01$; REM sleep: $F_{(3,20)} = 10.17$, $P < 0.01$; NREM sleep: $F_{(3,20)} = 26.79$, $P < 0.01$. ** $P < 0.01$, Newman-Keuls test.

decreased the time in wakefulness in rats during the first 3 h post-injection (Newman-Keuls test, $P < 0.01$), accompanied by increased time spent in REM and NREM sleep (Newman-Keuls test, $P < 0.01$) (Fig. 3B). In contrast, compared to the two administrations of ACSF, application of ACSF + orexin A (10 pmol) induced an elevation of wakefulness accompanied by a significant reduction of NREM sleep but not of REM sleep (Newman-Keuls test, wakefulness and NREM sleep: $P < 0.01$; REM sleep: $P > 0.05$). And the differences in the three behavioral states were significant between APV (10 nmol) + ACSF administration and ACSF + orexin A treatment (Newman-Keuls test, $P < 0.01$). In the presence of APV (10 nmol), application of orexin A (10 pmol) partially blocked the inhibitory action of APV on wakefulness by increasing the time spent in wakefulness and decreasing REM and NREM sleep (Newman-Keuls test, wakefulness and NREM sleep: $P < 0.01$; REM sleep: $P < 0.05$ versus APV followed by ACSF treatment), but there was no significant difference between ACSF + ACSF administration and APV + orexin A in the first 3 h post-injection (Newman-Keuls test, $P > 0.05$). And significant differences in the time in wakefulness, REM and NREM sleep during the first 3 h-session were found between ACSF and APV followed by orexin A (Newman-Keuls test, $P < 0.01$).

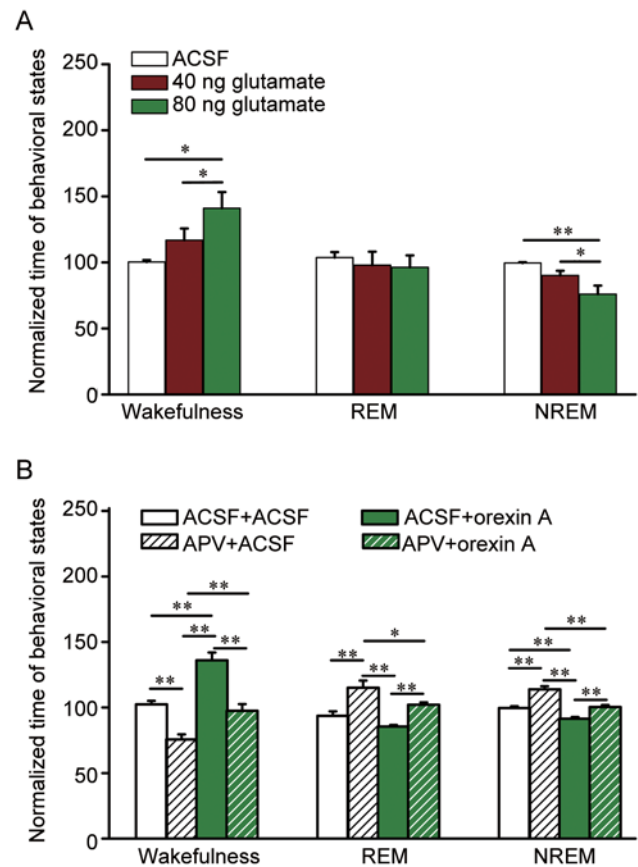


Fig. 3. Effects of glutamate and NMDA receptor antagonist APV on sleep and wakefulness. **A:** Normalized time spent in wakefulness, NREM, and REM sleep for the first 3 h after microinjection of ACSF, 40 ng or 80 ng glutamate. One-way ANOVA, wakefulness: $F_{(2,15)} = 5.55$, $P < 0.05$; NREM sleep: $F_{(2,15)} = 7.98$, $P < 0.01$; REM sleep: one-way ANOVA, $F_{(2,15)} = 3.39$, $P = 0.06$. * $P < 0.05$, ** $P < 0.01$, Newman-Keuls test. **B:** Pooled data showing the normalized time in behavioral states during the first 3 h after application of the NMDA receptor antagonist APV (10 nmol) and orexin A (10 pmol). One-way ANOVA, wakefulness: $F_{(3,20)} = 29.99$, $P < 0.01$; REM sleep: $F_{(3,20)} = 13.75$, $P < 0.01$; NREM sleep: $F_{(3,20)} = 31.10$, $P < 0.01$. * $P < 0.05$, ** $P < 0.01$, Newman-Keuls test.

Effect of Orexin A on Adenosine-induced Changes of Sleep and Wakefulness

Recent behavioral experiments with adenosine antagonists *in vivo* have suggested that orexin neurons are another important target involved in the hypnotic action of adenosine^[16, 17, 19, 27]. In this study, we further explored the role of exogenous adenosine in the regulation of sleep and wakefulness in the lateral hypothalamus. Analysis of the

EEG and EMG signals during the first 3 h post-injection of drugs revealed that, compared to the ACSF treatment, both 20 nmol and 10 nmol adenosine increased the time in NREM sleep but not in REM sleep with a concomitant reduction in the time in wakefulness (Newman-Keuls test, $P < 0.01$), whereas no evident changes in the three behavioral states were observed after application of 1 nmol adenosine (Newman-Keuls test, $P > 0.05$) (Fig. 4A).

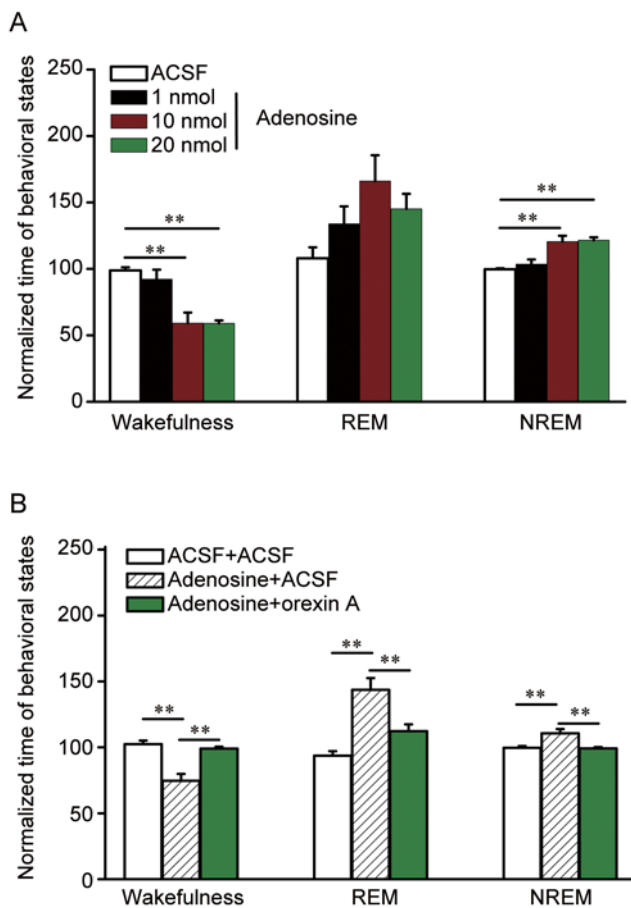


Fig. 4. Effect of orexin A on sleep-promoting action of adenosine injected into the lateral hypothalamus. **A:** Pooled data showing the normalized time in behavioral states during the first 3 h after application of adenosine and ACSF. One-way ANOVA, wakefulness: $F_{(3,24)} = 14.76$, $P < 0.01$; NREM sleep: $F_{(3,24)} = 13.71$, $P < 0.01$; REM sleep: $F_{(3,24)} = 1.47$, $P = 0.25$. $**P < 0.01$, Newman-Keuls test. **B:** Pooled data showing the comparison of normalized time in behavioral states during the first 3 h after application of 10 nmol adenosine and 10 pmol orexin A. One-way ANOVA: wakefulness, $F_{(2,17)} = 18.82$, $P < 0.01$; REM sleep, $F_{(2,17)} = 14.59$, $P < 0.01$; NREM sleep, $F_{(2,17)} = 9.17$, $P < 0.01$. $**P < 0.01$, Newman-Keuls test.

Whether the excitatory effect of orexin A on these orexin neurons could reverse the sleep propensity induced by adenosine was little known. During the first 3 h post-injection, compared to ACSF microinjection, adenosine (10 nmol) administration induced an increase in REM and NREM sleep with a concomitant reduction of wakefulness (Newman-Keuls test, $P < 0.01$). However, no significant changes in behavioral state were found after application of 10 nmol adenosine followed by 10 pmol orexin A during the first 3 h post-injection (Newman-Keuls test, $P > 0.05$) (Fig. 4B).

DISCUSSION

The main finding of this study was that exogenous application of orexin A into the lateral hypothalamus *in vivo* exerted an arousal-promoting effect through activation of orexin receptor 1. This excitatory action of orexin A may be realized by increasing glutamatergic transmission in the lateral hypothalamus. Furthermore, the excitatory effect of orexin A reversed the sleep-promoting effect of exogenous adenosine in the lateral hypothalamus.

The arousal-promoting action of the orexin system in the central nervous system (CNS) by activation of multiple subcortical arousal systems including the basal forebrain^[28], tuberomammillary nucleus^[23, 29] and locus coeruleus^[30] has been well documented. In this study, we found that enhancement of wakefulness in rats was induced by microinjection of orexin A into the lateral hypothalamus where these orexin neurons are located. This suggests that orexins exert a strong excitatory effect in the lateral hypothalamus, and this is mediated by orexin receptor 1, in that pretreatment with a selective orexin receptor 1 antagonist completely blocked the arousal-promoting action of orexin A. *In vitro* electrophysiological studies have demonstrated that the exogenous application of orexin increases the firing rates of orexin neurons through the activation of glutamatergic input to these neurons^[15, 16]. Consistently in this study, the arousal-promoting effect was not detected after blockade of glutamatergic transmission to these neurons using an NMDA receptor antagonist, strongly suggesting that the arousal-promoting action of orexin A is realized by directly exciting glutamatergic input to orexin neurons through the activation of orexin receptor 1. Thus, these findings demonstrate that the positive feedback

from excitatory glutamatergic input to orexin neurons may function in keeping orexin neurons firing continuously in wakefulness, which is essential for orexins to excite subcortical systems to promote and maintain wakefulness.

Consistent with the previous reports^[31, 32], we also found that administration of glutamate into the lateral hypothalamus increased wakefulness in a dose-dependent manner. It should be noted that application of the NMDA receptor antagonist alone reduced wakefulness and increased sleep, whereas no changes were found after orexin receptor 1 antagonist administration alone. These findings suggest that *in vivo*, endogenous orexins are mainly released into other subcortical arousal systems including the basal forebrain, tuberomammillary nucleus, and locus coeruleus, where orexin could excite these neurons directly and eventually promote wakefulness; and the lateral hypothalamus, where orexin neurons are located is not the major target in the arousal-promoting action of these neuropeptides. We therefore speculated that the activation of orexin neurons needs other excitatory synaptic inputs in the CNS. Our data strongly support the idea that the excitatory effects of glutamatergic synaptic transmission on orexin neurons play a key role in exciting these neurons to promote wakefulness *in vivo*. In addition, the decreased time in wakefulness caused by the NMDA receptor antagonist nearly recovered after application of orexin A, indicating that besides NMDA receptors, AMPA receptors may also contribute to the excitatory action of glutamate on orexin neurons induced by orexin A. In fact, a previous experiment with glutamate receptor antagonists showed that microinjection of AMPA into the perifornical lateral hypothalamus of rats increases the number of orexin neurons immunoreactive for c-Fos^[32].

In addition to the key role in promoting wakefulness, abundant evidence has demonstrated that orexin neurons are a potential target in the sleep-producing effect of endogenous adenosine, in which blockade of adenosine A1 receptors in the lateral hypothalamus induces a significant increase in wakefulness with a concomitant reduction in sleep^[17, 19]. Consistently, we found that the exogenous application of adenosine into the lateral hypothalamus enhanced sleep. These data confirmed the involvement of orexin neurons in the regulation of sleep homeostasis by endogenous adenosine. Moreover, a study by Liu *et al.*

revealed that the mechanism underlying this adenosine-induced suppression may be through inhibition of excitatory glutamatergic synaptic input to orexin neurons *via* adenosine A1 receptors^[27].

Furthermore, we found no significant difference in sleep and wakefulness between control and orexin A following adenosine injection, which suggests that this sleep-promoting effect of exogenous adenosine can be blocked by application of orexin A into the same area. This suggests that the excitatory effect of orexin A on orexin neurons in the lateral hypothalamus reverses the sleep propensity induced by adenosine. Neuronal activity in wakefulness is associated with increased neuronal metabolism. As a product of cell metabolism and is ubiquity in the CNS, adenosine accumulates during wakefulness and progressively increases the propensity to sleep^[33, 34]. Indeed, our previous studies have provided evidence that under sustained or stronger synaptic transmission in orexin neurons, endogenous adenosine is generated and inhibits the excitability of orexin neurons *via* inhibiting glutamatergic transmission in acute hypothalamic slices^[16]. Moreover, the previous study *in vitro* showed that orexin excites the orexin neurons *via* local glutamatergic transmission^[15]. Thus, the indirect excitatory effect of orexin might offset the inhibitory action of adenosine on orexin neurons and consequently reverse the sleep-promoting effect of adenosine. The modulation of orexin neurons plays an important role in regulating sleep and wakefulness, especially under prolonged wakefulness in which sleep pressure is enhanced rapidly due to the large release of endogenous adenosine^[35]. Caffeine, a nonselective adenosine receptor antagonist, is a widely used stimulant that effectively reverses the depressant effects of increasing sleep propensity^[36], although the side-effect of drug-dependence has restricted its therapeutic use as an arousal-promoting agent^[37]. It is therefore necessary to find other available drugs or measures to abolish the increase of sleep propensity. Our findings of the reversal of the sleep-promoting effect by orexin A provides a possibility that orexins may be a potential candidate to reduce the sleep propensity induced by adenosine, independent of the blockade of adenosine receptors.

In conclusion, we speculate that pharmacological manipulation of the orexin system including orexin neurons

and orexins may open up a new avenue for the regulation of sleep and wakefulness, especially under the condition of sleep propensity induced by adenosine.

ACKNOWLEDGEMENTS

This work was supported by the National Natural Science Foundation of China (81071074).

Received date: 2013-10-08; Accepted date: 2014-01-23

REFERENCES

- [1] Sakurai T, Amemiya A, Ishii M, Matsuzaki I, Chemelli RM, Tanaka H, *et al.* Orexins and orexin receptors: a family of hypothalamic neuropeptides and G protein-coupled receptors that regulate feeding behavior. *Cell* 1998, 92: 573–585.
- [2] Sakurai T. The neural circuit of orexin (hypocretin): maintaining sleep and wakefulness. *Nat Rev Neurosci* 2007, 8: 171–181.
- [3] Adamantidis AR, Zhang F, Aravanis AM, Deisseroth K, de Lecea L. Neural substrates of awakening probed with optogenetic control of hypocretin neurons. *Nature* 2007, 450: 420–424.
- [4] de Lecea L, Kilduff TS, Peyron C, Gao X, Foye PE, Danielson PE, *et al.* The hypocretins: hypothalamus-specific peptides with neuroexcitatory activity. *Proc Natl Acad Sci U S A* 1998, 95: 322–327.
- [5] Sakurai T, Mieda M, Tsujino N. The orexin system: roles in sleep/wake regulation. *Ann N Y Acad Sci* 2010, 1200: 149–161.
- [6] Xia J, Chen X, Song C, Ye J, Yu Z, Hu Z. Postsynaptic excitation of prefrontal cortical pyramidal neurons by hypocretin-1/orexin A through the inhibition of potassium currents. *J Neurosci Res* 2005, 82: 729–736.
- [7] Xia JX, Fan SY, Yan J, Chen F, Li Y, Yu ZP, *et al.* Orexin A-induced extracellular calcium influx in prefrontal cortex neurons involves L-type calcium channels. *J Physiol Biochem* 2009, 65: 125–136.
- [8] Alexandre C, Andermann ML, Scammell TE. Control of arousal by the orexin neurons. *Curr Opin Neurobiol* 2013, 23: 752–759.
- [9] Li B, Chen F, Ye J, Chen X, Yan J, Li Y, *et al.* The modulation of orexin A on HCN currents of pyramidal neurons in mouse prelimbic cortex. *Cereb Cortex* 2010, 20: 1756–1767.
- [10] Chen XW, Mu Y, Huang HP, Guo N, Zhang B, Fan SY, *et al.* Hypocretin-1 potentiates NMDA receptor-mediated somatodendritic secretion from locus ceruleus neurons. *J Neurosci* 2008, 28: 3202–3208.
- [11] Chemelli RM, Willie JT, Sinton CM, Elmquist JK, Scammell T, Lee C, *et al.* Narcolepsy in orexin knockout mice: molecular genetics of sleep regulation. *Cell* 1999, 98: 437–451.
- [12] Sasaki K, Suzuki M, Mieda M, Tsujino N, Roth B, Sakurai T. Pharmacogenetic modulation of orexin neurons alters sleep/wakefulness states in mice. *PLoS One* 2011, 6: e20360.
- [13] Tabuchi S, Tsunematsu T, Kilduff TS, Sugio S, Xu M, Tanaka KF, *et al.* Influence of inhibitory serotonergic inputs to orexin/hypocretin neurons on the diurnal rhythm of sleep and wakefulness. *Sleep* 2013, 36: 1391–1404.
- [14] Zhang XY, Yu L, Zhuang QX, Zhu JN, Wang JJ. Central functions of the orexinergic system. *Neurosci Bull* 2013, 29: 355–365.
- [15] Li Y, Gao XB, Sakurai T, van den Pol AN. Hypocretin/Orexin excites hypocretin neurons via a local glutamate neuron-A potential mechanism for orchestrating the hypothalamic arousal system. *Neuron* 2002, 36: 1169–1181.
- [16] Xia J, Chen F, Ye J, Yan J, Wang H, Duan S, *et al.* Activity-dependent release of adenosine inhibits the glutamatergic synaptic transmission and plasticity in the hypothalamic hypocretin/orexin neurons. *Neuroscience* 2009, 162: 980–988.
- [17] Alam MN, Kumar S, Rai S, Methippara M, Szymusiak R, McGinty D. Role of adenosine A(1) receptor in the perifornical-lateral hypothalamic area in sleep-wake regulation in rats. *Brain Res* 2009, 1304: 96–104.
- [18] Rai S, Kumar S, Alam MA, Szymusiak R, McGinty D, Alam MN. A1 receptor mediated adenosinergic regulation of perifornical-lateral hypothalamic area neurons in freely behaving rats. *Neuroscience* 2010, 167: 40–48.
- [19] Thakkar MM, Engemann SC, Walsh KM, Sahota PK. Adenosine and the homeostatic control of sleep: effects of A1 receptor blockade in the perifornical lateral hypothalamus on sleep-wakefulness. *Neuroscience* 2008, 153: 875–880.
- [20] Chen L, Thakkar MM, Winston S, Bolortuya Y, Basheer R, McCarley RW. REM sleep changes in rats induced by siRNA-mediated orexin knockdown. *Eur J Neurosci* 2006, 24: 2039–2048.
- [21] Jia X, Yan J, Xia J, Xiong J, Wang T, Chen Y, *et al.* Arousal effects of orexin A on acute alcohol intoxication-induced coma in rats. *Neuropharmacology* 2012, 62: 775–783.
- [22] Paxinos G, Watson C. *The Rat Brain in Stereotaxic Coordinates*. San Diego, 1998.
- [23] Huang ZL, Qu WM, Mochizuki T, Eguchi N, Watanabe T, *et al.* Arousal effect of orexin A depends on activation of the histaminergic system. *Proc Natl Acad Sci U S A* 2001, 98: 9965–9970.
- [24] Huang ZL, Sato Y, Mochizuki T, Okada T, Qu WM, Yamatodani A, *et al.* Prostaglandin E2 activates the histaminergic system via the EP4 receptor to induce wakefulness in rats. *J Neurosci* 2003, 23: 5975–5983.

- [25] Oishi Y, Huang ZL, Fredholm BB, Urade Y, Hayaishi O. Adenosine in the tuberomammillary nucleus inhibits the histaminergic system via A1 receptors and promotes non-rapid eye movement sleep. *Proc Natl Acad Sci U S A* 2008, 105: 19992–19997.
- [26] Kushikata T, Hirota K, Yoshida H, Kudo M, Lambert DG, Smart D, *et al.* Orexinergic neurons and barbiturate anesthesia. *Neuroscience* 2003, 121: 855–863.
- [27] Liu ZW, Gao XB. Adenosine inhibits activity of hypocretin/orexin neurons by the A1 receptor in the lateral hypothalamus: a possible sleep-promoting effect. *J Neurophysiol* 2007, 97: 837–848.
- [28] Dong H, Niu J, Su B, Zhu Z, Lv Y, Li Y, *et al.* Activation of orexin signal in basal forebrain facilitates the emergence from sevoflurane anesthesia in rat. *Neuropeptides* 2009, 43: 179–185.
- [29] Eriksson KS, Sergeeva O, Brown RE, Haas HL. Orexin/hypocretin excites the histaminergic neurons of the tuberomammillary nucleus. *J Neurosci* 2001, 21: 9273–9279.
- [30] Chen L, McKenna JT, Bolortuya Y, Winston S, Thakkar MM, Basheer R, *et al.* Knockdown of orexin type 1 receptor in rat locus coeruleus increases REM sleep during the dark period. *Eur J Neurosci* 2010, 32: 1528–1536.
- [31] Alam MA, Mallick BN. Glutamic acid stimulation of the perifornical-lateral hypothalamic area promotes arousal and inhibits non-REM/REM sleep. *Neurosci Lett* 2008, 439: 281–286.
- [32] Li FW, Deurveilher S, Semba K. Behavioural and neuronal activation after microinjections of AMPA and NMDA into the perifornical lateral hypothalamus in rats. *Behav Brain Res* 2011, 224: 376–386.
- [33] Rainnie DG, Grunze HC, McCarley RW, Greene RW. Adenosine inhibition of mesopontine cholinergic neurons: implications for EEG arousal. *Science* 1994, 263: 689–692.
- [34] Porkka-Heiskanen T, Strecker RE, McCarley RW. Brain site-specificity of extracellular adenosine concentration changes during sleep deprivation and spontaneous sleep: an in vivo microdialysis study. *Neuroscience* 2000, 99: 507–517.
- [35] Zhang N, Liu HT. Effects of sleep deprivation on cognitive functions. *Neurosci Bull* 2008, 24: 45–48.
- [36] Landolt HP, Retey JV, Tonz K, Gottselig JM, Khatami R, Buckelmuller I, *et al.* Caffeine attenuates waking and sleep electroencephalographic markers of sleep homeostasis in humans. *Neuropsychopharmacology* 2004, 29: 1933–1939.
- [37] Daly JW, Fredholm BB. Caffeine--an atypical drug of dependence. *Drug Alcohol Depend* 1998, 51: 199–206.

Brief Instructions to Authors

Neuroscience Bulletin (NB) is a SCI journal publishes Original Research Articles, Report and Reviews on basic and clinical neuroscience research bimonthly via Springer Science and Business Media. In addition, NB also publishes other types of articles such as Research Highlights, Perspectives, Brief Communications, and Methods.

Manuscript Submission

Manuscripts should be submitted through our online submission system, ScholarOne Manuscripts, at <http://mc03.manuscriptcentral.com/nsb> or <http://www.neurosci.cn>.

Manuscript file types that we accept for online submission include Word, WordPerfect, and TXT. For Figure submission, we accept JPEG, TIFF, or AI files. Required items differ for each article type and are specified during the submission process.

The submitted manuscript should be accompanied with a signed "Neuroscience Bulletin copyright transfer statement and submission form" stating that all work is original, has not been published previously, and is not under consideration for publication elsewhere. The corresponding author responsible for the originality, legality and validity of the work must sign the form.

Manuscript Preparation

NB considers manuscripts of the following types:

Research Article

A research article contains original research materials and presents compelling data on conceptual advances in any area of neuroscience. The total character count of all sections of the main text (including references and figure legends but excluding supplemental data) should not exceed 60,000, including spaces. Up to 8 figures and/or tables are allowed for the entire manuscript. The minimum requirement of a submitted research article is 40,000 characters total and at least 6 figures. The submitted manuscript should be a substantial novel research study, organizing a story with complex mechanisms elucidated using multiple techniques or approaches. It should provide mechanistic insights into a particular aspect of neuroscience field. References are limited to 100.

Report

In addition to research articles, NB also publishes short-format papers that report single exciting message in a particular field of neuroscience. Research observations should contain enough novelty and demonstrate physiological/functional significance. Manuscripts for reports can be up to approximately 30,000 characters (including spaces). The number of Figures in Reports should be limited to 4. Reports follow the same general organization as research articles except that the sections of Results and Discussion should be combined (denoted as Results and Discussion). References are limited to 50.

Review

Authoritative reviews contribute greatly to our journal and we are interested in comprehensive articles that are fairly and well written to describe recent development in any field of neuroscience. The authors are expected to cover controversies in the field and propose their own viewpoints in an unbiased and justifiable way. Reviews are typically at the similar length with research articles and schematic illustrations are strongly encouraged. In particular, the scope of the review should not be dominated by the authors' own work.

Others

All other types of articles including **Research Highlight**, **Perspective**, **Brief Communication**, and **Method** are also being considered upon enquiry. The article type should be specified in the author's cover letter. For Brief Communication and Method, the article should begin with an unreferenced abstract about 100 words. For Perspective, Brief Communication, and Method, the total character count should not exceed 20,000 and the display items should be limited to 2. Subheadings are discouraged. References are limited to 20. For Perspective, the article should contain discussion on recent primary research literature similarly as Review. Yet, Perspective is shorter in length and focuses on a narrower scope. It is possible that in Perspective authors advocate a position over a controversial issue or a speculative hypothesis. For Brief Communication, the article reports a concise message conveyed by primary research data of high quality and broad interest. In addition, please note that NB no longer accepts Method on neurosurgery pathway, surgical techniques, or any other clinical related technical studies. On the other hand, NB welcomes Method discussing new advances on research techniques in any field of basic neuroscience (For a glance, please see our Special Issue on "new techniques and approaches for neuroscience").

Please note that NB intends to publish high quality research articles as the major part of the journal. Short reports and articles of other formats are only considered if the research work provides a major scientific breakthrough. The number of these other articles is limited in every issue.

Accepted and published manuscripts are expected to comply with journal policies on these formats and NB editors reserve the right to return manuscripts that are not in accordance with the instructions. During initial submission, NB will consider manuscripts based on the scientific merit even if they slightly exceed the required length. Once accepted for publication, however, the authors will be asked to shorten the manuscript to fit the journal's format.

Manuscript Revision

Upon peer-reviews, the authors may be asked to revise the manuscript. If the authors have substantial reasons to believe that their manuscript was treated unfairly, they may appeal for reconsideration. Revision should be completed within four (minor revision) or eight weeks (major revision). The authors should provide a cover letter and a point-to-point response for addressing the reviewers' comments. The editor will notify the corresponding author upon the acceptance of the manuscript. Accepted papers will be processed to advanced online publication as soon as possible.

Proofs

A PDF proof will be sent to the authors for them to correct last minute errors on the manuscript.

Page Charges

Page charges for the printed form are as follows: RMB400 for each text page, RMB500 for each page containing black-and-white figures, RMB1500 for the first page containing color figures, RMB1000 for the second color figure page, and RMB800 for the rest. The corresponding author will receive an invoice on all the publication-related charges once the manuscript is accepted for publication and enters the editing process.

If you are in China, make checks or money orders payable to:

Beneficiary's Name (帐户名称): Shanghai Institutes of Biological Sciences, Chinese Academy of Sciences (中国科学院上海生命科学研究所)

Beneficiary's A/C NO. (帐号): 033924-00801048006

Beneficiary's Bank(开户行): Fenglin Branch of Xuhui District, Agricultural Bank of China (农行徐汇区枫林支行)

If you are in China, payment can also be mailed by Post Office to the Editorial Office of Neuroscience Bulletin.

Editorial Office of Neuroscience Bulletin (《神经科学通报》编辑部收):

Room 405, Building 31B, 319 YueYang Road, Shanghai 200031, China (200031, 上海市岳阳路319号31B楼405室).

Tel: +86-21-54922863; Fax: +86-21-54922833; E-mail: nsb@sibs.ac.cn

(Updated November, 2013)

NEUROSCIENCE BULLETIN

Editor-in-Chief

Shumin Duan
(Zhejiang University, Hangzhou, China)

Consulting Editors

Yizhang Chen
(Second Military Medical University, Shanghai, China)
Muming Poo
(Institute of Neuroscience, CAS, Shanghai, China)
Larry R. Squire
(University of California-San Diego, USA)
Charles F. Stevens
(The Salk Institute, San Diego, USA)
Xiongli Yang
(Fudan University, Shanghai, China)

Executive Associate Editor

Iain C. Bruce (Zhejiang University, Hangzhou, China)

Associate Editors

Zhong Chen (Zhejiang University, Hangzhou, China)
Tianming Gao (South Medical University, Guangzhou, China)
Shihui Han (Peking University, Beijing, China)

Cheng He (Second Military Medical University, Shanghai, China)
Margaret S. Ho (Tongji University, Shanghai, China)
Ru-Rong Ji (Duke University, Durham, USA)
Tianzi Jiang (Institute of Automation, CAS, Beijing, China)
Tao Li (West China Hospital, Sichuan University, Chengdu, China)
Mengsheng Qiu (Hangzhou Normal University, Hangzhou, China)
Fu-Dong Shi (St. Joseph's Hospital and Medical Center, Phoenix, USA)
You Wan (Peking University, Beijing, China)
Jian-Zhi Wang (Huazhong University of Science and Technology, Wuhan, China)
Zhi-Ying Wu (Huashan Hospital, Shanghai Medical College, Fudan University, Shanghai, China)
Tianle Xu (Shanghai Jiaotong University, Shanghai, China)
Dai Zhang (Peking University, Beijing, China)
Zhi-Jun Zhang (Southeast University, Nanjing, China)
Chunjiu Zhong (Fudan University, Shanghai, China)
Yimin Zou (University of California-San Diego, USA)

Editorial Board

Philippe Ascher (Paris Diderot University, Paris, France)
Ben A. Barres (Stanford University, San Francisco, USA)
Guo-Qiang Bi (University of Science and Technology of China, Hefei, China)
Ying-Shing Chan (The University of Hong Kong, Hong Kong, China)
Jun Chen (The Fourth Military Medical University, Xi'an, China)
Sheng-Di Chen (Shanghai Jiaotong University, Shanghai, China)
Yiping Du (Zhejiang University, Hangzhou, China)
Ming Fan (Academy of Military Medicine, Beijing, China)
Richard S. Frackowiak (University of Lausanne, Lausanne, Switzerland)
Tamás F. Freund (Institute of Experimental Medicine of the Hungarian Academy of Sciences, Budapest, Hungary)
Charles Gilbert (The Rockefeller University, New York, USA)
Xiaosong Gu (Nantong University, Nantong, China)
Aike Guo (Institute of Neuroscience, CAS, Shanghai, China)
Philip G. Haydon (Tufts University, Boston, USA)
Joe Herbert (University of Cambridge, Cambridge, UK)
Zhi-An Hu (Third Military Medical University, Chongqing, China)
Kazuhide Inoue (Kyushu University, Fukuoka, Japan)
Yong-Hua Ji (Shanghai University, Shanghai, China)
Kai-Da Jiang (Shanghai Mental Health Center, Shanghai Jiaotong University School of Medicine, Shanghai, China)
Yu-Wu Jiang (Peking University First Hospital, Beijing, China)
Helmut Kettenmann (Max-Delbrück Center for Molecular Medicine, Berlin, Germany)
O.A. Krishtal (Bogomoletz Institute of Physiology, Kiev, Ukraine)
Robert H. LaMotte (Yale University School of Medicine, New Haven, USA)
Pierre Lavenex (University of Fribourg, Fribourg, Switzerland)

Juan Lerma (Instituto de Neurociencias de Alicante, Alicante, Spain)

Bao-Ming Li (Nanchang University, Nanchang, China)

Yun-Qing Li (The Fourth Military Medical University, Xi'an, China)

David J. Linden (Johns Hopkins University, Baltimore, USA)

Stuart A. Lipton (Sanford-Burnham Medical Research Institute and University of California at San Diego, San Diego, USA)

Bai Lu (GlaxoSmithKline [China] Investment Co., Ltd., Shanghai, China)

Yi-Cheng Lu (Changzheng Hospital, Second Military Medical University, Shanghai, China)

Bridget Lumb (University of Bristol, Bristol, UK)

Jian-Hong Luo (Zhejiang University, Hangzhou, China)

Zhen-Ge Luo (Institute of Neuroscience, CAS, Shanghai, China)

Lan Ma (Fudan University, Shanghai, China)

Robert C. Malenka (Stanford University, Stanford, USA)

Manuel S. Malmierca (Universidad de Salamanca, Salamanca, Spain)

John H.R. Maunsell (Harvard Medical School, Houston, USA)

Lin Mei (Georgia Regents University, Augusta, USA)

Earl K. Miller (Massachusetts Institute of Technology, Cambridge, USA)

Enrico Mugnaini (Northwestern University, Feinberg School of Medicine, Chicago, USA)

Vladimir Parpura (University of Alabama at Birmingham, Birmingham, USA)

Bruce R. Ransom (University of Washington, Seattle, USA)

Yi Rao (Peking University, Beijing, China)

Ferdinando Rossi (Università di Torino, Torino, Italy)

Huai-Zhen Ruan (Third Military Medical University, Chongqing, China)

Tom E. Salt (University College London, London, UK)

Joshua R. Sanes (Harvard University, Boston, USA)

Michael N. Shadlen (Columbia University, New York, USA)

Morgan Sheng (Genentech, Inc., South San Francisco, USA)

Sangram S. Sisodia (The University of Chicago, Chicago, USA)

Peter Somogyi (University of Oxford, Oxford, UK)

Feng-Yan Sun (Fudan University, Shanghai, China)

Dick F. Swaab (Netherlands Institute for Neuroscience, Amsterdam, Netherlands)

Keiji Tanaka (RIKEN Brain Science Institute, Tokyo, Japan)

Alexej Verkhratsky (The University of Manchester, Manchester, UK)

Steven R. Vincent (University of British Columbia, Vancouver, Canada)

Jian-Jun Wang (Nanjing University, Nanjing, China)

Wei Wang (Huazhong University of Science and Technology, Wuhan, China)

Wei Wang (Zhejiang University, Hangzhou, China)

Xu-Chu Weng (Hangzhou Normal University, Hangzhou, China)

William Wisden (Imperial College London, London, UK)

Jun-Xia Xie (Qingdao University, Qingdao, China)

Lin Xu (Kunming Institute of Zoology, CAS, Kunming, China)

Albert Cheung Hoi Yu (Peking University, Beijing, China)

Xu Zhang (Institute of Neuroscience, CAS, Shanghai, China)

Yu-Qiu Zhang (Fudan University, Shanghai, China)

Zhong-Xin Zhao (Changzheng Hospital, Second Military Medical University, Shanghai, China)

Ping Zheng (Fudan University, Shanghai, China)

Jiang-Ning Zhou (University of Science and Technology of China, Hefei, China)

Richard E. Zigmond (Case Western Reserve University, Cleveland, USA)

Copyright

Submission of a manuscript implies: that the work described has not been published before (except in the form of an abstract or as part of a published lecture, review, or thesis); that it is not under consideration for publication elsewhere; that its publication has been approved by all co-authors, if any, as well as – tacitly or explicitly – by the responsible authorities at the institution where the work was carried out. The author warrants that his/her contribution is original and that he/she has full power to make this grant. The author signs for and accepts responsibility for releasing this material on behalf of any and all co-authors. Transfer of copyright to Shanghai Institutes for Biological Sciences of Chinese Academy of Sciences and Springer becomes effective if and when the article is accepted for publication. After submission of the Copyright Transfer Statement signed by the corresponding author, changes of authorship or in the order of the authors listed will not be accepted by Shanghai Institutes for Biological Sciences of Chinese Academy of Sciences and Springer. The copyright covers the exclusive right (for U.S. government employees: to the extent transferable) to reproduce and distribute the article, including reprints, translations, photographic reproductions, microform, electronic form (offline, online) or other reproductions of similar nature.

An author may self-archive the English language version of his/her article on his/her own website and his/her institution's repository; however he/she may not use the publisher's PDF version which is posted on www.springerlink.com. Furthermore, the author may only post his/her version provided acknowledgement is given to the original source of publication and a link must be accompanied by the following text: "The original publication is available at springerlink.com".

All articles published in this journal are protected by copyright, which covers the exclusive rights to reproduce and distribute the article (e.g., as offprints), as well as all translation rights. No material published in this journal may be reproduced photographically or stored on microfilm, in electronic data bases, video disks, etc., without first obtaining written permission from the publishers. The use of general descriptive names, trade names, trademarks, etc., in this publication, even if not specifically identified, does not imply that these names are not protected by the relevant laws and regulations. While the advice and information in this journal is believed to be true and accurate at the date of its going to press, neither the authors, the editors, nor the publishers can accept any legal responsibility for any errors or omissions that may be made. The publisher makes no warranty, express or implied, with respect to the material contained herein.

Special regulations for photocopies in the USA: Photocopies may be made for personal or in-house use beyond the limitations stipulated under Section 107 or 108 of U.S. Copyright Law, provided a fee is paid. All fees should be paid to the Copyright Clearance Center, Inc., 222 Rosewood Drive, Danvers, MA 01923, USA, Tel.: +1-978-7508400, Fax: +1-978-6468600, <http://www.copyright.com>, stating the ISSN of the journal, the volume, and the first and last page numbers of each article copied. The copyright owner's consent does not include copying for general distribution, promotion, new works, or resale. In these cases, specific written permission must first be obtained from the publishers.

Subscription information

ISSN print edition: 1673-7067

ISSN electronic edition: 1995-8218

Volume 30 (6 issues) will appear in 2014

Subscription rates

For information on subscription rates please contact:
Customer Service

North and South America: journals-ny@springer.com

Outside North and South America:
subscriptions@springer.com

Orders and inquiries:

North and South America:

Springer New York, Inc.

Journal Fulfillment

P.O. Box 2485

Secaucus, NJ 07096 USA

Tel: 1-800-SPRINGER or 1-201-348-4033

Fax: 1-201-348-4505

Email: journals-ny@springer.com

Outside North and South America:

Springer Distribution Center

Customer Service Journals

Haberstr. 7

69126 Heidelberg, Germany

Tel: +49-6221-345-0, Fax: +49-6221-345-4229

Email: subscriptions@springer.com

Cancellations must be received by September 30 to take effect at the end of the same year.

Changes of address: Allow for six weeks for all changes to become effective. All communications should include both old and new addresses (with postal codes) and should be accompanied by a mailing label from a recent issue. According to § 4 Sect. 3 of the German Postal Services Data Protection Regulations, if a subscriber's address changes, the German Federal Post Office can inform the publisher of the new address even if the subscriber has not submitted a formal application for mail to be forwarded. Subscribers not in agreement with this procedure may send a written complaint to Customer Service Journals within 14 days of publication of this issue.

Microform editions are available from: ProQuest. Further information available at <http://www.il.proquest.com/uni>

Electronic edition

An electronic version is available at springerlink.com.

Production

Printed in People's Republic of China

Springer-Verlag is part of Springer Science+Business Media



NEUROSCIENCE BULLETIN

Impact Factor **1.832**

2013 Journal Citation Reports (Thomson Reuters, 2014)

Indexed/Abstracted by

Science Citation Index
Neuroscience Citation Index
Biological Abstracts
Biosis Previews
Medline/PubMed

Index Medicus
Chemical Abstracts
IndexCopernicus
Scopus
Excerpta Medica

NEUROSCIENCE BULLETIN 神经科学通报(Bimonthly)

Vol.30 No.5 October 1, 2014

Sponsored by: Shanghai Institutes for Biological Sciences, Chinese Academy of Sciences, the Chinese Neuroscience Society and the Second Military Medical University

Editor-in-Chief: Shumin Duan

Edited by: Editorial Board of *Neuroscience Bulletin*

319 Yueyang Road, Building 31B, Room 405, Shanghai 200031, China

Phone: +86-21-54922863; Fax: +86-21-54922833

E-mail: nsb@sibs.ac.cn; <http://www.neurosci.cn>

Editors: Bin Wei, Xu Jiang, Yefei Li

Published by: Shanghai Institutes for Biological Sciences, Chinese Academy of Sciences (319 Yueyang Road, Shanghai 200031)

Printed by: Shanghai Tu Yu Printing Co., Ltd. (No.28 Lane 23 Yingao Road, Shanghai 200439)

Overseas Distributed by: Springer Science+Business Media

Home Distributed by: Local Post Offices

ISSN 1673-7067

CN 31-1975/R

Post Office Code Number: 4-608

Permit of Ad. Number: 3100420080068

Price: ¥ 50.00

ISSN 1673-7067



9 771673 706148